NASA/CR—2013-217820 PMF–01766

Advanced Concept Studies for Supersonic Commercial Transports Entering Service in the 2018 to 2020 Period

Phase I Final Report

John Morgenstern, Nicole Norstrud, Jack Sokhey, Steve Martens, and Juan J. Alonso
Lockheed Martin Corporation, Palmdale, California

February 2013

NASA STI Program . . . in Profile

Since its founding, NASA has been dedicated to the advancement of aeronautics and space science. The NASA Scientific and Technical Information (STI) program plays a key part in helping NASA maintain this important role.

The NASA STI Program operates under the auspices of the Agency Chief Information Officer. It collects, organizes, provides for archiving, and disseminates NASA's STI. The NASA STI program provides access to the NASA Aeronautics and Space Database and its public interface, the NASA Technical Reports Server, thus providing one of the largest collections of aeronautical and space science STI in the world. Results are published in both non-NASA channels and by NASA in the NASA STI Report Series, which includes the following report types:

- TECHNICAL PUBLICATION. Reports of completed research or a major significant phase of research that present the results of NASA programs and include extensive data or theoretical analysis. Includes compilations of significant scientific and technical data and information deemed to be of continuing reference value. NASA counterpart of peer-reviewed formal professional papers but has less stringent limitations on manuscript length and extent of graphic presentations.

- TECHNICAL MEMORANDUM. Scientific and technical findings that are preliminary or of specialized interest, e.g., quick release reports, working papers, and bibliographies that contain minimal annotation. Does not contain extensive analysis.

- CONTRACTOR REPORT. Scientific and technical findings by NASA-sponsored contractors and grantees.

- CONFERENCE PUBLICATION. Collected papers from scientific and technical conferences, symposia, seminars, or other meetings sponsored or cosponsored by NASA.

- SPECIAL PUBLICATION. Scientific, technical, or historical information from NASA programs, projects, and missions, often concerned with subjects having substantial public interest.

- TECHNICAL TRANSLATION. English-language translations of foreign scientific and technical material pertinent to NASA's mission.

Specialized services also include creating custom thesauri, building customized databases, organizing and publishing research results.

For more information about the NASA STI program, see the following:

- Access the NASA STI program home page at *http://www.sti.nasa.gov*

- E-mail your question to *help@sti.nasa.gov*

- Fax your question to the NASA STI Information Desk at 443–757–5803

- Phone the NASA STI Information Desk at 443–757–5802

- Write to:
  STI Information Desk
  NASA Center for AeroSpace Information
  7115 Standard Drive
  Hanover, MD 21076–1320

NASA/CR—2013-217820 PMF–01766

Advanced Concept Studies for Supersonic Commercial Transports Entering Service in the 2018 to 2020 Period

Phase I Final Report

John Morgenstern, Nicole Norstrud, Jack Sokhey, Steve Martens, and Juan J. Alonso
Lockheed Martin Corporation, Palmdale, California

Prepared under Contract NNC10CA02C

National Aeronautics and
Space Administration

Glenn Research Center
Cleveland, Ohio 44135

February 2013

Acknowledgments

This work was funded by the NASA N+2 Supersonic program administered by Peter Coen at the NASA Langley Research Center and Clayton Meyers at the NASA Glenn Research Center under prime contract (Lockheed Martin (LM)) NNC10CA02C. LM would like to thank them and many others at NASA including Susan Cliff, Don Durston, Bruce Storms, Maureen Delgado, Jon Seidel, Teresa Monaco, Lori Ozoroski, Richard Campbell, Eric Walker, Floyd Wilcox, and Linda Bangert for their helpful contributions, editorial support and encouragement on this program. LM would also like to acknowledge GE Global Research Center including specifically Steve Martens and Phil Vyers; Rolls Royce Liberty Works including Jack (Jagdish) Sokhey, Travis Jonas and Jeff Peters; and Stanford University including Juan Alonso and his team, for contributing written material, data, and ideas for the N+2 Base Program final report. Nicole Norstrud and John Morgenstern would also like to acknowledge LM's many people who supported this program including Michael Buonanno, Robert Langberg, Sonny Chai, Frank Marconi, Victor Lyman, Marc Stelmack, Tony Pilon, David Pehrson, Chandler Clifton, Tom Anderson, Ken Hajic, Neal Nuttall, Ida Antonucci, Radhika Goel, Nguyen Nguyen, John Vedder, Shane Ganzel and any others who contributed.

This report contains preliminary findings, subject to revision as analysis proceeds.

Level of Review: This material has been technically reviewed by NASA technical management.

Available from

NASA Center for Aerospace Information
7115 Standard Drive
Hanover, MD 21076–1320

National Technical Information Service
5301 Shawnee Road
Alexandria, VA 22312

Available electronically at http://www.sti.nasa.gov

Contents

Advanced Concept Studies for Supersonic Commercial Transports Entering Service in the 2018 to 2020 Period

Phase I Final Report

John Morgenstern, Nicole Norstrud, Jack Sokhey, Steve Martens, and Juan J. Alonso
Lockheed Martin Corporation
Palmdale, California 93599

1.0 Executive Summary

Lockheed Martin Aeronautics Company (LM), working in conjunction with General Electric Global Research (GE GR), Rolls-Royce Liberty Works (RRLW), and Stanford University, herein presents results from the "N+2 Supersonic Validations" contract's initial 22 month phase, addressing the NASA solicitation "Advanced Concept Studies for Supersonic Commercial Transports Entering Service in the 2018–2020 Period." This report version adds documentation of an additional three month low boom test task. The key technical objective of this effort was to validate integrated airframe and propulsion technologies and design methodologies. These capabilities aspired to produce a viable supersonic vehicle design with environmental and performance characteristics, illustrated by the configuration in Figure 1. Supersonic testing of both airframe and propulsion technologies (including LM3: 97-023 low boom testing and April-June nozzle acoustic testing) verified LM's supersonic low-boom design methodologies and both GE and RRLW's nozzle technologies for future implementation.

The N+2 program is aligned with NASA's Supersonic Project and is focused on providing system-level solutions capable of overcoming the environmental and performance/efficiency barriers to practical supersonic flight. NASA proposed "Initial Environmental Targets and Performance Goals for Future Supersonic Civil Aircraft (Ref. 1)," that are outlined in Table 1 along with the validated LM N+2 Phase I status. Under payload, the asterisk in "100 target for LM N+2 Effort,*" refers to LM's modified vehicle sizing target of 100 passengers which better matches LM's anticipated N+2 vehicle size. The LM N+2 studies are built upon LM's prior N+3 100 passenger design studies (Ref. 2). The LM N+2 program addresses low boom design and methodology validations with wind tunnel testing, performance and efficiency goals with system level analysis, and low noise validations with two nozzle (GE and RRLW) acoustic tests.

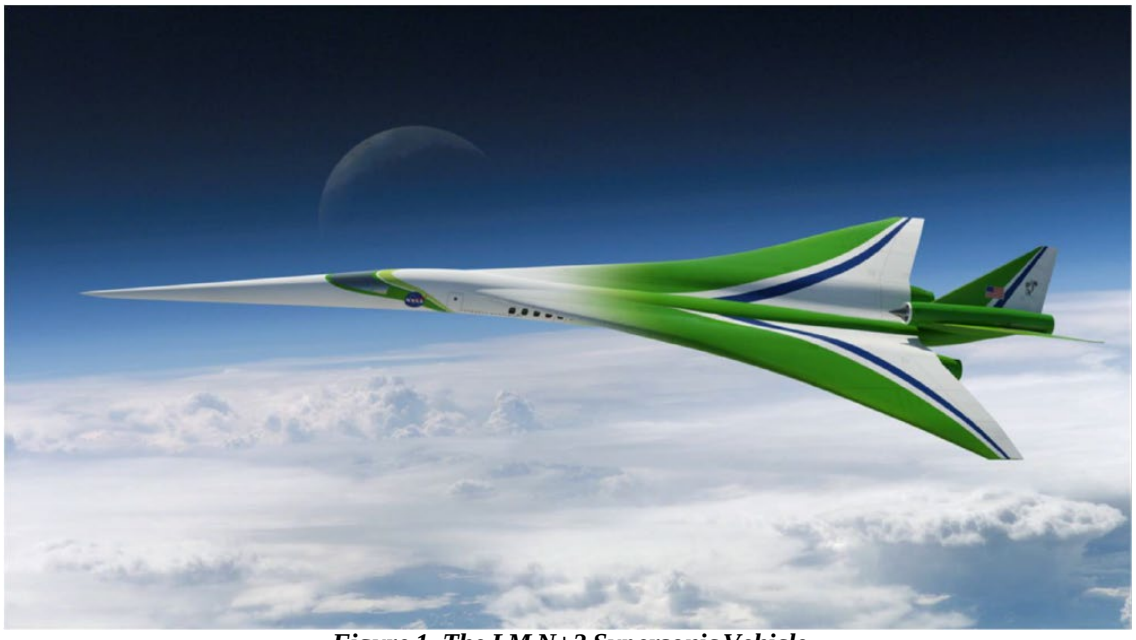

Figure 1. The LM N+2 Supersonic Vehicle

TABLE 1.—N+2 ENVIRONMENTAL AND PERFORMANCE GOALS AND VALIDATED PHASE I RESULTS

	NASA N+2 Supersonic Transport Initial Goals	LM N+2 Phase I Status
Environmental Goals		
Sonic Boom KEY GOAL	65–70 PLdB ~0.14–0.17 psf N-wave	79 PLdB ~0.26 psf N-wave
Airport Noise KEY GOAL (cumulative below stage 3)	10–20 EPNdB	22 EPNdB (predicted) (Targeting 26 EPNdB)
Cruise Emissions	<10 EINOx	5 EINOx (predicted)
Performance Goals		
Cruise Speed	Mach 1.6–1.8	Mach 1.6
Range	4000 nm	4000–5500 nm
Payload (passengers)	35–70 (100 target for LM N+2 Effort*)	82
Fuel Efficiency KEY GOAL (passenger-nm per lb of fuel)	3.0	3.1

To address low boom, our efforts focused on three major tests conducted at the NASA Ames Research Center (ARC) 9x7 facility: LM1: Measurement Hardware Validation Test (97-0220), LM2: Spiked Nacelle Sonic Boom Validation Test (97-0223), and LM3: Low Boom Validation Model Test (97-0231). To support the LM1 Test, the Model Support Apparatus (MSA) was fabricated to provide universal connectivity for new and legacy models as well as connect to the recently developed Linear Actuator. The SEEB-Aft Lift Relaxation (ALR) axisymmetric model was fabricated with a well-known pressure-flat magnitude to calibrate the wind tunnel measurement apparatus. The intent was to use the SEEB-ALR calibration body prior to all Ames supersonic testing as the normal pre-test verification procedure. Another axisymmetric model was fabricated with a signature matching the design target N+2 Optimum Signature (OptSig) as a representative validation of the new hardware's ability to measure the upcoming full configuration model. Results from the LM1 Test provided insight into the difficulties of obtaining accurate low boom pressure measurements that are several times lower than the ambient flow field distortions of the tunnel and the increased measurement distortions seen by a 420 orifice rail when the distortion changes at each new orifice measurement position in tunnel. During the LM1 Test, a procedure was tried whereby the SEEB-ALR model was measured at multiple positions every 2 in. throughout the maximum available translation range. The averaged distortion of the model's flat pressure was used to determine a distortion correction for each measurement orifice. When the correction calibration was applied to model measurements taken at different positions—repeatability and CFD matching showed a 2/3 variation reduction. In spite of this improvement, the overall accuracy assessment showed that ground loudness was not likely to robustly validate predictions to the desired less than 2 PLdB of difference. More improvements were needed for LM3 Test success.

The Spiked Nacelle Sonic Boom Validation Test (LM2) provided incremental validations between CFD and operational propulsion effects, particularly inlet centerbody spike supersonic spillage, subsonic mass flow spillage and exhaust effects. A pre-existing, LM proprietary HS3 (3rd High Speed QSST 4.7 percent scale model) configuration was re-tested. The test configuration variations included: nacelles with spikes and subsonic mass flow variation screens, hollow supersonic flow-through nacelles, and nacelles-off to cost effectively validate CFD modeling of propulsion operational variations in the Ames 9´ 7 facility. The above LM1 Test fidelity concerns did not apply to the much larger (over 6 ft long) model and pressures measured in LM2. In this report, the incremental results show how CFD should be applied to achieve a good match.

Developing a low boom configuration capable of meeting the N+2 low boom targets was a key goal for the N+2 program. During the LM Phase I effort, LM successfully designed, refined, fabricated and (scale) tested a low boom trijet vehicle capable of achieving an average of 79 PLdB for its entire cruise sonic boom carpet. Efforts for Multiple Disciplinary Analysis and Optimization (MDAO) optimization and reducing sonic boom demonstrated that optimization is an effective way to match undertrack and

off-track sonic boom targets simultaneously, and specific advice on weighting/prioritizing the angles is presented. Improvements to multiple off-track angle loudness's were achieved with relatively small compromise to undertrack loudness. These results demonstrate the level of difficulty inherent in simultaneous under and off-track low boom design.

Validating these PLdB measurements required the calibration and testing improvements identified in the LM1 Test as well as further improvements to achieve the required accuracy robustly. Low boom model support hardware was improved to minimize interference on sonic boom measurement. LM designed and fabricated a 22.4 in. (0.8 percent scale) low boom model with both a sting and highly swept blade support. The model had removable flow-through nacelles and a replaceable tail to verify the aft lift increment that has a strong effect on aft signature shaping. The model was accurately fabricated with most of the geometry within 0.003 to –0.001 in. (0.08 to –0.03 mm) of the specified geometry.

Further examination of the LM1 measurements was used to understand their cause and develop alternative testing procedures to reduce distortion effects on the Low Boom Configuration Validation Test (LM3 Test). The new LM3 procedures measured the model repeatedly while translating its position in the tunnel, averaging out the measurement distortions that change with position. Also, the SEEB-ALR model was measured at multiple positions throughout the maximum available translation range to calibrate the distorted orifice measurements over as much of the Blade Rail as possible, improving measurement accuracy. The LM3 Test was executed in the NASA Ames 9´ 7 facility in October of 2011. The new testing procedures reduced measurement distortion by two orders-of-magnitude and matched CFD predictions with better than needed precision. Propagating measurements to the ground validated predictions with less than 1 PLdB of difference.

In coordination with our propulsion suppliers, LM conducted 2D and 3D CFD analyses, to design and develop an inlet capable of achieving N+2 goals. The LM inlet is an axisymmetric, bleed-less, external compression type with a design Mach number of 1.6. Two main trade studies were conducted for the development of the N+2 inlet looking at performance optimization and inlet length. The resulting inlet (AE40-TB121) has a 50 percent diffuser length reduction from the baseline. Benefits include decreased weight, improved total pressure recovery, and easier wing-mounted integration for structure and low boom without increased drag. There was an option in the contract for NASA to fund fabrication and testing of an inlet model. Inlet installation and testing remain a potential future activity under the N+2 Supersonic Validations program.

1.1 Stanford

Stanford University, in collaboration with LM and NASA, developed an adjoint-based capability for the inverse shape design of supersonic configurations. Stanford derived, implemented, and tested a preliminary version of an adjoint solver that is able to produce sensitivities (gradients) of cost functions derived from the aircraft's sonic boom distribution with respect to arbitrary numbers of design variables that affect the shape of the aircraft. Using CAPRI, a CAD-neutral software interface, Stanford successfully applied the adjoint based techniques to the N+2 trijet configuration. The Stanford Final Report is attached in Appendix C (Ref. 3).

1.2 RRLW

Based on thrust requirements, inlet characteristics and goals provided by LM, RRLW provided propulsion system definitions and experimental validations to address the N+2 airport noise and performance goals. RRLW designed, developed, and fabricated a 15 percent scale variable geometry exhaust nozzle that was tested at the NASA GRC AAPL in May 2011. The RRLW final report is attached in Appendix A (Ref. 4).

1.3 GE GR

Based on thrust requirements, inlet characteristics and goals provided by LM, GE developed an N+2 propulsion system definition designed to meet or exceed the goals set by NASA. A variable cycle engine was optimized for the N+2 airport noise goals. GE GR designed, developed, and fabricated a 9 percent scale noise suppressing nozzle that was tested at the NASA GRC AAPL in June 2011. The GE GR final report is attached in Appendix B (Ref. 5).

1.4 Recommendations

Recommended Phase II efforts include continued systems level validation testing and methodology verifications for both low boom and nozzle designs. A summary list of recommendations for Phase II and beyond is highlighted below, with updates considering the excellent low boom validations achieved in the LM3 Test (97-0231):

1.5 Low Boom Goal

- Achieve most of the last 4 PLdB reduction low boom loudness possible with our current design's target sonic boom signature and either hold that level or achieve further reduction of the low boom off-track to the edge of the carpet.
- Using productivity and accuracy improving procedures refined from LM3 lessons learned, validate an improved low boom design; and by doing so, demonstrate the maturity of these measurement procedures for wind tunnel low boom design validation.
- For comparison with NASA Dryden flight boom demonstrations, perform a high resolution CFD vehicle starting boom prediction. Compare our propagation methodology's (no turbulence) ground sonic boom to measured sonic boom statistically, at various turbulence levels, to quantify the overpressure and loudness variation expected from a real atmosphere. (Past, lower resolution comparisons indicate that atmospheric rounding of measurements typically reduces overpressure 20 to 25 percent).
- Develop a way to demonstrate and validate low boom loudness, like our Optimum Signature, after propagation through a real atmosphere that is affordable by the N+2 Supersonic Validations program.

1.6 Airport Noise Goal

- Develop a refined analysis procedure that models tonal and separation noises accurately. Refine acoustic nozzle designs to eliminate tonal and separation noise.
- Refine cycle parameters for new low boom tri-jet requirements and noise conditions.
- Refine noise estimates—particularly at cutback and approach—with jet, fan and airframe noise sources with best low noise technology projections to see if the estimated sideline constraint needs to be adjusted to achieve the overall cumulative noise goal.
- Predict low noise fan noise acceptability with inlet distortion interaction, inlet acoustic lining and auxiliary inlet with soft choke for approach noise reduction and devise affordable validation tests.

1.7 Cruise Emission Goal

- Continue to monitor technology development and integrate projected consequences of temperature limits, etc. into cycle models and performance assessments.

1.8 Performance Goals

- In looking for a good flow quality tunnel for low sonic boom measurements, it was found that the NASA Glenn 10´ 10 tunnel has uniquely good flow attributes, but at a minimum speed of Mach 2.0. Mach 2.0 is the design speed for our swept Natural Laminar Flow (NLF) wing from the DARPA QSP program. Continue to investigate the 10´ 10 for suitability to retest the Natural Laminar Flow (NLF) model.
- Find an affordable way to develop and validate NLF under representative flow conditions (including lower turbulence than current wind tunnels).
- Implement existing and new N+2 MDAO methodologies. Use them to optimize performance while integrating technologies like NLF and variable cycle engines that are being validated in this N+2 Supersonic Validations program. Use system assessments of the validated results to predict the potential performance of a future vehicle.

2.0 Introduction

2.1 Subject/Relevancy

The National Aeronautics and Space Administration's (NASA) Supersonics Project is aligned with the Aeronautics Research Mission Directorate (ARMD) principles of maintaining intellectual stewardship of aeronautical core competencies for the nation in the supersonic flight regime and of focusing research in areas that are appropriate to NASA's unique capabilities. The Supersonics Project is a broad-based effort designed to develop knowledge, capabilities and technologies that support vehicles that fly in the supersonic speed regime. A major focus of this effort is eliminating the efficiency, environmental and performance barriers to practical supersonic cruise vehicles.

The Supersonic project invests a significant portion of its allocated budget in NASA Research Announcement (NRA) solicitations—including the N+2 Supersonics Validation program. The objective of the NRA investment is to stimulate innovation in integrated transportation concepts and to create an environment for collaboration among NASA researchers, commercial organizations, and academia. This investment is primarily focused at foundational level research, but has also been used to aid the project in developing integrated systems concepts. These concepts can be used to both conduct trade studies to determine the requirements for future supersonic aircraft and to assess the effectiveness of the project's work content at overcoming the barriers to supersonic flight. LM's N+2 Supersonic Validations contract fits into NASA's N+2 Supersonic Program as shown in Figure 2.

The N+2 Supersonic Validations program (supersonic vehicle anticipated to enter service in 2018–2020) directly aligns with these NRA and Supersonic Project goals and focuses on the validation of methodologies to successfully design and develop a low boom supersonic air vehicle. The N+2 effort is divided into elements that focus on foundational, discipline, multidiscipline and integrated system level challenges. To achieve these multi-faceted goals, the N+2 effort requires multi-discipline analysis and optimization (MDAO) efforts between airframe and propulsion industries to address system integration. Integrated vehicle design is performed to simultaneously achieve supersonic cruise efficiency, low sonic boom signatures, as well as low take-off noise. Integrated design concerns include:

- Sonic Boom Reduction
- Airport Noise
- Cruise Efficiency
- Light Weight Structure for Airframe/Propulsion Systems
- Aero-Propulso-Servo-Elasticity
- High Altitude Emissions

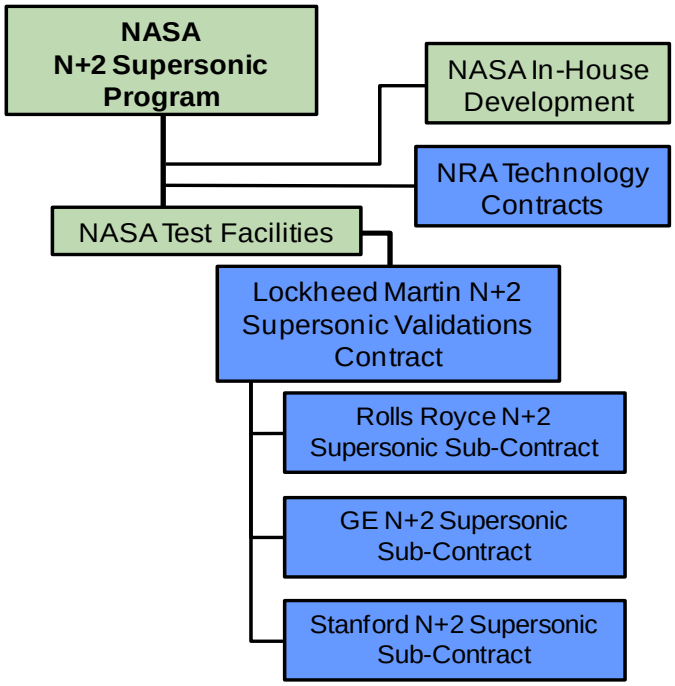

Figure 2. LM N+2 Organization

A key element of the Supersonics Project (and N+2 program) is systems level validation testing, which leverages the substantial investments made by the project (both internally and through the NRA). These system level validations provide proven capabilities that address the efficiency, environmental and performance challenges of future supersonic aircraft. The LM N+2 program conducted low boom testing and nozzle testing to achieve these goals.

The N+2 Supersonic program generated knowledge to benefit the Nation. Therefore, this report (and related papers at technical conferences) seeks to share the program's findings, disseminate test results, and validate component and system analysis tools that will support the design of an environmentally and economically viable product.

2.2 Purpose

This final report (PMF-01765) fulfills the NASA sponsored program "N+2 Supersonic Validations" program's final reporting requirements for the December 2009 through September 2011 initial phase, plus the LM3 wind tunnel test task that concluded December 2011. The N+2 program is focused on validating tools and technologies for integrated supersonic vehicle design that is traceable to a full scale N+2 vehicle class. The program focused on the design, development, test and validation at a systems level for both low boom and low airport noise. This program is committed to overcoming significant performance (cruise speed, range, payload and fuel efficiency) and environmental (sonic boom, airport noise, and cruise emission) challenges. The NASA solicitation's N+2 initial goals are illustrated in Table 2 along with LM's target status. Differences are displayed in red text.

For sonic boom, our less stringent target status differs for reasons based upon both technology limitation and requirement severity. Our current low boom technologies achieved 79 PLdB (Phase I status summarized in Table 1) with a relatively small performance penalty. Further improvements of more than a few PLdB would require large increases in vehicle length with greater penalties to weight and fuel efficiency. We have found a knee in the curve with our current techniques, beyond which loudness reductions become abruptly more costly.

TABLE 2.—N+2 ENVIRONMENTAL AND PERFORMANCE TARGET UPDATES

N+2 Small Supersonic Airliner (2020)	NASA's Initial Goals	LM's Target Status
Environmental Goals		
Sonic Boom (PLdB)	65 - 70	≤ 78 Threshold, ≤ 73 Ideal
Airport Noise (cum below Stage 3)	10 - 20 EPNdB	25 - 30 EPNdB
Cruise Emissions (g/kg fuel)	< 10 EINOx	< 10 EINOx
Performance Goals		
Cruise Speed	Mach 1.6 - 1.8	Mach 1.6 - 1.8
Range (nm)	4000	4000 - 5500
Payload (passengers)	35 - 70	70 - 100
Fuel Efficiency (passenger-nm per lb fuel)	3.0	> 3.0

With regard to requirement severity, we suspect that 65–70 PLdB may be more severe than necessary. Our guidelines indicate that loudness should not be greater than 78 PLdB for supersonic over land flight and would ideally be less than 73 PLdB. Though our Phase I design was above 78 PLdB, achieving the targets in subsequent N+2 Phases is possible without substantial penalty. A substantial penalty in efficiency (e.g., greater than 10 percent) is unacceptable for the vehicle capability that we are targeting.

For the other goal differences—airport noise, range and passenger payload—our targets are increases in capability relative to NASA's initial goals. The latest subsonic aircraft are coming out with cumulative noise 20 to 30 EPNdB below Stage 3 limits, so the initial goal would have been significantly louder than subsonic aircraft. Because we employed variable cycle engine technology, high aerodynamic efficiency high-lift systems and operational procedures (integrated to exploit our vehicles unique characteristics); we were able to achieve lower airport noise targets without the weight penalty of higher thrust and greater wing span needed in prior studies. With the high efficiency that was achieved, sizing the vehicle for trans-Pacific range (5000+ nm) became beneficial, and sizing for a greater passenger load better matches our anticipated N+2 vehicle size.

Meeting or surpassing these goals stimulates innovation and advances the pursuit of revolutionary conceptual designs. On-going studies are improving fuel efficiency. System-level multi-disciplinary analysis and optimization (MDAO) and out of the box thinking enables larger improvements needed for successful supersonic transportation. We strive to foster an environment of innovation and excitement for future supersonic travel.

Overall, the N+2 effort is demonstrating proven capabilities for successful supersonic transportation. Capabilities are proven through design and testing validations that satisfy the efficiency, environmental, and performance barriers to practical supersonic flight. The results in this report have advanced tools and technologies necessary for integrated supersonic design, especially for low boom test validation.

2.3 Objectives

To pursue the purpose of providing propulsion, airframe, and vehicle system-level experimental validation of tools and technologies, the LM N+2 validation effort is guided with the following objectives:

Objective 1: Leverage our foundation in supersonic aircraft development along with recent experience and patented methodology for low boom design to execute a comprehensive program of experimental validations aimed at addressing NASA's goals for the N+2 effort, and position NASA for intermediate demonstrations or flight tests.

Objective 2: Use LM ADP's expertise as system integrators and RRLW's and GE GR's expertise in engines to increase the Technology Readiness Levels (TRLs) of integrated propulsion/airframe technologies.

Objective 3: Address two significant challenges for an N+2 vehicle: constraining the boom signature (particularly the aft shock) by applying LM ADP and Stanford's advanced MDAO boom shaping while maximizing aerodynamic efficiency, and (applying RRLW/GE GR's expertise) balancing propulsive cruise efficiency with airport noise constraints.

Objective 4: Forge productive collaborations with NASA research personnel and facilities that will foster future government/industry supersonic technology development efforts.

2.4 Scope

The LM N+2 Supersonic Validations program conducts tool and methodology validations as well as systems level experimental validations in support of environmental challenges facing efficient, supersonic flight. Building upon the work done by LM on the N+3 Supersonic System Studies program (2), the N+2 program encompasses an integrated airframe and propulsion test validation program, validating the capabilities needed to meet environmental and performance goals for future supersonic commercial vehicles. Essential low boom aft-shock testing was conducted to validate current MDAO methodologies with the following high fidelity assets:

- Blade Rail sonic boom measurement apparatus
- Linear Actuator for translating model X position up to 24 in.
- Model support apparatus (MSA) including pitch and sideforce balances with aft taper and cylindrical mounts and front cylindrical mount compatible with a wide range of new and existing models
- MK2D 1.5 in. Balance Adapters with aft taper to linear actuator and front cylindrical and front taper mounts that additionally connect to new Boeing low boom models
- SEEB-ALR calibration axisymmetric model with a SEEB flat-top signature modified to include Aft Lift Relaxation (SEEB is a computer program (Ref. 6) that calculates low boom signatures and theoretical potential) which reduces the equivalent area needed at the aft end of a vehicle
- OptSig signature measurement validation axisymmetric model that produces the design target N+2 optimum signature
- HS3 large-scale QSST operational nacelle simulation model
- N+2 Low Boom wind tunnel model (1021-01 configuration)

Essential supporting technologies of MDAO and natural laminar flow are being assessed and validated with cumulative, incremental testing. Essential supersonic propulsion systems were integrated with all low boom vehicle system requirements. Two propulsion systems were developed, one by each engine company, such that the full vehicle system met airport field length performance and acoustic noise requirements. The integrated low noise nozzle predictions were experimentally tested to validate their estimations of noise and performance on the low boom vehicle. LM is committed to helping NASA successfully validate their goals through tests that are traceable to a representative N+2 supersonic configuration achievable in the 2020+ time frame as well as socialize the resulting capability with the broadest possible audience. The LM N+2 Supersonic Validations program's initial phase encompassed the following:

- Three low boom wind tunnel tests at the NASA Ames 9´ 7
  - Testing of the SEEB-ALR, OptSig and legacy LBWT Models with the new MSA balance and Blade Rail sonic boom measurement apparatus—LM1
  - Spiked Nacelle Sonic Boom Validation—LM2
  - N+2 Low Boom configuration model—LM3

  - Also utilizing MK2D 1.5 in. Balance, balance Adapters and retesting of SEEB-ALR, OptSig and Boeing AS2 models
- Nozzle NATR (Nozzle Aeroacoustic Test Rig) tests at the NASA Glenn Acoustic facility
  - RRLW nozzle testing
  - GE GR nozzle testing
- Coordination with Boeing and NASA
  - Blade Rail sonic boom measurement apparatus for the Ames 9´ 7 tunnel
  - Linear Actuator for model X translation
  - Lessons learned from data on past sonic boom measurement rail difficulties
- Coordination with Stanford University on adjoint-based low boom design optimization

3.0 LM Phase I Work Breakdown Structure

LM Aeronautics is responsible for the overall design, development, fabrication, testing, and technology verification necessary to realize a visionary vehicle capable of achieving the supersonic N+2 environmental and performance goals. A combination of advanced design methodology and an integrated system approach was required to verify an advanced concept vehicle serviceable in the 2018-2020 timeframe. Figure 3 illustrates the overall work breakdown structure (WBS) of the tasks and duties required for the initial program phase, which also lays out the structure for this final report. Our efforts focused on nine major products:

1. Measurement Hardware Validation Test, LM1 (WBS 3.1-2)
2. Spiked Nacelle Sonic Boom Validation, LM2 (WBS 3.4)
3. Low Boom Validation Model Test, LM3 (WBS 3.3)
4. MDAO N+2 Solver (WBS 3.8)
5. Inlet Testing (WBS 3.9)
6. NATR Test 1 RRLW Nozzle (WBS 3.12)
7. NATR Test 2 GE GR Nozzle (WBS 3.13)
8. Optimization with Stanford University (WBS 3.6)
9. Vehicle System Integration Analysis (WBS 3.7, 3.9)

Each of these nine products had supporting tasks, WBS 3.1-3.13, to ensure that the program executed on time and within budget. The WBS encompassed all work necessary to oversee and direct the execution of the N+2 Phase 1 Program.

LM1: **Measurement Hardware Validation Test (97-0220)**: For this mid-phase Ames wind tunnel test, LM was responsible for the design and fabrication of the Model Support Apparatus (WBS 3.1) as well as the SEEB-ALR and OptSig models (WBS 3.2). A Low Boom Data Quality task was added (WBS 3.16) to help develop, test and assess a new sonic boom measurement rail—intended to satisfy everyone's needs. NASA had Boeing manage fabrication of the new measurement "Blade Rail" and NASA managed fabrication of the Linear Actuator. These test components were made available early for this test in November 2010. The objective was to validate all new hardware prior to the coming LM3 low boom configuration test. The high resolution of the hardware, and the SEEB-ALR calibration model in particular, helped identify, understand and partially remove (through calibration) causes of measurement distortion inherent to measuring the low sonic boom models. Adequate accuracy for low boom validation was not robustly achieved in this test with the new hardware; however, analysis of the data led to further measurement procedure changes that resulted in success—adequate LM3 test accuracy for validation of aft shock low boom.

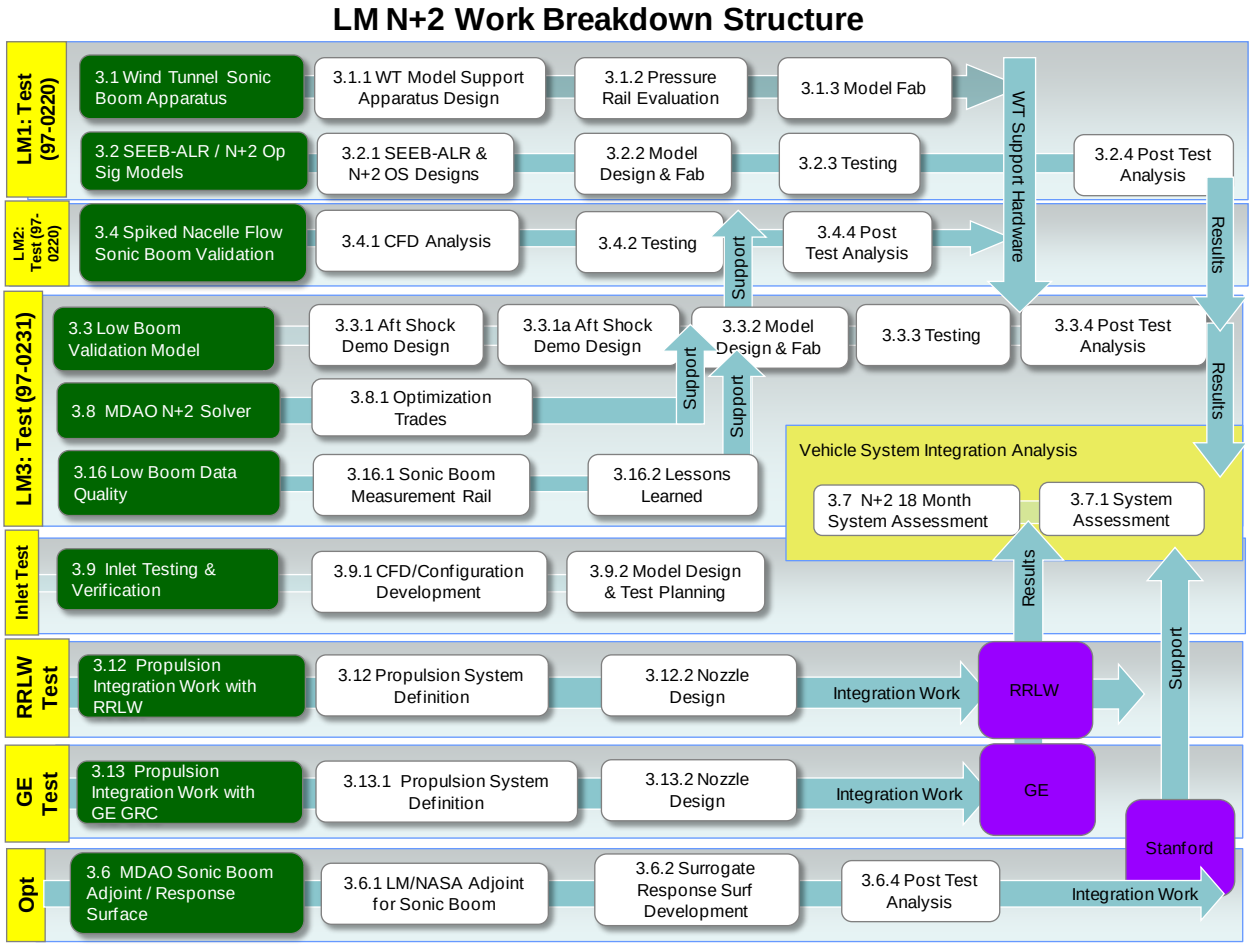

Figure 3. LM work breakdown structure for N+2 phase 1 program

LM2: **Spiked Nacelle Sonic Boom Validation Test (97-0223)**: Immediately following LM1, a pre-existing, large (4.7 percent, over 6 ft long) Quiet Small Supersonic Transport (QSST) model, designated "HS3," was re-tested in the Ames 9´ 7 wind tunnel with the objective of validating prediction accuracy for an operational propulsion system (WBS 3.4). The large QSST model was fabricated with complex nacelles including the inlet spike, internal pitot flow measurement rakes, internal screens for adjusting mass flow and convergent-divergent exhaust nozzles. Previous performance testing had identified the configuration needed to match the operational inlet flow, but no sonic boom measurements had been taken. The LM2 test performed a validation of operational nacelle CFD modeling with minimal program cost. Because of the large model size and the large magnitude of the nacelle flow disturbances, the measurement issues of LM1 did not detract from this test, and validation of pre-test predictions were successful. This report documents the CFD modeling resolution and boundary conditions used to achieve successful operational flow predictions.

LM3: **Low Boom Validation Model and Test (97-0231)**: The third Ames sonic boom test focused on measuring the LM N+2 Low Boom configuration 1021-01 model (designed under WBS 3.3 and tested under WBS 3.16), which was fabricated at 0.8 percent scale. The design effort supporting this test was concentrated on creating a vehicle with very low aft shock loudness. To better measure the aft shock, two different model supports, a sting and a blade, were built that produced very little change to the sonic boom signature. The two supports also provided redundancy for prediction removal of their interference. The LM3 test was conducted in the Ames 9´ 7 facility from the 13th through the 20th of October 2011. The configuration design status at the end of 2010 had a low boom aft signature at 0 degrees undertrack out to

10 degrees of roll, but sonic boom farther from the flight track at a roll angle of 20° increased in loudness by more the 6 PLdB. Also the LM1 test at the end of 2010 measured large calibration distortions and did not robustly achieve validation of the similar OptSig model's signature. Further refinements were implemented in methodology, low boom design and measurement technique. In May 2011, the 1021-01 design combined multiple firsts in low boom design: high efficiency, practical structural thickness and low boom demonstration throughout its sonic boom carpet at Mach 1.6. Also, new test procedures were developed that improved upon the calibration corrections achieved in LM1 and virtually eliminated measurement distortion in LM3. The procedures implemented in LM3 were so effective that an order-of-magnitude better accuracy was achieved relative to the best previous sonic boom testing results. Both model support concepts' measurements matched their predicted small sonic boom interference, and resulted in matching vehicle predictions when their interference was removed—yielding two sets of validating measurements for the low boom aft shock predictions. The October testing utilized the new Blade Rail, MSA, Linear Actuator and SEEB-ALR calibration model to achieve the excellent 1021-01 Low Boom model measurements. The test and following data analysis through the end of December 2011 were supported by the additional 3.16 Low Boom Data Quality task.

MDAO N+2 Solver: The Low Boom configuration design work ran many analyses that produced multiple outputs for sonic boom characteristics at multiple roll angles with L/D efficiency—all as a function of various design parameter variations. The design spaces resulting from these analyses were used in this study to understand what solvers should be best (WBS 3.8) to use with the methodology being developed in WBS 3.6.

Inlet Test: Inlet Testing and Verification tasking (WBS 3.9) began with CFD design and analysis to address cruise performance, low-speed auxiliary inlet refinement and flow controls for performance, operability, and acoustic-related improvements. Concept design and test planning was conducted in Phase I but the option (Option B-WBS 3.15) to perform testing was not exercised.

RRLW Nozzle Test: The first Nozzle Aeroacoustic Test Rig (NATR) Test was conducted with RRLW in May 2011. Work under this effort (WBS 3.12) includes collaboration between LM and RRLW to define a propulsion system definition, make nozzle noise predictions, streamline engine accessories, design, fabricate, and test a low noise N+2 nozzle. Results from these efforts are outlined in detail in *Appendix A—RRLW Final Report* (Ref. 4).

GE GR Nozzle Test: The second NATR test was conducted with GE GR in May/June of 2011. Work under this effort (WBS 3.13) includes collaboration between LM and GE GR to define a propulsion system definition, make nozzle noise predictions, evaluate flow control technologies, perform an inlet distortion evaluation, design, fabricate, and test a low noise N+2 nozzle. Results from these efforts are outlined in detail in *Appendix B—GE GR Final Report* (Ref. 5).

Optimization: WBS element 3.6 includes the optimization development effort LM performed in conjunction with Stanford University. Specifically, LM/Stanford improved upon the adjoint-based capability for the inverse shape design for low sonic boom supersonic configurations. The main objective of our effort was to derive, implement, and test a preliminary version of an adjoint solver that is able to produce sensitivities (gradients) of cost functions derived from the aircraft's sonic boom with respect to arbitrary numbers of design variables that affect the shape of the aircraft. Results from these efforts are outlined in detail in *Appendix C—Stanford Final Report* (Ref. 3).

Vehicle System Integration Analysis: LM traces/scales results of the Phase I program test measurements and studies to assess their impact on the vehicle system performance, status versus N+2 goals, and maturity and risk of technologies/capabilities in this task (WBS 3.7). Vehicle system integration and analysis supports low boom design, development, and optimization for future N+2 phases.

4.0 LM1: Measurement Hardware Validation Test (Ames 97-0220)

4.1 Wind Tunnel Sonic Boom Apparatus (WBS 3.1)

The Base Program contained two sonic boom tests (Tasks 3.1 to 3.4 and 3.14) that were intended to validate a LM designed/developed measurement apparatus and model support motion components. The new low boom wind tunnel measurement hardware was needed to cost-effectively and accurately measure aft shock as well as measure six roll angles (defining the entire boom carpet) and sonic boom flight conditions. Accurate measurements of multi-shock signatures' magnitude and spacing were required to correctly validate N+2 signature loudness.

4.1.1 Background

To measure a model at various distances requires the ability to change height and forward-aft position to keep the shock waves hitting a fixed measurement apparatus. The primary planned facility, the NASA Ames 9′ 7, has wall to wall height adjustment, angle-of-attack (with a fixed model position when angle and height are both adjusted) and sideslip angle capability (causing lateral translation of the model since there is no lateral translation capability). However, the Ames tunnel did not have forward-aft translation and remote roll capabilities. Remote translation and roll mechanisms were added forward of the facility support and motion system. NASA had a suitable remote roll mechanism and translation mechanism they had used previously, but the translation mechanism's actuation was in need of refurbishment. NASA decided to design and build a new translation mechanism—the linear actuator (LA). NASA incorporated everyone's input during the design process and made a compact, streamlined, structurally rigid mechanism. In addition, the LA has a taper fit connection on its forward end which has improved testing flexibility and convenience.

For improved static pressure measurements, NASA built and tested three new measurement rails prior to N+2, that mounted 1.25, 5.25, and 14 in. distance off the wall. Measurements with all three rails produced results that seemed to differ from previous, single point measurement probes, and it was desired to do a thorough review of the prior data before designing any new measurement apparatus. LM performed analysis of these rails which is discussed in Section 4.1.3.1.

4.1.2 Measurement Hardware Approach

With model pitch, yaw and height provided by the Ames 9′ 7 facility plus roll and translation mechanisms part of the support strut, the remaining model support challenges were reducing support interference, measuring model lift and interconnecting components. In prior sonic boom testing, sting mounting and blade mounting have been used to attach the model to wind tunnel support hardware. Particularly for aft shock validation, a blade attachment is likely to provide less interference over a sting balance. However, to further quantify and isolate attachment interference—dual mounting with a top blade and rear sting provides two chances to match analysis to measurement and allows the possibility for measuring both and differencing a measurement of each interference.

Prior low boom testing has used either small balances (usually without axial force) or have had balances built into the aft end of the model sting. Even for the 22 in. low boom model made for this program (Task 3.3), the flow is unable to transition like the full scale airplane making it a few times smaller than what is desired for drag measurement. So the purpose of a low boom model balance is to get model lift within 1.5 percent of the desired value, which is required to match sonic boom. Using a typical balance inside the model requires an air gap between the model and the model support. The model distortion to accommodate the sting must now be larger in diameter, and for the blade there is the additional problem that the air gap now covers a long longitudinal distance down the model where pressure is generally more varied than for a sting. While such a blade gap may not cause a significant flow-field change, it is a difficult problem to solve with CFD, especially since it is difficult to eliminate uncertainty if measurements do not match predictions. Therefore for sonic boom, we prefer to have a balance back in the model sting (or blade). Surrounding a balance in the aft end of a sting leads to a much

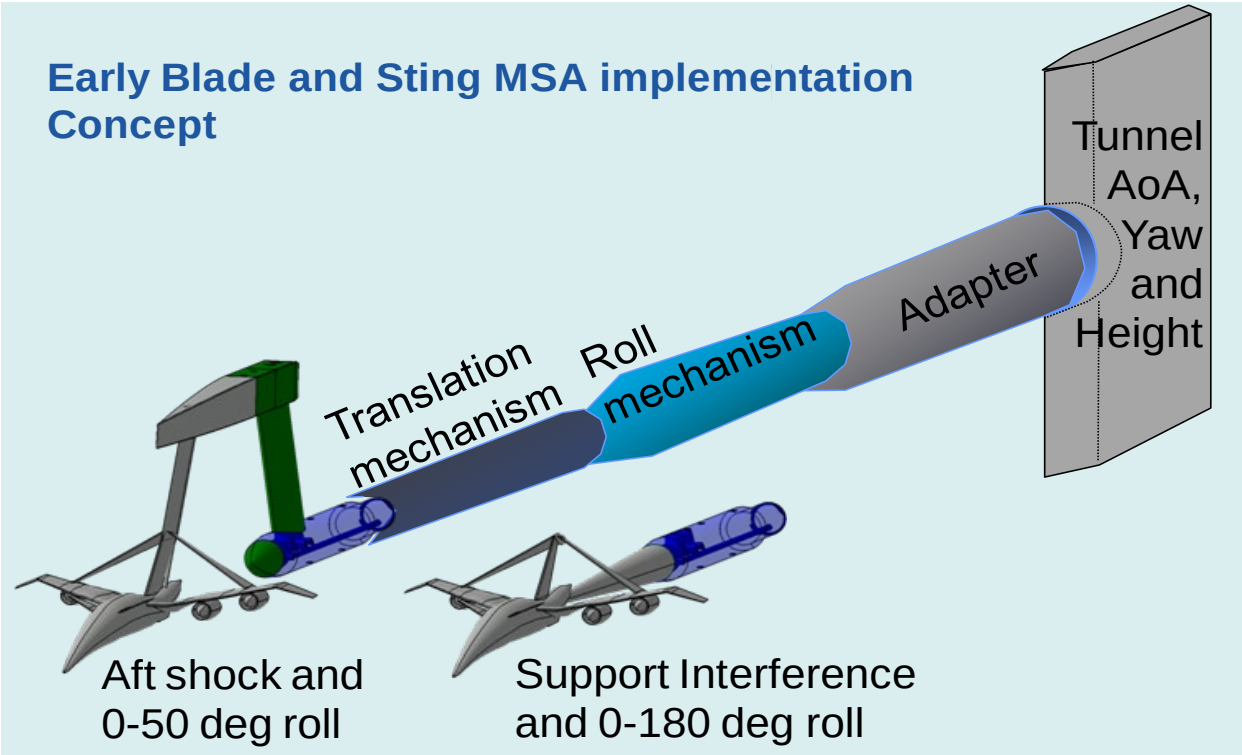

Figure 4. Keeping the Model in the Same Position with Sting and Blade was Deemed Unnecessary, Simplifying the Final Design

larger diameter, and consequent flow-field disturbance. This type of balance also creates a larger diameter than is necessary. A balance built into the sting (or one with a front end attachment instead of surrounding attachment) allows for a smaller sting flow-field disturbance. For multiple test models, being able to reuse such a sting balance also saves cost.

An early MSA concept, Figure 4, had a different attachment points for the blade (green) and sting that kept the model in the same location. After review with NASA it was agreed that using the same attachment, with the facility offsetting the lower position for the blade mounted model, worked fine for stress and force measurement in other testing, while resulting in a much simpler and less costly MSA fabrication.

4.1.3 Wind Tunnel Model Support Apparatus (MSA) Design

In collaboration with NASA, LM fabricated a universal wind tunnel sonic boom measurement apparatus that improves productivity and accuracy for all future boom testing. The Model Support Apparatus (MSA) was designed to accommodate the needs of all N+2 participants, specifically NASA, LM, and Boeing. The intent was to reduce a signature measurement from 50 min to approximately 30 sec. A major feature of the model support apparatus is changeable model mounts: high blade mounts for minimal aft signature distortion and alternate sting mounts. By measuring both mounts separately and together, their distortion pressure increments can be differenced and subtracted entirely to increase measurement accuracy for N+2 configuration testing.

The MSA (Fig. 5) was made to interconnect the many components we plan to use in future sonic boom testing. And it was designed with both sting and blade mountings in mind. A 0.25 in. diameter shaft runs its length to carry instrumentation wires and its own balance wires. The MSA matches the connecting cylinder (male end) and set screws of the NASA Langley Angle of Attack (AoA) mechanism on its aft end (four set screw flats allowing 90° rotation increments), which is used to overcome angle/position limitations. The MSA has a sleeve adapter that goes over that cylindrical aft end to directly connect it to the LA (LM does not anticipate using the AoA mechanism at NASA Ames). The front of the

MSA repeats the same connection type (female end) for our models with a top pin, in addition to the set screws, for a compatible but more secure and repeatable hold location. While working to also minimize the interference of sting and blade mountings individually with the MSA, we realized that attachment interference is configuration specific and would have to be left as part of the Low Boom model design. The final MSA arrangement is shown in Figure 6.

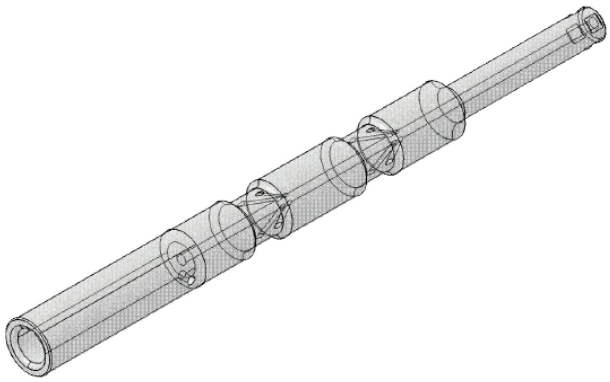

Figure 5. MSA without Sleeve Adapter and Strain Gage Covers Removed

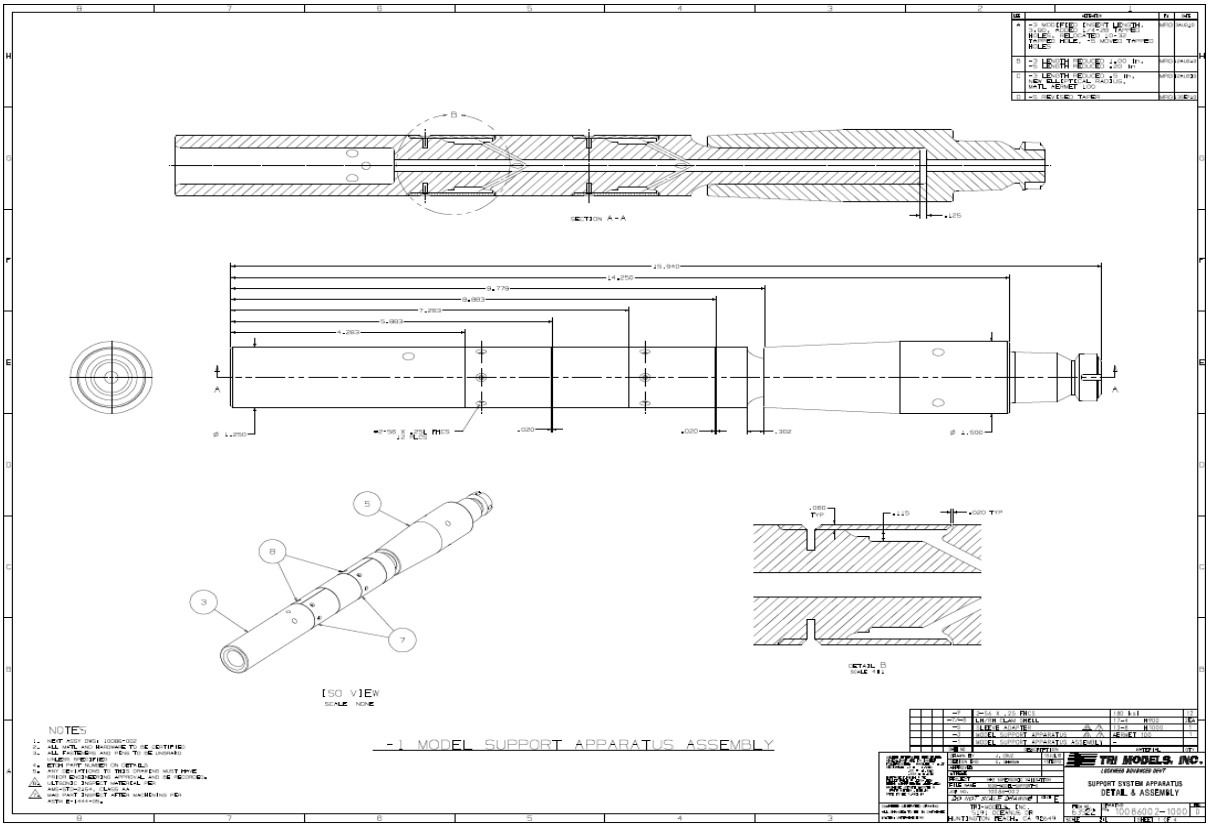

Figure 6. Final MSA Assembled with Strain Gage Covers and Sleeve Adapter

4.1.3.1 Pressure Rails Evaluation and Recommendation

Under the pressure rail and evaluation and recommendation subtask we examined the large sonic boom database that NASA measured in 2008 (consisting of a new 385 orifice wall rail 1.25 or 5.25 in. from the wall), new 160 orifice mast rail 18 in. from the wall, and legacy single orifice 10 and 10.5 in. probes. Our evaluation addressed whether an existing NASA pressure rail was adequate for the planned LM and Boeing sonic boom tests as well as help guide the design of the Boeing measurement rail device. The Boeing blade rail was used in our N+2 Hardware Validation Test or LM1 Test 97-0220 (described in subtask 3.2.3). Our initial report and recommendations changed as the N+2 program progressed. After extensive CFD analysis, the LM1 test, the Boeing test with a new 480 orifice 1.5 in. wide Flat-Top Rail mounted 2 in. from the wall, and data analysis we believe we can explain the shortcomings of these 2008 measurements.

The most important differences between the three measurement rails were their cross-sectional shape, distance from the wall, and local flow-field variations, Figures 7 and 8. When sonic booms (like other acoustic sound waves) reflect off a tunnel wall (or hard flat ground, etc.) there is a doubling of their pressure magnitude on the wall. On the Legacy Probes, Figure 9, the static pressure orifices are on the sides of the needle-like probe, which keeps any reflection from the pressure orifices. On both the Wall Rail and Mast Rail, the pressure ports are on top where there is reflection of the sonic boom. Both the Wall Rail and Mast Rail are narrow, 2 and 1.44 in. respectively, and do not have a flat-top shape. We initially tried to match Legacy Probe and Rail measurements by using an intermediate reflection factor between 1.0 and 2.0, as shown in Figures 10 and 11.

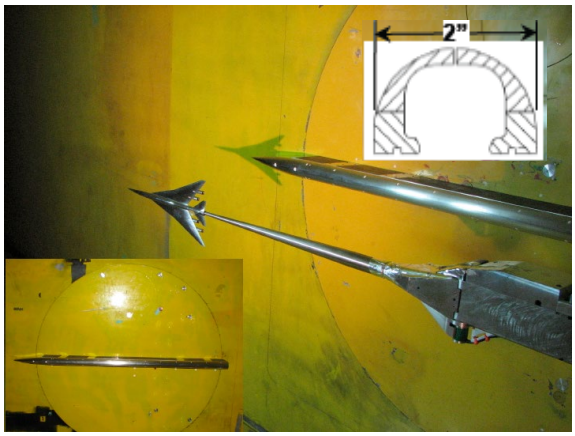

Figure 7. Wall Rail with Standoff for Orifices 5.25” from Wall (and Model)

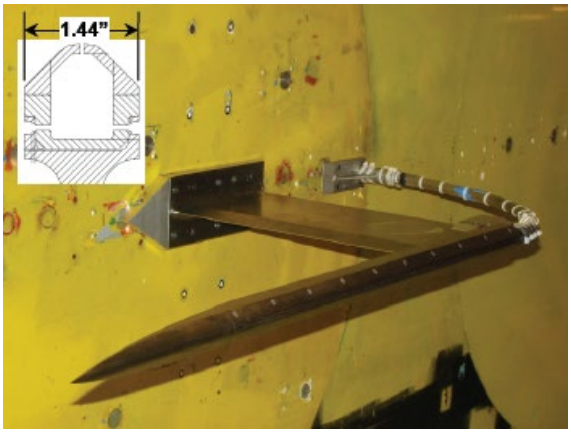

Figure 8. Mast Rail 18” from Wall

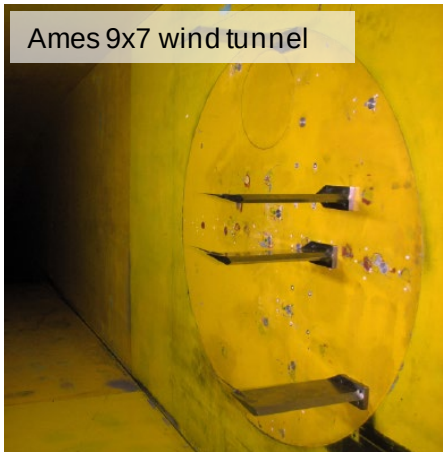

Figure 9. Legacy Single Orifice Probes 10” from Wall

While the reflecting factor seems to match in Figure 10 (except at 0.9 the match is not precise enough for our configuration signatures), the reflection factor does not match using a single multiplier in Figure 11. A later CFD CART3D analysis by NASA for our SEEB-ALR model (described in Section 4.2) measured by a flat-top Boeing rail, 1.5 in. wide and 2 in. from the wall, illustrates more complexity in Figure 12.

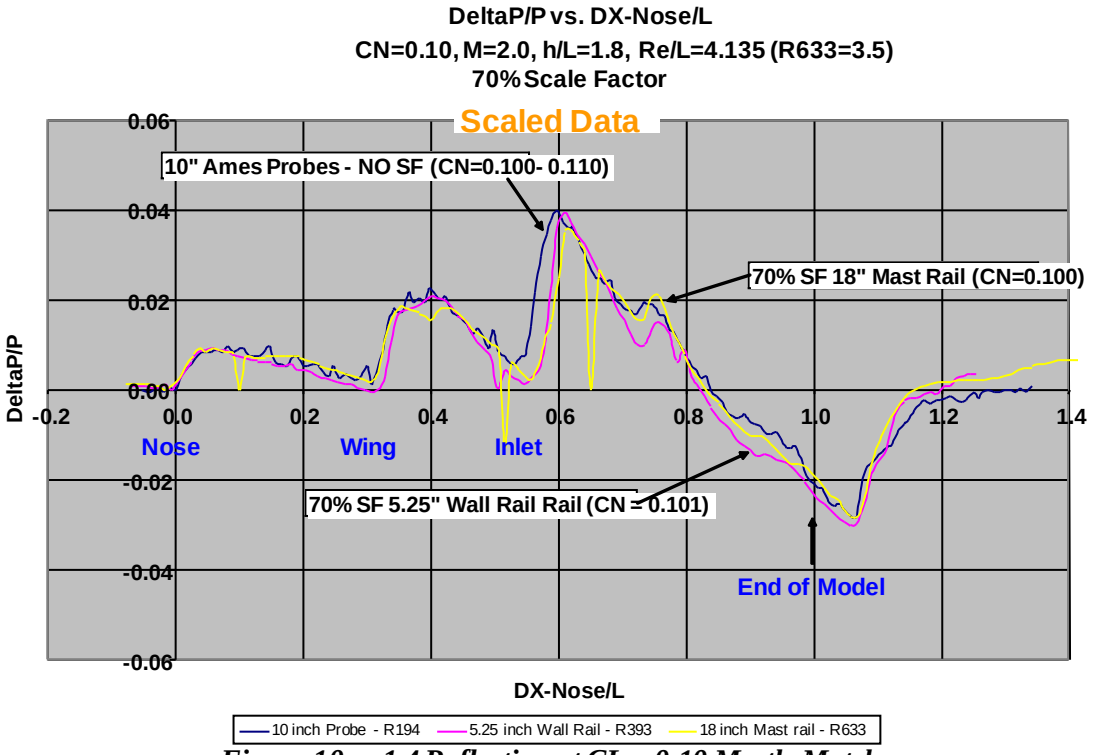

Figure 10. x1.4 Reflection at CL = 0.10 Mostly Matches

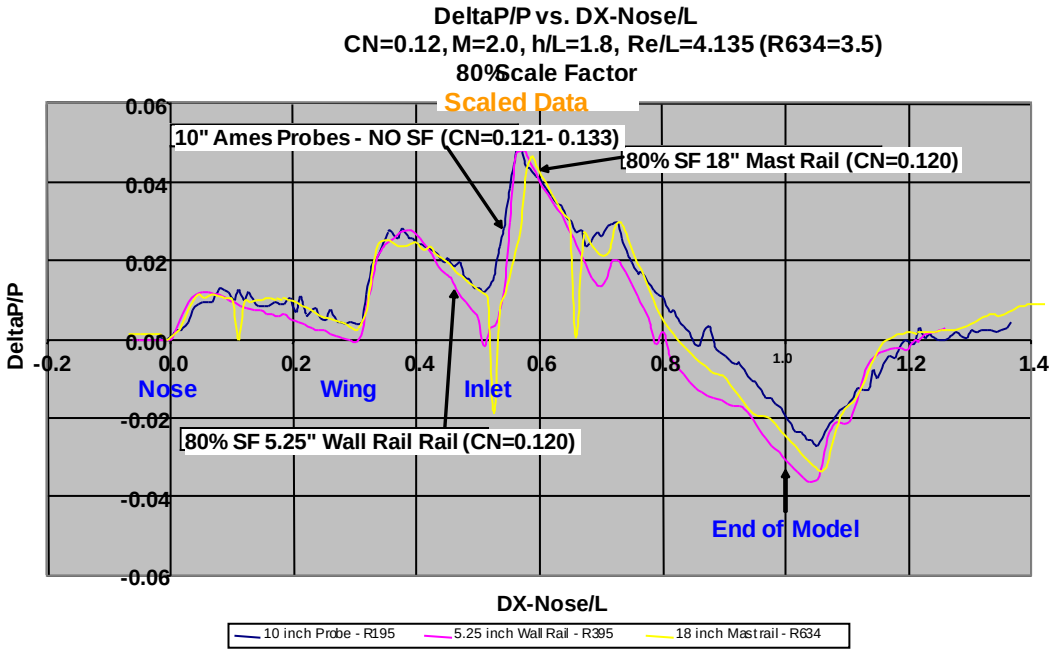

Figure 11. x1.6 Reflection at CL = 0.12 Not Matching

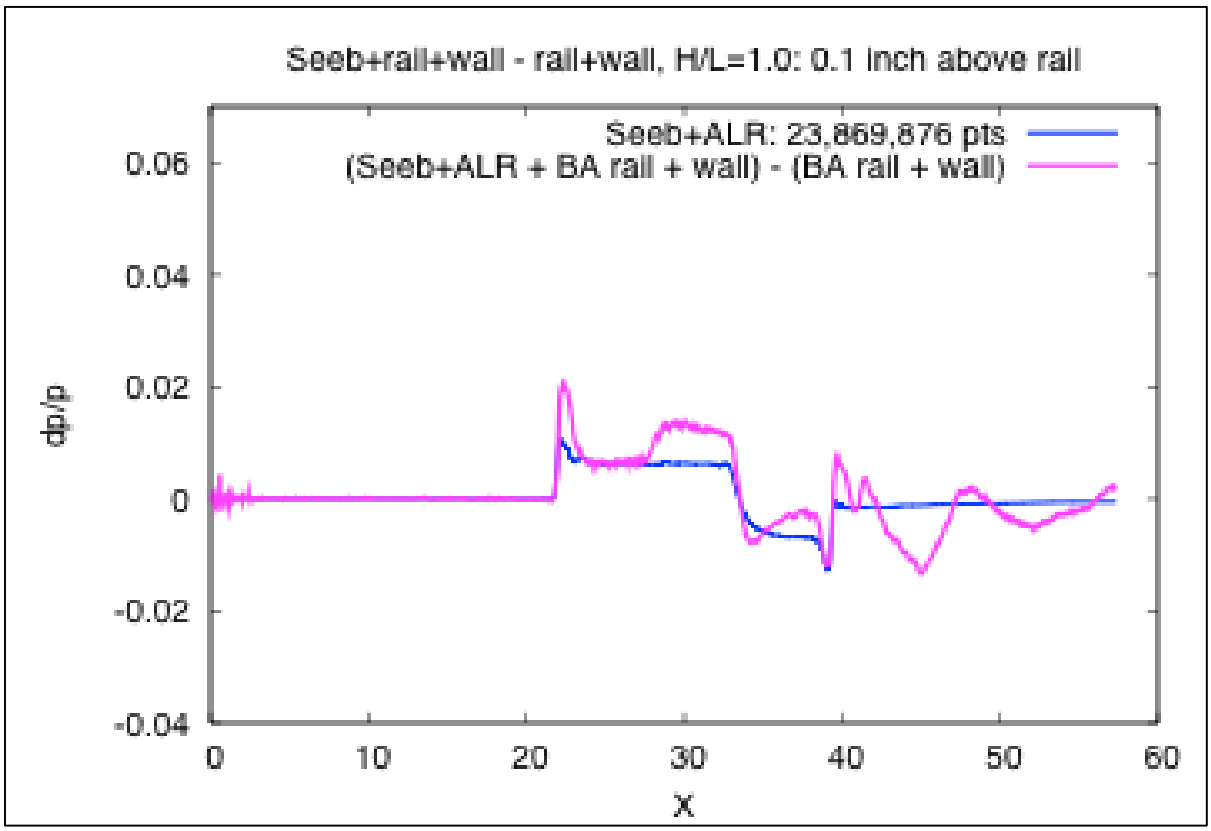

Figure 12. CFD of SEEB-ALR Signature and SEEB-ALR Signature Reflecting Off 2" Rail

When the sonic boom first strikes the flat-top of the rail there is a 2.0 strength reflection, but the reflection does not occur 0.75 in. from the orifices at the edge of the Boeing rail. At the Mach 1.6 shock angle, the loss of reflected pressure takes 1 in. to propagate to the orifices; where after, the doubling is lost. But it is not just a 2.0 to 1.0 switch in this case; doubling is displaced from 1 in. earlier in the signature (looks simpler with a flat-top). The signature travels past the rail 2 in., reflects off the wall, then back up 2 in. then to the center of the rail orifices which delays it by 6 in. A superposition of the original signature with some magnitude reduction for turning 90° at the edge of the rail occurs as well as an expansion into the extra 2 in. of air above the rail that was not in the wall reflection. Also, the superimposed signature is smeared from reflecting off the subsonic boundary layer at the wall, which was not reflected in the CFD analysis. The Wall Rail at 1.25 in. from the wall has these same two problems, which explains its distorted measurements. The Wall Rail at 5.25 in. is far enough that, for the model size and higher Mach number, the signature does not reflect back until it is behind the vehicle (and often hidden in the model support shocks). Both the Wall and Mast Rails have initial, then lost reflection multipliers with displacement. They also have rounding on their upper surface that starts a reflection factor reduction in less distance than a shock wave from the edge of the Rail to the center orifices. With more complicated signatures and changing pressures, these distortions are harder to discreetly identify. Looking at other sonic boom test measurements taken close to the wall or with top orifices on their rail, these same distortions appear to be imbedded in their measurements. Test engineers have attributed the differences with their analysis as being close enough or unexplained.

Further, all supersonic wind tunnels have ambient flow-field distortions as large as or larger than the model pressure disturbances we are trying to measure. We have found that there are better and worse locations in every tunnel and ambient flow variability magnitude can vary 2 to 3 times between rail orifices located near or next to each other.

LM designed a pressure measurement apparatus that addresses the wall reflection and rail refection issues by making its measurements on a flat plate. The plate is wide enough that its edge reflection relief is outside the Mach cone of the signature, so no reflected pressure is ever lost, Figures 13 and 14. Having this width also eliminates the wall reflection problem because nothing can propagate from the edge to the orifices in less distance than the signature length theoretically allowing it to be mounted on the wall with as low as zero offset distance. The plate is installed just beyond the tunnel boundary layer.

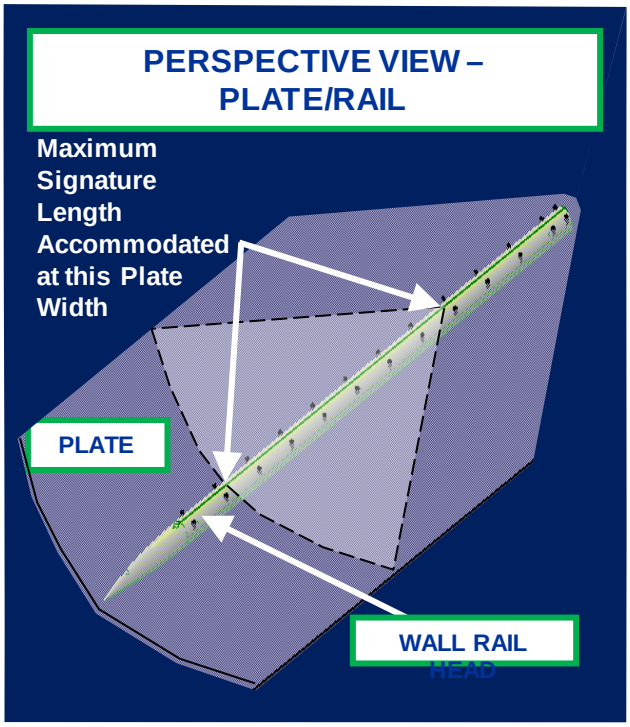

Figure 13. Plate Measurement Apparatus Incorporating Wall Rail

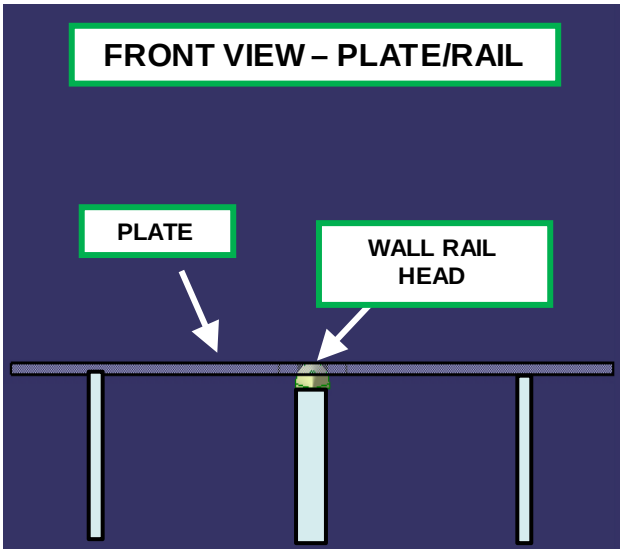

Figure 14. Plate Measurement Off-Set from Wall Concept

It was believed that two outer support plates could mount the plate in the tunnel with minimal disturbance to the flow. Based off of past inlet design experience, we believed the disturbance through the plates had a small enough contraction to easily flow at supersonic flow. Without CFD analysis to verify this assumption, NASA opted not to fund the LM plate design.

A cost savings idea was conceived for implementation of this concept by adding the plate onto NASA's existing wall rail. The intent was to reduce costs by using existing hardware. The wall rail measured 48 in. in length and 32 in. in width to accommodate a 30 in. signature (adequate for at least a 24 in. model). There are advantages to the measurement plate over the currently preferred Blade Rail. The plate doubles the sonic boom pressures and ambient disturbances traveling in the plane of the boom propagation from the vehicle to the rail, but it does not double the perpendicular ambient disturbances which are generally larger in the Ames 9´ 7. There is the potential for reduced ambient flow variations providing increase in measurement resolution. The plate concept can also be mounted near the wall at lower Mach numbers but with greater span; whereas, a blade rail needs to increase in height (2 ft for Mach 1.2 and 3 ft for Mach 1.1) to stay away from wall reflections.

NASA also designed a rail that avoids the aforementioned problems, first making the orifices far enough from the wall to insure that model reflections are displaced behind the primary measurement for the largest model and lowest Mach number (lowest angle). The Boeing blade rail has orifices 14 in. from the wall (allowing up to 24 in. models at Mach 1.55), Figure 15. It has upward facing orifices positioned on a 0.1 in. diameter half circle at the tip of the Blade Rail. The wall-side edge of the Blade Rail is 1 in. thick to accommodate wind tunnel start-up loads, with a straight taper from 1 in. root to 0.1 in. tip. It has 420 orifices along 66 in. of length (0.157 in. spacing) providing over 150 signature points from a 22 in. model (Task 3.3). In CFD analysis, it was found that this edge diameter caused the orifices to have no (1.0) reflection increase in signature strength. Also a later study indicated that the tip location seemed to have the least ambient distortion from changes in flow angularity perpendicular to the rail, which is the direction of larger flow angularity distortions in the Ames 9´ 7 tunnel.

Regarding the assessment of the new blade rail, we summarize the flow-field distortions that were found to be problematic in the LM1 Test. Several procedures and test changes were developed to enhance the accuracy of measuring such small model disturbances in a wind tunnel flow-field. Their implementation and results are covered in the Section 4.2.

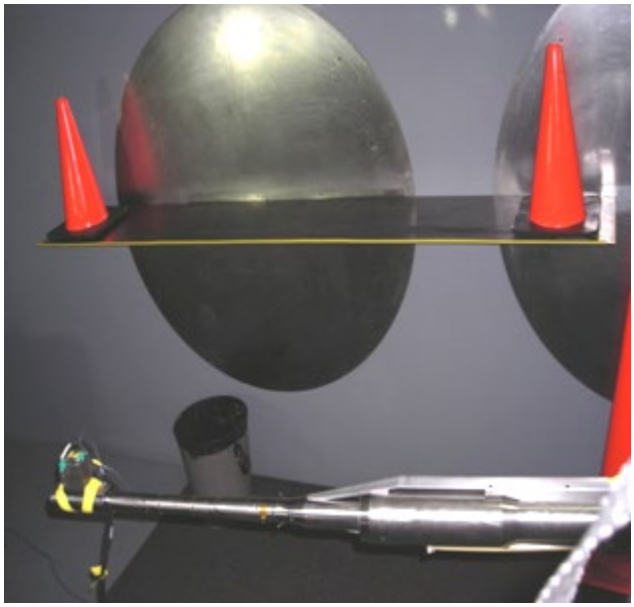

Figure 15. Boeing Blade Rail (under Safety Cones and Edge Protector) in Ames 9x7.

4.1.4 Results

The LM N+2 plan employed two wind tunnel test entries, the first (12 months into the program) to test the model support and measurement apparatus with the validation models from Task 3.2 and spiked nacelle model from Task 3.4. After validating the new hardware, the second test would measure the low boom model design from Task 3.3, originally planned for month 16 of the program. The first test revealed problems with making measurements of the required accuracy that were eventually theorized to result from trying to make highly accurate model pressure measurements that are several times smaller than the ambient flow-field distortions of a high quality supersonic tunnel. Based on the many curious details of the measurements from the first test, a calibration procedure using the SEEB-ALR model (described in Section 4.2) was developed that reduced distortions in the measurements by two-thirds; and additionally, new measurement procedures were proposed that seemed capable of reducing distortions by another 2/3. The combined improvement is needed to validate our low boom signature loudness, and these procedures are implemented in the delayed second test as described in Task 3.17.

The results of using the Task 3.1 MSA with the Task 3.2 models, since they were tested together, are covered together in Section 4.2.

4.2 SEEB-ALR/N+2 Optimum Signature Models (WBS 3.2)

4.2.1 Description

Task 3.2 was created to validate the new sonic boom measurement apparatus and calibrate it prior to testing. Several past boom tests have recorded distorted measurements that have nullified the entire test. For the Phase I Program, new measurement hardware was fabricated to conduct calibration testing (LM1 Test 97-0220) prior to the low boom model test (LM3 Test 97-0231). To validate the pressure response of a new measurement rail, a flat-top pressure distribution with a well-known pressure change was required. The intent was to translate the calibration model over the measurement rail before every low boom test to validate that the pressure orifices are reading the expected value (erroneous ones would be dropped). Based on prior testing experience, measurements should not be taken around ambient shocks. Any shocks evident in the ambient rail measurement should be avoided when positioning the model signature on the rail. The new measurement rails were made 2.5 to 5 times longer than the model signatures to make measurement location flexible at any Mach and distance condition when combined with model support translation capability. Before flat-top validation testing, the measurement apparatus is run with the model moved out of the way to measure the zero reference pressures of each orifice and to determine the best location for signature measurements. Then the validation model, with the ideal well known flat-top pressure magnitude, was measured and used to validate/calibrate readings. The flat-top pressure matches the well-known SEEB-code value, which is easily verified/repeated by far-field area, singularity or CFD methodology. Plus, a flat-top signature from an axisymmetric body is a stable validation shape, dropping in magnitude only by 1/3 while maintaining the same flat-top shape. The axisymmetric body is useable for all Mach numbers from Mach 1.2 to 3.0. Our proposed validation models, pre-test validation procedures and NASA's new measurement Blade Rail help provide rapid, undistorted, and accurate measurements for future boom testing—saving test costs, distortion uncertainty, rework and schedule risk. However, the LM1 Test revealed that getting accurate measurements is even more challenging than the aforementioned procedures can achieve. Having accurate measurements, sufficient data, and enough time to understand the measurement distortions measured in LM1 Test was pivotal. Our understanding of the results from the LM1 Test led to improved calibration and measurement procedures to achieve the required accuracy. If successful, the LM3 Test will provide higher measurement accuracy than previously achieved.

4.2.2 Approach

Two axisymmetric models were designed for the validation of the new measurement hardware along with new test procedures to measure models in the best flow along the rail. In initial planning, three concepts emerged as ideal for validation testing. (1) A SEEB flat-top type signature was chosen as the best way to check pressure measurement accuracy. (2) The second was a pressure signature that matched the target signature being used for the N+2 Low Boom configuration design. Accurately measuring the second signature would be similar to measuring the final Low Boom design signature. (3) The third was to validate a new kind of signature, a (LM proprietary) SEEB theory extension for minimum sonic boom with a reduced target equivalent area at the aft end of the vehicle—the natural shape of all non-low boom vehicle equivalent areas. Validating this minimization theory extension reduces the aft lift needed for low boom that is far in excess of aft lift needed for minimum drag. The theory extension is called Aft Lift Relaxation or ALR (akin to Christine Darden's "Nose Bluntness Relaxation,") and the amount of ALR is quantified by the ratio of maximum equivalent area/final equivalent area of the target distribution. ALR has the potential for improving the performance of low boom designs and making it easier to achieve low boom without detrimental impacts such as greater trim, too much aft lift, insufficient aft area, and center-of-gravity too far aft.

To test the three validation concepts, two axisymmetric "javelin" models were designed. The ALR extension to the SEEB theory modifies the aft shaping of the standard minimization signatures. As a result, a flat-top signature was chosen that would combine the objectives of checking pressure measurement accuracy and validate the ALR concept.

Figure 16 shows that the SEEB-ALR model has a maximum equivalent area 5 percent greater than the final area. Figure 17 shows the predicted ground signature from the SEEB-ALR model with its balanced front and aft shocks and long duration flat regions. Particular care was taken in the design and CAD definition of the SEEB-ALR model to make the flat regions as flat and smooth as possible to make the validation pressures accurate. Due to the small (0.006) scale chosen for the calibration model length (18 in.), meeting tolerance was difficult. Fabricated model inspection measurements were used to generate an as-built geometry for analysis. Without smoothing the measured points and using a linear analysis method without dissipation, the geometry was found to have accurate pressure flats, as shown in Figure 18. The as-built geometry should measure as completely flat given viscosity, measurement oversampling, and position oscillation (about ±0.15 in.) of the model during wind tunnel measurements. The measurement of the Aft Lift Relaxation extension to the SEEB theory improves ALR's maturity, advancing its TRL to 4.

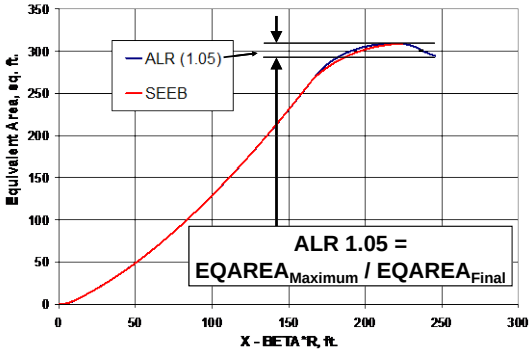

Figure 16. More Practical SEEB-ALR Target with 5% Area Drop at Aft End

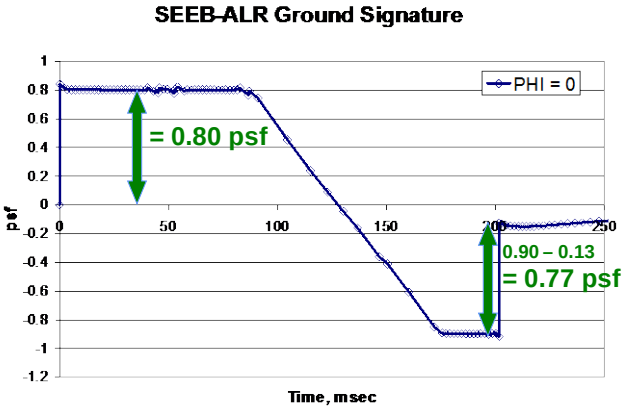

Figure 17. SEEB-ALR Design also Provides Flat-Top Pressure Validation

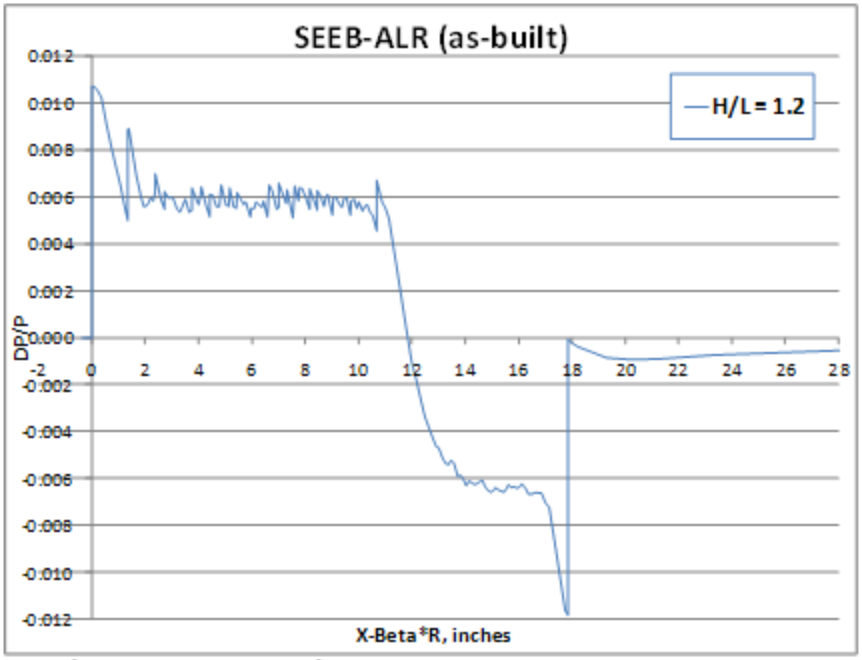

Figure 18. As-Built Geometry Shows Accurate Flat Regions in Linear Analysis

The other "javelin" axisymmetric model was shaped to match the N+2 target signature, which was similar to the Low Boom model of the LM3 Test, and titled "OptSig". This OptSig model used a target signature shape that was discovered and developed initially from the N+3 Supersonic Systems Studies program. The discrete component of (even blended) practical airplane shapes results in multi-shock signatures. But multi-shock signatures approximating a ramp shape signature can be similarly quiet once shock rounding is applied. A multi-shock signature shape optimization was run to find the shape that yields minimum vehicle length for the low boom loudness desired. Length is minimized as a surrogate for vehicle weight and thereby/performance. The optimum signature shape was used as a design target for the Low Boom configuration design in Task 3.3 and tested in the LM3 Test. For the LM1 Test, the OptSig model created a signature representative of the LM Low Boom configuration, and the new Blade Rail was used to try to measure its signature with enough precision so the propagated ground signature loudness would yield repeatable loudness from repeated measurements.

The weight of the current N+2 vehicle, 354,000 lb mass take-off weight (MTOW), was used for both the SEEB-ALR and OptSig models. For the axisymmetric models, all of the equivalent area is represented with volume (no lift). So the nose of the OptSig model is very similar to the nose of the Low Boom vehicle; however, once the wing starts on the Low Boom vehicle—its fuselage cross-section area remains constant through the cabin. The SEEB-ALR final area is zero, while the OptSig model has to simulate the lift with its volume and ends with a non-zero cross-section proportional to its weight (and adjusted by the altitude for which it is intended). This ending area is carried back with a constant section for approximately one foot to allow the complete recompression to ambient to be simulated. The overall OptSig model length was made to be 29.25 in. to match the NASA LBWT model, allowing similar location variations in the tunnel. The SEEB-ALR model was made to initially match a 230 ft long SEEB distribution with another 15 ft added to accommodate adding ALR while maintaining close similarity to a non-ALR baseline SEEB distribution shown in Figure 16. The OptSig model was kept at 230 ft in length similar to the Low Boom configuration.

The OptSig design process is outlined in six steps in Figures 19 to 24. The optimized ground target comes from the findings and optimization study in our N+3 Supersonic Systems Studies report (and planned Applied Aero 2012 AIAA paper) (Ref. 7). The ground target has a smooth initial ramp because the nearly axisymmetric forebody of the Low Boom vehicle is able to achieve this shape. This optimum signature is reverse propagated back to a starting signature, so the equivalent area can be calculated and used to determine the necessary area distribution of the axisymmetric body.

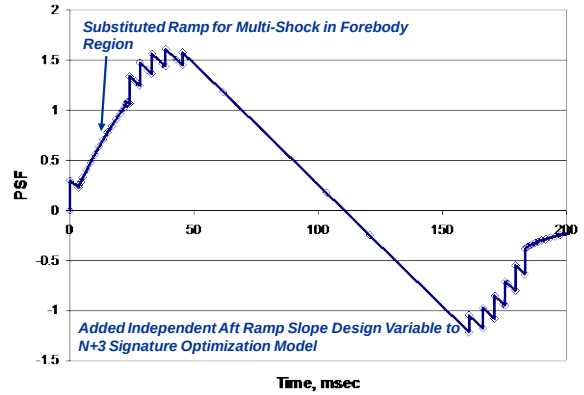

Figure 19.
(1) Optimized Ground Target

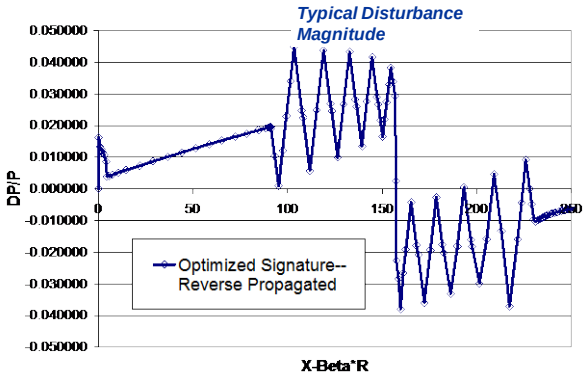

Figure 20.
(2) Reverse Propagation

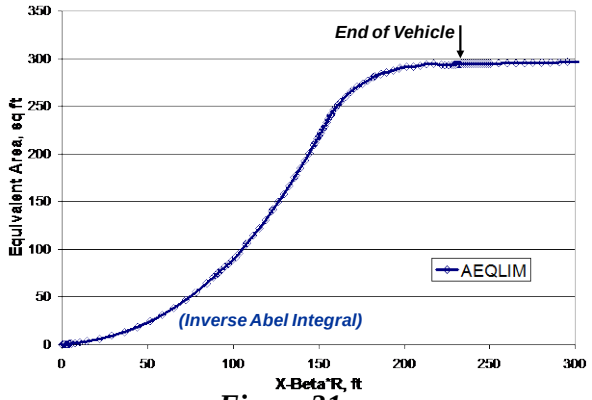

Figure 21.
(3) Integrate Target Equivalent Area

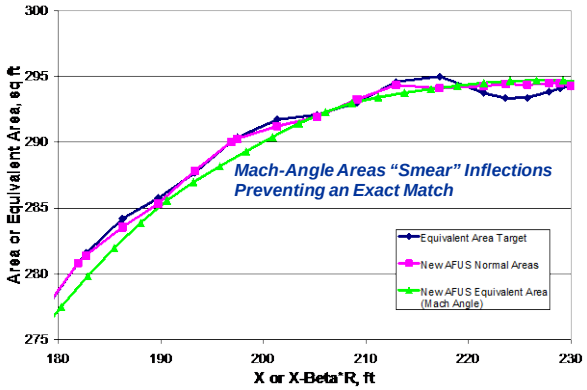

Figure 22.
(4) Match Mach-Angle Area with Normal Area Distribution

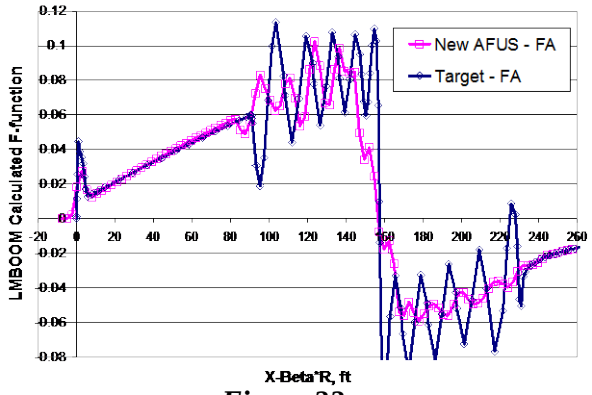

Figure 23.
(5) Approximate Starting OptSig Characteristics

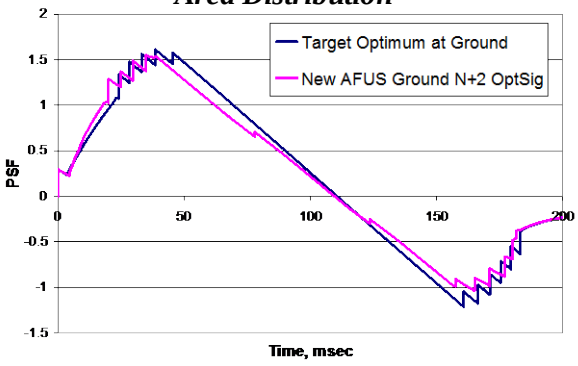

Figure 24.
(6) Final Ground N+2 OptSig

However as shown in (4), equivalent area is a Mach angle cut area distribution that cannot be exactly met by an axisymmetric body when the Mach angle cuts "smear" across a range of fuselage stations. But a shape (4) can be made that nearly matches the desired ground signature (6). The linear starting signature in (5) shows similar shape but with a reduced disturbance magnitude on the rear ramp. Part of the difference is due to the approximations of far-field volume cuts. CFD results in Figure 25 produce a closer match to the target of (5). The final model geometries are shown in Figure 26.

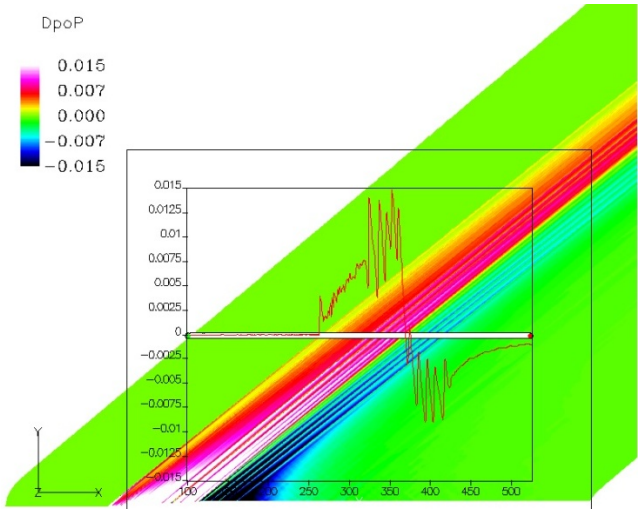

Figure25. OptSig from CFD++ (Radial Solution)

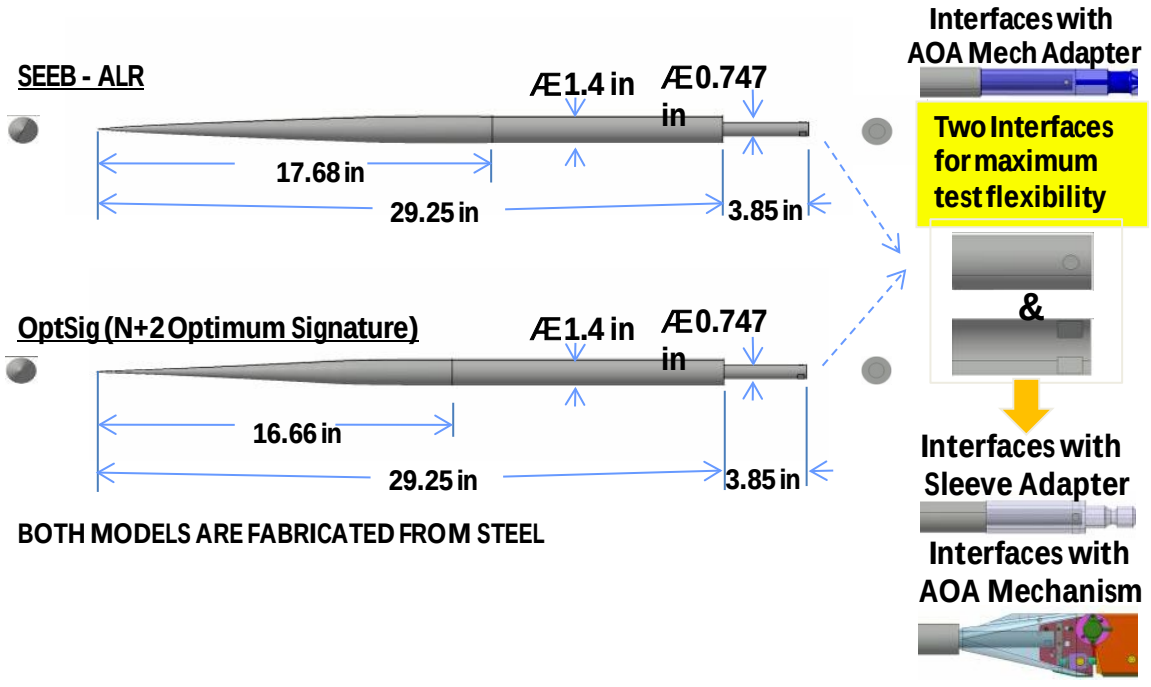

Figure 26. Axi-Symmetric "Javelin" Models' Geometry

In conclusion, the low boom axisymmetric modified SEEB-ALR or “aft lift relaxation” body was planned to be used hereafter for measurement apparatus calibration and pre-test verification. A second low boom axisymmetric body of the N+2 Optimum Signature (OptSig) will be used to validate measurement of a representative N+2 Low Boom signature in the future LM3 Test.

4.2.3 Results From Test LM1 (Ames 97–0220): Measurement Hardware Validation

This first test occurred 11 months into the Base Program. After evaluating test results from previous rail designs, both LM and Boeing concluded that measurement rail redesign was needed for low boom configuration validation. The SEEB-ALR and OptSig models were fabricated for testing with the MSA and the new measurement apparatus. Pre-test predictions were completed. Because of the intent to use the SEEB-ALR model for all pre-test measurement calibration and validation, Boeing was invited to attend all LM testing. NASA also prepared existing models for potential testing (LM1 Test) but only ended up testing the LBWT model developed during NASA’s High Speed Research program of the 1990’s. Under a similar contract, Boeing fabricated a new measurement blade rail.

The main objective of LM1 Test was to validate the Boeing blade rail and new measurement procedures relative to the accuracy required to validate the Low Boom configuration’s sonic boom. In general, we wanted the loudness of a measurement propagated to the ground and to be accurate within ±2 PLdB. In specific signature attributes, this should equate to measuring the signature propagated to the ground such that all shock pressure change magnitudes are within ±0.02 psf (±1 Pa) and shock positions are within ±2 msec. These measurements are more precise than previously achieved, so we added calibration models and new test procedures to find the best tunnel flow and improve measurement accuracy.

The LM1 test began with measuring the SEEB-ALR model to match its known pressure with the new Blade Rail measured pressure, Figure 27. Immediately the SEEB-ALR model revealed problems with pressure measurement accuracy. The expected flat-top signature (shown previously in Fig. 18) was distorted with seemingly random variations of up to ±20 percent from the known flat pressure (but generally centered on the expected pressure) at an H/L of 1.2 (H = 21.2 in.).

Measurement averaging was performed for 60 sec to reduce variability in both model measurements and ambient measurements, which are differenced to get the pressure change due to the model. As shown in Figure 28, there were ambient tunnel pressure changes larger than the model pressure change being measured. H/Ls of 0.6, 1.2, 1.8, 2.4 and XRAMs of 0, 12 and 24 in. were measured to identify the best measurement locations. For shorter signatures of 12 in., locations could be found with distortions less than ±10 percent. During the test, real-time plots of the measurements started to overlay measurements from different distances—showing how the measurement slope variations appeared to repeat with the same ratio from the expected flat value at the same Rail location (for the same Mach and density test condition), Figure 29. To see if the repetition was precise enough to be used as a calibration, we decided

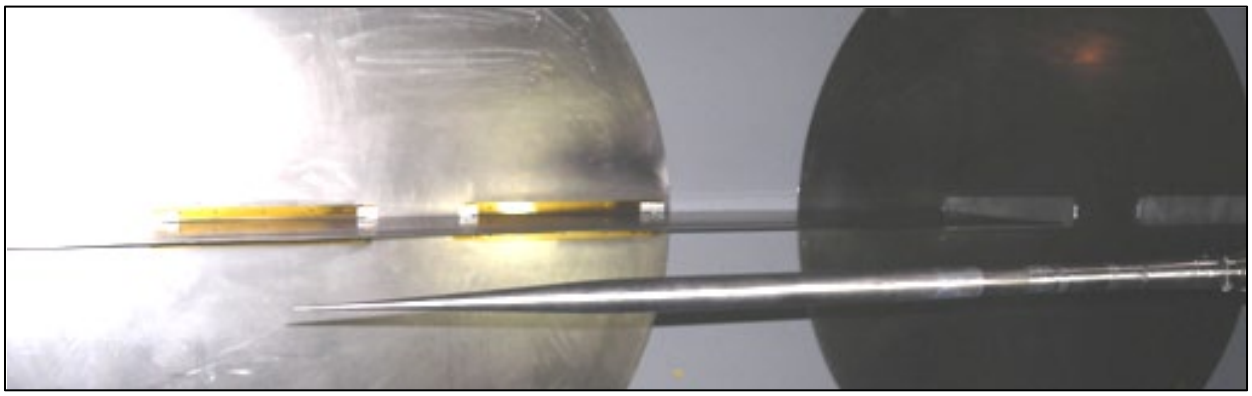

Figure 27. OptSig Model in Ames 9x7 with Blade Rail

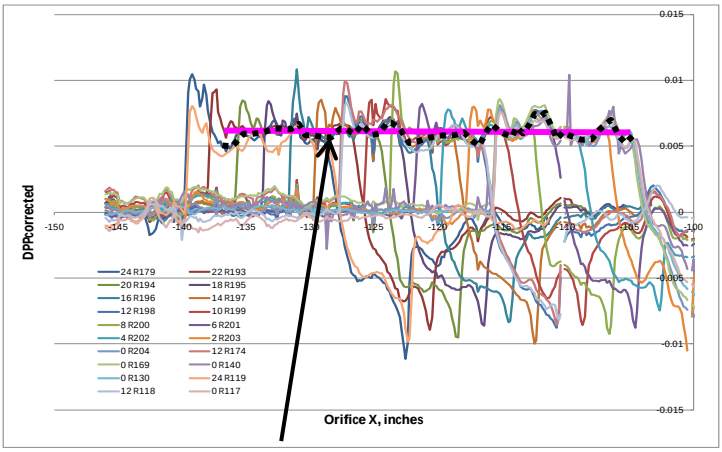

Figure 28. Variations of +/- 20% of Flat-Top Pressure Repeated at the Same Rail Position Despite Different Model Position

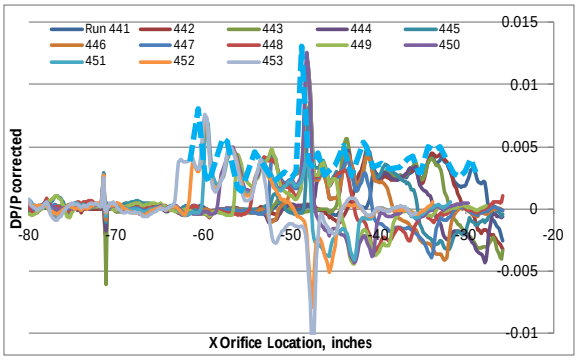

H/L=4.25

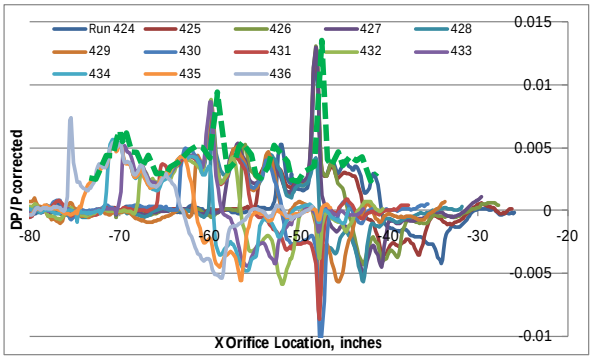

H/L=3.7

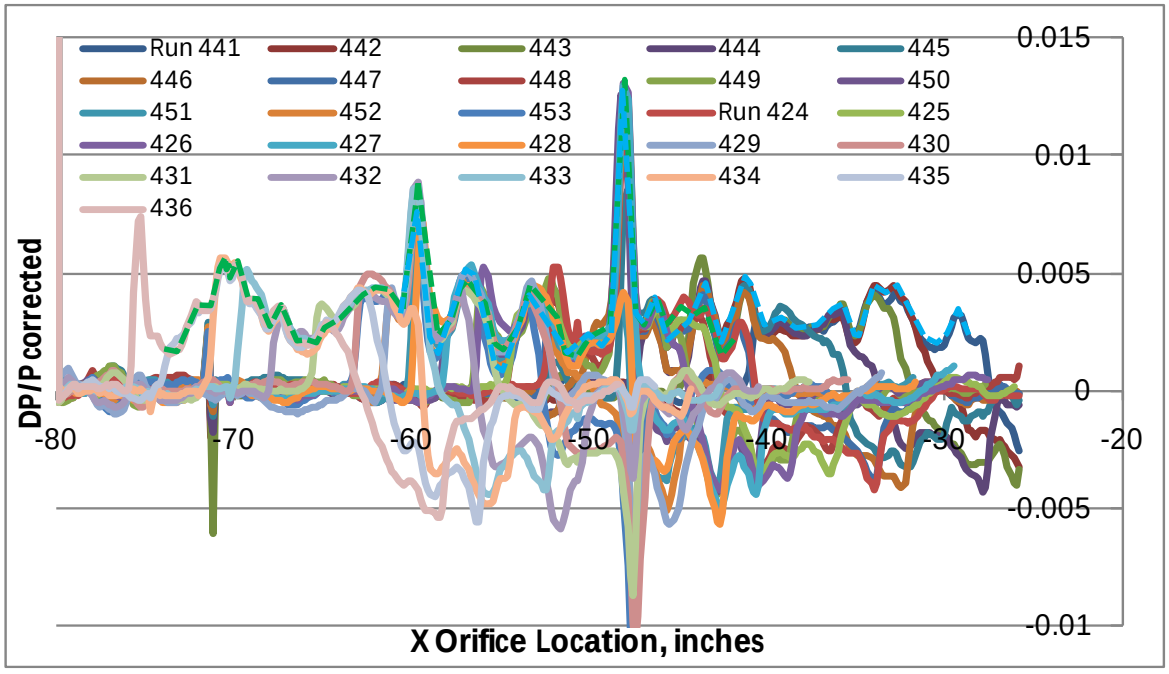

Figure 29. Distortion Pattern Overlays from Different Measurement Distances

to translate the model in 2 in. increments, providing 4 repeats from different portions of the 8 in. front flat. Figure 28 shows the SEEB-ALR measurements from moving the model every 2 in. of XRAM travel (plus 7 repeats) with the dotted black line showing the ±20 percent variability of the clustered data from the front flat portion of the signature compared with the magenta line showing the actual value of the front pressure flat. The flat pressure does show a repeating slope variation with position on the rail. Further testing revealed that the slope variation pattern changes completely when tunnel Mach was changed and when the rail position was moved from the forward to the aft window blank. Hence, the variations follow X-Beta*R Mach lines in the tunnel and do not seem to be linked to any details of the measurement Blade Rail or its instrumentation.

Further testing revealed more curious properties of the pressure measurement slope variation pattern. The rail pattern measured from different model locations with H/L of 4.25 and 3.7 had similar flat distortion magnitude at the same location on the rail. Also the distortion was becoming a larger fraction of the flat pressure at larger distances, ±50 percent at H/L of 4.25. The distortion pattern repeated for the negative pressure flat of the aft portion of SEEB-ALR signature. A similar slope variation pattern was seen but with a curious difference—the pattern shifted 4 pressure orifices further back on the rail, as shown in Figure 30.

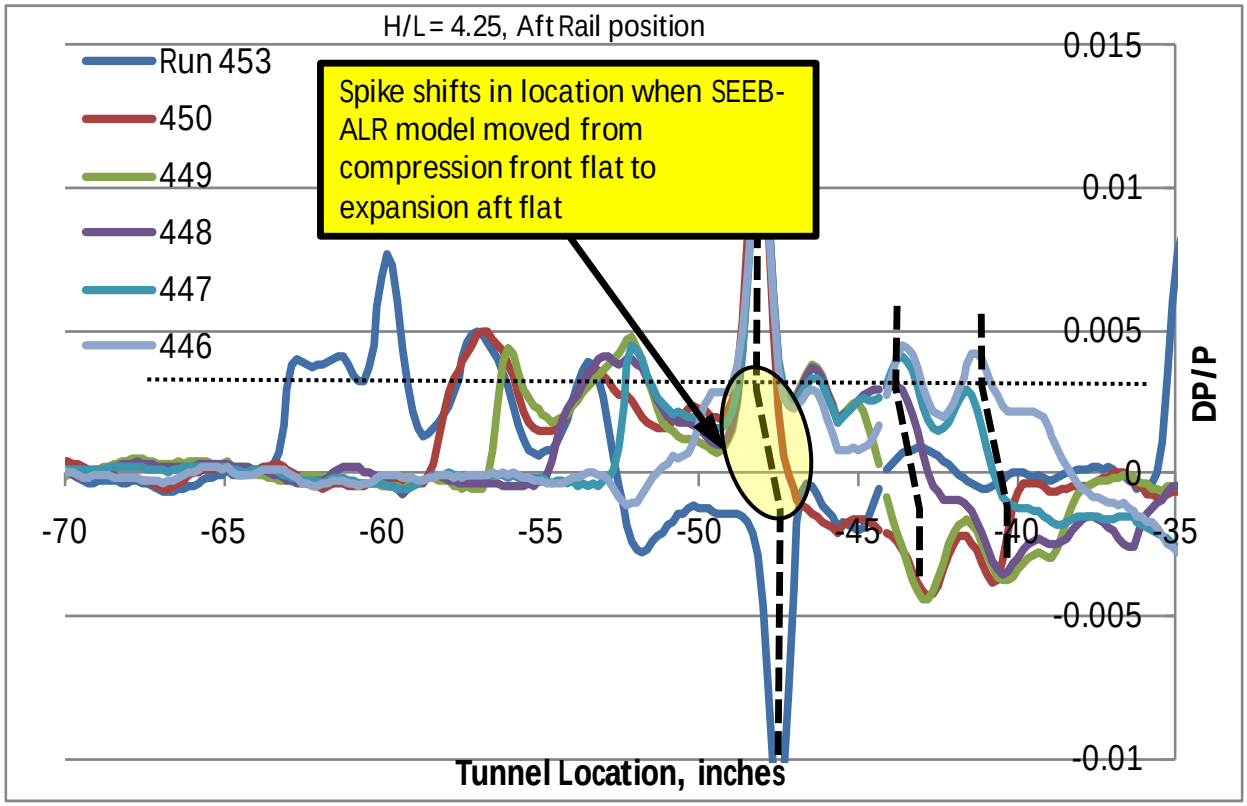

Figure 30. Measurement Sensitivity Spikes Shift with Model Induced Mach Angle Changes

The 4 orifice shift corresponds to the Mach angle shift due to the SEEB-ALR model itself when its pressure disturbance shifts from its positive flat to its negative flat. There are 3 portions of the SEEB-ALR model that produce a flat pressure: the 8 in. front flat, the 2 in. aft flat, and the 11 in. of near zero pressure trailing the signature (where the model has a constant diameter with the area of the cross-section matching the equivalent area of the lift the model was designed to match). The application of ALR makes the trailing delta pressure start close to zero, instead of the significant negative delta pressure at the end of a flat-top that requires more distance to recompress to near zero (ambient). The measurement in the tunnel was subtracted by the predicted value, then the average flat pressure was added back in (to see them separately on the plot), and the points outside the three flat regions were dropped to more clearly see the measurement difference from prediction in Figure 31.

The pattern is from H/L = 1.2 and shows repeatability with more scatter seen in the trailing signature measurement. At this closer distance, the signature trailing measurement shows a substantial distortion pattern (difference from ambient) even though the model is producing zero pressure change. This distortion is not a pressure measurement slope change. At greater H/L distances the distortion is larger relative to the signature (±50 versus ±20 percent at this closer distance), and the mirrored repeatability with 4 orifice shift is more identifiable. To quantify the average slope distortion, the ratio of measurement/prediction for all the repeats of the front flat and aft flat (note, aft ratio is positive) were averaged and plotted in Figure 32. The first plot contains no shift and the second plot with the front/aft ratio patterns are shifted in location to account for the model induced Mach angle change over the propagation distance. The shifted data has a better match, but there is still a difference that may not be due to variations. Since the mismatch represents an offset whereby both the front and aft pressure change flats are shifted in the same direction, the difference was compared with the offset from the signature trailing measurement of Figure 31. The comparison plot in Figure 33 shows an encouraging offset match between the offset calculated from the front and aft flats and the offset from the signature trailing flat.

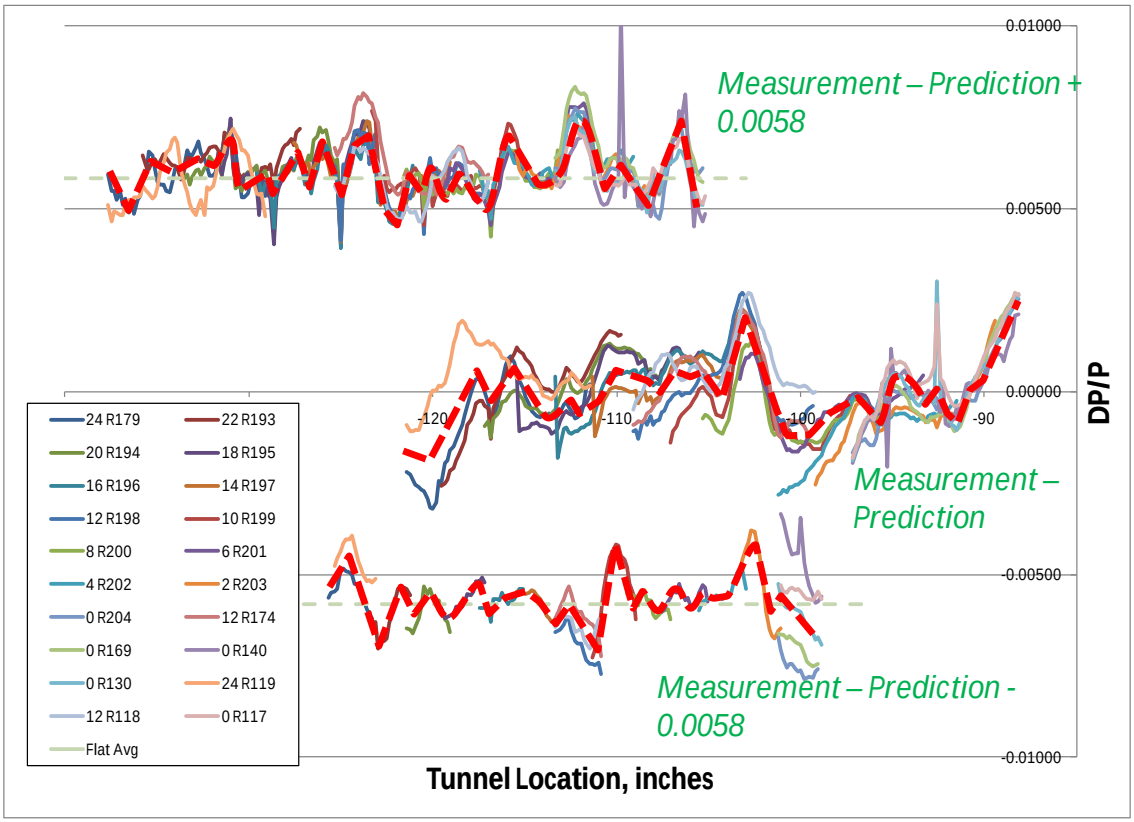

Figure 31. Measurement Differenced by Prediction

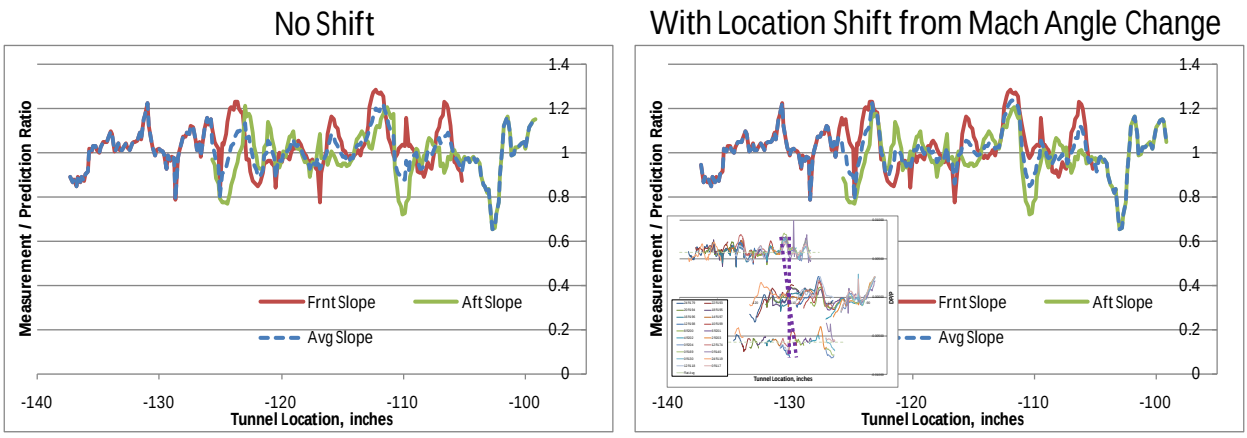

Figure 32. Offset Ratios Align Best with Model Induced Mach Angle Changes

Measurement sensitivity slope variations measured from the positive front flat and the negative aft flat have some mismatch offset—that offset correlates with the offset measured from the zero pressure trailer. Meaning a similar offset is measured from the positive, zero and negative flat regions.

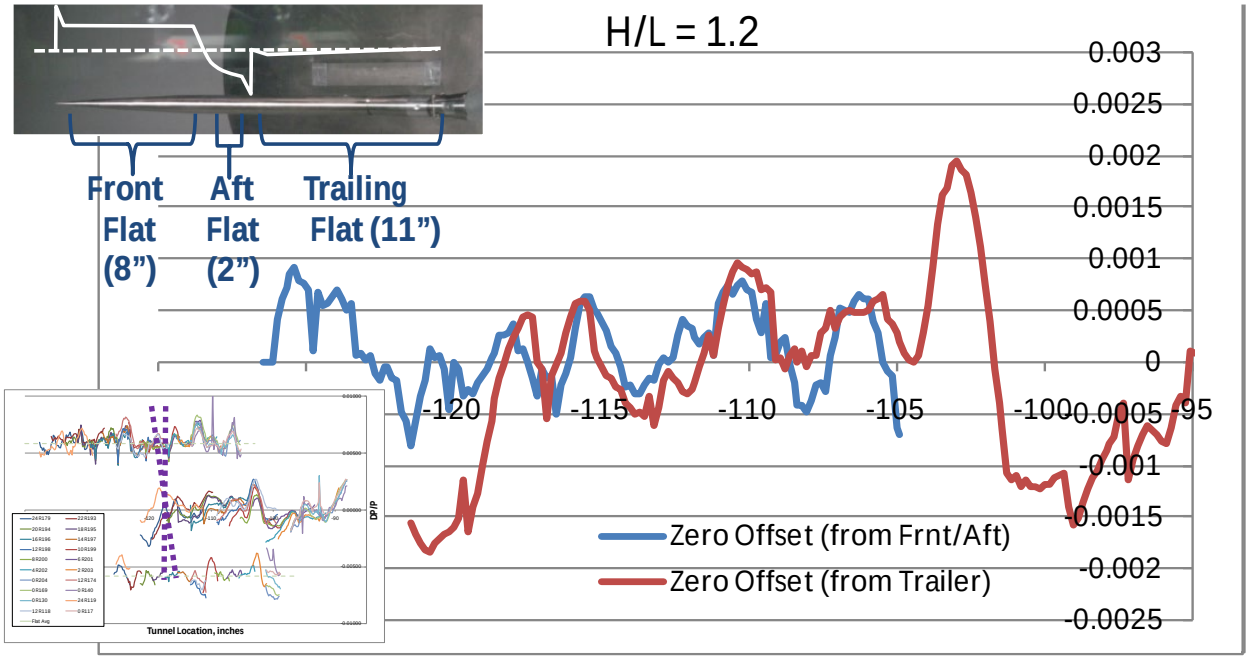

Figure 33. Zero Offsets from Front/Aft Flats and Trailer Match

The measurement slope distortion magnitude (repeating distortion pattern from averaging the ratio of the front and aft flats) becomes much larger (not just a larger percent of the weaker signature, larger in absolute magnitude too) at farther distances. However, the offset magnitude seems to stay in proportion with the signature magnitude getting weaker, by square root of distance ratio, at farther distances. Also, unlike the slope distortion, the offset magnitude pattern is different for any change in model distance from the rail.

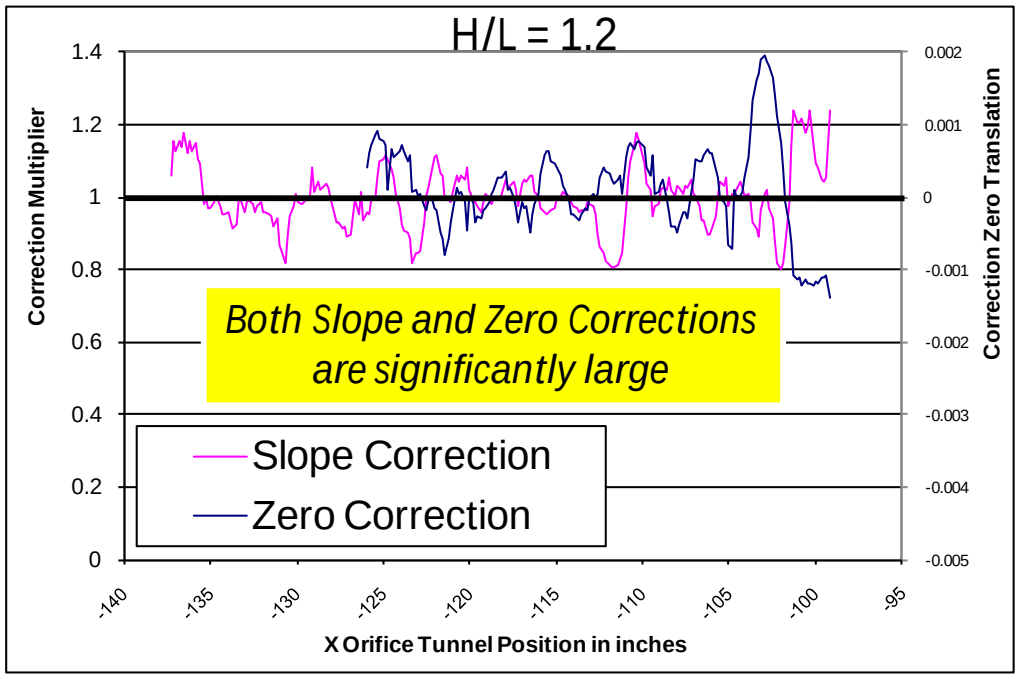

Figure 34. Calibrated Slope and Zero Correction

The SEEB-ALR measurement hardware validation model was used to quantify a measurement slope variation with a different value for each orifice, a measurement offset variation with a different value for each orifice, and each model distance from the measurement rail. This slope and intercept calibration was then assessed for its accuracy when used as a measurement correction. By applying the reciprocal of the distortion ratio and subtracting the offset (from the current measurement distance), a calibrated measurement results. Figure 34 shows a plot of this correction multiplier and zero (offset) correction (dual axes). For the axes' ranges in the plot, a 1.2 multiplier was applied to a 0.0005 delta P over P [DP/P] like the SEEB-ALR flat-top DP/P which matches the secondary axis 0.001 correction value. The effect of the slope and zero corrections were of similar magnitude and similar to the desired accuracy of 0.001 at H/L = 1.2. So the correction was small but not insignificant.

In Figure 35, the OptSig model produced a signature similar to the Low Boom configuration; and therefore, was a relevant case for assessing the accuracy of calibrated measurements. Five signature measurements at three different XRAM positions (0, 12, 24 ft) from the Linear Actuator were assessed. The upper two plots showed their measured location on the Blade Rail. The lower two plots had the signature noses aligned for comparison. In the wind tunnel, models are cantilevered far ahead of the supporting strut and (combined with turbulence from the flow) results in model vibration. For this model and support hardware, it looked like a relatively low ±0.1 in. of motion, which led to the signature measurements being averaged and rounded over a corresponding distance. The refined CFD prediction (data from flow-field pictured in Fig. 25) exhibits extreme spikes, which are nicely matched in position and magnitude after accounting for the wind tunnel measurement rounding. The calibrated measurements on the right matched better and were more consistent with one another. Particularly interesting is the uncalibrated measurement bump at 4.5 in. at the end of the front ramp of the signature that was seen in measurements with XRAM of 0 and 12 in. The bump does not match the prediction; however, despite the fact that it repeats in measurements taken from two XRAM positions, the calibrated measurements changed to match the prediction. However, the calibration did not improve the overall aft signature expansion magnitude difference. Despite rounding the CFD, the measurements had the same average pressure for the spiked part of the front multi-shock ramp approximation. The aft signature measurement always had less expansion than the prediction, so the average expansion was less in the measurement.

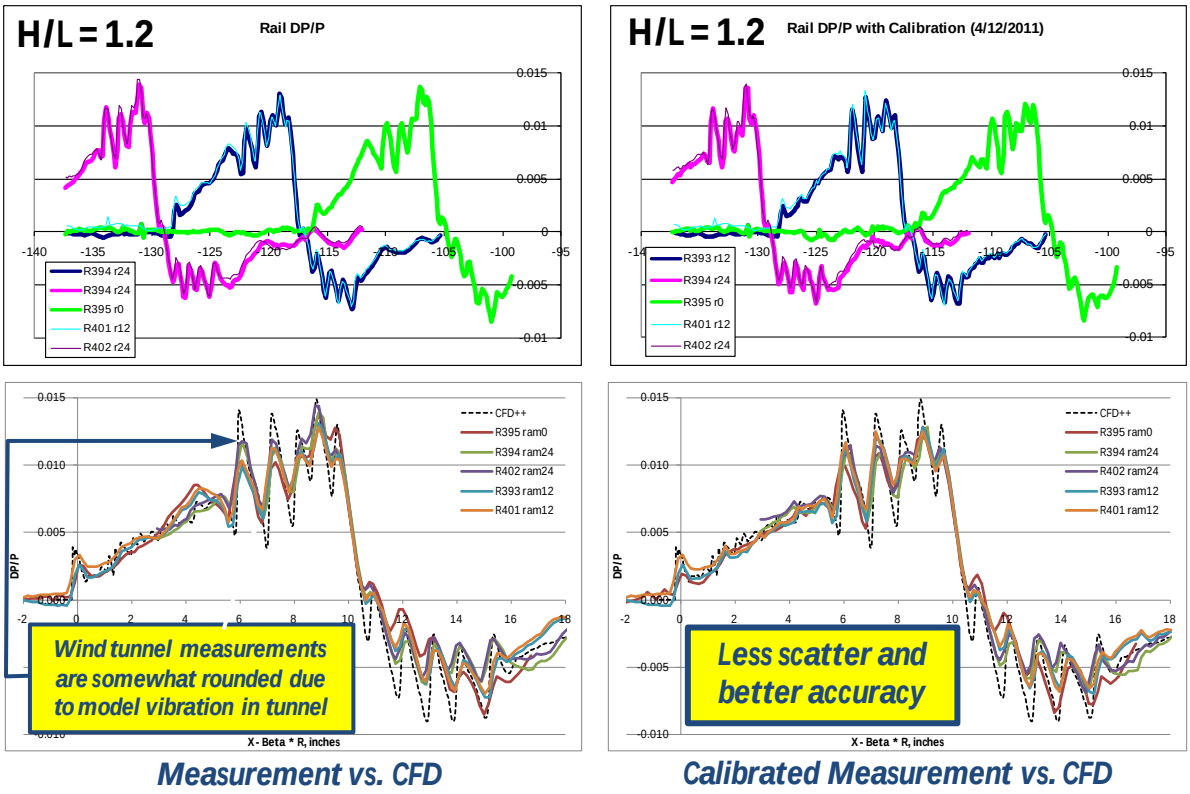

Figure 35. Slope and Zero Correction Improves OptSig Measurements

To quantify the significance of the differences between the measurements, the calibrated measurements and the CFD prediction, the signatures were propagated to the ground using modified linear theory methodology. Ideally the same shocks, with similar pressure change magnitude and similar separation would be present, resulting in a loudness difference of less than 2 PLdB. Figure 36 shows the propagated ground signatures with comments. The average uncalibrated measurement is in dashed red. It had three significant signature differences described in the figure, resulting in more than 2 PLdB difference. The average calibrated measurement, in green, had a very small front shock difference and a more significant coalescence of two of the six aft shocks. While the loudness difference with the prediction was only 1.3 PLdB the difference from two shocks coalescing could have been more than 2 PLdB for a signature where the coalescing shocks happened to be bigger. So the improvement of these calibrated measurements was not seen as being reliably good enough to achieve our goal of better than ±2 PLdB accuracy for any relevant signature.

However, several non-ideal circumstances of these calibrated signatures should be considered for improvement in future testing. The flow for an XRAM of 18 in. looked best for measurements at this distance, but these measurements were trying to survey the flow and were not rerun after finding the best location. The best reference measurement seemed to be one done at the same height and XRAM = 0, but that only worked for measurement XRAM of 18 (greater than model length or more so the measurement is fully ahead of the reference signature location). A smaller calibration XRAM step size was required to get aft signature overlap and repeats with XRAM min and max repeats. In addition, the calibration should be performed as close to the measurements as possible and at as close of conditions as possible (e.g., Same outside weather, humidity, etc.). Acting as the biggest non-optimum for the LM1 measurements, some runs were spread over different weeks.

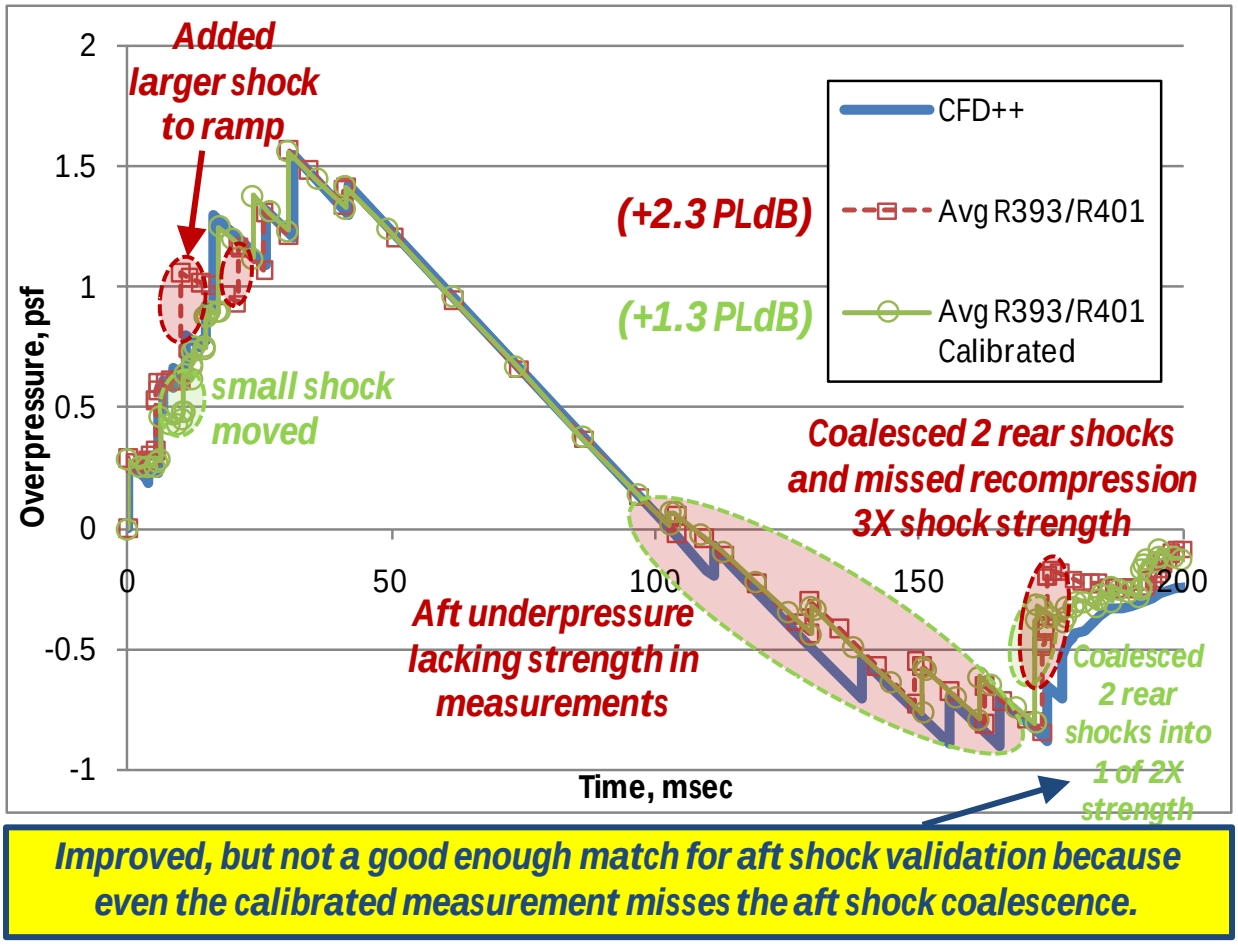

Figure 36. OptSig Propagation to the Ground

Many improvements to calibration and measurement procedures were implemented in the LM3 Low Boom Configuration Test (Ames 97–0231) under Task 3.17 described in Section 6.1.6. A description of the flow-field and a theory of the physics responsible for the observed measurement distortions are presented. Procedures for calibrating and reducing measurement distortion were developed with great success. The resulting measurement accuracy validated the Low Boom design, advancing the program to consider future testing at closer to full scale and closer to realistic atmospheric conditions. A potential factor to improve measurement accuracy includes performing calibration and test measurements within a close timeframe.

5.0 LM2: Spiked Nacelle Flow Sonic Boom Validation (97–0223, WBS 3.4)

5.1 CFD Analysis (WBS 3.4.1)

CFD analyses were performed on the existing Quiet SuperSonic Transport (QSST) High Speed (HS) 3 model to compare and measure operational nacelle effects. Using the 4.7 percent scale representation of the QSST model, the three flow configurations analyzed included; nacelle off, flow-through nacelle and a spiked nacelle at two different mass flow ratios. These runs provide a measure of the nacelle inlet spill, exhaust effects and provide data to validate CFD modeling of propulsion operational effects on full configuration.

CFD solutions were generated using CFD++—a commercial code from Metacomp Technologies. Solution adaptive grid was used to accurately capture the shock wave system which is critical for understanding and optimizing the vehicle's aerodynamic performance. CFD++ is an unstructured Euler and Navier-Stokes flow solver with advanced numerical scheme for computing flows at all flow regimes from low subsonic to high supersonic Mach number flows. A range of Reynolds Averaged Navier-Stokes (RANS) turbulence models ranging from the one-equation Spalart/Almaras model to two-equation k-epsilon models including the realizable and the non-linear models which offer improved predictions and many advantages of the full Reynolds-stress transport model. The k-epsilon turbulence model was used for all HS3 CFD computations.

Shock capturing for accurate predictions of the shock wave system is critical for understanding and optimizing the vehicle's aerodynamic performance. Grid adaptation by clustering grid points towards regions of high flow gradients enables more accurate flow solution with correspondingly fewer grid points and a faster run time. The flow feature based adaptation code (OptiGrid) was used with a driving function based on the pressure gradients to resolve shocks. OptiGrid was fully coupled with the CFD++ flow solver to modify the mesh in order to minimize errors and capture any flow feature accurately and efficiently.

The computational model developed for the HS3 test (Fig. 37(a)) shows a side view of the symmetry plane. The unstructured mesh has a total of about 15M cells. The adapted grid using OptiGrid (Fig. 37(b)) shows mesh clustering down running shocks.

Most of the nacelle-off cases were run inviscid to speed up the computational time and to avoid errors in the adaption method's reading of viscous solutions. Justification for running inviscid was investigated with a limited number of viscous runs. Viscosity was seen to smooth sharp disturbances and lower peak pressures, but the impulse tended to be the same—and impulse is most important for sonic boom matching. Inviscid and viscous solutions also showed the same change in sonic boom from changes in airflow.

Computations were made for a spiked nacelle at two different inlet mass flow ratios (MFR) (defined as the ratio of actual inlet airflow to the airflow of a theoretical stream tube in the freestream with a cross sectional area equal to the inlet capture area). A specified pressure boundary condition was imposed to target a specific MFR that is close to the experimental values obtained with screens of porosities of 82 and 71 percent. Increased spillage is indicated at the lower MFR case resulting in a higher pressure peak.

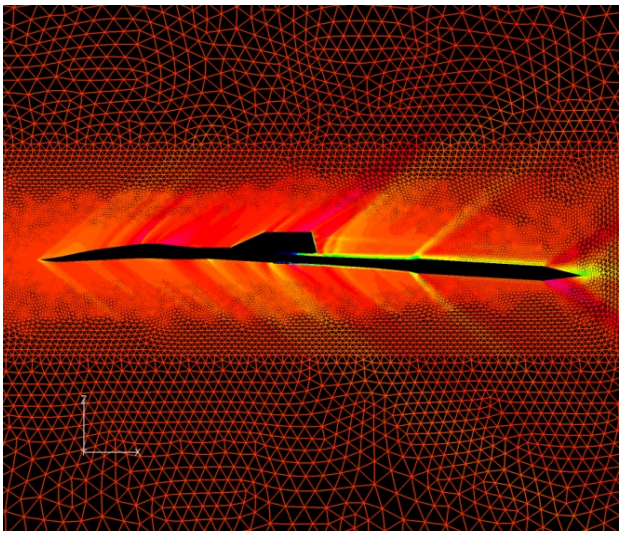

Figure 37a. Initial grid

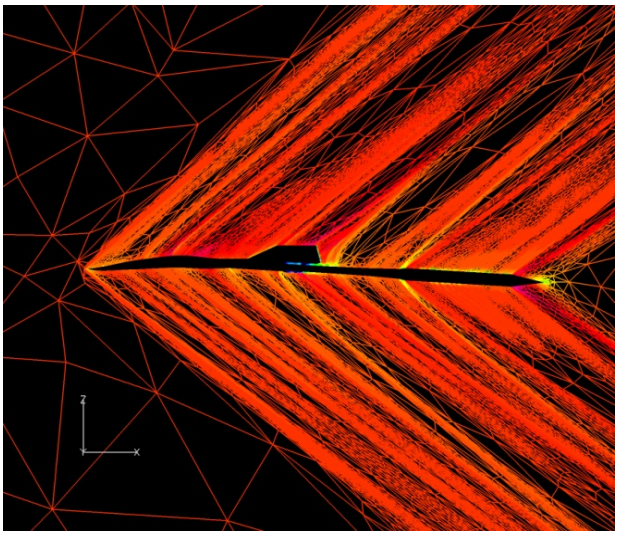

Figure 37b. Optimized (adapted) grid

5.2 Installation and Test (WBS 3.4.2)

LM2: Spiked Nacelle Sonic Boom Validation Testing (97–0223) of the HS3 model was performed in the NASA Ames 9´ 7 ft facility just after the LM1 Measurement Hardware Validation test. The purpose of the one-week test was to validate CFD predictions for operational nacelle conditions using existing hardware to reduce costs. The HS3 configuration (4.7 percent QSST) was previously tested in the Ames Unitary Plan Wind Tunnels in September of 2006.

For the spiked nacelle test, the base model remained the same for all measurements with the exception of the engine nacelle inlet geometry. Two nacelle geometries, one with and one without a spike, were investigated. The geometry with a spike included two different screen configurations; screen 82 and screen 71. The model contained 12 static pressure taps on the body and wing but were not utilized during the test. Due to its size, the model was not mounted on the linear actuator, but directly to the Ames SR-47 0° primary adapter with the SR-34 extension. The Lockheed model uses a rear sting mount for the six-component balance (LMSW-597).

The maximum normal force expected from the Lockheed QSST model was approximately 395 lb (C_N = 0.165, q = 540 psf, Re = 2.5 million/ft, M = 1.8), and the desired resolution of normal force was approximately 4 lb (C_N = 0.002), which is about 1 percent of the maximum force. The maximum pitching moment expected is about –113.7 in.-lb (C_M = –0.00292, q = 540 psf), and the desired resolution is roughly 15 in.-lb (C_M = 0.0003), about 13 percent of maximum.

The model was mounted in wings-vertical and wings-horizontal orientations (0° and 90°) with the majority of the testing with model lower surface facing the north wall. The Boeing 14-in. high sonic-boom pressure rail was mounted at mid height on the north wall and positioned in the rear window blank. The tip of the rail was instrumented with 420 pressure taps that were plumbed directly to PSI top plates for ease of installation and checkout. The distance between the model and the pressure rail (h/L) was varied using the strut heave.

Tolerances for the tunnel flow parameters q, P_T, P_S, T_T, T_S, Reynolds number, and humidity were expected to be the “standard” tolerances used in most tests. Humidity was kept low enough so there was no visible moisture in the test section. The standard tunnel operation started data runs with humidity at 202 ppm or less, with maximum variation of ±25 ppm.

LM, in conjunction with NASA, developed a run matrix that included testing the HS3 model with nacelles off, flow through nacelles, and two spiked nacelles with screens 82 and 71 representing 82 and 71 percent mass flow blockage. Two height/length (H/L) were tested at H/L = 0.302 and 0.496. Sampling duration lasted 5, 10, 20, 30, 45, and 60 sec for a total of 60 sec for data acquisition.

The LM Run matrix highlights include:

- Re = 2.5 million/ft, M = 1.6
- Angle of attack variation for 1, 1.1, and 0.5 of cruise CL (0.15)
- h/L variation: 2-3 locations
- Various nacelle configurations
  - Two nacelle geometries (one with spike)
  - Two screens for nacelle with spike (82 and 71)
  - Nacelles off
- Two roll angles: 0°, 90°
- Pressure rail in aft window blank

A sampling of the run matrix is highlighted in Figure 38.

Lockheed Nacelle Effects Sonic Boom Test 97-0223
Run Matrix — Ames 9x7-Ft Supersonic WT
December 2–9, 2010

Row shading: Reference runs; Repeat runs; Pitch or yaw runs; Imported reference runs; Wind-off rail check points

Black text: user input
Blue text: calculations (do not modify

Nacelles	Screens	Mach	P_T (psf)	Re/L (10^6/ft)	q (psf)	Humidity Target (ppm)	Comments, Run Details (indicate if reference run)	Desired h/L	Model h "above" rail (h/L * L)	Alpha Schedule	Sampling Rate (Hz)	Sampling Duration (sec)	Time Between Start of Data Pts (sec)	Time of Data Acq. (sec)	Model C_L	Model Alpha (deg)	Model Beta (deg)	Model Roll Angle (deg)
		All models run in Mach-PT mode, except SLE, run in Mach-Re mode														Alpha	Beta	Roll m2r
			2116.2	#######														
acelles, inverted stream angle runs, phi = 180°																		
		1.6	1,225	2.408	516	202	Imported ref. run 408 from Test 220				10	60	1	60				
		1.8	1,450	2.667	572	202	Imported ref. run 410?? from Test 220				10	60	1	60				
		1.6	1,450	2.851	611	202	Imported ref. run 407 from Test 220				10	60	1	60				
Flow-thru	None	0.0	2150, 700				Wind-off ref. and data points at atm & 700 psf, 1-sec durations				10	1	1	1				
Off	None	1.6	1,450	2.851	611	202	Imported ref. run 407 from Test 220		0.00		10	60	1	60				
Flow-thru	None	1.6	1,450	2.851	611	400	Pitch run	0.493	39.14	A0	10	1	1	5	0	-1.636	-0.5	180°
Flow-thru	None	1.6	1,450	2.851	611	400	Pitch run	0.493	39.14	A0	10	1	1	5	0	-1.636	-1.2	180°
Flow-thru	None	1.6	1,450	2.851	611	400	Pitch run	0.273	21.68	A0	10	1	1	5	0	-1.636	0	180°
Flow-thru	None	1.6	1,450	2.851	611	400	Pitch run	0.493	39.14	A0	10	1	1	5	0	-1.636	0	180°
acelles, upright stream angle runs and signature runs, phi = 0°									*0.00*									
Flow-thru	None	0.0	2150, 1450				Wind-off ref. and data points at atm & 1450 psf, 1-sec durations				10	1	1	1				
Flow-thru	None	1.6	1,450	2.851	611	202	Pitch run, alpha = -3 to +3	0.47	37.32	A0	10	1	1	5	0	-1.636	0	0°
Flow-thru	None	1.6	1,450	2.851	611	202	Pitch run, alpha = -3 to 0 (higher alpha's too close to strut)	0.28	22.23	A0	10	1	1	5	0	-1.636	0	0°
Flow-thru	None	1.6	1,450	2.851	611	202	Reference run, 77:25. This pt reset as frametype 38 (60-sec pt) to turn off this run as ref. run, being replaced by imported run 407.	0.99	78.61	T1	10	5,10,20,30,45,60	5	60	0.451	8.499	0	0°
Off	None	1.6	1,450	2.851	611	202	Imported ref. run 407 from Test 220		0.00		10	60	1	60				
Flow-thru	None	1.6	1,450	2.851	611	202	Set CL to within ±0.001, note alphas,	0.47	37.32	T1	10	5,10,20,30,45,60	5	60	0.075	0.049	0	0°
Flow-thru	None	1.6	1,450	2.851	611	202	use these alphas for rest of test	0.47	37.32	T1	10	5,10,20,30,45,60	5	60	0.15	1.735	0	0°
Flow-thru	None	1.6	1,450	2.851	611	202		0.47	37.32	T1	10	5,10,20,30,45,60	5	60	0.165	2.072	0	0°
Flow-thru	None	1.6	1,450	2.851	611	202		0.333	26.44	T1	10	5,10,20,30,45,60	5	60	0.165	2.072	0	0°
Flow-thru	None	1.6	1,450	2.851	611	202		0.333	26.44	T1	10	5,10,20,30,45,60	5	60	0.15	1.735	0	0°
Flow-thru	None	1.6	1,450	2.851	611	202		0.333	26.44	T1	10	5,10,20,30,45,60	5	60	0.075	0.049	0	0°
Flow-thru	None	1.6	1,450	2.851	611	202	"Reference" run with no FT 35 pts	0.99	78.61	T1	10	5,10,20,30,45,60	5	60	0.451	8.499	0	0°
Flow-thru	None	1.6	1,450	2.851	611	202	Pitch run, alpha = -3 to 3	0.333	26.44	A0	10	1	1	5	0	-1.636	0	0°

Figure 38. N+2 HS3 Run Matrix Sampling

5.3 Results (WBS 3.4.3)

During the spiked nacelle test, comparisons of the pressure signature tested on the HS3 model and those obtained from CFD were obtained. Figure 39 illustrates the incremental results of CFD predictions as they compare to HS3 test results. From these results it is evident that CFD can accurately predict sonic boom increments from an operating nacelle including inlet spillage and mass flow variations.

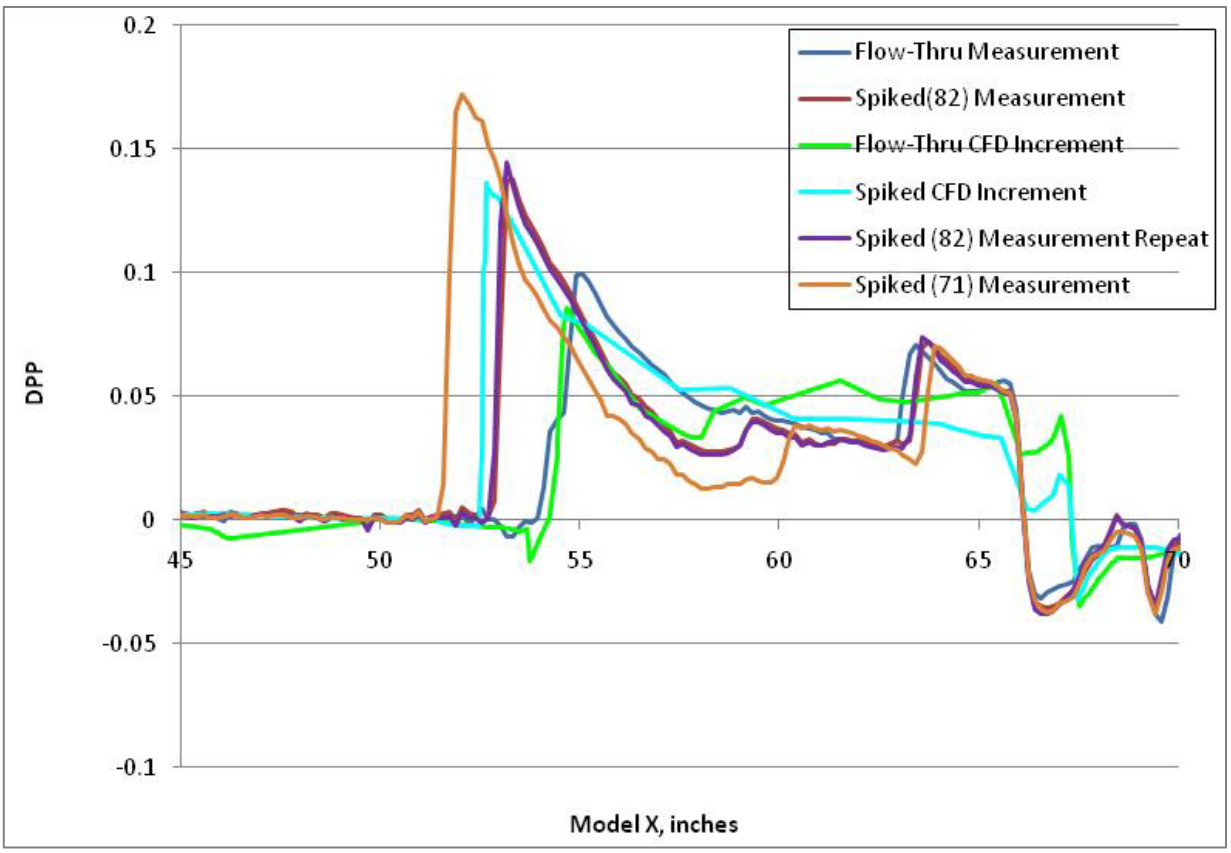

Figure 39. CFD and Test increments

6.0 LM3: Low Boom Validation Model and Test (97-0231)

6.1 Low Boom Validation Model (WBS 3.3)

6.1.1 Aft Shock Demo Design (WBS 3.3.1)

The objective of the N+2 low boom validation model activity was to develop a supersonic transport design shaped for front and aft sonic boom signatures. The loudness undertrack and up to 20 degrees off-track was requested by NASA to be a no more than 85 PLdB at maximum fuel weight start of cruise, for at maximum fuel load 4000 nm range mission, and a 1 msec/psf shock rise time. Obviously, this maximum weight is a worst case condition. Also, this 1 msec/psf rise time is worse than the 3 msec/psf (and often even larger for our weak shocks) typical for real atmospheric measurements; however, this level was fine for a design requirement. Furthermore, an assessment of typical aircraft loudness will also be shown for the final design (Section 6.1.2 in Fig. 60(b)). This effort used the final N+3 design from NASA contract NNC08CA84C as the starting point for the vehicle design and concluded with a successful design that met this intermediate N+2 loudness requirement. And while this loudness requirement does not meet the 65 to 70 PLdB of NASA's initial goal, our average loudness assessment of 79 PLdB is getting very close to what we believe would be acceptable for over land flight; while just as importantly, this design maintains characteristics and performance suitable for a practical and successful transport. On-going refinements will further reduce loudness while improving upon the performance that already meets the initial performance goal.

6.1.1.1 Design Methodology

The N+2 aft shock demo design effort was performed using a Rapid Conceptual Design (RCD) model that facilitates the prediction of sonic boom signatures using CFD (Fig. 40). This model uses CATIA V5 for lofting and surface mesh generation, AFLR3 for volume grid generation, and can be used with multiple CFD solvers such as CFD++. At the start of the N+2 design effort a combination of CFD++ and Optigrid were respectively used for generation of the flow solution and adaptation of the volume grid to improve resolution of the sonic boom features. During the course of the program, the model was significantly enhanced to incorporate superior flow solution and adaptation procedures as described later in this report.

The low boom design process begins with the creation of a parametric CATIA V5 loft that represents the essential features of the configuration being investigated. Power copies are used to rapidly generate different aircraft concepts and are joined and trimmed, resulting in a watertight loft suitable for meshing. A surface mesh is then created from the loft in the CATIA V5 FMS workbench. Mesh parameters including size and structure and tailored to produce a quality surface triangulation with a reasonable number of elements. For this program, surface triangulations were typically about 100,000 elements.

A major benefit of using the FMS license within CATIA for surface meshing, as opposed to traditional CFD meshing packages, is that the mesh is fully associative with the surface geometry, meaning, new meshes can be generated "hands off". The surface mesh is then used to grow a volume mesh using AFLR3 (Fig. 41). AFLR3 is a relatively robust tetrahedron grid generator that produces the UGRID files required by the different flow solvers used on the N+2 program.

Both the NASA FUN3D and commercial CFD++ flow solvers were used to perform design work on the N+2 program. At the start of the program, CFD++ was used with the commercial feature-based grid adaptation program Optigrid to generate flow solutions for design studies. However, it was found to be difficult to tweak control parameters in Optigrid to achieve good results at large distances from the body. The ability of FUN3D to perform adjoint-based adaptation led to its adoption for further work, and yielded improved results compared to the CFD++/Optigrid approach. Towards the end of the Phase I design work on N+2, a method inspired by work performed at NASA was implemented in CFD++ that combines an unstructured grid around the vehicle with a structured grid of Mach-aligned stretched prisms, Figure 42. This new method yielded results superior to those of the adjoint-adapted FUN3D approach and at lower computational cost.

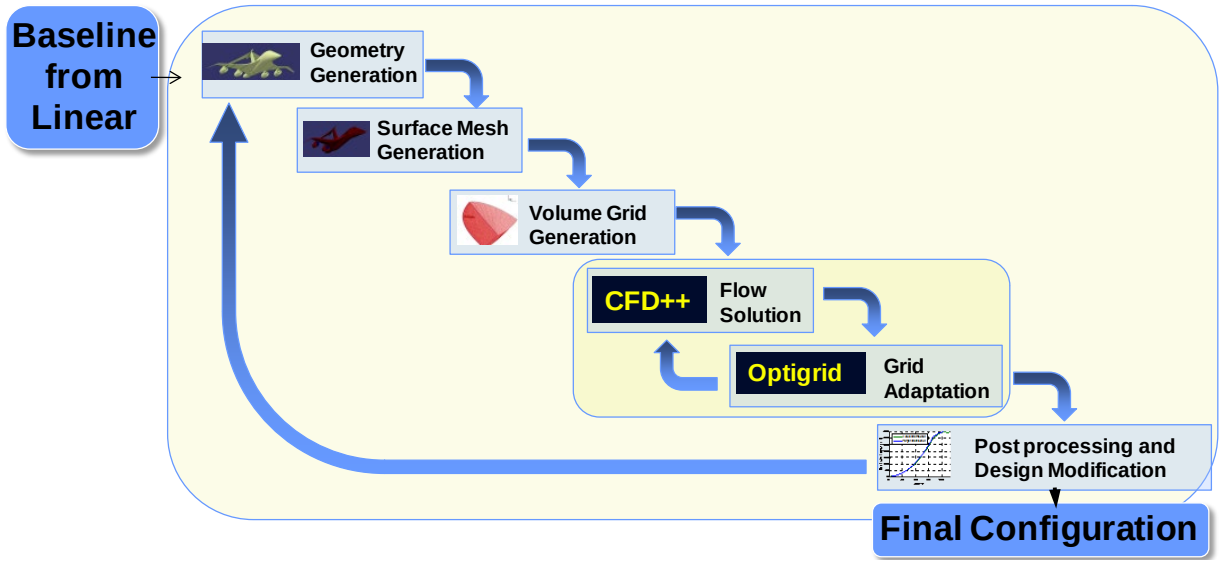

Figure 40. N+2 design tools enabled rapid iteration of low boom concepts

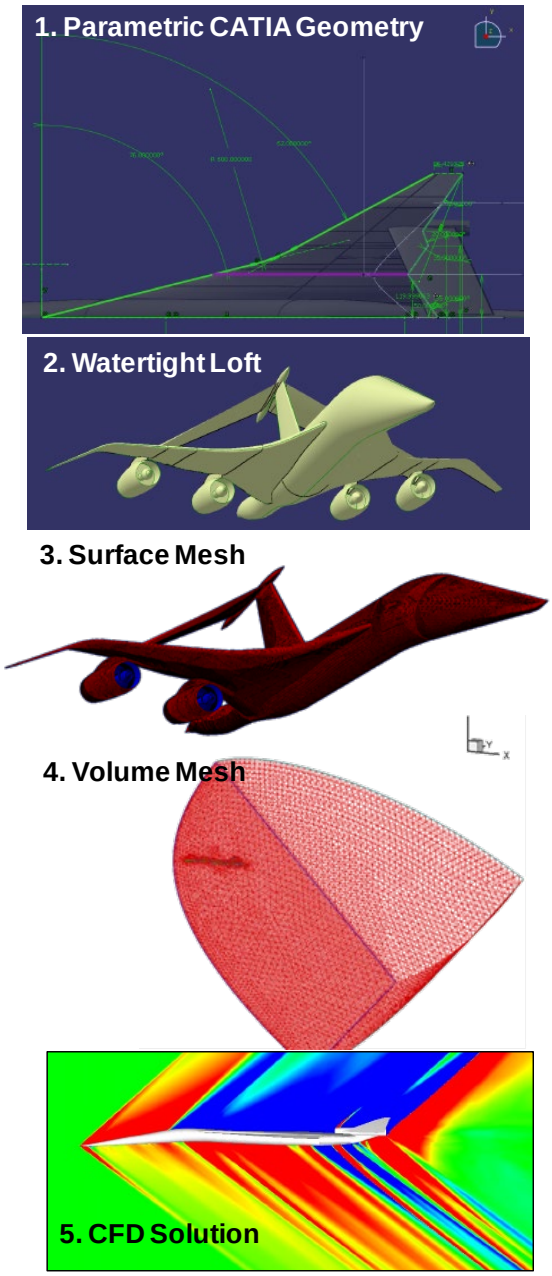

Figure 41. Associativity between parametric CAD and CFD models enables rapid generation and evaluation of low boom design concepts

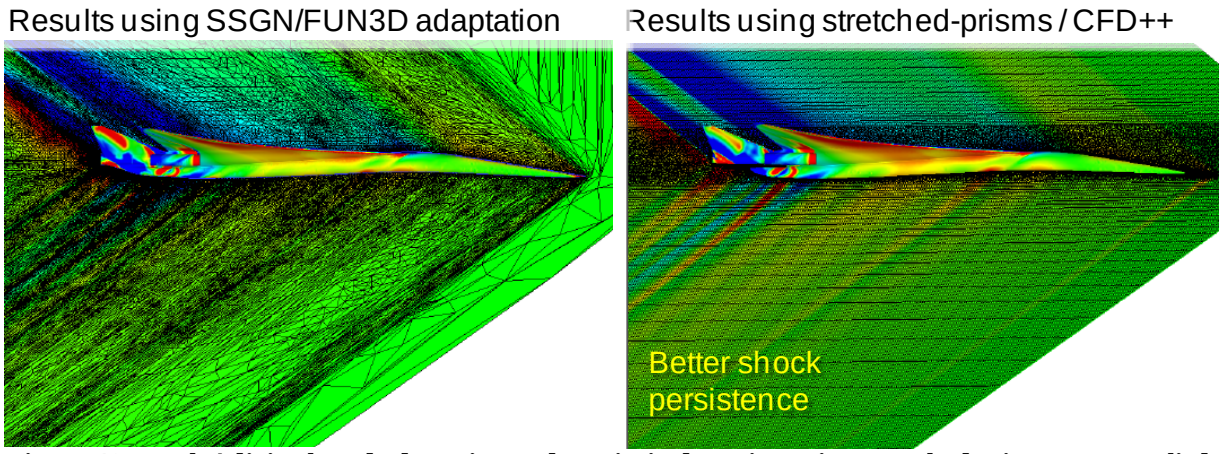

Figure 42. Both Adjoint-based adaptation and a-priori adaptation using stretched prisms were applied during the N+2 low boom design process

6.1.1.2 Configuration Design

The N+3 design (Fig. 43) was designed using linear analysis tools to have an undertrack shaped boom signature; however at the conclusion of that contract, the N+3 design had not been analyzed using more accurate Euler-based sonic boom analysis tools. Analysis of the N+3 design using Euler-based methods revealed that the inverted V-tail was not producing as much lift as predicted by the linear tools due to interference with the wing. For constant lift, this requires more lift from the wing and results in an N-wave ground signature undertrack.

The baseline design was modified as shown in Figure 44 in an attempt to recover the good low-boom performance predicted by the linear analysis tools. Relatively good shaping was achieved on the front portion of the ground signature, but it proved time intensive to prevent coalescence of the aft signature with the inverted-V configuration. Although the inverted-V design provided aeroelastic advantages over other configurations, the N+2 team decided to take the design path that offered the least resistance. A modified configuration was developed with a conventional empennage instead of the inverted V-tail. This new configuration, dubbed the "2+2", improved performance relative to the baseline and prevented complete coalescence of the aft signature (Fig. 45).

The inability to completely meet the 85 PL dB goal using manual design iterations led to a change in approach for N+2 low boom design work. Drawing upon method development efforts that had been on-going under IRAD, we developed a new Trijet configuration that uses an aft centerline nacelle with a V-tail for aft lift generation (Fig. 46). Engine scale of the new configuration was increased to keep constant thrust.

The new Trijet configuration was designed using a response-surface based approach for matching the equivalent area distributions as predicted by CFD to the target OptSig equivalent area distribution, Figure 47. In this approach, a number of design variables thought to have an impact on the aft portion of the signature were selected and used as inputs to create a Design of Experiments (DOE).

This DOE was used to execute approximately 50 separate CFD runs as required to create the response surface equations that represent the sonic boom. After regression was performed in JMP, the equations were imported into Microsoft Excel (Microsoft Corporation), where Excel Solver was used to minimize the deviation from the target OptSig distribution (Fig. 48). A well tolerated modification was made to the undertrack signature to improve off-track performance for minimal undertrack loudness penalty. Over the rest of the distribution, the optimizer was able to successfully achieve a deviation (expressed in equivalent area) of less than a square foot over the entire length. This precision of signature matching had not been possible to achieve with manual design methods.

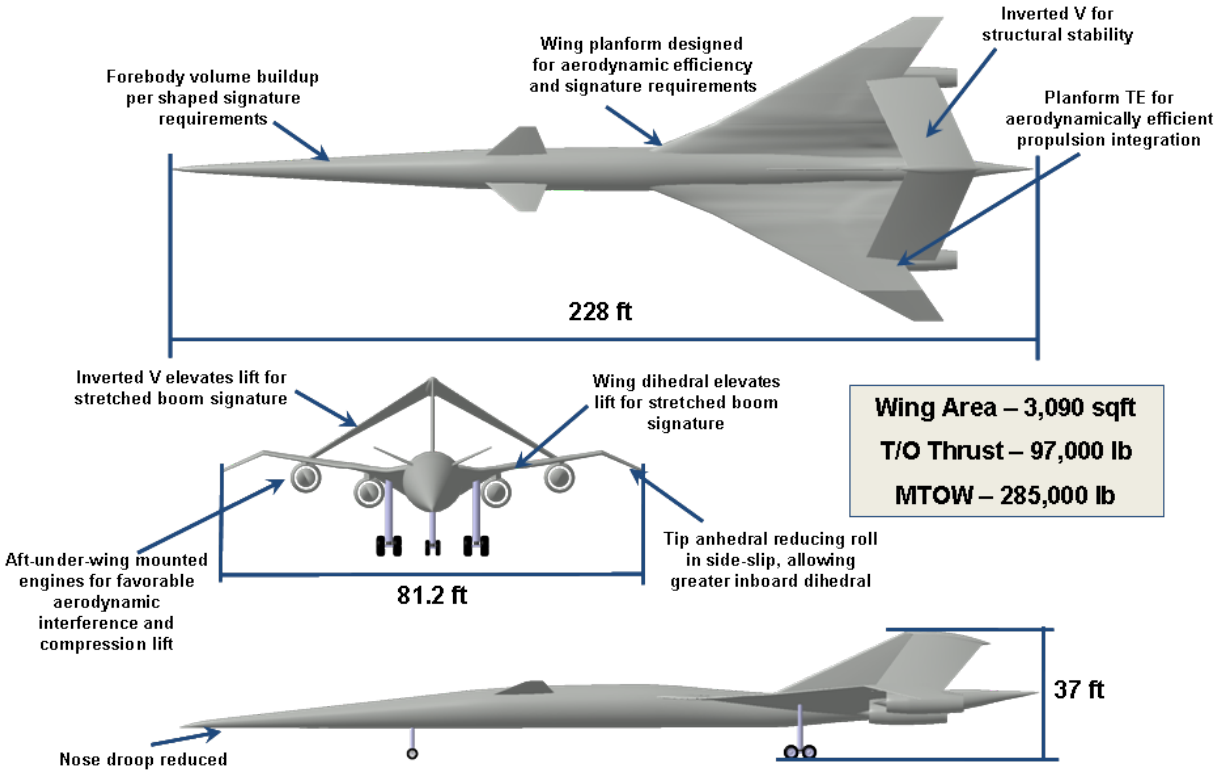

Figure 43. The N+3 design represented the start for N+2 design activities

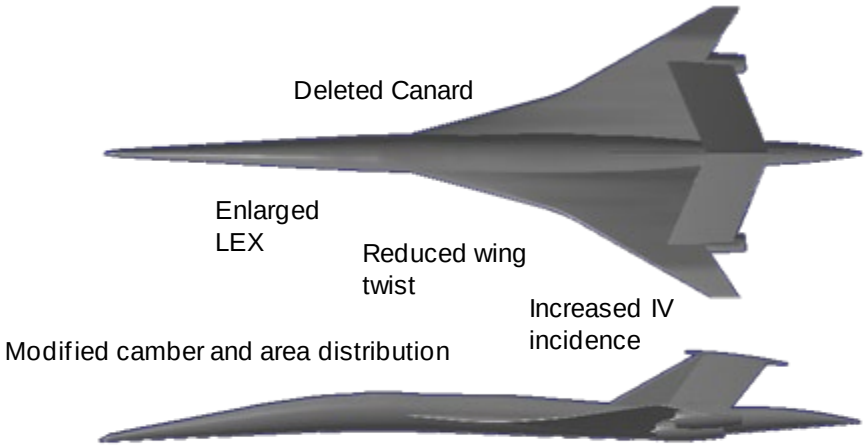

Figure 44. Modifications to the baseline N+2 improved the front signature significantly but were unable to prevent coalescence of the aft signature

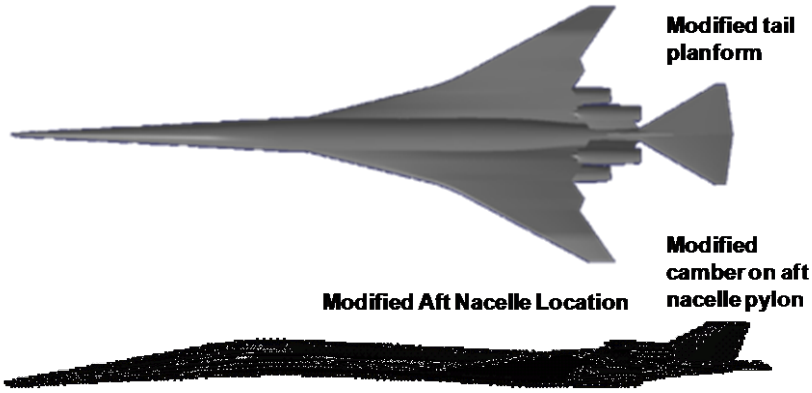

Figure 45. The "2+2" alternate configuration improved aft signature shaping relative to the Inverted-V configuration but did not meet the 85 dB loudness goal

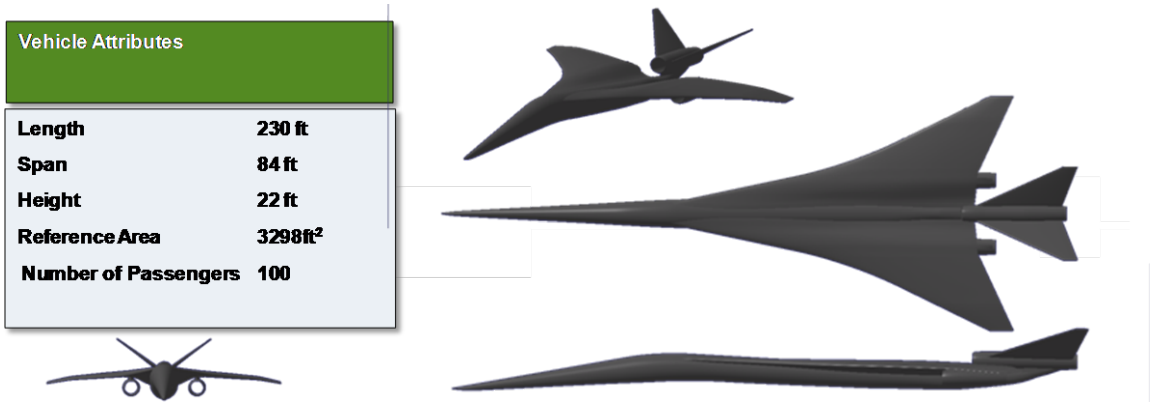

Figure 46. The Trijet configuration was adopted for boom refinement studies based upon promising earlier promising results from the 2+2 concept, but takes advantage of a V tail to stretch lift aft and improve the rear signature

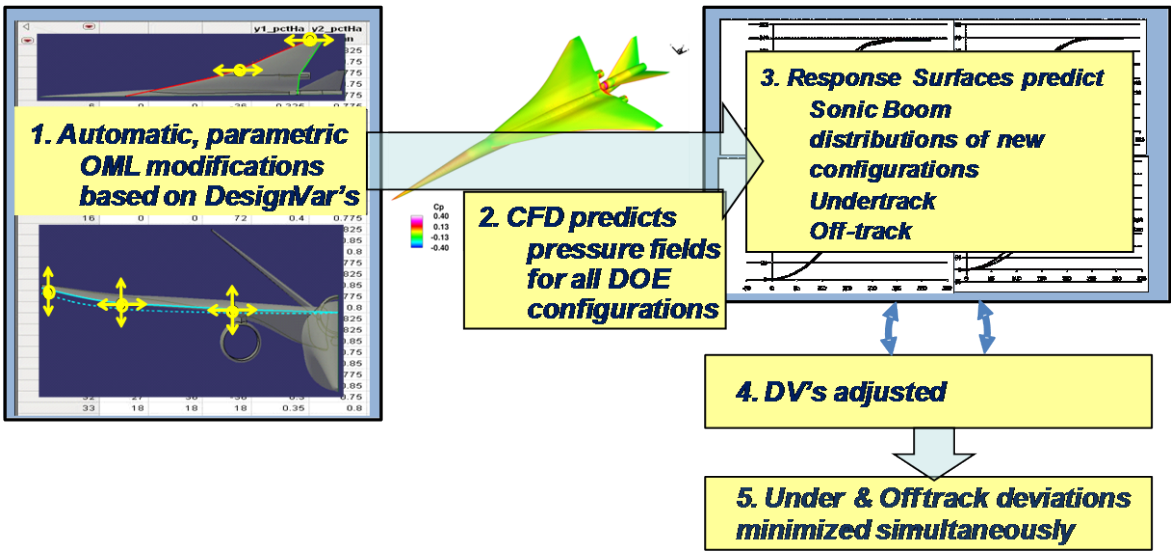

Figure 47. Response surfaces of the vehicle's equivalent area distribution were generated and optimized to minimize deviation from the optimum signature targets

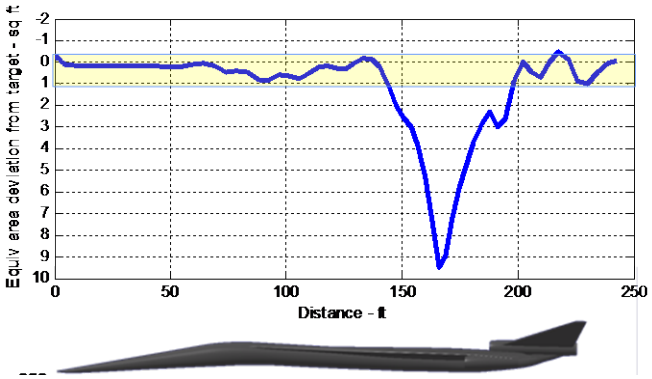

Figure 48. The response surface method was used to match the undertrack to within ±1 sq ft

The near-field signature of the optimized configuration, shown in Figure 49, was propagated using typical far-field methodology after applying a near-to-far correction method (4) using LMBOOM. The signature was extracted from the CFD solution at both 0.5 body lengths and 1 body length, and yielded similar results when propagated to 3 BL and to the ground. This near-to-far correction methodology's ability to extract signatures from the CFD solution closer to the body, while retaining accuracy, significantly reduces computing requirements for low boom design work.

The ground signatures of the January low boom Trijet configuration at start of cruise (SOC) and end of cruise (EOC) are shown in Figure 50. The SOC undertrack signature is slightly quieter than the 85 dB PL loudness goal and exhibits a well-shaped aft ramp.

At 10 and 20 degrees off track the signature remains shaped, however the aft ramp combines into two shocks with a significant impact on loudness for those cases. For all cases, the EOC loudness values are 4 to 5 dB quieter than the SOC values due to the need for left lift and corresponding higher altitude.

The increased loudness off-track was not surprising since undertrack loudness had been the goal of the design work up to that point. It was felt that off-track loudness could be improved without significantly impacting undertrack loudness, so additional design work continued, eventually resulting in the QR4 configuration (Fig. 51).

6.1.1.3 Winglet Studies

6.1.1.3.1 Description

CFD visualization of the QR3 low-boom configuration showed that the expanding low-pressure region coming off the upper wing surface intensifies the boom signature between 30 and 60 degree off-track. Three winglet concepts, as shown in Figure 52, were investigated to modify the shape of the expansion bubble: upward-swept blended winglet; downward-swept blended winglet; and wing tip fence.

6.1.1.3.2 Results

As shown in Figure 53, the wing closeout concepts evaluated have incremental effects on the expansion bubble, but did not significantly lower the off-track boom strength.

As a boom signature control feature, the winglet/wingtip fence has negligible effect on the off-track loudness.

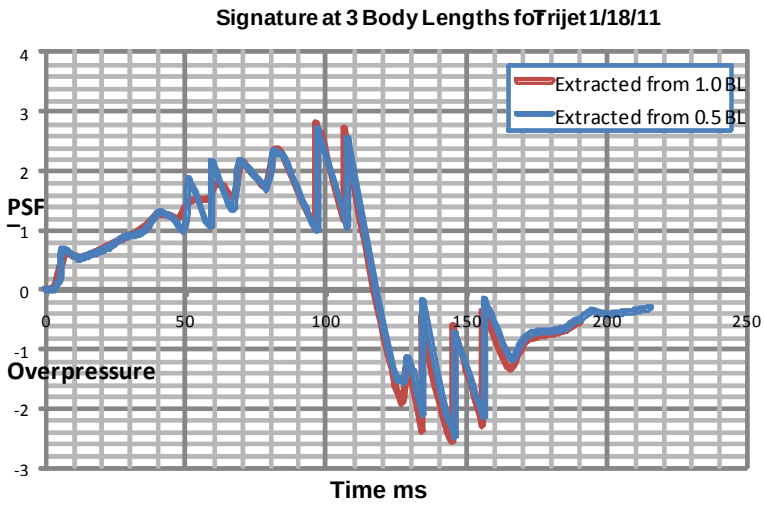

Figure 49. Use of the near-field cylinder correction method permits extrapolation of signatures from CFD solutions at only 0.5-1 body lengths, significantly reducing computational burden

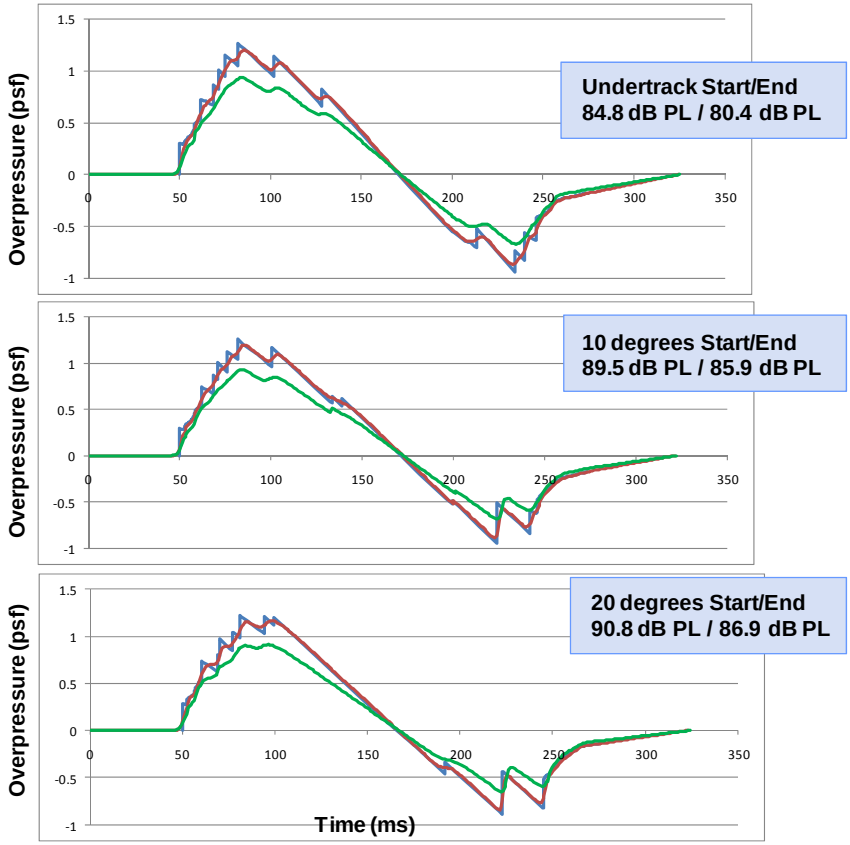

Figure 50. The loudness of the optimized Trijet configuration was reduced to below the 85 PL dB undertrack

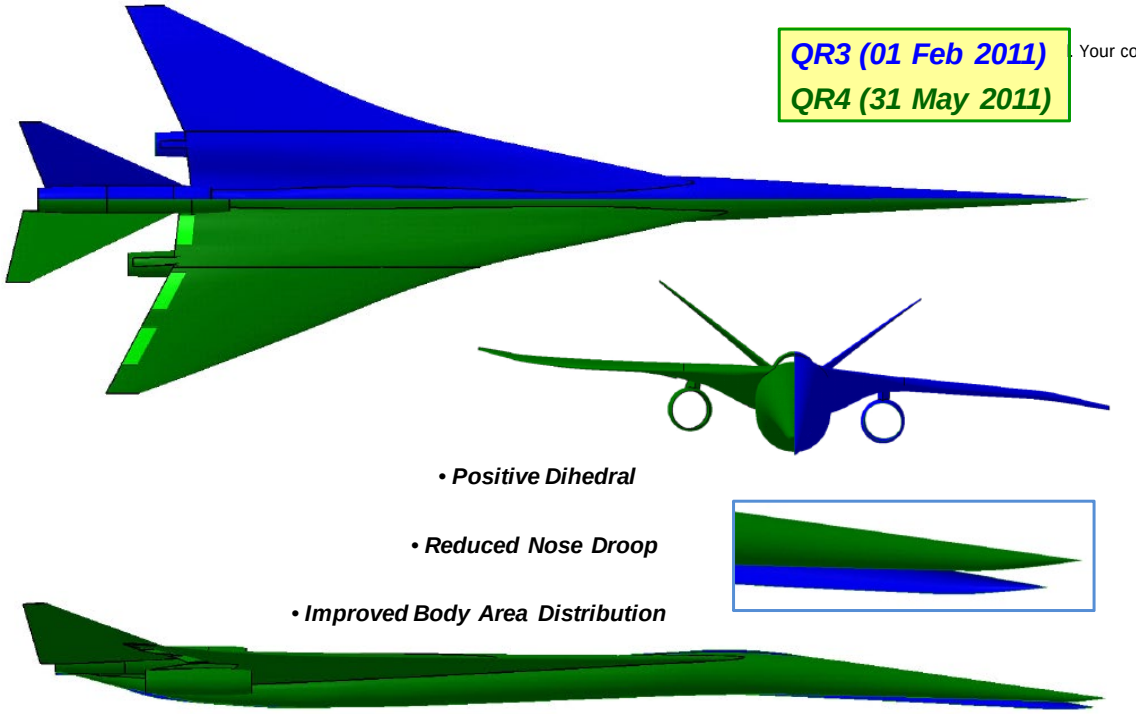

Figure 51. The design of the trijet N+2 configuration was significantly modified between QR3 and QR4 to improve off track loudness while retaining good under-track performance

Figure 52. Winglet concepts

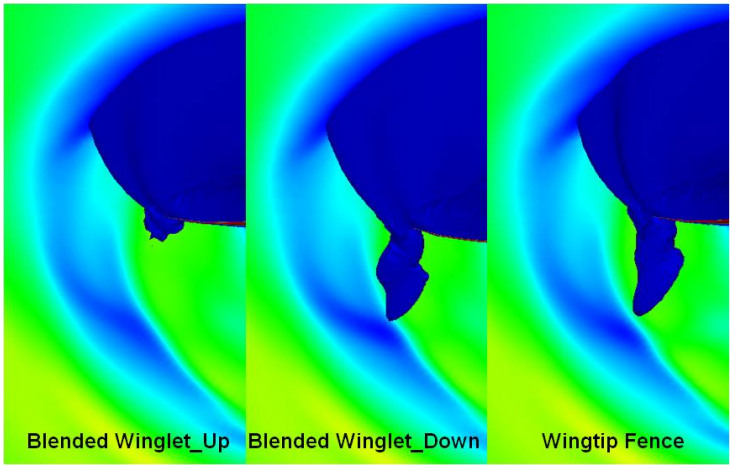

Figure 53. Winglet concepts

6.1.1.4 Area Rule Studies

6.1.1.4.1 Description

Three concepts were evaluated to smooth out the off-track area distribution: anti-shock bodies; outboard relocation of the tail; and wing trailing edge extension. In the first concept, the wing-mounted engine pylon was extended aft and enlarged to provide additional cross-section volume. In the second concept, the v-tail was divided up and relocated to the wing-mounted engine pylon to improve the wing-tail overlap at higher off-track angles. In the last concept, a trailing edge (TE) extension was added between the fuselage and wing-mounted engine pylon to provide structural support and additional lift and volume.

6.1.1.4.2 Results

Figure 54 shows the 30 degree off-track area distribution comparison of the various concepts evaluated. As shown, the TE extension concept removed the discontinuity in the area curve around FS 2,450, resulting in improved L/D at cruise. In addition, the TE extension provided structural relief to the pylon supporting the engine the tail, potentially lowering the structure weight.

6.1.2 Final Phase I Low Boom Design Refinement

These modifications significantly improved the aft portion of the signature in the recompression region off-track by eliminating the strong expansion regions that had been present in the QR3 Trijet design (Fig. 55). The ground signatures for the QR4 configuration at the SOC weight and altitude (Fig. 56) show that the QR4 Trijet rounds to 85 PLdB (1 msec/psf) and lower from undertrack to 30 degrees off track (and at carpet edge, too), and over the full carpet at mid-cruise and EOC conditions. The general trend is that loudness should typically decrease off track, due to lift generally decreasing as cosine of the roll angle away from the vehicle centerline and the greater propagation distance through the atmosphere; however for the QR4 configuration, some aft shock separation breaks down beyond 20 degrees and coalesce into a larger shock while increasing loudness. These small anomalies should be cleaned up in the on-going refinement work by further effort and application of the Adjoint-based optimization methods currently being developed with Stanford.

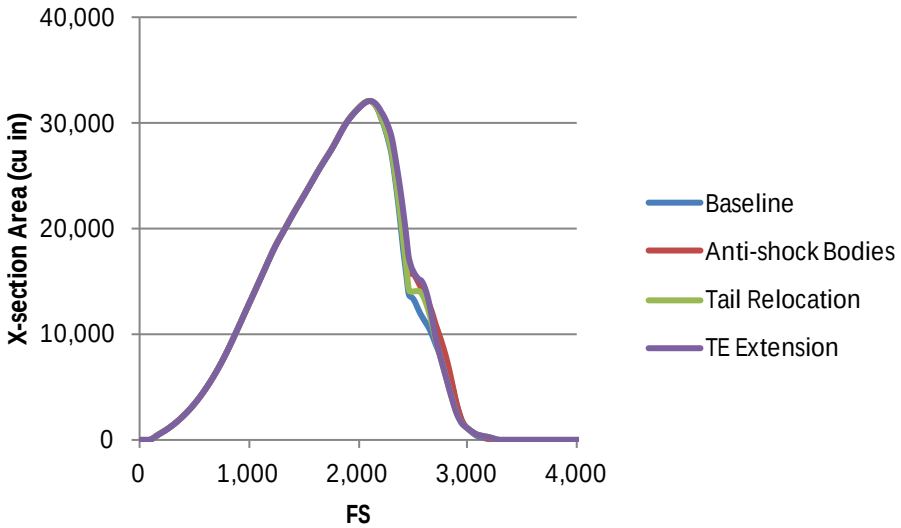

Figure 54. Area distribution comparison

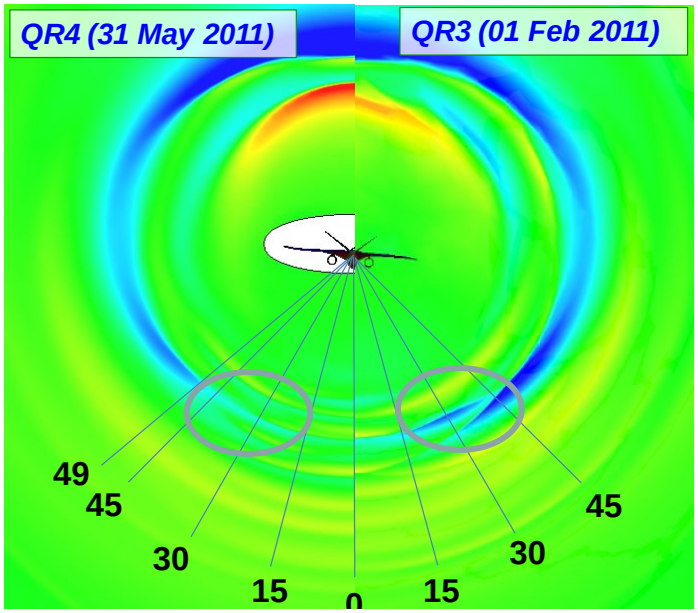

Figure 55. Design refinements between QR3 and QR4 significantly reduced the magnitude of the expansion spike and resulted in a shaped signature to almost 40 degrees off-track

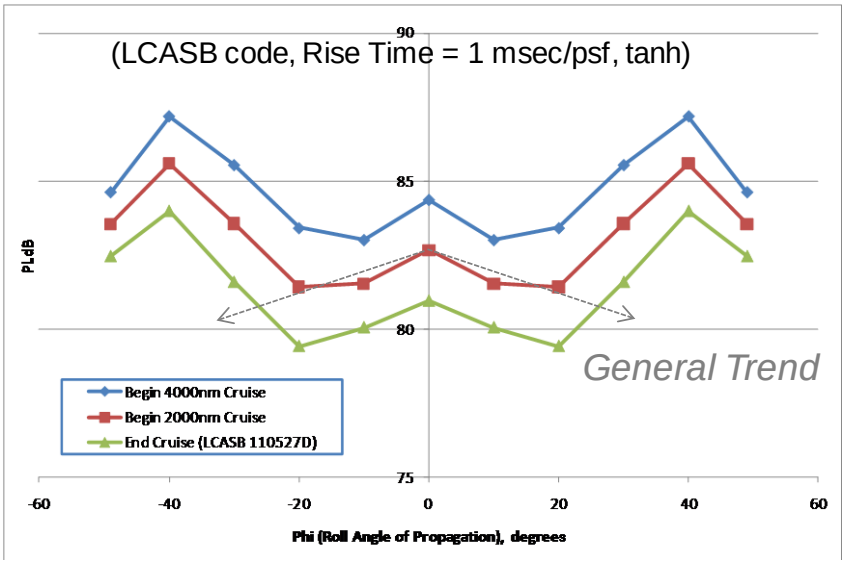

Figure 56. The QR4 1021-01 (N+2) Trijet configuration maintains a loudness level below 85 dB PL up to 28 degrees off-track at the start of cruise, and over the full carpet and mid-cruise and end-of-cruise

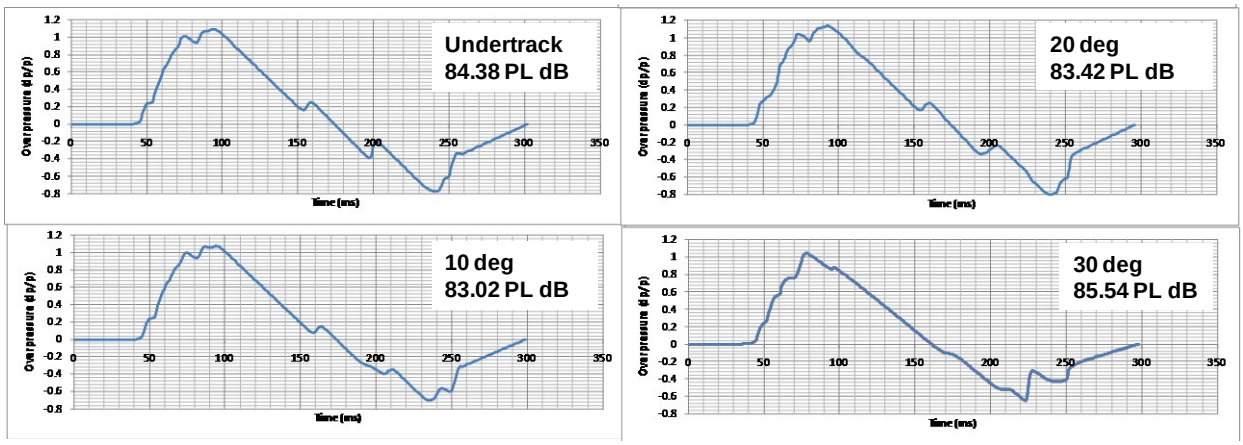

Figure 57. The QR4 N+2 Trijet configuration maintains a loudness level below 85 dB PL up to 30 degrees off-track at the start of cruise for the 4000 nm cruise mission

The SOC maximum fuel weight signatures for the QR4 configuration, Figure 57, show that the aft signature is well shaped into small enough multi-shocks for them to blend into a ramp up to 20°. At 30 degrees off-track, the aft signature is split into two more distinct small shocks, resulting in a slightly higher loudness of 85.5 PLdB (1 msec/psf). This trend continues through approximately 40 degrees off track, at which point loudness again begins to decrease up until cutoff around 49°. The front signature remains well shaped for the entire carpet.

However as mentioned earlier the above requirement comparisons use a minimal rise time of 1 msec/psf; whereas, real atmospheric measurements show 3 msec/psf. (and the trend goes to increasingly larger slope values as shock strength gets lower than 0.3 psf; however, this old data does not have sufficient accuracy to know that loudness reduces correspondingly.) Our analysis of routes in our N+3 study (2) indicates the frequency distribution of route distance for determining an average. Combining the average route distance, average from SOC to EOC and using 3 msec/psf, we have generated the average, which is also the typical, loudness for each roll angle as plotted in Figure 58. As can be seen from the plot, a representative typical loudness for this vehicle from this methodology is 79 PLdB.

Low boom design without considering aerodynamic performance can result in unrealistic configurations due to poor lift to drag ratio or stability and control problems. The Trijet N+2 configuration has been designed to maintain good aerodynamic performance simultaneously with low sonic boom. One of the initial concerns with the Trijet configuration was that the top mounted nacelle would experience problems at low speed and high angle of attack. Navier-Stokes CFD predictions (Fig. 59) show that the vortices from the leading edge extensions on the wings form a stable system that promotes good flow quality to the engine.

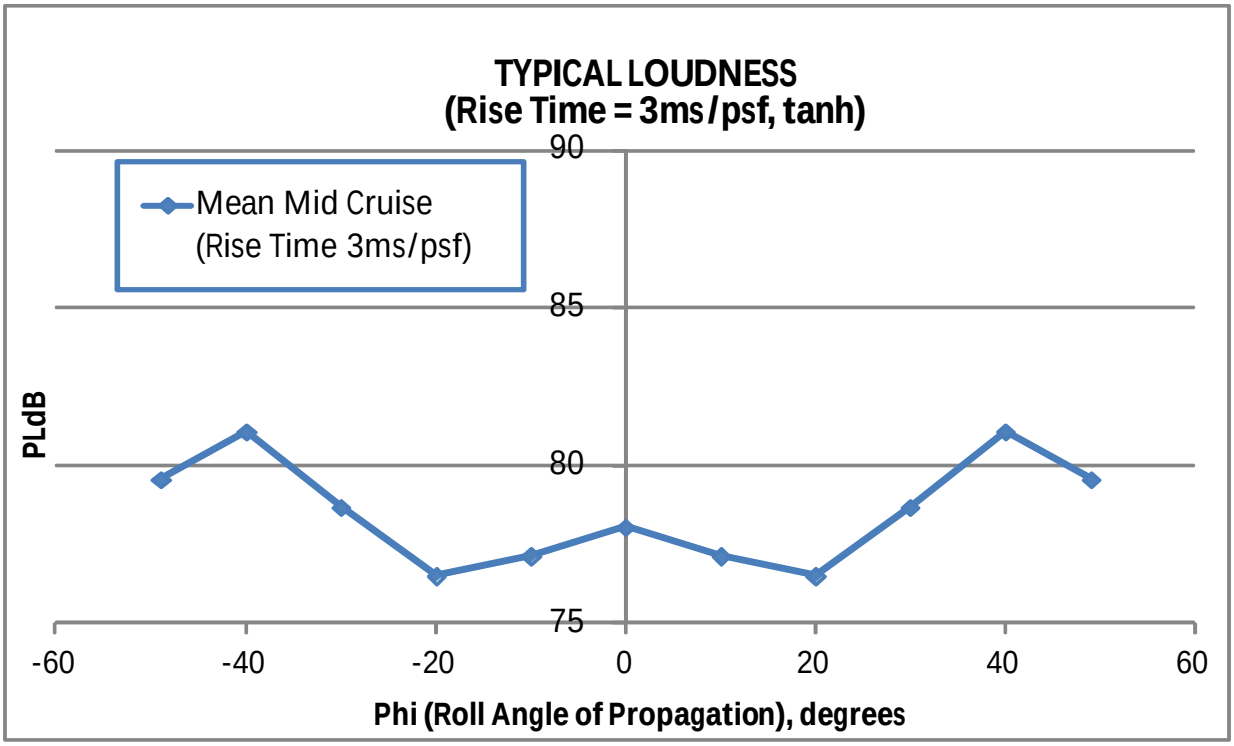

Figure 58. Using methodology matching typically measured rise time and using an averaged operational weight, the above trend intends to portray the average typical vehicle loudness versus roll angle

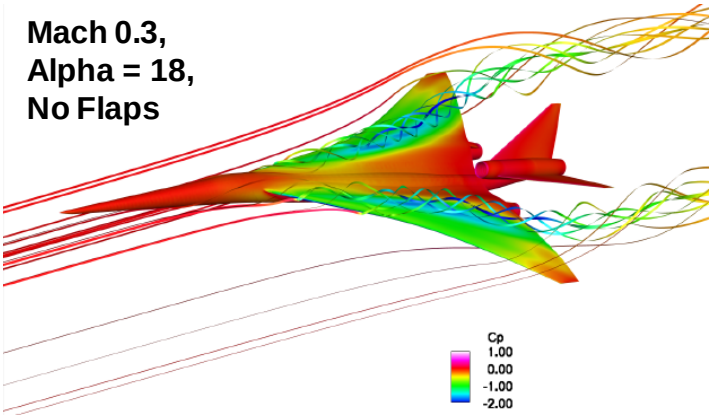

Figure 59. The wing vortex system maintains good quality airflow to the centerline nacelle even at high AOA

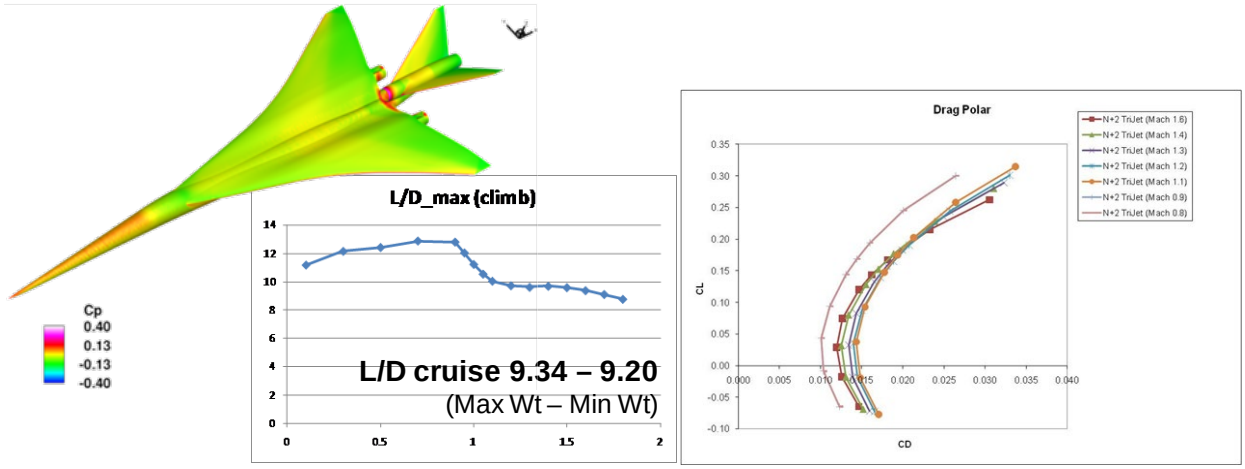

Figure 60. The QR4 1021-01 (N+2) Trijet design simultaneously achieves low sonic boom and good supersonic L/D due to careful attention to wave drag reduction during the low boom design process

Aerodynamic performance was also predicted using N-S CFD, Figure 60. The results show that the Trijet configuration exhibits very good L/D, ranging between 9.2 and 9.34 during cruise depending on weight, due to Reynolds number variation. This good aero performance allows the Trijet configuration to meet N+2 performance goals with a reasonable gross weight, simplifying the task of low sonic boom design.

6.1.3 Vehicle Packaging

6.1.3.1 Description

A preliminary vehicle packaging study was performed to identify and evaluate potential changes required on the low-boom optimized design to accommodate passenger cabin and subsystems integration. Notional layout based on the QR4 baseline configuration is shown in Figure 61. The landing gear is of traditional tricycle placement, with the twin nose gear retracts forward and the duel-twin main gear retracts forward and inboard. The fuel is located in the wing and the center wing box, with approximately 3,850 ft^3 of total usable fuel volume. The passenger cabin is located forward of the main gear wheel well. Approximately 650 ft^3 of cargo space is located aft of the wheel well. ECS and electrical/hydraulic are tentatively located aft of the cargo hold.

A three-class, 80-passenger cabin layout is shown in Figure 62. The business-class section contains four 58-in. pitch seats arranged two-abreast. The premium economy-class section contains 20 38-in. pitch seats in a one-plus-two arrangement, with the center seat in the first row removed to improve aisle clearance. The economy-class section contains 56 32-in. pitch seats in a two-plus-two arrangement. The notional cabin features three galleys, four lavatories, and closet/overhead bin with combined storage volume of approximately 250 ft^3.

A total of six exits are incorporated in the cabin layout: two 72-in.-by-42-in. passenger/service doors located between the business- and premium economy-class sections; two 56-in.-by-30-in. emergency exits located between the premium economy- and economy-class sections; and two 56-in.-by-30-in. emergency exits located at the rear of the cabin.

6.1.3.2 Results

The cross-section of the passenger cabin is illustrated in Figure 63. The QR4 circular cross-section resulted in reduced leg room for the outboard passengers. A composite cross-section was proposed to eliminate wall encroachment while retaining the same cross-section area.

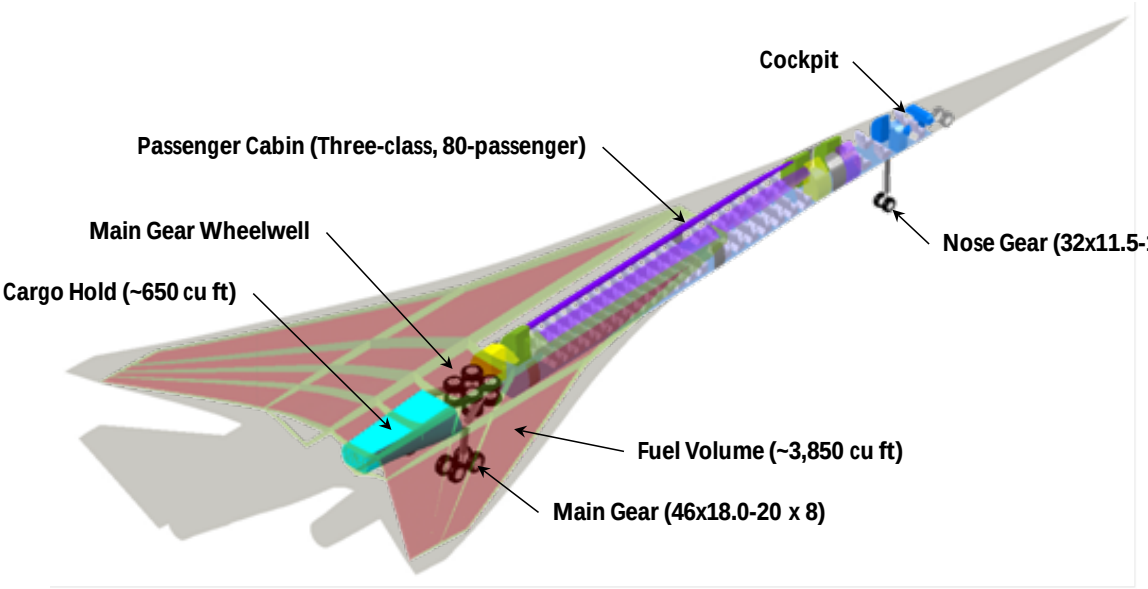

Figure 61. LM N+Notional vehicle layout

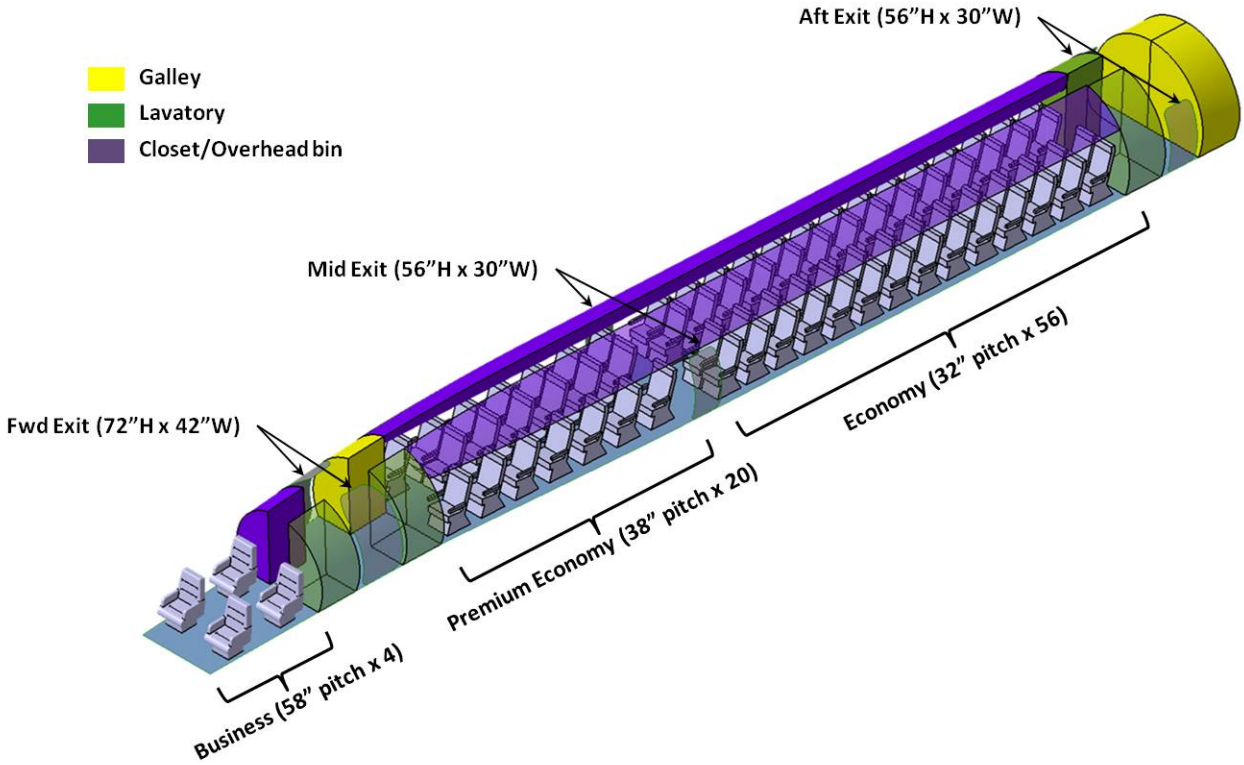

Figure 62. N+2 80-passenger, three-class cabin layout

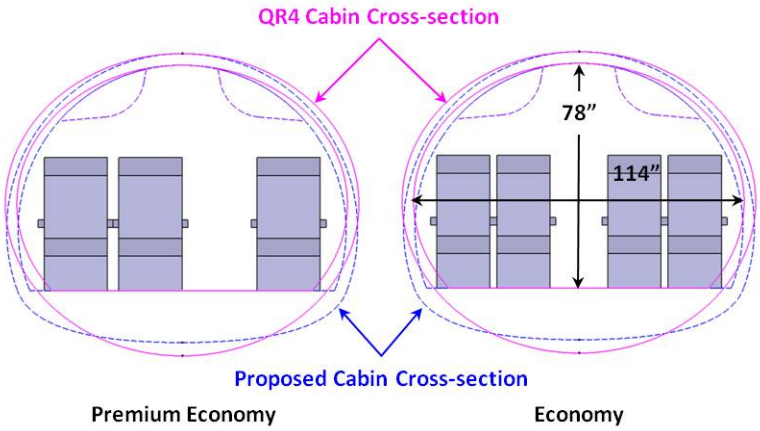

Figure 63. Cabin cross-section

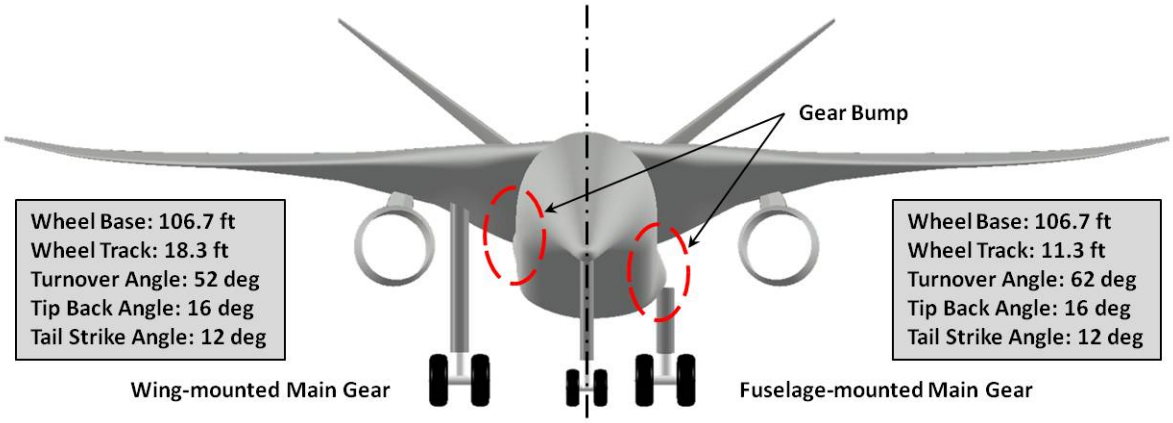

Figure 64. Main gear placement

Figure 64 shows the two main gear placements evaluated in the packaging effort. Both concepts have their own advantages and drawbacks. Low turnover angle is the most desirable feature for wing-mounted concept. However, the longer strut means increased gear weight, and requires shortening of the passenger cabin by one row of economy seating to store the gear. The lateral location of the main gear also increases the possibilities of the wing-mounted engines ingesting foreign objects liberated from the wheel well. As of the fuselage-mounted concept, the biggest drawback is that the turnover angle approaches the acceptable safety limit. The shorter strut results in a lighter gear weight, but the weight saving could be offset by the protruding trunion support structure. For both concepts, bear bumps are required to enclose the stowed gear.

6.1.3.3 Conclusions

Additional trades involve fuselage cross-section shape, passenger capacity, and operating safety margin are needed to further refine the vehicle layout. Also, impacts to aerodynamic performance and sonic boom signature due to outer mold-line (OML) modification required to accommodate packaging issues need to be evaluated and quantified.

6.1.4 Model Design and Fabrication (WBS 3.3.2)

6.1.4.1 Model and Model Support Design

After achieving the loudness goals with the QR4 1021-01 configuration, model design for the 0.008-scale low boom test model was initiated (Fig. 65). This 22.3-in. long model is designed to interface with the existing Model Support Apparatus (MSA) used for the first two N+2 low boom wind tunnel tests. The primary objective of this wind tunnel test is to validate the aft-signature performance of the Trijet configuration. The model has been designed with removable flow-through nacelles and a replaceable tail with two incidence settings. The two angles allow for the calculation of the aft lift increment that is critical to aft signature shaping.

Previous experience emphasized the importance of minimizing the influence of the model support on the signature, and several designs were investigated under the N+2 program for this task. The first support type considered was a highly swept blade, shown in Figure 66.

The blade was highly swept to keep it behind the Mach cone while minimizing the strength of the shock, and the wing was used to shield the influence of the shock below the vehicle. Positioning of the blade is critical, since a forward location allows the shock to spill around the wind leading edge, and an aft position causes interference with the signature contribution of the centerline nacelle and empennage.

The sting concept presented at the bottom of Figure 66 is similar to many traditional wind tunnel model supports, but has been designed and positioned to minimize the influence of the sting on the signature to the maximum extent possible. The majority of the sting area growth occurs within the hole left in the equivalent area distribution to account for the off-track relative movement of the nacelle shocks, and therefore does not coalesce with the front part of the signature.

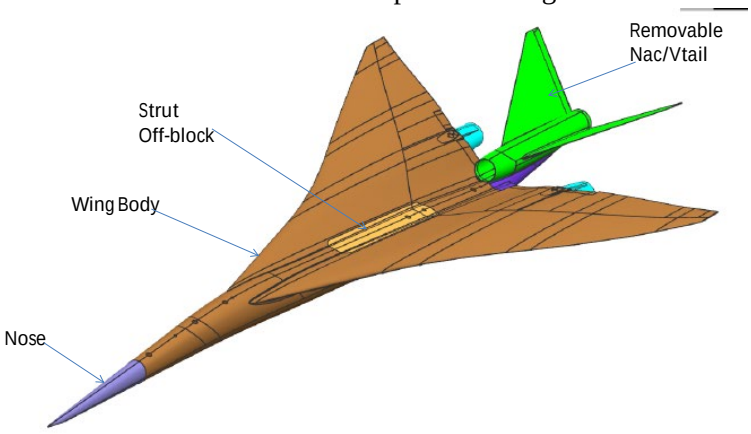

Figure 65. The 0.008 scale wind tunnel model of the QR4 configuration has removable nacelles and a two position tail to capture important sonic boom increments

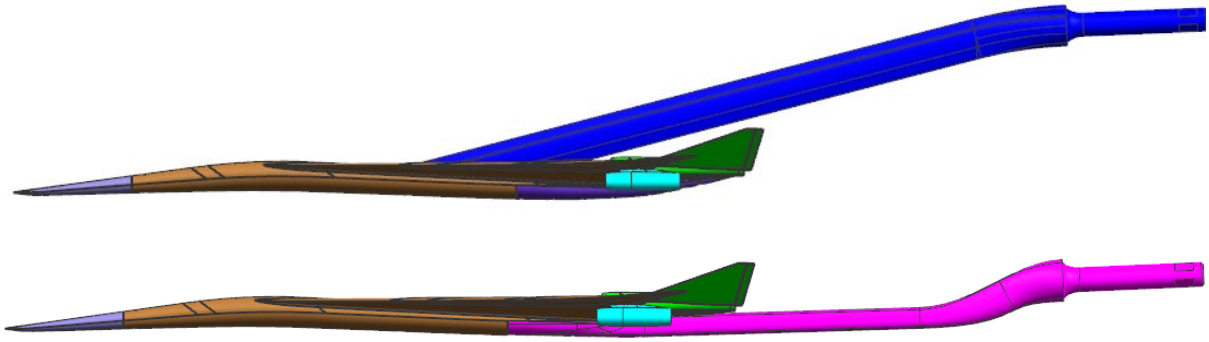

Figure 66. Both a sting and blade support system were designed and fabricated for the low boom test to reduce risk due to viscous effects at model scale

Figure 67. Difference between model aft fuselage design (blade support) and aft sting support

The preferred configuration at the start of the support work was the highly swept blade configuration. Inviscid predictions of the blade support showed good results, however viscous simulations at wind tunnel Reynolds numbers indicated that there could be a potential problem with the centerline inlet ingesting the boundary layer air from the blade (Fig. 68). This causes a stronger nacelle shock and could potentially lead to problems getting a good signature measurement in the wind tunnel. Even though the signature prediction off-body remained good for this case, experience has shown that CFD can sometimes under-predict (or over-predict) this type of phenomenon. Caution was therefore warranted for the second wind tunnel entry.

The sting support shown in Figure 67 does not exhibit the same problem. Original plans were to delete the sting support from the program and use only the swept blade for model support. However, based upon these results it was decided to fabricate and test both supports.

Predictions for wind tunnel model scale sonic boom were made using both laminar and turbulent boundary layers. Due to the relatively low Reynolds number of the test, significant laminar flow may be present. CFD predictions indicate that it is desirable to have trip discs on the wing upper surface. Experience suggests that these trip discs may not transition the flow, but should at least energize the boundary layer inhibiting separation. Figure 69 presents a plot with surface pressures and stream traces for the laminar and turbulent runs. For the laminar case, the nacelle cowl and blade support causes shock-induced separation while the flow remains attached for the turbulent condition. We have modified our wind tunnel run schedule to investigate the use of transition discs early during the October 2011 entry to ensure good results from the test.

The influence of the blade on the aft signature measurement is examined in Figure 70. The data show that the blade mount has a minimal impact on the signature for measurements taken between undertrack and 25 degrees off-track, with a gradually increasing influence beyond that point due to the compression and expansion generated by the blade spilling over the wing. Even for higher angles (up to and including cutoff), the blade remained effective. For measurements to the side and above the configuration, the sting mount provides smaller distortion of the signature and is the preferred support system.

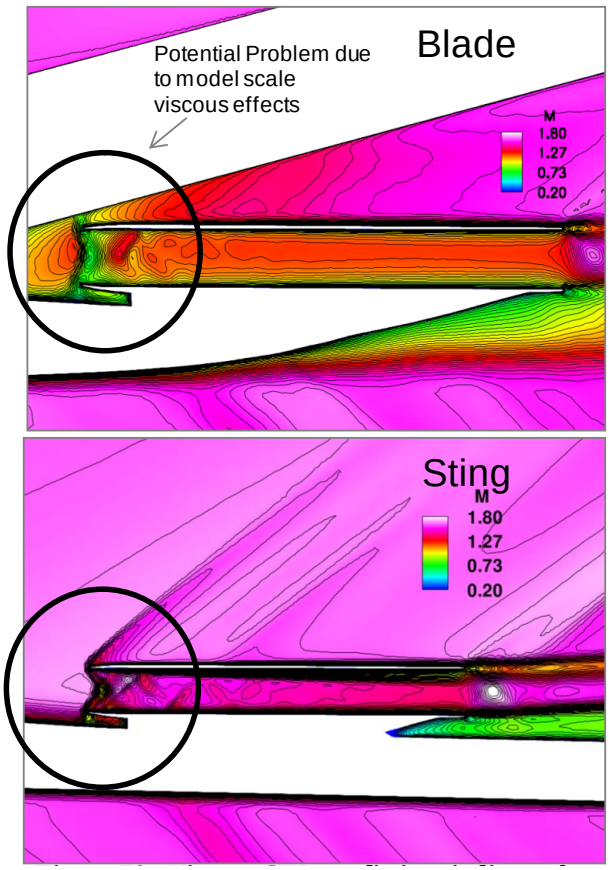

Figure 68. Viscous CFD predictions indicate the potential for a interaction between the blade mount and the centerline nacelle

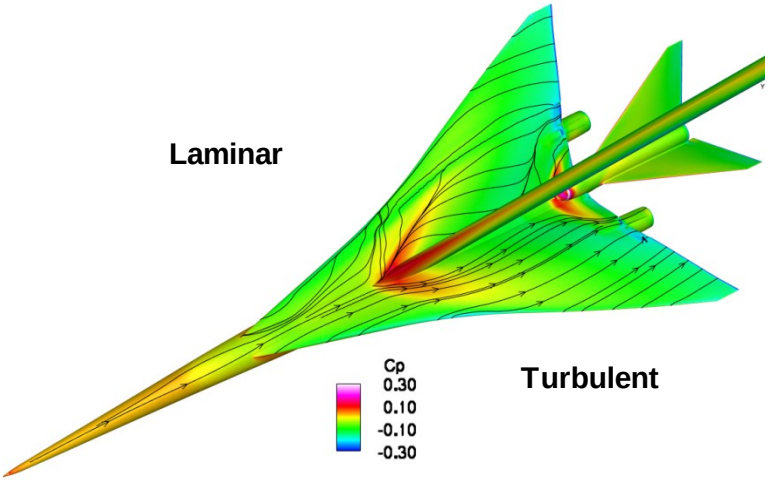

Figure 69. Viscous CFD results at model scale indicate that the blade mount may cause shock-induced separation on the upper surface of the wing if the boundary layer is laminar, suggesting it may be desirable to use grit to force transition on the upper surface during the test

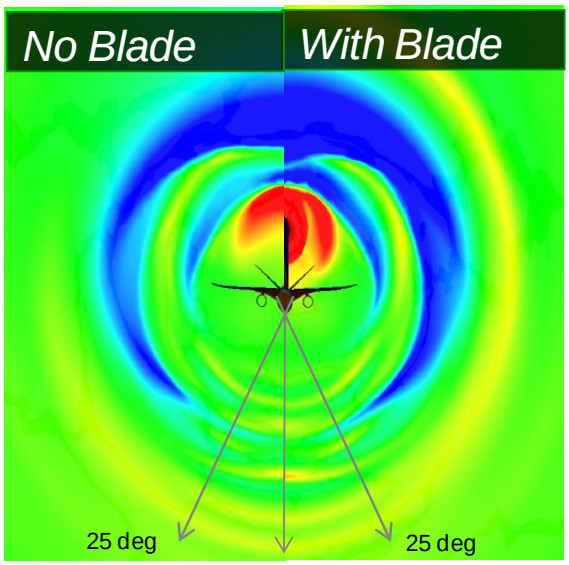

Figure 70. The highly swept blade support has a minimal impact on the measured pressure signature from directly undertrack to approximately 25 degrees off-track

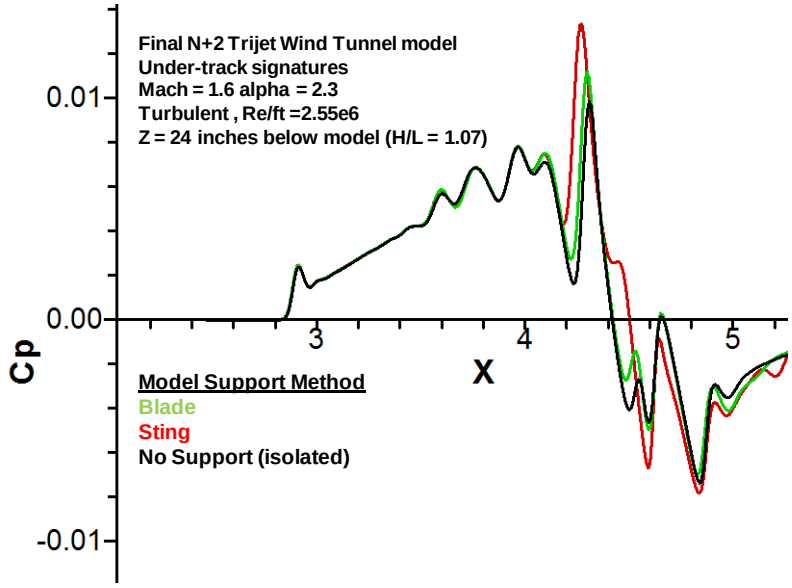

Figure 71. The subsonic sweep blade mount results in a smaller pressure difference from the isolated model than the sting mount for undertrack signature measurements

Figure 71 compares undertrack signatures of the two model supports with the signature of an unsupported model floating in the tunnel. The signature of the unsupported model is slightly different than that of the full scale Trijet configuration due to the larger influence of the viscous effects due to the low Reynolds number as well as a number of minor modifications that were required to fabricate the model, including fillets and thickened trailing edges and nacelle cowls. The results show that while both supports require only a moderate increment to remove their influence, the blade is predicted to require a smaller increment under track as expected.

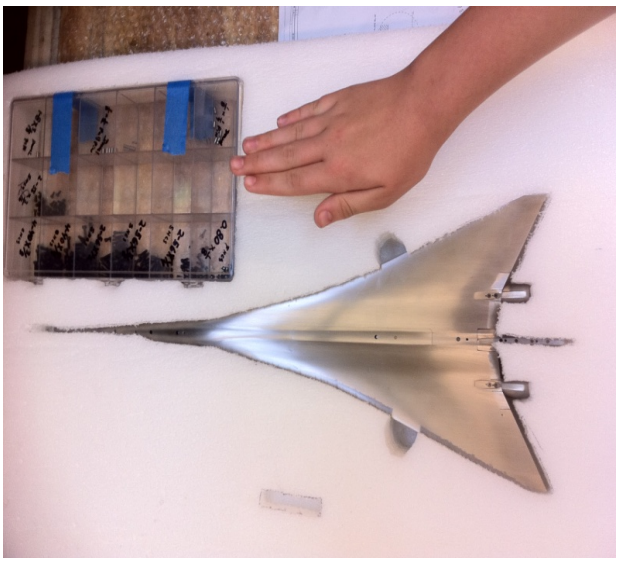

Figure 72. At 22.396 in. in length, the 1021-01 configuration is our largest sonic boom model

6.1.4.2 Model Fabrication

The model fabrication subcontractor was Tri Models Inc., who produced the tight tolerance axi-body models used in the LM1 test. The low boom model, sting, blade, and support hardware designs were released at the beginning of June, to support delivery to NASA Ames by the end of September 2011, which was successfully achieved. The low boom model was built at 0.008 scale and just over 22 in. in length—larger than our previous largest 15.6 in. sonic boom model Figure 72. The model was fabricated out of 13-8 high strength stainless steel and designed to meet all tunnel stress requirements. Having designed the full scale configuration to be practical, the model stress analyses had safety factors well above the 4.0 desired by the facility with the single exception of the sting, which was fabricated from Vasco 300 steel to meet this stress margin.

The sting was made at a minimum cross section to reduce geometrical distortion and therefore, flow field distortion. It was made taller in height than width corresponding to the greater wing load than sideforce load. The blade attaches with no model geometric distortion, and its flow field distortion is reduced by being primarily on the model upper surface. The blade thickness was sized to a minimum at the vehicle, which necessitated a slightly increasing thickness going away from the model to counter the increasing moment arm from the model's load. However, since the blade's chord is over 12 times its thickness (at the vehicle) the pitch stiffness is over 2 orders of magnitude greater than if it had been minimally sized to the load. The stiffness of the model (especially its blade mount in pitch), the stiffness of the large 1.5 in. diameter balance and its adapter, and the stiffness of the new Linear Actuator served to reduce model pitch vibrations in the tunnel to about ±0.1 in. (for the blade and ±0.25 in. for the sting, versus ±0.3 in. for typical previous (smaller) sonic boom models. Vibrations in pitch smear shocks and reduce their peak amplitudes by averaging the signature over that vibration distance times Beta (sqrt(M^2-1). So for this model, smearing relative to length should be about 0.006*L for the blade and 0.014*L for the sting, versus 0.03*L for a legacy 12 in. model and more for a smaller model. This reduction of shock amplitude in wind tunnel measurements needs to be taken into account in any CFD to measurement comparison and will be referred to again in the prediction comparison sub-section 6.1.10 LM3 Test Results. (e.g., AIAA–2004–4846 (Ref. 8) Figure 5 and AIAA–2004–4536 (Ref. 9) Figure 4 applied a ±0.15 in. sinusoidal averaging to relatively sharp CFD data in order to match the measured data.)

To accurately machine the model, all "sharp" model edges were defined with a minimum finite thickness of 0.007 in. and the model maintained 0.100 in. thickness within 1.000 in. of any edge, which

the model met without modification. The model quality inspection revealed that the majority of the model was within –0.001 to 0.003 in. of geometry definition, which is sufficient for CFD prediction validation of signatures without reanalyzing an updated geometry. The only portions of the model likely to make a noticeable but insignificant difference are the nacelle thickness (typically 0.002 in. too small on the inside and 0.003 in. too large on the outside—in other words 0.005 in. too thick) and forebody waviness. (At the time of this writing, NASA was considering generating an updated as-built geometry from the many inspection measurements provided by Tri Models, 17 wing cuts, 50 body cuts, etc.) The Final assembly drawings for the model, sting, and blade are shown in Figure 73. The baseline model configuration is shown in Figure 74. The (rounded) rectangular bumps on the wing upper trailing edge above the wing mounted nacelles were added to allow the nacelles to be attached with larger, less delicate screws and pins. The bumps' location and shaping were designed, and shown with analysis, to have no significant effect on the sonic boom.

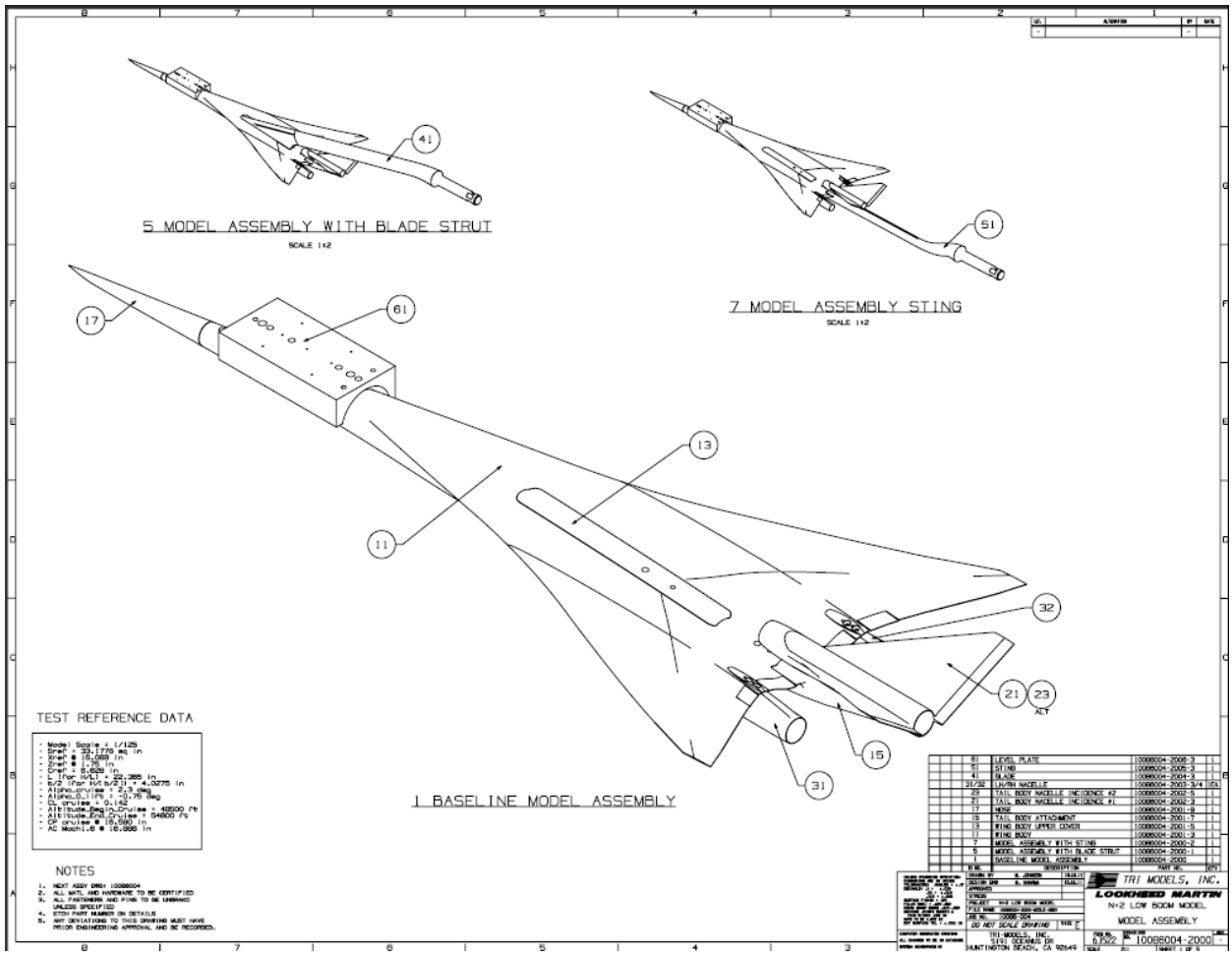

Figure 73. Assembly drawings of the LM N+2 Low Boom Model and support hardware

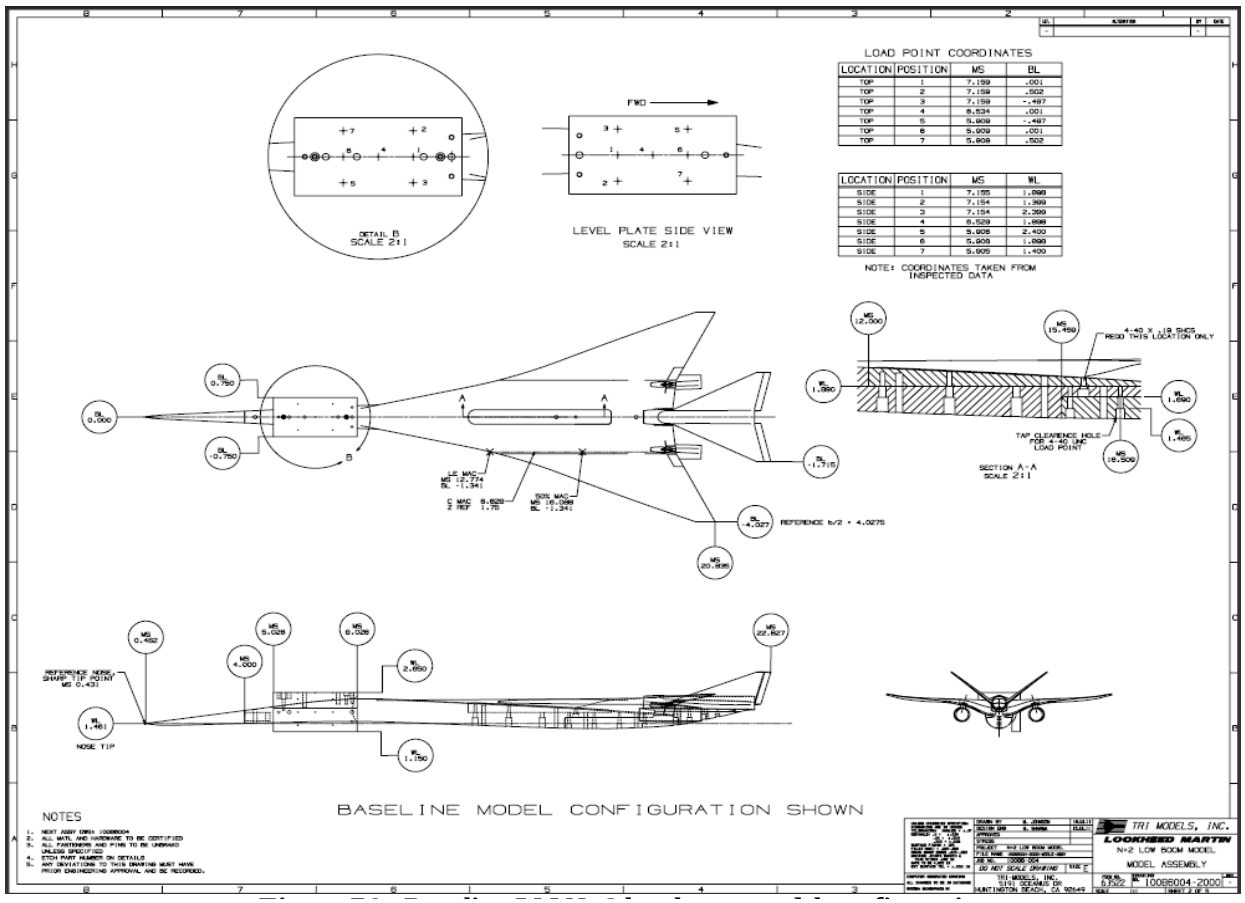

Figure 74. Baseline LM N+2 low boom model configuration

On-going test calibration of the MSA balance by NASA indicated that its error could be as large as 6 percent of the desired low boom model value, when 1.5 percent precision was needed for acceptable matching of the low boom signature. An existing 1.5 in. diameter balance was identified to have better precision but was felt to be more reliable as a high precision device. The MSA was retained in the test plan as the back-up balance and was also used as a spacer to locate the SEEB-ALR model farther forward in the tunnel to align its calibration range with the low boom model. To use the existing 1.5 in. balance, two adapters were also fabricated by Tri Models to match the cylindrical MSA mount (used by all LM models) and to match the AS2's model taper mount as shown in Figure 75.

6.1.5 LM3 Test Planning (WBS 3.3.3)

The prior LM1 test recorded measurements of the OptSig model, which after calibration, resulted in ground signature loudness within 2 PLdB of the prediction—the validation accuracy goal. However, there were significant discrepancies that would have resulted in greater than 2 PLdB difference if located in other positions of the signature; therefore, better measurements were needed to ensure that the desired validation accuracy was reliably achieved. To do so, the distortions remaining in LM1 calibrated measurements needed to be reduced an additional three times. The LM1 calibration process had already reduced distortion three times relative to the uncalibrated LM1 measurements. So for the LM3 test, sources of measurement inaccuracy were postulated and test changes were planned to create improvements.

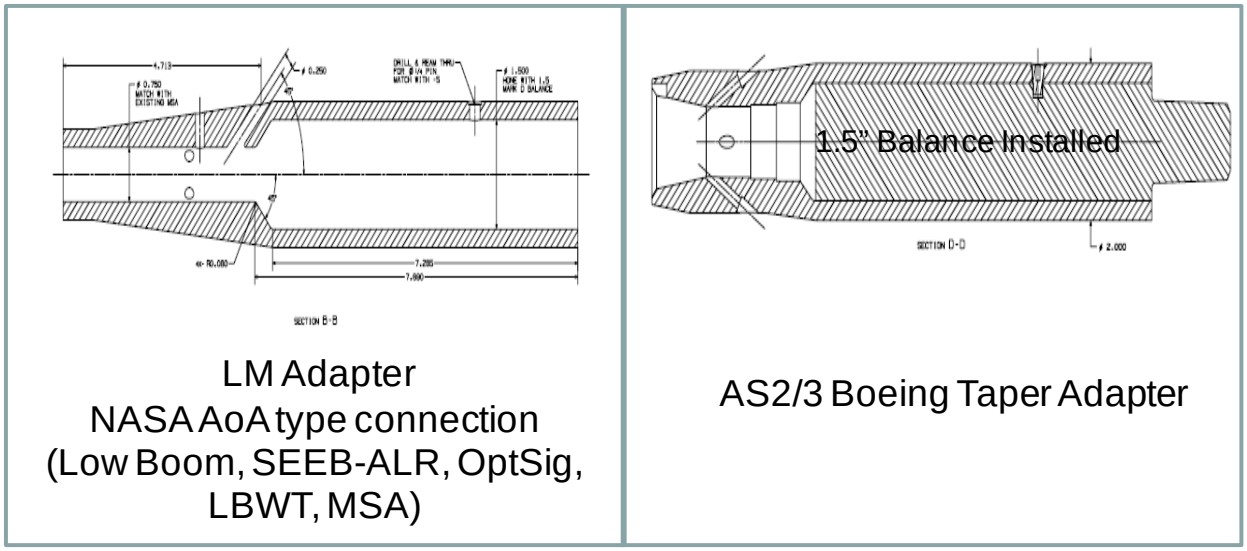

Figure 75. 1.5 in. Balance Adapters

Sources of Measurement Inaccuracy—Based on LM1 and prior sonic boom wind tunnel measurement testing, the following issues were to be addressed:

- Solving this first issue, discovered by LM1, was the most critical to LM3 success.
  - Flow-field pressure measurement distortions (of both slope and intercept) due to ambient static pressure variations interacting with the model and its signature propagation
- Still, the following issues would have degraded LM3 success.
  - Dynamic noise, random and oscillating
  - Test condition variations through long full signature measurement times
  - Effect of pressure orifices at rail edge, facing incoming pressures
  - Model support location limitations (with every model angle change the tunnel programming returns the model to a reference height [auto-height hold], model location moves with Dalpha at non-zero roll
  - Model tunnel location bouncing relative to measurement
  - Model fidelity (as-built accuracy, CAD geometry precision, model flexibility)
  - Model support geometrical and flow distortions, like cavity flow
  - Balance and pressure measurement accuracy: the MSA balance failed during LM1 apparently due to a broken wire found after the test, the PSI modules (15 psid) measuring the Blade Rail pressure have a spec precision <0.1 percent that is less than what is needed; however, they have in practice been providing much better than their spec precision and seem to be providing a sufficiently precise <0.005 percent of their full scale range (which is a lot of precision from a device).

Improvement Changes—Several changes were discussed to improve measurement accuracy:

- Using a 1.5 in. balance, which while its spec does not have a better resolution than the MSA, it is a higher precision, more reliable, temp compensated device. The MSA was rewired and calibrated to be available as a back-up
- Two alphas were run for most every signature case, so that interpolations could always be made for any correction to CL
- One more sensitive 0.4 psid PSI module was connected to 64 Blade Rail orifices in parallel with the existing 15 psid psi modules and measured the low boom and OptSig models (however the analysis was not available for this report)
- The model and new model supporting hardware, including the 1.5 in. balance and adapter and Linear Actuator, were made relatively stiff and reduce model vibration in the tunnel
- The model was made with both sting and blade supports, both with minimal impact on the measured signature, and two ways to measure the aft shock
- The nacelles' internal duct has a small linear increase in radius to keep the boundary layer growth from increasing spillage with a more difficult to predict flow—keeps the flow field more like the full scale configuration. While a linear increase in radius does not provide the best counter to internal boundary layer growth, it allowed the duct to be cut with a more precise and less expensive wire EDM process.
- The model was designed relatively thick and defined with a finite minimum edge thickness to aid accurate fabrication milling, and was made almost twice the length of previous low boom models to improve fabrication accuracy, increase the boom disturbance magnitude and improve nacelle internal flow with a higher Re#.

Several changes were implemented in the LM3 97-0231 test to overcome the spatially distributed distortion, its varying shift of measurement slope and intercept at each orifice, and reduced measurement variability.

- Every signature was made from averaging multiple measurements taken across a range of Linear Actuator (Xram) positions
- References taken at the end of data runs seem to work consistently better than references taken in front, but front references are needed for real-time checking of the results. So, short front references and long end references were taken for all data. Further, end references were done at the same height; however, for the low boom model such a reference intrudes into the last couple inches of the signature, so a second end reference was taken (+7.2 in. in height) for the aft shock plus recompression. The second end reference was used but was replaced with the first end reference ahead of the aft shock if that reference worked better.
- An improved calibration of the Blade Rail was made with the SEEB-ALR model by moving it in 1 in. increments (instead of 2 in.) with extra end repeats (so the ends had repeats like the overlaps in the middle) plus two runs at +4.8 in. height at 0 in. Xram to extend the calibration further aft.
- High variability orifices were identified and excluded from measurements
- Facility controls of pressure, humidity, motion control and pressure measurement were all examined and experimented upon to improve flow field and measurement quality

6.1.6 LM3 Test Description

The LM3 test was planned to validate a configuration capable of achieving sonic boom levels acceptable for over land flight. Since we do not know what will eventually be ruled as acceptable, our 1021-01 configuration represents our best guess of an acceptably low sonic boom vehicle. The goal of the LM3 test was to demonstrate testing techniques that measure sonic boom signatures with sufficient accuracy to validate its ground sonic boom loudness to < 2 PLdB. To help achieve this measurement

accuracy, the SEEB-ALR model was also measured to calibrate the Blade Rail sonic boom measurement apparatus. The OptSig model (SEEB-ALR and OptSig described in 4.2.2) was measured as another low boom signature example. The AS2 model from Boeing's 97-0229 test was also measured as a test to test comparison, particularly comparing measurements from the 14 in. tall Blade Rail with the 2 in. tall rail from the 97-0229 test. The LM3 test planned to measure four different models (AS2 and OptSig were lower priority). The 1021-01 configuration had four measurement geometries total, including:

- Baseline shape blade-mounted
- Baseline shape sting-mounted
- Wing nacelles off
- Alternate tail incidence (cross combinations and their mixed increments were not desired to be tested)

The 1021-01 model was made with both blade and sting model supports. The blade was swept greater than the Mach cone angle to create a minimal flow field disturbance. It also had the minimal thickness needed to meet stress and the longest chord possible to keep its disturbance limited above the wing. The blade resulted in a fairly slender 8 percent thickness where it met the vehicle. A concern was whether the blade caused a significant change to the wing upper surface flow, especially if analyzed with a laminar boundary layer (which was likely at the wind tunnel Re#). Using viscous analysis, the signature change due to the blade was found to be small and acceptable, even with the laminar boundary layer. However, analyses of such complex flows are prone to greater uncertainty. Three steps were taken to minimize the risk: an alternate sting support was built, oil flow visualization was run (described in Section 6.1.7) and trip discs were placed on the vehicle to inhibit flow separation.

The sting was predicted to produce a larger disturbance than the blade (under the vehicle), but the disturbance was very small and an acceptable change to the vehicle signature. The sting produced very little flow impact, and it was deemed a low risk alternative if we found that the blade flow was not what we expected or could not match with analysis. Oil flow visualization was performed to help identify mismatches with our flow prediction if our sonic boom analysis did not match measurements. The trip discs were employed to help reduce flow separation risk. They were not intended to trip the flow, and it is likely the flow was too difficult to trip at this low Re#. The trip discs were intended to act like vortex generators. They energized the boundary layer to help prevent separation. They were limited to the wing upper surface, blade, and a row across the upper surface wing root, and fuselage just ahead of the center nacelle (Fig. 76) to help attach fuselage flow through the center nacelle shock and attach the aft fuselage flow under the center nacelle. The subsonic swept trailing edge of the blade was prone to (vortex) flow separation. The blade was unswept, in front of the nacelle, to move any separation above the nacelle to reduce interaction.

All sonic boom measurements were made from one of two measurement series types as shown in Figure 77. Most measurements were taken with the 4 in. translation at the closer 21.2 in. height above the rail. The translation was limited to the greatest 4 in. of Linear Actuator extension to keep the model ahead of the Blade Rail shock (strong enough to change flow angularity up to 2° as measured in the LM1 test). Measuring at the closest distance made the signature pressure greater and reduced part of the flow field distortion effect. Twenty-six measurements were made by moving the model 0.1575 in. between measurements. The increment matched the orifice spacing on the rail, and made lining up the signatures for averaging easier by shifting orifice alignment without the need for interpolation. The other measurement series type was done at a height of 31.8 in., which allows for 16 in. of translation before running into the Blade Rail shock. The same number of measurements was taken, to facilitate comparison, with a 4 orifice spacing of 0.63 in. between them. This translation distance had the benefit of averaging the measurements across a greater length of the static pressure fluctuations. LM1 calibrations indicated that this would be about 3 to 5 periods of static pressure fluctuations, which would be enough to average 26 measurements of a good absolute level. It was important that this was the case, because 16 in. of translation meant that the aft shock measurements would be behind the zone that the SEEB-ALR

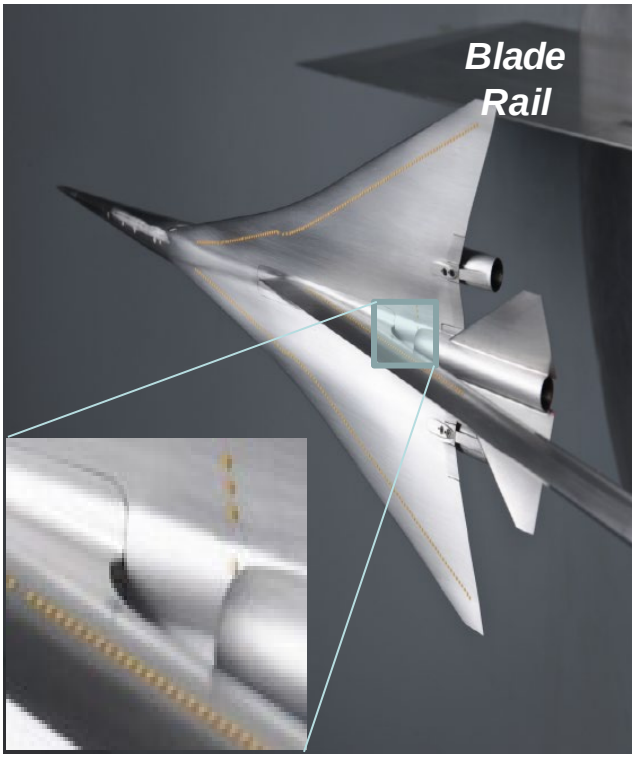

Figure 76. Model above Blade Rail with yellow trip discs and inset highlighting blade—nacelle region discs and unswept blade trailing edge in front of nacelle.

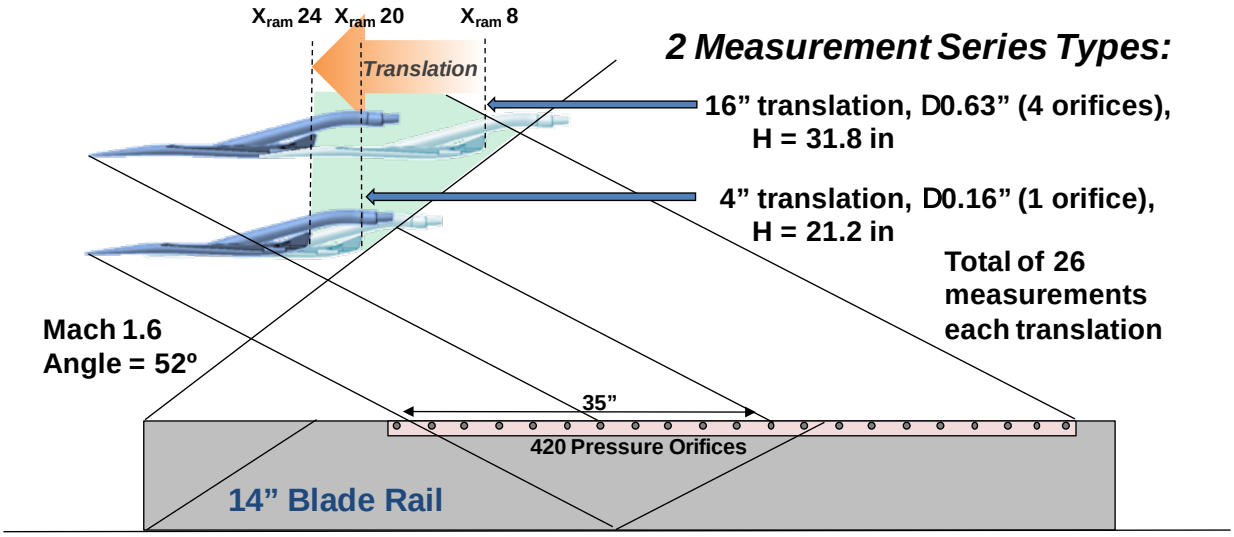

Figure 77. New procedures for 2 types of sonic boom measurement

model could calibrate. So 4 in. of translation would have a tendency to have too much of its measurements concentrated in a local low or high pressure fluctuation, making averages biased in absolute level; however, the SEEB-ALR calibration should be able to reliably correct the averages (and correct each individual measurement partially) to the right absolute level. Also, the same 21.2 and 31.8 in. heights were also used in the LM1 test, allowing test-to-test comparisons to better understand flow field measurement characteristics. We looked for patterns that indicated a calibration from one test could be used for the next.

Pretest Calibration and Hardware Checkout—Pre-test calibration and hardware check-out started September 26, 2011. Tunnel installation began Tuesday, October 11th. Data acquisition started near 6 a.m. Thursday, October 13th, stopped for the weekend, and completed (Run 1017 of LM3) near 6 p.m. on Thursday, October 20, running 2 shifts per day. The first runs were made with configuration stack: SEEB-ALR model, MSA, 1.5 in. Balance and its Adapter, Linear Actuator and Roll Mechanism all mounted with a conical adapter to the tunnel support strut (strut adjusts height, AoA and Beta). This looks like Figure 78 with the 1021-01 blade mounted model replaced by the SEEB-ALR model and MSA. Testing in the Ames 9´ 7 was oriented horizontally, instead of the typical vertically, to get the best results from the tunnel. Height was defined as horizontal separation from the wall mounted Blade Rail edge to the model reference center (MRC) (or the nose for the axi-symmetric models SEEB-ALR, OptSig, AS2).

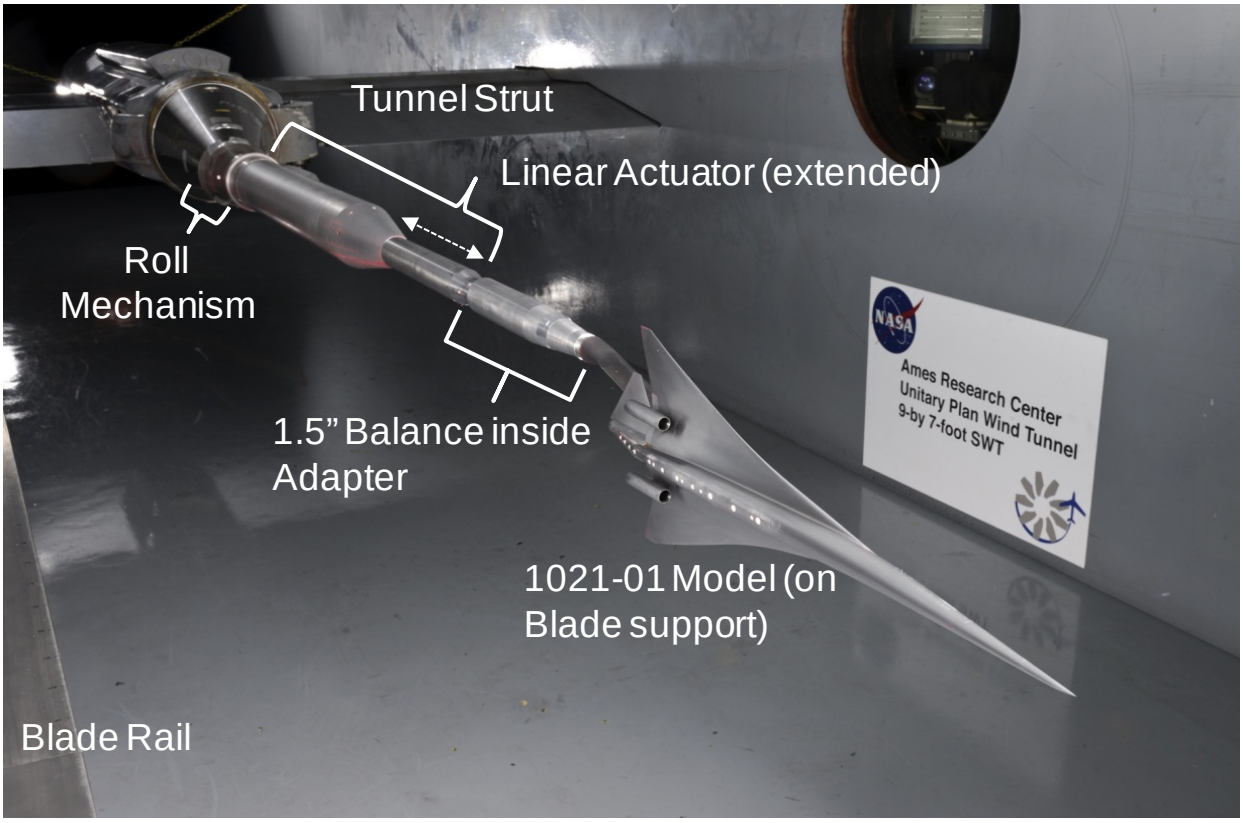

Figure 78. 1021-01 Model (on blade), balance and actuation equipment

SEEB-ALR—The test started with the SEEB-ALR model being used to perform an initial blade rail calibration and to examine the flow field at two or three tunnel pressures. The SEEB-ALR model's flat-top signature made flow-field variations easy to identify and quantify. This model was used to develop a linear calibration for each Blade Rail pressure orifice (described in Section 6.1.9). Another objective of these initial calibration runs was to investigate three different measurement heights and 2 or 3 tunnel pressures (Re#) for flow measurement quality. However, during these initial runs, we had difficulty holding the humidity requirement of no more than ±3 ppm change during a run series. The tunnel had to be stopped during the 3rd height SEEB-ALR measurement. In the previous tests, 97-0221 and 97-0222, the effect of humidity changes on sonic boom measurement was investigated and shown to substantially shift measurements. The ±3 ppm humidity requirement was based on those tests. The test was restarted at the next planned higher pressure and appeared to make humidity control easier to achieve. While the higher pressure incurred more electricity cost, less lost time off humidity made up for it. However, throughout the test more than half of the productive time was lost due to failure to maintain humidity consistency (spent adjusting dry airflow, replenishing dry air tanks, etc.). Relief in stringency of the humidity requirement would greatly improve productivity.

1021-01 Low Boom Configuration—Next the 1021-01 Low Boom model was supposed to traverse with the Linear Actuator at the 3 planned measurement heights running alpha and beta sweeps to measure flow angularity. However with time running short before the weekend stop, only one height was run so that the model could perform sonic boom measurement translations. The data was examined over the weekend and used to make refinements to the next week's test plan. In this case measurement fidelity looked encouraging but the humidity constraint limited productivity. As a result, we ran the highest priority runs including all 4 models and the comparison with the higher sensitivity pressure module. The following week of testing started with the model reconfigured to sting-mount (with the model change, like many others, done off tunnel time by dedicated LM personnel). It was desired to determine if one mounting was working better, so it could be used for the rest of the model test options. We found that the model bounced a lot more in pitch with the sting support. While this still resulted in less signature smearing than in previous testing, the extremely stable blade mount was used for the remaining testing.

Nacelle Off—Nacelle off testing was run next. Although precise comparisons were not done (nacelle off CFD was unavailable), the increment was approximately what was expected. Oil flow visualizations (later in Section 6.1.7) indicated that flow around and through the nacelles matched expectations. With matched measurement results and behaved oil flow, it was decided to skip running the alternate tail incidence in favor of running different measurement types (like the 16 in. translation at 31.8 in. height). Alternative roll angles were also run. Two alphas were run for almost every case, and interpolations were made to a corrected CL. After examining the sonic boom data, there were indications that the balance absolute CL values were a little low, but the incremental CL measurement differences between two nearby alphas accurately (and adequately) discerned the difference.

AS2 Model—After the low boom model, the AS2 model was run for test to test comparisons. Eight measurements at a height of 30 in. over 24 in. translation (with some varying spacing) were given a partial new process without any calibration. The results were good and could be exact with a few more measurements or with calibration (needed to be run at a calibrated height 21.2 or 31.8 in.).

Higher Sensitivity Pressure Modules—The higher sensitivity pressure module was run last with a pressure tubing "T" split to attach the new module and still remain similarly attached to the old modules. This was done to exactly match measuring identical pressures. The 1021-01 Low Boom configuration and the OptSig models were run with the new gauge measuring in parallel. Analysis of the results has not been completed.

6.1.7 LM3 Oil Flow Visualization

Oil flow visualization was used to verify whether flow was matching predictions. If flow did not match predictions, oil flow could have identified the difference, and we could have tried to modify our analysis to match. As it turned out, running at either the original Re# of 2.55 or 4.5 M/ft the flow stayed fully attached. The trip discs were not removed to see if the flow separated. However, during initial supersonic flow start-up in the tunnel, the Re# was only 1.3 M/ft and separated flow (like the above laminar seen in Fig. 79) on the wing. (Watching this dynamically changing few minutes of separated flow finally explained the region of more evacuated oil at 1/3 and at 2/3 of span ahead of the trip discs). Oil flow visualization was experimented with concurrently during most sonic boom measurement series. Movies of oil flow development, Figure 80, were taken throughout and Schlieren photography was also taken during the first week. However, the reflective decals placed on the tunnel wall for the ARBOSS Schlieren photography pulled off into the flow during testing and corrupted the first week's sonic boom measurements.

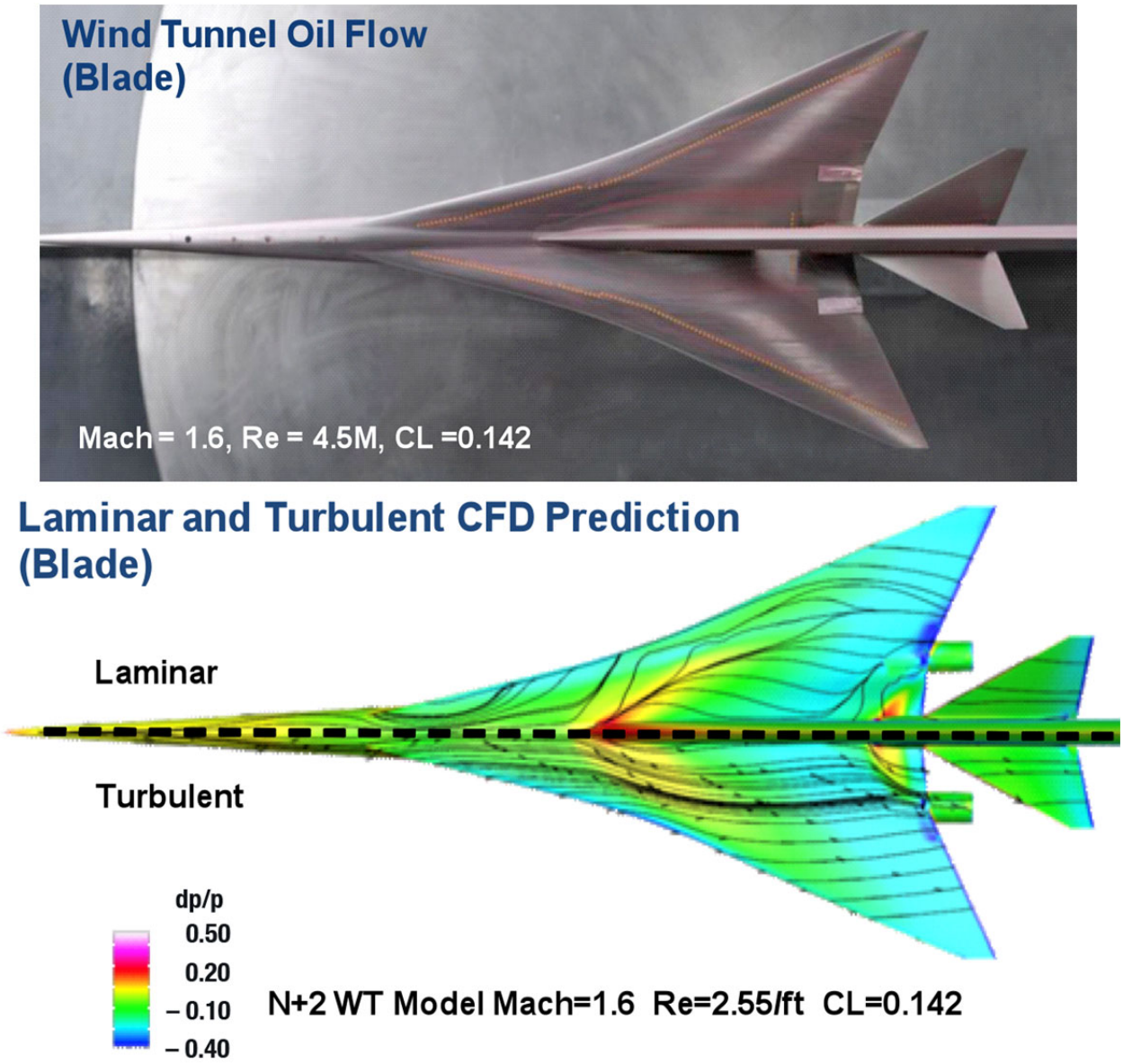

Figure 79. Oil flow showing fully attached like turbulent

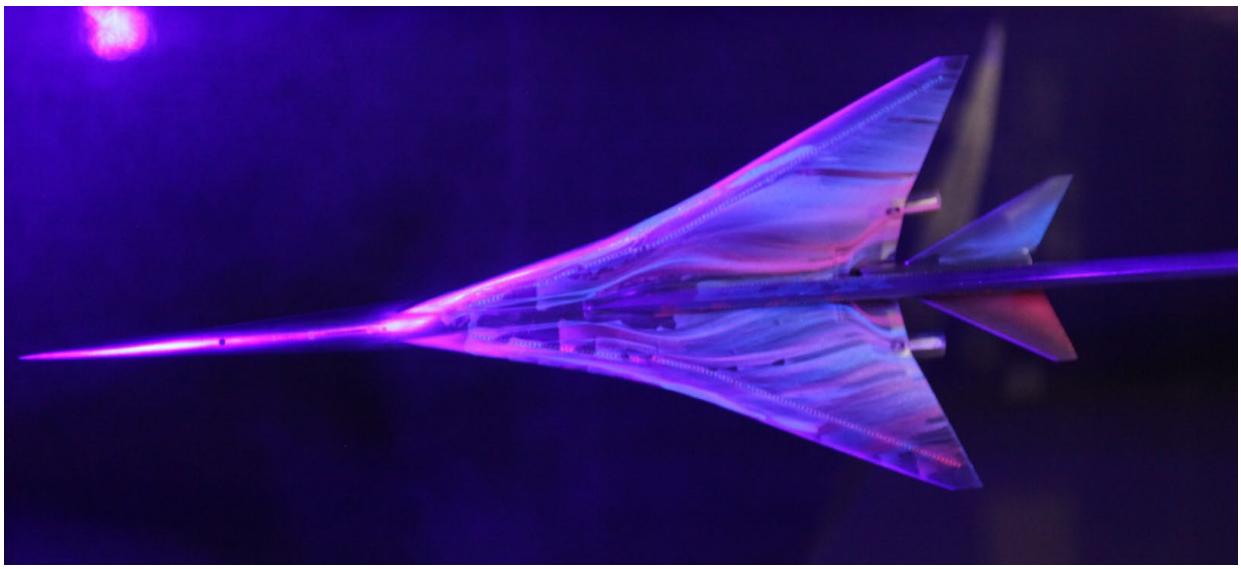

Figure 80. Movie recordings of fluorescent oil flow development were taken throughout tunnel start-up pattern changes

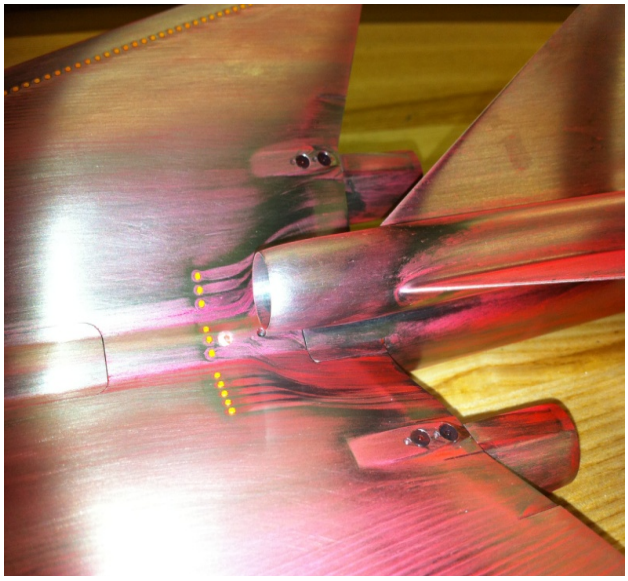

Figure 81. Flow around Center Nacelle Nicely Attached

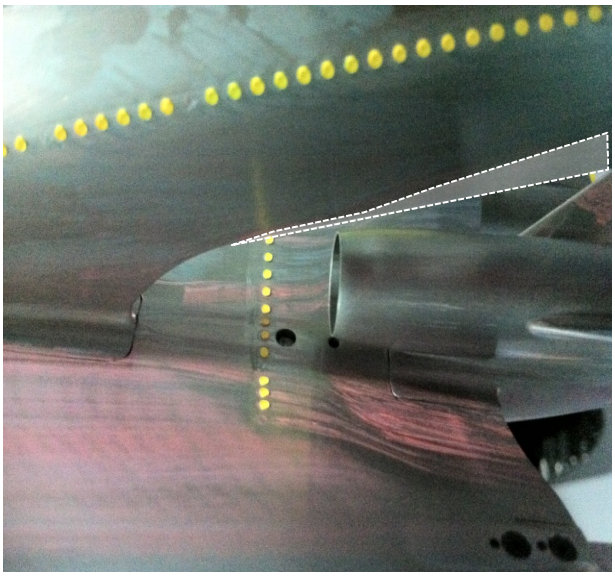

Figure 82. Blade Flow Separation Above Nacelle and Induced by Nacelle Shock

All flow at cruise conditions was attached and turbulent everywhere (Fig. 81). Although our past experience with transition detection by sublimation suggests that this model's flow was stubbornly laminar. We believe the CFD's laminar separations may be overpredicted and flow turbulence and trip discs may have increased flow attachment. The only significant region of separated flow was on the blade trailing edge, where it was expected. The separation appeared to be encouraged by the center nacelle shock's strong, swept, adverse pressure gradient impingement, and may not have occurred there without the center nacelle's shock impingement, Figure 82. The sonic boom difference between laminar and turbulent was small, Figure 83, and was due to a combination of the flow field difference and boundary layer thickness difference. Typically having the expected laminar flow on a model (and similarly attached flow) makes a better sonic boom match with the thin full scale boundary layer.

At full scale, Euler predictions of sonic boom match viscous predictions because the boundary layers are so thin. Finally, the sting-mounted predicted and measured surface flows were attached and well behaved except for a laminar inboard wing, upper surface, and vortex flow separation, Figure 84. The lower surface oil, Figure 85, had regions where the oil was wiped clean in the nacelle shock impingement region. Careful, direct examination at the time of the streamlines ahead of the clean region and following, showed only straight streamlines without any indication of separated streamlines in between.

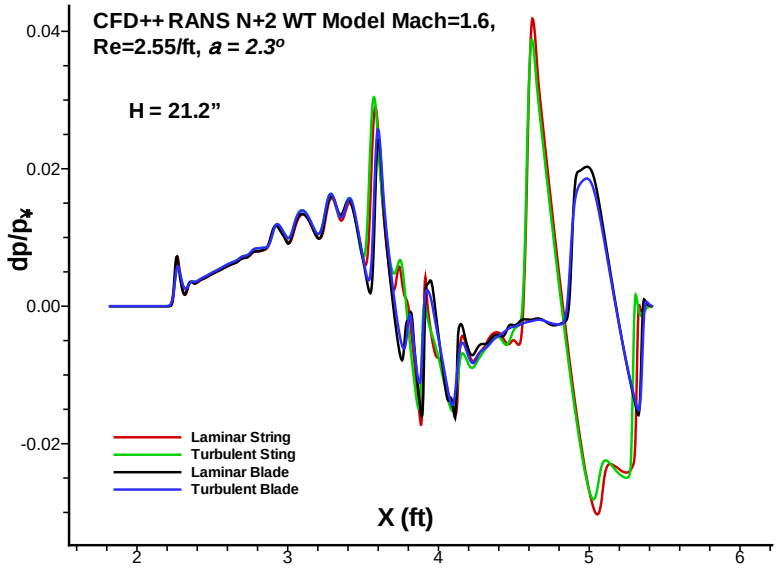

Figure 83. Signature Difference Between Laminar and Turbulent

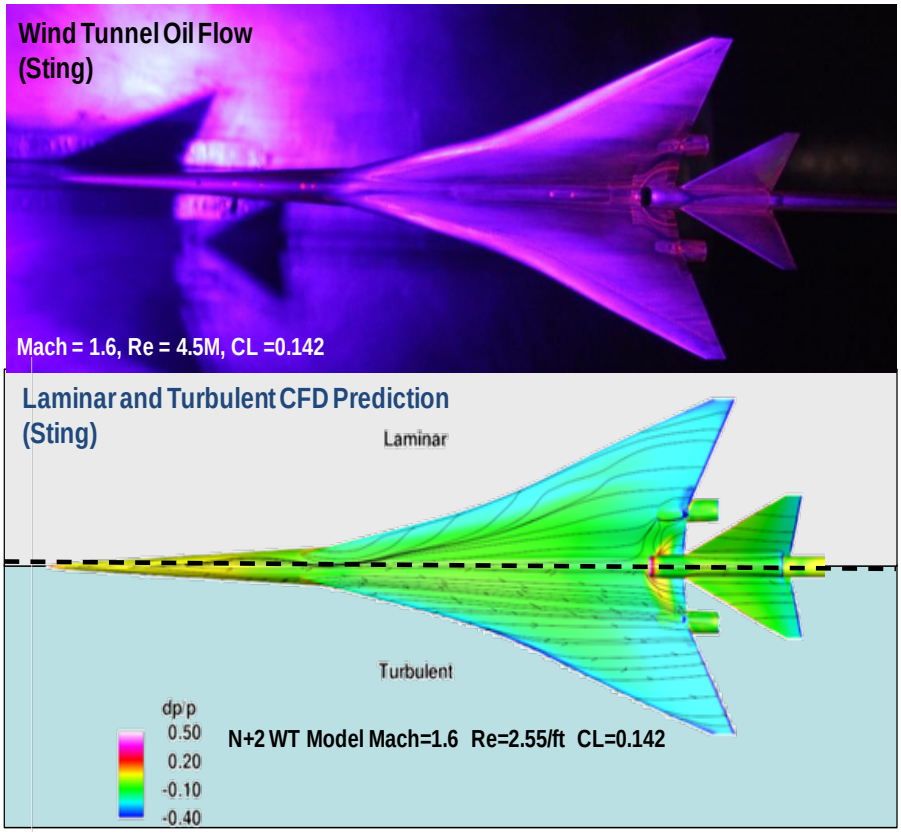

Figure 84. Oil flow showing fully attached like turbulent

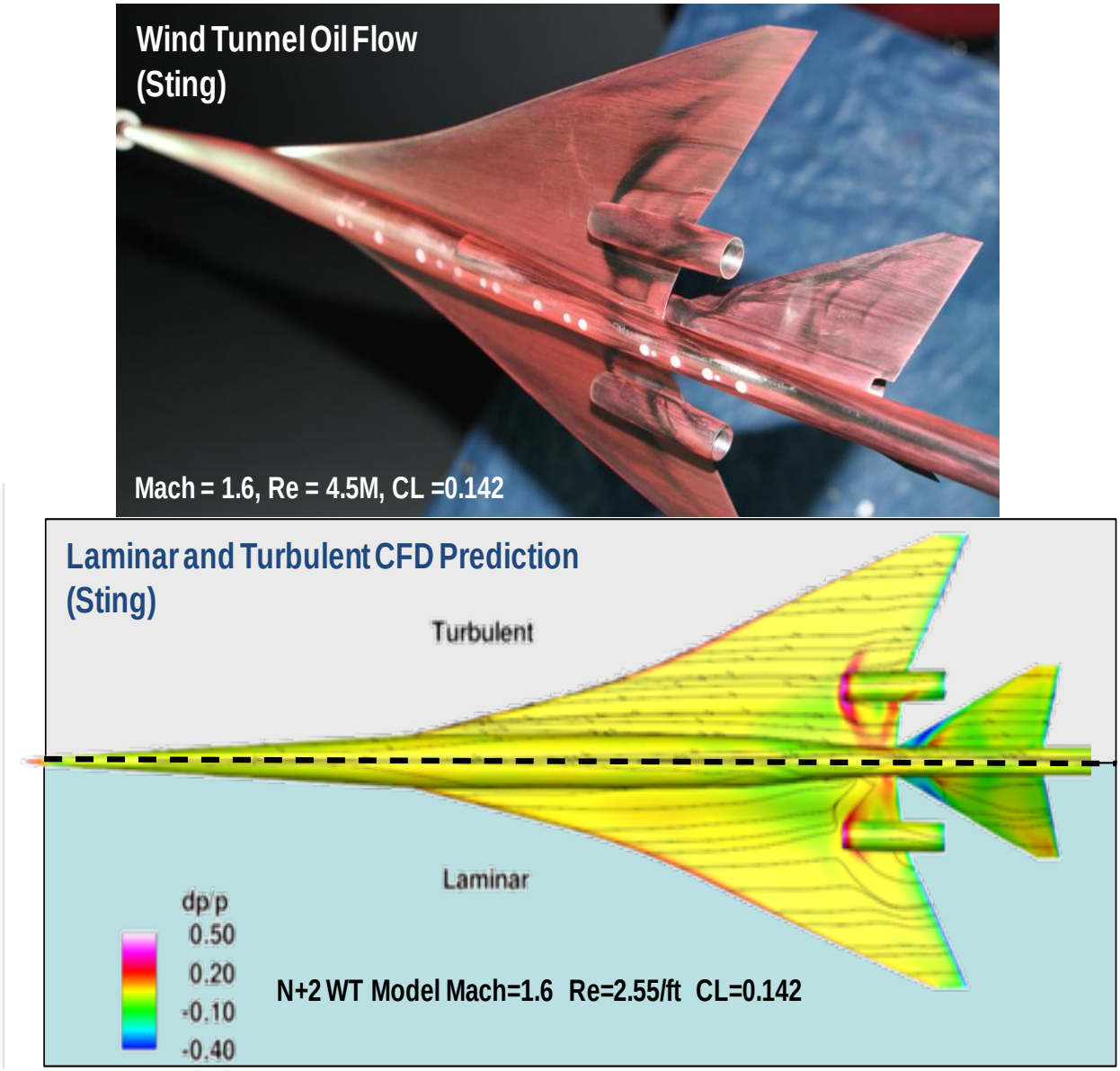

Figure 85. Oil flow showing fully attached like turbulent on lower surface

6.1.8 LM3 Four Signature Processing Techniques

The following is a summary of the signature processing techniques and results. Calibration is described in Section 6.1.9 and results are in Section 6.1.10. For each of the two measurement translation types (illustrated in Fig. 77) there were two techniques investigated for processing signatures. The first two were for 16 in. translations and the second two were for the 4 in. translations. The 16 in. translations were intended to cover enough periods of the static pressure oscillations (with enough measurement samples) so that the average would match the correct absolute level. With enough samples and translation to average out the distortions to the correct level, the Averaged Over Distance technique (1) does not require the calibration (unlike the 4 in. translation). This was an important attribute because the length of the signature plus 16 in. of translation meant that much of the measurements would be outside of the fully calibrated zone available from the SEEB-ALR's flat signature portions (calibration Section 6.1.9). Thereby, calibrated Average Over Distance (2) shows less of a calibration improvement than when used

on the 4 in. translations. However, the reliability of 16 in. averaging provided better results than calibration. Although applying the calibration improved on the signature, averaging by itself provided such good results that adding calibration did not make a significant change to cases with 26 measurements. In the LM1 test it was determined that some measurement orifices had more variability than the others. Results showed that orifices located where the static pressure around it was changing rapidly had as much as three times the variability in pressure measurements than orifices where the ambient pressure was relatively constant. The third signature processing technique (3) investigated whether excluding high variability orifices would yield better measurements. We ultimately found that while low variability orifices did yield better measurements, averaging measurements from more locations was so powerful at eliminating the spatially distributed distortions that technique (4) of averaging all orifices worked better than excluding high variability orifices. Averaging over longer distances appears to be the most efficient way to get accurate signatures of very low sonic boom in the Ames 9´ 7 wind tunnel with a uniform flow field and "shock diamond" variations (variations small enough that several periods could be translated across with our new Linear Actuator).

Calibration could be done more efficiently and effectively with a model designed specifically for the application. Whether calibration is cost effective depends on the number of runs over which its cost in time would be applied in order to improve accuracy and reduce the number of samples needed for the required accuracy. To be justified for efficiency the calibration would require many measurements to be made for each Mach number run as well as reduced measurements. However, even if its cost is not fully justified on an efficiency basis, the results of running such a flat-top validation model give a lot of insight into the flow field in which measurements are being made. Such insight has led to the successful test procedures implemented on the LM3 test and will yield more payoffs in future testing. For example, Averaged Over Distance should also be used to accurately measure a model with surface pressure orifices.

6.1.9 LM3 Blade Rail Calibration

It was apparent from the LM1 data analysis and comparisons of static pressure variations of all supersonic tunnels around the world that even high quality flow has spatially varying distortions to pressure measurement slope and zero offset. These distortions critically affect the accurate measurements of low sonic boom pressure disturbances. The flat-top pressure regions of the SEEB-ALR model offer an effective means of calibrating the measurement rail to improve its measurement accuracy. The LM1 test also showed that a separate calibration was required for each Mach number and measurement height desired. Since all of LM3 was planned for a cruise condition of Mach 1.6, this test required only 2 height calibrations. The calibration itself is (mostly) the same as any other microphone or pressure transducer calibration. A known pressure and a zero are measured and a slope and intercept correction are calculated that make the pressure measurement signal equate to the known pressure and zero. A more detailed description and tutorial of the calibration process is planned for a technical paper (Refs. 10 to 12) for the June 2012 AIAA Applied Aerodynamics conference.

CALIBRATION SIMPLIFIED

Definition: difference or ratio between the value the rail orifice was supposed to measure and what it is measuring

Calibration from SEEB-ALR w/MSA

Step 1 - Zero Offset correction determination:

Trailer Flat [0] – Measured Trailer = **Zero Offset** correction

Step 2 – Slope correction determination:

Front Flat [+] / (Measured Front – **Zero Offset**) = **Slope** correction

Application to Model:

Having observed in the LM1 test that a correction of 20 to 50 percent was required to match the flat-top pressure, considerable effort was spent trying to understand its source and understand why such large distortion values had not been noticed previously. For prior sonic boom testing with a single point measurement probe the distortion would only be experienced at one point (or sometimes two points when the probe was on a track and had to be moved to measure a vehicle longer than the model translation available (Refs. 13 and 14). As a result its variability was not appreciated. Finally, the observation was made that for most typical low sonic boom models, the signature consisted of a saw tooth pattern of three shocks in front and one shock aft. Once a shock coalesces a portion of the signature, they (all the distortions of that portion) become averaged together. Without long flat shaped portions in a signature (or many small short shocks) the distortion becomes averaged and much harder to discern. Such as the Averaged Over Distance procedure, such signatures are already partly averaged and need fewer additional samples averaged to accurately measure the strength of their shocks. Or conversely, the latest low amplitude sonic boom designs have a long, shallow ramp shaped forebody followed by many small and short shocks. Therefore, flow field distortions of the signature have become many times more apparent, and now require distortion elimination through calibration and averaging or lots of averaging.

For the LM3 test the SEEB-ALR model's 9 in. front flat and 11 in. trailer flat provided a (similar in amplitude to the model pressures we will measure) positive signal and (nearly) zero signal respectively, for making a linear, slope and zero, calibration at each Blade Rail orifice. Or more specifically, it provided the signals for a calibration at each orifice that they both traverse. The full calibration range is limited to the portion of the Blade Rail that both the front flat and trailer can be made to cover with 24 in. of translation capability. Also, to position the calibrated range to best cover the Low Boom model's signature, the SEEB-ALR model was mounted on the MSA that was mounted on the balance adapter. This stack positions the front flat to cover the Low Boom model's aft signature through 20 to 24 in. of Xram travel. However, the slope calibration was not available to cover the aft signature for the other 12 in. during 16 in. Xram traverses.

For LM3 calibration measurements, the SEEB-ALR model was measured at Linear Actuator Xram's of 0 to 24—1 in. at a time for a total of 25 measurements. Moving one inch at a time was not necessary for calibration with the front and trailer flats. The model could have, for example, been measured at just 0, 8, 16, and 24 in. (and 6.25 times longer duration to get the same total measurement oversampling time) and the calibration would have worked the same. However, measuring every inch also allowed an Averaged Over Distance signature to be processed for the SEEB-ALR model from the same data.

The flat portions of the 25 SEEB-ALR measurements are plotted together in Figure 86. The average value of the Front Flat [+] and the Trailer Flat [0] are highlighted with a transparent dashed red line. From Step One (above), the difference between what the Trailer flat was supposed to be (near zero) minus the measured Trailer Flat equaled the Zero Offset correction. For comparison, the average Leader ahead of the vehicle illustrated that the value of the Trailer Flat was significantly greater than the noise floor of the Leader. The non-zero value of the measured Trailer Flat was believed to be due to shock waves coming from the wall where the Blade Rail was mounted and reflecting off the aft (11 in. long, 1.4 in. diameter, cylindrical) section of the SEEB-ALR model. These reflections only occur when a model is there, so they were not in the ambient reference measurement. (When the model changes in height the Zero Offset pattern shifts in location on the rail in a corresponding manner.) This understanding of the source of the Zero Offset also leads to a substantial limitation in the accuracy of calibration in general. The strength of the reflection is going to be different for differently shaped models, e.g., the Low Boom model is going to create a different Zero Offset reflection than the SEEB-ALR model upon which the calibration was determined. To achieve better calibration accuracy, we need a more accurate way to simulate the Zero Offset reflection than using an axi-body for a winged configuration. We could try to scale the Zero Offset magnitude by the model's local span to see if the correlation improves. The validity of such a scaling might be investigated in a future test with measurements of a highly swept, triangular, delta planform flat plate's reflection. Future improvements aside, the current calibration process does seem to consistently improve measurements.

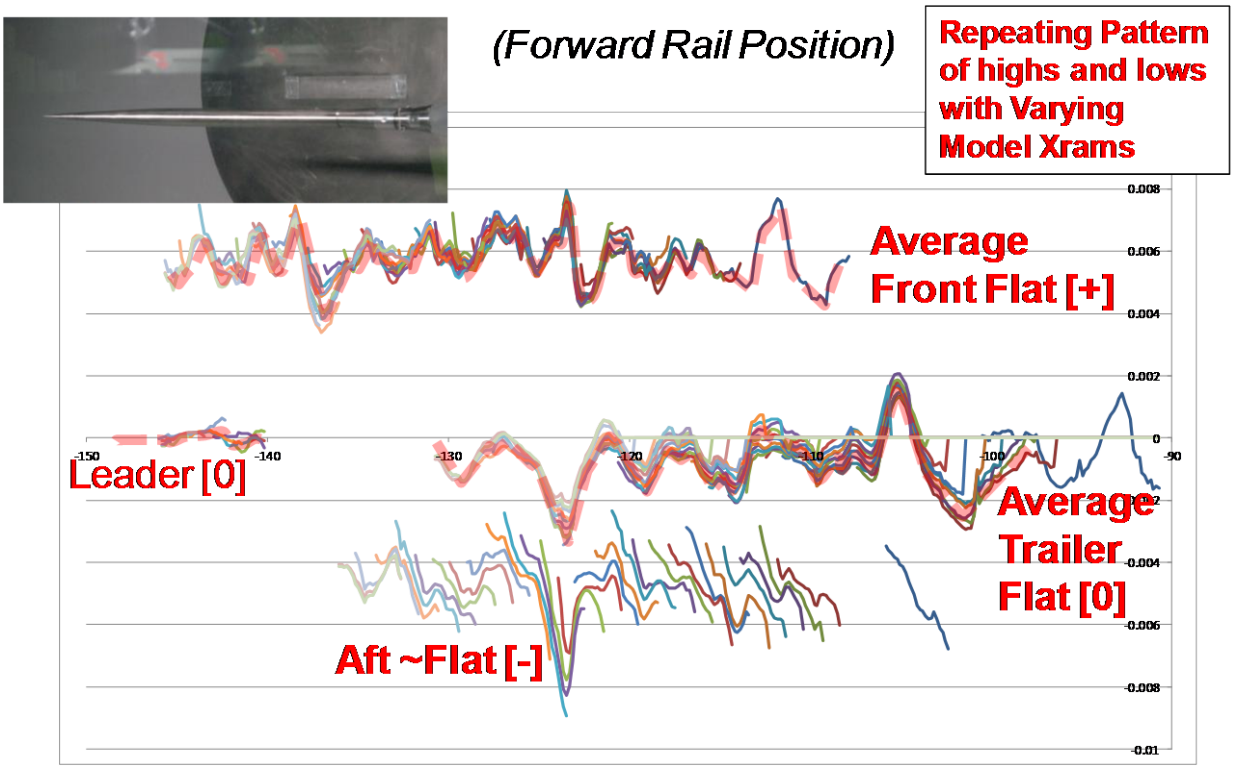

Figure 86. Pattern of distortion zero and slope repeatability

After the Zero Offset correction is determined, the Slope correction can then be determined from step two (above). The slope correction is the ratio of what the flat was supposed to be versus what was measured, after the zero correction has first been removed. Additional information that is in Reference 10 illustrates that slight compressions and expansions traveling along with the signature seem to explain the source of this correction and why it is correctly applied as a multiplier. The application of the full calibration process applied herein also includes a correction location adjustment for the Mach angle change created by the model itself. The adjustment is used on all data shown. It improves measurement correlations and is supported by physics; however, the complexity of its explanation is deferred to Reference 10.

The final calibration resulting from the process described is shown in the Figure 87 plot. The calibration's Slope ratio and Zero Offset increment are plotted at the X of the orifice that they represent. An analysis was performed using the calibration to quantify the difference between averaging over 4 and 16 in. for 26 measurements. The calibration indicates that the 16 in. translation is approximately 3 times more accurate in absolute signature level, with most of the improvement present by 12 in. of translation. The preceding analysis is another example of the value of the SEEB-ALR calibration analyses. The benefit of applying the calibration is shown in the following sub-section 6.1.10 LM3 Test Results.

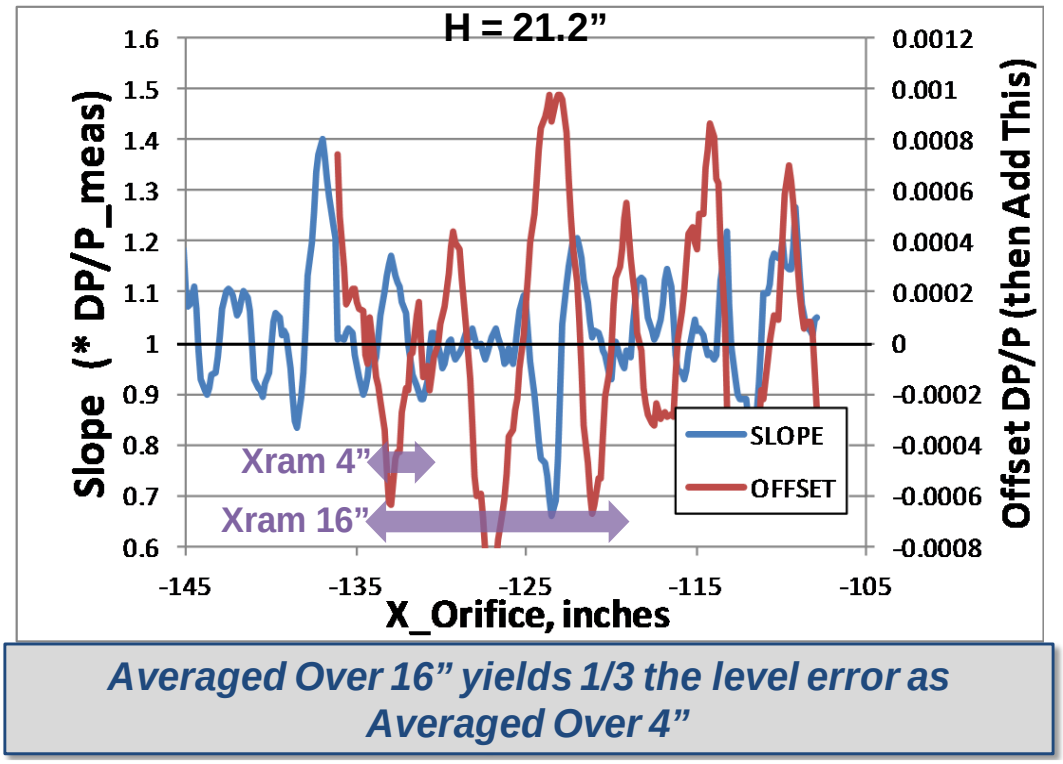

Figure 87. Slope and zero (offset) correction for each orifice based on SEEB-ALR measurements

6.1.10 LM3 Test Analysis and Results (WBS 3.3.4)

AVERAGED OVER DISTANCE (Technique 1)

1021-01 Low Boom Configuration, 16 in. Translations—Starting with signature processing technique, (1) Averaged Over Distance, the inset in Figure 88 shows a compilation of all the measurements that were averaged to make the final signature. For this technique, the signatures were first translated into alignment. Then the average at each orifice was determined after first discarding the highest and lowest values. This was found to help eliminate oscillations that occurred with the measurement spacing, 0.63 in. in this case. The oscillations were caused by measurement orifices with peaked sensitivity, either low or high. Discarding the highest and lowest values had the effect of dropping the most peaked orifice measurements, which tended to be the same orifices again and again. In an interesting parallel, the Average Over Distance technique (1) was analogous to technique (3) Calibrated Excluding High Variability Orifices; except, the most statically distortion peaked measurements were excluded, instead of the most dynamically variable orifices. Eliminating high/low measurements was only necessary when translating by more than one orifice at a time or when not using calibration (in these cases oscillations was not a problem).

Another difficulty in testing came from variations in lift that occur while translating the model. Changes in lift as small as 2 percent can significantly change sonic boom, and lift for the case of Figure 88 varied 12 percent during the 16 in. translation. Even the short sonic boom propagation of 31.8 in. complicates the variation further, because (even though the initial change in lift produces a linear and smoothly distributed change in the signature) shock coalescence concentrates the lift increment into a very spiked distribution, as shown in Figure 89 in blue. The inset plot in the figure shows two CLs from both measured averages and CFD predictions. Greater lift causes stronger shocks to move forward and stronger expansions to move back. This second-order movement of the shocks is termed aging (or steepening, or stretching) of the signature and is the primary concern of sonic boom minimization by

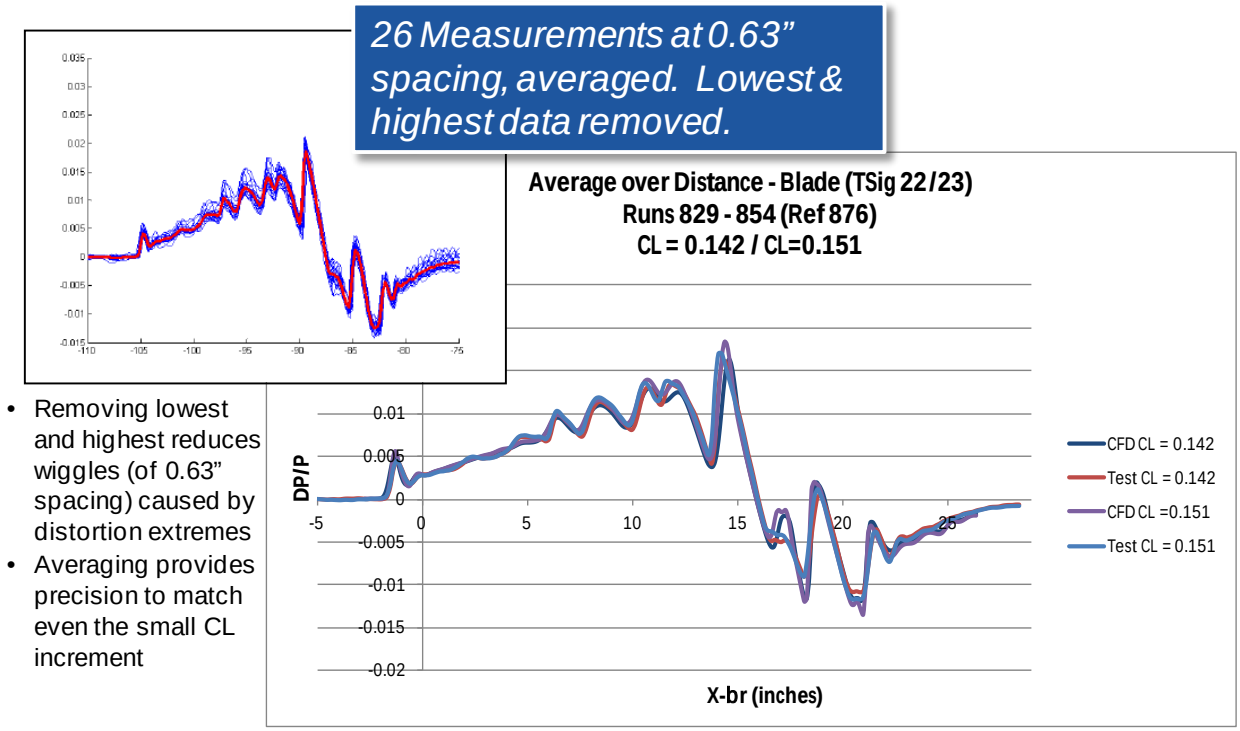

Figure 88. Pre-Test CFD Matches Measurement with Remarkable Precision

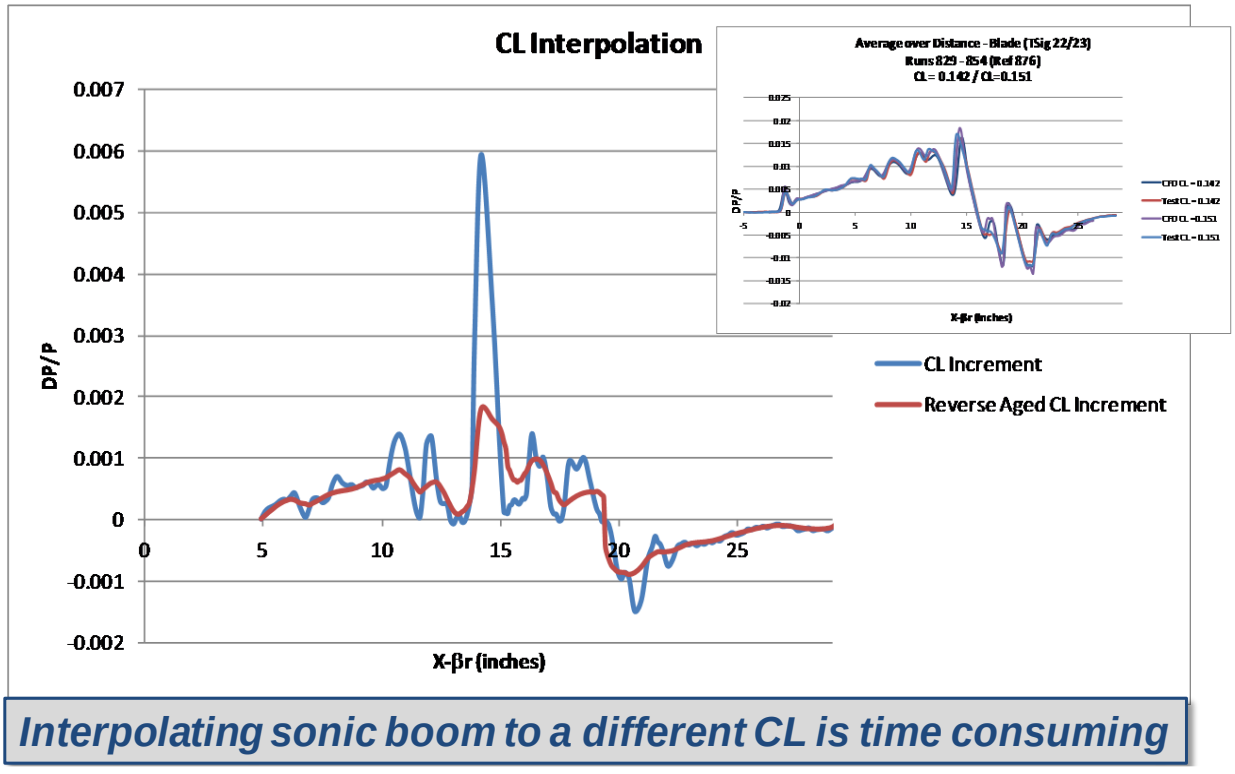

Figure 89. CL increment initially coalesced at each shock into spikes

signature shaping. By just averaging the signatures together at different CLs, the averaged signatures shocks become more rounded. For the red line of Figure 88, the signatures were first "reverse-aged" and then the sonic boom increment due to different CLs was calculated with a reduced spiked result. For the Averaged Over Distance signatures shown in Figure 89, each measurement was first reverse-aged, and then a (reverse aged, red line) sonic boom CL increment was applied to interpolate the signature to the desired CL of 0.142 or 0.151. Finally, each measurement was "re-aged" and averaged together to make the final signature. In this case, the additional effort resulted in a slight (line width size) increase in shocks' minimum and maximum peak strengths. There was no difference in the propagation of the processed signature. The cases where the CL varied as much as 30 percent, the reverse-aging and CL interpolation made a more significant sharpening of the signature and slight propagation change.

SEEB-ALR—As mentioned in sub-section 6.1.9 LM3 Blade Rail Calibration, the SEEB-ALR calibration measurements were also suitable for processing an Averaged Over Distance signature, which is plotted in Figure 90. The prediction of the SEEB-ALR model was made using CFD++ in a radial 2-D solution. The geometry was re-lofted from the fabrication quality inspection data, so it accurately contains every small imperfection that could be measured to ±0.0003 precision. Using a radial CFD solution was efficient and 1.4 million cells were used (swept at the Mach angle) for a high resolution prediction. In the solution, even small wiggles on the front flat of the signature prediction matched inflections in the geometry. The measured Averaged Over Distance signature also matched the small wiggles of the front flat with precision better than ±0.0003 DP/P. There was the aforementioned slight rounding of the measurement due to vibration of the model in the tunnel; whereas, the CFD prediction rightly showed the shocks as being more peaked. The aft expansion portion of the signature however, had approximately 20 percent lower expansion strength in the measurement than the CFD prediction. This over-prediction of the expansion strength was also seen from the radial CFD solution of the OptSig model. At a future time we would like to perform a very high resolution 3-D analysis to assess whether this type of radial CFD expansion prediction is missing significant detail.

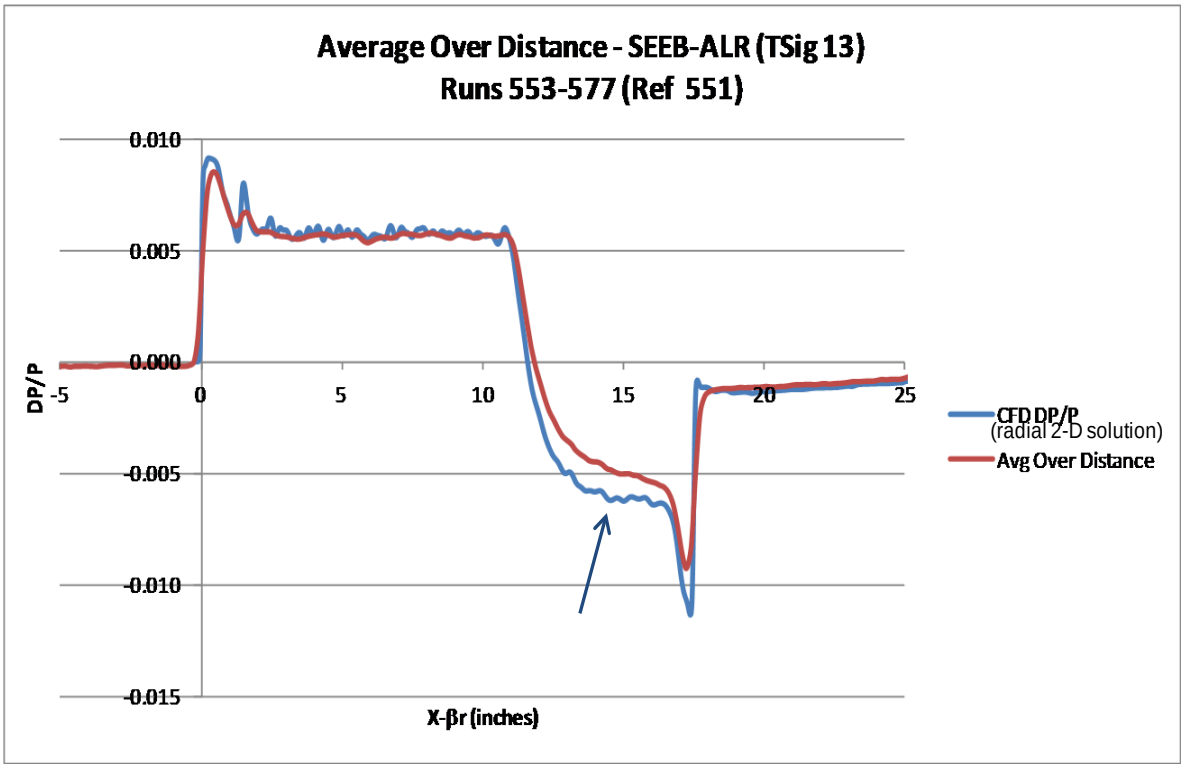

Figure 90. Great front signature match but aft level mismatch with CFD was unexpected

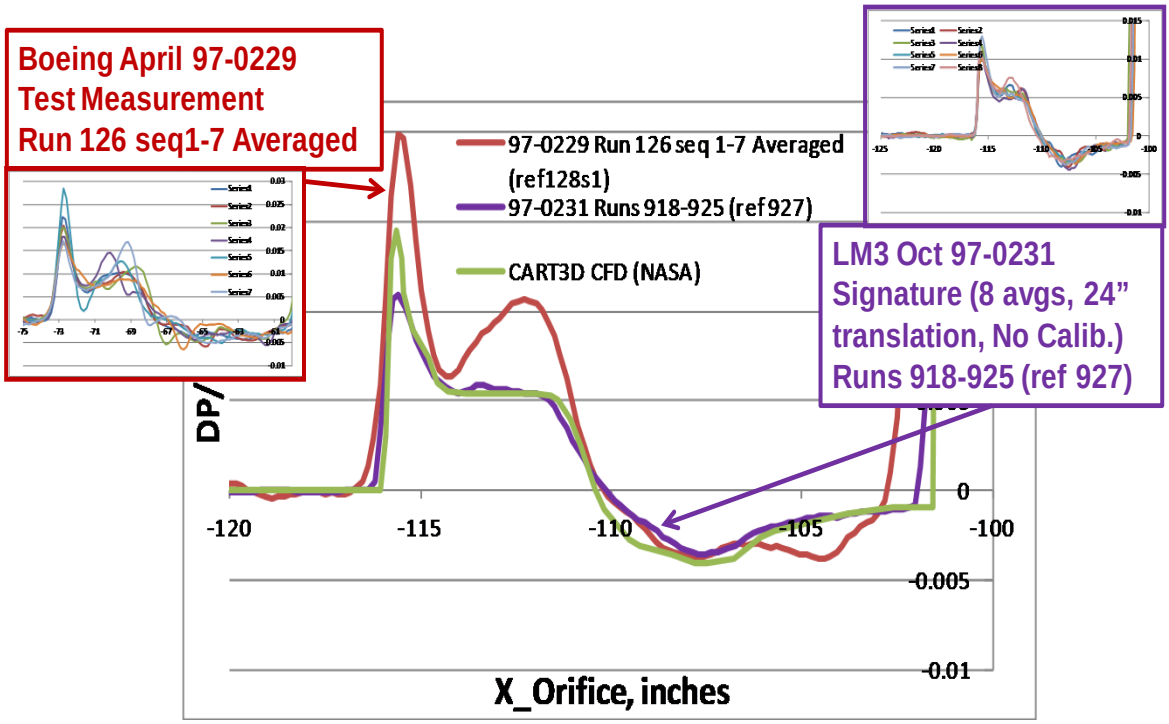

Figure 91. LM3 Good Match from 8 (90 sec) Measurements and Partial New Process. 97-0229 with 7 (2 sec) Measurements Converging with Reflections

AS2—The AS2 model from the 97-0229 test was rerun in the LM3 test to provide a test-to-test, and more specifically, a measurement rail-to-rail comparison. The 97-0229 test used a 2 in. tall and 1.5 in. wide wall Rail versus the 14 in. tall 0.1 in. diameter edge Blade Rail. The aligned individual measurements are shown in the corner plots for each rail in Figure 91. The 97-0229 measurements are only 2 sec sample times and were taken at different heights (without the Linear Actuator) of 24 to 36 in. every 2 in. Before averaging the signatures they were scaled in amplitude by the square root of their height over their rail divided by 30, to match the 30 in. measurement and prediction height of the other plot lines. Even though the sample time was short, averaging of the 7 measurements made the sampling time equivalent to 14 sec, and the averaged red line in the main plot had a much smoother leader—quantifying the reduced noise variability of the averaged signature. Compared with the "free air" CART3D CFD prediction (provided by NASA), the 2 in. rail measure doubled the nose shock strength, dropped to nearly the same flat pressure 1 in. behind that shock, bulged to a peak, doubled the flat pressure 4 in. behind the nose shock, followed the expansion prediction for the next 5 in., then bulged again to twice the expansion strength in the next 2 to 3 in. (followed by a model support shock).

This behavior seems to follow a pattern of measuring reflections, also seen in CFD modeling with the following consequences listed. First, the nose shock reflected from the flat-top rail until 0.75 in. from the center, where it propagated past the rail edge without reflection. That relief of the reflection shock at the edge of the rail took 1 in. to propagate to the center of the rail; thereafter, the signature doubling was lost. Then the front shock spike reflected off the subsonic portion of the wind tunnel wall boundary layer, became somewhat diffused, and traveled from the wall (around the edge) another inch to the centerline orifices. There was not an exact 1.0 or 2.0 factor after the front shock because the signature was an integral of what happened before. Different portions of the signature were doubled, relieved, reflected off the wall and overlapped in a complex fashion that caused strong non-intuitive distortions of the signature—following the first inch of simple 2.0 nose shock reflection. Averaging Over Distance was very effective at removing flow field distortions and reducing variability through summing sampling time, but it retained reflections inherit to the measurement rail.

The 97–0231 test measurements were translated from 0 to 24 in. with a 4 in. spacing to match measurements taken in 97–0229, not as an actual Averaged Over Distance translation series. Regardless, the measurements were similar. We decided to apply the process to this reduced measurement translation. The individual measurements used a 90 sec sampling time, so their noise level was much lower and the averaged blue line in the main plot had a leader almost exactly on zero. The averaged signature front shock peak was approximately 25 percent lower than the prediction; however, the measured shock began sooner and had the same impulse area—providing a matching propagation with the prediction. The rest of the signature was also a good match. With only 8 samples and no calibration applied, it does not have the same accuracy produced for the low boom model in Figure 100. However, it was sufficient to validate this prediction and solidify differences with the 97–0229 measurement rail.

CALIBRATED AVERAGE OVER DISTANCE (Technique 2)

LBWT—Applying calibration to the already accurate Averaged Over Distance signatures of Figure 100 produced barely discernable changes. We decided to add calibration to the LM1 measurements of the LBWT model Averaged Over Distance in Figure 92. There were 13 measurements of the LBWT vehicle taken over 24 in. every 2 in. However, the CL variation of the measurements was greater than 75 percent, which made the averaging smear the shocks greatly. By dropping the highest CL measurements runs 9 to 12, the remaining 9 runs' CL variation was reduced to 30 percent. The inset plots in the upper corners show the signatures before averaging, on the left without calibration, and on the right with calibration. The tighter overlap of the calibrated data is noticeable in the inset plot and leads to a sharper main shock in the averaged data. As the data accuracy became better with averaging, the improvement from calibration gets smaller, which was expected. The calibration improvements to the individual measurements of the inset plot are more dramatic.

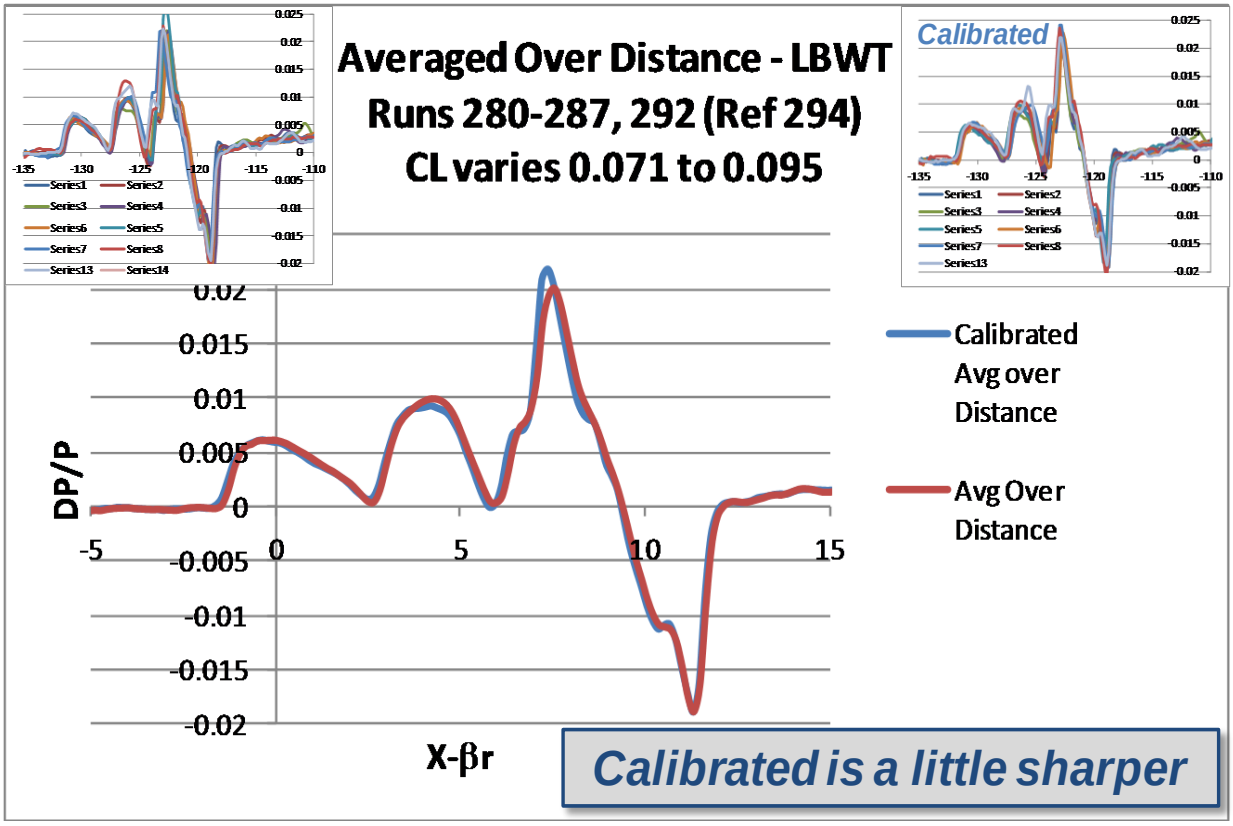

Figure 92. Technique applied to LM1 with only 9 measurements and large CL variation

CALIBRATED EXCLUDED HIGH VARIABILITY ORIFICES (Technique 3)

1021-01 Low Boom Configuration, 4 in. Translations—One leading thought for making higher accuracy measurements was to use orifices that had lower variability. It had been observed in LM1 data that orifice measurement variations could differ by a factor of 3 from location to location. These areas of high orifice variability were also linked to rapidly changing static pressure variation around that orifice. We wanted to determine if more accurate measurements and shorter sampling times could be used if higher variability orifices were excluded. To first identify the higher variability orifices, plots were made of the 45 two second sample time measurements from the reference run shown in Figure 93.

Regions of high and low variability are easily identified in such plots of the rail. Orifices with < ±0.001 DP/P were defined as low variability, making the other orifices high variability. Figure 94 compares signatures made from 26 measurements of a 4 in. translation by averaging the low variability orifices (above) and the high variability orifices (below). You can see that the low variability orifices appear to provide a better signature.

Translations were set to 4 in. for these cases to allow for measurement at the closer height of 21.2 in. and get the best full calibration coverage. Measurement at the closer height was thought to be better for accuracy because of slightly stronger signature amplitude and reduced pressure slope correction magnitude. The closer distance did have greater near-field distortion. Together with our near-field to far-field correcting cylinder method, we have confidence in propagation from near-field measurements. Figure 95 shows the improvement from applying a full calibration for a 4 in. translation. The measurement moved closer to the CFD throughout.

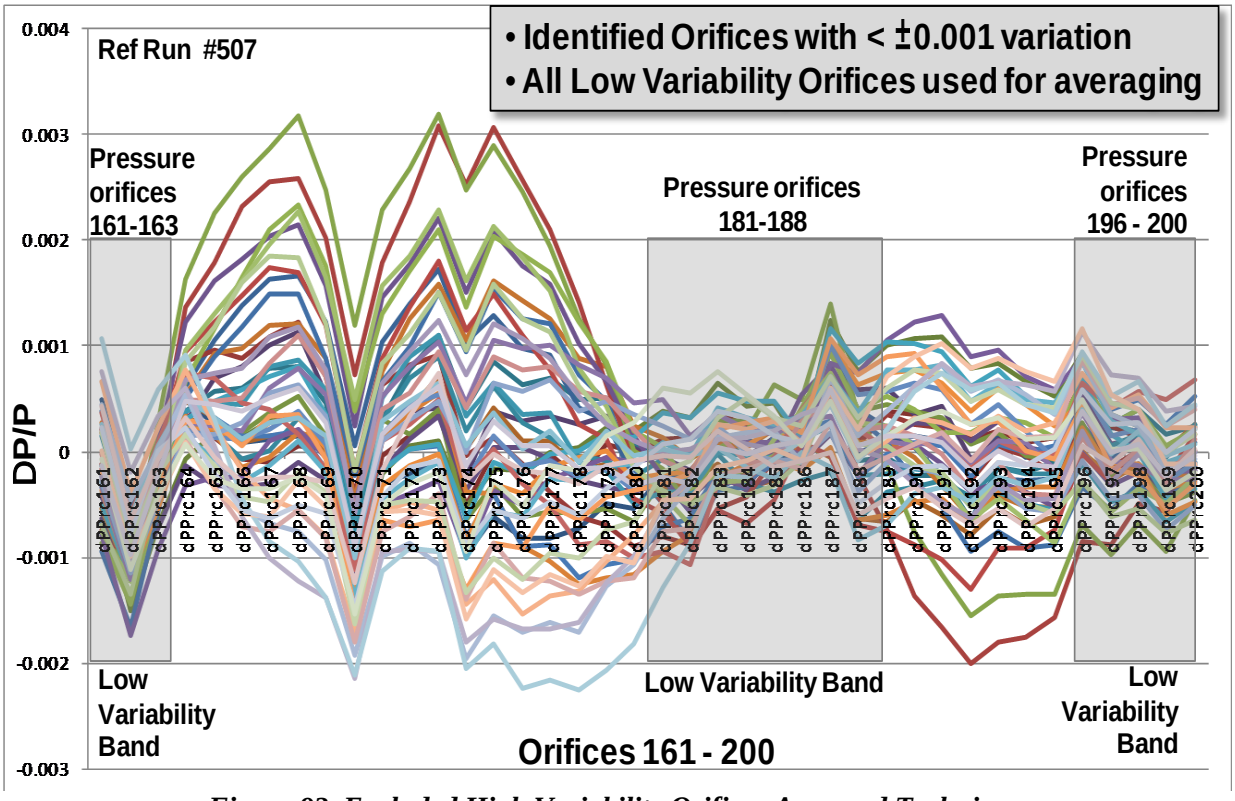

Figure 93. Excluded High Variability Orifices Averaged Technique

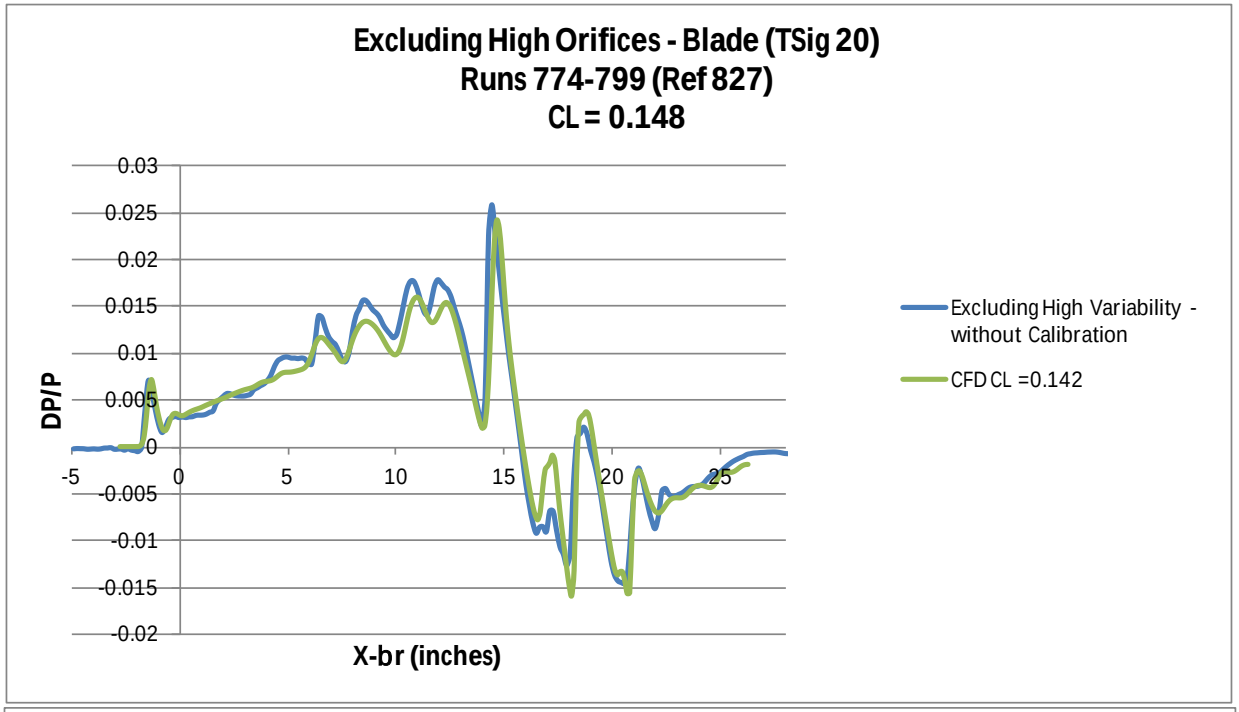

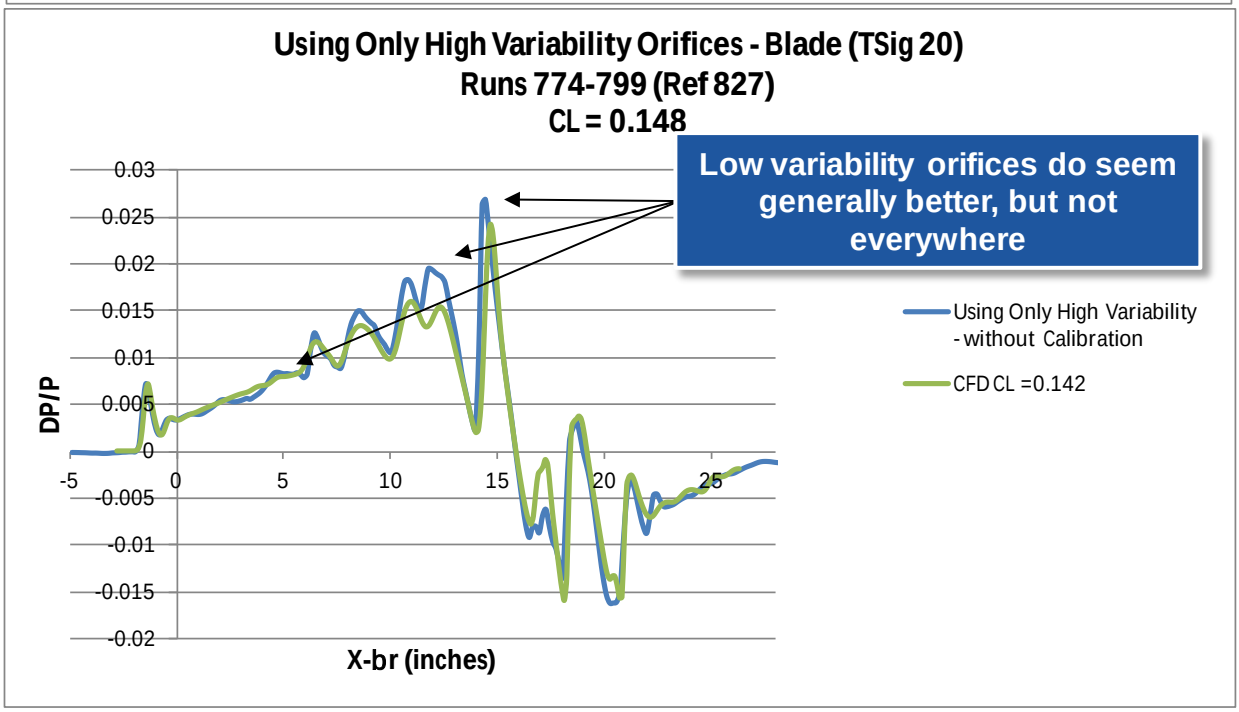

Figure 94. Low variability versus high variability orifices

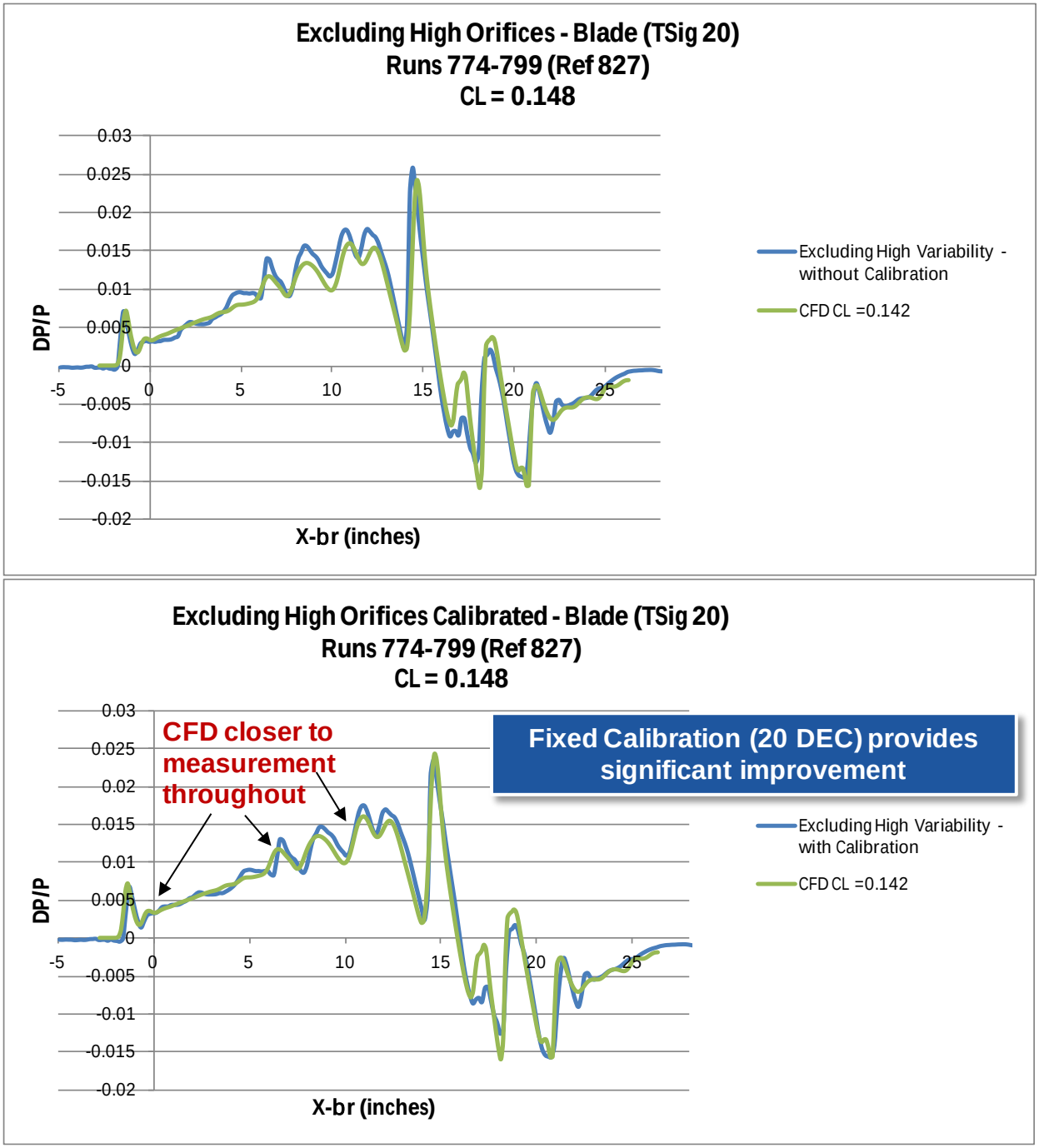

Figure 95. Calibration provides significant improvement

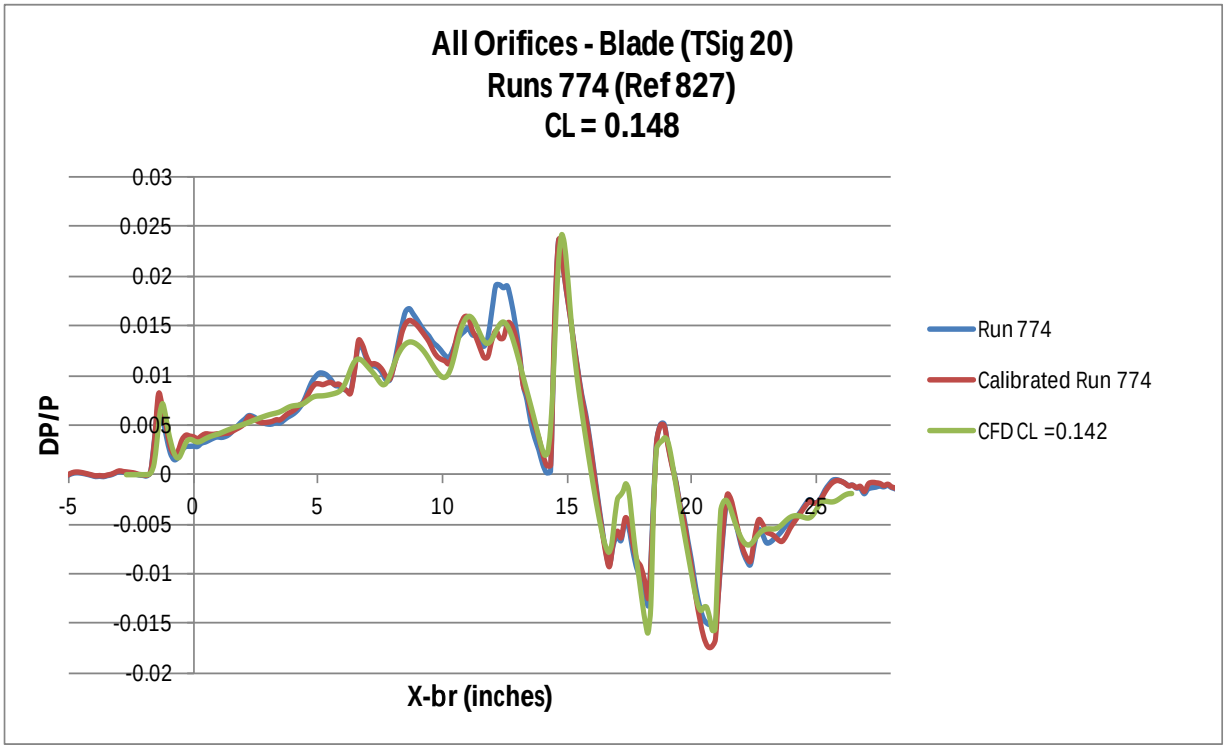

Figure 96. Calibration provides necessary improvement, but improvement is less necessary as runs available to average increases

Figure 96 shows the effect of calibration on just a single measurement. The effect was more dramatic for a single measurement than for an averaged signature. As averaging reduces distortion, averaging also reduces calibration magnitude (like shock coalescence averages, and thereby also reduces distortion). In this case, calibration was particularly helpful for a single or a small numbers of averaged signatures. Calibration eliminated high/low spiked values and the need to drop high/low values before averaging.

CALIBRATED ALL ORIFICES AVERAGED (Technique 4)

Based on the highly effective success of averaging, it was only natural to wonder if we would be better off using all orifices with low and high variability to see if more averaging was more effective than excluding high variability orifices. The Figure 97 comparison shows that using all orifices provided a slightly better signature. It was also easier to process averaging all orifices. So for the 4 in. translations, using calibration and averaging all orifices was our chosen technique for processing signatures from our measurements. However, the Calibrated All Orifices Averaged match, Figure 98, did not look quite as good as the Averaged Over Distance match. Hence, we plan to favor longer translations in future testing. Such measurements also did not require the laborious calibration calculations. Although with the many things learned from calibration studies, future improved calibration studies will still be contemplated.

Figure 99 is a further example of Calibrated All Orifices Averaged for the OptSig axi-body geometry. Like the SEEB-ALR model, the geometry for the OptSig model was a highly accurate geometry that was re-lofted from the fabrication quality inspection data. It accurately contained every small imperfection that could be measured to ±0.0003 precision. A similar radial CFD large 1.4 million cell grid was used employing Mach angle sweep for extremely high resolution solution. As can be seen in comparison (Fig. 98), the OptSig sonic boom signature had similar characteristics to the Low Boom configuration. It had a small nose shock followed by a smooth ramp with slightly decreasing slope for half of the front signature. Then the rest of the front ramp had 5 close together shocks whose average overpressure continues the reducing slope front ramp signature. There was a small shock in the expansion

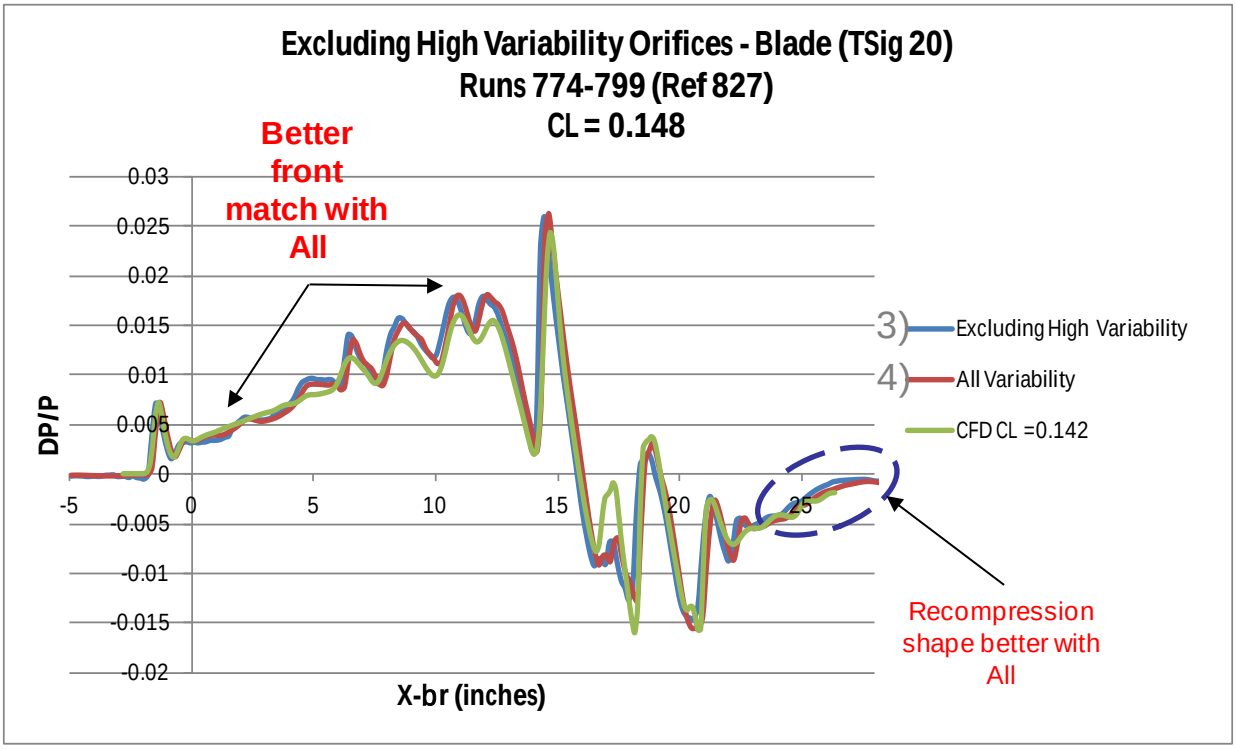

Figure 97. Averaging All Orifices (4) better than Excluding High Variability Orifices (3), and easier to process

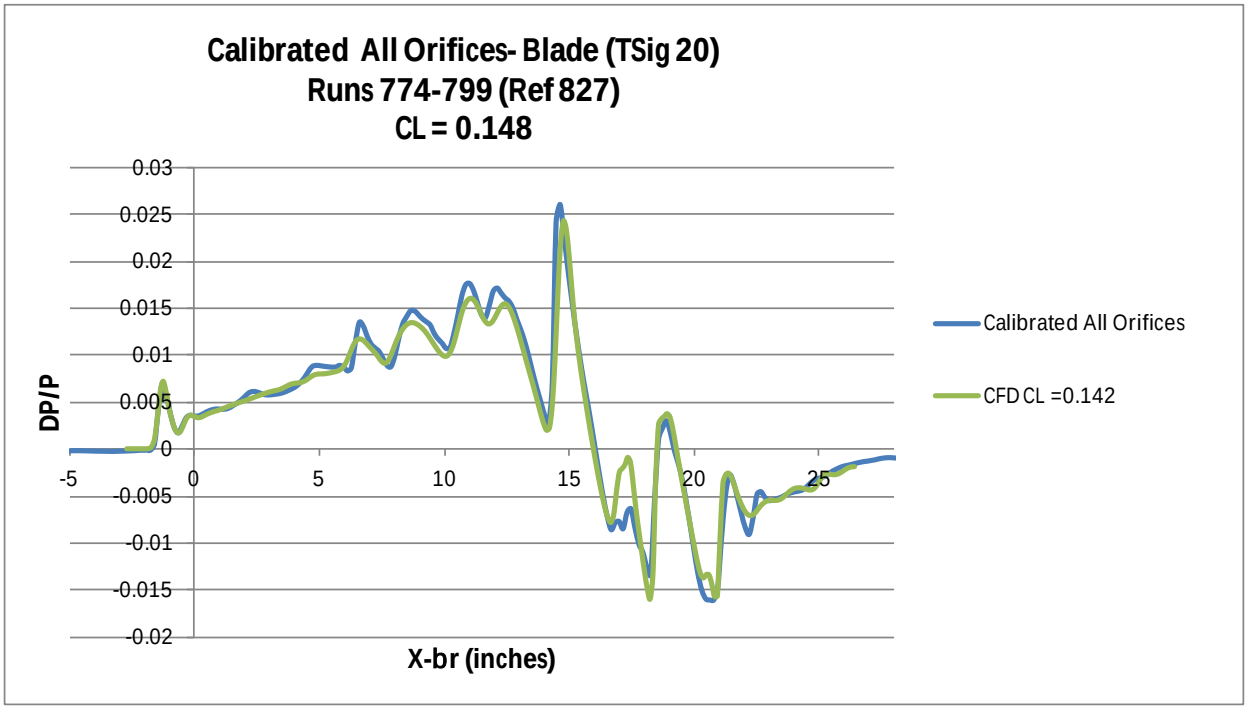

Figure 98. Calibrated (if available) All Orifices best process for signatures

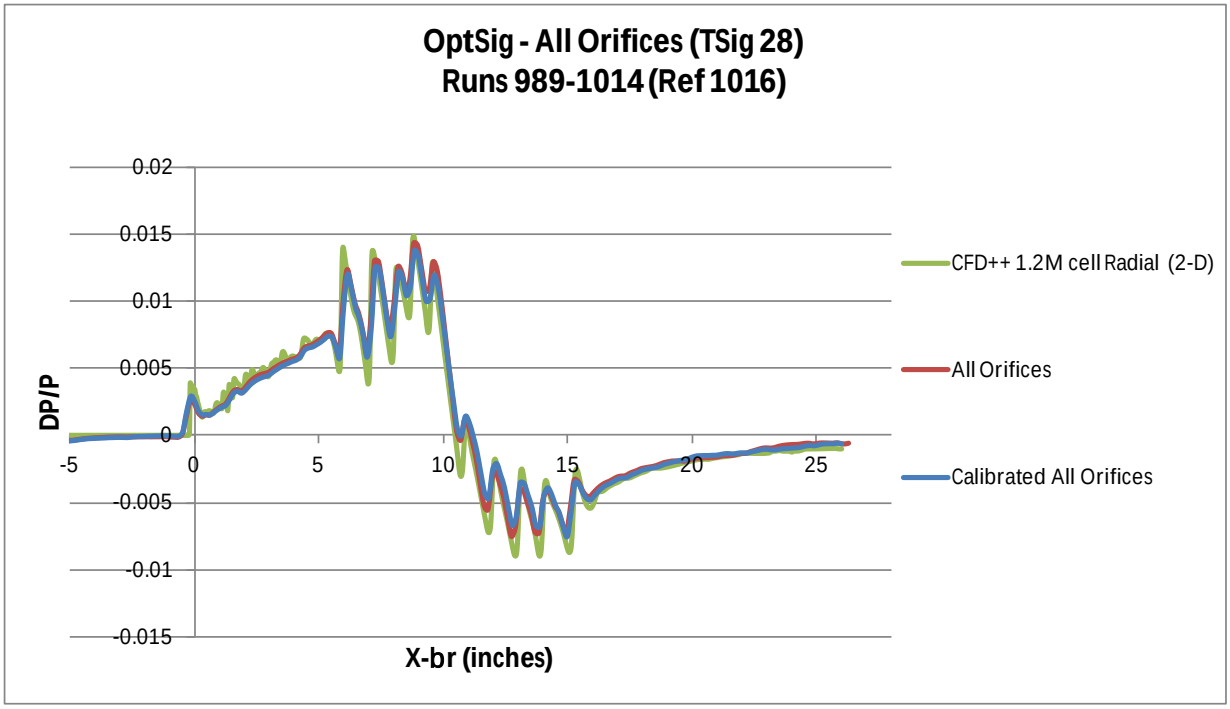

Figure 99. Calibration improves front shock match and recompression shape, but less initial aft expansion than Radial (2-D) CFD (like SEEB-ALR)

near zero DP/P followed by 4 stacked shocks that comprised the aft signature with a weak expansion DP/P near –0.005, followed by a slow recompression to ambient. These characteristics were also present in the Low Boom configuration design throughout the roll angles whose sonic boom intercepts the ground (about –50° to 50° at Mach 1.6). The All Orifices Averaged signature is shown along with the Calibrated All Orifices Averaged signature. The calibration brings the amplitude of the front ramp shocks down slightly to better match the prediction. It also made the aft shocks' amplitudes weaker which matched the prediction less well; however, the calibration better matched the measurement/prediction discrepancy seen with the SEEB-ALR model and similar radial CFD++ solution.

6.1.11 LM3 Test Validation Accuracy Assessment

The chosen criteria for sonic boom test validation success was defined to be a propogated ground signature with the wind tunnel measured sonic boom difference less than 2 PLdB. Based on problems encountered with previous measurement rails, the LM1 test was conceived as a readiness review to validate that the new Blade Rail had the accuracy to meet the aforementioned sonic boom goal for the upcoming Low Boom configuration tested in LM3. The SEEB-ALR model's flat-top signature was intended to validate that the Blade Rail was measuring the correct flat-top overpressure. The SEEB-ALR model fulfilled a double role of validating the –aft lift relaxation [of 1.05] concept. The SEEB-ALR low boom signature was successfully achieved with an equivalent area that reached a peak area/radius that dropped 5 percent in equivalent area while maintaining its minimized low sonic boom signature. We have the fundamental capability of designing for practical equivalent area distributions that do not have to increase at all times through their trailing edge the way the initial George-Seebass-Darden distributions are designed. Then the OptSig model's representative low boom signature would be a surragate for the future Low Boom configuration.

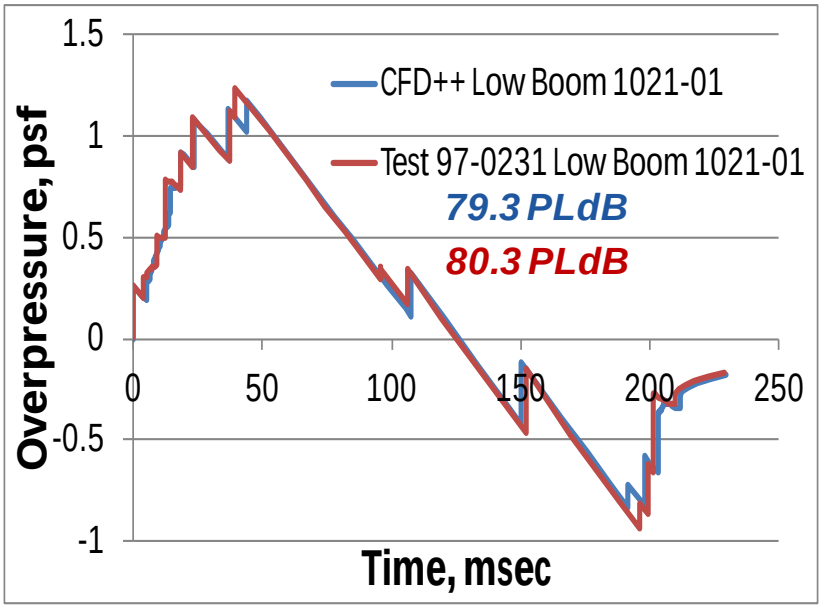

Figure 100. Matching measurement produces matching ground propagation within 1 PLdB of prediction

Measurement of the high fidelity SEEB-ALR geometry revealed a whole new world of flow field distortions that challenged making accurate sonic boom measurements. Measurement of the OptSig geometry produced a 2.3 PLdB difference with prediction. However, a new calibration procedure was developed during the test on-the-fly. The application of the calibration reduced the OptSig measurement difference to 1.3 PLdB—but partially through luck. If the same measurement differences had fallen in a different location, the loudness difference could have been more than 2 PLdB. We determined that the measurement capability had to be improved to robustly achieve the validation goal. Many improvements were implemented in 6.1.5 Test Planning with Averaging Over Distance technique. The improvements provided effective elimination of measurement distortion. The propagation of the final measurement difference to the ground is illustrated in Figure 100. It shows that the processed measurement is less than 1 PLdB different than the prediction, and it would always result in similar results regardless of location.

6.1.12 Efficiency Improvements for Future Testing

After determining that the Average over Distance technique provided the easiest and most cost effective manner to post process data, the next step was to investigate methods that further improve testing efficiency. We looked at reducing duration, number of samples, and translation distance required to obtain accurate data while reducing total testing time. For the LM3 test, the majority of test runs were a 90 second average for each of the 26 measurements taken along the blade rail. The total run time for a single pressure signature was approximately 48 min (26 measurements x [90 sec run time + 20 sec transition] = 48 min). To improve on these times, we looked at 30 sec averaged data and compared it with 2 4, 5, 8, 10, 15, 20, and 25 sec averaged duration of the same data. Figure 101 highlights the insignificant variation seen between a 2 sec and a 30 sec duration time for each measurement. Although only one comparison is shown in Figure 101, all of the reduced averaged durations results in the same conclusion. The ability to reduce a 30 sec averaged signature to a 2 sec averaged signature cuts the signature measurement time by 1/5. These values are dependent on tunnel hardware pause/move times, and a 90 sec reference run is still required after signature measurements. The potential for total signature measurement time is approximately between 6 to 20 min for the highest accuracy with shorter times possible for incremental off-design measurements. Dramatically reducing the measurement time improves efficiency and reduces costs for future signature testing.

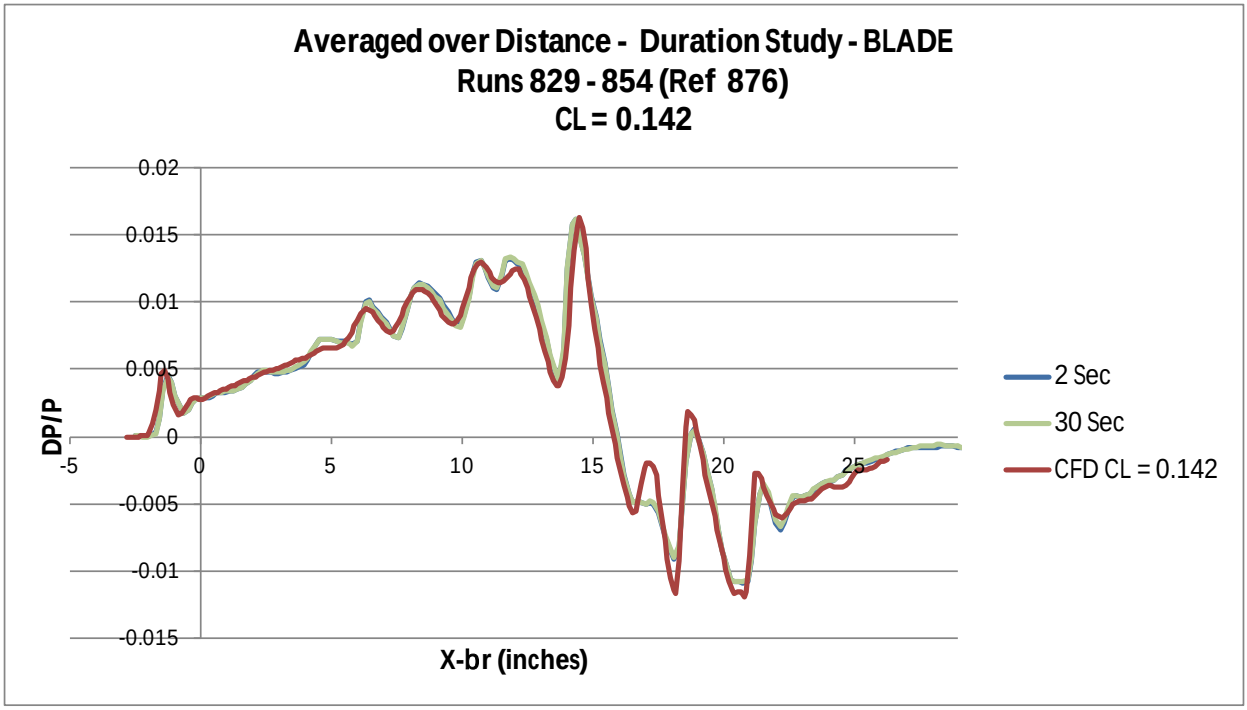

Figure 101. Insignificant variation between the 2 and 30 sec sampling when Averaging 26 Over Distance

Next, the minimum number of measurements within a constant translation distance was looked at to further improve efficiencies. Taking runs 829 through 854 (blade mounted low boom configuration at CL = 0.142) we plotted 13 through 26 equally spaced measurements while keeping the translation distance constant (16.2 in.), Figure 102. Results of the sampling study using Average Over Distance technique showed that a minimum of 13 measurements (versus 26) is required to produce similar results with a 2 sec duration time over 16.2 in. Averaging lower than 13 measurements resulted in obvious deviation from the 26 measurement curve. The greater the number of measurements, the more accurate the results. As an initial approximation, a 2 sec duration sample time with 18 measurements over 16.2 in translation provided accurate results while further improving upon signature measurement efficiency.

Lastly, we looked at translation distance as a means to improve on wind tunnel efficiencies. Looking at the same data set as the previous two studies (Runs 829 to 854), 13 measurements were held constant while the translation distance was changed from 8.06 to 16.2 in. (Consistent data was not available in this translation series for 13 measurements in less than 8 in. of translation.) Figure 103 does not definitively define a minimum length of translation required to achieve sufficient accuracy. Insignificant (to loudness) but noticeable variation in the curves was evident as the translation distance changed. The plot suggests that translation as short as 8 in. may be sufficient; whereas, 4 in. used for the results in Figures 94 to 98 did not seem to provide enough translation through the measurement distortion highs and lows to achieve accurate absolute DP/P levels.

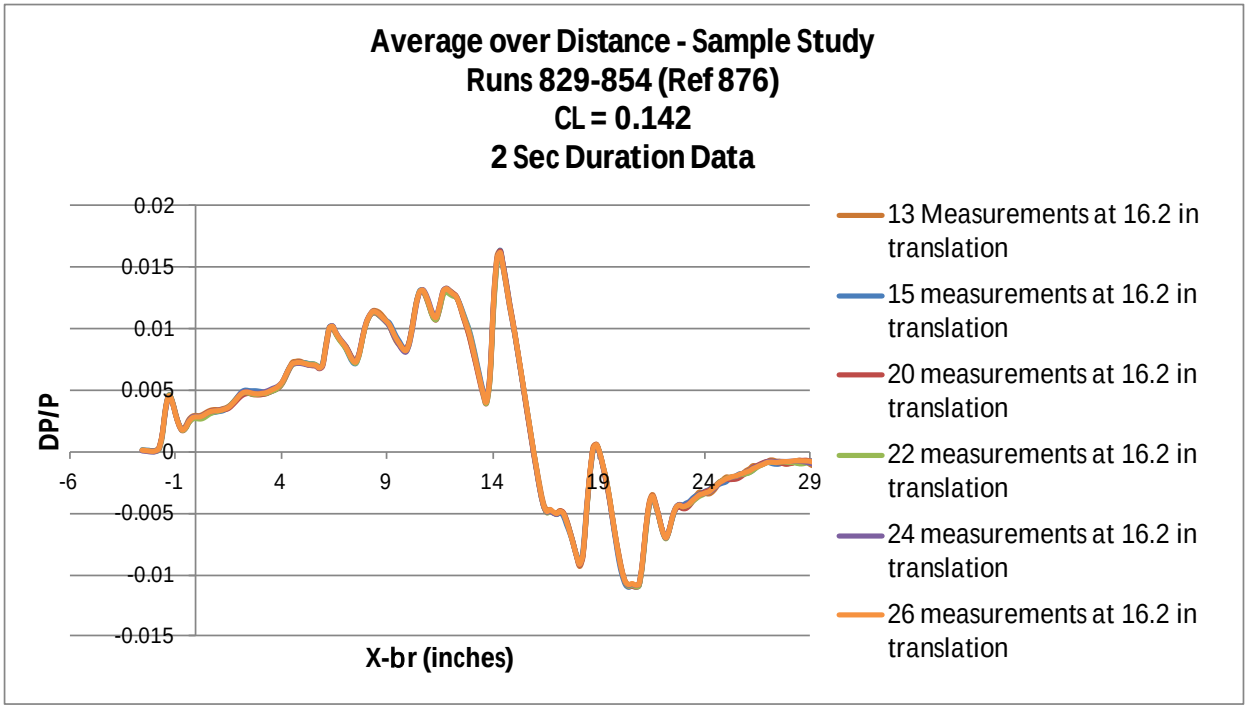

Figure 102. Initial approximation: reduce testing to 2 sec samples and 18 measurements

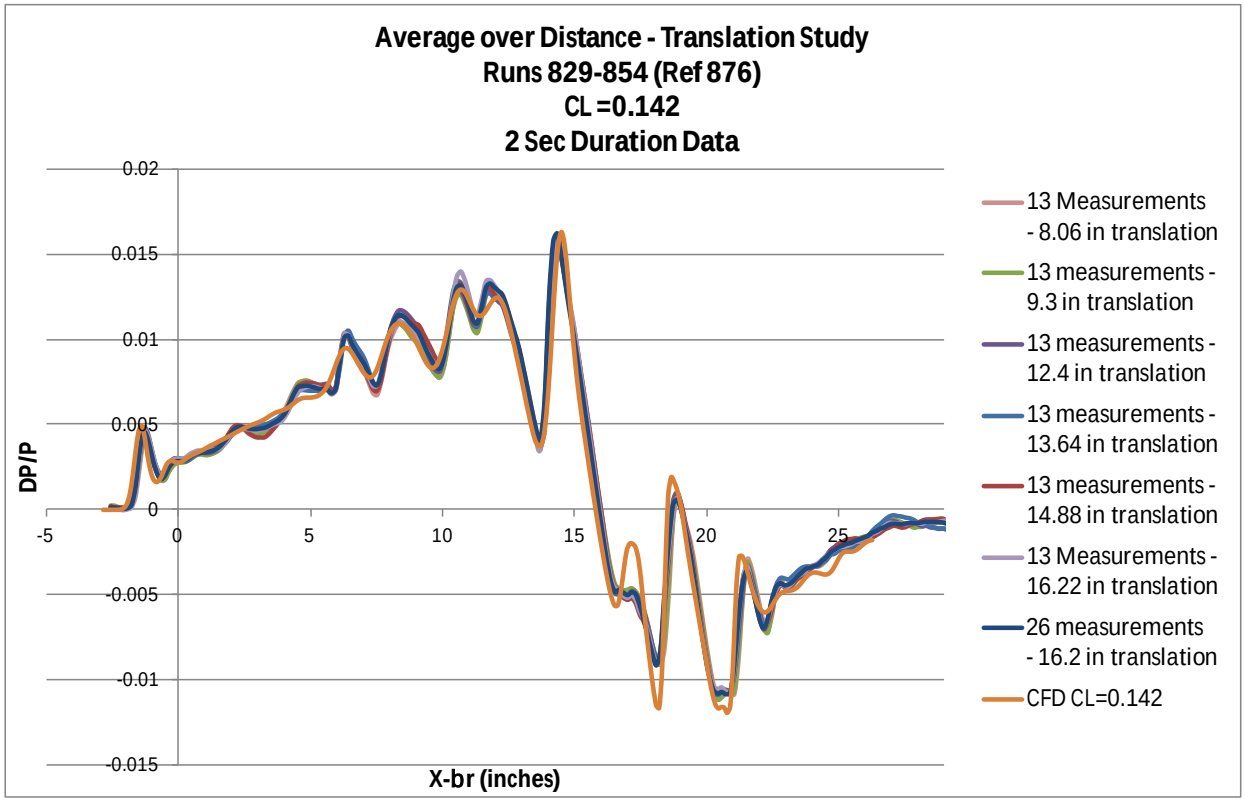

Figure 103. It is not definitively clear the minimum length of translation required to achieve sufficient accuracy

6.2 MDAO N+2 Solver (WBS 3.8)

6.2.1 Description

This task entailed research to assess the effectiveness of different optimization methods and problem formulations on reducing sonic boom. The benchmark problem used for this effort included 6 configuration design variables with length scale factors on the $SonicBoom_{targ}$ associated with both undertrack and multiple off-track signatures. The 6 configuration variables, listed in Table 3, defined wing twist and planform geometry at key points shown in Figure 104 and Figure 105. The optimizers adjusted these variables to make the vehicle's sonic boom conform to a target signature.

A total of 12 optimization problem formulations were considered during this task. They represent combinations of 4 different sonic boom error metrics, which served as objective or constraint functions, and 3 means of trading undertrack and off-track signatures within an optimization.

The basic error metric was a root-mean-square (RMS) function composed of differences between the target ($SonicBoom_{targ}$) and that produced by the vehicle ($SonicBoom_{veh}$) at equally distributed points along the vehicle's length.

TABLE 3.—MDAO CONFIGURATION DESIGN VARIABLES

Design variable	Lower bound	Upper bound
Wing twist (inboard)	0.8 deg	2.4 deg
Wing twist (outboard)	5.25 deg	7.25 deg
Wing twist (tip)	0.25 deg	2.25 deg
LE X location (middle)	–40 in. (from QR3 baseline)	+30 in. (from QR3)
LE X location (tip)	–30 in. (from QR3 baseline)	+40 in. (from QR3)
LE radius of curvature	1950 in.	2550 in.

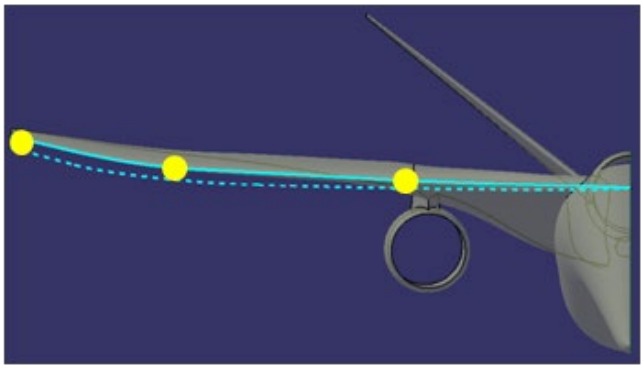

Figure 104. MDAO Wing Twist Design Variables

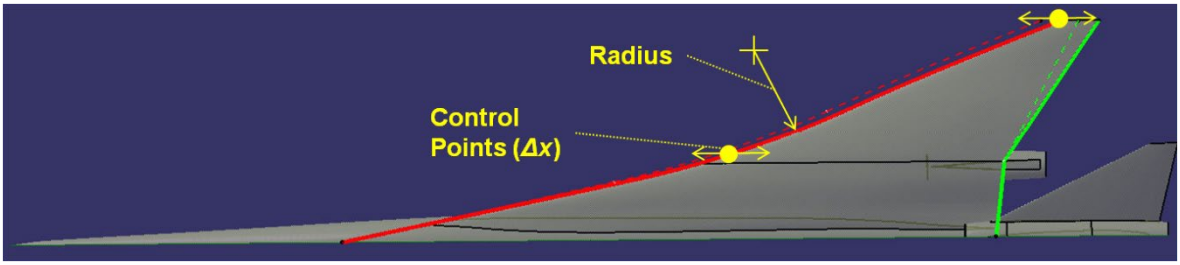

Figure 105. MDAO Planform Design Variables

$$RMS = \left(\frac{\sum_{i=1}^{n} \left(SonicBoom_{veh} - SonicBoom_{targ} \right)_i^2}{n} \right)^{1/2}$$

The remaining metrics were formulated such that they would be dominated by points where the vehicle's $\text{SonicBoom}_{\text{veh}}$ exceeds the target. The first was a weighted RMS function:

$$RMSwgt = \left(\frac{\sum_{i=1}^{n} wgt_i \left(SonicBoom_{veh} - SonicBoom_{targ} \right)_i^2}{n} \right)^{1/2}$$

Where the "weights" wgt_i increased the contribution of individual error terms by an order of magnitude at points where the vehicle's $SonicBoom_{veh}$ exceeded the target:

$$wgt_i = \begin{cases} 1 & \text{if } SonicBoom_{veh} \leq SonicBoom_{targ} \\ 10 & \text{if } SonicBoom_{veh} > SonicBoom_{targ} \end{cases}$$

Another alternative was the mean error between the vehicle and target $SonicBoom_{vehq}$ curves, simply:

$$\mu_{err} = \frac{\sum_{i=1}^{n} (SonicBoom_{veh} - SonicBoom_{targ})_i}{n}$$

Finally, the "mean overshoot" is the average of those individual error terms corresponding to locations where the vehicle's $SonicBoom_{veh}$ exceeds the target:

$$\mu_{over} = \frac{\sum_{i=1}^{n} k_i (SonicBoom_{veh} - SonicBoom_{targ})_i}{n}$$

Where

$$k_i = \begin{cases} 0 & \text{if } SonicBoom_{veh} \leq SonicBoom_{targ} \\ 1 & \text{if } SonicBoom_{veh} > SonicBoom_{targ} \end{cases}$$

The objective functions minimized during optimization were comprised of the above metrics evaluated for signatures undertrack and 10, 20, and 30 degrees off-track. When the basic RMS error metric was used, the objective function *F(RMS)* took the form:

$$F(RMS) = \frac{w_{under} RMS_{under} + w_{10} RMS_{10} + w_{20} RMS_{20} + w_{30} RMS_{30}}{w_{under} + w_{10} + w_{20} + w_{30}}$$

where the subscripts *under, 10, 20,* and *30* indicate signatures undertrack and 10, 20, and 30 degrees off-track, respectively. The *w* terms are referred to as *"Signature Weighting Coefficients"* and act as weights of undertrack and off-track error metrics relative to one another during optimization.

Alternative objective functions took exactly the same form as *F(RMS)* above, but were based on the weighted RMS metric (RMS_{wgt}) and mean $\text{SonicBoom}_{\text{veh}}$ overshoot (μ_{over}). Finally, one formulation also sought to minimize *F(RMS),* but was constrained such that the mean $\text{SonicBoom}_{\text{veh}}$ error (μ_{err}) was less than zero.

The 12 optimization problem formulations are summarized in Table 4. The first formulation minimized the basic *RMS* error metric associated with the undertrack signature. The 2nd, 3rd, and 4th formulations also operated only on the undertrack signature, but used alternative error metrics to make the optimizer prioritize points where the vehicle sonic boom exceeded the target. Finally, these 4 formulations were repeated while incorporating the off-track signatures.

TABLE 4.—MDAO PROBLEM FORMULATIONS

#	*Optimization formulation*		*Signature weighting coefficients*			
	Minimize:	***Subject to:***	w_{under}	w_{10}	w_{20}	w_{30}
1	*F(RMS)*	-	1	0	0	0
2	$F(RMS_{wgt})$	-	1	0	0	0
3	*F(RMS)*	$\mu_{err} < 0$	1	0	0	0
4	$(F(RMS)+F(\mu_{over}))/2$	-	1	0	0	0
5	*F(RMS)*	-	1	1	1	1
6	$F(RMS_{wgt})$	-	1	1	1	1
7	*F(RMS)*	$\mu_{err} < 0$	1	1	1	1
8	$(F(RMS)+F(\mu_{over}))/2$	-	1	1	1	1
9	*F(RMS)*	-	1	0.5	0.25	0.1
10	$F(RMS_{wgt})$	-	1	0.5	0.25	0.1
11	*F(RMS)*	$\mu_{err} < 0$	1	0.5	0.25	0.1
12	$(F(RMS)+F(\mu_{over}))/2$	-	1	0.5	0.25	0.1

The 12 formulations above were solved using three different optimization methods; each implemented using a different tool, for a total of 36 test cases. These methods and tools are summarized in Table 5. All of them included both global and local search elements to combine broad exploration of the design space (global) with efficient convergence to an optimum (local).

TABLE 5.—MDAO METHODS

Test cases	**Method(s) implemented [Tool used]**
1-12	*Sequential Approximate*: Approximation-based gradient optimization followed by pattern search; process repeated until convergence [ModelCenter – Design Explorer]
13-24	*Multi-Method Uncoupled*: Genetic algorithm, pattern search, and gradient optimization executed sequentially [DAKOTA]
25-36	*Gradient Multi-start*: Gradient-based optimization initialized from multiple starting points, selected via Latin Hypercube [ModelCenter – DOT]

In all of the above formulations, the vehicle's sonic boom (undertrack and off-track) were evaluated using a series of response surface approximations constructed from CFD results. Sixty-five different combinations of the design variables listed in Table 1 comprised the Design of Experiments (DOE) array for which SonicBoom_{veh} distributions were obtained through CFD. Based on those results, values of the derivative $d(SonicBoom_{veh})/d(x - \beta \cdot r)$ were approximated at 128 equally distributed points along the length of the vehicle. Each time one of the optimizers in this task needed to evaluate the objective function, the underlying SonicBoom_{veh} were predicted based on those incremental contributions to SonicBoom_{veh}.

6.2.2 Results

6.2.2.1 Overview

The results of the 36 optimization test cases are summarized in Table 6. Each row of the table lists the final objective function value (F_{obj}) and the number of function evaluations *(# eval)* for the corresponding formulation using each of the 3 tools and methods considered. For comparison, the objective value at the geometric center of the design space is listed in the 2nd column of the table (the center is used as a baseline for comparison because none of the methods operated from a single starting point). The highlighted cells indicate the lowest objective value identified for each formulation.

TABLE 6.—MDAO RESULTS SUMMARY

Form #	--	***Sequential approximate***		***Multi-method uncoupled***		***Gradient multi-start***	
	F_{obj}*(center)*	F_{obj}	*# eval*	F_{obj}	*# eval*	F_{obj}	*# eval*
1	20.91	0.982	185	1.381	1913	**0.946**	1021
2	14.30	**0.924**	191	1.214	1510	0.974	1199
3	20.91	1.809	173	1.349	1985	**1.230**	474
4	10.47	0.851	185	0.643	1937	**0.624**	868
5	14.66	1.866	189	1.825	2052	**1.596**	2328
6	45.60	4.650	189	1.708	2050	**1.382**	2216
7	14.66	1.773	198	**1.686**	2046	2.052	2108
8	7.38	1.563	192	1.117	2058	**1.002**	2746
9	18.46	1.388	200	**1.134**	2044	1.253	2473
10	51.13	2.331	189	**0.987**	2058	1.071	2247
11	18.46	**1.212**	200	1.256	2048	1.390	1090
12	9.25	0.950	175	0.901	2045	**0.757**	2234

In terms of objective function minimization, the "Gradient Multi-Start" method (several executions of a gradient-based optimizer, each initiated from a different, random starting point) was the most effective, identifying the lowest observed objective function for 7 of the 12 problem formulations. This was a somewhat surprising result in that the global (exploratory) element of this method-multiple starting points- was purely random in nature.

In terms of efficiency (objective function improvement per number of function evaluations), "Sequential Approximate" optimization consistently required an order of magnitude fewer function evaluations to achieve comparable reductions in the objective functions. During this task, runs that required 1000's of evaluations were tractable because the function evaluations themselves consisted of approximation-based predictions of SonicBoom_{veh} as previously discussed. Typically, the time rate of function evaluations during optimization was between 40 and 50 evaluations/minute when the optimizer and SonicBoom_{veh} prediction tools were running on a PC desktop and approximately 100 evaluations/

minute when those tools were running in the background. In any case, the substantially lower computational cost of Sequential Approximate optimization was attributed to its use of internally constructed response surface approximations and illustrates the benefits of that approach.

6.2.2.2 Preventing Sonic Boom Overshoot

The initial root-mean-square (RMS) error metric was a basic gauge of how closely the $SonicBoom_{veh}$ distribution conformed to the target. The other objective functions considered, as well as the constraint requiring that mean error $\mu_{err}<0$, were all modifications to the basic RMS metric intended to prioritize the elimination of "overshoots" of the $SonicBoom_{targ}$ distribution. In other words, the goal was to maintain conformity to the target distribution as closely as possible, with an additional measure to force the vehicle's $SonicBoom_{veh}$ to be less than the corresponding target at every point.

Figures 106 to 108 depict the mean $SonicBoom_{veh}$ overshoot (μ_{over}) of the solutions obtained in each of the 36 test cases. Each figure contains results for one set of signature weighting coefficients (Table 4). Figure 106 includes cases that focused only on the undertrack signature (3, lines 1-4); Figure 107 includes those in which under-and off-track signatures were weighted equally (3, lines 5-8); Figure 110 includes those in which under-and off-track signatures were weighted differently (Table 4, lines 9-12). The 3 groups of bars within each figure correspond to the three optimization methods investigated (Table 5). The 4 bars within each group correspond to the 4 different objective functions considered.

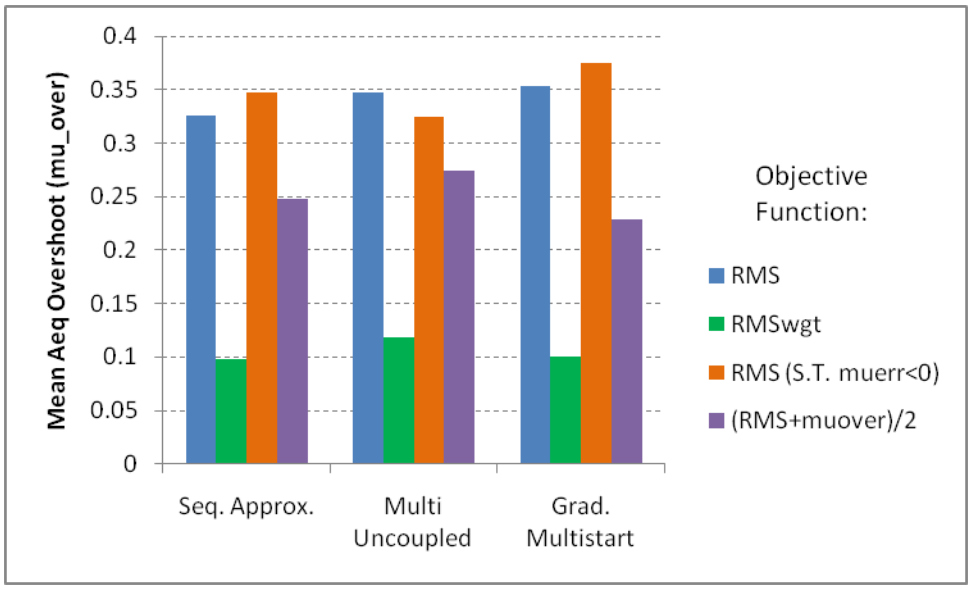

Figure 106. Mean $SonicBoom_{veh}$ Overshoot of Optimal Designs (Undertrack Only)

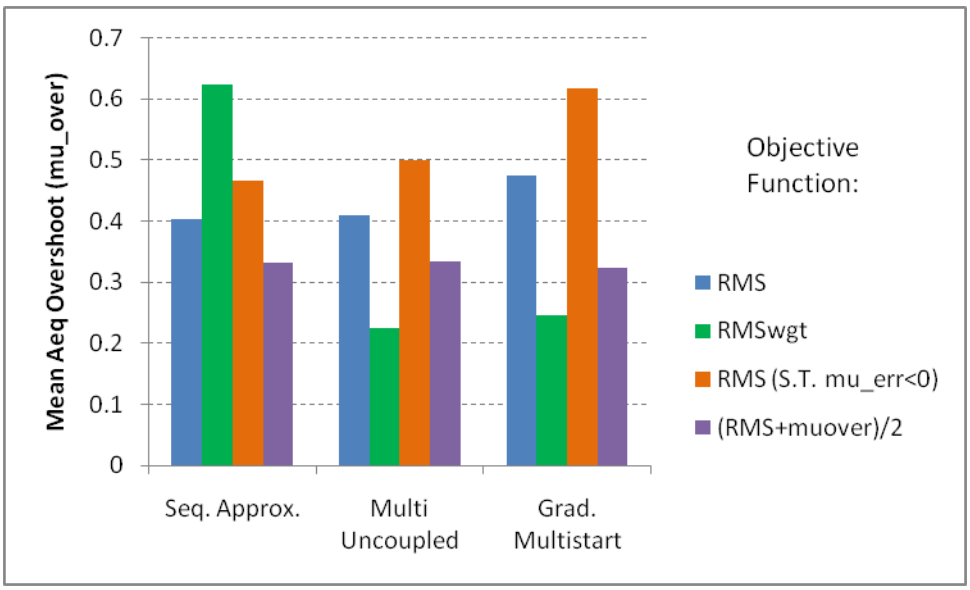

Figure 107. Mean SonicBoom$_{veh}$ Overshoot of Optimal Designs (Under and Off-track (Ref. 1))

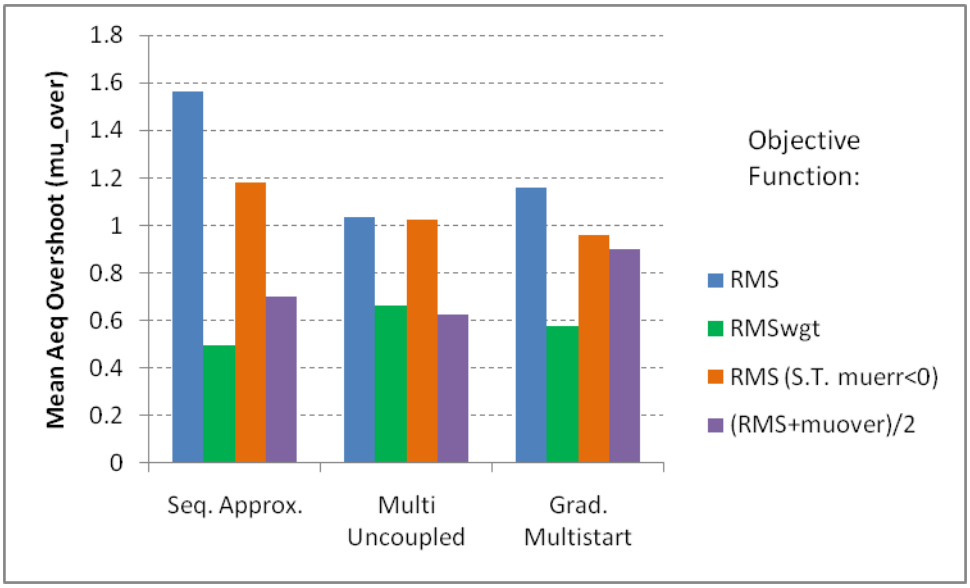

Figure 108. Mean SonicBoom$_{veh}$ Overshoot of Optimal Designs (Under and Off-track (Ref. 2))

In general, minimizing the weighted RMS function was the most effective way to prevent SonicBoom$_{veh}$ overshoot. The 36 test cases run comprise 9 unique combinations of signature weighting coefficients and optimization methods (3 variants of each), shown by the 9 (total) groups of bars contained in Figures 106 to 108. In 7 of those 9 groups, the lowest mean SonicBoom$_{veh}$ overshoot (μ_{over}) was exhibited by the solution obtained by minimizing the weighted RMS function (RMS_{wgt}; green bars in Figures). In one additional group (Fig. 107, center group), the mean SonicBoom$_{veh}$ overshoot obtained by minimizing RMS_{wgt} exceeded but was within 6 percent of the lowest value obtained in that group.

6.2.2.3 Simultaneous Undertrack and Off-Track Signature Management

The other specific issue investigated was how to best improve both the undertrack and off-track sonic boom signatures simultaneously. While a solution that matches multiple $SonicBoom_{targ}$ distributions is ideal, there is no guarantee that such a solution exists when vehicle geometry is defined by a limited number of design variables (such as the 6 considered here). In this investigation, 2 means of incorporating off-track signatures were compared in terms of the resultant improvements in off-track performance and any adverse effects on undertrack performance. The off-track signatures were accounted for during optimization through the use of signature weighting coefficients as listed in Table 4. Two combinations of them were considered: one which assigned equal priority (weighting coefficients) to signatures undertrack through 30 degrees off-track (Table 4, lines 5–8), and another which assigned declining priority as the off-track angle increased (Table 4, lines 9–12).

The results of this study are detailed in Tables 7 to 10. The first table includes values of the basic RMS error metric (RMS) broken down by components associated with signatures undertrack and 10, 20, and 30 degrees off-track. The rows of the table include the values of those components at solutions obtained using different optimization methods and signature weighting coefficients. For solutions that incorporated off-track signatures (the 2nd and 3rd row within each method), the percent change refers to the difference between the indicated value and the undertrack-only value. Finally, the last 2 rows of Table 6 indicate the average change (among the 3 optimization methods considered) in each RMS component caused by the introduction off-track signatures in the optimization objective.

Tables 8, 9, and 10 are analogous to Table 7, except they include the alternative error metrics that were minimized in other test cases: the weighted RMS function (Table 7), the constrained RMS minimization (Table 9) and the average of the RMS error and mean overshoot (Table 10).

TABLE 7.—BASIC RMS ERROR COMPONENTS BY ANGLE

Method	Sig. Wgt. Coef's $\{w_{under}, w10, w20, w30\}$	*RMS (undertrack)*	*RMS (10° offtrack)*	*RMS (20° offtrack)*	*RMS (30° offtrack)*
Sequential Approximate Opt.	{1, 0, 0, 0}	0.982	7.761	10.903	7.988
	{1, 1, 1, 1}	1.317 (+34.1%)	1.310 (–83.1%)	1.769 (–83.8%)	3.066 (–61.6%)
	{1, 0.5, 0.25, 0.1}	1.191 (+21.3%)	1.275 (–83.6%)	1.609 (–85.2%)	3.372 (–57.8%)
Multi-Method Uncoupled	{1, 0, 0, 0}	1.381	1.450	3.785	3.734
	{1, 1, 1, 1}	1.430 (+3.5%)	1.071 (–26.2%)	1.673 (–55.8%)	3.127 (–16.2%)
	{1, 0.5, 0.25, 0.1}	0.930 (-32.7%)	0.992 (–31.6%)	1.549 (–59.1%)	2.846 (–23.8%)
Gradient Multistart	{1, 0, 0, 0}	0.946	3.219	3.129	5.523
	{1, 1, 1, 1}	0.920 (–2.7%)	0.955 (–70.3%)	1.573 (–49.7%)	2.938 (–46.8%)
	{1, 0.5, 0.25, 0.1}	1.051 (11.2%)	1.090 (–66.1%)	1.675 (–46.5%)	3.032 (–45.1%)
Average %-change: {1,0,0,0} to {1,1,1,1}		***+11.6%***	***–59.9%***	***–63.1%***	***–41.6%***
Average %-change: {1,0,0,0} to {1, 0.5, 0.25, 0.1}		***–0.1%***	***–60.4%***	***–63.6%***	***–42.2%***

TABLE 8.—WEIGHTED RMS ERROR COMPONENTS BY ANGLE

Method	Sig. Wgt. Coef's $\{w_{under}, w10, w20, w30\}$	*RMSwgt (undertrack)*	*RMSwgt (10° offtrack)*	*RMSwgt (20° offtrack)*	*RMSwgt (30° offtrack)*
Sequential Approximate Opt.	{1, 0, 0, 0}	0.924	11.859	5.526	3.116
	{1, 1, 1, 1}	3.437 (+271.8%)	3.648 (–69.2%)	5.249 (–5.0%)	6.266 (+101.1%)
	{1, 0.5, 0.25, 0.1}	1.762 (+90.6%)	1.589 (–86.6%)	4.608 (–16.6%)	6.045 (+94.0%)
Multi-Method Uncoupled	{1, 0, 0, 0}	1.214	3.990	2.190	4.143
	{1, 1, 1, 1}	1.183 (–2.6%)	1.188 (–70.2%)	1.496 (–31.7%)	2.965 (–28.4%)
	{1, 0.5, 0.25, 0.1}	0.918 (–24.4%)	0.623 (–84.4%)	1.207 (–44.9%)	2.948 (–28.8%)
Gradient Multistart	{1, 0, 0, 0}	0.974	2.222	1.794	8.746
	{1, 1, 1, 1}	0.896 (–8.0%)	0.891 (–59.9%)	1.277 (–28.8%)	2.462 (–71.8%)
	{1, 0.5, 0.25, 0.1}	1.077 (+10.6%)	0.962 (–56.7%)	0.976 (–45.6%)	1.791 (–79.5%)
Average %-change: {1,0,0,0} to {1,1,1,1}		***+87.1%***	***–66.4%***	***–21.8%***	***+0.3%***
Average %-change: {1,0,0,0} to {1, 0.5, 0.25, 0.1}		***+25.6%***	***–75.9%***	***–35.7%***	***–4.8%***

TABLE 9.—CONSTRAINED RMS ERROR COMPONENTS BY ANGLE

Method	Sig. Wgt. Coef's $\{w_{under}, w10, w20, w30\}$	*RMS (undertrack)*	*RMS (10° offtrack)*	*RMS (20° offtrack)*	*RMS (30° offtrack)*
Sequential Approximate Opt.	{1, 0, 0, 0}	1.809	3.590	6.628	4.450
	{1, 1, 1, 1}	1.353 (–25.2%)	1.251 (–65.2%)	1.665 (–74.9%)	2.822 (–36.6%)
	{1, 0.5, 0.25, 0.1}	1.027 (–43.2%)	1.047 (–70.8%)	1.605 (–75.8%)	2.905 (–34.7%)
Multi-Method Uncoupled	{1, 0, 0, 0}	1.349	9.627	9.535	10.100
	{1, 1, 1, 1}	1.034 (–23.3%)	0.972 (–89.9%)	1.628 (–82.9%)	3.108 (–69.2%)
	{1, 0.5, 0.25, 0.1}	1.068 (–20.8%)	1.120 (–88.4%)	1.632 (–82.9%)	2.871 (–71.6%)
Gradient Multistart	{1, 0, 0, 0}	1.230	2.847	3.017	5.530
	{1, 1, 1, 1}	1.255 (2.1%)	1.366 (–52.0%)	2.031 (–32.7%)	3.555 (–35.7%)

	{1, 0.5, 0.25, 0.1}	1.184 (–3.7%)	1.123 (–60.6%)	2.037 (–32.5%)	3.167 (–42.7%)
	Average %-change: {1,0,0,0} to {1,1,1,1}	***–15.5%***	***–69.0%***	***–63.5%***	***–47.2%***
	Average %-change: {1,0,0,0} to {1, 0.5, 0.25, 0.1}	***–22.6%***	***–73.3%***	***–63.7%***	***–49.7%***

TABLE 10.—BASIC RMS/MEAN OVERSHOOT COMPONENTS BY ANGLE

Method	Sig. Wgt. Coef's $\{w_{under}, w10, w20, w30\}$	*(RMS+μ_{over})/2 (undertrack)*	*(RMS+μ_{over})/2 (10° Offtrack)*	*(RMS+μ_{over})/2 (20° Offtrack)*	*(RMS+μ_{over})/2 (30° Offtrack)*
Sequential Approximate Opt.	{1, 0, 0, 0}	0.851	0.925	2.162	2.417
	{1, 1, 1, 1}	2.494 (+193.2%)	0.849 (–8.2%)	1.025 (–52.6%)	1.883 (–22.1%)
	{1, 0.5, 0.25, 0.1}	0.884 (+3.9%)	0.802 (–13.2%)	1.077 (–50.2%)	2.031 (–16.0%)
Multi-Method Uncoupled	{1, 0, 0, 0}	0.643	5.296	6.918	5.369
	{1, 1, 1, 1}	0.893 (+38.9%)	0.705 (–86.7%)	1.001 (–85.5%)	1.868 (–65.2%)
	{1, 0.5, 0.25, 0.1}	0.862 (+34.1%)	0.812 (–84.7%)	0.946 (–86.3%)	1.618 (–69.9%)
Gradient Multistart	{1, 0, 0, 0}	0.624	1.561	1.547	4.364
	{1, 1, 1, 1}	0.681 (+9.1%)	0.675 (–56.7%)	0.916 (–40.8%)	1.735 (–60.2%)
	{1, 0.5, 0.25, 0.1}	0.612 (–1.9%)	0.646 (–58.6%)	1.049 (–32.2%)	2.033 (–53.4%)
	Average %-change: {1,0,0,0} to {1,1,1,1}	***+80.4%***	***–50.5%***	***–59.6%***	***–49.2%***
	Average %-change: {1,0,0,0} to {1, 0.5, 0.25, 0.1}	***+12.0%***	***–52.2%***	***–56.3%***	***–46.4%***

The most important results in Tables 7 to 10 are those in the last 2 rows of each table. They show that while the 2 combinations of signature weighting coefficients yielded comparable improvements in the off-track components of each objective function, weighting all signatures equally tended to have a much more adverse effect on the undertrack signature. These results are illustrated graphically in Figures 109 to 112, which depict the percent changes in objective function components attributable to the incorporation of off-track signatures. Beginning with Figure 109, the red bars depict the percent difference in the undertrack and off-track components of *F(RMS)* between the solution obtained by optimizing only RMS_{under} and that obtained by weighting the undertrack and 3 off-track components equally. The green bars depict the percent difference in the undertrack-only solution and that obtained using declining weights for off-track components. The undertrack-only solution was the baseline for comparison in both cases. Figures 110 to 112 are analogous to Figure 110, but they depict changes in the other objective functions.

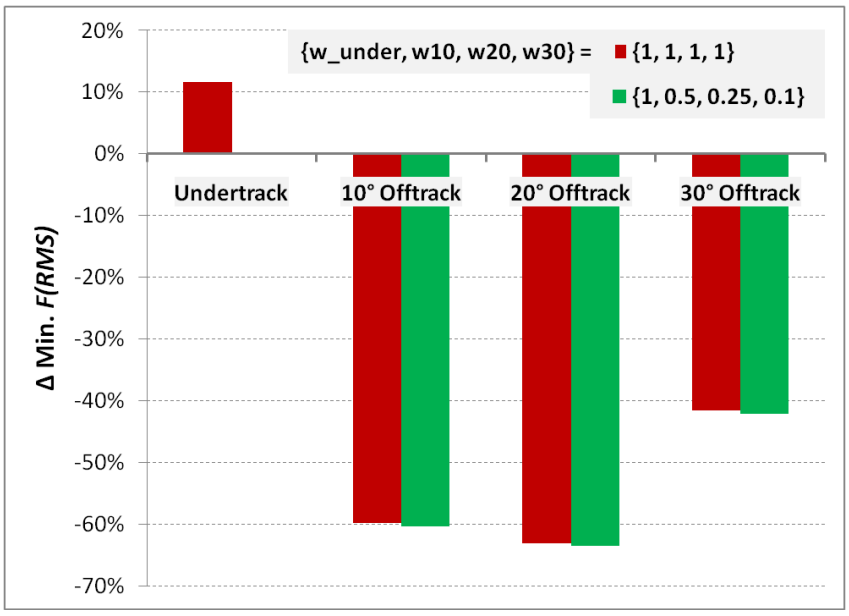

Figure 109. Effect of Off-Track Signature Weighting on Basic RMS Error Components

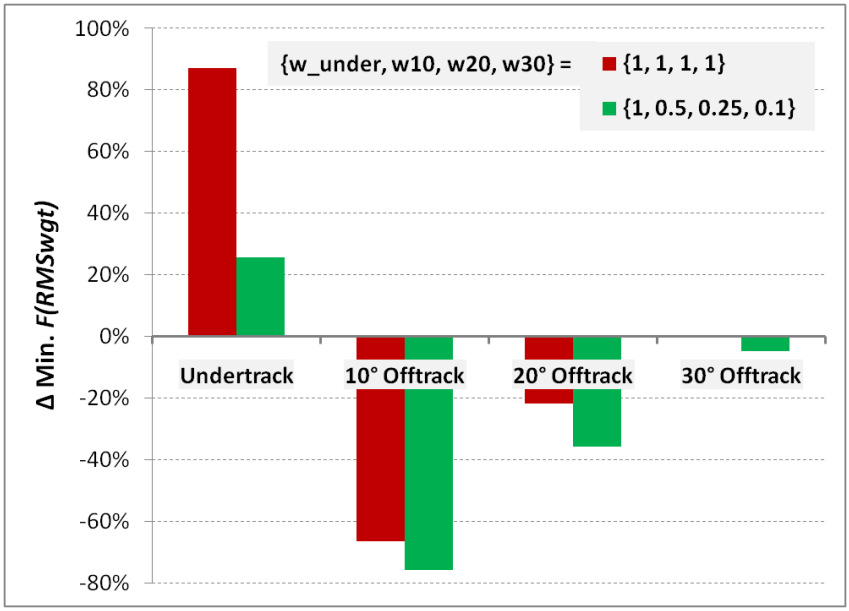

Figure 110. Effect of Off-Track Signature Weighting on Weighted RMS Error Components

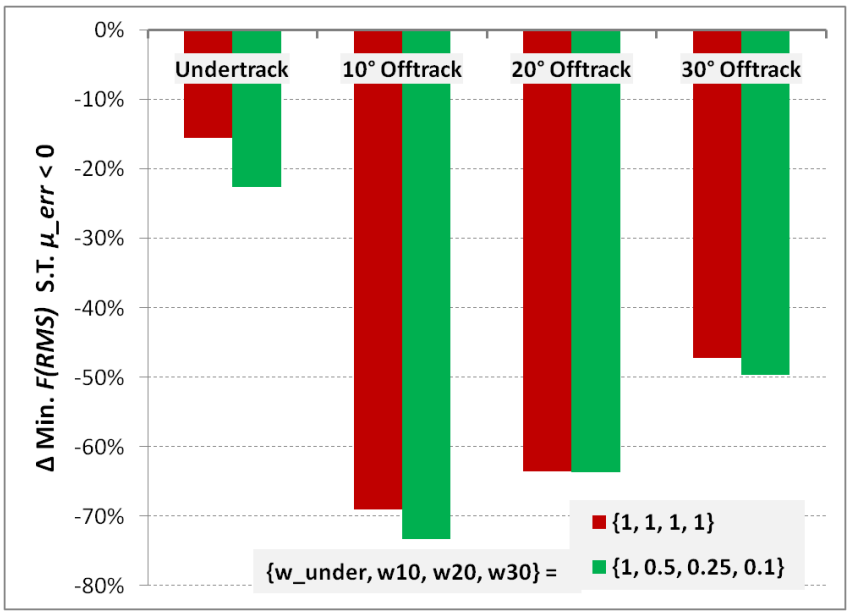

Figure 111. Effect of Off-Track Signature Weighting on Constrained RMS Error Components

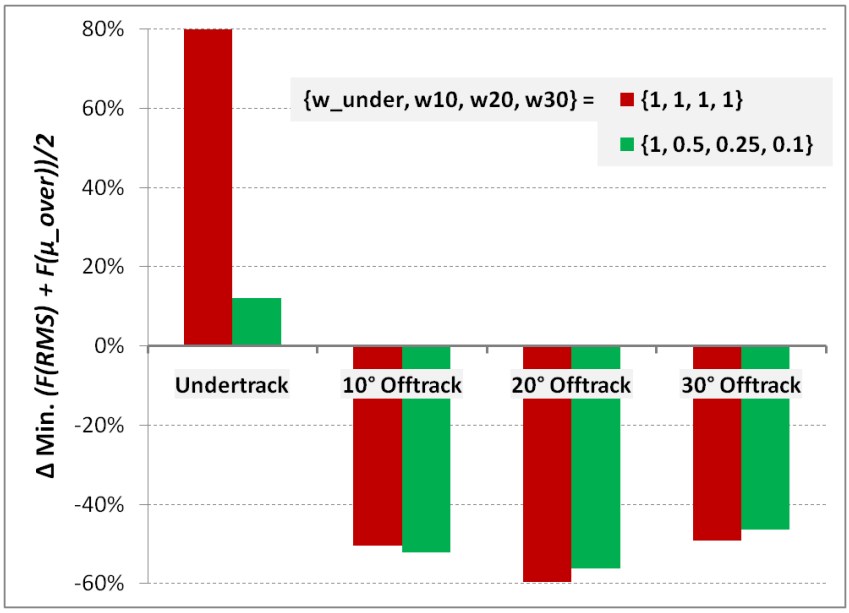

Figure 112. Effect of Off-Track Signature Weighting on Basic RMS/Mean Overshoot Error Components

As can be seen in Figure 109 to 112, improvements in off-track signatures were comparable and consistent for both methods of weighting the off-track results. However, assigning equal priority (weight) to both the undertrack and off-track signatures often resulted in the undertrack performance being compromised, sometimes substantially. The reason for this is that it becomes more difficult to match the desired $\text{SonicBoom}_{\text{targ}}$ as the off-track angle increases. Therefore, the components of the various error metrics associated with off-track performance tended to dominate the optimization objectives that included them. The better approach was to include the off-track signatures but at progressively lower

priority (weight) than the undertrack signature. As demonstrated by these results, this enabled the optimizers to address and improve off-track performance with reduced impact on the undertrack signature.

The research in this task focused on optimizers' ability to reduce sonic boom by matching the $SonicBoom_{targ}$ associated with one or more target ground signatures. This problem was of particular interest because low-boom shaping was the top priority of the N+2 design effort and because matching multiple (undertrack and off-track) signatures presented a unique challenge. Another question of interest would be whether the optimizers' performance is markedly different when the objective and/or constraints contain other performance parameters, such as L/D. Whereas all optimizers employ mathematical algorithms that are independent of the physics underlying the objective and constraint evaluations, absent further research it is anticipated that the methods investigated would exhibit similar performance regardless of the physical nature of the objective function.

6.2.2.4 Summary and Conclusions

Three dozen test cases were executed, collectively representing different optimization algorithms, $SonicBoom_{targ}$ objective functions, and combinations of undertrack and off-track signatures. Results indicated that the most effective way to prevent the vehicle's $SonicBoom_{veh}$ from exceeding the corresponding target(s) was by minimizing a weighted root-mean square (RMS) error metric. Points where the $SonicBoom_{veh}$ exceeds its target contribute more heavily to such an objective function than do points where it falls short, making the former a higher priority for the optimizer. Results also demonstrated that it is possible to effectively tailor both undertrack and off-track signatures simultaneously using $SonicBoom_{targ\text{-}veh}$-based optimization. Doing so requires the corresponding $SonicBoom_{veh}$ metrics to be weighted (prioritized) such that the most difficult signatures to match (furthest off-track) do not dominate the objective function and compromise undertrack performance.

7.0 Inlet Testing and Verification

7.1 Inlet Testing and Verification (WBS 3.9)

7.1.1 CFD/Configuration Development

7.1.1.1 Description

The N+2 inlet is an axisymmetric, bleedless, external compression type with a design Mach number of 1.6. Previous experience was used for a starting point and two main trade studies were conducted for the development of the N+2 inlet. AE-40N-1 refers to the inlet version serving as the N+2 baseline.

The first study quantifies performance changes resulting from modifications in the baseline compression surface. The second study compares the effects of varying subsonic diffuser length downstream of the baseline center body compression. This latter study shows much potential for vehicle performance improvement.

7.1.1.1.1 CFD Code Comparison

Before either of the previously mentioned studies was begun, *CFD++* solutions were run and compared with previous analyses for consistency. The solutions were nearly identical qualitatively as well as numerically, and off-design points showed similar agreement. It was therefore determined that using *CFD++* for this effort was acceptable.

Metrics by which 3-D inlet CFD solutions can be compared are engine face total pressure recovery, engine face distortion (or distribution of this recovery), mass flow ratio, and external nacelle drag. However, the first trade study, which compares different compression surfaces, uses 2-D axisymmetric CFD to quickly generate solutions. Therefore, engine face total pressure recovery (referred to as pressure recovery, or simply recovery henceforth) and mass flow ratio (referred to as MFR) are the only measureable variables by which comparisons were made.

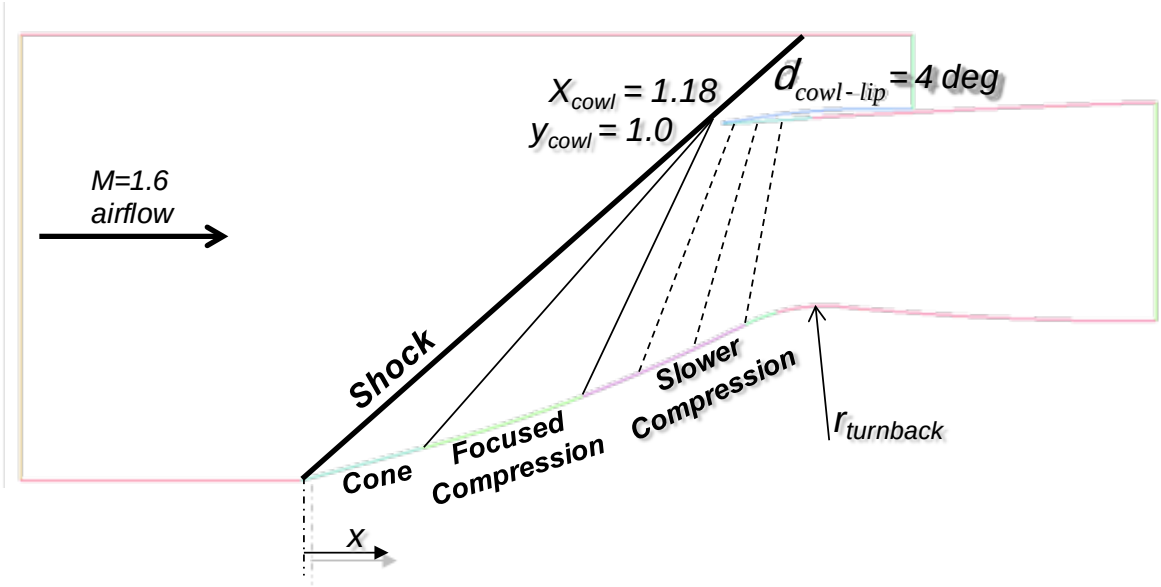

Figure 113. Sample 2-D CFD Domain and Geometry Features of the Inlet

7.1.1.1.2 Compression Surface Variations

Figure 113 shows an example domain used for the 2-D axisymmetric CFD cases. The basic inlet geometry features are highlighted. A leading edge cone angle causes an initial shock, followed by a compression surface focused just upstream and outboard of the cowl lip. The cowl lip angle is set as aggressively as possible without detaching the shock wave. Downstream of the focused compression is a section of "slower" compression, or less aggressive compression, followed by a section which forms the minimum area, or throat, and ultimately leads into a subsonic diffuser. Throughout this analysis, the cone angle and cowl lip angle were constrained to their baseline values. Varying too many of the features was considered too broad a task.

Although the permutations on the variables left unconstrained have not been exhausted here, quite a few combinations were examined, though none showed more than barely perceptible benefits to performance.

7.1.1.1.2.1 Turnback Radius Sensitivity Study

Because the flow is still supersonic as it approaches the turnback, expansion waves cause local flow acceleration before the normal shock at the throat. It was hoped that by delaying the turnback, this acceleration of the flow could be minimized, thereby reducing recovery loss through the normal shock.

Simply translating the baseline turnback aft wards in a flow-wise direction cannot be done, as the minimum area would move far downstream of the normal shock. So as turnback was delayed, the turnback radius was required to decrease, keeping the minimum area to throat area ratio above 0.98. As the turnback station is moved aft, initially there is a slight tradeoff between mass flow and peak recovery, but there is only performance loss as it is moved past x = 1.26.

7.1.1.1.2.2 Modified Compression Study

Other variations on the baseline compression geometry included configurations which increased compression after the focused compression to achieve lower Mach number near the wall, as well as configurations which moved the focal point of compression further outboard while maintaining the amount of compression before turnback. In all cases, no benefit was achieved and generally, the shock at the cowl detaches, causing spillage as well as recovery loss. Below in Figure 114 is a Mach contour of an attempt at raising compression which results in shock detachment at the lip.

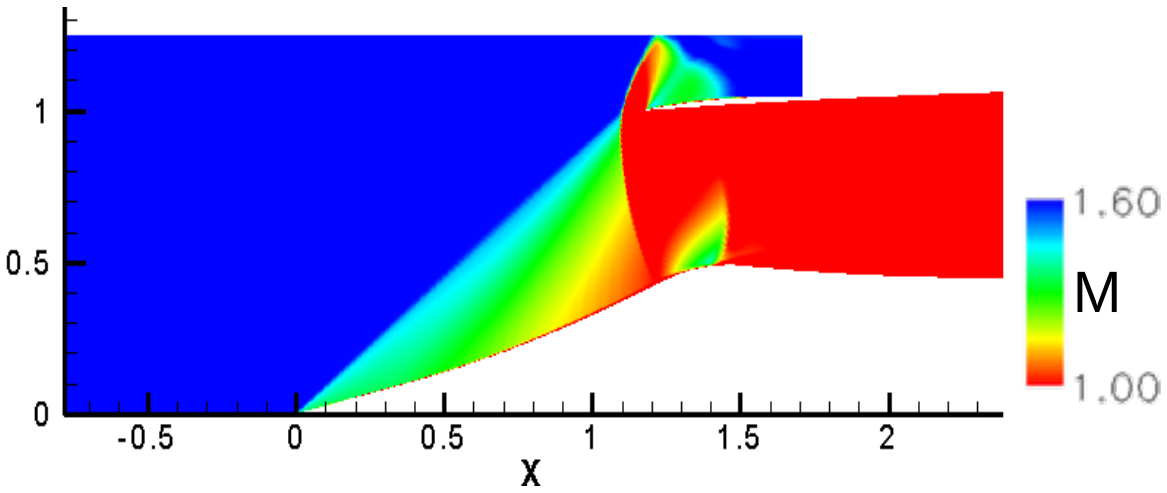

Figure 114. 2-D CFD Solution of Inlet with Compression Increased Over Baseline

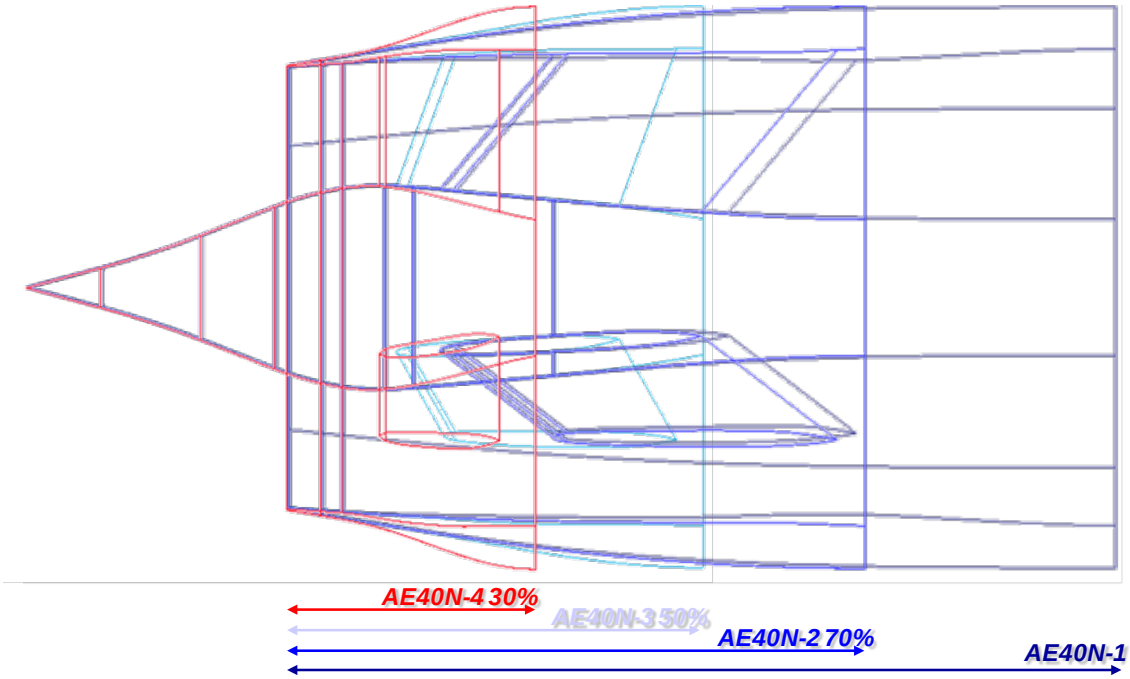

Figure 115. Side View of Inlets Used in Diffuser Length Study

The conclusion of this study is that there is little improvement to be gained by modifying the compression surface, as it is already optimized for M = 1.6 cruise.

7.1.1.1.3 Subsonic Diffuser Length Study

Another analysis has been done to determine what performance costs would be associated with shortening the subsonic diffuser in order to significantly reduce the nacelle weight. The unknowns prior to this study were the effects on engine face recovery and distortion due to diffuser length reduction, as well as the extent of increase in external nacelle drag due to the increased cowl angle required to package the engine. Figure 115 shows the different diffuser lengths for which FNS 3-D CFD solutions were generated. It should be noted that the N-4 nacelle can be reshaped for lower drag.

7.1.1.1.3.1 Diffuser Length Effects on Inlet Performance and Drag

Total pressure recovery improves with decreasing diffuser length until somewhere between 30 and 50 percent (N-4 and N-3) of the baseline length, when performance drops off quickly. The increased recovery present in the shorter, more aggressive N-2 and N-3 diffusers is a result of a thinner boundary layer due to the shorter length. As diffuser length is reduced to 70 percent, represented by N-2, any increase in nacelle drag is negligible, suggesting a tradeoff between more pressure drag for less viscous drag. Drag does increase as the diffuser length is reduced further, and dramatically so when reduced to 30 percent of baseline length, N-4.

Figure 116 shows symmetry plane Mach contours and engine face recovery contours for each of the 4 diffusers analyzed at two conditions: one representing critical operation (a, 40 lbs/(s ft^2)) and one representing supercritical operation (b, 42 lbs/(s ft^2)).

Because the normal shock is pulled back into the inlet during supercritical operation, the cowl lip shock is visible in the N-1 and N-2 diffusers (the longer diffusers), and the near sonic flow (red) indicates that the shock from the cowl lip is nearing detachment. This supports the conclusion from the first study that there is little room for improvement with respect to the compression surface, that further compression will detach the shock. As the diffuser is shortened, the normal shock can be seen creeping upstream towards the lip for the same supercritical condition in the Mach contours of Figure 116(b), until increased supercritical spillage occurs in N-4. It is clear that N-4 represents a diffuser that is too short for consideration on this vehicle.

As stated before, the overall boundary layer thickness of the diffusers in critical operation, shown in Figure 116(a), decreases as diffuser length decreases. However the Mach contours show that there is actually a boundary layer thickness increase on the center body, but a decrease on the outboard side of greater influence. It is also apparent that when the diffuser becomes too aggressive, or short, as in N-4, the boundary layer separates causing the sharp gradient seen as an almost instantaneous blue-to-red change in the pressure recovery contour versus the blue-to-yellow-to-red of N-1, -2, and -3 diffusers.

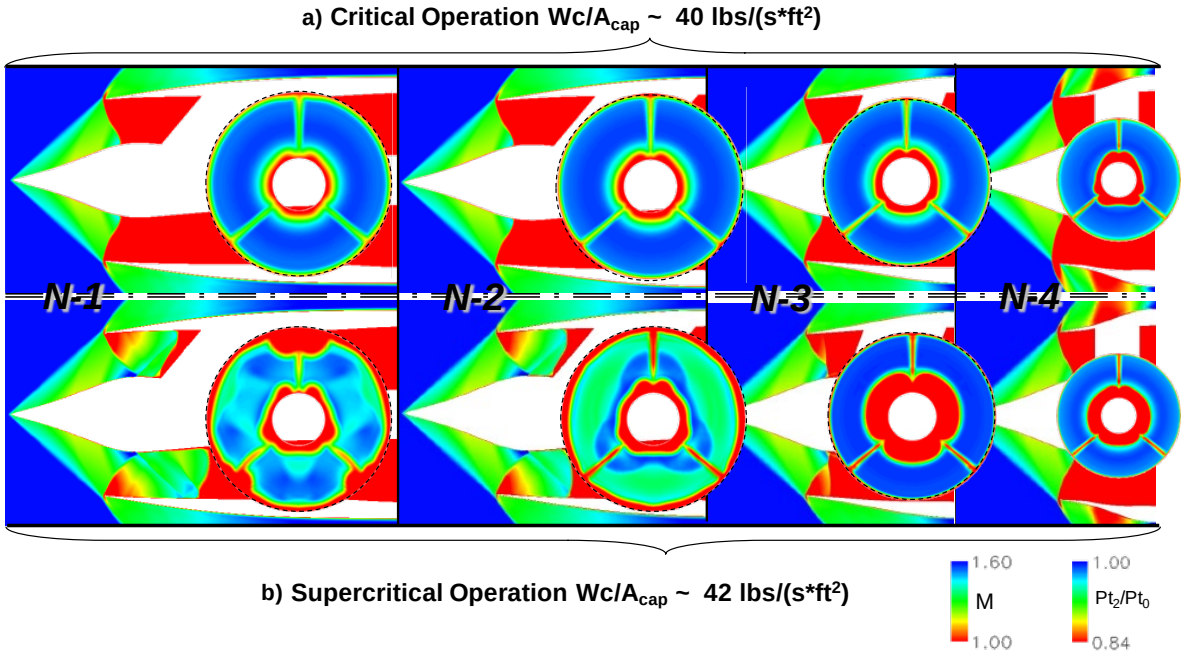

Figure 116. Symmetry Plane Mach Contours and Engine Face Recovery Contours Comparing Diffuser Length at Critical and Supercritical Operation

	Relative to N-1		
	N-2	N-3	N-4
~Cd change at cruise *(Fdrag / (Q * Acap))*	0.003	0.034	0.166
	Engine dependent		
Weight Reduction *(lbs)*	2130-2867	3312-4223	4352-5340
Fuel fraction gain *(%)*	1.4-1.9	2.2-2.8	2.8-3.5

Figure 117. Diffuser-Shortening Effects on Nacelle Drag and Weight

7.1.1.1.3.2 Diffuser Length Effect on Nacelle Weight

The following results in Figure 117 compare the different diffusers based on their predicted nacelle weights and drag coefficients. From the data presented thus far, it is clear that reducing diffuser length to 70 percent is a no-lose design change offering: an increase in total pressure recovery, a reduction in nacelle weight by well over a ton, and no appreciable drag increase. The optimum tradeoff of drag increase and weight decrease likely falls between the cases presented here, but the determination of this solution falls outside of the scope of this effort.

7.1.1.1.3.3 Angle-of-Attack Effect on Engine Face Distortion

Before completely accepting a shorter subsonic diffuser as a design improvement, 3-D FNS CFD was performed on the same diffusers to quantify the effects of angle-of-attack on engine face characteristics such as total pressure recovery and distortion. It should be noted that CFD is not yet a reliable tool for predicting distortion levels; it has a tendency to under-predict the magnitude of distortion. So in this study, CFD distortion predictions are used to observe trends as opposed to quantify the actual distortion levels of the different diffuser designs.

The different configurations are compared in Figure 118 based on a radial distortion parameter, $DPRP_{max}$, defined by ARP1420, commonly used in the engine industry for quantifying radial distortion. Distortion values were compiled using 40 sample locations representative of a standard 40-probe rake typical in wind tunnel tests. With the exception of N-4, the shorter diffusers show distortion very similar to, though lower than, the baseline at no angle-of-attack.

CFD solutions were generated for 2 and 4 degrees of alpha as well, and the results are plotted in Figures 119 and 120. Figure 119 compares the baseline diffuser, N-1, with the most aggressively shortened diffuser that does not reduce performance, N-3. Cane curves for the two configurations are presented for alpha = 0° and 4°, showing that N-3 pressure recovery and MFR respond very similarly to that of N-1 during flight at angles of attack.

A comparison of distortion for these same configurations and conditions is presented in Figure 120. As angle-of-attack is changed from 0° to 4°, it is apparent that the rise in distortion intensity is greater in the shorter N-3 diffuser than the rise in the baseline N-1 diffuser. In other words, engine face distortion is more sensitive to angle-of-attack in shorter diffusers than in longer diffusers, an expected result.

7.1.2 Model Design and Test Planning

There was an option in the contract for NASA to fund fabrication and testing of an inlet model, but NASA had limited funding and did not feel the inlet was as critical as other tests for its low sonic boom emphasis. Inlet installation and testing remains a potential future activity under the N+2 Supersonic Validations program.

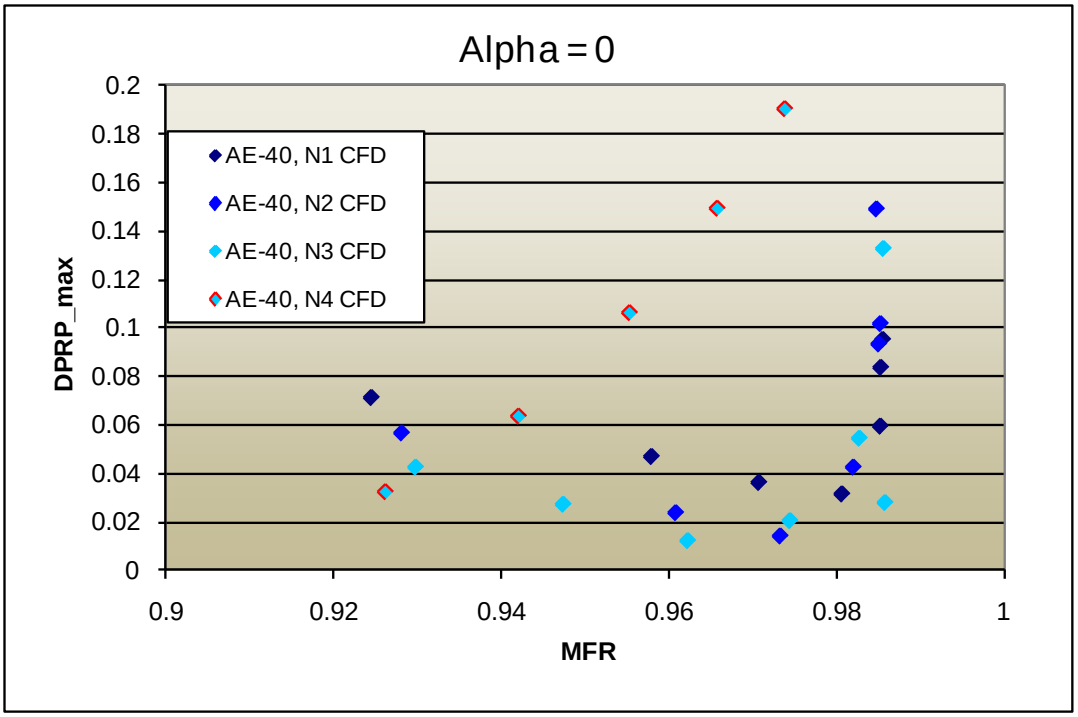

Figure 118. Diffuser-Shortening Effects on Engine Face Distortion

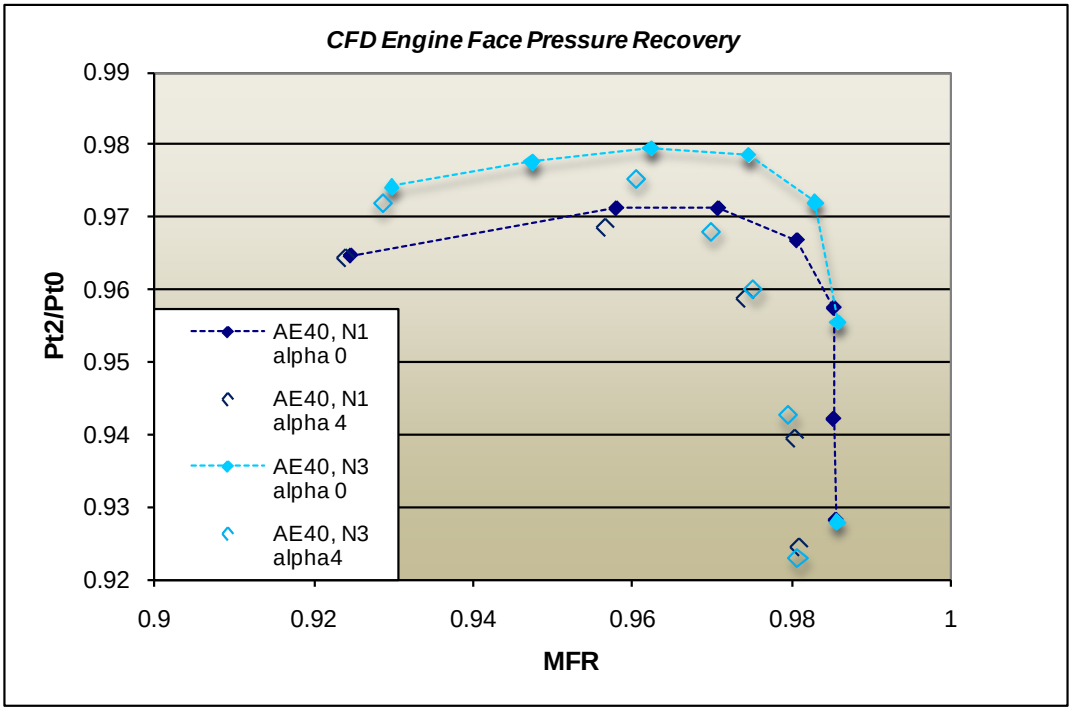

Figure 119. Angle-of-Attack Effects on Engine Face Recovery

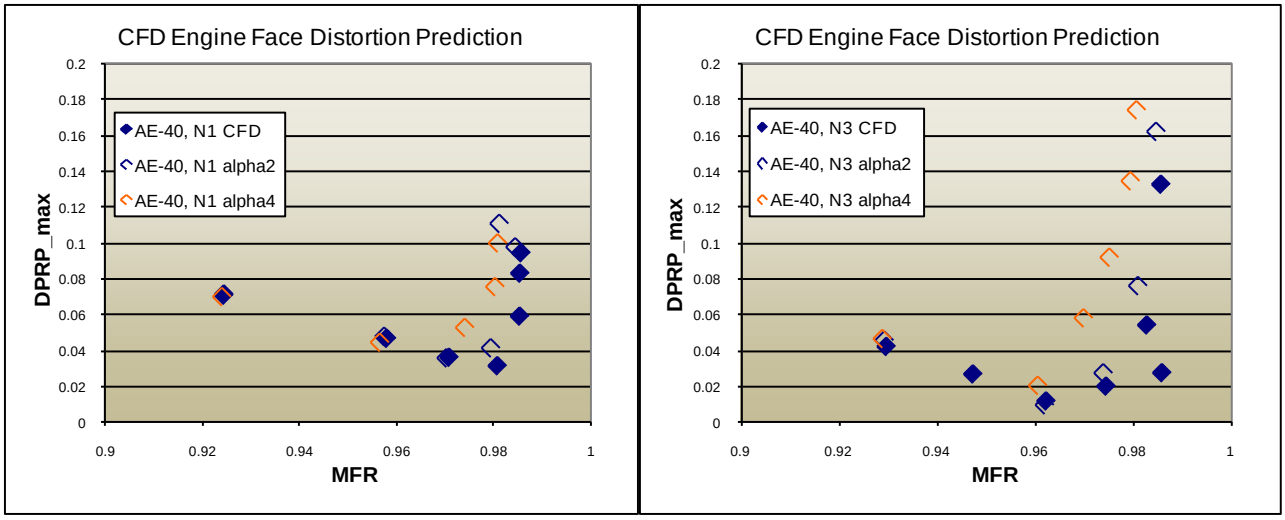

Figure 120. Angle-of-Attack Effects on Engine Face Distortion

8.0 MDAO Sonic Boom Adjoint/Response Surface

8.1 Adjoint for Sonic Boom (WBS 3.6)

The Adjoint for Sonic Boom effort is provided in more detail under Appendix C—The Stanford University Final Report (Ref. 3).

9.0 Integrated N+2 Vehicle Analysis

9.1 Description

This Phase I effort focused on developing and validating low boom measurement and design technology along with propulsion nozzle acoustics and cycle technology. These are the major challenges to be addressed for viable supersonic transportation and the requested focus of the NASA N+2 Supersonic Validations solicitation. Since Concorde SST days, NASA has had three major supersonic research programs: Advanced Supersonic Technology (AST) of the 1970s, Supersonic Cruise Research (SCR) of the early 1980s and High Speed Research (HSR) throughout the 1990s. In NASA's HSR program, low sonic boom was dropped for being too difficult and immature a technology at the time; and propulsion noise and the final, long, heavy propulsion system solution reduced the attractiveness of such a huge development program and contributed to its cancellation. Regarding sonic boom even for long range commercial traffic, 75 percent of current flying is over land. Without supersonic flight over land, the market limitation reduces the number of vehicles estimated for an aircraft program, and aircraft launch viability is often discussed in terms of how many planes need to be sold to break-even. And for propulsion, airline voluntary accelerated phase-out of noisier old aircraft (non-Stage 3) during HSR led to increasing noise stringency, which further impacted the already increasing weight estimates of technology implementations needed to meet the initial noise goals. The high performance solution developed during SCR, with engines under the wing and aft, turned out to be particularly sensitive to propulsion weight increases. Increased engine and nozzle weight suspended behind the rear wing spar not only required more wing strength, but flexibility leading to flutter and aeroelastic problems required even more weight to increase stiffness and greatly complicated vehicle control. So improvements in these two areas are known to particularly improve the viability and prospect of future supersonic transportation.

9.2 Approach

The focus on low boom and propulsion noise was reflected in the tasking and budget distribution. Tasks 3.1, 2, 3, 4, 6, 8, and 9 all have a strong impact on low boom and 3.9 (again), 12 and 13 are primarily propulsion and achieving its low noise goal. (3.5 was deferred to Year 3 and 3.7, 10, and 11 are supporting tasks). To validate low boom, the N+2 Program invested in the design and development of accurate measurement hardware. This turned out to be key. The new quieter optimum signature shaping, developed in the N+3Supersonic Systems Studies program, requires greater measurement accuracy than ever before to achieve accurate signature loudness validation (as much as ±0.0001 DP/P accuracy needed, versus the only ±0.001 accuracy achieved in many prior sonic boom wind tunnel tests). As detailed earlier, this greater accuracy is only achievable with a known calibration model and testing procedures for rigorously reducing sources of variability. The success of the Low Boom Configuration test (LM3) is validation that the theories suggested as the sources of measurement distortions were applicable models for determining procedures that reduced measurement distortions by an order of magnitude. The other great effort in low boom validation was developing a configuration design good enough to meet the low boom goal without abandoning practical vehicle attributes that make the low boom success meaningless from a system assessment standpoint. (Though perhaps still useful as a low boom test example; however, our OptSig model was an easier way to fabricate a representative test example.) Task 3.4 utilized an existing, expensive, large scale model to get high resolution (from large scale) nacelle effect measurements that validated the accuracy of our CFD operating propulsion system effects modeling. This validated prediction methodology was used for the low boom results that follow.

The low boom and airport noise goals are shown in Figure 121, along with emissions and performance goals. LM adjusted some of the goals for greater stringency to better match with our supersonic transportation studies. The only large change from a technology and capability standpoint, was

LM N+2 Environmental & Performance Goals (2020)	
ENVIRONMENTAL GOALS	
Sonic Boom	**65-70 PLdB**
Airport Noise (cumulative from stage 3)	**-20 to -30 EPNLdB** **Sideline (PLR) <= S3 -5**
Cruise Emissions (Cruise NOx g/kg of fuel)	**< 10**
PERFORMANCE GOALS	
Cruise Speed	**Mach 1.6 – 1.8**
Range	**4000 - 5500 nm**
Payload (passengers)	**35-100**
Fuel Efficiency (passenger-nm / pound of fuel)	**> 3.0**

Figure 121. Entries in Blue Reflect Greater LM Stringency than NASA's N+2 Goals

our airport noise change. Instead of the NASA N+2 goal of –10 to –20 cumulative noise difference from stage 3 levels, we worked for –20 to –30. Most of the subsonic vehicles being delivered today are in the –20 to –30 range. On the other hand, quieter airport noise results in much larger penalties for a supersonic transport than for subsonic ones, which indicates that technology improvement is necessary to keep such an aggressive goal from ruining performance viability. Past studies of supersonic business jets and N+3 Supersonic Systems Studies had suggested a combination of technologies that might work with the inclusion of our propulsion partners, GE and Rolls Royce. The other changes, allowing ranges up to 5500 nm and up to 100 passengers (instead of 70) can be achieved just by sizing a vehicle larger, so they do not dictate technology by themselves. (More passengers have a benefit on fuel efficiency but more range is a detriment to it). Our reasoning for the change was two-fold. We want to build on low boom design progress in our N+3 study with a 100 passenger vehicle and we found that adding one engine to our N+1 study vehicle (allowing more sales and viability of a common supersonic engine) resulted in a vehicle with more range or payload than the original N+2 goal numbers.

The airport noise and emissions results were validated through engine cycle studies based on the product experience and methodologies developed for the same by GE and Rolls Royce. For the important airport noise goal, cycle studies were supplemented with acoustic nozzle test measurements of a large scale nozzle at representative jet velocities, accurate temperature hot flow and forward flow speed from Mach 0.0 to 0.3. Performance assessments compared to the performance goals are performed with validated aerodynamic (CFD), weight and design methodologies and experience. Measurements are added for the newer characteristic of low boom and later may be used to enhance accuracy of aerodynamic forces, moments and natural laminar flow (NLF) boundary layer drag reduction. Some fan noise measurements are also desired especially for approach noise where it is typically a dominant noise source.

9.3 Results

Sonic boom design predictions used direct CAD surface gridding, Mach aligned volume grids and Euler CFD++ solutions. Solution cylinders of DP/P wrapping around the vehicle were extracted for use with a 10^{th} order Fourier-fit singularity near-field to far-field correction methodology linked to ray tube tracing acoustic propagation in a real atmosphere with non-linear aging. The Mach aligned grid and near-field correction methodology gives accurate and virtually identical sonic boom when propagated from H/(b/2) of 2.7 to 11 (H/L of 0.5 to 2.0) without the need to run CFD beyond H/(b/2) of 20 (H/L of 3.6) to get enough outside the near-field for accurate direct propagation. The sonic boom results are now so repeatable that various loudness calculation methods have much more variability than the ground signature calculation. The target signature shape for low boom is in general a multi-shock ramp signature with ramp rounding more toward sinusoidal in shape that came from a parametric signature shape optimization for minimum vehicle length required for the desired loudness constraint. For our N+2 vehicle weight and the chosen length, the target signature is equivalent in loudness to a 0.22 psf N-wave (by various loudness calculation codes). The sonic boom analysis of the final geometry developed in Task 3.3 (extended 8 months to achieve better low boom results that NASA wanted). As plotted in Figure 122, the under-track loudness (and everywhere except a little louder from the 40 degree roll angle) at maximum weight is equivalent to a 0.26 psf N-wave just 4 PLdB above the minimum target. As illustrated in Figure 123, its more than 1 PLdB quieter than the loudness of the ideal (SEEB) minimum shock ramp signature for the same weight and length. And the whole low boom carpet is within 6 percent of the ideal ramp. This is important because it is not necessarily that difficult to achieve low boom at very low weight and long length, but such a vehicle would be too heavy for competitive or even viable performance. For a low boom vehicle to also be practical over water, it cannot sacrifice more than perhaps 10 percent in efficiency versus a non-low boom design. 10 percent is an estimate based on an efficiency difference that justifies fleet replacement, but there is a breakpoint even if the precise number is a little different. Too much performance lost to achieve low boom indicates the need for different designs for over land and over water—splitting the (expanded) market.

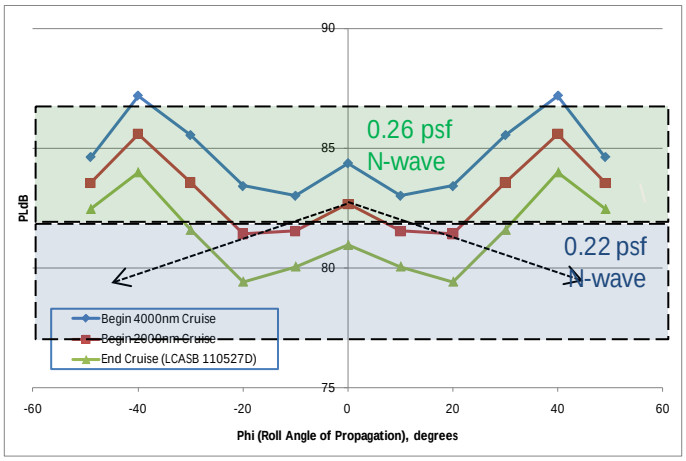

Figure 122. Current Low Boom Equivalent to 0.26 psf N-wave, Nearing Taget of 0.22 psf N-wave

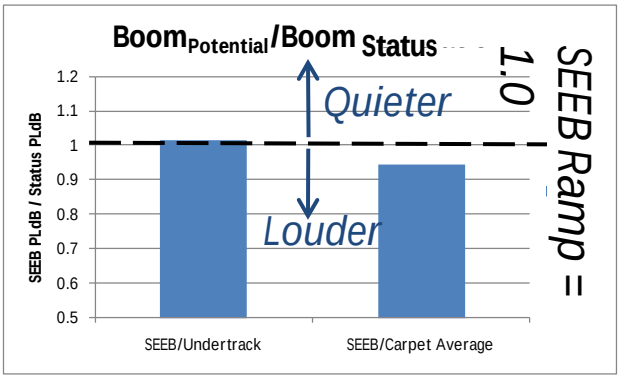

Figure 123. Current Low Boom Under-Track Better than SEEB

So just as important as very low boom loudness is high performance, which generally requires good efficiency and thick structure. Figure 124 shows that the low boom design is close to its performance before shaping and along a highly optimized vehicle L/D aerodynamic efficiency trendline. Figure 125 shows very smooth, distributed and weak pressures at cruise that generally indicate good performance, and a wing vortex at limit low speed conditions that is well separated from buffeting the V-tails or center engine with high pressure at the engine inlets. Compared to the non-low boom Technology Configuration (TC) of HSR, this low boom design has the same wing loading, same required total propulsion thrust-to-weight ratio for the same takeoff field length. However it has a 35 percent lower aspect ratio and greater wing spar thickness/span ratio, leading to less wing weight and flexibility. As a tri-jet, the outboard wing engines are much closer to the body, the propulsion system is much lighter with the nozzle being especially lighter and closer to the wing structure, reducing dynamic structural problems that complicated control systems and reduced the TC's performance. Further, improvements like increased design method sophistication controls lift for low boom while the cabin has a constant cross-section for better packaging and simpler structure, visible in Figure 126. In summary, this low boom configuration also combines high performance and simplifying, practical design parameters.

Like indicated in the description, a propulsion system that efficiently achieves low airport noise is the other focus of the Base Program and excellence in low airport noise is achieved along with efficiency with this design and its integrated propulsion system. LM and its propulsion suppliers worked together closely to achieve a high level of optimization while eliminating unfavorable interactions. Again sophistication in design methodology allows the high performance positioning of the engines below the

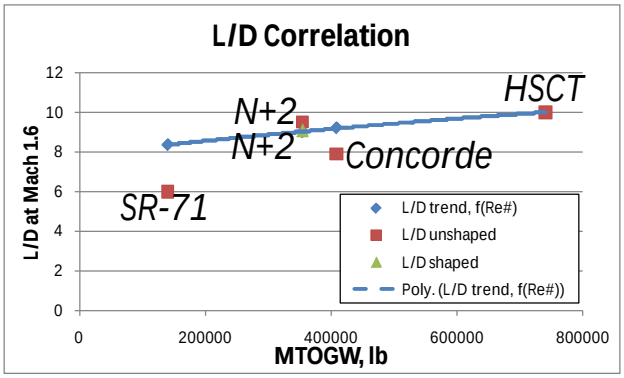

Figure 124. L/D with Low Boom Near Best Trend

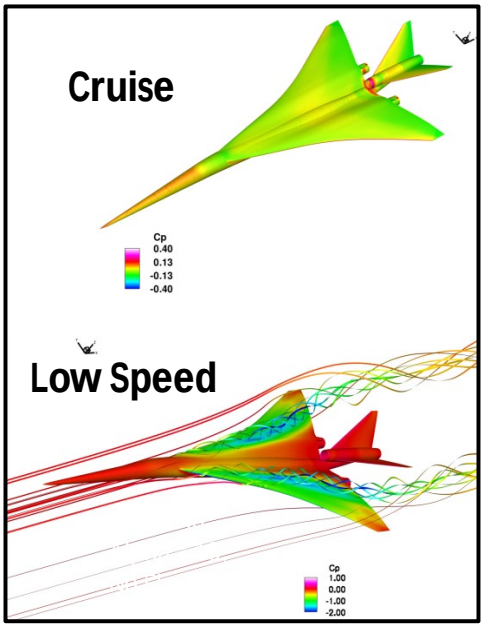

Figure 125. Smooth Flow at Cruise, Well-Controlled at Low Speed

Figure 126. Careful Control of Lift Can Achieve Low Boom with a Constant Cabin Cross-Section

wing and aft, without any increase in low boom loudness above the minimum for this vehicle weight and length. Our design matches the HSR TC's wing loading, T/W required, and field length with a 35 percent lower aspect ratio. This is possible from a slightly higher performing Kreuger flap, but mostly from performing takeoff calculations differently to better utilize a supersonic aircraft's unique characteristics—without reducing safety margins, Figure 127. Most of the takeoff procedural change benefit has been taken to improve performance by offsetting the shorter wing span, with just a couple dB improvement in cutback noise attributed to the difference in throttle shown in Figure 128. So the majority of the increased noise burden has been put on the propulsion system, now required to meet stage 3 –5 dB sideline, instead of the stage 3 –1 dB of the TC (cumulative –10 dB for the TC instead of N+2 –20 to –30). But any effective noise reducing nozzle technologies can reduce the weight incurred by the engine solving the entire problem. Nozzles were analyzed and predicted to have great performance potential, so acoustic validation of the nozzles at large scale and representative conditions was tested in NASA's Acoustic Test Rig (NATR). However, specific implementation features produced some tonal and separated flow noise that increased levels at their design conditions. Diagnostic measurements have located and characterized these noise sources. Existing and emerging methodology should be useable to eliminate these noise sources if sufficient resources are available to generate an accurate model and determine the shape changes needed for the model to predict success.

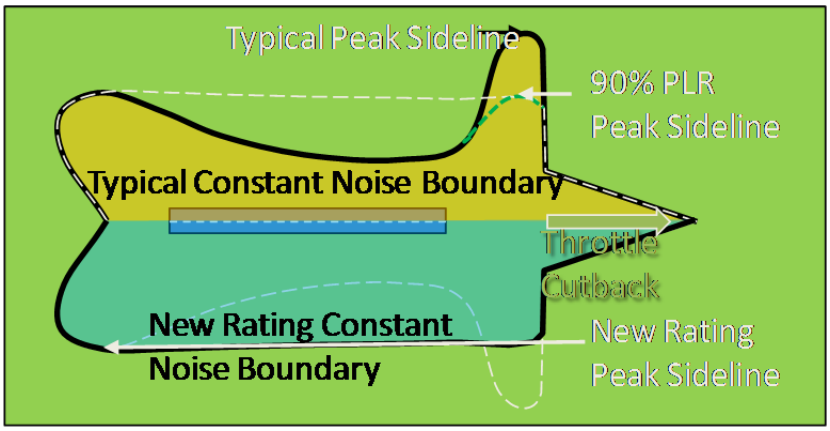

Figure 127. Engine Designed for Sideline Noise Compliance with Best Performance

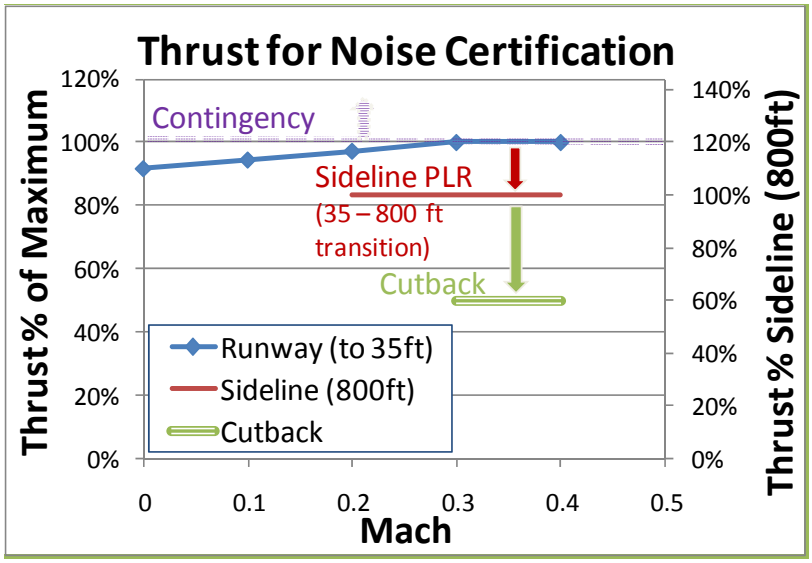

Figure 128. Engine Designed for Noise Compliance with Best Performance

Despite the more stringent noise, our total propulsion system weight is 30 percent lower than the HSR TC's rather poor value of less than 3. Primarily a lighter low noise engine, but also lighter material and system weight, were the big reasons for going to a lower cruise Mach than HSR and even Concorde. But strangely reversed from the total system, our best N+2 cycle alone (no inlet, no nozzle) sea level static thrust-to-weight ratio (SLS T/W) is more than 15 percent worse than HSR, contrary to our later technology availability date and less stringent EINOx goal. N+2 has much higher BPR, but subsonic cycle SLS T/W tends to vary little with BPR, so N+2 SLS T/W seems rather low. Studying this deficit in T/W and the size, weight and thrust values that cause it might uncover a source and a point to a way to make it less deficient. (In some past studies throttle was originally reduced to meet noise, then other features of the engine were reduced so that the throttle could not be turned back up simply without redesigning other constraining features; however, by redesigning the constraints, turning up the throttle plus increasing BPR to keep noise low, the poor engine only T/W was eliminated.)

The cycle concepts were developed with temperature limits compatible with combustor technology being developed to meet the EINOx goal. Combustor technology is being developed in separate programs, outside of N+2. As long as combustor technology continues to be pursued, monitored and integrated into these system study concepts, the emission goal should be reachable by our N+2 cycles.

The low boom vehicle design and its propulsion system integration appear capable of meeting the performance goals, particularly range and efficiency. Substantial further improvements are predicted with the application of natural laminar flow technology and MDAO methodology if it continues to be developed and validated in this on-going N+2 program. However, ascent trajectories that maintain low boom levels can require 15 to 30 percent more thrust than available from our current cycles without some means of augmentation. The poor SFC of afterburning used for this short portion of climb does not seem to substantially reduce range, so it is currently a leading solution, but more study with an actual design capable of low boom climb is needed to better quantify thrust and other requirements for such a unique trajectory.

9.4 Summary

The LM N+2 Low Boom Configuration achieved the best full carpet low boom signature and performance possible in the vehicle size and weight class. Design tools worked with great accuracy and repeatability. The Low Boom Configuration was tested in October 2011 with all new calibration and test procedures and improved measurement accuracy by two orders-of-magnitude. The measurements validated all predicted sonic boom, matching within 1 PLdB. The configuration was also predicted to have high L/D with good structural thickness and generally practical design parameters; therefore, it was designed to have very good performance.

A low noise propulsion concept successfully integrated with the low boom design. The propulsion concepts were predicted to achieve the low noise goal, but acoustic testing revealed additional noise sources that need to be reduced or eliminated through careful redesign with the latest tools. Total propulsion weight was improved from prior study solutions, with the exception of the engine cycle. Study of this greater weight is recommended for future weight reduction. Further performance improvements are expected with the application of NLF and MDAO methodology.

10.0 Conclusions

10.1 Environmental Goals

10.1.1 Low Boom Goal

- The low boom signature necessary for acceptable supersonic flight over land appears to be reachable with practical supersonic vehicle designs. However to become confident in this assertion we need:
  - Further low boom level refinement
  - Low boom in climb, descent and cruise

- Quantification of reduction in loudness in a real atmosphere relative to our (no turbulence) prediction methodology
- Validation of low boom human acceptability indoors

· Sonic boom can be accurately measured in the wind tunnel and was validated in the October 2011 test
· Sonic boom impact of an operating vehicle propulsion system can be accurately modeled with CFD if the all mass flows, pressure and temperature conditions are accurately enforced, along with typical grid alignment, densities and adaptations for the flow features being modeled
· Now that low boom has been validated (3.17), a validation that shows goal loudness can be achieved when propagated through atmospheric variations is needed

10.1.2 Airport Noise Goal

The NASA airport noise goal of a cumulative –10 to –20 EPNLdB relative to stage 3 limits was adjusted to –20 to –30 to keep pace with expected subsonic aircraft levels. We attempted to take advantage of the better noise potential indicated by recent studies at cruise Mach of 1.6 to 1.8, reduced from Mach 2.4 of HSR. To achieve –20 to –30 cumulative, a sideline noise level of –5 dB from stage 3 was estimated to be necessary (provided sideline noise technology did not fail to help at cutback and approach conditions). Studies were performed of variable cycle engines with integrated noise suppressing nozzle technology. These propulsion concepts were themselves integrated into a low boom supersonic vehicle design. Takeoff and landing trajectory and propulsion characteristics were determined integrated on a vehicle representative of a design that could meet all environmental and performance requirements.

· Engine cycle and nozzle concepts are predicted to meet the sideline goal and the cumulative –20 to –30 from stage 3 overall goal when integrated with a representative vehicle
· Acoustic validation testing of large scale nozzle concepts at representative conditions indicated the concepts potential of meeting their predicted noise; however, specific implementation features produced tonal and separated flow noise that increased levels at their design conditions. Diagnostic measurements have located and characterized these noise sources. Existing and emerging methodology should be useable to eliminate these noise sources if sufficient resources are available to generate an accurate model and determine the shape changes needed for the model to predict success.
· Two vehicle operational differences could further reduce supersonic noise compared to subsonic vehicles due to: the greater drop in supersonic vehicle weight for flight distance reductions from the maximum and the ability to keep more noise inside the airport boundary through the greater maneuver capability of this supersonic vehicle (and supersonic vehicles in general). The technology and performance reduction incurred to meet the airport noise goal could be significantly lessened by exploiting these two operational differences.

10.1.3 Cruise Emission Goal

The cycle concepts were developed with temperature limits compatible with combustor technology being developed to meet the EINOx goal. As long as combustor technology continues to be pursued, monitored and integrated into these system study concepts, the emission goal should be reachable.

10.1.4 Performance Goals

The low boom vehicle design and its propulsion system integration appear capable of meeting the performance goals, particularly range and efficiency.

Substantial further improvements are predicted with the application of natural laminar flow technology and MDAO methodology if it continues to be developed and validated in this on-going N+2 program.

11.0 Recommendations

Recommended Phase 2 efforts include continued systems level validation testing and methodology verifications for both low boom and nozzle designs. A summary list of recommendations for Phase 2 and beyond is highlighted below, with updates considering the excellent low boom validations achieved in the LM3 Test (97-0231):

11.1 Low Boom Goal

- Achieve most of the last 4 PLdB reduction low boom loudness possible with our current design's target sonic boom signature and either hold that level or achieve further reduction of the low boom off-track to the edge of the carpet.
- Using productivity and accuracy improving procedures refined from LM3 lessons learned, validate an improved low boom design; and by doing so, demonstrate the maturity of these measurement procedures for wind tunnel low boom design validation.
- For comparison with NASA Dryden flight boom demonstrations, perform a high resolution CFD vehicle starting boom prediction. Compare our propagation methodology's (no turbulence) ground sonic boom to measured sonic boom statistically, at various turbulence levels, to quantify the overpressure and loudness variation expected from a real atmosphere. (Past, lower resolution comparisons indicate that atmospheric rounding of measurements typically reduces overpressure 20 to 25 percent).
- Develop a way to demonstrate and validate low boom loudness, like our Optimum Signature, after propagation through a real atmosphere that is affordable by the N+2 Supersonic Validations program.

11.1.1 Airport Noise Goal

- Develop a refined analysis procedure that models tonal and separation noises accurately. Refine acoustic nozzle designs to eliminate tonal and separation noise.
- Refine cycle parameters for new low boom tri-jet requirements and noise conditions.
- Refine noise estimates—particularly at cutback and approach—with jet, fan and airframe noise sources with best low noise technology projections to see if the estimated sideline constraint needs to be adjusted to achieve the overall cumulative noise goal.
- Predict low noise fan noise acceptability with inlet distortion interaction, inlet acoustic lining and auxiliary inlet with soft choke for approach noise reduction and devise affordable validation tests.

11.1.2 Cruise Emission Goal

Continue to monitor technology development and integrate projected consequences of temperature limits, etc. into cycle models and performance assessments.

11.1.3 Performance Goals

- In looking for a good flow quality tunnel for low sonic boom measurements, it was found that the NASA Glenn 10′ 10 tunnel has uniquely good flow attributes, but at a minimum speed of Mach 2.0. Mach 2.0 is the design speed for our swept Natural Laminar Flow (NLF) wing from the DARPA QSP program. Continue to investigate the 10′ 10 for suitability to retest the Natural Laminar Flow (NLF) model.
- Find an affordable way to develop and validate NLF under representative flow conditions (including lower turbulence than current wind tunnels).
- Implement existing and new N+2 MDAO methodologies. Use them to optimize performance while integrating technologies like NLF and variable cycle engines that are being validated in this N+2 Supersonic Validations program. Use system assessments of the validated results to predict the potential performance of a future vehicle.

Lockheed Martin Aeronautics Company

N+2 Supersonic Validations: Phase I

In Response To:

Contract Requirement - deliverables

Submitted By:

Rolls-Royce North American Technologies Inc. (LibertyWorksÒ)
2059 South Tibbs Avenue, Indianapolis, IN 46241
(or) P.O. Box 7162, Indianapolis, IN 46207-7162

Dr. Jack (Jagdish) S. Sokhey
Principal Investigator

Final Contract Report,

EDNS 00000981602
26 July 2011, (Revised (2/6/2012)

Table of Contents

Table of Figures

List of Tables

1. Summary

This constitutes the final report as required by the NASA N+2 Supersonic Validations Program, Government Contract # NNC10CA02C, LM Subcontract # XF3179080E. A summary of four program tasks which include the development of a new three-stream engine definition for Lockheed-Martin's N+2 Supersonic vehicle requirements and the corresponding design concept of a Mixer-Ejector variable geometry C-D exhaust nozzle. The exhaust nozzle was then designed using CFD analysis to meet the N+2 vehicle performance requirements at Take-off, a transonic transition point at M = 1.1 and nominal cruise at M = 1.6 without afterburner. Key sizing operating points turned out to be the transonic drag/thrust performance, and the acoustical sideline take-off noise requirements. A model scale (0.15) design of the Mixer-Ejector, variable area, and convergent divergent nozzle for acoustical testing at NASA GRC AAPL was designed, fabricated and tested in April-May 2011. Test model details, test plan and the analysis of test results are presented.

The 0.15 scale model nozzle hardware was designed by ASE FluiDyne and it required geometry modifications to the nozzle configuration to integrate with the facility interface requiring a large increase in boat-tail angle, the addition of structural brackets to hold divergent fairings and mechanical design features to allow manual actuation. These resulted in some performance compromise to both aerodynamic and acoustics. Still, the nozzle tests indicated that the nozzle provides reasonable suppression to the required take-off jet noise, and very close to N+2 supersonic acoustic cumulative noise levels required for supersonic aircraft application. Jet noise levels close to a corresponding subsonic reference mixed flow nozzles within margin of error were demonstrated. In particular, two configurations, with DF=12º and ED=9.5º and another, with DF=10º and ED=12.5º were best performers, and a possible minimum exists here. As the propulsion system matures, mixer-ejector nozzle design changes will be required to control general broadband noise at frequencies greater than 1 kHz and the generation of very strong tones in the model appears to be related to the third stream pressure ratio. A list of recommendations have been provided for Phase II Program and bring the development of ejector-mixer nozzle acoustic program to TRL = 4.

2. Introduction

Rolls-Royce has a unique insight and interest into supersonic aircraft propulsion for commercial applications, having provided engines for the only supersonic airliner to enter revenue service. The company remains keenly interested in the development of
.

new supersonic applications for civil aviation. The development of affordable propulsion systems for such applications that can meet the low far field noise requirements during take-off and landing, and while also satisfying a low drag and a low boom acoustic signature at the supersonic cruise, remains a daunting task. Variable cycle engines can emulate existing low noise high bypass ratio engines when operating at low altitude near airports and adapt to provide highly efficient propulsion for supersonic cruise operation. Innovative exhaust system concepts that can complement engine variability and adaptability to such supersonic aircraft have been developed; however, they will require validation.

RR strategy is consistent with NASA's N+2 Supersonic Validations Program to advance fundamental technologies for a viable and safer supersonic transportation. Mixer-Ejector supersonic nozzle with Variable Exit Areas has been in main focus for civil applications; to generate a required thrust, while enhancing Acoustical technology Data Base. An efficient exhaust system at Cruise and through transonic flight regimes and a quite operation at take-off and landing is the main focus of this work.

2.1 Background

Rolls-Royce NA Technologies Inc (LibertyWorks) has been working with NASA and its commercial supersonic programs since 2000 with QSSP Program where Rolls-Royce and Lockheed-Martin (LM) designed and tested the first generation of mixer-ejector nozzle. There were additional cooperation with LM and Gulf Stream Aircraft (GAC) on Supersonic Business Jets (SSBJ) when additional studies on a number of supersonic engine installations were investigated. RR conducted significant research at its University Technology center (Purdue U.) and also at University of Illinois to advance supersonic technology as quickly as possible. This program has offered another opportunity to address future community acoustical issues for supersonic flight on land in cooperation with LM and is pleased to support on the following Statement of Work.

2.2 Scope and Statement of Work (SOW)

This SOW supports Lockheed-Martin's overall objective for this contract is to perform integrated validations of tools and technologies for the N+2 Supersonic Validations NRA. Rolls Royce Liberty Works (RRLW) will assist LM with the development and testing, and integrated propulsion validations for innovative propulsion systems and technologies that meet environmentally friendly emissions, community noise requirements, and low sonic boom. This document addresses 17 month base program task3.12 listed below, ending in June 2011 (Phase I).

Task 3.12 Variable Cycle Propulsion System Development and Aero-acoustic Nozzle Design and Testing Work – 5 sub-tasks (Base)

Each RRLW task will involve reviews and reporting procedures similar to those shown in table below. This will include the development and engineering of sub-contractors, the technical data for work plan document, final report, and modifications/updates to the following year plan and Recovery Act reporting requirements where applicable. The optional programs following the base program may or may not be linked with other optional programs as described in the appropriate task details. Optional programs are linked to follow the roadmap for supersonic technology readiness at RR LibertyWorks for developing a viable propulsion system to meet NASA and LM goals for N+2 Air vehicles.

Report Description	Delivery	Content
Monthly Technical/Schedule Progress	After each month	Technical progress, schedule progress, identify problems and propose corrective action, and identify work planned for next month
Work Plan	Within 30 days of start	Detailed schedule of sub-tasks, milestones and deliverables for schedule tracking
Kick-Off Plan Review	Within first month or two	Communication of planned work, technical approach, schedule, and coordination of GFE/GFI and collaborations with NASA
Quarterly Review	Every 3 months after start (excluding mid-term and final report month)	Technical progress to date including data from subcontractors
Mid-Term Oral Review	At halfway month of Program period	Technical progress and development to date
Final Report	Final month of Program period	Disclosure of all major developments and technical progress
Following Year Plan Modification/Updates	At End of Base Program	Any needed changes to the following year plan based on insight and progress during this portion

Task 3.12.1: Propulsion System Definition

RRLW shall collaborate with LM to define propulsion system from a commercial version of Variable Cycle Engine Technology Applications cycle to N+2 SS aircraft as a baseline and conduct the required trade studies listed below. RRLW engineers will define a preliminary engine and inlet/engine interface requirements tailored for an integrated LM N+2 propulsion system. The design cycle will be secured by export control and proprietary protections as appropriate, and all documentation provided to NASA must clearly note what restrictions apply. In addition to the protected design documentation, a non-proprietary version will also be provided to NASA.

1. Coordinate with LM to get aircraft defined to appropriate mission requirements, NASA performance goals in NASA's solicitation Table etc., to size and select a variable cycle engine to model. Create a baseline model for the commercial supersonic N+2 aircraft application.
2. Create NPSS Model and exercise required studies for the selected Variable Cycle Engine Technology Payoffs and input/output files for final configuration. Appropriate RRLW proprietary data restrictions will apply as needed to the embedded engine component data.

3. Provide airflow schedule, thrust and operability limits etc., to design the test model parameters and provide a basis for exhaust nozzle design for validation testing. Compare conventional VCE with the Variable Cycle Engine cycle model data.
4. Conceptual engine configuration with preliminary details to fit LM N+2 aircraft - given space, necessary performance data, data inputs used in NPSS model.
5. Nozzle Noise Prediction: RRLW shall provide standard noise analysis / prediction from Task 1 cycle data and LM revised aircraft performance at Noise Certification points (sideline, flyover, approach) and future noise regulations, project targets. The noise prediction approach will be based on correlated noise data rather than computer flow simulation. Supports Noise Task 3.12.4.
6. Engine Accessory Study: RRLW shall perform a limited conceptual mechanical layout study for relocating and reshaping accessories into engine general assembly. LM will determine consequential nacelle changes and overall effect of the vehicle performance. Ongoing Support for LM and Coordination, weekly meetings, data transfer etc.

Deliverables:

(1) RRLW final cycle configuration – NPSS data packs for two iterations
(2) RRLW final cycle conceptual flow-path and associated PD details, component performance data and any supporting engine cycle.

Task 3.12.2 Nozzle Aerodynamic Design

RRLW will identify the improvement opportunities on the current baseline nozzle configuration and modify flow path to enhance the aerodynamic and the noise performance, review nozzle requirements, participate in the current NASA HVC nozzle test at NASA GRC, analyze the test data and formulate the nozzle design requirements for the next design. RRLW will identify the improvement opportunities on current baseline nozzle configuration and layout a new aerodynamic design.

- 2D /3D flow analysis may be used to evaluate nozzle design concepts, study and identify improved configurations and formulate a design plan. A limited 3D-CFD flow analysis of final configurations will be conducted for design, validations and other exhaust performance assessments.
- Develop a scale model configuration of the nozzle and other modifications for testing and validation. Addition CFD analysis may be conducted if needed.
- Complete final geometry definition (IGES format) for nozzle model procurement; i.e., design and fabrication.

Deliverables:

(3) Provide IGES format geometry, a validation CFD solution and grid files.

Review: A review of nozzle model design modifications and analysis results shall be

performed before NASA authorizes modification, fabrication, installation and test.

Task 3.12.3 Model Nozzle Procurement

RRLW will manage nozzle procurement, mechanical design oversight and technical guidance to subcontractor (currently ASE is a sole source for model)

1. Complete a SOW for nozzle model design and start procurement process. Award model design and fabrication contract based on agreed criterion and provide subcontractor oversight during design, fabrication and delivery. During the design process, RRLW will explore the possibility of maximizing customer value by using as many existing HVC nozzle hardware parts as possible.
2. Nozzle Mechanical Design: RRLW has experienced subcontractors (such as ASE) to design the nozzle model and required modifications. Design will include pressure / temperature instrumentation and but no actuation systems.
3. The model test hardware will be designed to interface with the facility rig drawings provided by NASA GRC. All model hardware will be documented in a hardware design report to show compliance with NASA/TM-2006-212939 “Aero-Acoustic Propulsion Laboratory Nozzle Acoustic Test Rig User Manual.” for completing the aerodynamic and acoustic testing at NATR Rig.
4. Nozzle Fabrication: RRLW will use a subcontractor (e.g., ASE) to fabricate parts hardware and modifications to the nozzle design.
5. Model Assembly and Delivery of model w/ required documentation.

Deliverables:

(4) Nozzle model modified parts and interface hardware
(5) Model documentation: drawings, support hardware, stress/quality report.

Task 3.12.4 Model Nozzle Installation and Test

The nozzle will be installed at the NASA Glenn Research Center Aero-Acoustic Propulsion Laboratory (AAPL) facility using the Nozzle Aero-acoustics Test Rig (NATR). The existing rig will be used to install the new model components and other design modification parts. Particle Image Velocimetry (PIV) may be used to the map the time mean velocity field and measurements of turbulence quantities if NASA allows. These acoustic and flow field datasets, along with model pressure and temperature instrumentation, if needed, will be made available for post-test analysis and reported after test completion.

1. RRLW shall provide test planning and shall include defining test requirements (objectives, test matrix, priorities) generating a test plan and coordination with the NASA facility. A final Test Matrix will be developed with customer input.
2. RRLW will provide on-site engineering support during NATR testing (Two weeks or10 days) and additional mechanic support for model installation and model modification if required at a nominal cost.

3. Selection and prioritization of test runs shall be coordinated with NASA to ensure that the highest priority data is obtained during the test.
   - NASA will deploy the AAPL far field microphone array which to measure the far field sound pressure level spectrum and directivity for the models and provide standard data acquisition equipment and support.
   - Particle Image Velocimetry (PIV) will be requested to be used to the map the time mean velocity field and measurements of turbulence quantities.
4. Post Test support: Data Reduction, analysis, validations and reporting will be provided both at and off-site as required.
5. Travel to Test site – 6 trips (15 days coverage, mechanic -5 days)

Deliverable:

(6) Test plan
(7) Test and post-test analysis summary report

Task 3.12.5 Program Management and Reporting

This task support the management of tasks 3.12.1-4 and includes the program management, business management, loads review, Internal Gated Reviews required, Periodic Program Reviews, Final reviews, monthly reports, ASE reviews, the associated travel, audits, and contracts related issues.

2.3 Program Schedule

The 16 month program schedule from January 2010 to June 2011 is shown below.

Task Name	Duration	Start	Finish
Base Program N+2 Exhaust System	362 days?	Mon 1/4/10	Tue 5/24/11
Task 1 Propulsion Systems Definition	210 days	Mon 1/4/10	Fri 10/22/10
1.1 Coordination with LM & Trade Studies	44 days	Mon 1/4/10	Thu 3/4/10
1.2 Create Engine Model (i-NPSS Mode)	110 days	Fri 3/5/10	Thu 8/5/10
1.3 Engine Conceptual Design - Perf- Maps	25 days	Mon 3/29/10	Fri 4/30/10
1.4 Cycle Optimization/UKICE Model	30 days	Mon 5/10/10	Fri 6/18/10
1.5 Noise Predictions	30 days	Mon 6/28/10	Fri 8/6/10
1.6 Engine Accessory Study	20 days	Mon 8/2/10	Fri 8/27/10
1.7 Ongoing LM Support	195 days	Mon 1/25/10	Fri 10/22/10
Task 2 Nozzle Aerodynamic Design	169 days?	Wed 3/31/10	Mon 11/22/10
2.1 Nozzle CAD Model Development	50 days	Thu 7/15/10	Wed 9/22/10
2.2 HCE Test Coverage and Data Analysis	44 days?	Wed 3/31/10	Mon 5/31/10
2.3 Nozzle Component Design Studies	45 days?	Tue 6/1/10	Mon 8/2/10
2.4 CFD Analysis	60 days	Tue 8/3/10	Mon 10/25/10
2.5 Create Design Geometry Data	20 days?	Tue 10/26/10	Mon 11/22/10
Task 3 Model Nozzle Procurement	81 days	Tue 11/23/10	Tue 3/15/11
3.1 Coordination	10 days	Tue 11/23/10	Mon 12/6/10
3.2 Nozzle Mechanical Design	33 days	Tue 12/7/10	Thu 1/20/11
3.3 Nozzle Fabrication	38 days	Fri 1/21/11	Tue 3/15/11
3.4 Model Delivery	0 days	Tue 3/15/11	Tue 3/15/11
Task 4 Model Installation and Testing	92 days	Mon 1/17/11	Tue 5/24/11
4.1 Test Planning	25 days	Mon 1/17/11	Fri 2/18/11
4.2 Test Set-Up	5 days	Wed 3/16/11	Tue 3/22/11
4.3 Conduct Testing	15 days	Wed 3/23/11	Tue 4/12/11
4.4 Data Reduction and Reporting	30 days	Wed 4/13/11	Tue 5/24/11

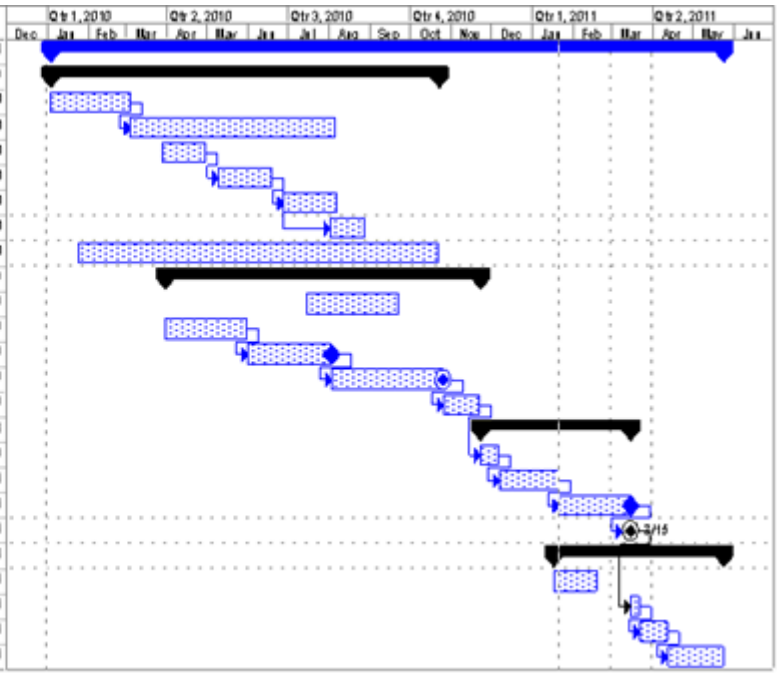

3. Propulsion Systems Definition

3.1 N+2 Engine Requirements

The design requirements of the propulsion system for the LM N+2 Aircraft arrangement shown in Figure 1 is provided in Table 1. For the four engines per vehicle aircraft, the thrust requirements at three operating conditions, namely, rolling take-off, a transonic pinch point and the nominal cruise operation are shown in Table 1 along with required bleed, horsepower extraction and acoustical requirements.

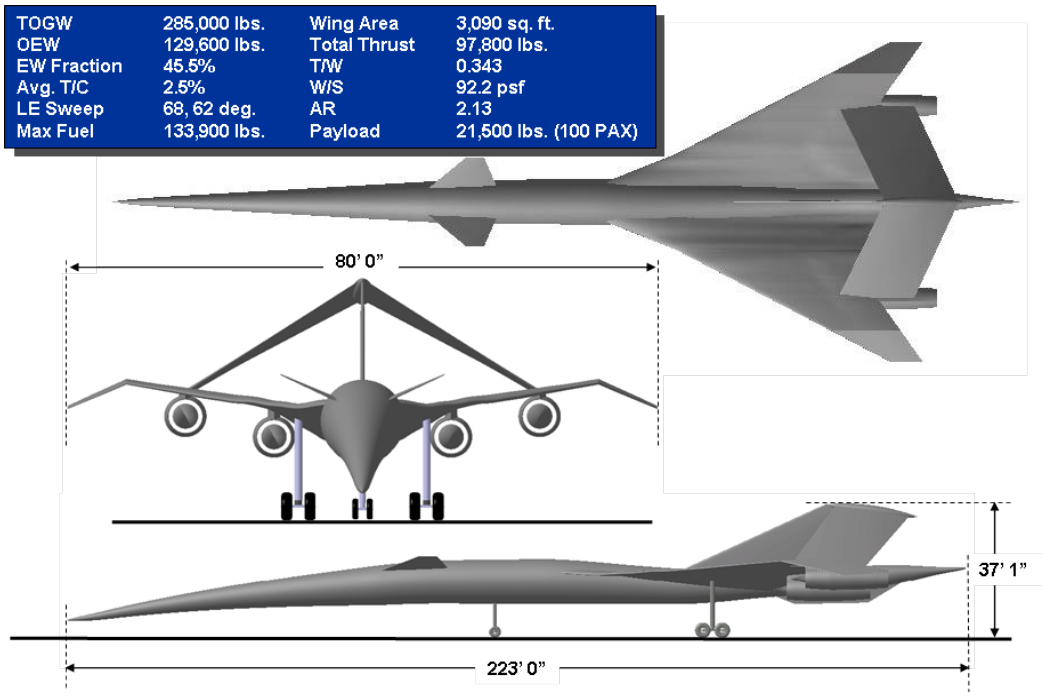

Figure 1 N+2 LM General Arrangement

The Lockheed-Martin N+2 Low Boom Aircraft must meet the environmental targets and the performance goals for Y2020 described below.

Sonic Boom	**60-70 PNdB**
Airport Noise (Cumulative)	**Stage 3 minus 20 EPNdB (with 90% PLR)**
Cruise Emissions	**< 10 NOx g/kg of fuel**
Cruise Speed	**Mach 1.6**
Range with 100 PAX	**4000- 5500 nm**
Fuel Efficiency	**>3.0 Passenger-miles /Lb fuel**
Max Take-Off Weight (MTOW)	**354,000 Lbs**

Table 1 Propulsion System Requirements – 4 Engines per Vehicle

Thrust Requirements (Per Engine)

Mach Number (Free-Stream)	Altitude (ft)	Installed Thrust (lbf)		Inlet+Boattail Drag Cd (base; Capture Area, Std day)
0.3	0	24,500 @ 20C day		0
1.1	35,000	7,800 +10C day		0.113
1.6	50,000	6,000 +5C day		0.0039

Engine Bleed and Horsepower Extractions (nominal per engine) **Range Sensitivity**

Horsepower	80		Conversion Factors
Engine Bleed - Fan	1.25 lbm/sec @10 psi		1% Cruise thrust = +22.8% nm Range
Engine Bleed - Intermediate	1.50 lbm/sec @75 psi		1% Cruise SFC = -55.6 nm Range
T Fuel to Engine (Avg)	155F (235F Limit) (ground 250F limit)		Cd +0.0001 CR = -35.0 nm Range

LM also provided the inlet recovery, engine turndown and the drag characteristics as a function of local Mach number as an input to the installed engine cycle deck. Additional data that was used included in the installed drag (Figure 2) and the boat-tail (after-body) drag of the supersonic exhaust nozzle based on a single axi-symmetric C-D nozzle. In the absence of more accurate information, it was assumed that these characteristics will apply to the Mixer-Ejector nozzle profile.

Note:

In February 2011, LM updated their aircraft and optimized their supersonic aircraft with engine performance requirements based on a three-engine per vehicle. Most of the performance and acoustics data presented in this report are based an original four-engine aircraft configuration. A new section has been added to the end of the report to address the impact of three-engine vehicle configuration on the Propulsion System, the Mixer-Ejector nozzle design and the projected acoustic performance characteristics.

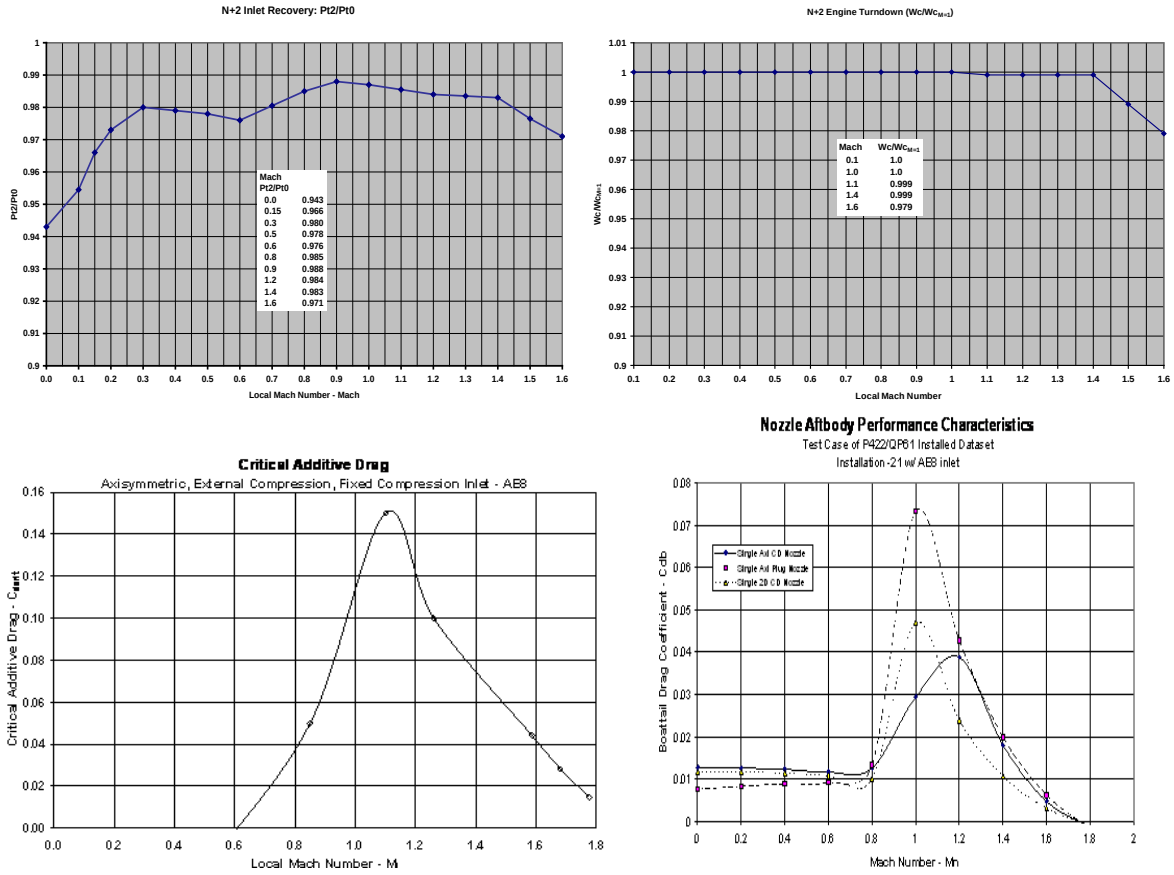

Figure 2 Inlet and Nozzle After-body Drag Characteristic Requirements

3.2 Three-Stream N+2 Engine Cycle Model

N+2 engine cycle was developed to meet the requirements of the LM N+2 Supersonic Commercial Jet Aircraft with mission performance requirements listed above. A baseline standard fixed engine configuration was used as basis of developing a variable area three-stream configuration. It is assumed that a commercial version of three-stream variable cycle will be developed by Rolls-Royce for the N+2 aircraft time-frame. A new ejector module to the NPSS simulation was developed where only the third-stream from two stage fan was used to drive the required free-stream ejector. Following is a list of technologies that were incorporated into this N+2, two-spool engine cycle.

1. Variable Inlet Guide Vanes
2. Light Weight Fan Structure
3. Active Flow Control
4. Hybrid Compressor disks
5. Modulated-Cooled Cooling Air
6. Advanced Tip Clearance Control

7. Variable three-stream architecture
8. Variable area third-stream and core-stream nozzle
9. Variable Area Ejector Nozzle

The Parametric Study Process illustrated in Figure 3, for the propulsion system is iterative in nature and required JMP optimization of the response surface that provided a minimum Cruise SFC and minimum inlet fan diameter while maintaining average exhaust nozzle velocities to take-off noise requirements. It was assumed based on our internal studies that this velocity should be less than 1100 feet per second.

With the mixed flow nozzle throat fixed, the third stream throat or exit areas have to be variable at all conditions. The nozzle ejector door is in closed position during supersonic cruise (M = 1.6) condition, allowing the mixer-ejector nozzle to ideally expand as a convergent-divergent nozzle. The ejector doors are contoured internally to simulate each stream to fully expand to exit ambient pressure. The variable engine cycle flow balance requires a variable throat area third-stream from transonic to supersonic cruise. Thus an additional restriction imposed on the third stream by requiring an actuation system to significantly vary the third stream exit area as required.

During the iterative process, a baseline conventional cycle, the 3-stream engine cycle with and without ejector open at take-off with fixed and variable throats were studied. The aerodynamic performance was also compared while improvements in installed drag characteristics for inlet and ejector nozzle and other changes were incorporated. The optimization activity continued over several months as it required an integration between RRLW and LM to optimize engine propulsion system to N+2 aircraft mission requirements. Generally, the engine cycle with ejector on the NPSS took longer to converge and required close monitoring, especially at off design points. At take-off operations, the cycle was optimized to a minimum cruise SFC and a minimum inlet diameter. The optimization process continued after each feed back from LM on the operation of the data back with N+2 aircraft mission study.

Final data package for the N+2 engine was finalized and delivered to LM before the nozzle design activity commenced. Final ejector pumping or entrainment using the third-stream was adjusted to a more realistic value of about 0.6. The final ejector performance was validated using a simple 1-D ejector analysis flow predictions, and then confirmed by a more accurate three-dimensional CFD analysis.

Figure 4 provides a summary of all cycle engine optimization runs completed on the fixed engine, the variable engine, an optimum variable engine and the optimum engines with ejector. Each point represents an engine with varying parameters but responding to an average exit velocity (1-D Analysis) as a function of engine fan inlet diameter. As may be noted, the engine diameter generally decreased by as much as 10% with variable cycle engine outperforming a fixed engine. Due to slow convergence of ejector model developed for the NPSS cycle, only limited solutions were evaluated, and on the

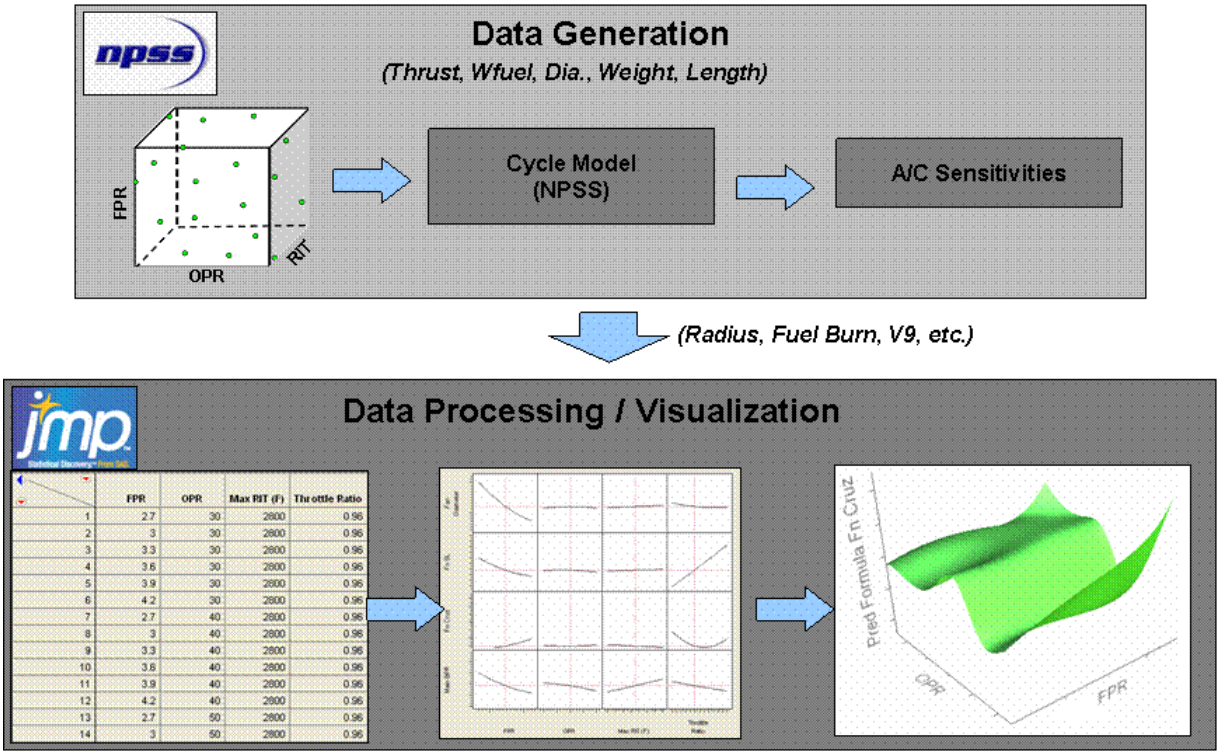

Figure 3 Parametric Study process

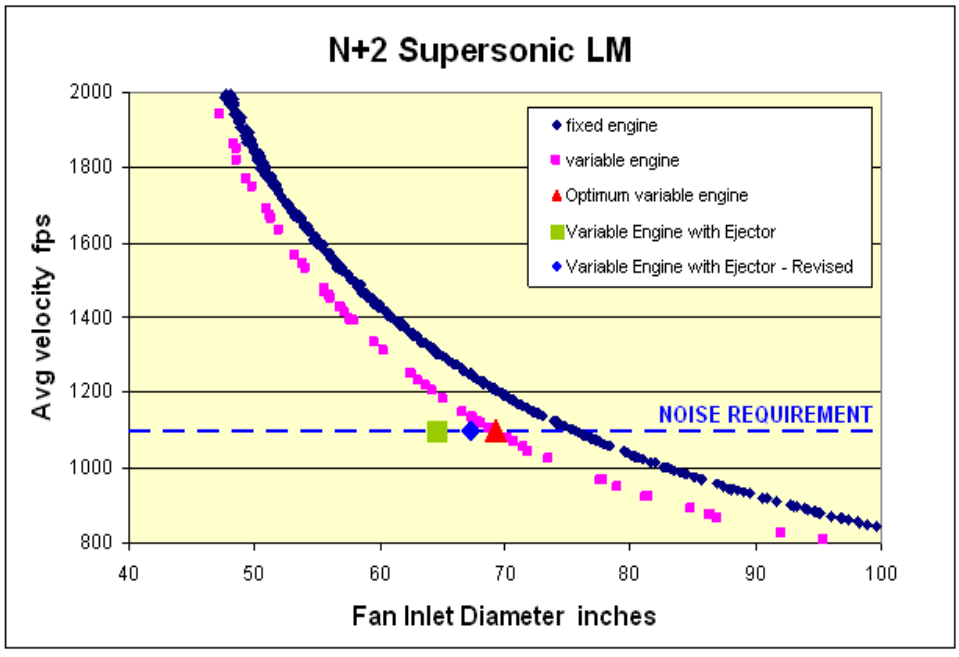

Figure 4 Engine Model Dimensions

average the engine size (fan diameter) was reduced by 3 to 4 inches. Additional opening of nozzle ejector doors may provide additional thrust augmentation and engine size can be reduced. At the noise requirement of 1100 ft per second, the engine inlet approaches 65.6 to 67.2 inches depending upon ejector efficiency.

Additional proprietary information on engine parameters, dimensions, weights and comparisons are tabulated in Appendix A, along with details of nozzle design, key enabling features for nozzle acoustical suppression.

3.3 Noise Predictions

Meeting FAA noise limits during take-off and approach is currently a large obstacle prohibiting supersonic commercial aircraft certification. Variable engine cycle technology on the Lockheed Martin N+2 supersonic business jet is one solution which may provide the high bypass ratio required for low noise take-off, while also allowing supersonic cruise at a low bypass ratio.

Therefore, community noise levels are an important aspect of the N+2 supersonic validations program, with a goal of achieving Stage 4 – 10. Early predictions of engine noise were made using VN02, a proprietary Rolls-Royce noise prediction program which considers all engine noise sources. The program is based on empirical correlations to a large database of test data. As the engine design matures, advanced methods for predicting engine noise estimates are critical to success. Additionally, the airframe noise will influence final EPNL margins, and should be considered in the future.

Preliminary Engine Noise Predictions:

Predictions were made during in the first half of the contract, and the results were reported in QR2. A brief review of the noise model and the results follows.

Jet Noise Source

One major source of uncertainty was the effect of the third stream on jet noise; no previous test bed noise data existed for three stream nozzles. To perform the noise prediction, the model considered the sum of the bypass and third stream mass flow rates and assumed a fully mixed flow. This assumption allowed VN02 to correlate the jet conditions to an existing database and calculate the noise levels. The jet cycle conditions analyzed in the prediction program are presented in Table 2 below. The “Representative Fan” is derived from the conditions in the bypass stream (Mixer-Cold) and the third stream, including entrained flow from the ejector stream. The jet noise correlations did not account for the directivity effect of an elliptical nozzle or for any acoustic effect of the installed ejector.

Table 2 Predicted Engine Cycle Conditions

Flow Rate [lbm/sec]	Sideline	Cutback	Approach
Mixer Hot	144.8	119.4	76.0
Mixer Cold	613.7	548.1	407.9
3rdStream+Free Air	297.0	240.2	30.0
Representative Fan	910.7	788.3	437.9
Pt [psia]			
Mixer Hot	22.84	20.21	17.09
Mixer Cold	22.99	20.66	17.63
3rd Stream+Free Air	18.57	17.90	17.17
Representative Fan	21.55	19.82	17.60
Tt [R]			
Mixer Hot	1562.6	1430.6	1228.9
Mixer Cold	637.7	614.7	582.9
3rd Stream+Free Air	602.6	596.1	581.2
Representative Fan	626.2	609.0	582.8
Isentropic Vel. [ft/sec]			
Core	1542.5	1295.4	826.1
Representative Bypass	922.6	822.5	615.2
Fully Mixed	1007.6	884.7	646.4

Turbomachinery Noise Sources

In addition to the jet noise predictions of the fan, the combustor, and the LP turbine were considered in the engine noise prediction. Under the scope of the project, some uncertainty in the turbomachinery detailed design was unavoidable. However, based on the engine performance cycles at the noise assessment points, preliminary models of these engine noise sources were developed.

Detailed fan design was out of scope for the engine preliminary design, so the noise generated from the two-stage fan is a source of uncertainty. A simplified fan noise source was modeled by scaling existing LibertyWorks fan noise models. The gap to chord ratio of the 2nd stage fan was set to 0.5 to reduce influence of acoustic interaction effects. Additionally, an inlet liner and a “representative” bypass liner were modeled to help attenuate fan noise. The effect of lined co-annular flow (treatment on both third stream and bypass ducts) on fan noise was not considered.

A noise model for the LP turbine was included in the prediction, using preliminary design tools to estimate the aerodynamic effects which drive turbine noise. Blade and vane counts were set to reduce the number of high frequency tones which propagate into the free field.

Trajectory

Lockheed Martin provided take-off and approach trajectories which were used to predict flyover EPNL at the acoustic assessment points, as described in Figure 5 below.

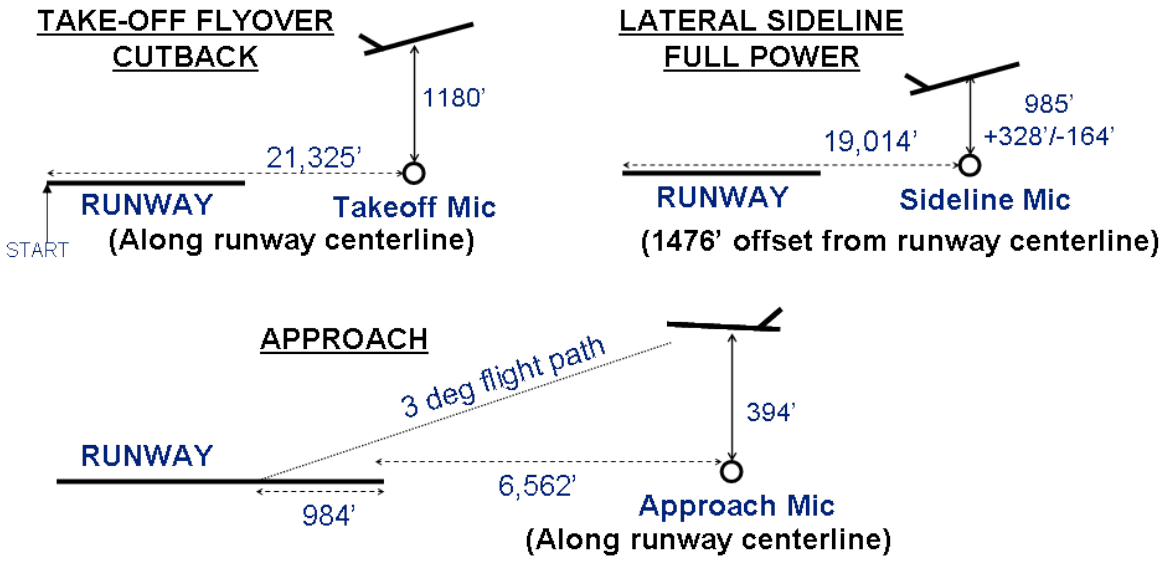

Figure 5 N+2 Trajectory Operating Conditions for Noise Predictions

Regarding engine power requirements along the trajectory, it is important to note that according to FAR36 Appendix B36.7 (b)-Stage 3.

> "For the purpose of determining the lateral noise level, the reference flight path must be calculated using full takeoff power throughout the test run without a reduction in thrust or power."

For Stage 4 noise certification, an aircraft with 4 engines must maintain full thrust until reaching an altitude of 689 feet, and this number increases to 853 feet for a 3 nacelle configuration. The take-off thrust schedule for the N+2 trajectory, calls for a reduction to 90% throttle once aircraft reaches an altitude of 35 feet for obstacle clearance. Under current federal regulations, this feature will require special approval from the FAA. Sideline (lateral) noise predictions were made at 90% throttle, and it can be assumed that the EPNL margin would significantly decrease if the engine was operating at 100%.

Predicted engine-only EPNL margins are listed in Table 3 below.

Table 3 Predicted engine-only EPNL margins

Measurement Point	Stage 3 Limit [dB EPNL]	Predicted [dB EPNL]	Margin [dB]
Sideline	**99.6**	**93.4**	**6.2**
Take-Off	**101**	**95.1**	**5.9**
Approach	**103**	**96.9**	**6.2**
		Stage 3 Margin	**18.3**
		Stage 4 Margin	**8.3**

Based on the predicted margin of Stage 4 – 8.3 dB, the N+2 goal of Stage 4-10 dB is feasible. However, considerable uncertainty exists due to some of the assumptions in the model as described in the previous paragraphs. Additionally, the inclusion of airframe noise from flaps and landing gear will reduce margin, particularly at approach.

Results from three stream jet noise testing performed at NASA Glenn Research Center in April and May of 2011 will provide the dataset needed to update jet noise correlation capability and reduce uncertainty in the noise prediction. Additional follow on activities to reduce uncertainty in noise prediction include a detailed design study of a 2-stage fan for low noise, and trajectory optimization studies to reduce cumulative EPNL margin.

4. Aerodynamic Design of Mixer-Ejector Nozzle

The current N+2 Mixer-Ejector nozzle design is derived from a number of propulsion and noise suppression technology programs at Rolls-Royce such as QSST, QSP with Lockheed-Martin and SSBJ with Gulf-stream Aircraft. The movable petals or doors around nozzle throat are based on the evolution of the Concorde nozzle design which provided variations in primary nozzle area. These “ejector doors” are used to entrain the ambient air during low speed operations and provide thrust augmentation, while they provide an efficient CD nozzle for supersonic operation. Ejector doors can double as thrust reverser during landing, and may be used at other alternative settings at such as high subsonic and transonic regimes if desired.

Earlier mixer-ejector nozzles for supersonic business jet (SSBJ) were based on Rolls-Royce Highly Variable Cycle (HVC) with variable area mixer ejector nozzle (Figure 6). Original designs tested in 2003, were modified to specific program design objectives to provide improvement in performance and acoustics. A generic version of this design and test hardware was delivered to NASA in 2009 (Reference 1) and was tested as HVC10 by NASA at HFJER (AAPL) model testing rig as shown in Figure 7.

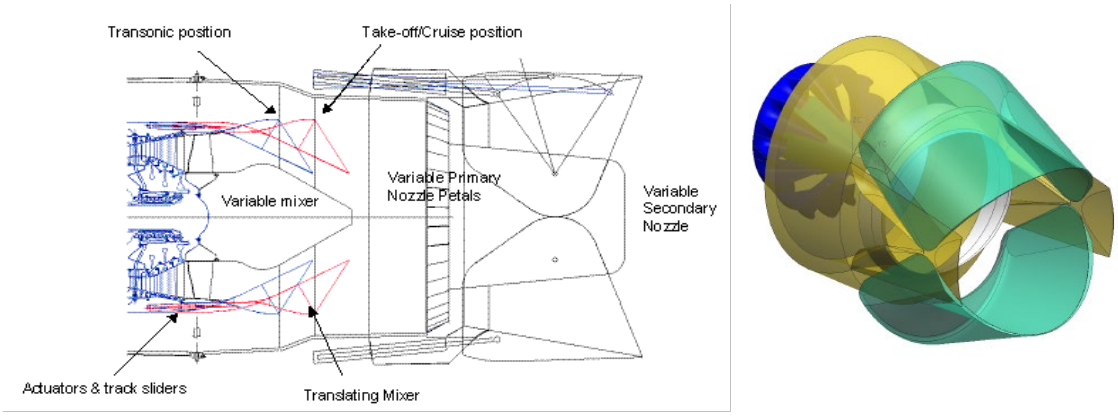

Figure 6 Rolls-Royce Highly Variable Cycle (HVC) Mixer-Ejector Nozzle

More stringent noise requirements for N+2 Supersonic Propulsion required the lower average exhaust velocities and therefore, lower operating pressure ratios for core, and bypass streams. The engine bypass ratio was increased while keeping the operating fan pressure ratio low to achieve low noise targets. The divergent area of the C-D nozzle was also modified to avoid flow separation as the flows mix before plume exit. However, the main nozzle with fixed throat area improved feasibility for a lighter-weight nozzle with more circular cross-section. But the advanced new variable cycle turbofan engines engine cycle required a separate annular fan third stream, and it must be used

efficiently to maintain superior thrust performance. Thus, the N+2 Mixer-Ejector nozzle became an opportunity to drive ejector to augment thrust as well as reduce jet noise.

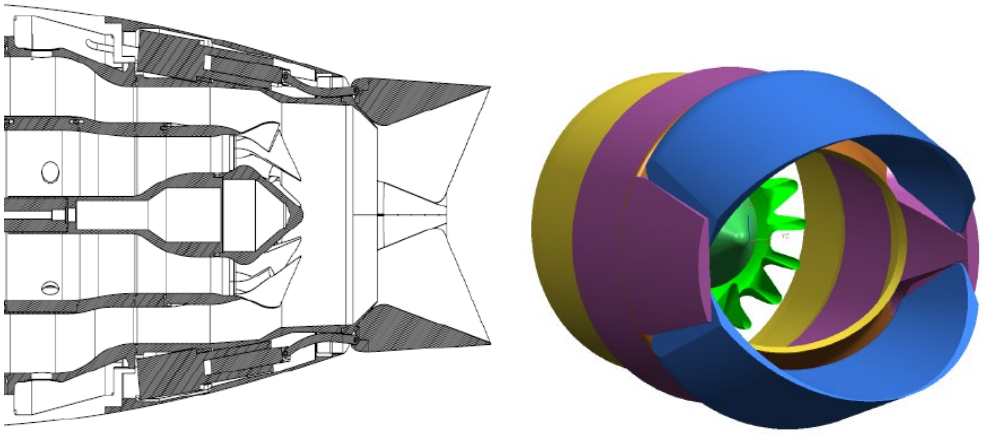

Figure 7 HVC10 Mixer-Ejector Nozzle Design

The final version of the Mixer-ejector nozzle, discussed here, represents a new three-stream exhaust system that will be investigated for acoustical benefits while meeting other super-sonic mission performance goals. The N+2 Mixer-Ejector nozzle utilizes a 16 lobed mixer configuration from previous mixer-ejector nozzles including HVC10 (Figure 6-7) but has significantly different geometry and operating conditions. Appendix A provides proprietary design information on the evolution process for the mixer-ejector nozzle concept, and additional CFD analysis results. Initially, 2D-CFD results were used to evaluate trends followed by 3D CFD analysis was conducted in steps, to down select desired geometrical features of the nozzle configuration. Final nozzle design flow path was selected after a limited amount of CFD to fit the program cost and schedule.

4.1 Reynolds Averaged Viscous Flow Analysis (RANS)

The modeling of the nozzle configurations was conducted using Siemens CAD NX6 system (Formerly UG) which modeled configuration as a 90 degree sector to take advantage of nozzle symmetry. Each flow configuration was then meshed for finite-difference CFD grid using ICEM unstructured grid generation code. Flow grid generation involved a tetrahedral volume, boundary layer regions with prisms and additional grid refinements for plume boundaries. The complex flow geometry was simplified further to smooth out minor features, too fine thicknesses and cavities, thus to keep overall grid size reasonable for CFD analysis. The CFD analysis conducted was based on LW experience and employed ANSYS Fluent Version 6.3 with density based formulation and a rationalized k-e turbulence model. The flow analysis solved a set of 3-D Viscous, Turbulent, Reynolds Averaged, Navier-Stokes' Equations. A computational based modeling design and analysis methodology was employed to obtain flow solutions or characteristics (as illustrated in Figure 8).Initial concept development studies were conducted using a two-dimensional (or axi-symmetic) flow analysis to understand and

establish geometrical variables required for cruise, transonic and take-off performance conditions. The ejector doors are in “closed” stowed position for supersonic cruse operation but must be opened to entrain ambient flow for take-off. The required several nozzle flow-path design iterations for include area variations, and accommodations to a realistic actuator mechanism. The nozzle design near nozzle throat and divergent sections was changed several times using 3D (UG) modeling tools to achieve reasonable design at all three design conditions. The final three nozzle design also required additional area variations to perform as anticipated.

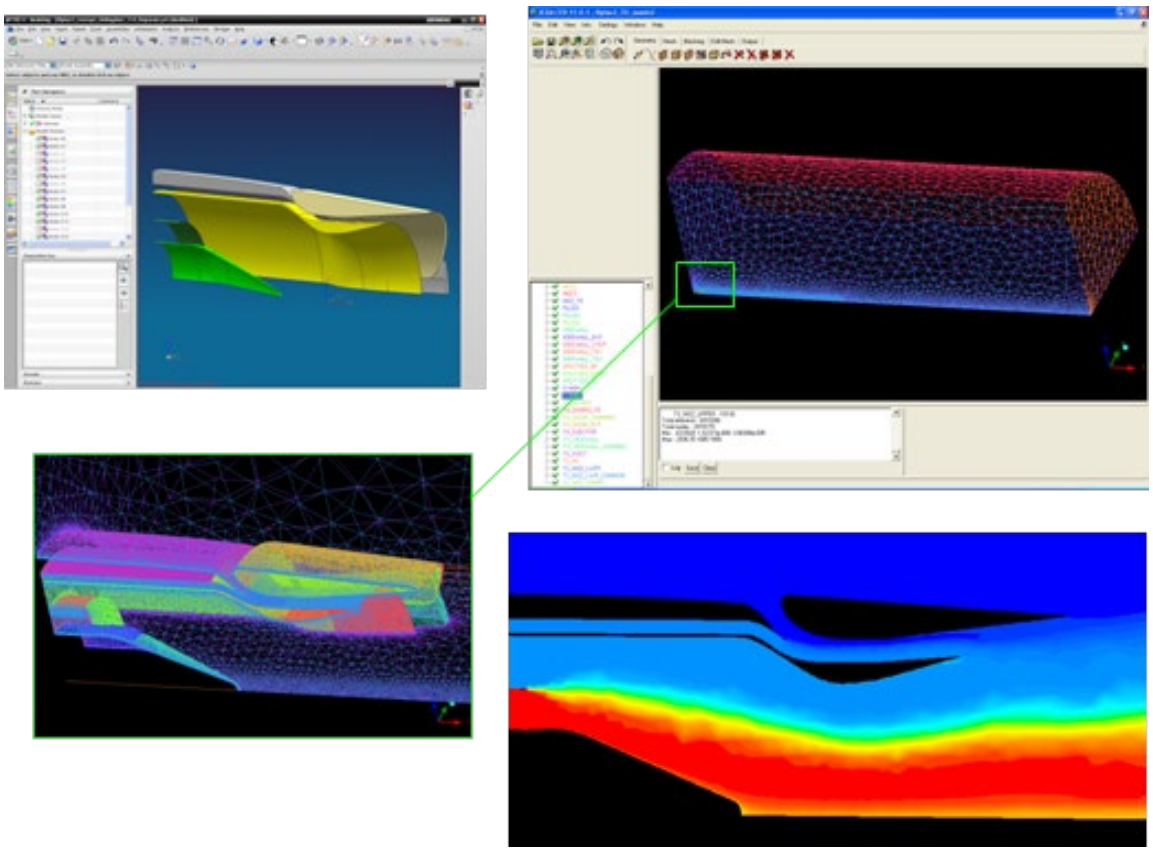

Figure 8 CFD Based Analysis and Design System

As the design concepts developed, 3-D CFD analyses were conducted at both M=1.6 Cruise, and 0.3M take-off to make sure that design improvements are indicated at both conditions. As take-off configuration is dominated by acoustical performance, it was essential to look at local Mach numbers and velocities. The levels of generation and dissipation of turbulent plays a significant part in keeping low noise levels. Even with improved CFD flow resolution, the acoustical tones and screeches cannot be predicted by type of RANS CFD analysis; therefore, general guidelines to avoid flow separation, vortex generation and shedding were applied. An aerodynamically efficient configuration is usually considered a good place to start, keeping low Mach numbers through nozzle

throat areas, low turbulence kinetic energy levels in the exhaust plume and eliminate turbulent wakes caused by local nozzle features.

4.2 Flow Analysis at Take-Off Configuration

The CFD results of the final mixer-ejector geometry (Configuration 7) are presented here. Figure 9 shows calculated static pressure distributions for full scale nozzle at take-off settings. Nominal ejector door opening of 9.5 degrees and the divergent flap set at 10 degrees provided adequate pumping levels closed to expectations. With the TO free-stream flow at 0.3M, the exit plume Mach numbers remained subsonic (M ~0.90) along 0 and 90 degree cuts without any unsteady effects (Figure 10). The temperature mixing (see Figure 11) downstream of the cut-back lobe mixer was targeted at 70%. Peak temperatures near the nozzle throat were well below 860ºR, a value which eliminated hot spots and allows lighter weight material for the mixer-ejector nozzle design. The mean turbulent kinetic energy (tke) levels in the plume showed increase near the side walls of the nozzle due to higher shear, but these values remained below 1000 m2/s2. The turbulent kinetic energy peaked at a station one diameter down stream of the nozzle exit indicating slower dissipation in the wake. Overall, the CFD predictions indicate a significant improvement over previous ejector-mixer nozzle designs.

The CFD analysis was used to study and reduce high velocity or choked regions within the nozzle flow path, in the ejector door cavities, and areas where the flow streams interacted with each other. This goal was achieved in the final the final mixer-ejector design. CFD analysis was also conducted at lower power “sideline” point and in general results were similar to full power case but with lower Mach numbers. These details are Rolls-Royce proprietary and presented in the Appendix A.

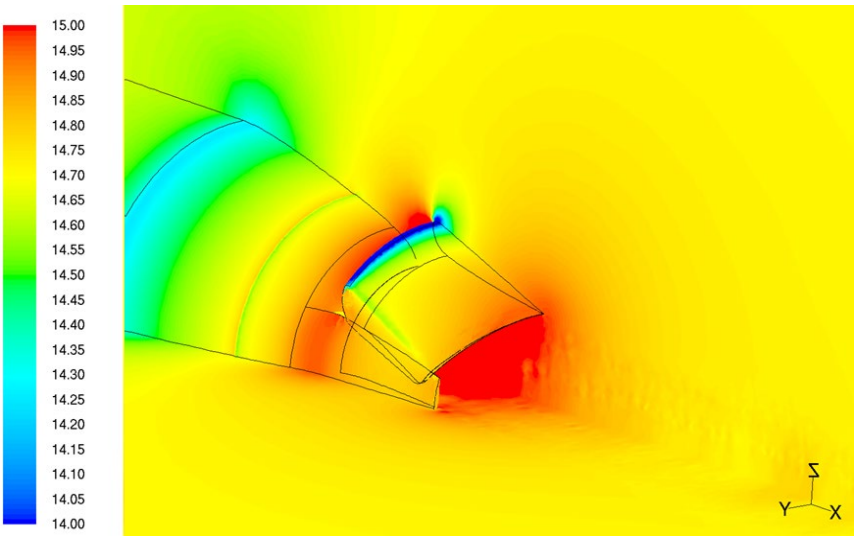

Figure 9 Static pressure distribution for N+2 ejector nozzle at TO, M = 0.3(fs)

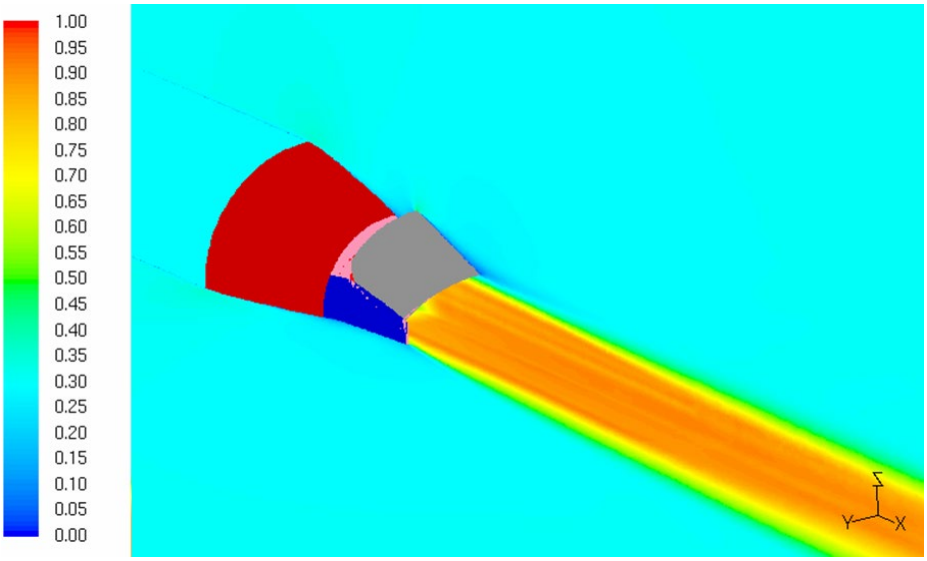

Figure 10 N+2 Mixer-ejector plume Mach numbers at TO, M=0.3(fs)

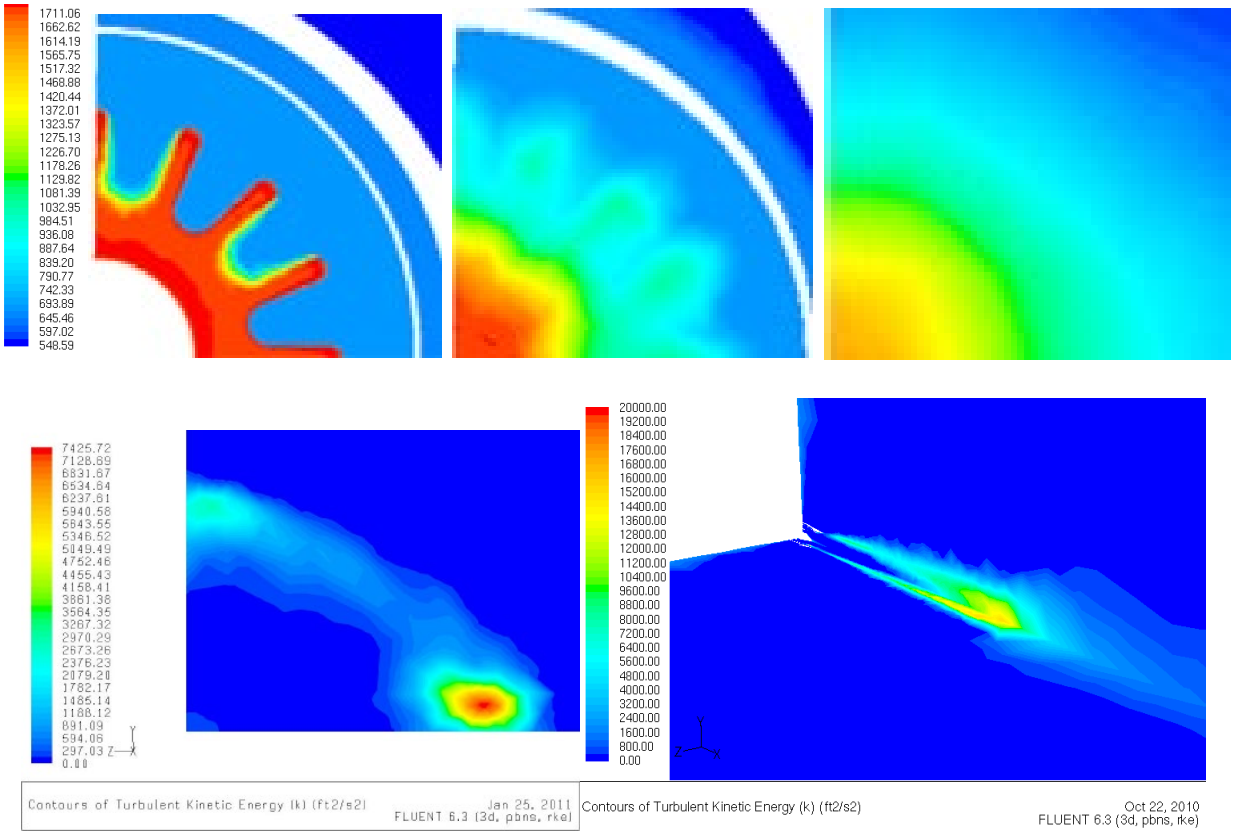

Figure 11 N+2 Mixer-ejector plume axial Cuts, at TO, 0.3M; total temperatures at stations 3, 10 & 14 (top); Turbulence ke values at station14 and an axial cut are also shown (bottom)

Flow path lines were studied and indicated minor separation regions inside the nozzle passages; however, it did not create any wakes in the exit plume region. The leading edge of the divergent flap (DF) was modified and its impact was evaluated by an additional CFD analysis conducted for the 0.15 scale nozzle model design. The nozzle flow path had to be modified to accommodate very thin trailing edges and the simulation of the manual actuation hardware brackets near the nozzle throat area. These CFD results are also included in Appendix A and indicate that the nozzle performance had gotten slightly worse due to lower ejector flow and higher internal Mach numbers especially in third stream flow. The turbulence kinetic energy levels had doubled in value compared to full scale CFD calculations and the flow around the DF brackets indicated flow vortices not noted before. CFD modeling was clearly did not represent the local geometry details. By this time, the nozzle design and model fabrication by ASE FluiDyne was already completed to allow any last minute improvements to the design.

4.3 Flow Analysis at Cruise Configuration

The analysis at Supersonic Cruise was conducted initially using an axi-symmetric nozzle configuration to understand the full expansion characteristics of the convergent – divergent nozzle. A couple of design iterations were completed to set up required flow areas to simulate the cruise operation of the engine. This provided initial geometry required for the ejector doors both internal contours and the external boat tail angle of 4.6º, consistent with N+2 low drag propulsion requirements.

Figure 12 shows that the exit plume is relatively parallel, nearly axi-symmetric and efficient as implied by total pressure contours, as the shocks generated by ejector doors and trailing edges are isentropic. Additional data is presented in Appendix A. Predicted Nozzle Cruise Thrust and mass flows matched the desired propulsion requirements within 1% of the cycle values.

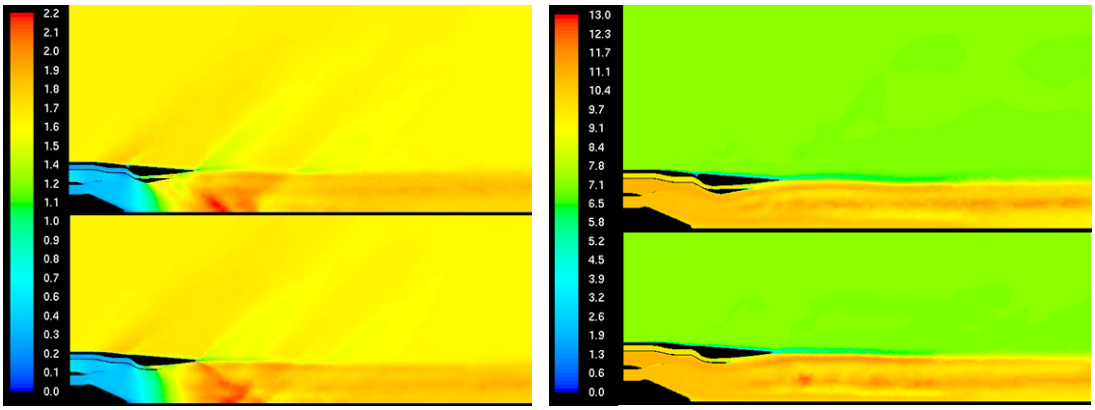

Figure 12 N+2 Mixer-ejector nozzle with Mach numbers and total pressures at Cruise, along 0º and 90º axial cuts, M = 1.6, altitude= 50,000 ft.

4.4 Reference Nozzle Design

The reference nozzle was designed to provide a nozzle configuration for comparing acoustical performance of the mixer ejector nozzle. Two reference configurations were designed; one with the lobed mixer used in the mixer-ejector nozzle and the other used an annular splitter mixer. This designed was verified using CFD analysis to make sure the core splitter nozzle has adequate “clean” mixing with the annular fan flow. Third stream flow is annular and represents propulsion cycle flows scaled from corresponding mixer ejector nozzle. Results of CFD analysis are shown below in Figure 13-15.

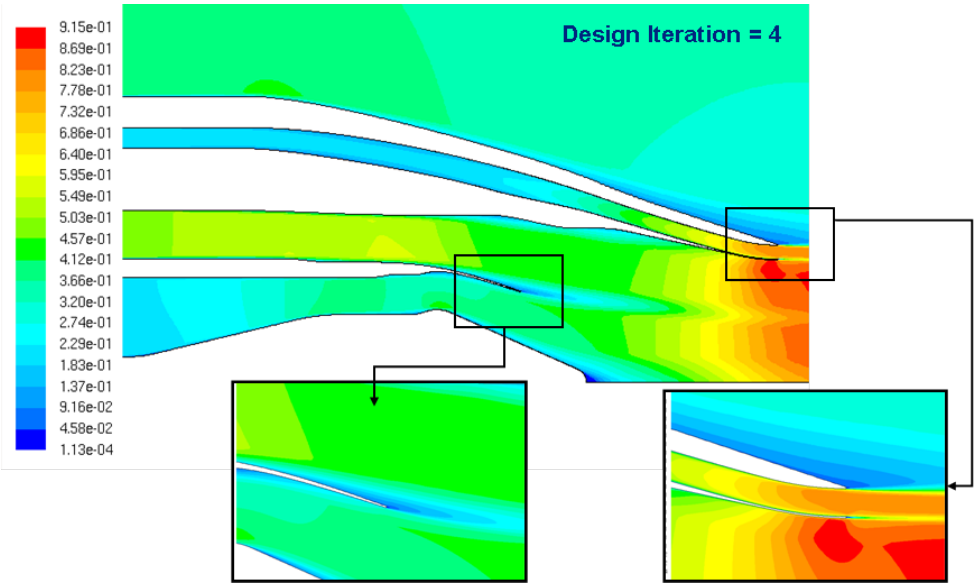

Figure 13 N+2 Reference nozzle Mach number distributions, axial cuts, TO, 0.3M

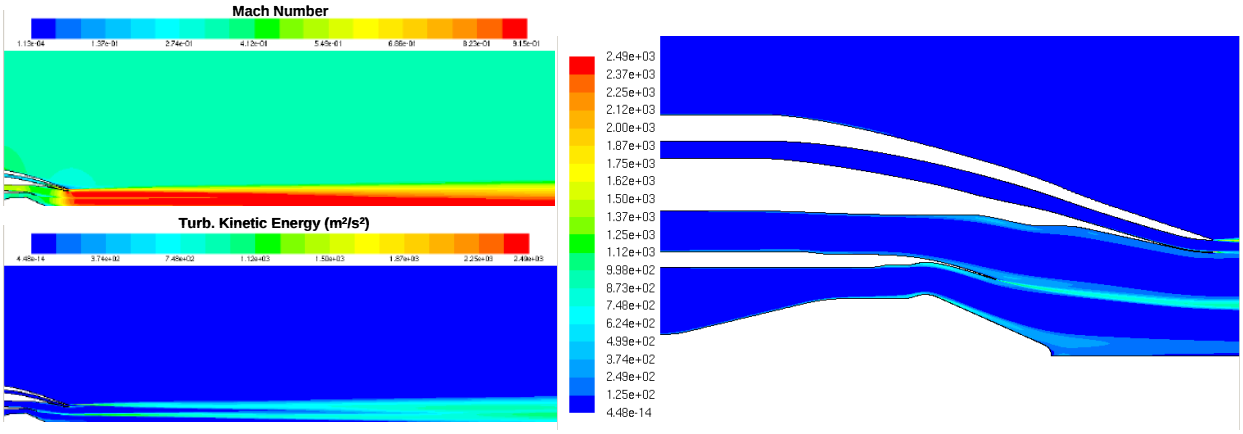

Figure 14 Reference nozzle plume Mach numbers (Max =0.91) and Turbulence kinetic energy tke (Max= 800m2/s2), TO, 0.3M

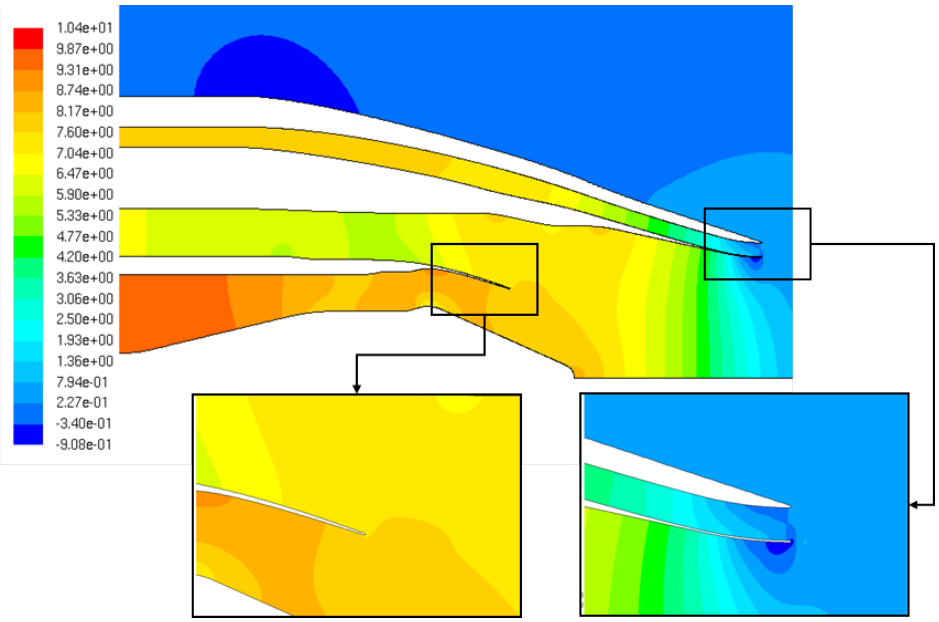

Figure 15 Reference nozzle static pressure distributions, axial cuts, TO, 0.3 M

5. Mechanical design: N+2 Mixer-Ejector Nozzle

5.1 Model Design and Analysis

The mechanical design and analysis of the scale model was presented by the model vendor ASE FluiDyne during final Rig Review in February 2011. The model geometry is configured to fit on to the NASA Glen Nozzle Acoustic Test Rig (NATR) for acoustic evaluation and has a scale factor of ~ 0.15 to keep same mixer hardware as was used during HVC10 program and fit N+2 exhaust nozzle. Nozzle Configuration is of high bypass-ratio of 5+ and is configured with a 16 lobed internal mixer which mixes the core and bypass flows before exhausting through the variable area throat. Downstream of the nozzle throat is a pair of “Concorde style” buckets or ejector doors (ED) form the divergent cuff of the nozzle and provide the correct expansion of the flow. Additional nozzle geometrical features are provided to allow area variability and nozzle expansion under check at all operating conditions. Appendix B provides design details, stress analysis, and required set of model drawings.

To meet the basic requirements of the model test nozzle, LW provided ASE with documents and data as summarized below.

· Safe operation – comply with the factors of safety requirements for NASA Facility per “Aero-Acoustic Propulsion Laboratory - Nozzle Acoustic Test Rig User Manual,” by R.H. Soeder and S. P. Wnuk ,GRC, Ohio, and R.A. Loew , Sierra Lobo, Inc., Ohio, NASA TM 2006-212939, Nov 2006.

· Operational range of exhaust test conditions from the proposed engine cycle and from the desired test matrix. Surface pressure and temperature loads on model surfaces ere obtained from CFD analysis at key design points
· Manual actuation scheme required to control nozzle throat areas and engine flows
· Required design variability range for ejector door settings, nozzle geometric throat and Exit station areas
· Easy handling of model changes - light-weight construction
· Test Conditions: Temperature < 1400°F, Pressure < 50 psi
· Design and manufacture in accordance with R-R quality procedures, DNS87529 Issue 1, “Aero-thermal test vehicle mechanical and instrumentation specification”.

5.2 Model Hardware and Configurations

To meet the requirement of operating at engine exhaust conditions the model has been manufactured primarily from stainless steel. Non-pressure containing parts that are only exposed to low ambient conditions flow are manufactured other Steel alloys and also aluminum. FEA and Joint analysis was conducted for all new parts, while axial lengths accounted for estimated thermal growth in mixer and plug. Based on Material Properties of the model hardware used are shown in Figure 16, model met structural requirements at most severe pressure and thermal loads (Appendix B).

To avoid any major changes to the NATR rig facility, the rig-model interface was chosen to be the plane just down stream of the item termed, “Charging Station Fan”. The model geometry is designed to allow manual assembly of various model test configurations on the test rig. All Model design drawings have been provided separately as required by NASA SOW and Contract.

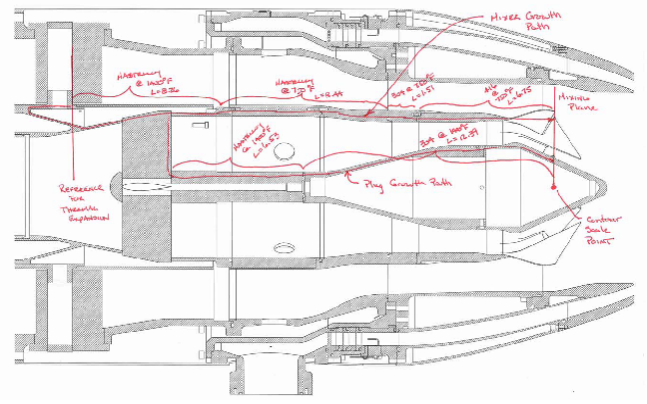

Material Properties
Room Temperature

Material	Tensile Strength	Yield Strength	Allowable Stress
15-5 PH Stainless Steel Condition H925	190,000	174,800	38000
15-5 PH Stainless Steel Condition H1025	170,000	165,000	34000
416 Stainless Steel Annealed	75,000	40,000	13333
304 Stainless Steel	85,000	38,000	12667
6061-T6 Aluminum	45,000	40,000	9000
7075-T6 Aluminum	83,000	73,000	16600

Figure 16 Structural materials and thermal growth

6. Acoustical Test Plan

The purpose of the current test is to determine the far field acoustical radiation of the ejector nozzle as a function of various nozzle parameters as well as nozzle orientation relative to the microphone plane (model clocking angle). Data may be used in updating nozzle design, and developing an optimum configuration. In addition, data base may be generated to support jet noise predictions for a variable cycle Propulsion System.

6.1 Test Objectives

Testing is designed to address the following objectives:

1. Understand and document the impact of nozzle on Far-field noise spectral directivity, EPNL and narrowband spectral content.
2. Understand the impact of observation plane on the acoustic radiation of the Ejector Nozzle
3. Document and optimize the noise source distribution generated by the ejector nozzle
4. Understand and document the impact of ejector flow-field on the ejector and the exhaust nozzle performance
5. Document ejector nozzle performance nozzle with surface static pressures and flow measurements.
6. Validate prediction tools -turbulent velocity and turbulence kinetic energy field to support development of acoustic 3-stream noise model.

6.2 Facility and Test Interface

The tests will be conducted at NASA Glenn Research Center, in their Aero Acoustic Propulsion Laboratory (AAPL), which is housed in a 65 foot radius anechoic geodesic hemispherical dome. Acoustic wedges cover the walls of the dome and approximately half of the floor area. AAPL is acoustically cleaned for all acoustic test runs using acoustic wedges on the front and microphone sides of all rigs and on the facility floor. No untreated objects can be within 40 feet and within view of N+2 exhaust nozzle. Ambient temperature, pressure, and relative humidity will be recorded within the dome.

Nozzle Aero-acoustic Test Rig (NATR) is contained within Aero-Acoustic Propulsion Laboratory (AAPL) provides the required airflows for the test article and a flight flow simulation capability. The NATR supply duct work is acoustically lined on both inside and outside, and consists of an annular ejector system connected to a plenum, followed by a long radius transition section to a low beta Venturi ASME nozzle. This flow exits through a second nozzle of 53 inch diameter and forms a free jet to simulate the effects of forward flight on the test article. Centerline of the free jet is located 10 feet above the floor and simulates free-stream Mach numbers in the jet up to 0.35. Acoustically treated wall separates NATR from the section of the dome building without acoustic treatment on the floor, preventing unwanted reflections from untreated floor and adjacent test rigs.

At the downstream end of the NATR is the High Flow Jet Exit Rig (HFJER) which has been modified for three flow stream flow capability. The heated air is delivered from NASA facility which supplies compressed air system to the test article via dual or triple flow streams as required. The modified flow rig is shown in Figure 17 along with three charging station instrumentation for each stream.

The nozzle test model (with adapter) attaches to the core stream charging station as shown in Figure 18. The fan stream and the outer third stream can also be heated as specified or may be operated at conditions matching those of the free jet. However, due to facility limitations, the fan and the third stream may have same temperature. Four rakes are installed in each stream to measure total pressures and temperatures to indicated setting conditions. Similarly, the free-stream pressure measurement using three rakes may be used to set the free-stream Mach number.

Ambient conditions may be recorded on the facility ESCORT computer. Relative humidity and temperature may be recorded both at 10' above the floor near the NATR and at the top-most region of the overhead microphone array, located roughly 60' above the floor. Ambient pressure is recorded as well.

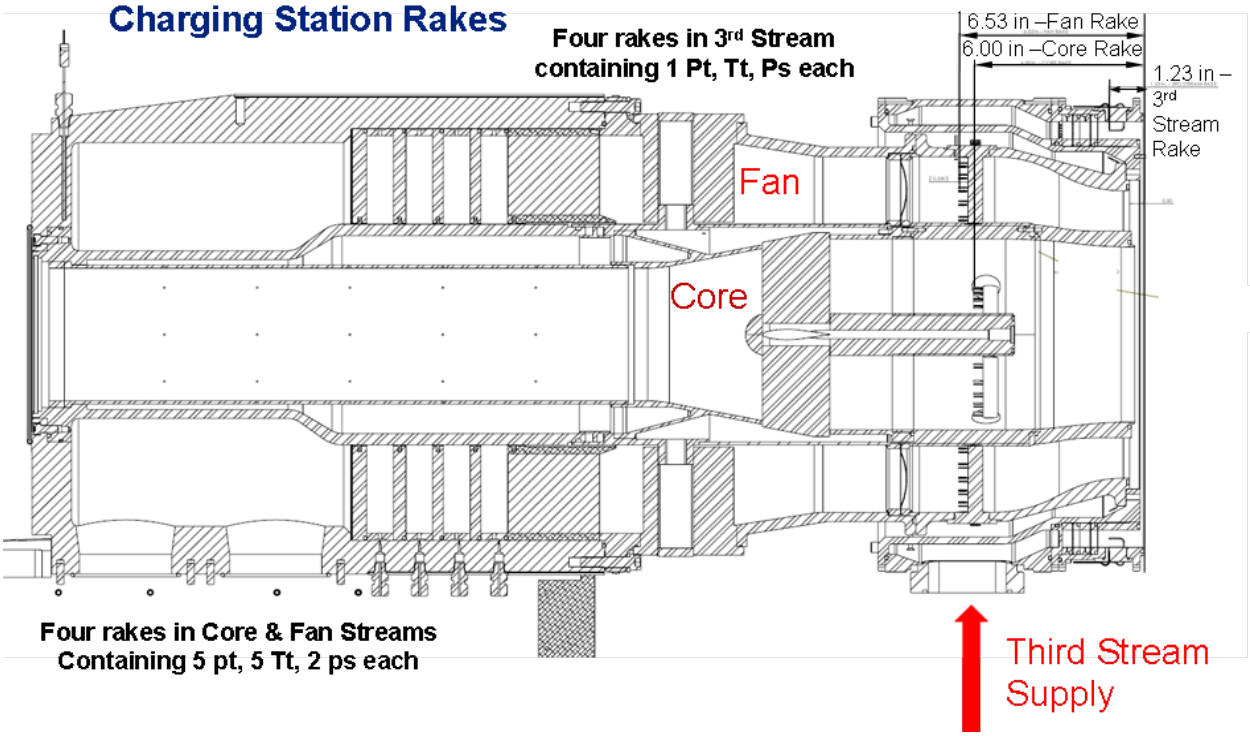

Figure 17 Modified HFJER Test Rig

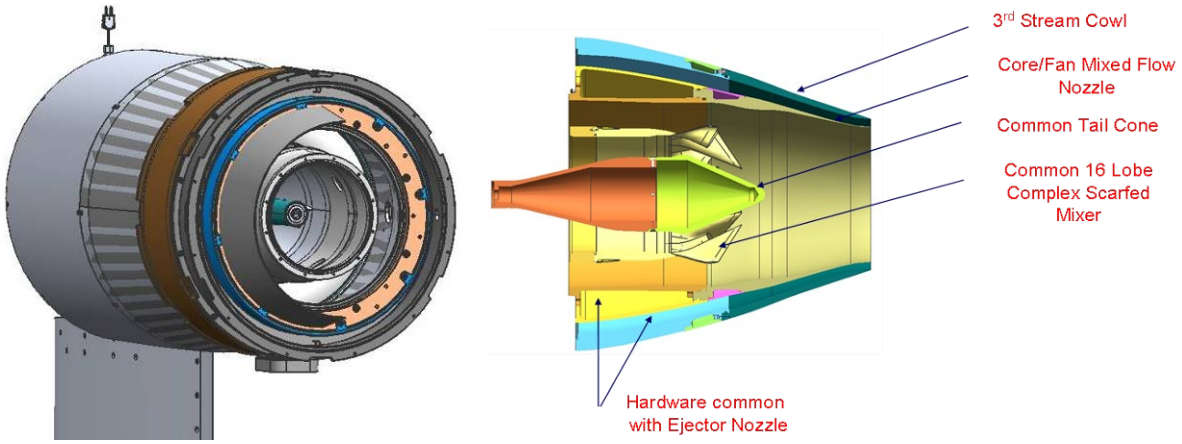

Figure 18 Modified HFJER (left) and N+2 Reference nozzle (right)

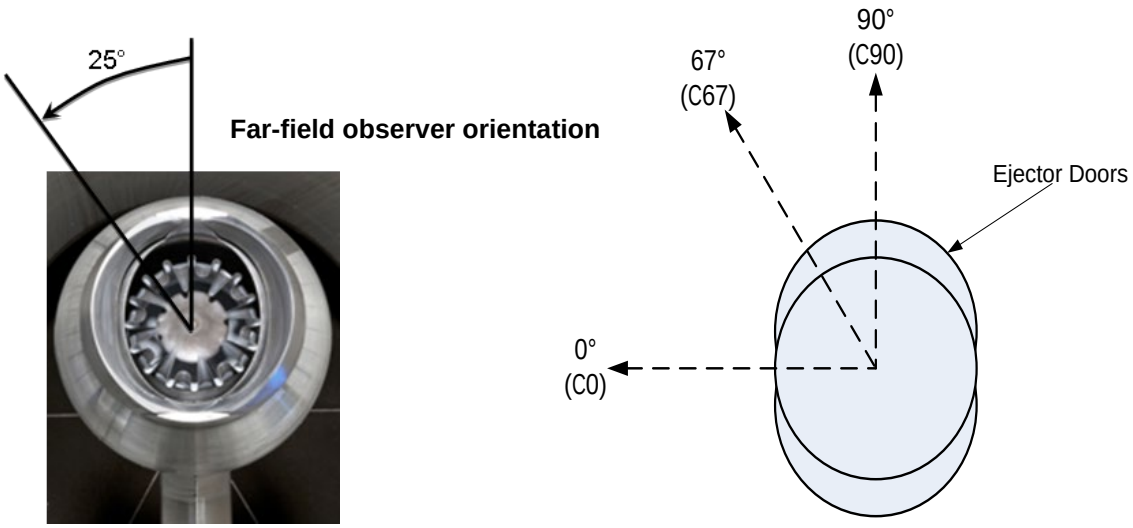

Figure 19 Far-field observer orientations: clocking positions for Ejector nozzle tests (ESCORT configuration names – C67, C90, C0).

6.3 Test Matrix and Procedures

Table 4 below lists nozzle configurations with various parametric variations for testing the ejector nozzle to determine an optimized position that corresponds to the lowest acoustical radiation signature. The Reference nozzle shown in Figure 18 (configuration on right) will be tested to compare acoustical performance with pre-test predictions. Baseline mixer-ejector nozzle (ENBL) with ED at 9.5º, DF at 10º and the third stream throat area set by two 0.075” thick spacer inserts (L10241-603) is shown in Appendix A. The nominal clocking position for conducting most of the testing is the “Sideline” setting as indicated in Figure 19 with ejector doors in vertical position and microphones arrays at ~23º from vertical or 67º form horizontal position of HFJER rig position as shown.

ESCORT uses C67 identification for the sideline setting and other positions to limited testing include C0 and C90 as indicated above which requires the nozzle rotation so that ejector doors are in line or normal to the microphone array respectively. Steps and gaps on model external surfaces are covered using aluminum tape or an RTV tape.

Table 4 Ejector nozzle parametric configuration matrix

Ejector Door Angle Settings		Set 3rd Stream Throat Area		Divergent Flap Angle setting	Comments/ Special settings	Clocking Position	Configuration
ID	Spacer	ID	deg	ID		ID	Nozzle ID
ED9.5	2	SP2	10	DF10	Nominal/baseline	C67	ENBL
ED9.5	2	SP2	10	DF10	Modified Cavity	C67	ENB1
ED9.5	2	SP2	10	DF10	TE Modification	C67	ENB2
ED9.5	2	SP2	10	DF10	Cleaned Baseline	C67	ENC
ED7.5 ED11 ED15 ED5 ED12.5	2	SP2	10	DF10	-Study effect of ejector door set -Limit only 4 ED Positions to vary	C67	ENC-D10/ E7.5 etc.
ED5-ED15	2	SP2	8	DF8	Only 4 selected ejector positions	C67	ENC-D8 /E….
ED5-ED15	2	SP2	12	DF12	Repeated as above	C67	ENC-D12 /E….
ED5-ED15	2	SP2	9 11	DF9/ DF11	DF9 or DF11 infer from test data	C67	ENC-D9 /E…. or ENC-D11/E…
ED5-ED15	1(-10%)	SP1	TBD	DF10/9/11	3rd Stream Area - best DF position	C67	ENC-D10/E… /S1
ED5-ED15	1(-10%)	SP1	TBD	DF---	3rd Stream Area – alt. DF Setting	C67	ENC-D…/E… /S1
ED5-ED15	0(-20%)	SP0	TBD	DF10/ 9/11	3rd Stream area – best DF position	C67	ENC-D10/E… /S0
ED---	2	SP2	TBD	DF--	Optimized Configuration	C67	ENCO
ED--	2	SP2	TBD	DF--	Flyover Clocking	C90	ENCO-C90
ED--	2	SP2	TBD	DF--	Pitch Axis	C0	ENCO-C0
ED--	2	SP2	TBD	DF--			
ED0	2	SP2	0.0	DF0	Closed position, test if needed	C0	Cruise

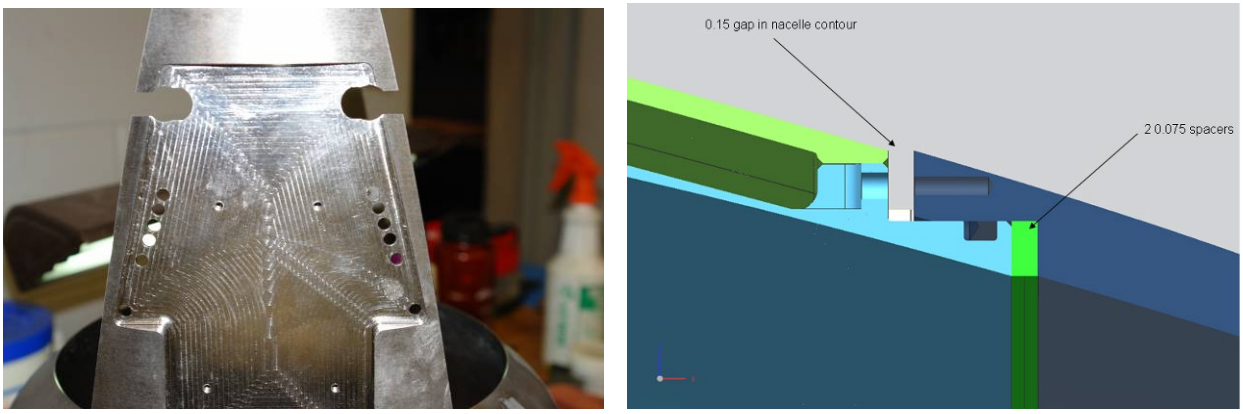

a b

Figure 20 Model details: side wall (a) -undercover plate with Pin holes to set ejector doors; Secondary nozzle split joint (b) - 2-third stream Spacers used to vary throat area

Figure 20 explains the changes required to set up the ejector doors positions using Pull pin and location for third stream spacer settings. Two reference nozzle configurations shown were designed and are compared in Figure 21.

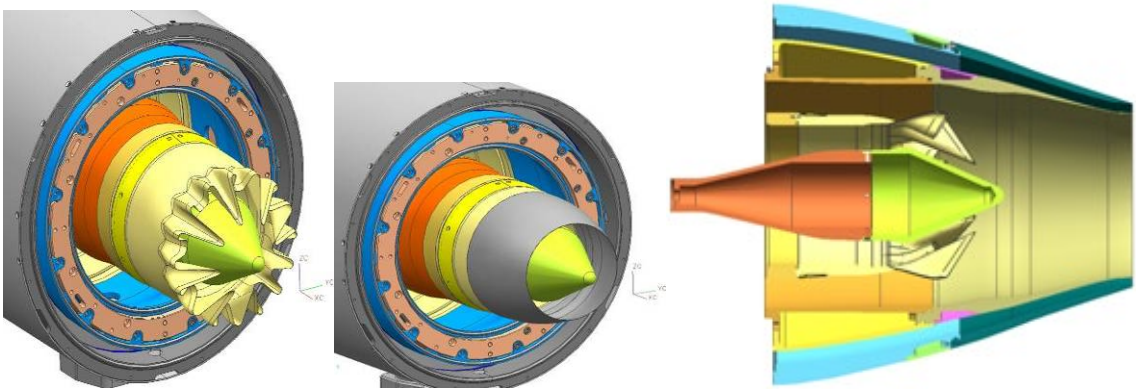

Figure 21 Reference Nozzles: PRFN (mixer Core), and SPFN (splitter core) – both nozzles have same external annular cowls (shown on right)

Test procedures followed the test objectives in chronological order. Pressure and Temperature ratios are set (unique as set points) using the area weighted averaged total pressures and temperatures from the charging station measurements, expanded to ambient conditions.

Initial runs were conducted to establish baseline ejector nozzle performance levels and “fixing” or “Covering” model related steps, gaps, cavities, trailing edge thicknesses and other mechanical features. This was done over four (4) runs to isolated noted changes and help establish ENBC configuration (Table 4), proceed with parametric optimization. A reduced matrix (Table 5), recommended by NASA was used to save test time during this phase of testing. It should be noted that each day, prior to a test configuration, the

background noise levels at the simulated free-stream mach numbers, is assessed and used in the acoustical calculations.

Table 5 Preliminary reduced set point matrix

GRC	NPRc	NPRb	NPRt	NTRc	NTRb	FJ Mach #	Ejector	Divergent Flap	Spacers	DataMAX	ESCORT
Setpoint				TTc/Tamb	TTf/Tamb		Deg	Deg	#		D021
003	1.72	1.71	1.57	3.2	1.27	0.30	9.5	10	2		
002	1.720	1.710	1.570	3.200	1.270	0.20	9.5	10	2		
032	1.600	1.600	1.450	3.200	1.250	0.20	9.5	10	2		
062	1.450	1.450	1.350	3.000	1.250	0.20	9.5	10	2		
061	1.450	1.450	1.350	3.000	1.250	0.10	9.5	10	2		

Once the final cleaned configuration was determined, a 9 set-point matrix list below (Table 6) will be used to conduct most acoustical tests. The parameters were studied in order by studying one parameter at a time. These include the ejector door angles (ED), divergent settings (DF), third stream throat areas (by replacing spacers) SP, clocking angles(C), and free-stream Mach. Again, for saving testing time, only a limited number of parameters were evaluated than originally planned. A typical Configuration list for each model set up test series is shown below.

Parametric Optimization Configurations:
Nozzle Configuration: Ejector Nozzle - ENC (Baseline, See Table 4)
Clocking Position: C67
Free-Stream Mach = 0.30
Ejector Door Positions: ED9.5, ED7.5, ED12.5, ED15, DF11, DF5
Divergent Flap Angles: DF10, DF8, DF12, DF9 or DF11
Spacer Settings: SP2 (2 Splitters), SP1 (1 splitter) and SP0 (no splitter)

Table 6 Ejector nozzle optimization test conditions matrix

Set Point	NPR,core Pt/Pamb	NPR,bp Pt/Pamb	NPR,3d Pt/Pamb	TR,core Tt/Tamb	TR,bp/3d Tt/Tamb	Notes
00	1.72	1.71	1.57	3.3	1.27	TO design
01	1.70	1.70	1.55	3.2	1.25	PR Map
02	1.65	1.65	1.50	3.2	1.25	“
03	1.60	1.60	1.45	3.2	1.25	“
04	1.55	1.55	1.40	3.0	1.25	“
06	1.45	1.45	1.35	3.0	1.20	“
08	1.35	1.35	1.30	2.8	1.20	“
10	1.61	1.62	1.31	3.0	1.20	Sideline
11	1.43	1.46	1.27	2.7	1.15	Cutback

For best ejector and divergent flap angles determined from the optimization test, the following selection of the set points given in Table 7 is used. The acoustic data may be repeated at two free-stream Mach numbers. The test article is cleaned by sealing cavities and smoothing of TE thickness and other beneficial features should be implemented based on objective. This extended test matrix was also employed for conducting testing reference configurations.

Table 7 Ejector nozzle full expanded test conditions matrix

Set Point	NPR,core Pt/Pamb	NPR,bp Pt/Pamb	NPR,3d Pt/Pamb	TR,core Tt/Tamb	TR,bp/3d Tt/Tamb	Notes
01	1.70	1.70	1.55	3.2	1.25	PR Map
02	1.65	1.65	1.50	3.2	1.25	"
03	1.60	1.60	1.45	3.2	1.25	"
05	1.50	1.50	1.40	3.2	1.25	"
07	1.40	1.40	1.35	3.0	1.25	"
09	1.30	1.30	1.30	2.8	1.20	"
10	1.61	1.62	1.31	3.0	1.20	Sideline
11	1.43	1.46	1.27	2.7	1.15	Cutback
12	1.70	1.60	1.50	3.2	1.25	Ptb/Ptc
13	1.60	1.70	1.50	3.2	1.25	variation
14	1.40	1.50	1.45	2.8	1.15	"
15	1.50	1.40	1.35	2.8	1.15	"
16	1.40	1.30	1.30	2.8	1.15	"
17	1.70	1.75	1.55	3.2	1.25	Max 1
18	1.75	1.80	1.55	3.2	1.25	Max 2

6.4 Instrumentation

Static pressure taps are located in the fan duct, ejector, (fan) nozzles, and sidewalls (attachment location for the ejector doors) and on the divergent flaps. The pressure taps are shown in Figure 22 and these locations of the fan duct pressure taps are shown in Tables 8-11 with coordinates, tap identifications, reference nozzle part, and angle (circumferential) location. The axial position X and circumferential position θ (degree) are defined in sketch shown. The estimated circumferential location of pressure taps in is indicated for ease in identification. Tables list the pressure taps that are separated to reflect the associated flow stream such as the primary stream – a mix of core and fan streams, the annular third stream, and the pressure scrubbed by ejector free-stream.

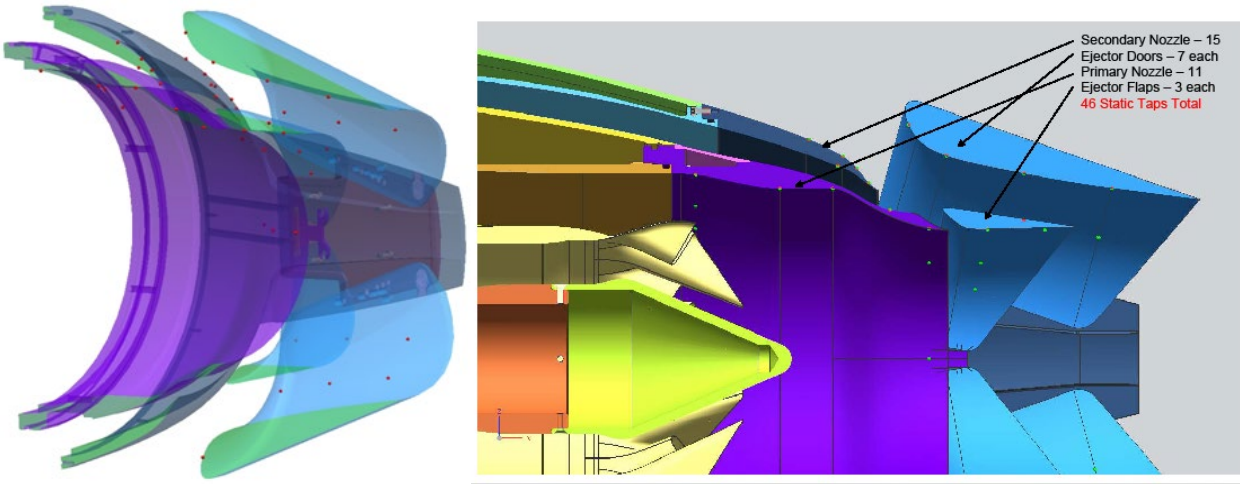

Figure 22 Ejector nozzle (patent peding) surface pressure instrumentation.

Table 8 Internal fan duct pressure taps

Pressure Tap	X (in)	Y(in)	Z(in)	Theta Location	Nozzle Part	Nozzle Description/ Remarks
PFD1	-6.6603	0.0000	4.9828	0 deg	L10241-002	Pri Nozzle -Fan duct
PFD2	-4.4496	0.0000	4.6130	0 deg	L10241-002	Pri Nozzle -Fan duct
PFD3	-3.0433	0.0000	4.6130	0 deg	L10241-002	Pri Nozzle -Fan duct
PFD4	-6.6603	3.5234	3.5234	45 deg	L10241-002	Pri Nozzle -Fan duct
PFD5	-6.6603	2.7683	4.1431	33.75 deg	L10241-002	Pri Nozzle -Fan duct
PFD6	-0.5000	0.0000	3.5258	0 deg	L10241-002	Primary nozzle -inner
PFD7	-0.5000	2.5984	2.5984	45 deg	L10241-002	Primary nozzle -inner
PFD8	-0.5000	3.8347	0.0000	90 deg	L10241-002	Primary nozzle -inner
DFI9	1.0488	0.0000	3.4924	0 deg	L10241-403	div flap-inner
DFI10	2.5488	0.0000	3.4793	0 deg	L10241-403	div flap-inner
DFI11	0.8572	2.5909	2.5909	45 deg	L10241-403	div flap-inner
DFI12	0.7054	3.2507	1.8768	60 deg	L10241-403	div flap-inner

Table 8 Internal Fan duct Pressures are greater than ambient depending upon the pressure ratios. Maximum Pressure 30 psia

Table 9 Outer fan duct third (third) stream pressure taps

Pressure Tap	X (in)	Y(in)	Z(in)	Theta Location	Nozzle Part	Nozzle Description/ Remarks
P3S13	-2.9050	0.0000	5.2154	0 deg	L10241-003	Sec Nozzle-3rd Stream
P3S14	-2.9050	3.6878	3.6878	45 deg	L10241-003	Sec Nozzle-3rd Stream
P3S15	-2.9050	5.2154	0.0000	90 deg	L10241-003	Sec Nozzle-3rd Stream
P3S16	-1.5338	0.0000	4.0336	0 deg	L10241-002	Pri Nozzle - outer
P3S17	-1.5338	2.8522	2.8522	45 deg	L10241-002	Pri Nozzle - outer
P3S18	-1.5338	4.0336	0.0000	90 deg	L10241-002	Pri Nozzle - outer
P3S19	1.8264	2.6998	2.6998	45 deg	L10241-403	div flap - outer
P3S20	2.0023	0.0000	3.7579	0 deg	L10241-403	div flap - outer

Table 9 Internal third stream duct Pressures are greater than ambient depending upon the pressure ratios. Maximum Pressure ~ 25 psia.

Table 10 Top Ejector door LE and inner door pressure taps

Pressure Tap	X (in)	Y(in)	Z(in)	Theta Location	Nozzle Part	Nozzle Description/ Remarks
PED21	-1.0463	0.0000	6.3349	0 deg	L10241-004	top eject door
PED22	-0.0420	0.0000	5.4935	0 deg	L10241-004	top eject door
PED23	2.0023	0.0000	5.0108	0 deg	L10241-004	top eject door
PED24	4.3225	0.0000	4.6186	0 deg	L10241-004	top eject door
PED25	-0.5477	3.6060	3.6060	45 deg	L10241-004	top eject door
PED26	1.6943	3.4103	3.4103	45 deg	L10241-004	top eject door
PED27	3.9646	3.2830	3.2830	45 deg	L10241-004	top eject door
PED28	-0.2797	2.6595	-4.6064	150 deg	L10241-004	bot eject door
PED29	4.1602	2.3170	-4.0132	150 deg	L10241-004	bot eject door
PED30	1.7738	2.4699	-4.2781	150 deg	L10241-004	bot eject door
PED31	-0.6509	3.8384	-3.2208	120 deg	L10241-004	bot eject door
PED32	1.4530	3.6727	-3.0818	120 deg	L10241-004	bot eject door
PED33	3.8851	3.5590	-2.9864	120 deg	L10241-004	bot eject door
PED34	-1.0463	0.0000	-6.3349	0 deg	L10241-004	bot eject door

Table 10 Ejector Stream Pressures may be below ambient. Maximum Pressure ~15 psia

Table 11 Ejector passage and cowl pressure taps

Pressure Tap	X (in)	Y(in)	Z(in)	Theta Location	Nozzle Part	Nozzle Description/ Remarks
PEP35	-2.4056	2.5766	4.4628	30 deg	L10241-003	Sec Nozzle - ejec pssg
PEP36	-2.0893	2.3830	4.1274	30 deg	L10241-003	Sec Nozzle - ejec pssg
PEP37	-2.7823	2.7409	4.7475	30 deg	L10241-003	Sec Nozzle - ejec pssg
PEP38	-3.6726	2.9687	5.1420	30 deg	L10241-003	Sec Nozzle - ejec pssg
PEP39	-3.6726	0.0000	5.9374	0 deg	L10241-003	Sec Nozzle - ejec pssg
PEP40	-2.7823	0.0000	5.4819	0 deg	L10241-003	Sec Nozzle - ejec pssg
PEP41	-2.4056	0.0000	5.1531	0 deg	L10241-003	Sec Nozzle - ejec pssg
PEP42	-2.0893	0.0000	4.7659	0 deg	L10241-003	Sec Nozzle - ejec pssg
PEP43	-2.0893	3.3700	3.3700	45 deg	L10241-003	Sec Nozzle - ejec pssg
PEP44	-2.4056	3.6438	3.6438	45 deg	L10241-003	Sec Nozzle - ejec pssg
PEP45	-2.7823	3.8763	3.8763	45 deg	L10241-003	Sec Nozzle - ejec pssg
PEP46	-3.6726	4.1984	4.1984	45 deg	L10241-003	Sec Nozzle - ejec pssg

Table 11 Ejector Stream Pressures may be below ambient. Maximum Pressure 15 psia

The overhead 24-microphone arc array (24U) is employed for the far-field spectral directivity. The 28-microphone sideline array (28L) available in the dome is not required by test. ¼" Pre-amps are used and the array is connected to a Data MAX acquisition computer. RTA personnel will be responsible for operation of far-field acoustic instrumentation with assistance from the AAPL technicians in calibration (Figure 23).

In addition to acoustic data, the data acquisition includes the surface static pressures (46 on various nozzle components), the charging station total and static conditions and raw thrust components data available from the existing load cells. This load cell data is only for reference and will not be processed.

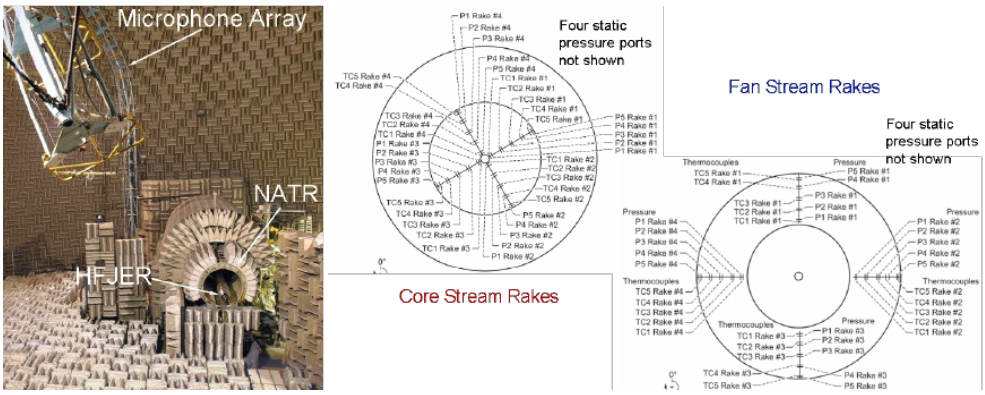

Figure 23 Microphone array and charging station total rake probes

7. Acoustic Test Results

7.1 Test Overview

Noise testing of the mixer-ejector nozzle system was performed at NASA Glenn Research Center form April 20 through May 12 following the test plan as previously discussed. During initial model check-out tests, tone contamination in the narrowband spectrum was discovered. This finding resulted in a test schedule delay as attempts were made to eliminate the tones source in the model. A temporary solution was identified which significantly reduced the tones, but follow-on design work is required to remove the tone-generating mechanism. Additionally, further analysis is required to fully understand the cause of the tones.

Due to the setback during test, a modified test matrix was then implemented to finish the testing by the required deadline. Despite the problems with the model early during the test, preliminary results were promising and configurations with low noise levels were identified. The mixer-ejector nozzle noise levels were referenced to a convergent reference nozzle as describe in the test plan. Additionally the effect of the reference nozzle lobed mixer was compared to a confluent splitter.

It is important to understand that while a nozzle ejector system typically reduces noise levels, the comparisons made here reference a conventional subsonic nozzle to one capable of supersonic flight. The goal of adding the mixer-ejector system is to bring the convergent-divergent nozzle noise levels back down to that of a conventional nozzle during take-off and approach. This ability is aided by the variable cycle of the engine.

The nozzle was tested at numerous configurations adjusting divergent flap angle and ejector door angle for various operating conditions simulating take-off conditions. Summaries of all the measured data for the test campaign are included in Appendix C. The test configurations along with test run identifications are tabulated chronologically in Table 12, with the start and end times of each configuration. Model ENC refers to the ejector nozzle configuration, PRFN refers to the primary reference nozzle with the lobed mixer, and SPFN refers to the splitter reference nozzle (no forced mixer). S refers to the number of spacer rings in the third stream. The “ED” designation refers to the ejector door angle which ranged from 7.5 to 15 degrees, and “DF” refers to the divergent flap angle which ranged from 8 to 12 degrees. “C” refers to the model clocking angle relative to the plane of the far-field microphone array at 0, 67, or 90 degrees. The Run ID start and end refers to the ESCORT identification number which was given to each data point which was acquired and processed. Under the Set Point Notes heading, “Non-std” refers to a non-standard set of set points which were acquired during initial model testing and tone investigations. Additionally, “Opt” refers to the optimization test matrix as described in Table 6, while “Exp” refers to the expanded test matrix as described in Table 7. Only limited test data is presented in this section at

conditions to facilitate the discussion of trends. Additional observations of the third stream throat area and the ejector nozzle azimuthal directivity are discussed.

Table 12 Log of configurations tested on the HFJER at NASA Glenn AAPL

Date	Time Start	Time End	Model	S	ED	DF	C	Run ID Start	Run ID End	Set Point Notes
4/21	10:25	14:55	ENC	S2	E95	DF10	C67	3	12	Non-std
4/22	9:56	11:20	ENC	S2	E95	DF10	C67	14	21	Non-std
4/22	13:10	13:17	ENC	S2	E95	DF10	C67	22	25	Non-std
4/25	9:25	10:31	ENC	S2	E95	DF0	C67	27	33	Non-std
4/25	13:53	14:53	ENC	S2	E95	DF12	C67	34	44	Non-std
4/26	9:40	11:04	ENC	S2	E95	DF12	C67	45	51	Non-std
4/26	12:12	12:33	ENC	S2	E95	DF12	C67	52	54	Non-std
4/26	15:45	16:54	ENC	S2	E95	DF12	C67	57	59	Non-std
4/27	13:35	15:23	ENC	S2	E95	DF8	C67	60	76	Opt
4/27	17:39	18:27	ENC	S2	E95	DF8	C67	77	79	Non-std
4/29	9:49	11:18	ENC	S2	E95	DF8	C67	81	95	Opt
4/29	12:07	13:23	ENC	S2	E125	DF8	C67	96	108	Opt
4/29	13:59	15:10	ENC	S2	E75	DF8	C67	110	123	Opt
4/29	16:26	17:26	ENC	S2	E15	DF8	C67	124	139	Opt
5/3	9:17	10:27	ENC	S2	E15	DF12	C67	140	154	Opt
5/3	11:34	12:37	ENC	S2	E125	DF12	C67	155	168	Opt
5/3	13:06	14:13	ENC	S2	E75	DF12	C67	170	182	Opt
5/3	14:49	16:11	ENC	S2	E95	DF12	C67	183	196	Opt
5/5	9:22	12:55	ENC	S2	E95	DF10	C67	197	229	Exp
5/5	13:33	16:22	ENC	S2	E125	DF10	C67	230	263	Exp
5/5	17:53	19:25	ENC	S2	E75	DF10	C67	264	281	Exp
5/6	10:35	12:03	ENC	S1	E75	DF10	C67	282	297	Opt
5/6	12:40	13:52	ENC	S1	E125	DF10	C67	298	314	Opt
5/6	14:31	16:00	ENC	S0	E125	DF10	C67	315	330	Opt
5/6	16:50	17:56	ENC	S0	E75	DF10	C67	331	344	Opt
5/9	11:12	12:35	ENC	S2	E75	DF10	C0	345	360	Opt
5/9	13:04	14:23	ENC	S2	E125	DF10	C0	361	377	Opt
5/10	9:22	10:30	ENC	S2	E75	DF10	C90	379	395	Opt
5/10	11:06	12:06	ENC	S2	E125	DF10	C90	396	410	Opt
5/11	9:44	13:09	PRFN	NA	NA	NA	NA	413	452	Exp
5/12	9:15	12:35	SPFN	NA	NA	NA	NA	453	490	Exp

7.2 Test Results

Data processing

The test data generated in the NASA Glenn AAPL facility was delivered as 1' polar, lossless, narrowband power spectral densities. The spectral density levels were obtained from 0 to 100 kHz in 12 Hz increments and at polar angles from 45 to160 degrees in 5 degree increments.

Additional processing to the data was performed for comparison to the preliminary aircraft noise predictions. To scale the noise data to full scale, the model scale factor of 0.1483 was applied to the data which shifted the data to lower frequencies and moved the source levels out to a 6.7' polar radius. Given the 12 Hz band width of the narrow band data, the spectral density level was converted to sound pressure level. Additionally, the data was synthesized into 1/3 octave bands from 50-10 kHz. This synthesis introduces some uncertainty when compared to data processed by standard 1/3 octave band filter sets due to the filter roll-off at the band limit frequencies.

However, this processing allowed the EPNL predictions to be made using a flyover simulation program and using the trajectories supplied for the initial predictions. Processing uncertainty with this method is +/- 1.5 EPNdB relative to those predictions, however, due to tone contamination and synthesis effects. However, since all the data was processed exactly the same way, the relative noise level comparisons can be made to investigate trends and find optimal configurations for low noise take-off.

Investigation of model-generated tones

First runs of the mixer-ejector model on test stand resulted in strong tones in the 6 to 11 kHz range, which was unacceptable due to the large increase in high frequency noise levels which resulted. Appling the model scale factor, full-scale frequencies would put tones in 900-1600 Hz range and would be severely penalized in the EPNL calculation, resulting in very little margin to Stage 4 requirements. Figure 24 shows the comparison of source noise levels of the first run with the baseline nozzle at 4 polar angles. Tone strength at some angles is in excess of 25 dB over the reference.

The investigation of the tone contamination issue followed the timeline shown below in Table 13. A series of modifications were made to the model to find the source of the tones.

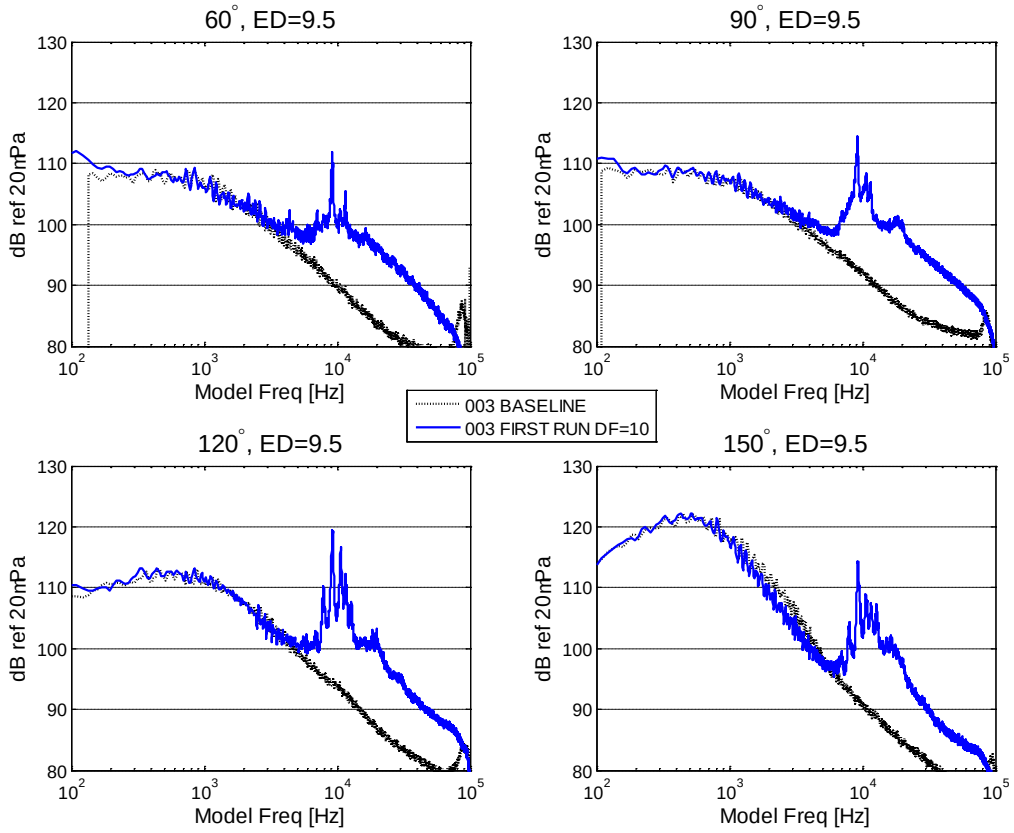

Figure 24 First run of mixer ejector system at set point 003 compared to reference nozzle. Divergent flaps set to 12 degrees, ejector doors set to 9.5 degrees, highlighting the tone contamination problem.

Table 13 Timeline: Actions taken to mitigate tone contamination in model acoustic data.

Date	Model Modification	Result/Observation	Action
21-April	Baseline, first run (DF=12, ED=9.5)	Large tones	Cover ejector door cavities (filled with putty), cover divergent flap hinge hardware
22-April (AM)	Everything covered per previous day action.	Fewer tones, tape came loose and blew out, still tone problem	Cover inside of divergent flap opening with tape
22-April (PM)	Covered divergent flap opening	Tones reduced, but came loose and blew out quickly	Close divergent flap (DF=0)

Date	Model Modification	Result/Observation	Action
25-April (PM)	Fully open flap (DF=12)	Tones still exist, damage noted to covers over cavities	Add Chevrons to divergent flap inlet, cover crescent “slivers” near hinge points with Ni-chrome strips (tack welded)
26-April (AM)	Chevrons and sliver covers applied to DF	Tones reduced but still present	Remove sliver covers
26-April (PM 1)	Chevrons only	Identical results, tones still present	Completely cover outside divergent flap openings with Ni-chrome strips, tape inside again (per 22-April)
26-April (PM 2)	Divergent flap covers applied	Tones are gone	Start with test matrix. Apply heat to fan stream, move flap to DF=8
27-April	DF=8, ED=9.5, test matrix, DF angle set to 8	Putty in ejector cavities blew out due to heat, mess	Clean ‘mess’, proceed with test with out ejector door cavity fill/covers. (tones are caused by divergent flap)

In summary of the efforts made to remove the problematic tones, divergent flap angle appears to have large effect on tone strength and high frequency broadband noise. It was noted that gap covers help reduce tones, and even eliminates tones at some conditions, as shown in Figure 25. The tone strength appeared to be a correlated to the third stream pressure ratio. Tones were not present if third stream pressure ratio was set to unity. Covers did result in a small decrease in bypass flow and small increase in core flow to meet the set point, which implies that some entrainment of flow from the third stream does exist.

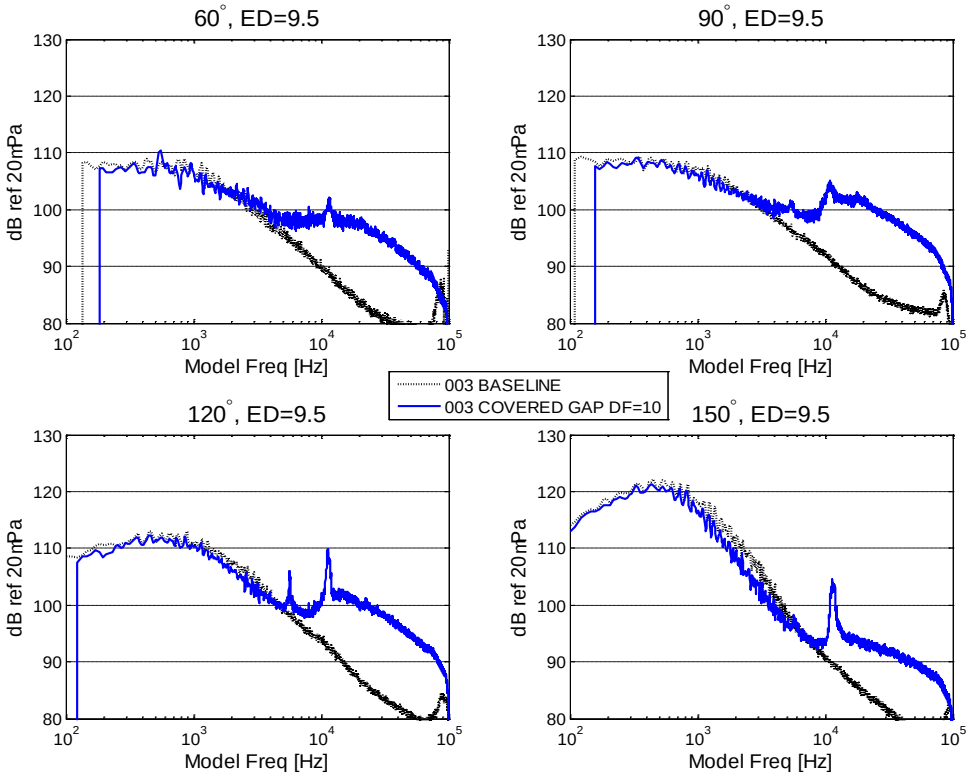

Figure 25 Repeat run of mixer ejector system with covered divergent flap gaps at set point 003 compared to reference nozzle. Divergent flaps set to 10 degrees, ejector doors set to 9.5 degrees, tones significantly reduced compared to Figure 23.

Additional observations during the tone investigation were also noted, but not fully understood as of the time of this report. Tones would appear at harmonic frequency intervals, but the relative strength changed with free-stream stream Mach number. Additionally, tone smearing was observed, where the bandwidth of the tone skirt would increase with the free stream Mach number. The frequency content was also dependent on the divergent flap and ejector door angle setting. Relative tone strength was also dependent on polar emission angle, with largest tones near 120 degrees. Residual tones were strongest at high operating conditions and diminish quickly as third stream pressure ratio decreases.

Residual tones were eliminated at the small divergent flap angle of 8 degrees, but it was noted that even with the covers applied, when the divergent flap moved to larger angles, residual tones existed. It was observed that the tone strength was linked to the third stream pressure ratio, as shown in Figure 26. Set point 103 represented the 90% power level setting for sideline noise conditions.

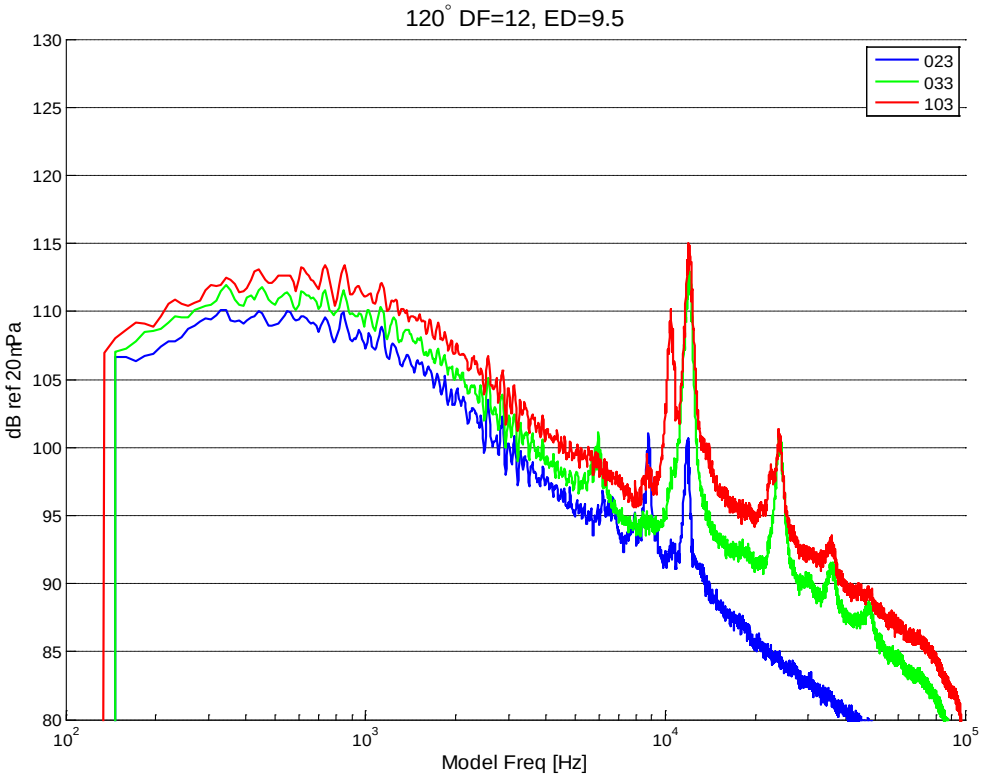

Figure 26 Effect of third stream pressure ratio on residual tone strength

7.3 Ejector Configuration Effect on Noise

For these comparison studies of ejector door angle and divergent flap angle, the spacer setting was set to the design third stream throat area, SP=2. The clocking angle was set to the representative sideline observer angle, or C=67. Any tones present in the data which contributed to the EPNL were penalized in the calculation for this analysis. In other words, no manual additional manipulation of the source spectra, were made. The set point of interest was 103, since that was closest to the conditions used in the preliminary noise predictions.

Two mixer ejector configurations were discovered which offered low noise relative to the reference nozzle noise levels. The divergent flap angle of 12 degrees with an ejector door angle set to 9.5 degrees, and the divergent flap angle of 10 degrees with an ejector door angle set to 12.5 degrees offered the same noise levels, which were slightly greater than the lobed mixer reference nozzle, as show in Figure 27. These mixer-ejector door configurations offered lower noise when compared to the annular reference nozzle with the splitter.

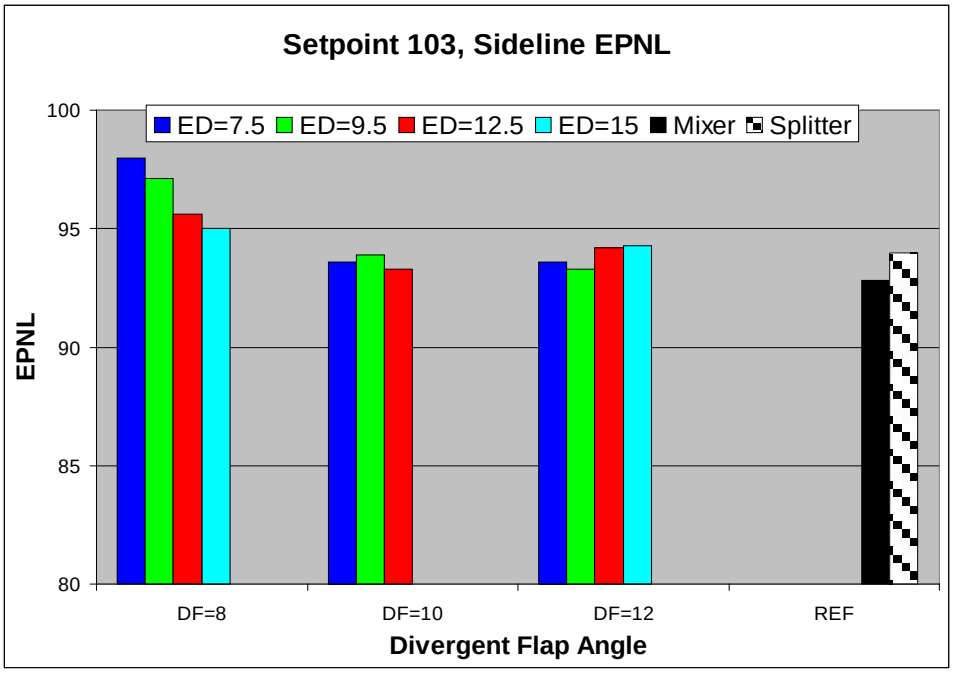

Figure 27 Effect of mixer-ejector configuration on EPNL and comparisons to reference nozzle

Further observations were made at this set point, and are consistent with trends in all the set points which are presented in Appendix C. However, the excessive tone contamination at high power set points may cause some inconsistencies. The largest effect the mixer-ejector system has on the jet noise spectrum is at frequencies greater than 1 kHz. For an 8 degree divergent flap angle, there was a strong trend of noise levels decreasing as ejector door angle opening increased, however this divergent flap angle increased high frequency noise to unacceptable levels compared to the reference nozzle. At the time of this report, the reason for the large noise increase at this divergent flap setting is not fully understood, and more testing would be beneficial to understand the complex flow effects happening in the nozzle.

No tone contamination existed in the 8 degree divergent flap angle setting, but one reason for the much greater EPNL was that the high frequency noise increase existed at forward emission angles and resulted in a longer flyover time duration during the calculation.

For 10 and 12 degree divergent flap angle setting, the effect of ejector door was less dominant, but residual tones existed which were affecting EPNL at some configurations. High frequency noise levels were more similar to reference nozzle, but tone contamination is more of a problem, especially at the 12 degree divergent flap setting. EPNL tone penalty was being applied due to the large source noise level increase at some 1/3 octave bands.

Another important observation is that the reference nozzle jet noise EPNL levels at sideline agree with the preliminary predicted jet noise contribution to the total engine EPNL. Recall the model did not include effects from the ejector doors, divergent flap, or third stream. Since configurations existed which were similar to the reference nozzle, it gives more confidence to the validity of the predictions. However, future predictions will include an updated jet noise model which incorporates the results from this test.

Clocking and third (third) stream throat area effect on noise

The elliptical shape of the mixer-ejector nozzle lends itself to a non-axisymmetric directivity. The azimuthal variation of noise was measured at two additional clocking angles, as described in the test plan for a divergent flap angle setting of 10 degrees only. The result for set point 103 is shown in Figure 28, but the trends are similar for all set points, and are available in Appendix C. As shown, the noise is slightly louder at the C0 location (sidewall hinge plane) and at the C90 location (ejector door midline plane). C0 noise levels were greater than both C67 and C90 measurements for every set point. The physics behind this amplification are not fully understood, but the results are consistent with previous testing of an elliptical ejector nozzle under the HVC program.

Spacer rings in the model allowed for variation of third stream throat area. The lowest noise levels were at a spacer setting of 2, which refers to the largest throat area setting. The divergent flap angle was set to 10 degrees in all of the spacer setting tests. This effect is less dominant than the effect of the ejector door angle setting as indicated in Figure 29. See Appendix C for charts at all set points.

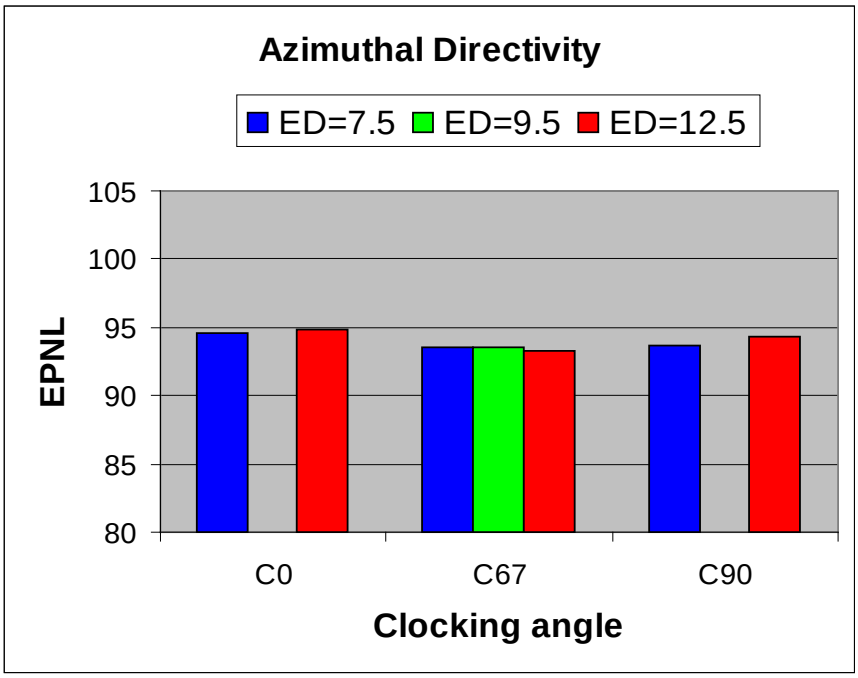

Figure 28 Effect of clocking angle (azimuthal directivity) on calculated EPNL (set point 103), all results at DF=10

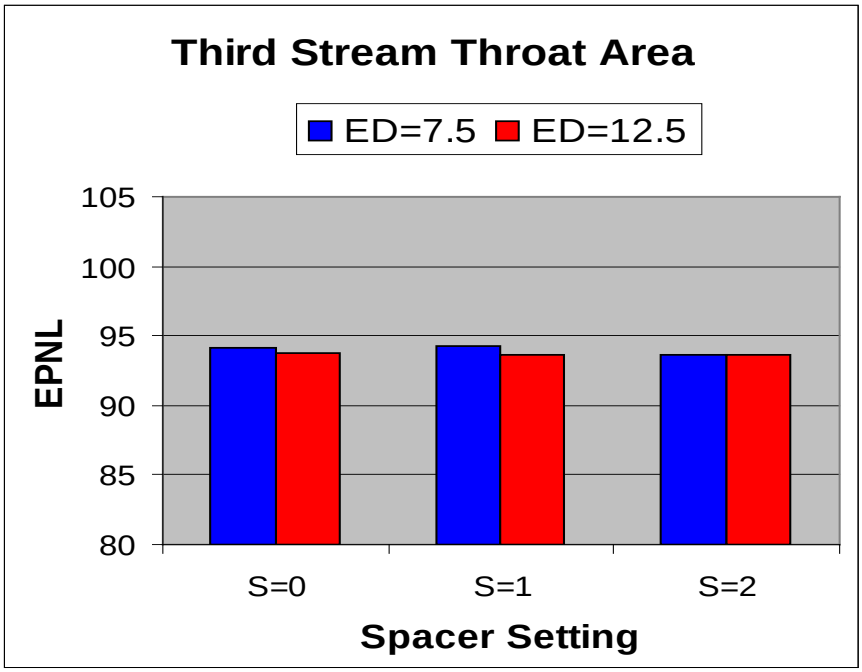

Figure 29 Effect of throat area change (spacers) on EPNL (set point 103), all results at DF=10

Impact of EPNL by model-generated tones

Design changes must be implemented to remove the tone problem with this mixer-ejector system, but this does present an interesting “what-if” scenario. Unfortunately, no automatic tone removal script was readily available to quickly remove the tones from the narrowband results and replace with smoothed jet noise data. To investigate this effect, the noise spectra from one of the optimum low-noise configurations, was manipulated at all angles to remove the tones to observe the effect on EPNL. This was done for two set points, 103 – the current sideline point, and 003 – the full power point which had the largest amount of tone contamination. Without the tonal noise, EPNL reduced by 3.5 dB at set point 003 as shown in Figure 30. This is about 1 EPNdB greater than the lobed reference nozzle EPNL at the same high power set point.

For set point 103, only an additional 0.4 dB of attenuation was gained, since the tone contamination from the third stream was much less prominent. However, the modified EPNL was well within the bounds of uncertainty of the reference nozzle level. The conclusion from this quick study was that the mixer-ejector jet noise EPNL will be roughly 1 dB greater than a reference nozzle due to high frequency noise increase at high power set points and nearly equivalent at reduced power levels. This is only possible if a design modification can remove the tone issues in the current model.

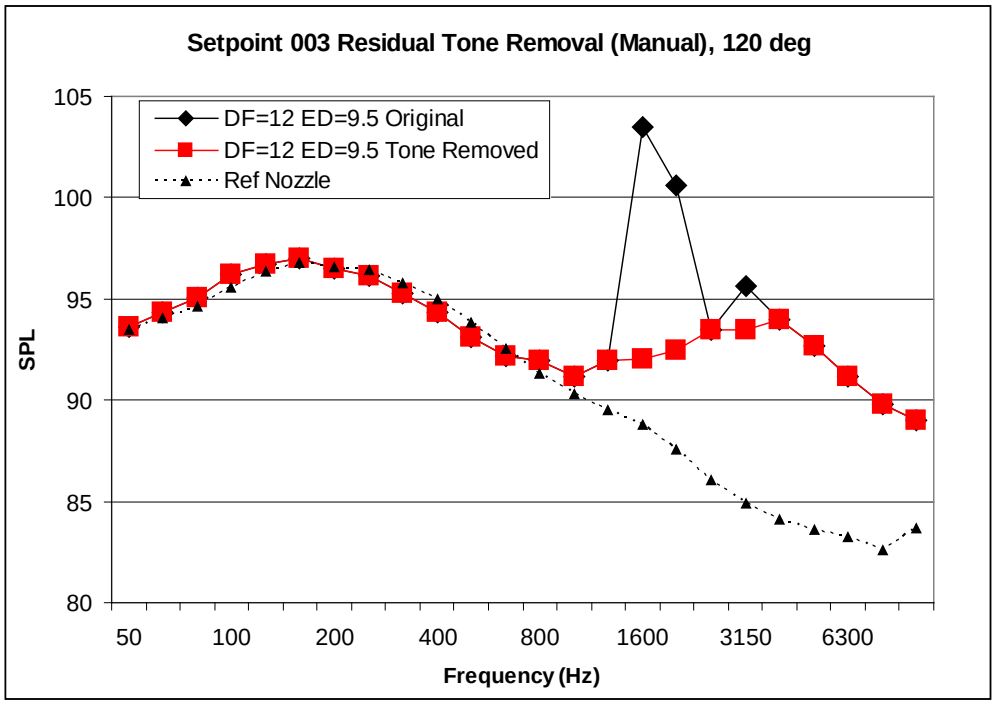

Figure 30 Source noise level comparisons with and without tonal contribution, example at 120 deg polar emission angle

7.4 Comparison with HVC10 Testing

Previous testing on a 2-stream mixer ejector nozzle under the HVC program was compared to the current N+2 program. Set point 103 was similar to 17013 in the previous test as described in Table 14. A graphical representation of the source PSD is shown in Figure 31. It is interesting to note that ejector noise increase seen in the HVC10 data does not exist in the N+2 data, and the reference nozzle data are very similar. It was calculated that the HVC10 nozzle was about 2.6 EPNdB louder than the reference, while the more recent N+2 three stream nozzle is just slightly above the reference, at 0.5 EPNdB. The same mixer hardware was used for both tests. The analysis shows that the 3 stream nozzle improves jet noise by 2 EPNdB.

Table 14 Set point comparison from two different models

Cycle Comparison	HVC10 17013	N+2 SUP 103
NPRC	1.6	1.61
NTRC	2.9	3
NPRB	1.6	1.62
NTRB	1.29	1.2
NPRT	N/A	1.31
MFJ	0.3	0.3
Delta EPNL (Ref-Ejector)	-2.57 (10 deg)	-0.50 (12 deg)

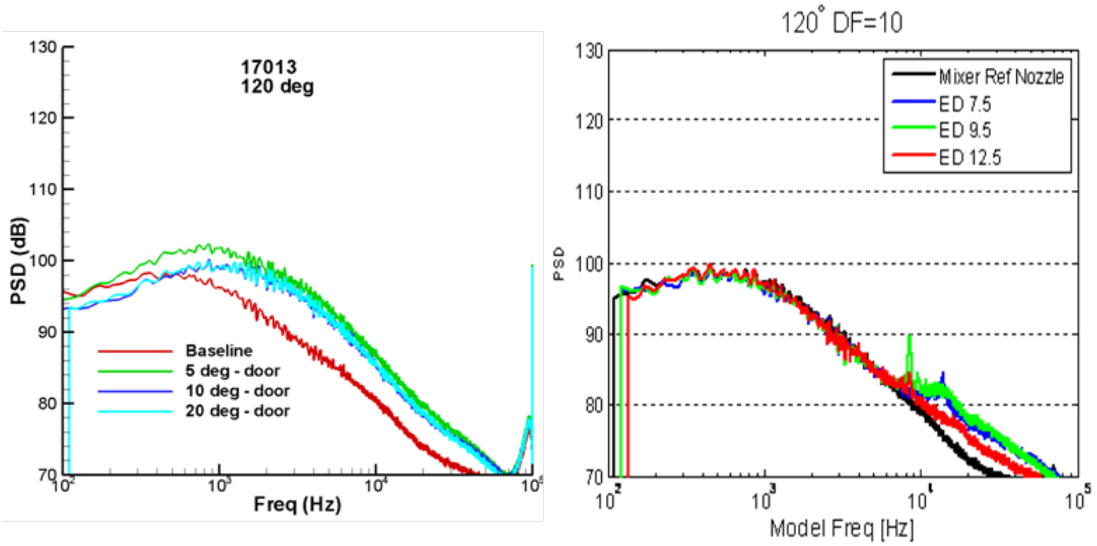

Figure 31 HVC10 data (left) compared to N+2 SUP data (right), showing that ejector noise had been significantly reduced

7.5 Estimates for 3-Nacelle Supersonic Aircraft

New EPNL estimates for a 3 nacelle configuration are discussed below.

After preliminary EPNL predictions were made, a change in aircraft sizing resulted in a switch to a three-nacelle configuration with a 1.29 scale factor increase in thrust per engine at sideline. With time and resources very short, new EPNL predictions could not be made under the contract; however, some experience-based scaling guidelines were applied to the results to generate new EPNL predictions. Key factors which were considered to affect noise were as follows:

- The reduction from 4 to 3 engines
- The reduction in MTOW from 354000 lbs to 322000 lbs
- Higher cutback altitude
- Differences in thrust at all noise certification points
- Increase in fan diameter

Due to the very large increase in approach thrust from 21,400 lbs to 35,400 lbs, new approach condition EPNL could not be determined with any confidence. Based on scaling guidelines, the Stage 3 approach limit would not be met. Therefore Stage 4 noise margin can not be defined or determined. However, an additional 0.5 EPNdB of margin was estimated at sideline and 0.6 EPNdB of margin was estimated at cutback as shown in Table X. It should be noted that due to the lower weight and reduction in number of engines, the Stage 3 limits from Table 1 are reduced. At cutback, the input for a three-nacelle configuration was reduced by 2.6 dB (Table 15).

Table 15 Updated EPNL estimates and Stage 3 limits for a 3 nacelle configuration, based on scaling the 4 nacelle prediction levels.

Measurement Point	Stage 3 Limit [dB EPNL]	Estimate [dB EPNL]	Margin [dB]
Sideline	99.3	92.6	-6.7
Take-Off	98.4	91.8	-6.6

7.6 Acoustic Performance Conclusions

While some design problems were made apparent during the test in the form of unwanted tonal noise, the results show that low jet noise levels can be achieved with a supersonic nozzle utilizing variable cycle technologies. While the noise levels are never below that of a conventional convergent nozzle, they are within ~1 dB at some optimal settings. The best configurations existed at the large divergent flap angle setting of 12 degrees, but the angle of the ejector door was also important to keep the noise low.

Using set point (103) as the representative sideline condition to calculate the EPNL, lowest jet noise levels were observed for two configurations: for a divergent flap angle of 12 degrees with an ejector door angle set to 9.5 degrees, and the divergent flap angle of 10 degrees with an ejector angle set to 12.5 degrees. The EPNL levels for the jet noise source were 0.5 EPNdB greater than the lobed reference nozzle PRFN. These configurations tended to be the among the best performers at other set point conditions as well, but due to tone sources contained in the data at some configurations, the level differences from the reference nozzle varied. Comparison at all set points can be found in Appendix C. It is worth noting that the reference with splitter SPFN performed at ~1.0 EPNdB higher than the mixer reference nozzle.

To aid redesign, there are two effects seen in the noise spectrum that need to be understood further. First, the general broadband noise increase at frequencies greater than 1 kHz existed in many configurations. The interaction of different parameters which drive this effect is not completely understood, and further understanding of how noise data trends with model configuration and with set point is needed. Second, the generation of very strong tones in the model appears to be related to the third stream pressure ratio, but more work needs to be done to identify the design features which would eliminate them. The effect of louder levels emitted at sidewall (0 deg clocking) may increase EPNL predictions at certain points along a low altitude trajectory, due to low slant angle from engine to microphone at sideline position. Based on comparisons of the reference nozzle to the ejector nozzle, a small reduction in predicted EPNL margin to Stage 4 may occur due to an increased high frequency jet noise. Follow-on design work to reduce tones generated by the third stream may help reduce the broadband high frequency noise as well.

There was good agreement in the comparison of reference nozzle test data and the noise predictions at the sideline condition. Recall the sideline prediction was 93.4 EPNdB, for engine noise only, dominated by jet noise. If the high frequency tones due to third stream flow can be removed through redesign, it was shown through manual manipulation of the source data that additional margin could be gained which would put the ejector nozzle on par with the reference nozzle noise levels.

8. Future Plans and Recommendations

Extensive acoustic test data but no aerodynamic data (except for selected surface pressures) was obtained and would required considerable analysis before design changes should be considered. Due to the limitations of steady-state CFD analysis (RANS Solutions) and the lack of reliable and validated unsteady-state CFD predictions, some of the noise characteristics such as tones cannot be predicted or explained. It is recommended that further development and validation in this direction is performed. The test data can provide more design information on optimizing the configurations for acoustics while meeting thrust requirements of the nozzle.

In near-term, the following recommendations are:

1. Detail Evaluation of Current Ejector-Mixer Configuration using PIV and internal phased Array measurements to provide more data on the jet flow effects caused by the nozzle divergent flap
2. Further analysis of the valuable three-stream acoustic test data to understand noise trends with various parameter variations, further discussed below.
3. Further CFD validation of Ejector-Mixer Model at selected test conditions which include accurate modeling of model design details, other turbulence models

There exists a wealth of measured three-stream jet data with and without an ejector from this test to conduct, more in-depth analysis and understanding of the nozzle acoustics. Future work could include efforts to analyze how a set point and configuration cause noise levels to trend, an investigation of jet flow effects on to divergent flap and ejector door angle, and an estimate of thrust differences of ejector system versus a reference nozzle. Additionally, the source of the tone excitation problem needs more attention to aid in any redesign activities. Questions still exist as to what is causing increased broadband noise levels at full scale frequencies greater than 1 kHz and what feature is generating strong tonal content at some configurations. Finally, there could be some benefit gained by a comparison with two stream ejector test data from the HVC10 model, which had very large increases in broadband noise due to the ejector.

With the redesign for three-nacelle vehicle, it is strongly recommended to go through the complete noise prediction process again, especially with the risk of unknown approach noise limit due to changes in thrust requirement.

For recommendations for Phase II Supersonic Validations, the suggestions include:

1. Small modifications to ejector-mixer nozzle to reduce third stream choking and shocks in the flow-field

2. Develop an unsteady flow analysis including large eddy simulation or direct numerical simulation CFD models to understand detail noise characteristics

3. Nozzle re-design to improve nozzle acoustic performance, including
    a. Improved aerodynamic shape of the ejector door and the divergent flaps
    b. Improved actuation system design
    c. New area variation concepts and actuation to improve both high speed and low speed performance
    d. Study the impact of increase in 3rd stream throat area seems to reduce noise – this observation should be explored further.

4. Nozzle optimization to including further improvements in ejector mixing including
    a. Other concepts -serrated, chevrons and variable area mixers.

Appendix A Propulsion System Design and CFD Analysis

Comparison of the current engine cycle performance without ejector and two iterations with ejector is shown below. Clearly, the ejector performance has significant effect of overall propulsion system and it is recommended that the ejector performance model is verified by testing. Many different cycle solutions are possible depending on desired average exhaust velocity target. The final propulsion system used here was based on the requirements provided for the N+2 vehicle with ejector model based on entrainment ratio of 0.6 obtained CFD analysis predictions.

Table A1 Data comparison between cycle iterations

	Variable Engine Cycle Style Datapack 1			Variable Engine Cycle with Ejector			Variable Cycle with Revised Ejector Setting		
	T/O	Trans	Cruise	T/O	Trans	Cruise	T/O	Trans	Cruise
Alt	0	35000	50000	0	35000	50000	0	35000	50000
Mn	0.3	1.1	1.6	0.3	1.1	1.6	0.3	1.1	1.6
Dtam C	10	10	0	10	10	0	10	10	0
Thrust	24500	7800	6000	24500	7800	6000	24500	7800	6000
SFC	0.530	0.890	0.937	0.560	0.878	0.938	0.574	0.979	0.956
Corrected Airflow	1077	1032	1010	943	914	895	980	985	950
Fan Pressure Ratio	1.65	1.87	1.62	1.83	1.99	1.74	1.66	1.93	1.60
Bypass Ratio	5.62	4.55	5.49	4.67	4.00	4.80	5.28	4.37	5.60
OPR	34.8	41.7	32.1	39.5	46.0	35.5	32.8	39.9	29.5
Avg exit Vel	1100	-	-	1100	-	-	1100	-	-
diameter	69.7			65.6	-	-	67.2	-	-
Weight	6500	-	-	6850	-	-	7500	-	-
Entrainment Ratio	-	-	-	0.8	0	0	0.5	0	0

The notional engine was developed that assumed an annular exhaust flow with core and fan flows are mixed via a lobed mixer and third stream used appropriately to interact with the 2 door ejector. The mixer-ejector nozzle design representing this cycle model, required a door opening (ED) of about 9.5 degrees. Subsequent geometrical changes to the nozzle flow path were made to achieve the predicted cycle performance at take-off, transonic and supersonic conditions. The overall engine length with the nozzle shown here is first order representation and more analysis will be required to determine the size and weight of many of the engine components. The weights shown in the above table include the dry engine weight plus the exhaust nozzle.

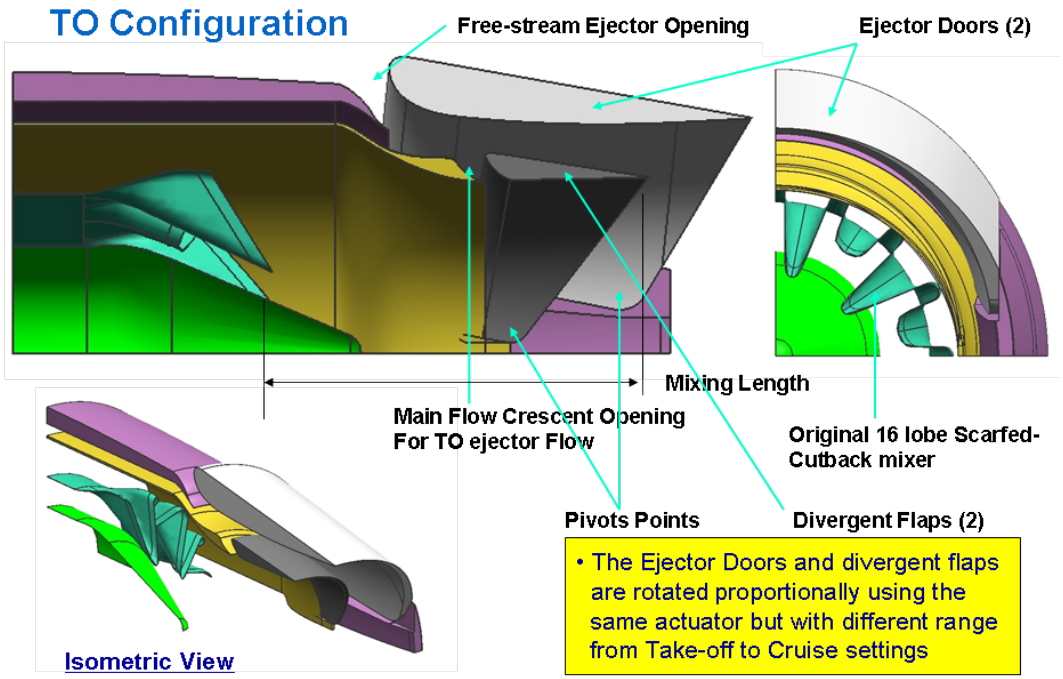

Mixer-ejector nozzle concept (patent pending)

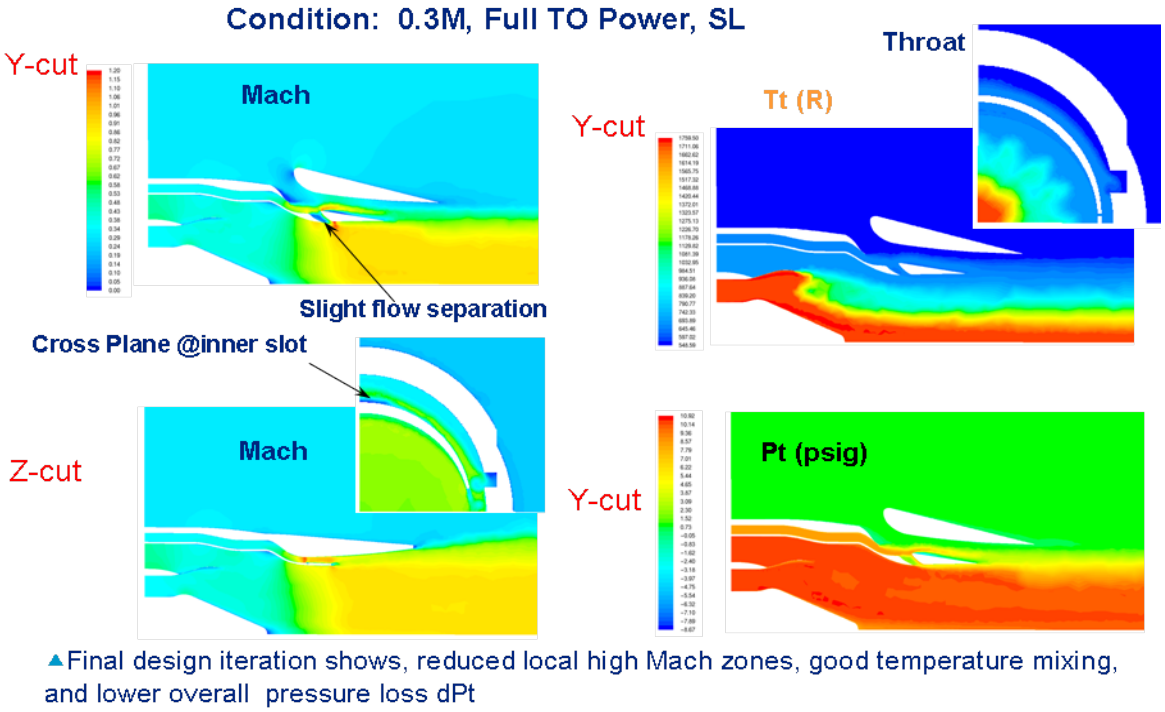

Mixer ejector nozzle Mach numbers and temperature contours at full power TO, 0.3M, axial top and side cuts (full scale)

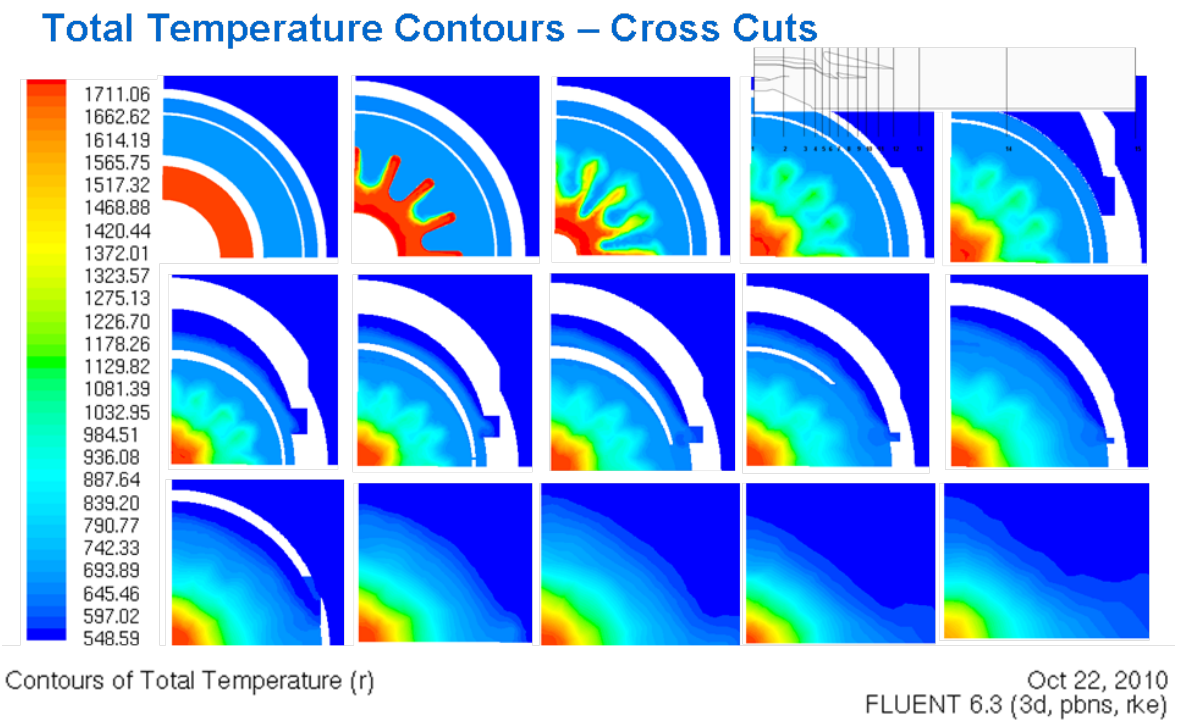

Mixer-ejector nozzle temperature contours at axial stations, full power TO, 0.3M

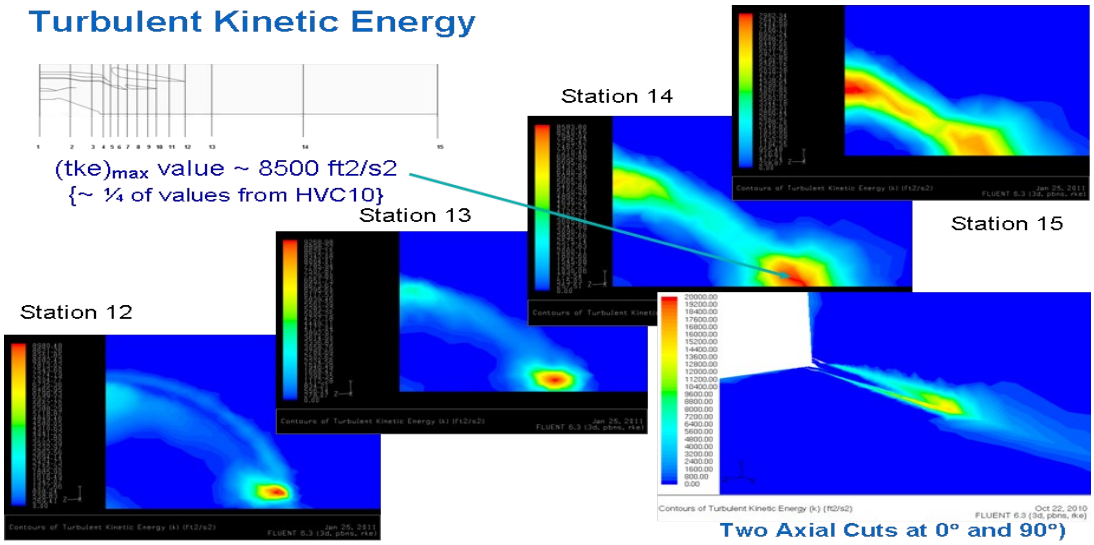

Mixer-ejector nozzle tke contours at axial station cuts, full power TO, 0.3M

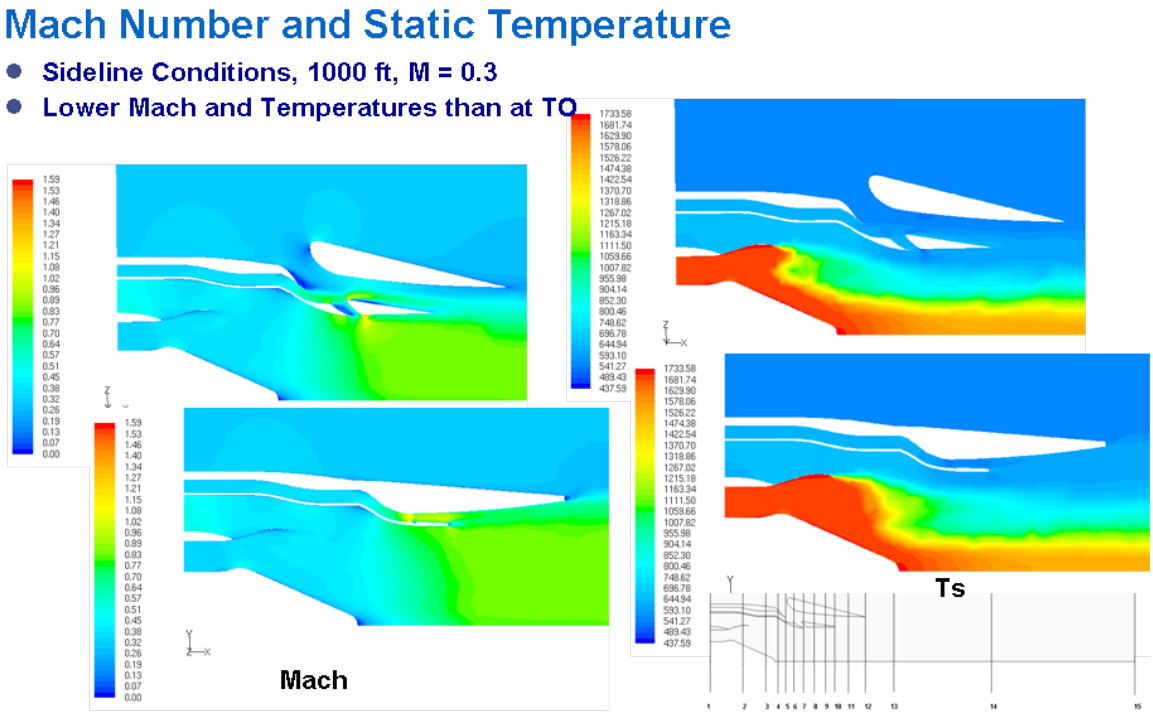

Mixer ejector nozzle Mach numbers and temperature contours at sideline, 0.3M, axial top and side cuts

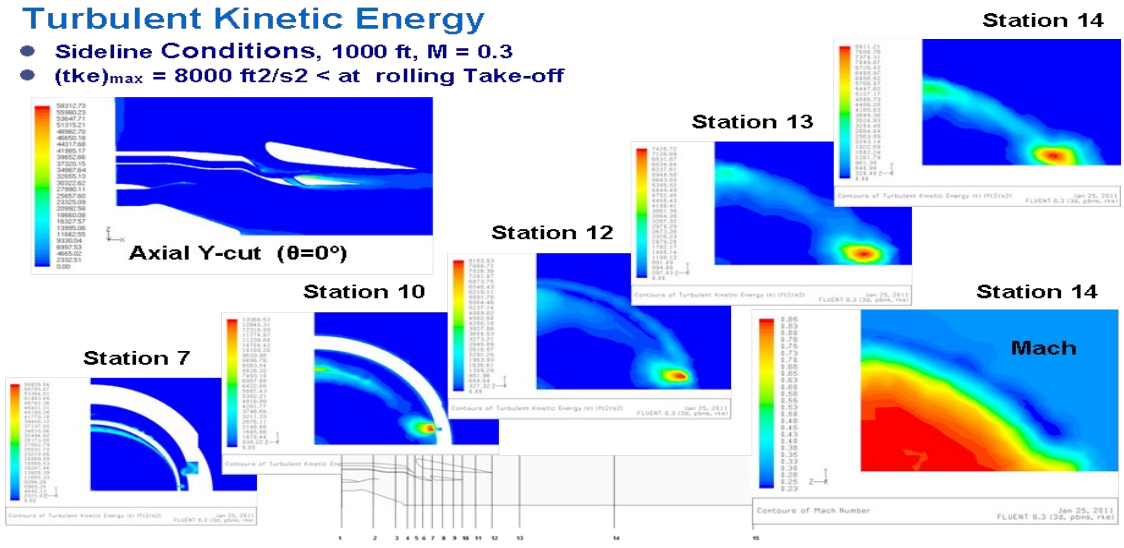

Mixer-ejector nozzle tke contours at axial station cuts at sideline, 0.3M

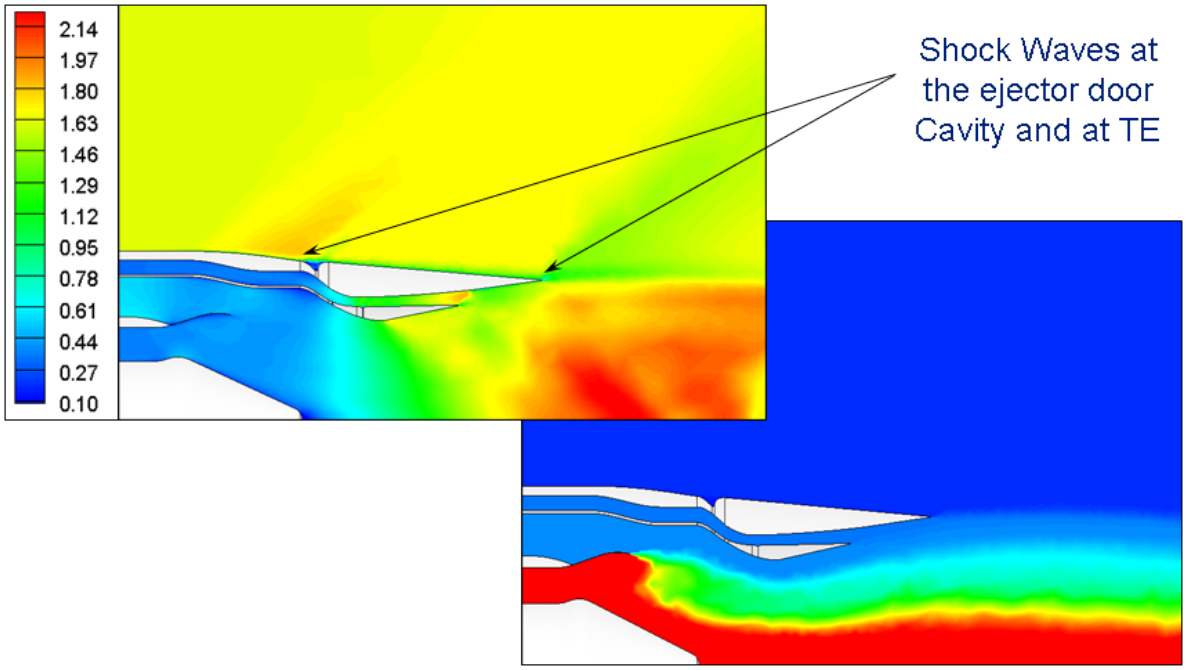

Cruise Mach and total temperature distributions, M = 1.6, Alt = 50,000 ft

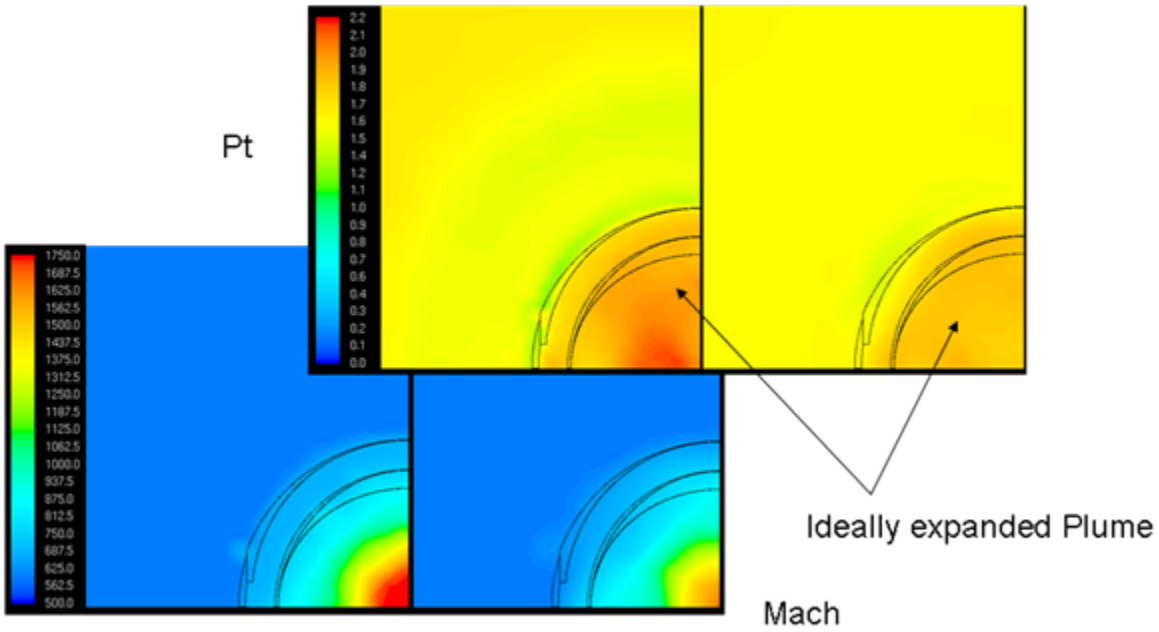

Cruise Mach and total pressure distributions in exit plume at L = 1D and 5D from nozzle exit, M = 1.6, Alt = 50kft

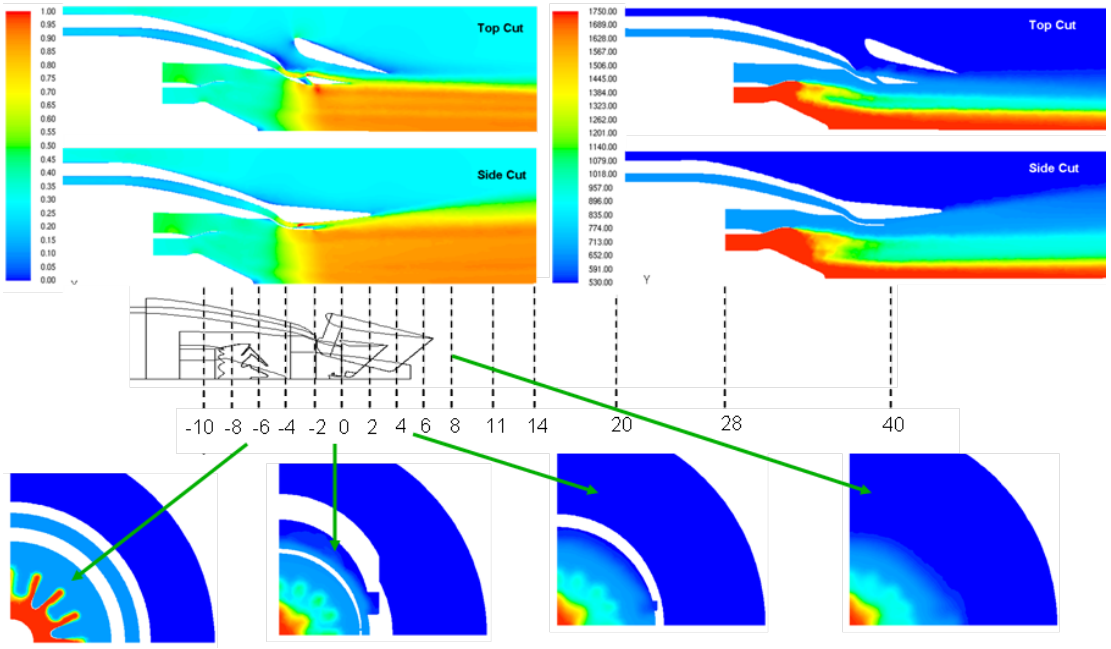

Mach Numbers and total temperatures for model scale mixer nozzle at full power TO, M=1.6, axial cuts and station cuts – reduced ejector flow

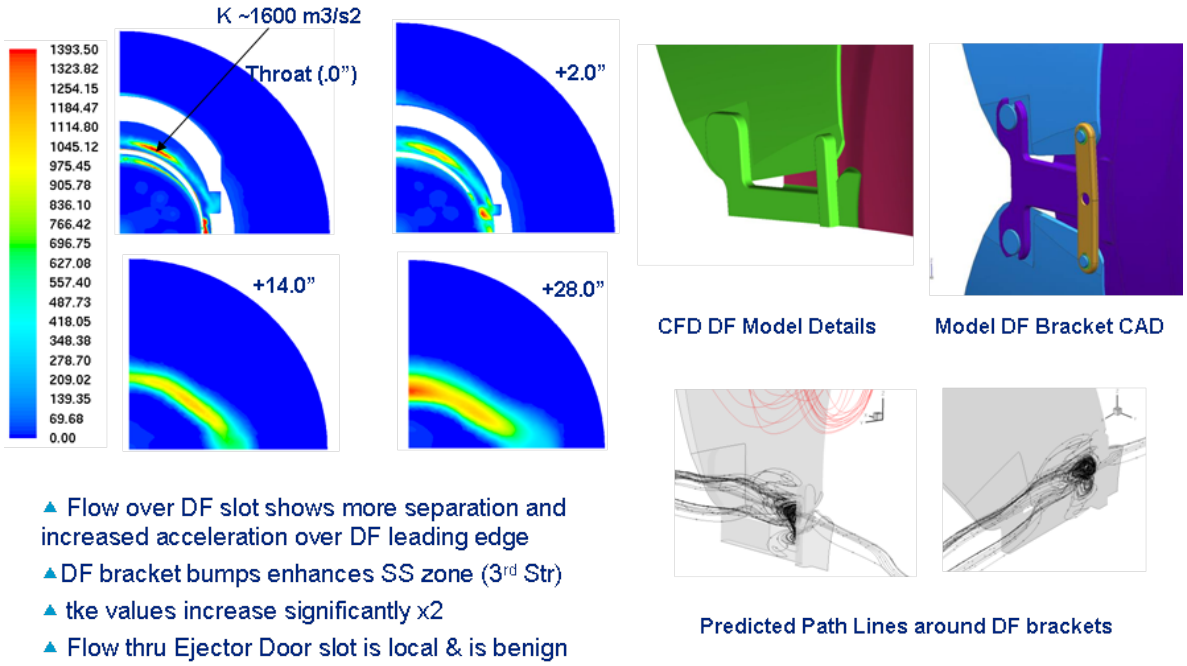

Turbulence kinetic energy tke predictions, axial cuts for nozzle at full power TO, M = 1.6. Comparison of CFD modeling of DF brackets shows difficulties in model geometry details.

The accuracy of CFD analysis was determined by computing gross quantities from the CFD solutions, such as mass flow and thrust in each stream and at selected stations. The following table at 100% TO power at 0.3M (Design point) compared the 1-D cycle data and 3D calculations. The ejector pumping was targeted at 50% with CFD predicting 49%. Subsequently, the third stream throat area was increased by 15% to compensate for losses in long third annular duct, upstream of the nozzle. Changes in third stream throat area had significant effect on performance and it was decided to test a few variations in throat areas.

Table A2 Comparison of Cycle and CFD calculated flow parameters

Exhaust System Model	Core Flow	Bypass Flow	3rd Stream Flow	Ejector Flow	Gross Thrust
CFD Predictions	159.2 lb/s	650.4 lb/s	198.4 lb/s	127.0 lb/s	35,276 lbf
PD671 Cycle Simulations	161.2 lb/s	639.91 lb/s	199.82 l	99.82 lb/s	36,376 lbf

Appendix B Model design Reports, & Drawings

The nozzle hardware during manufacturing inspection at ASE is shown below. The models were assembled on site (ASE) and delivered to NASA GRC in protective crates.

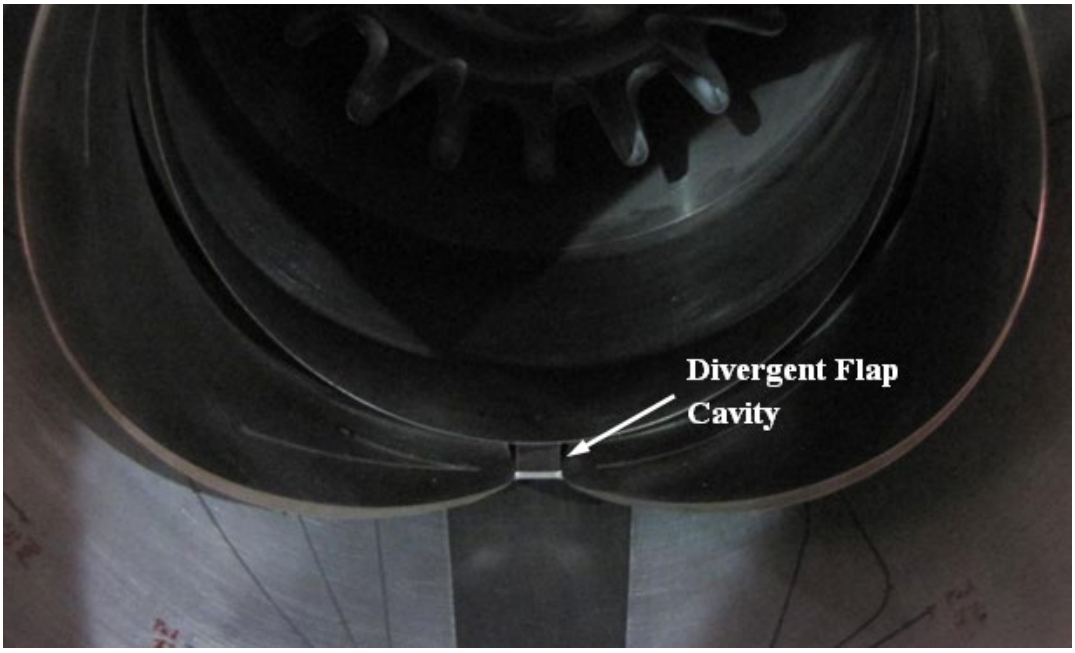
Divergent Flap
Cavity

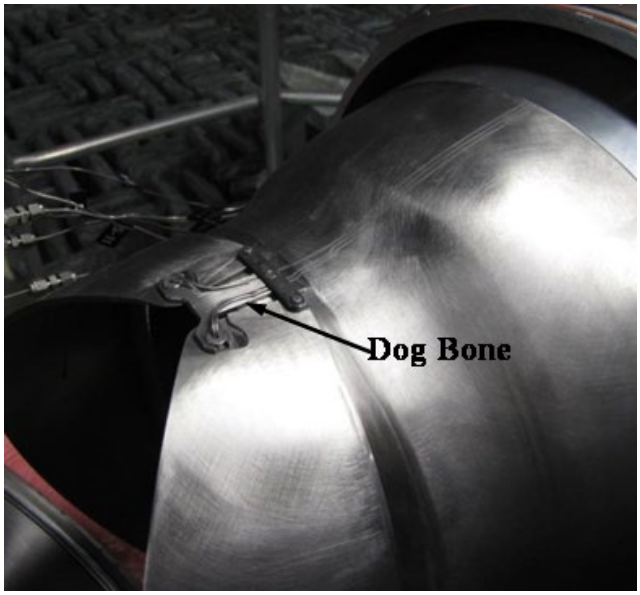
Dog Bone

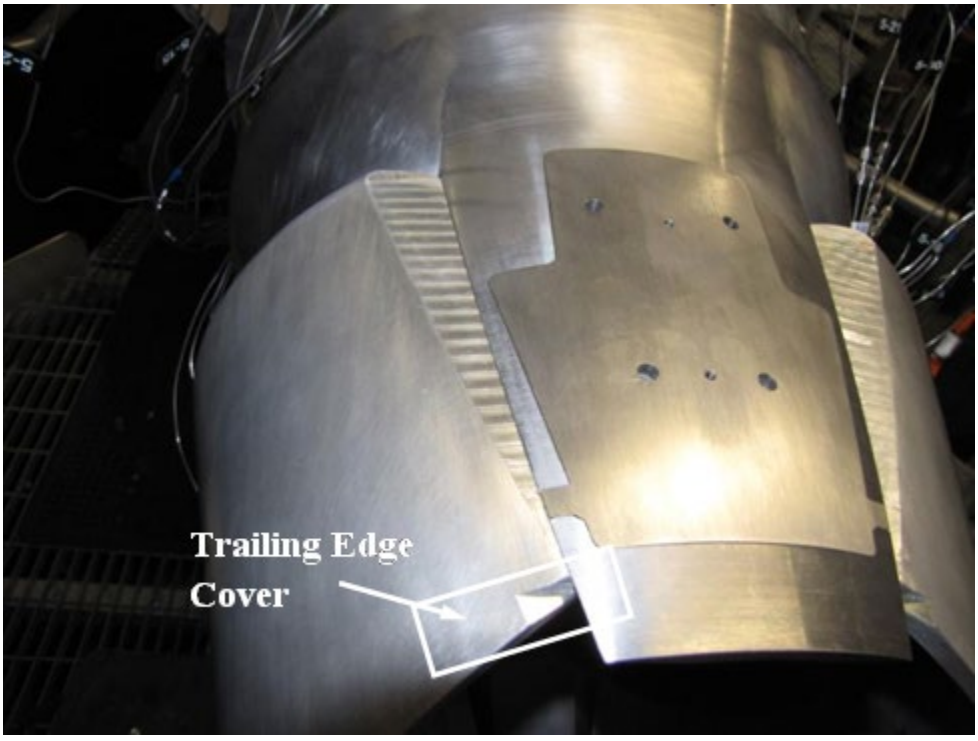
Trailing Edge
Cover

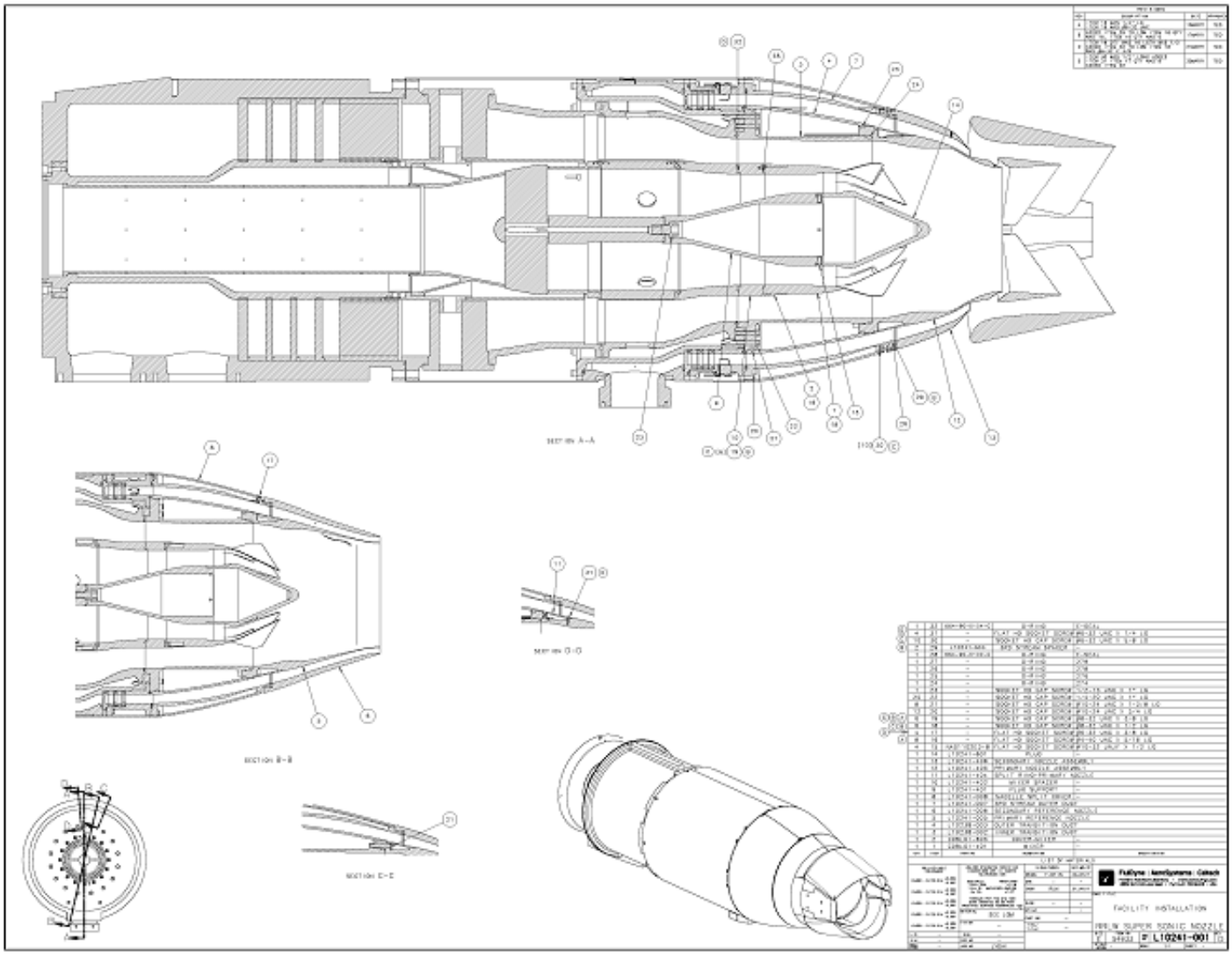

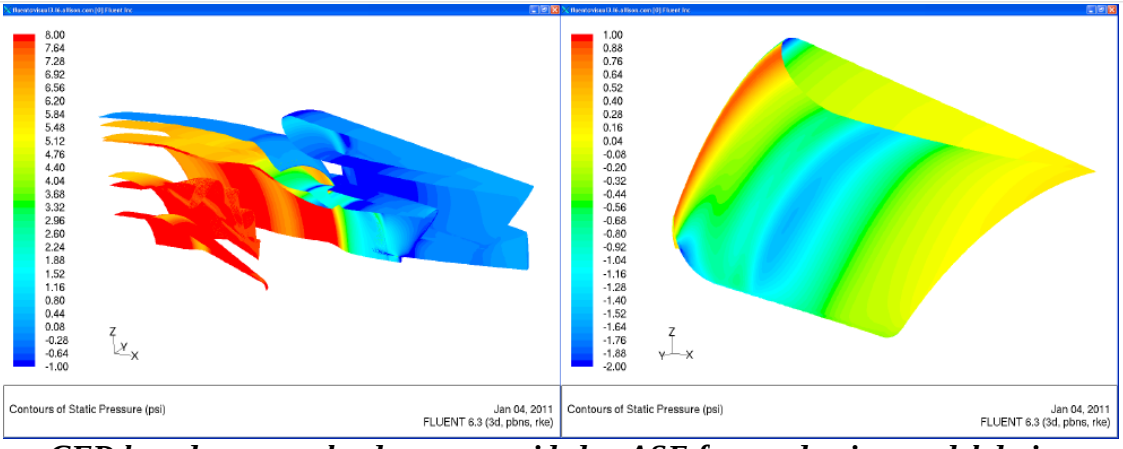

CFD based pressure loads were provided to ASE for conducting model design

Appendix C Acoustic Test Data

This appendix contains acoustic EPNL projections as well as full-scale acoustic source data at additional operating set points. Acoustic impact of divergent flap angle, ejector door angle, spacer setting, and clocking orientation are compared against the lobed reference nozzle. The splitter reference nozzle is also plotted for comparison. Plots of source noise levels in SPL at four (4) representative polar emission angles are on a 6.7' polar radius.

The set point conditions are referenced in the Table C1, with all data taken with a simulated flight of Mach 0.3, with exception to set point 08, which was taken at Mach 0.2. The third digit in the set point refers to the tenths of flight stream Mach Numbers.

Table C1 for frrstream Mach Mfs = 0.30

Set Point	NPR,core Pt/Pamb	NPR,bp Pt/Pamb	NPR,3d Pt/Pamb	TR,core Tt/Tamb	TR,bp/3d Tt/Tamb
003	1.72	1.71	1.57	3.3	1.27
013	1.70	1.70	1.55	3.2	1.25
023	1.65	1.65	1.50	3.2	1.25
033	1.60	1.60	1.45	3.2	1.25
043	1.55	1.55	1.40	3.0	1.25
063	1.45	1.45	1.35	3.0	1.20
083	1.35	1.35	1.30	2.8	1.20
103	1.61	1.62	1.31	3.0	1.20
113	1.43	1.46	1.27	2.7	1.15

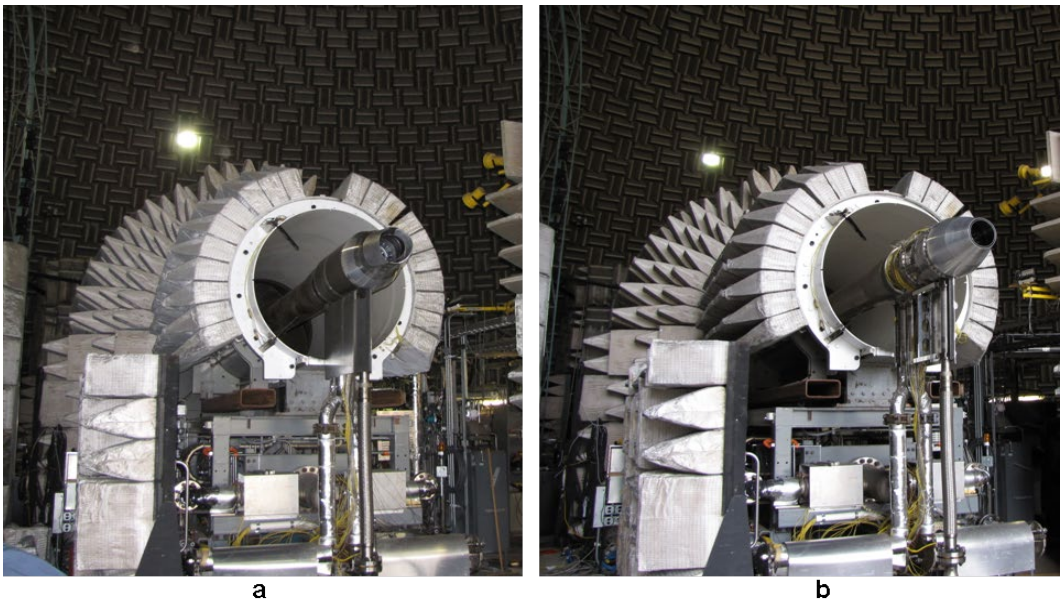

a b

HFJER at the NASA Glenn AAPL with the model installed, where (a) is the three stream ejector model and (b) is the three stream reference nozzle.

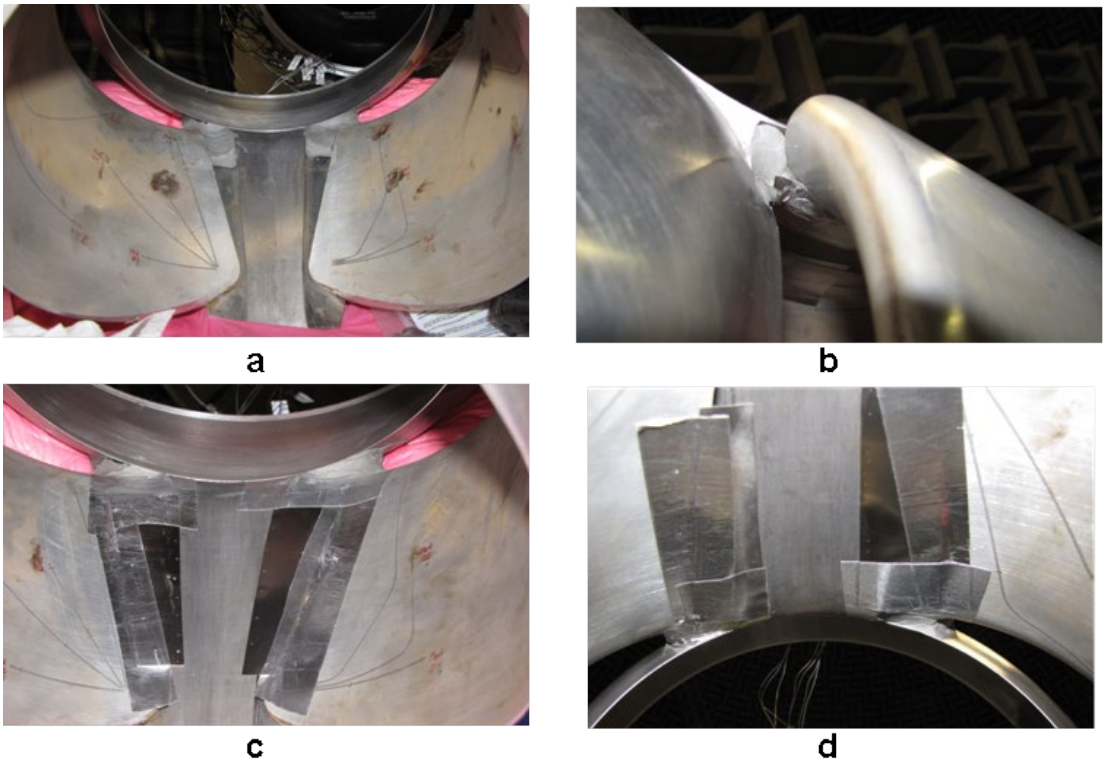

a b c d

Inside ejector along sidewall for tone investigation tests on April 22, 2011, where, (a) shows how putty was applied to cavities, (b) shows detail along ejector leading edge,( )c shows ni-chrome strips and tape covers on one side, and (d) shows the similar result on the top side. Putty was removed for testing with hot bypass air, since it created a mess.

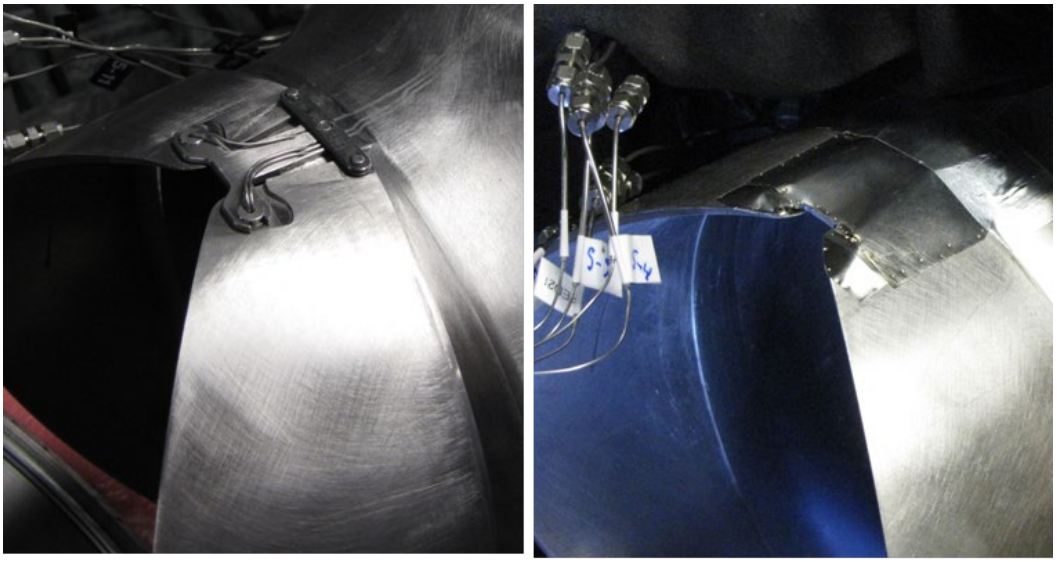

a b

Divergent flap hinge covers,(a) shows original hinge and (b) shows the covered hinge. This cover was maintained throughout the test campaign.

a b

Inside divergent flap opening for tone investigation tests on April 22, 2011, where (a) shows application before the test and (b) shows damage after the test.

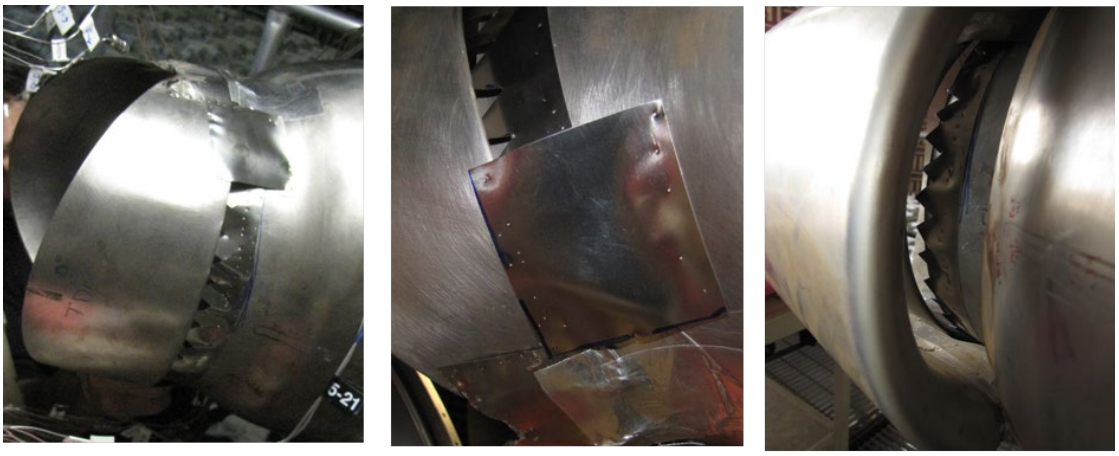

a b c

Chevrons and sliver covers (near hinge) fashioned from ni-chrome strips were tack welded to divergent flap opening for tone investigation tests on April 26, 2011, as shown in (a) and (b). The covers were removed to test chevrons-only in (c).

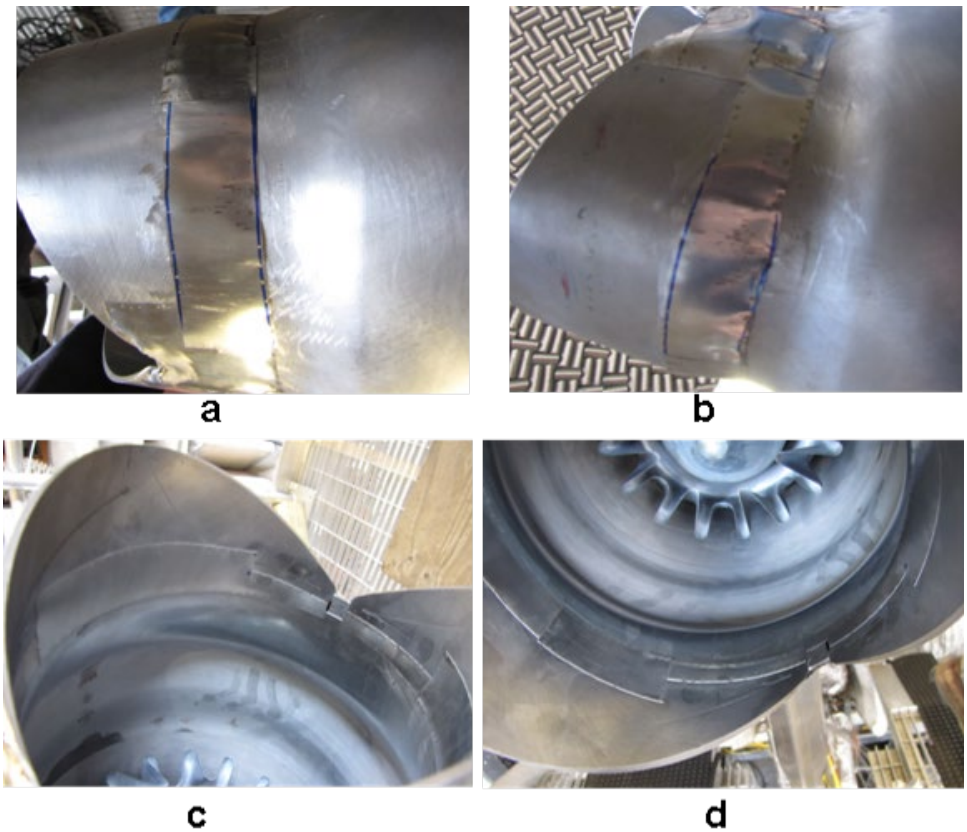

a b c d

Divergent flap covers fashioned from ni-chrome stripping were maintained throughout test campaign after it was decided that they performed well to reduce third-stream induced tones. Both the outer opening, as shown, in (a) and (b), and the inner opening (c) and (d) were covered.

SETPOINT 003

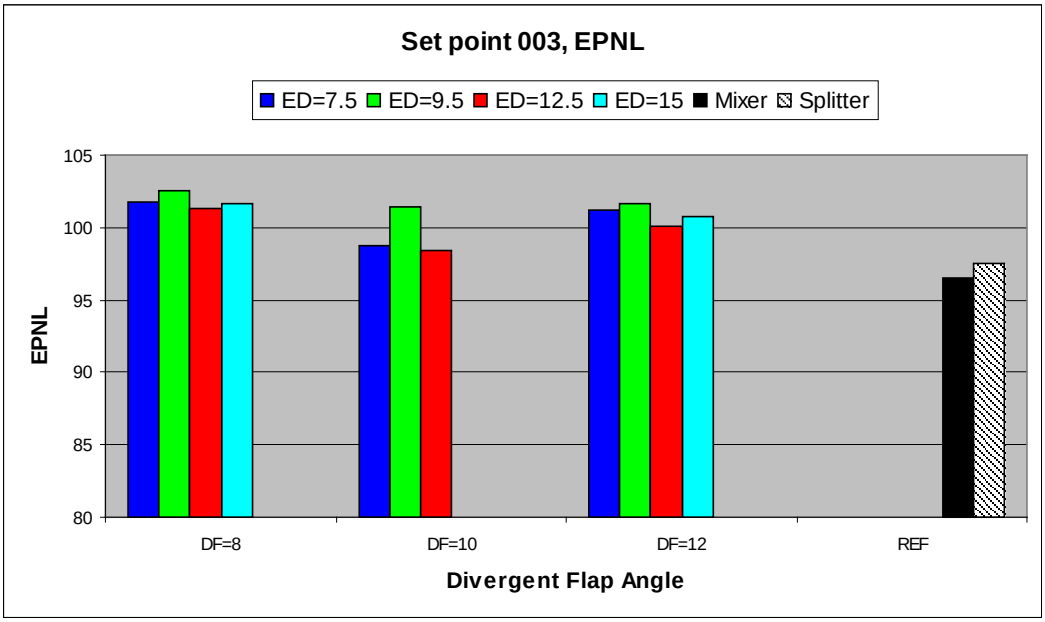

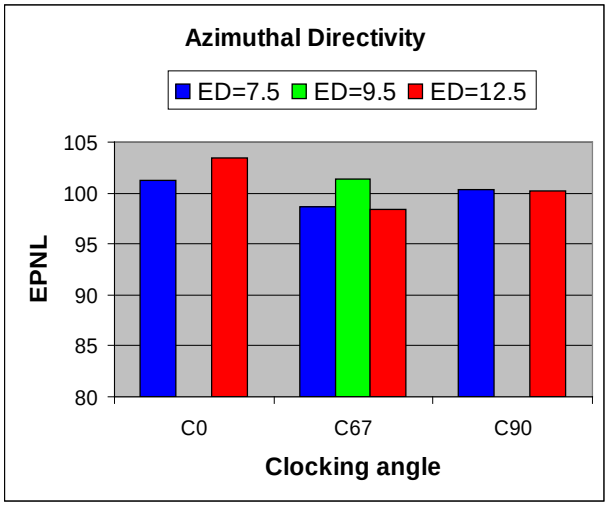

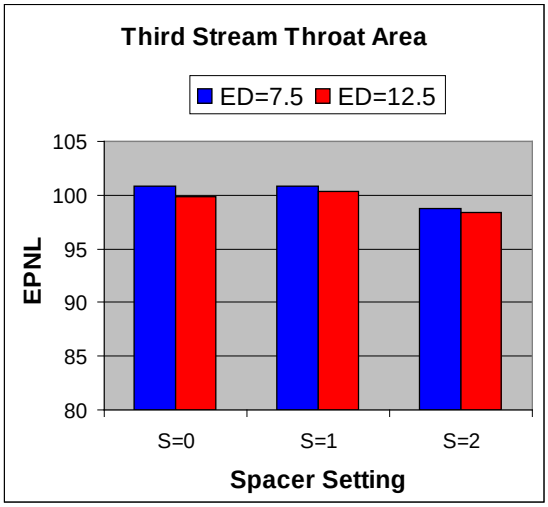

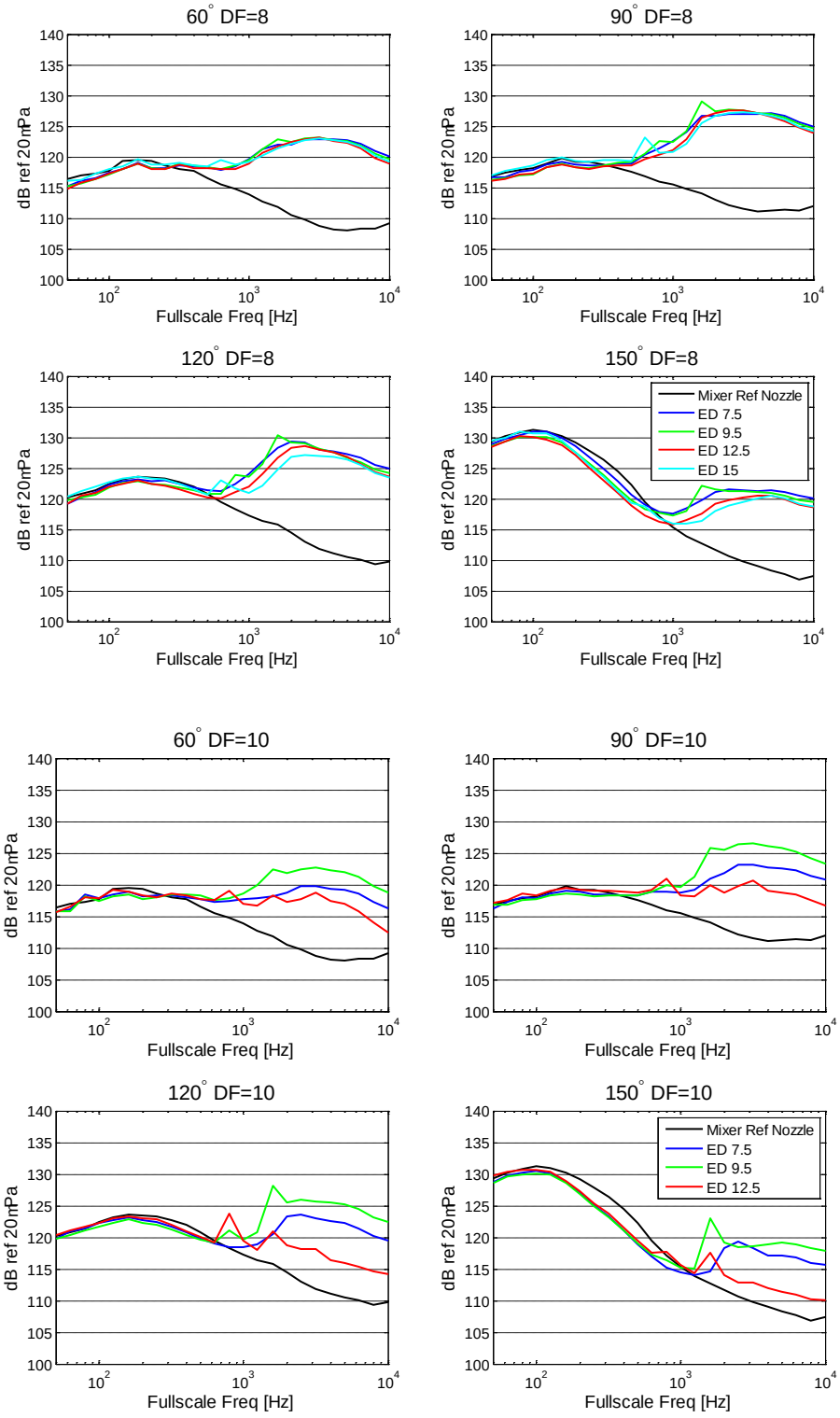
60° DF=8
90° DF=8
120° DF=8
150° DF=8
60° DF=10
90° DF=10
120° DF=10
150° DF=10
dB ref 20mPa
Fullscale Freq [Hz]
Mixer Ref Nozzle
ED 7.5
ED 9.5
ED 12.5
ED 15

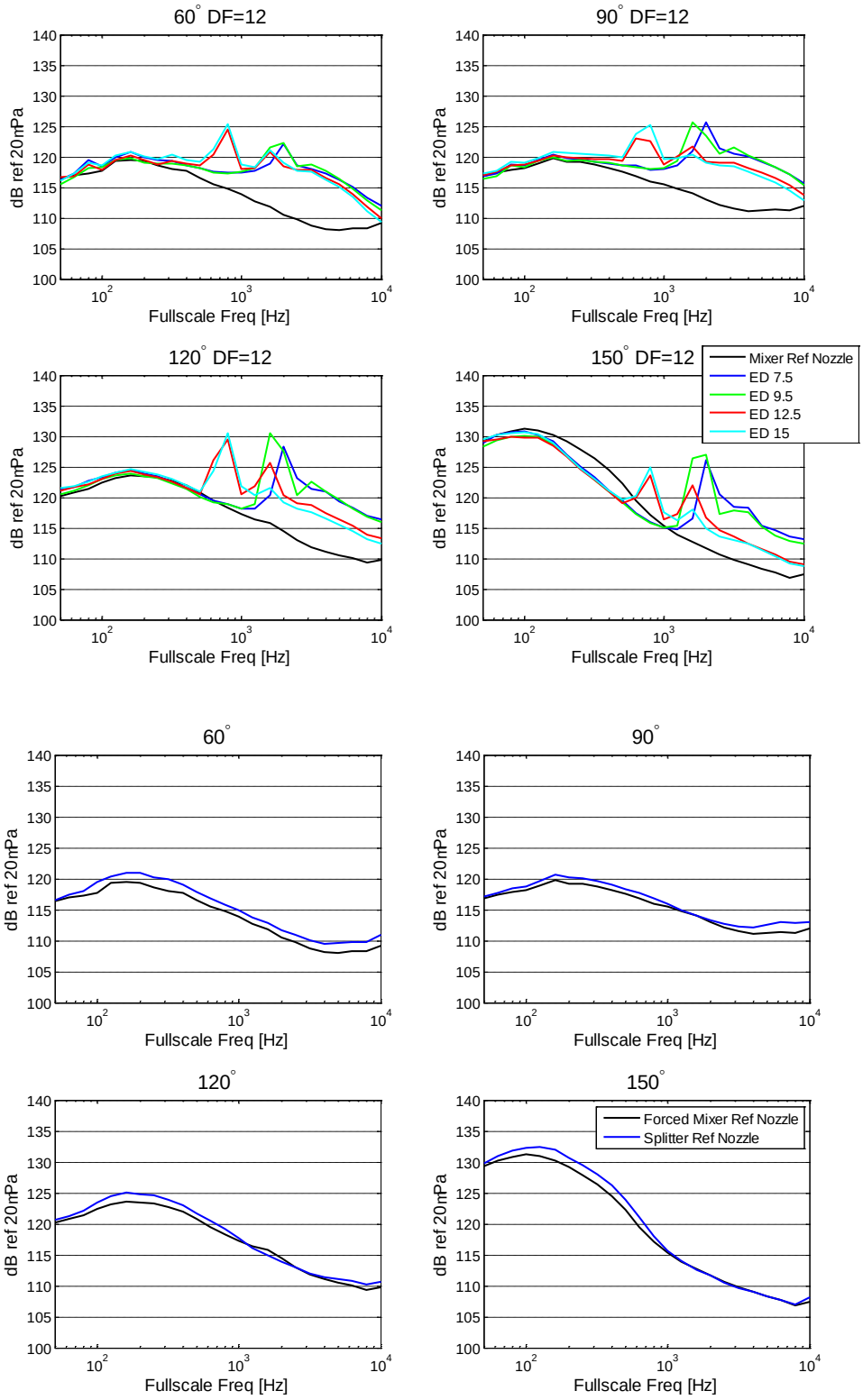
60° DF=12
90° DF=12
120° DF=12
150° DF=12
Mixer Ref Nozzle
ED 7.5
ED 9.5
ED 12.5
ED 15
60°
90°
120°
150°
Forced Mixer Ref Nozzle
Splitter Ref Nozzle
dB ref 20mPa
Fullscale Freq [Hz]

SETPOINT 013

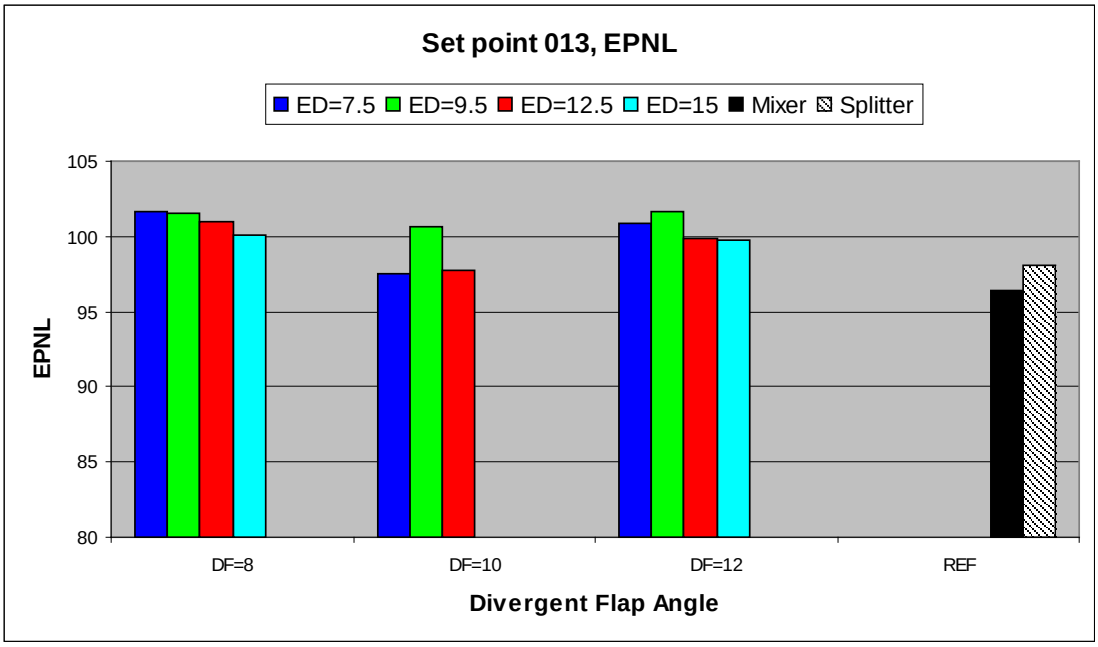

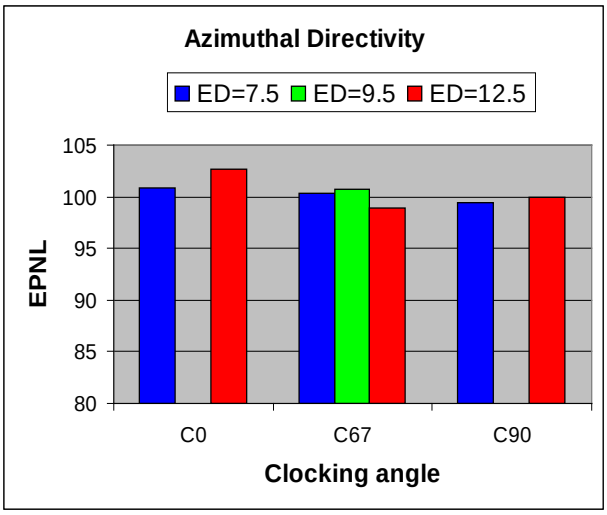

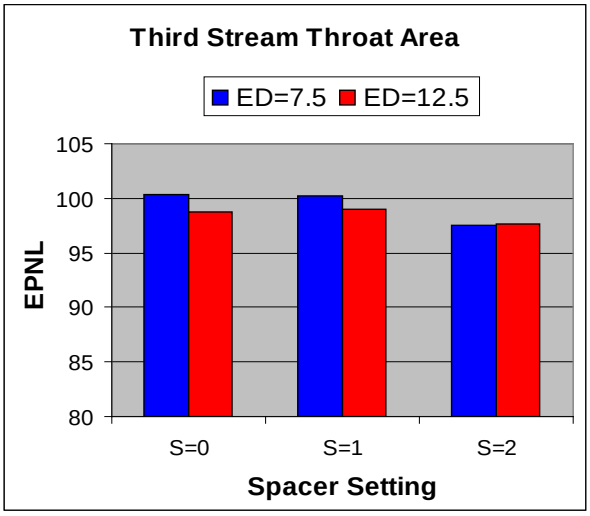

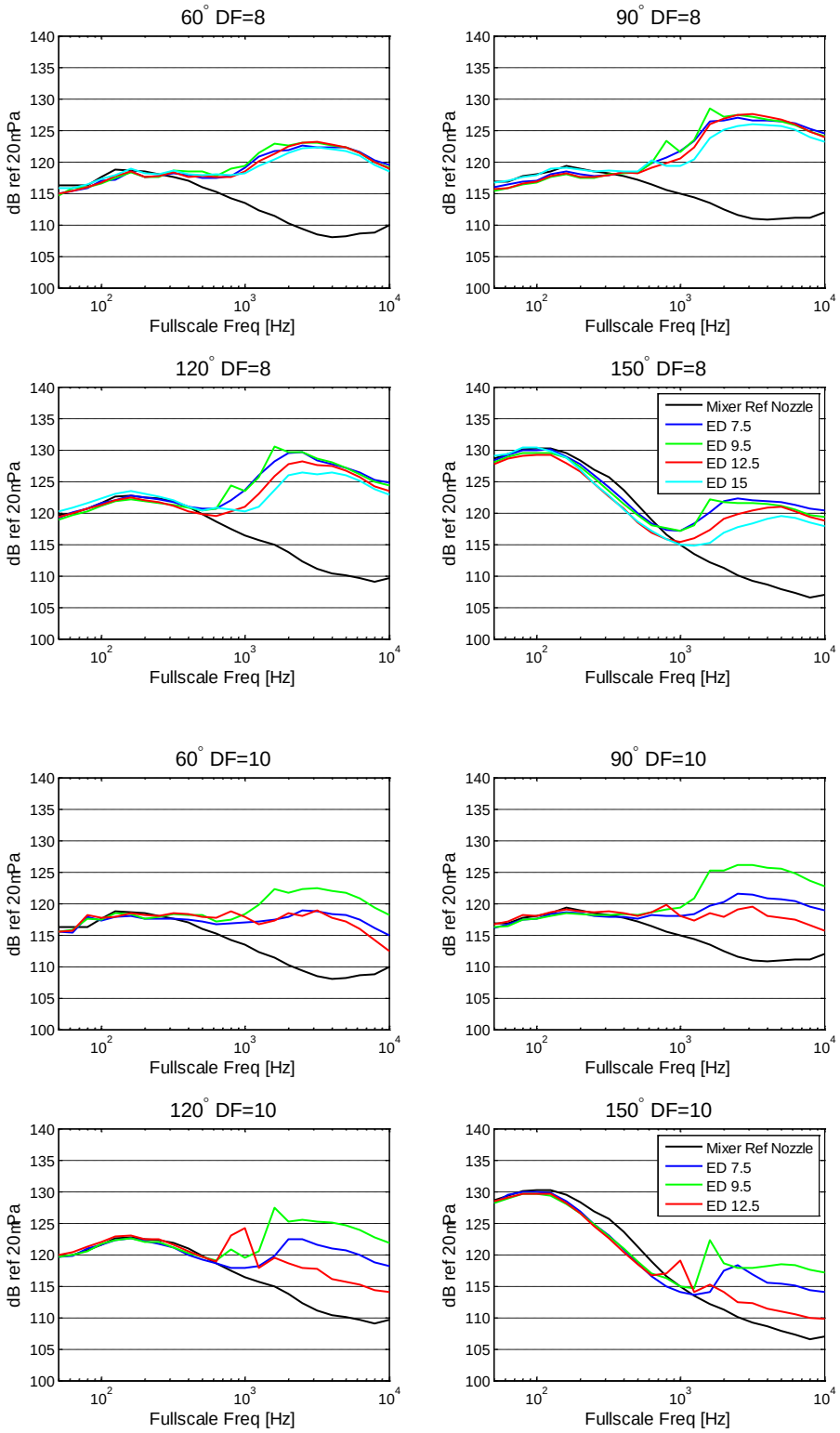
60° DF=8
90° DF=8
120° DF=8
150° DF=8
60° DF=10
90° DF=10
120° DF=10
150° DF=10
dB ref 20mPa
Fullscale Freq [Hz]
Mixer Ref Nozzle
ED 7.5
ED 9.5
ED 12.5
ED 15

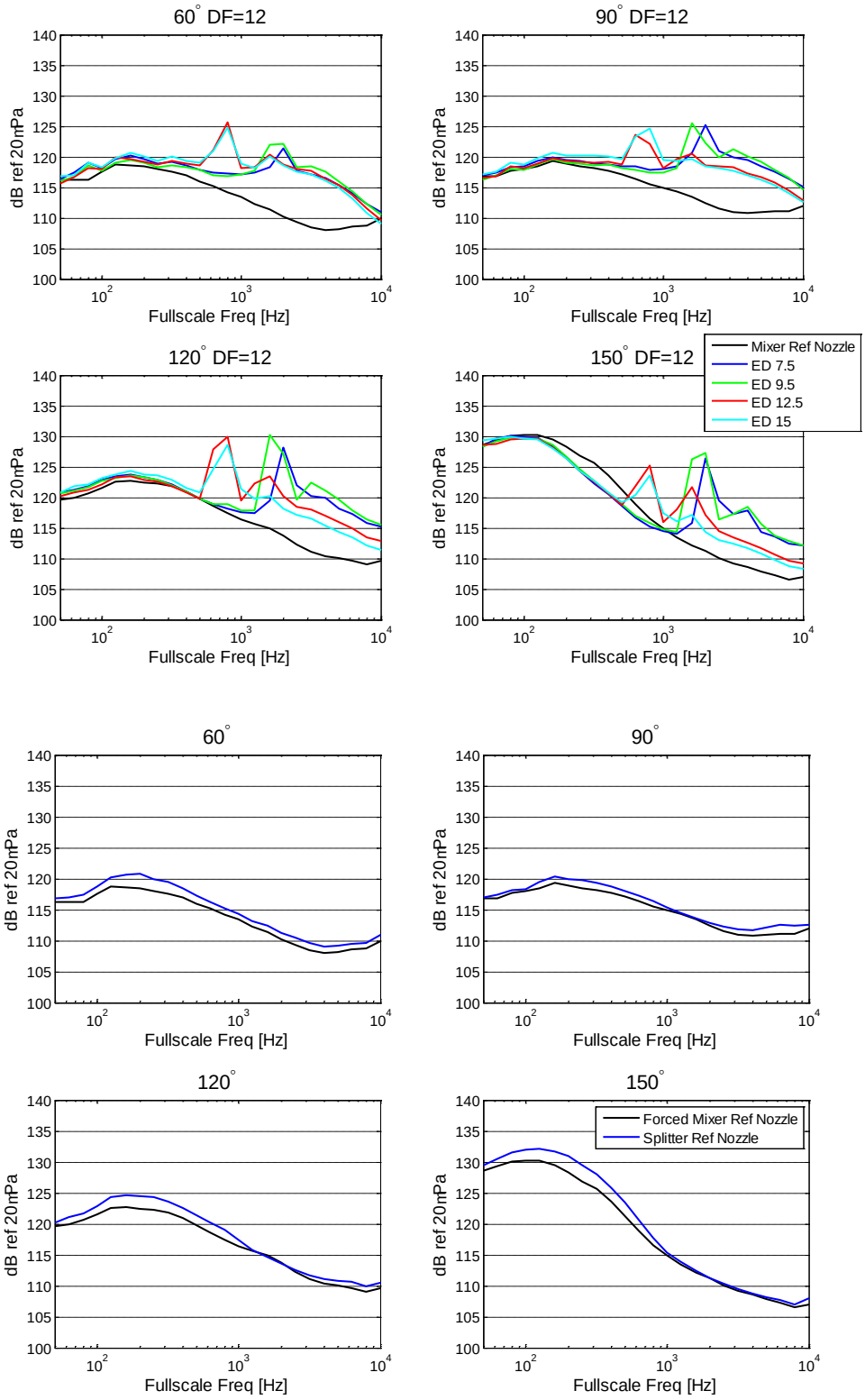
60° DF=12
90° DF=12
120° DF=12
150° DF=12
Mixer Ref Nozzle
ED 7.5
ED 9.5
ED 12.5
ED 15
60°
90°
120°
150°
Forced Mixer Ref Nozzle
Splitter Ref Nozzle
dB ref 20mPa
Fullscale Freq [Hz]

SETPOINT 023

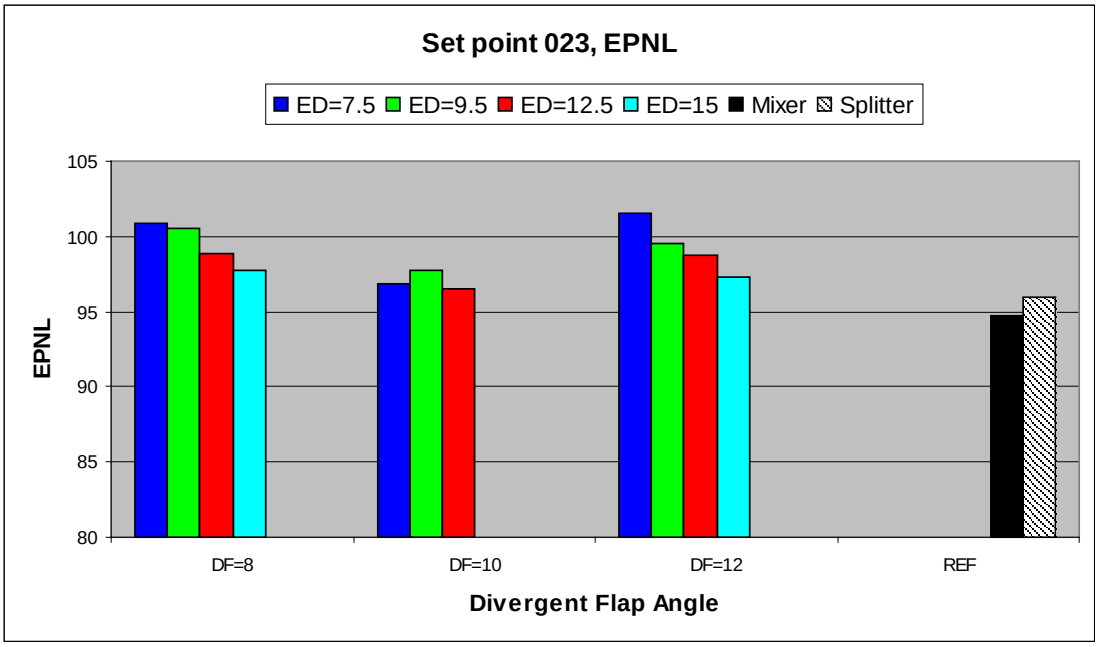

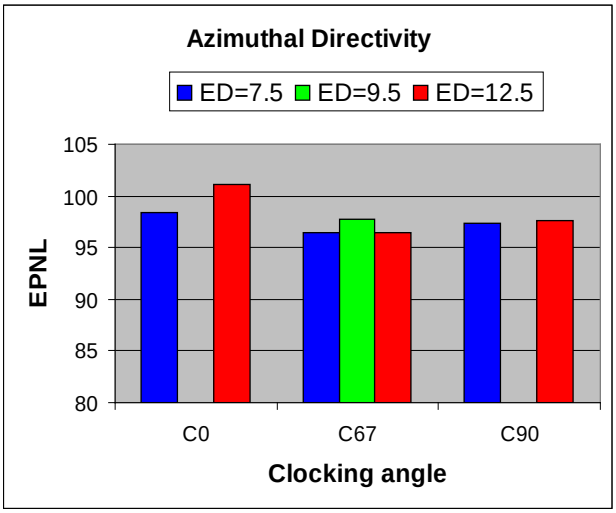

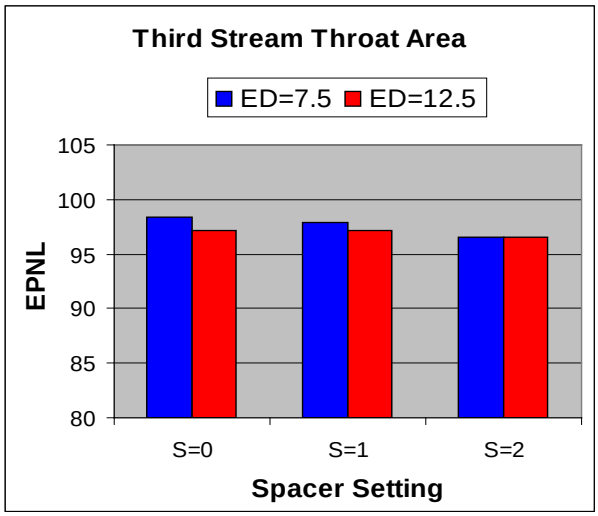

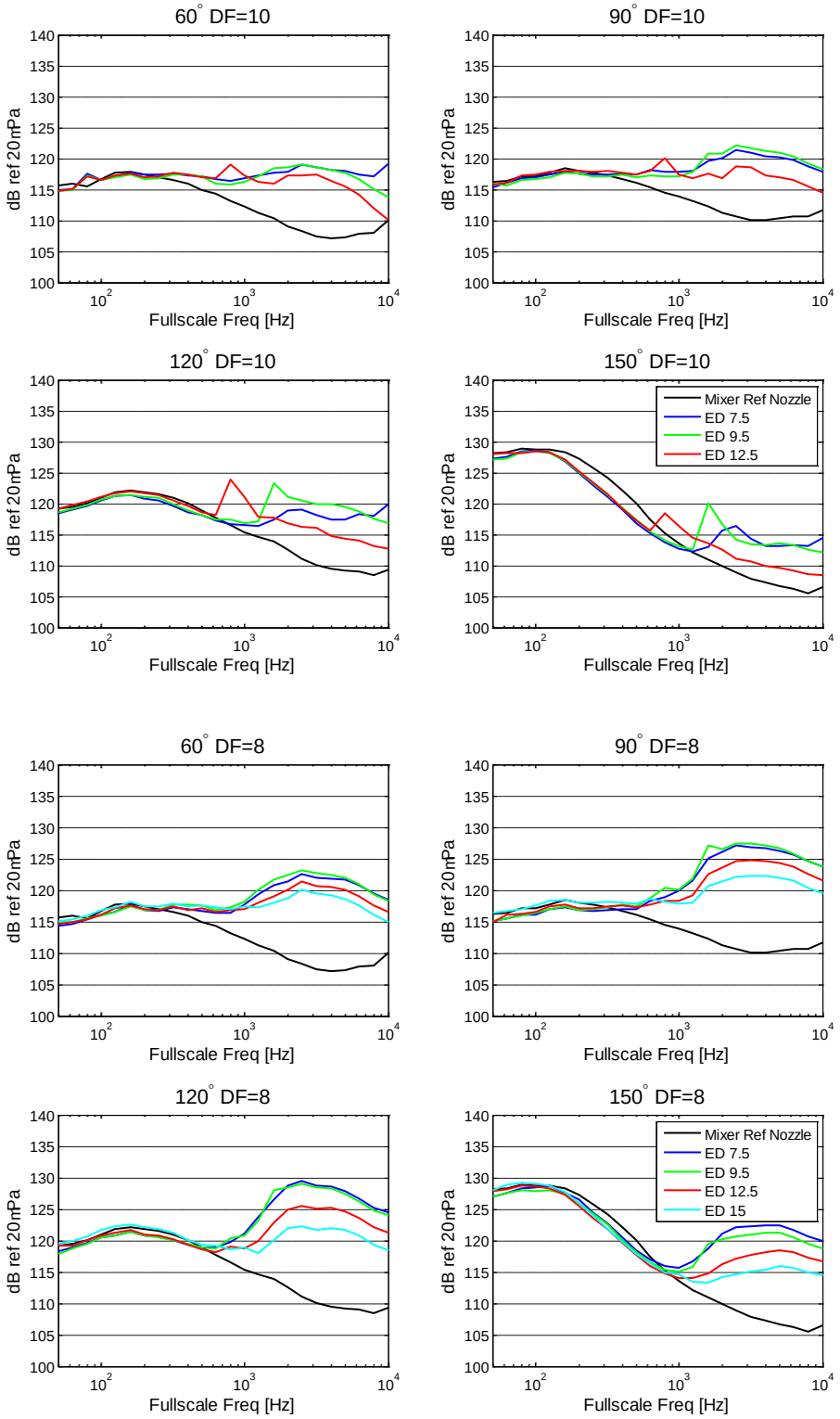
60° DF=10
90° DF=10
120° DF=10
150° DF=10
60° DF=8
90° DF=8
120° DF=8
150° DF=8
dB ref 20mPa
Fullscale Freq [Hz]
Mixer Ref Nozzle
ED 7.5
ED 9.5
ED 12.5
ED 15

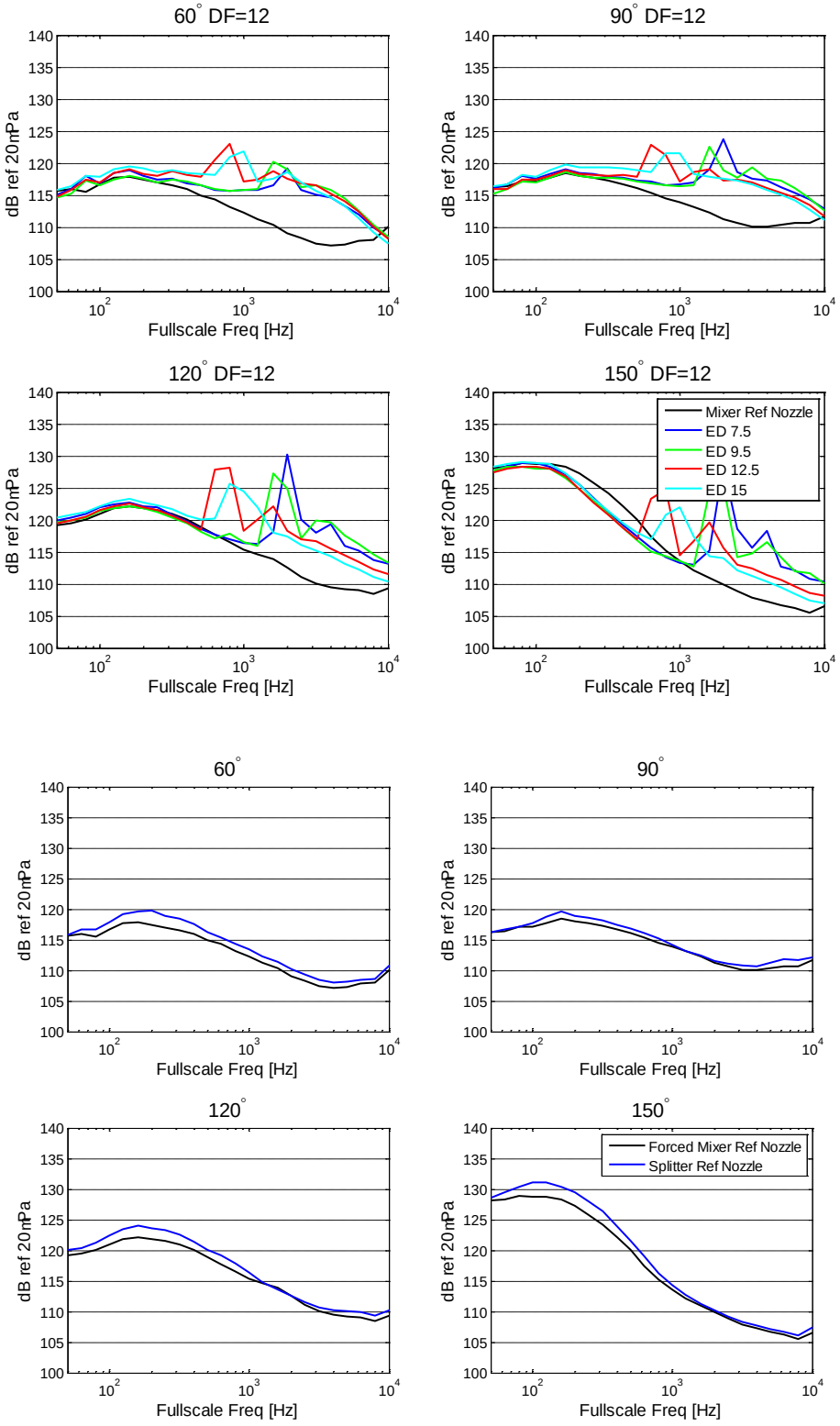
60° DF=12
90° DF=12
120° DF=12
150° DF=12
60°
90°
120°
150°
dB ref 20mPa
Fullscale Freq [Hz]
Mixer Ref Nozzle
ED 7.5
ED 9.5
ED 12.5
ED 15
Forced Mixer Ref Nozzle
Splitter Ref Nozzle

SETPOINT 033

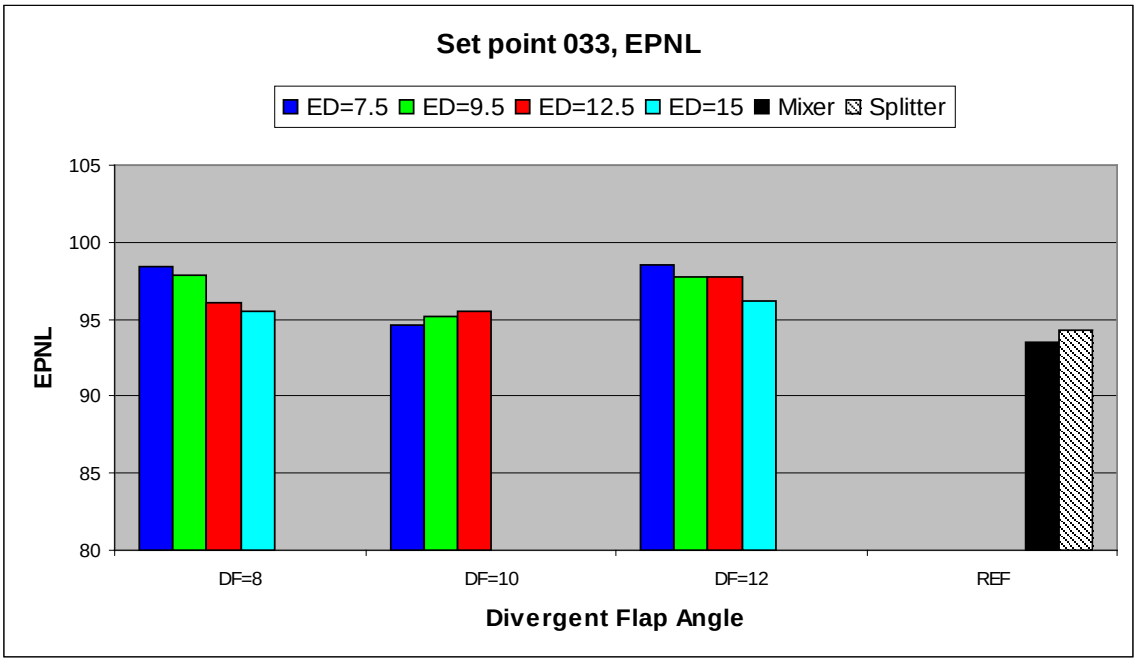

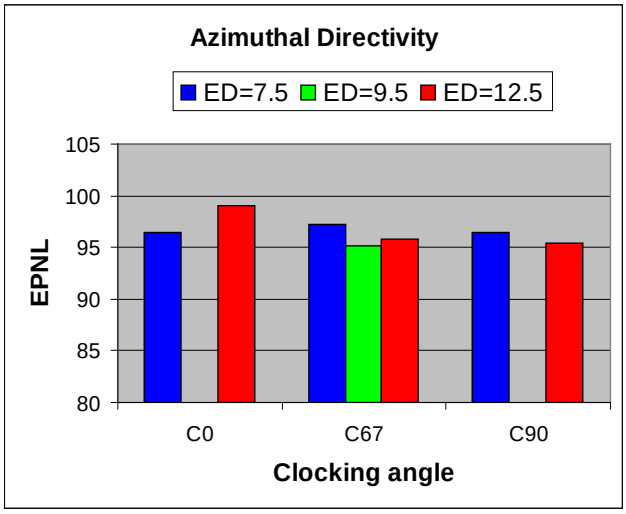

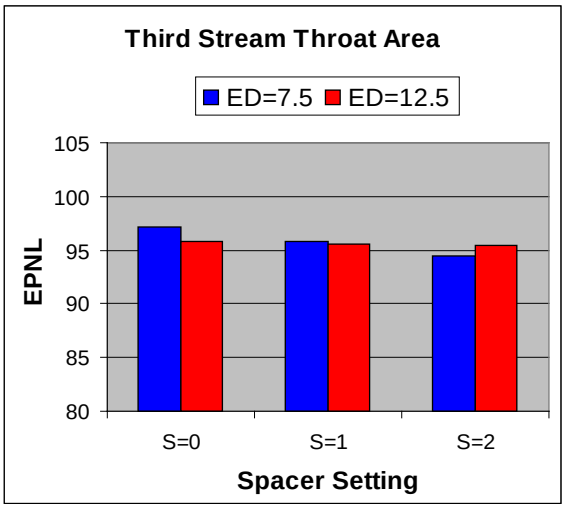

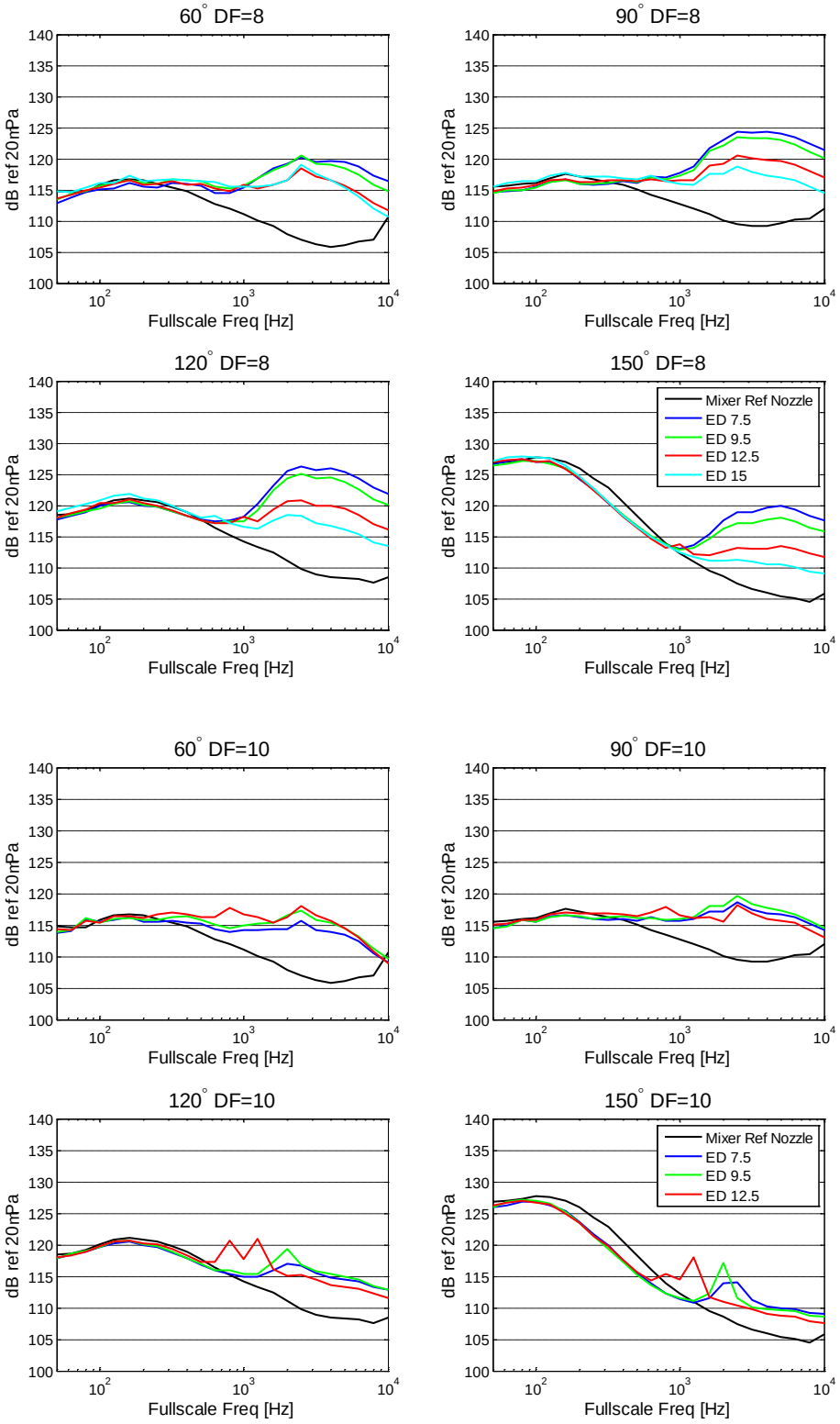
60° DF=8
90° DF=8
120° DF=8
150° DF=8
60° DF=10
90° DF=10
120° DF=10
150° DF=10
dB ref 20mPa
Fullscale Freq [Hz]
Mixer Ref Nozzle
ED 7.5
ED 9.5
ED 12.5
ED 15

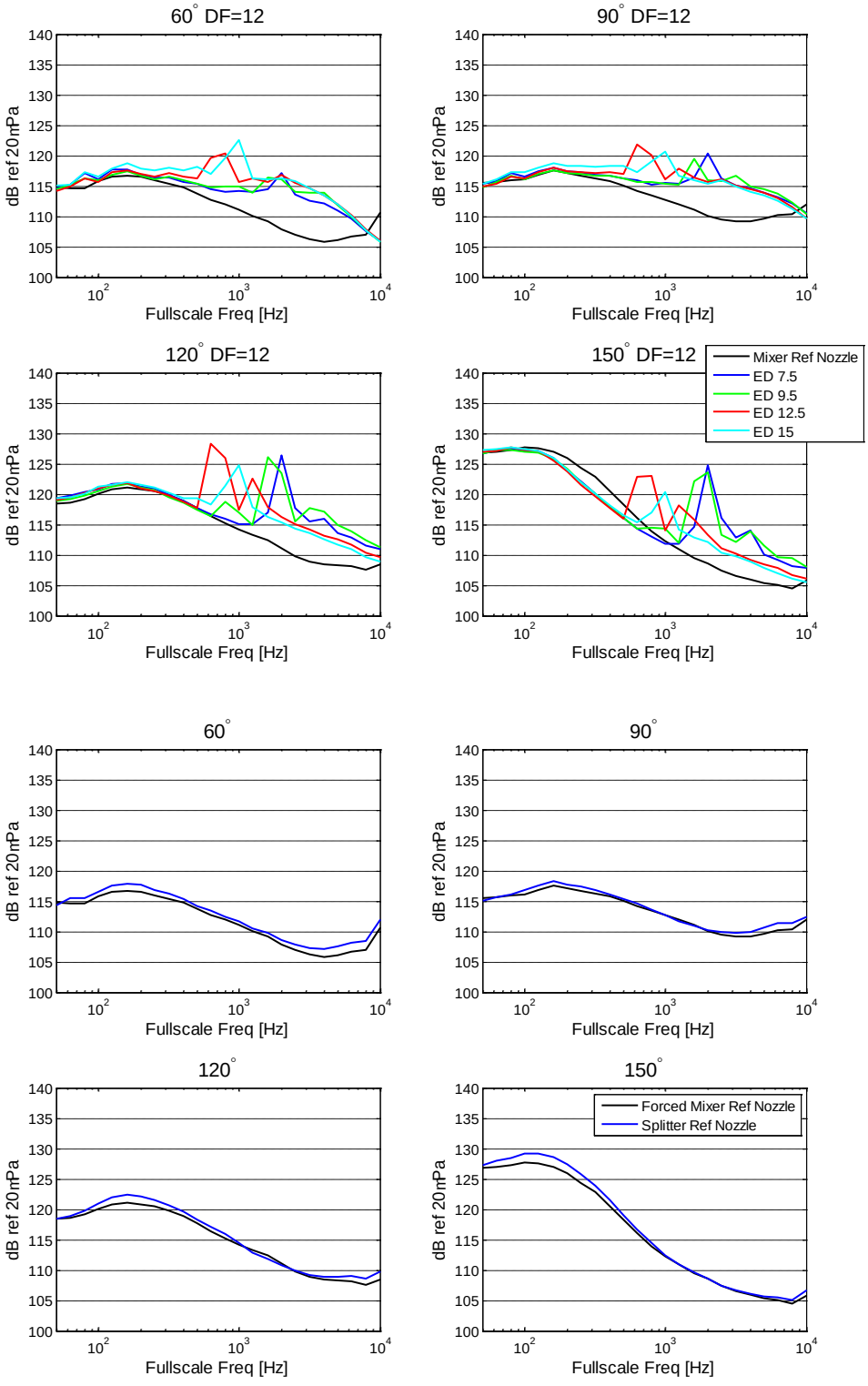
60° DF=12
90° DF=12
120° DF=12
150° DF=12
Mixer Ref Nozzle
ED 7.5
ED 9.5
ED 12.5
ED 15
60°
90°
120°
150°
Forced Mixer Ref Nozzle
Splitter Ref Nozzle
dB ref 20mPa
Fullscale Freq [Hz]

SETPOINT 043

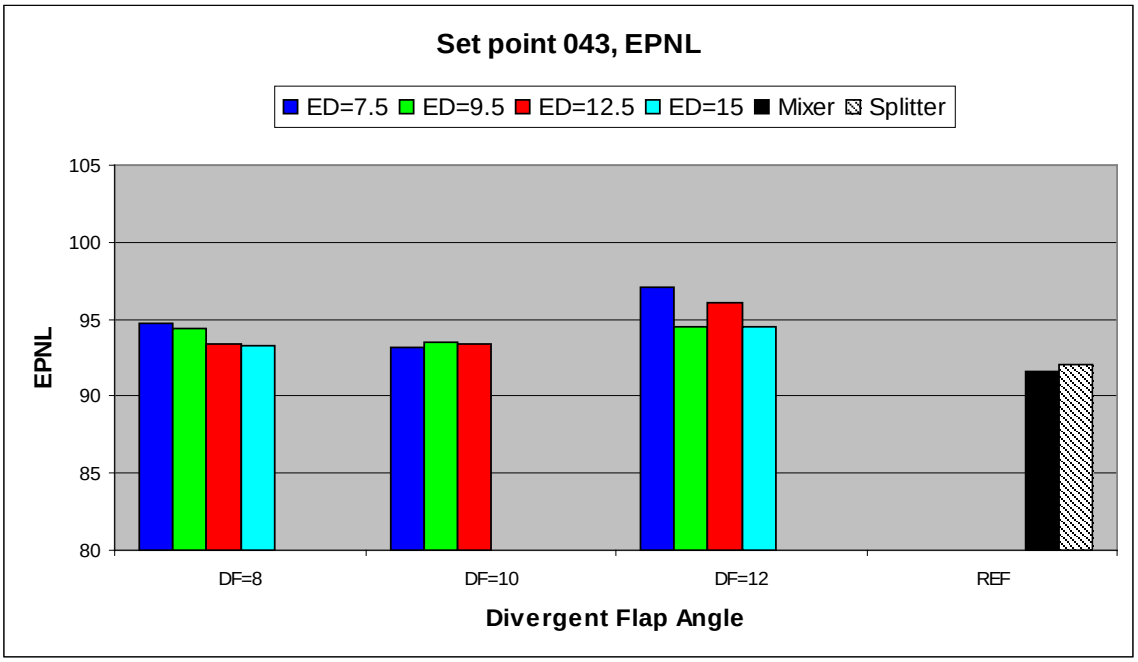

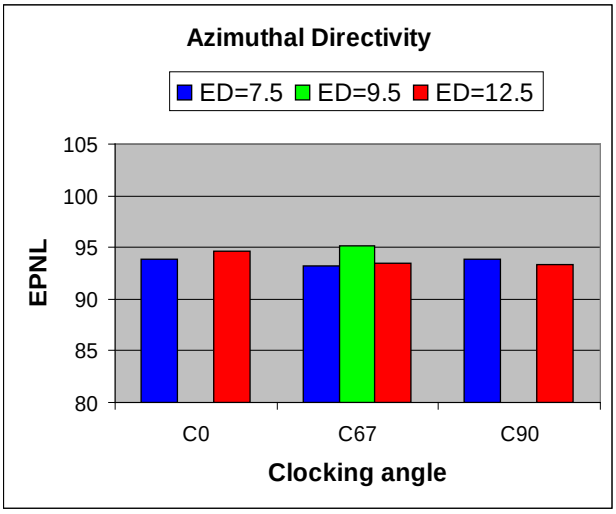

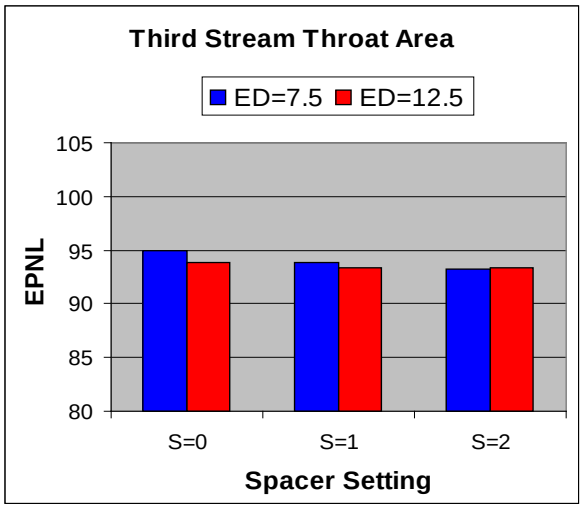

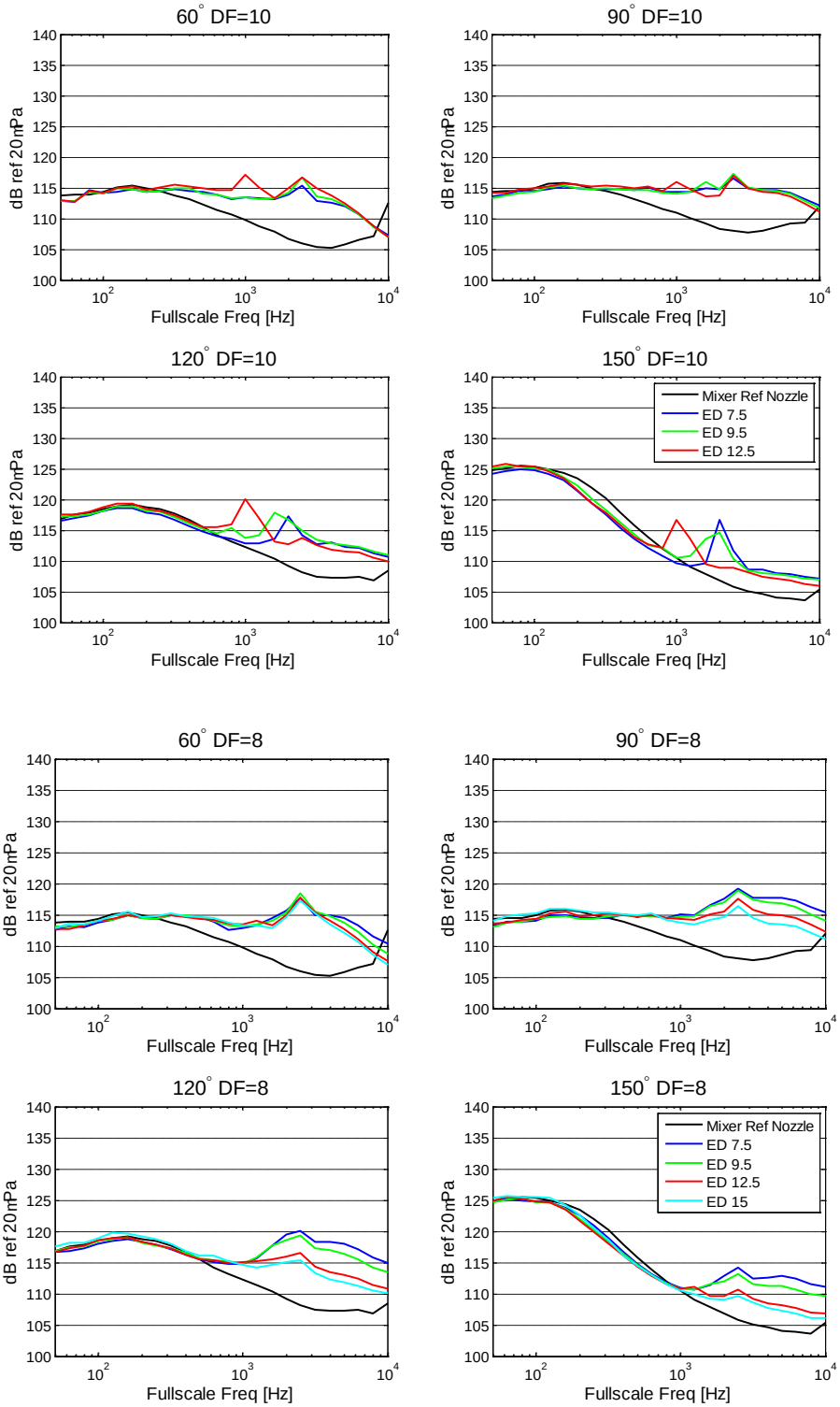
60° DF=10
90° DF=10
120° DF=10
150° DF=10
60° DF=8
90° DF=8
120° DF=8
150° DF=8
dB ref 20mPa
Fullscale Freq [Hz]
Mixer Ref Nozzle
ED 7.5
ED 9.5
ED 12.5
ED 15

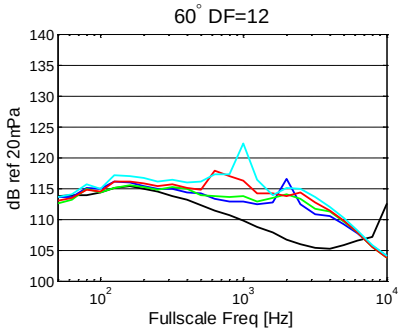
60° DF=12
dB ref 20mPa
Fullscale Freq [Hz]

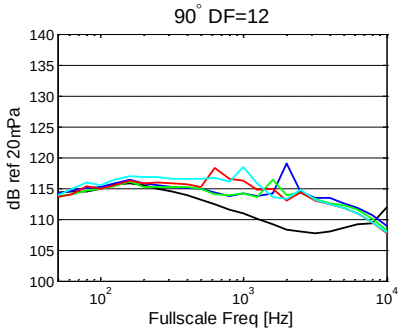
90° DF=12
dB ref 20mPa
Fullscale Freq [Hz]

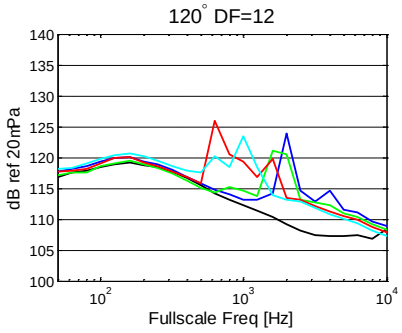
120° DF=12
dB ref 20mPa
Fullscale Freq [Hz]

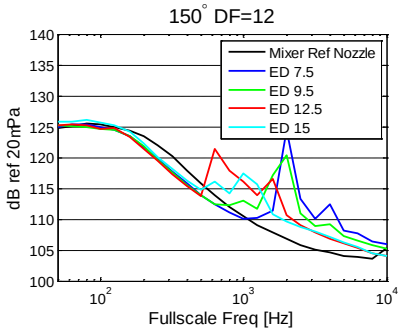
150° DF=12
Mixer Ref Nozzle
ED 7.5
ED 9.5
ED 12.5
ED 15
dB ref 20mPa
Fullscale Freq [Hz]

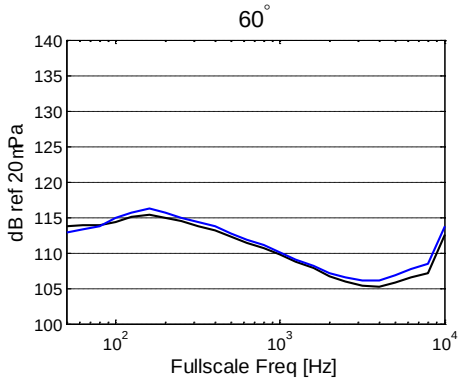
60°
dB ref 20mPa
Fullscale Freq [Hz]

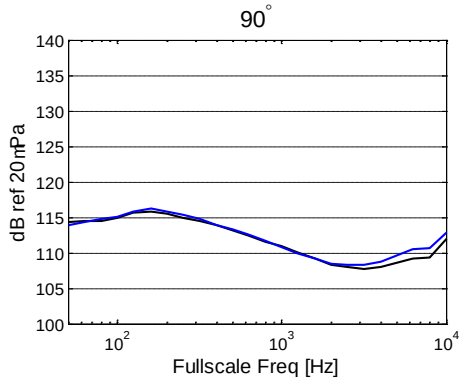
90°
dB ref 20mPa
Fullscale Freq [Hz]

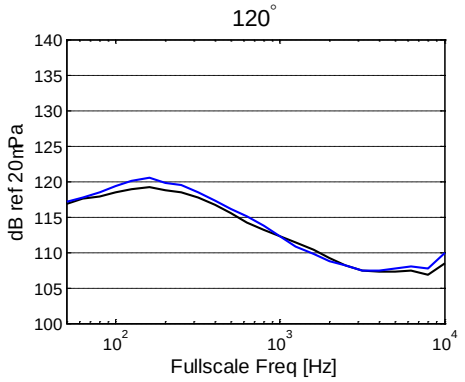
120°
dB ref 20mPa
Fullscale Freq [Hz]

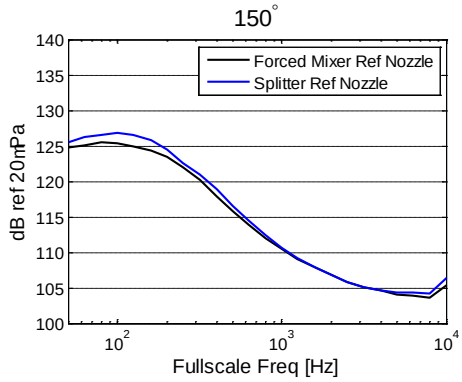
150°
Forced Mixer Ref Nozzle
Splitter Ref Nozzle
dB ref 20mPa
Fullscale Freq [Hz]

SETPOINT 063

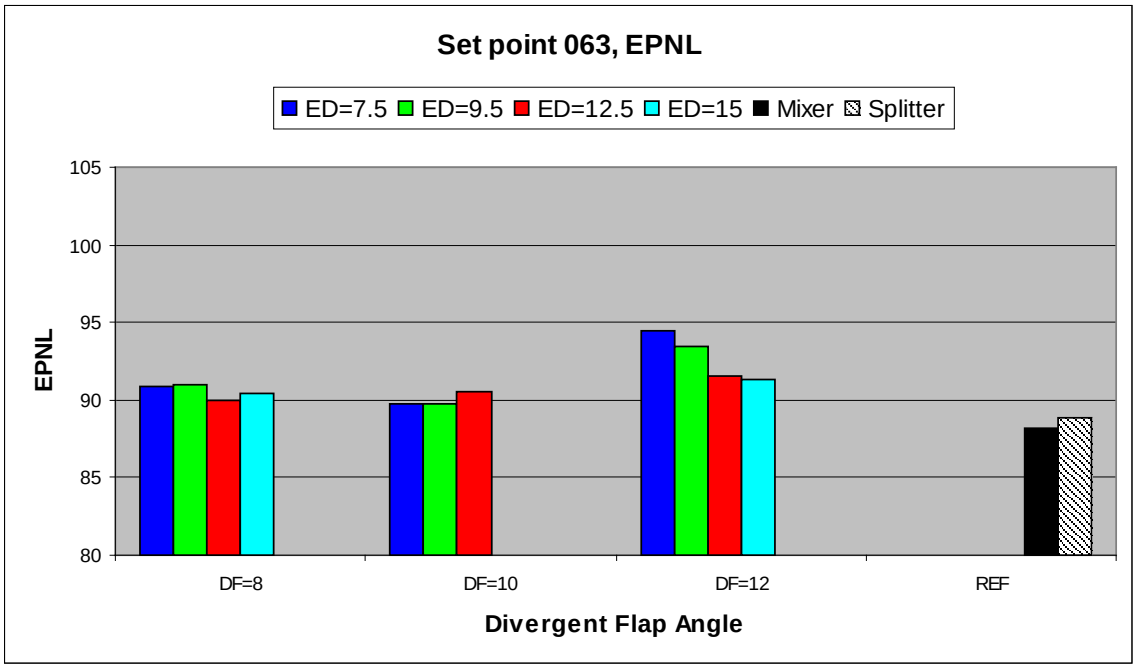

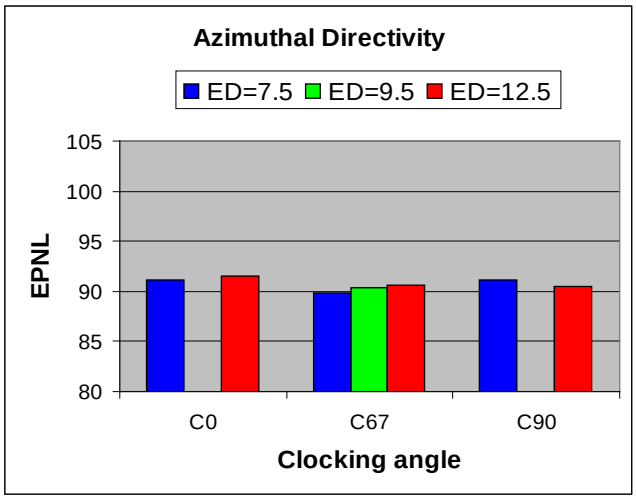

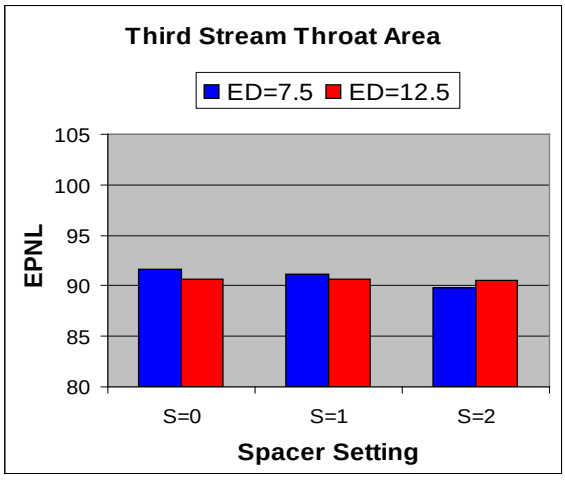

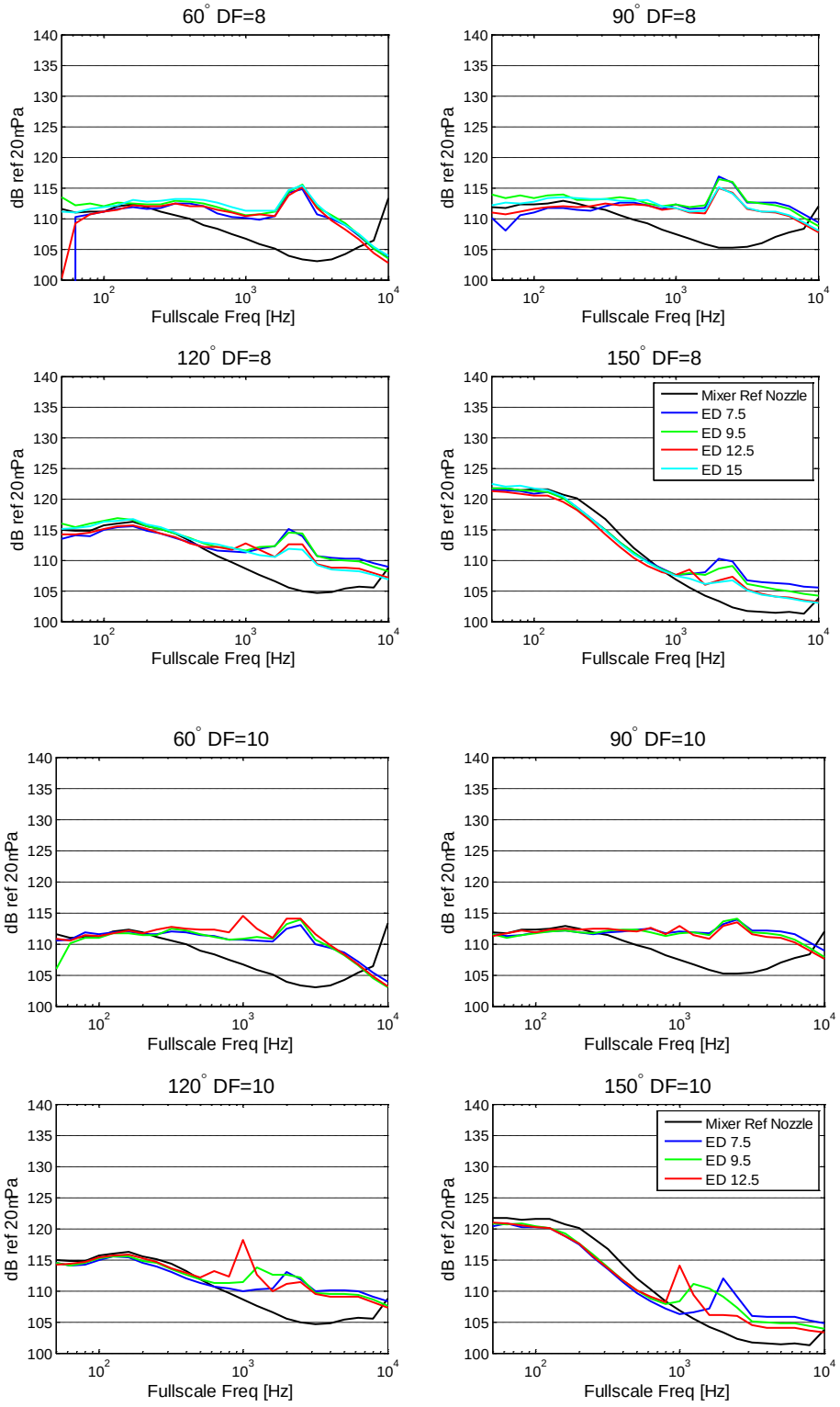
60° DF=8
90° DF=8
120° DF=8
150° DF=8
60° DF=10
90° DF=10
120° DF=10
150° DF=10
dB ref 20mPa
Fullscale Freq [Hz]
Mixer Ref Nozzle
ED 7.5
ED 9.5
ED 12.5
ED 15

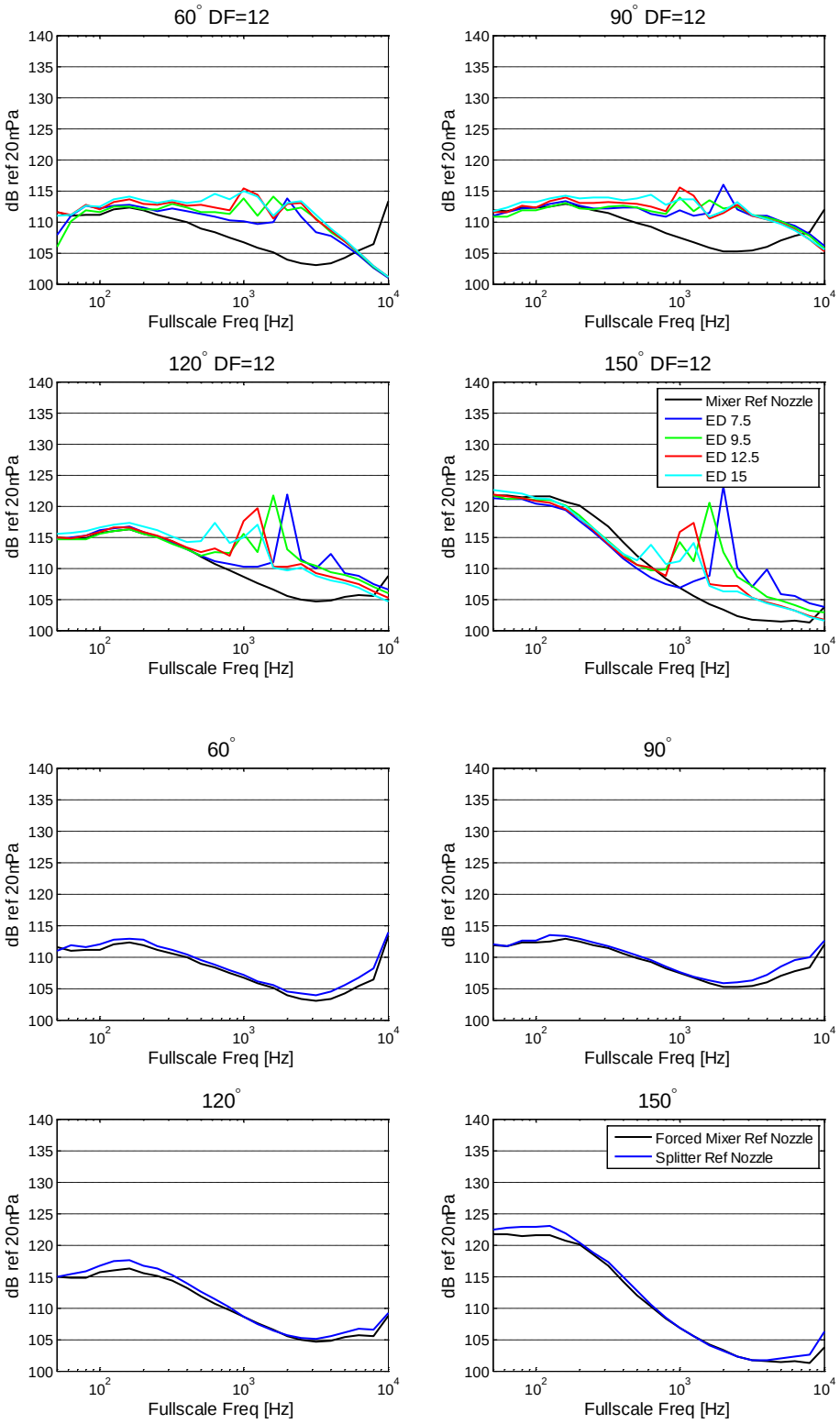
60° DF=12
90° DF=12
120° DF=12
150° DF=12
60°
90°
120°
150°
dB ref 20mPa
Fullscale Freq [Hz]
Mixer Ref Nozzle
ED 7.5
ED 9.5
ED 12.5
ED 15
Forced Mixer Ref Nozzle
Splitter Ref Nozzle

SETPOINT 082

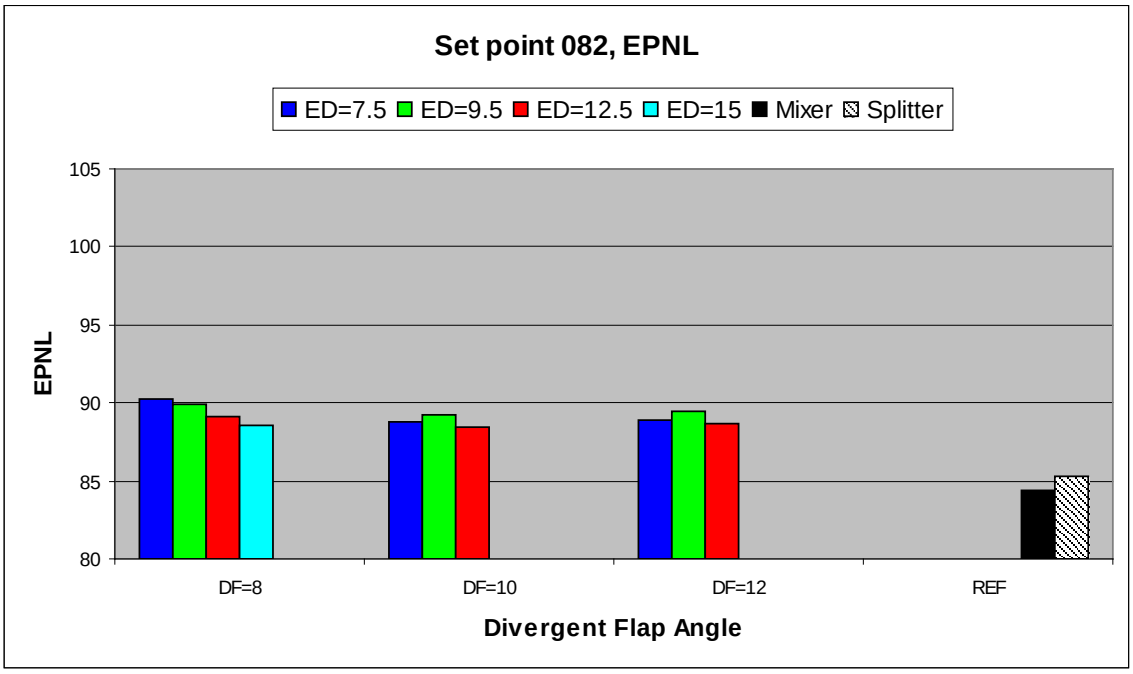

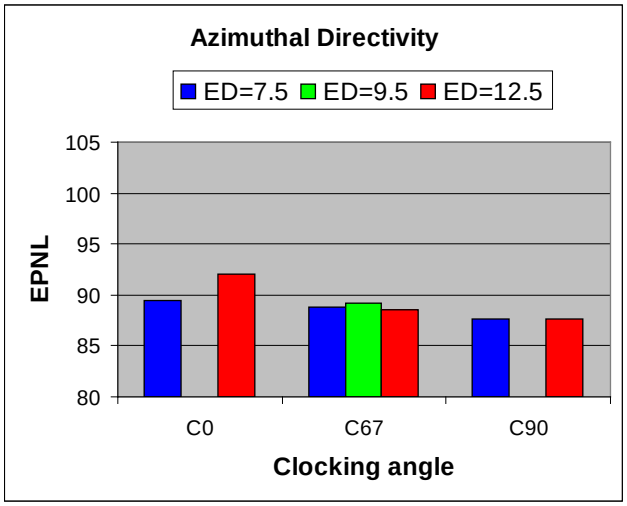

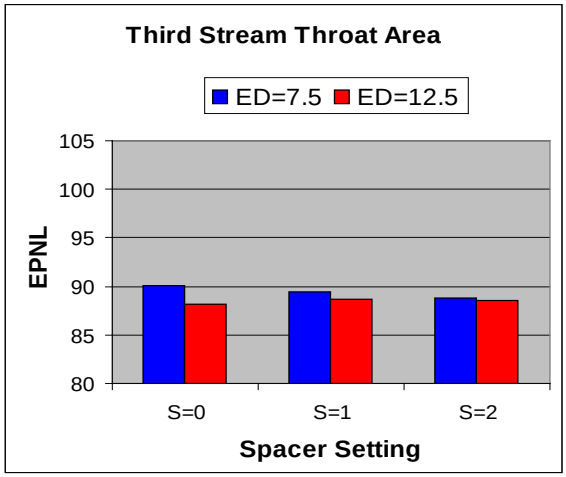

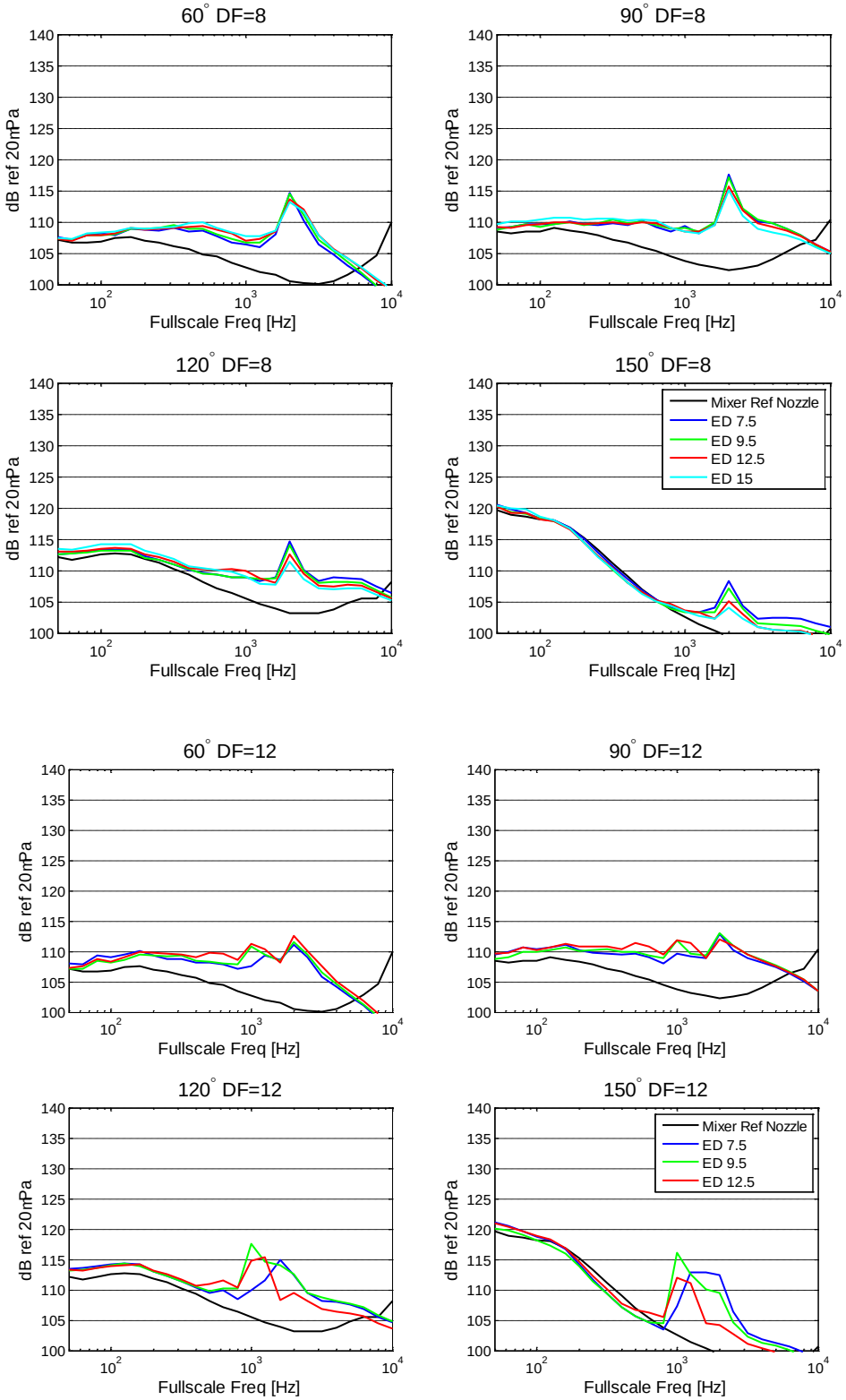
60° DF=8
90° DF=8
120° DF=8
150° DF=8
60° DF=12
90° DF=12
120° DF=12
150° DF=12
dB ref 20mPa
Fullscale Freq [Hz]
Mixer Ref Nozzle
ED 7.5
ED 9.5
ED 12.5
ED 15

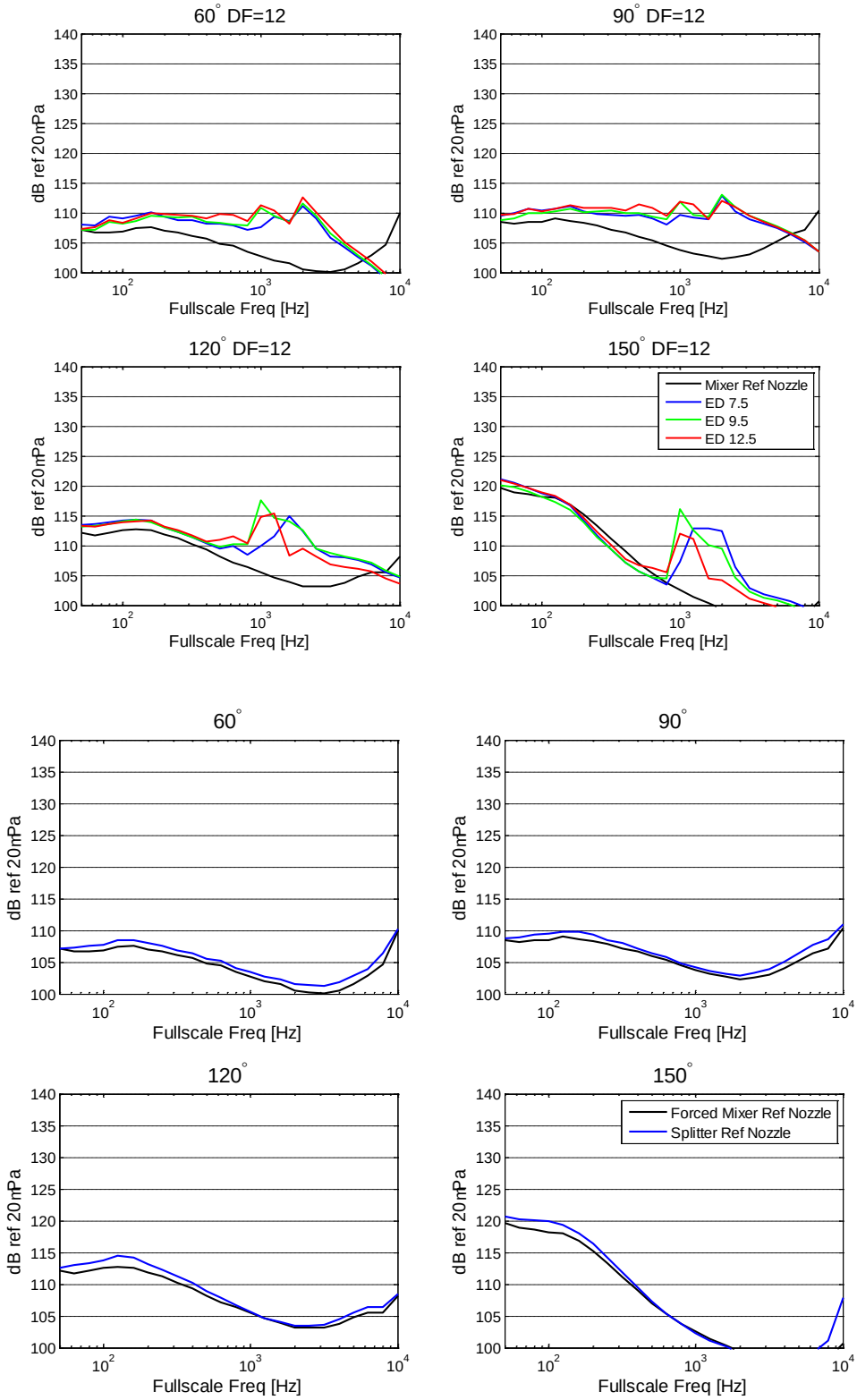
60° DF=12
90° DF=12
120° DF=12
150° DF=12
Mixer Ref Nozzle
ED 7.5
ED 9.5
ED 12.5
60°
90°
120°
150°
Forced Mixer Ref Nozzle
Splitter Ref Nozzle
dB ref 20mPa
Fullscale Freq [Hz]

SETPOINT 103

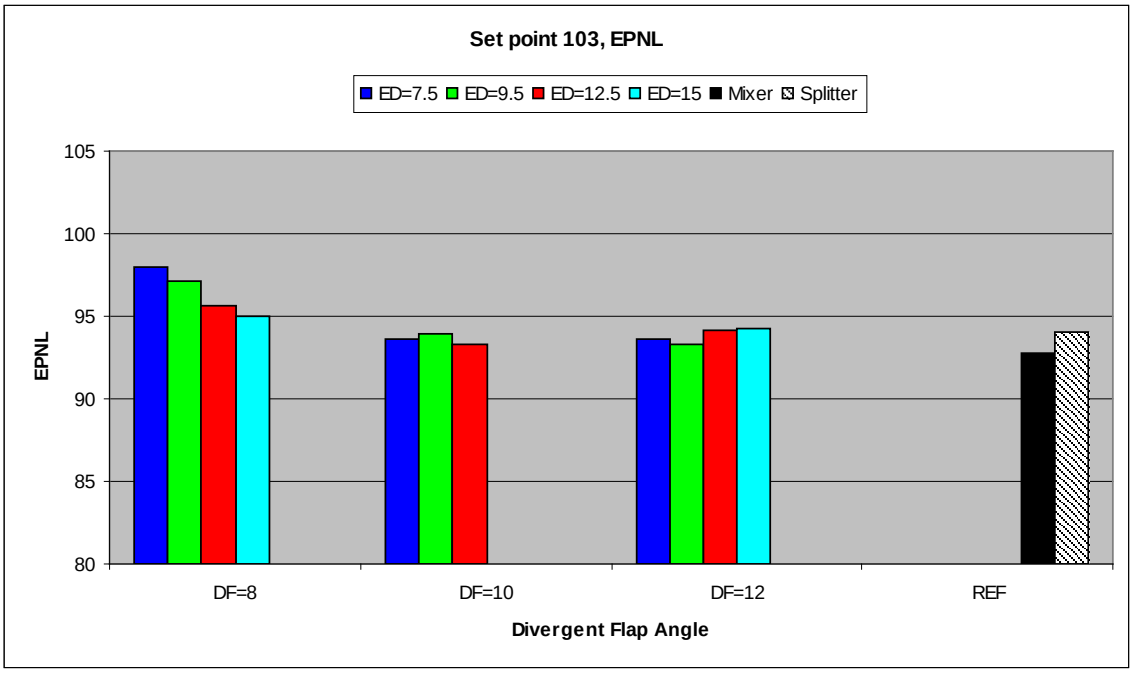

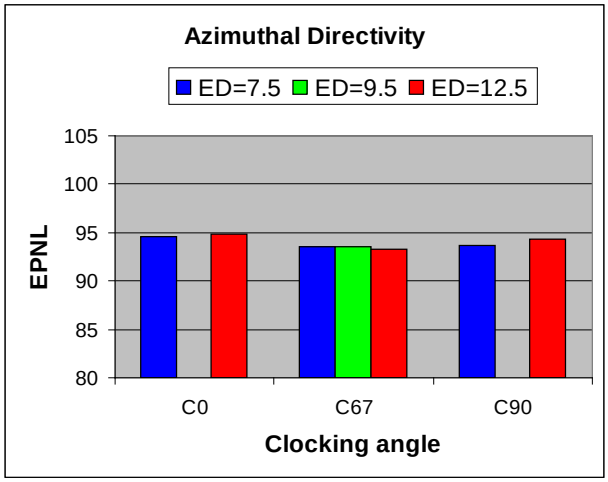

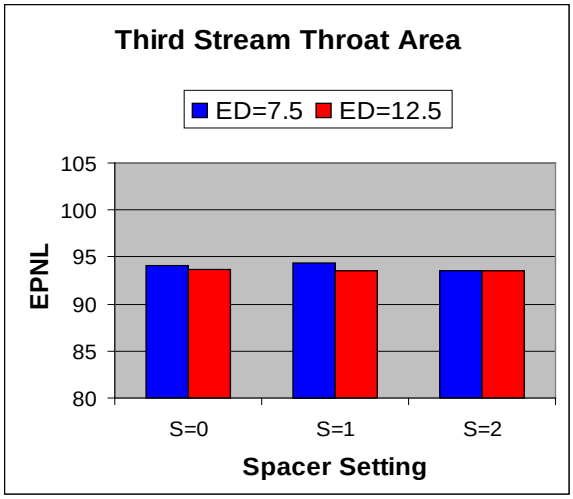

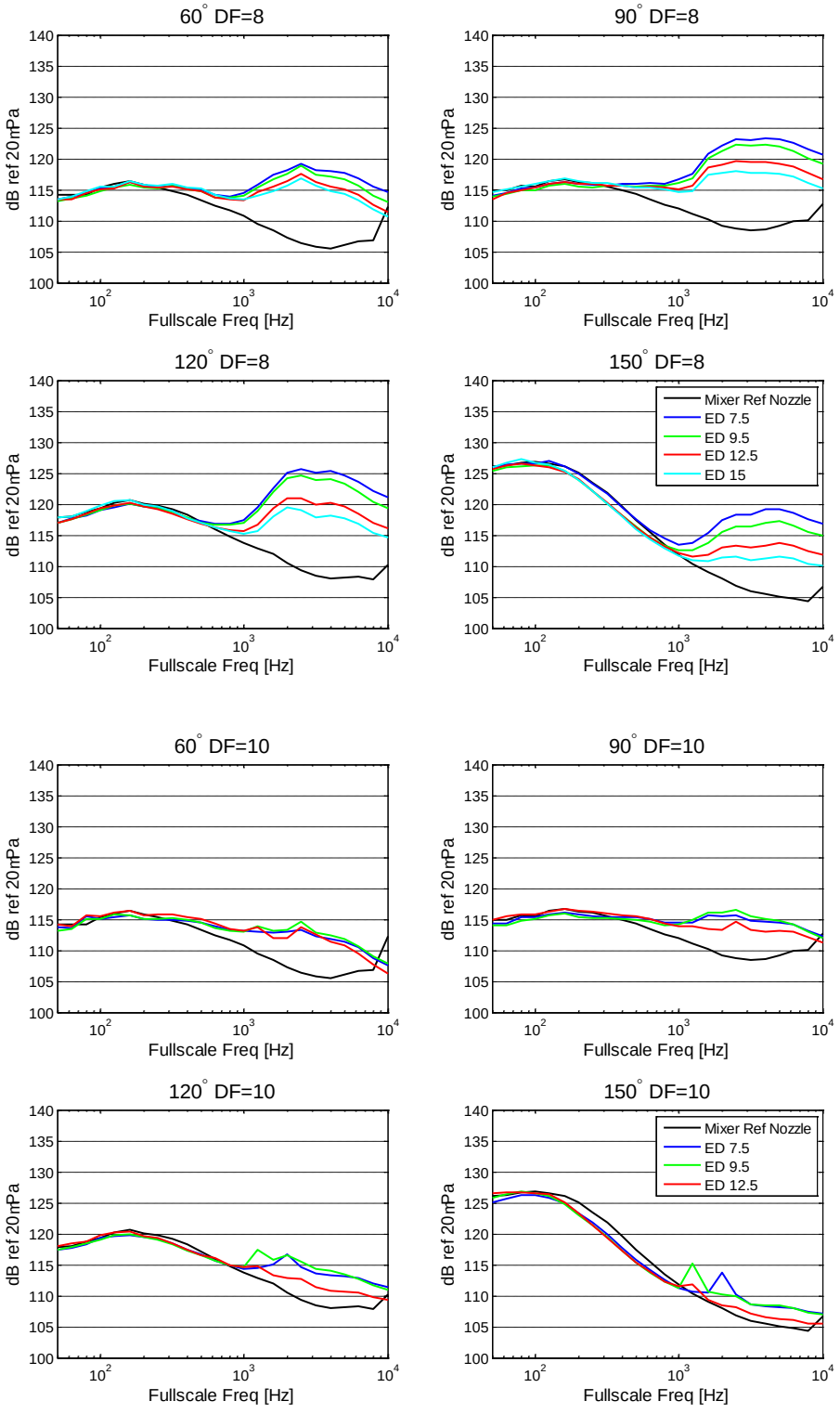
60° DF=8
90° DF=8
120° DF=8
150° DF=8
60° DF=10
90° DF=10
120° DF=10
150° DF=10
dB ref 20mPa
Fullscale Freq [Hz]
Mixer Ref Nozzle
ED 7.5
ED 9.5
ED 12.5
ED 15

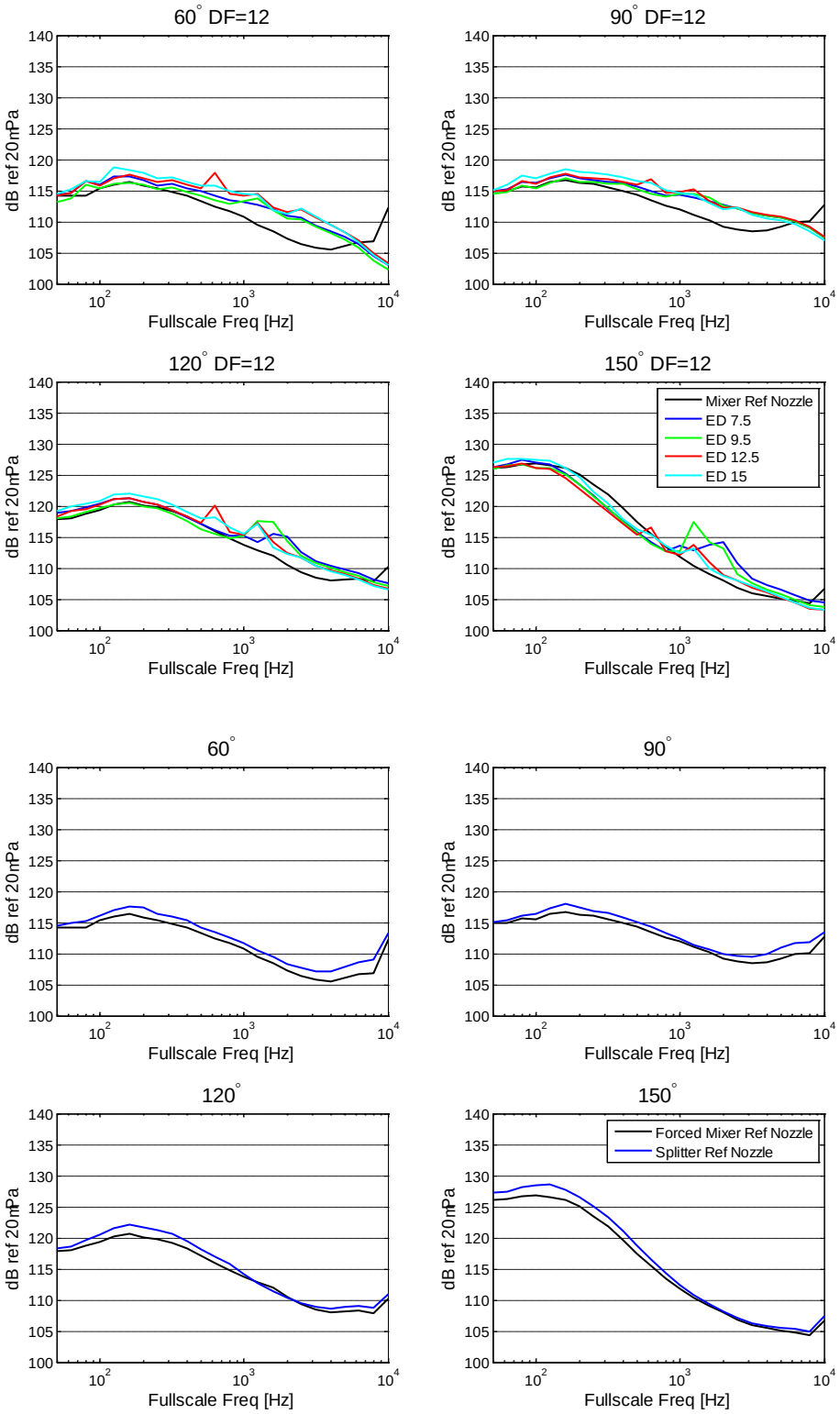
60° DF=12
90° DF=12
120° DF=12
150° DF=12
60°
90°
120°
150°
dB ref 20mPa
Fullscale Freq [Hz]
Mixer Ref Nozzle
ED 7.5
ED 9.5
ED 12.5
ED 15
Forced Mixer Ref Nozzle
Splitter Ref Nozzle

SETPOINT 113

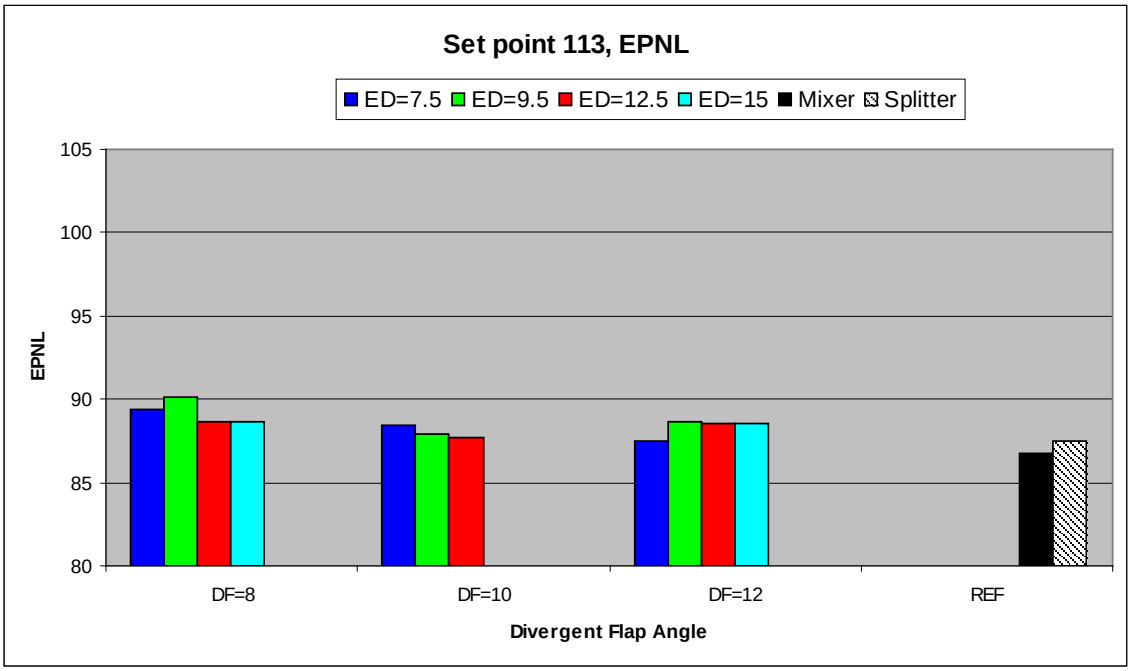

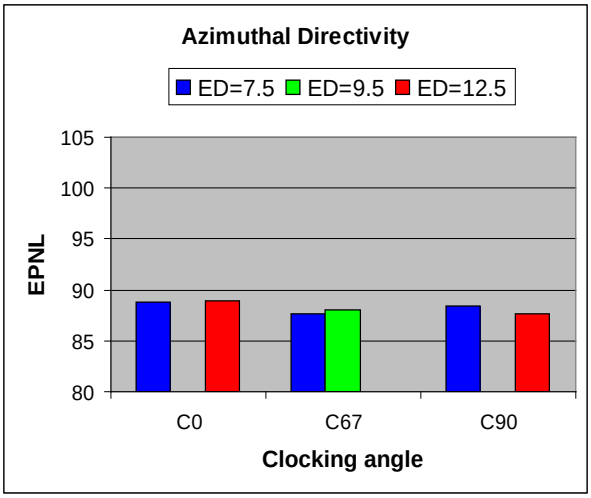

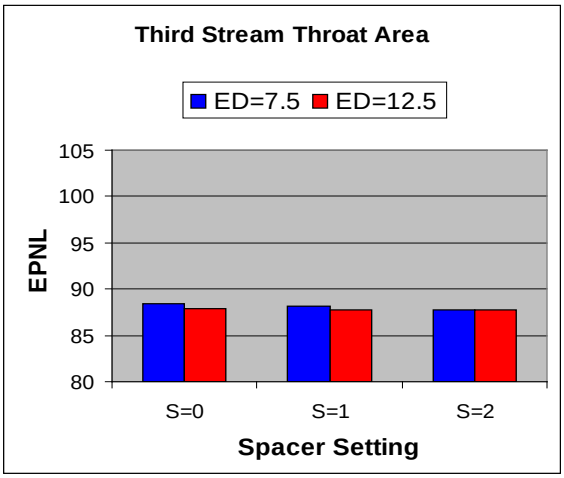

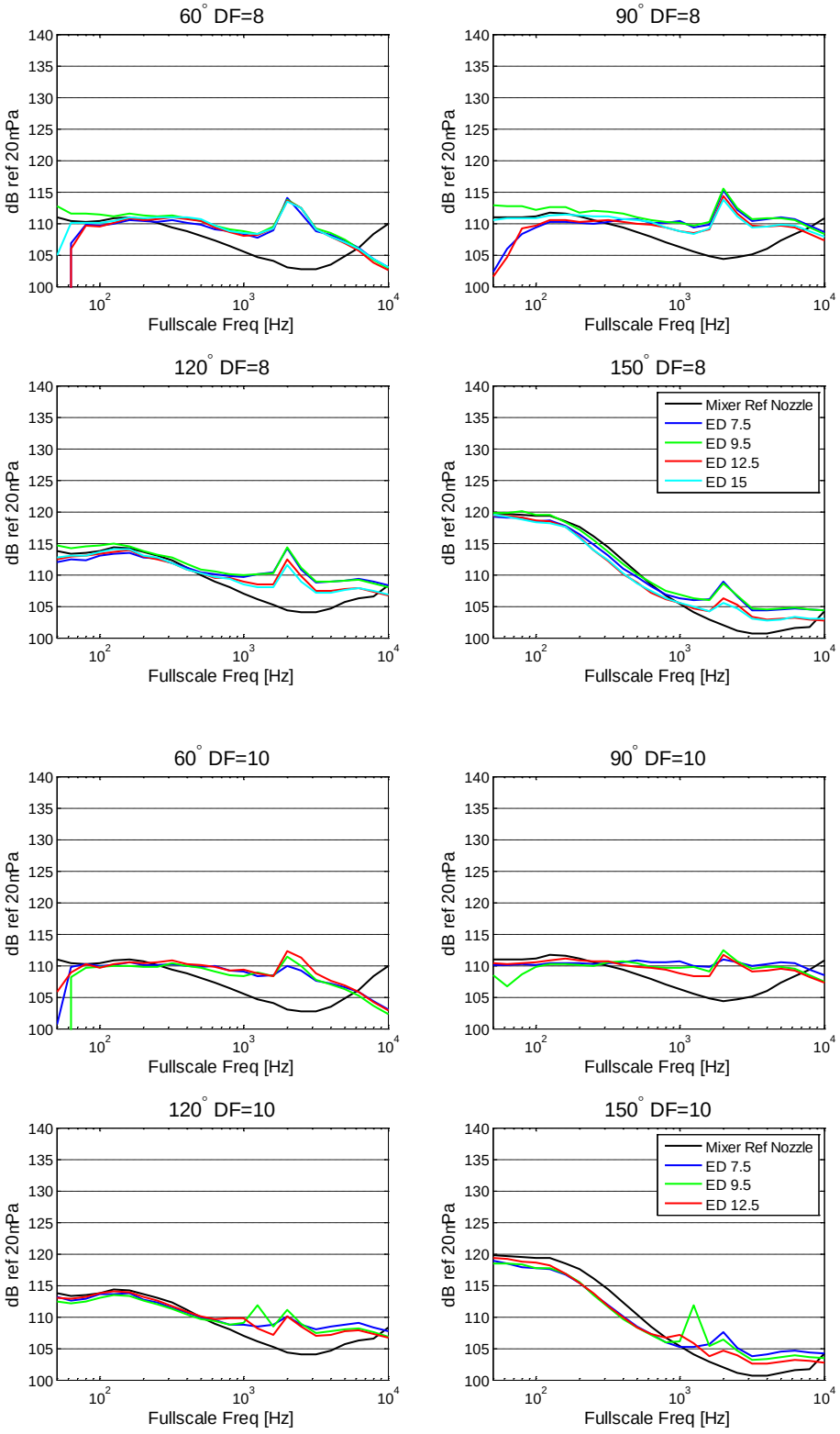
60° DF=8
90° DF=8
120° DF=8
150° DF=8
60° DF=10
90° DF=10
120° DF=10
150° DF=10
dB ref 20mPa
Fullscale Freq [Hz]
Mixer Ref Nozzle
ED 7.5
ED 9.5
ED 12.5
ED 15

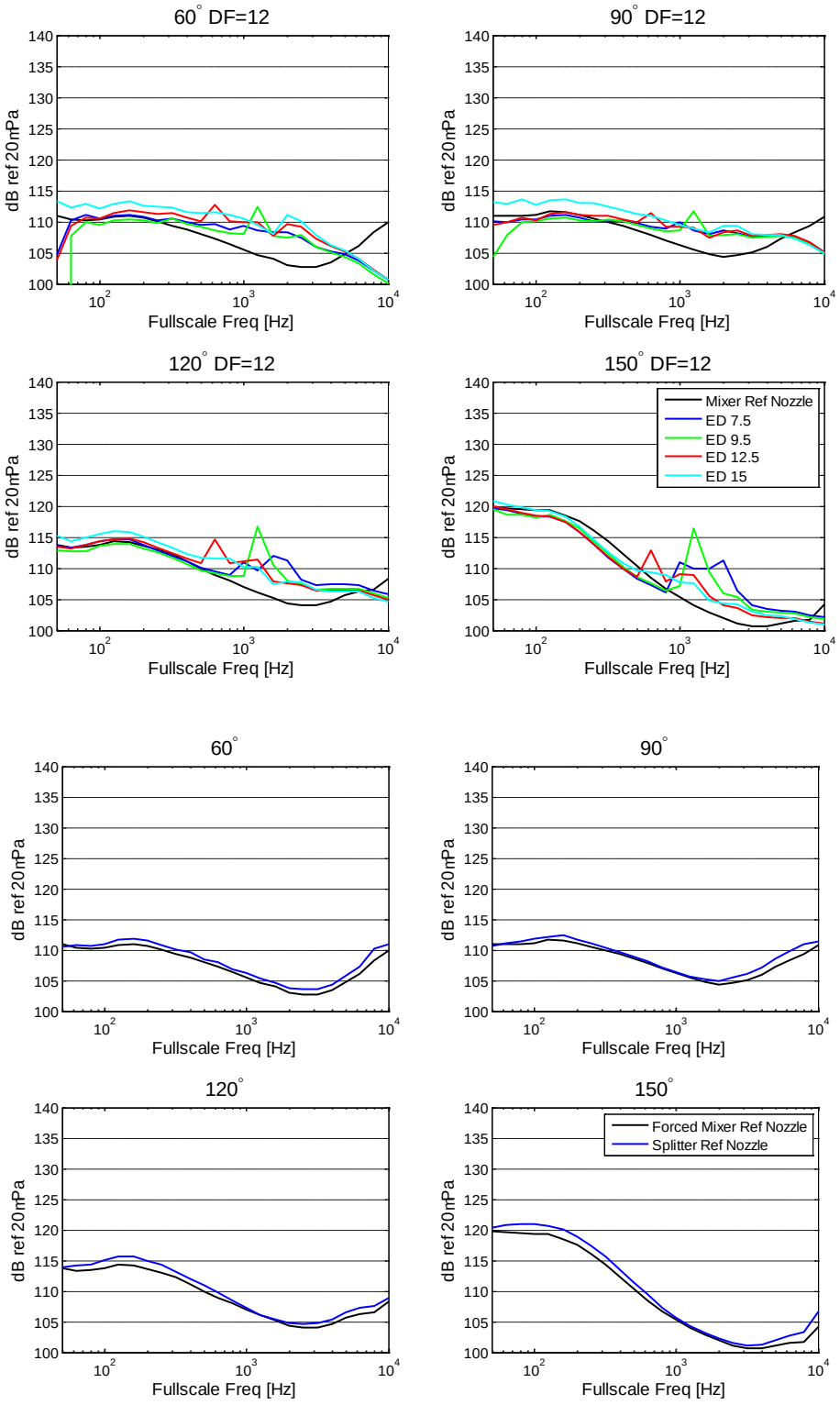
60° DF=12
90° DF=12
120° DF=12
150° DF=12
60°
90°
120°
150°
dB ref 20mPa
Fullscale Freq [Hz]
Mixer Ref Nozzle
ED 7.5
ED 9.5
ED 12.5
ED 15
Forced Mixer Ref Nozzle
Splitter Ref Nozzle

Appendix B.—GE GR Final Report

N+2 NRA – System Level Experimental Validations for Supersonic Transport Aircraft

Contract No. XF3178970E
Prime Contract (Lockheed Martin) NNC10CA02C

GE Global Research

Mugam Murugappan, Zac Nagel, Zhuyin Ren, Anupam Sharma, and Jixian Yao

GE Aviation

Steve Martens, Phil Viars and Stuart Hoelle

TABLE OF CONTENTS

EXECUTIVE SUMMARY

GE Global Research and Aviation supported Lockheed Martin in this NASA sponsored 'N+2 NRA – System Level Experimental Validations for Supersonic Transport Aircraft' program. Based on Lockheed Martin provided requirements and targets, GE modified a variable cycle engine propulsion system expected to meet or exceed the environmental goals set by NASA, from the recent N+3 program. This variable cycle engine propulsion system takes advantage of cooled cooling air to extend the overall pressure ratio of the engine and increase thermal efficiency. A low noise, high performance exhaust system takes advantage of the innovative variable cycle features, and two jet noise reduction technologies for lower noise capability. Heat addition is also incorporated in the exhaust to provide augmented transonic thrust and potential take-off noise abatement.

A scale model exhaust system incorporating two jet noise reduction technologies was designed, fabricated, and tested at NASA. The testing showed that the two jet noise reduction technologies do work, although there were excess noise sources at the lower cycle conditions due to nozzle flow separation. Heat addition was not found to be beneficial at cycles of interest for this program for take-off noise.

A list of technologies were compiled and ranked that could be applied to the supersonic inlet and fan module to help control the distortion that is present due the unique features of the Lockheed Martin supersonic inlet. These rankings were based on expected noise benefit, cost in terms of weight and performance, and a number of other risks.

The supersonic inlet was also combined with an existing single stage fan (SDT) and OGV configuration that was previously tested at NASA GRC to look at the acoustic impact of the distortion from the unique features of the supersonic inlet. The results show that the tonal noise source generated by the inlet distortion interacting with the fan was larger than the conventional noise source of the fan wakes interacting with the OGVs.

1 INTRODUCTION

GE Global Research and Aviation supported Lockheed Martin's contract from NASA on the N+2 System Level Experimental Validations for Supersonic Transport Aircraft. GE's support included propulsion system support through the modification of the variable cycle engine propulsion system to meet the vehicle requirements and environmental goals. The overall goals are shown in Figure 1. They cover sonic boom, airport noise, fuel efficiency, and emissions. The sonic boom, cruise speed, payload, and range were essentially used by Lockheed Martin to set the propulsion requirements that GE used to design the propulsion system. The airport noise, cruise emissions, and fuel efficiency were targets that GE assessed based on the propulsion system developed.

	N+1 Supersonic Business Class Aircraft (2015)	N+2 Small Supersonic Airliner (2020)	N+3 Efficient Multi-Mach Aircraft (Beyond 2030)
Environmental Goals			
Sonic Boom	65-70 PLdB	65-70 PldB	65-70 PLdB low boom flight 75-80 PLdB unrestricted flight
Airport Noise (cum below stage 3)	10 EPNdB	10-20 EPNdB	20-30 EPNdB
Cruise Emissions (Cruise NOx g/kg of fuel)	Equivalent to current Subsonic	< 10	< 5 & particulate and water vapor mitigation
Performance Goals			
Cruise Speed	Mach 1.6-1.8	Mach 1.6 -1.8	Mach 1.3 - 2.0 low boom flight Mach 1.3- 2.0 unrestricted flight
Range (n.mi.)	4000	4000	4000 - 5500
Payload (passengers)	6-20	35-70	100 - 200
Fuel Efficiency (passenger-miles per lb of fuel)	1.0	3.0	3.5 – 4.5

Figure 1 NASA Supersonic Goals.

The baseline propulsion system was a variable cycle engine with VAATE Phase III technology assumptions with an approximate 2018 TRL 6 technology availability date. The variable cycle engine architecture includes adaptive cycle features such as:

- Cooled Cooling Air (CCA) with modulated turbine cooling
- Low Noise/High Performance Exhaust System
- Controlled area turbine nozzle (CATN)
- Heat Addition

Together these technologies provide a propulsion system anticipated to meet the vehicle requirements and environmental goals.

GE also designed and fabricated a scale model exhaust system containing two jet noise reduction technologies. The jet noise reduction technologies are synergistic with the variable cycle features of the propulsion system. RANS CFD was run for the scale model to help design the features for good aero performance and structural integrity. RANS CFD was also run for both the sideline and cutback geometries and for a number of cycle conditions. The internal nozzle performance was calculated at each

condition. The scale model was tested at NASA GRC's HFJER facility in AAPL. The test was completed on schedule with no problems.

A list of technologies were compiled that could be applied to the supersonic inlet and fan module to help control the distortion that is present due the unique features of the supersonic inlet. These technologies were rated based on expected noise benefit, cost in terms of weight and performance, and a number of other risks. These Ratings result in a way to prioritize the technologies in terms of risk vs benefit and provide a method to determine which items to focus on.

The supersonic inlet was also combined with an existing single stage fan (SDT) and OGV configuration that was previously tested at NASA GRC to look at the acoustic impact of the inlet distortion due to the unique features of the Lockheed Martin supersonic inlet.

2 PROPULSION SYSTEM

2.1 PROPULSION SYSTEM OVERVIEW

The technology assumptions for this N+2 propulsion system were adjusted from a TRL 6 date of 2025 for the N+3 model to a TRL 6 date of 2018. The N+2 engine is a lower technology version of the conceptual NASA N+3 propulsion system delivered in 2009. The major impact of the lower technology level was designing to lower core temperatures, resulting in approximately 10% increase in weight. Also, for the N+2 program Lockheed Martin switched to a tri jet configuration and the engine was resized to the higher thrust requirements resulting in an increase in FPR and a larger engine size. In the end, the propulsion system is still designed to meet the N+2 airport noise and emissions goals.

2.1.1 TECHNICAL DESCRIPTION

2.1.1.1 VARIABLE CYCLE ENGINE PROPULSION SYSTEM

The advanced variable cycle engine uses VAATE Phase III level technologies with a TRL 6 date of 2018, and other technologies aimed at an entry into service (EIS) date of 2025. The engine architecture includes variable cycle features such as: Cooled Cooling Air (CCA) with modulated turbine cooling flow, high pressure (HP) controlled area turbine nozzle (CATN), and a variable area bypass injector (VABI). The high performance exhaust includes two jet noise reduction technologies. The exhaust also includes a heat addition capability.

2.1.1.2 COOLED COOLING AIR (CCA) ADVANCED THERMAL MANAGEMENT SYSTEM (TMS)

The CCA system, enables the engine to be designed at a higher overall pressure ratio (OPR) for improved thermal efficiency, by keeping the critical blade cooling air down to low levels. The CCA system reduces cooling flow requirements and enhances the high-pressure turbine (HPT) blade life. The system operates by removing a small portion of hot compressor discharge (CDP) air and ducting it out to a Surface Cooler heat exchanger. When mixed back in, this cooler air reduces the HPT blade cooling air which should enable achieving the hot section life margins required for sustained supersonic cruising at near maximum engine temperatures.

2.1.1.3 ADVANCED LOW NOX COMBUSTOR

As part of this program, an advanced low NOx combustor concept was assumed, leveraging work from the NASA Supersonic Low NOx Combustor contract studies. Meeting the N+2 cruise emission goal of EINOx = 10 g/kg fuel using a TAPS-type combustor will be a challenging goal for the supersonic N+2 program.

To achieve the N+2 NOx goal, an advanced technology development targeting an N+2 timeframe is necessary to reduce combustor residence time, cooling flow, pilot, and fuel/air mixing times. The beginnings of this development are currently being addressed in NASA Supersonic Low NOx Combustor contract studies. At the N+2 technology timing T4 will have to be limited to meet the goals.

2.1.2 EXHAUST SYSTEM

The exhaust system design is very important for supersonic vehicles since the nozzle performance is critical to the efficiency of the propulsion system as well as enabling jet noise technologies. The basic exhaust concept is a variable A8 and A9 axi-plug exhaust with a number of GE unique technologies added to improve performance and acoustics.

2.1.2.1 VARIABLE CYCLE ENGINE EXHAUST

The variable cycle engine propulsion system features an Axi-Plug exhaust system with two jet noise reduction technologies. The exhaust is cooled by bypass stream air. Some of the bypass air is used to cool the rear frame while some is used to cool the exhaust convergent nozzle upstream of the throat. Because of the variable cycle features, no bypass air is needed for the divergent section. Ceramic Matrix Composites (CMC) and other advanced composite materials are used extensively in the exhaust to minimize cooling requirements and weight.

2.1.2.2 HEAT ADDITION

The exhaust also has the capability of heat addition that is capable of augmenting the mixed temperature of the exhaust by a modest amount. The actual level of augmentation can be adjusted. There are no flame holders or fuel spray bars for the heat addition, so it has minimal impact on exhaust performance. Due to the low augmentation temperature and use of CMC materials, no additional cooling is required when the heat addition is used.

Heat addition is not intended to provide high levels of acceleration. The use of the heat addition may only prove beneficial during take-off where there might be some acoustic benefit and through climb pinch points where acceleration and ROC are low. For these types of aircraft, it is undesirable to have the engine sized by a pinch point, if it can be avoided. In follow-on detailed studies, the actual amount of heat addition could be adjusted to the minimum required at specific points in the mission.

2.1.2.3 VARIABLE GEOMETRY FEATURES

The exhaust has variable A8 and A9 (throat and exit area, respectively) capability through the use of a translating plug and cowl. The translating cowl also provides for a thrust reversing system. The center plug translates to control the inner exhaust throat and exit areas. The outer cowl has inner and outer translating shrouds that control the primary exhaust throat and exit area, respectively.

2.2 AIRFRAME REQRUIREMENTS

2.2.1 NASA N+3 GOALS

For the NASA N+3 Supersonic transport (SST) study, Lockheed Martin initially used a four engine, Mach 1.6 cruising, 100 PAX vehicle of approximately 300 klbs, similar to that shown in Figure 2. The overall objectives or goals for NASA NRA N+2 are shown in the table in Figure 3. The engine is expected to achieve challenging performance, acoustic and emissions goals:

- Stage III –26 dB at takeoff,
- Cruise EI NOx level no higher than 10 g/kg of fuel.
- Fuel Efficiency > 3.0 PAX nm/lb_{fuel}

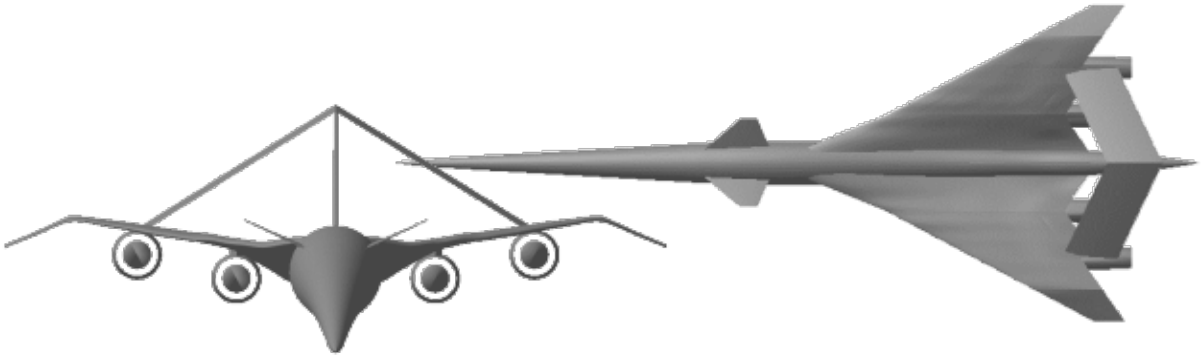

Figure 2 Lockheed Martin Quad-Jet 100 PAX Supersonic Transport.

N+2 Environmental Targets & Performance Goals (2020)	
ENVIRONMENTAL GOALS	
Sonic Boom	65-70 PLdB
Airport Noise (cumulative from stage 3)	-26 EPNdB (SL @ 90% PLR < S3 -5)
Cruise Emissions (Cruise NOx g/kg of fuel)	< 10
PERFORMANCE GOALS	
Cruise Speed	Mach 1.6
Range	4000 - 5500 nm
Payload (passengers, PAX)	100
Fuel Efficiency (PAX-miles per lb of fuel)	> 3.0

Figure 3 NASA N+2 Supersonic Goals / Requirements.

To best reflect overall mission efficiency, NASA also developed a Figure of Merit (FoM) for fuel efficiency around specific range and passenger load (PAX). The FoM is #PAX * (range / block fuel). Range/block fuel is specific range or V0 / fuel flow. Specific range can also be presented in terms of V_0 * (L/D) / (SFC) / Weight. The engine obviously has a direct impact on SFC, but the size of the engine can impact aircraft L/D and weight. Due to the impact of aircraft size on Sonic Boom, the passenger load (PAX) was focused at 100 and the range typically near 4,500 nm.

2.2.2 INSTALLATION EFFECTS

Lockheed Martin requested that propulsion installation effects be included in the installed engine data. To model these losses Lockheed Martin provided inlet performance updates. Inlet recovery was provided as a function of Mach number only. No off-design airflow characteristics were provided. The recommended inlet airflow schedule in terms of turndown ratio versus Mach is used to set airflow for the fan in the power management system. Along with the inlet recovery table, Lockheed Martin provided inlet critical additive drag (Cdcrit). Cdcrit is only provided as a function of Mach number. No off-design airflow characteristics were provided. Inlet drag then is Cdcrit * Q* Acap. There is no inlet bleed, so inlet drag only has a significant impact at transonic speeds. The inlet drag is represented in the installed thrust.

In addtion for the N+2 program Lockheed Martin provided plume impacts on nozzle afterbody drag. The Cd provided is also included as part of the installation drag.

The variable cycle engine propulsion system has an Axi-Plug exhaust with excellent nozzle performance and acoustic suppression capability. Since the nozzle has variable A9 capability, the area ratio can vary and high performance can be achieved for multiple operating conditions. Tests and CFD analysis have shown that overall exhaust performance can be relatively unaffected by multiple streams in the exhaust.

For customer offtakes, Lockheed Martin initially provided the table shown in Figure 4 for the Quad-jet configuration. These were updated later to 2.0 lb/s compressor interstage bleed, 1.67 lb/s bypass bleed, and 107 hp taken from the HP shaft for the Tri-jet configuration as shown in Figure 5.

Engine Bleed and HorsePower Extractions – Nominal (per engine) for Quad-jet		
Horsepower	80	
Engine Bleed - Fan	1.25 lbm/sec	10 psi
Engine Bleed - Intermediate	1.5 lbm/sec	75 psi
T Fuel to Engine (average)	155° F (235° F Limit)	(Ground 250° F Limit)

Figure 4 Lockheed Martin NASA N+2 Quad-jet Bleed and Horsepower extraction requirements.

Engine Bleed and HorsePower Extractions – Nominal (per engine) for Tri-jet		
Horsepower	106.7	
Engine Bleed - Fan	1.67 lbm/sec	10 psi
Engine Bleed - Intermediate	2.0 lbm/sec	75 psi
T Fuel to Engine (average)	155° F (235° F Limit)	(Ground 250° F Limit)

Figure 5 Lockheed Martin NASA N+2 Tri-jet Bleed and Horsepower extraction requirements.

2.2.3 THRUST REQUIREMENTS

When Lockheed Martin first kicked off the N+2 program their aircraft configuration was still a four engine aircraft, very similar to the previous N+3 configuration. Lockheed Martin's thrust requirements for the N+3 Quad-jet are shown in Figure 6.

Thrust Requirements (per engine) for N+3 Quad-Jet			
Mach Number	**Altitude – ft**	**Installed Thrust – lbf**	**Inlet & Boattail Drag: CD (Re: Capture Area, ISA)**
0.0 **0.3**	**0** **0**	**25,500 ISA+15C** **22,500 .ISA+15C**	**0** **0**
1.1	**35,000**	**7,000..ISA+10C day required** 8,000 desired (low boom)	**0.113**
1.6	**50,000**	**5,500 ISA+0C day desired**	**0.0039**

Figure 6 Lockheed Martin NASA N+2 Tri-jet Initial Supersonic Propulsion Requirements.

Lockheed Martin's N+2 updated Quad-Jet thrust requirements are shown in Figure 7. Takeoff, transonic and Mach 1.6 Top of Climb (TOC) thrust requirements are a little higher than the previous N+3 requirements. In addition Lockheed Martin is asking for TOC thrust capability up to ISA+5C which will impact core sizing temperatures.

Thrust Requirements (per engine) for N+2 Quad-Jet			
Mach Number	**Altitude – ft**	**Installed Thrust – lbf**	**Inlet & Boattail Drag: CD (Re: Capture Area, ISA)**
0.3	**0**	**24,500 .ISA+20C**	**0**
1.1	**35,000**	**7,800..ISA+10C day required**	**0.113**
1.6	**50,000**	**6,000 ISA+5C day desired**	**0.0039**

Figure 7 Lockheed Martin NASA N+2 Quad-jet Initial Supersonic Propulsion Requirements.

Later on in Phase 1 Lockheed Martin determined that they were going to change their N+2 configuration to a Tri-jet. Initial thrust requirements for the Tri-jet are shown in Figure 8. The ISA+5C TOC capability has now been dropped, but the TOC thrust requirement has gone up by a third. Also, note that Lockheed Martin has now requested that plug nozzle plume effects be included in the installed thrust.

Thrust Requirements (per engine) for N+2 Tri-Jet			
Mach Number	**Altitude – ft**	**Installed Thrust – lbf**	**Inlet & Boattail Drag: CD (Re: Capture Area, ISA)**
0.3 **0.3**	**0** **0**	**34,900 +15C day (Max 100%)** **29,100 +15C day (PLR 83.3%)**	**0** **0**
1.1	**35,000**	**8,600 +10C day required** 12,800 desired (low boom)	**0.113+0.042 (Plume)=0.155**
1.6	**50,000**	**8,600 +0C day desired**	**0.0039 + 0.0000 (ref)**

Figure 8 Lockheed Martin NASA N+2 Tri-jet Initial Supersonic Propulsion Requirements.

After the initial engine was sized, a final set of thrust requirements for this Phase were received, shown in Figure 9. The preliminary engine was still capable of meeting this thrust. Although it now has excess thrust at Mach 1.6 TOC, due to the progression of the four to the three engine configuration and relative changes between take-off, transonic, and cruise thrust requirements. A trade study of engine size and FPR might be desirable to best optimize the system FoM and noise.

Thrust Requirements (per engine) for N+2 Tri-Jet			
Mach Number	**Altitude – ft**	**Installed Thrust – lbf**	**Inlet & Boattail Drag: CD (Re: Capture Area, Std Day)**
0.3 **0.3**	**0** **0**	**34,900 +15C day (Max 100%)** **29,100 +15C day (PLR 83.3%)**	**0** **0**
1.1	**25,000** **35,000**	**15,600 +10C day required** 12,800 desired (low boom)	**0.113+0.042 (Plume)=0.155**
1.6	**50,000**	8,200 +0C day desired	**0.0039 + 0.0000 (ref)**

Figure 9 Lockheed Martin NASA N+2 Tri-jet Final Supersonic Propulsion Requirements.

2.3 PROPULSION SYSTEM DESIGN

2.3.1 VARIABLE CYCLE ENGINE PROPULSION SYSTEM

Based on prior IR&D studies supporting Lockheed designs, the variable engine cycle architecture is set to meet the program airport noise goals. The core is initially sized to keep max cycle average T41 under VAATE T41 limit throughout the flight envelope. The core pressure ratio (CPR) is set to keep the maximum cycle average T3 under VAATE T3 limits. The core operating line stall margin is initially set to ensure sufficient margin for operability concerns. The compressor is typically setup at a speed to limit

maximum physical speeds and T3. The core size and CPR for the design is then iterated again to stay within the T3 and T4 band discussed in Section 2.1.1.3 to meet the emissions goal.

Overall, each engine design is sized to match Lockheed Martin thrust requirements as defined in Section 2.2.3. Heat addition can either be on or off depending on demand. The Axi-Plug exhaust has partially variable A8 and A9, which can be adjusted to accommodate the heat addition and still maintain near peak efficiency across the operating range.

2.3.2 N+2 QUAD-JET SIZING

The first engine was designed to meet Lockheed Martin's Quad-Jet thrust requirements as shown in Figure 7. It was desired to maintain the same engine size as much as possible. Since T3 will need to be lower than the previous N+3 engine, OPR will be down and therefore, thermal efficiency will be lower. Since T4 and T41 are lower than the previous N+3 engine, the core will need to be larger, decreasing BPR and again lowering thermal efficiency. Lower thermal efficiency drives the engine's exhaust exit temperatures up, and therefore thrust. The drop in thermal efficiency made it possible to meet the N+2 Quad-Jet thrust requirements without changing the engine size

- Takeoff (Mach 0.3, SL) – 26400 lb (MB), 21200 lb (dry)
- Transonic (Mach 1.1, 35000 ft) - 10900 lb (MB), 7300 lb (dry)
- TOC (Mach 1.6, 50000 ft) - 6050 lb (dry)

As discussed in Section 2.2.2, the fuel lower heating value was assumed to be 18620 BTU/lbm to account for a T fuel of 155° F. This value is 1.2 % greater than the earlier N+3 value which will provide a comparable decrease in fuel burn.

The overall performance for this N+2 Quad-Jet engine relative to the N+3 design was expected to be

- Weight will increase by 10%
- Length will increase by 4%
- Thrust will increase by 4%
- Fuel flow will increase by 4.5%
- SFC will increase by 0.5%

2.3.3 N+2 TRI-JET SIZING

As mentioned earlier, later in the program, Lockheed Martin determined that a Tri-Jet configuration was better suited to meeting N+2 program goals. A preliminary study to resize the engine to Lockheed Martin's initial tri-jet thrust requirements (Figure 9) was conducted. A target of 35,000 lbs of thrust at SLS max was set. The engine was also sized to achieve 15,000 lbs of thrust at the transonic pinch point to provide additional transonic climb margin. TOC thrust at Mach 1.6 was set at 8,600 lbs of thrust. Since the three engine TOC thrust requirement is up somewhat relative to the previous 4 engine thrust requirement, the FPR was increased to minimize the size impact. The variable cycle engine propulsion system has additional noise suppression capability over a regular turbofan at higher FPR's. The thrust capability of this new engine would be

- Takeoff (Mach 0.3, SL) – 37k lb (heat addition), 30k lb (dry)

- Transonic (Mach 1.1, 35000 ft) - 15k lb (heat addition), 10k lb (dry)
- TOC (Mach 1.6, 50000 ft) - 8640 lb (dry)

The engine airflow is a little more than one third higher than the original airflow size of the Quad-jet engine to meet the relatively higher thrust requirements.

As was mentioned, earlier the final Tri-jet thrust requirements (Figure 9) came late in this Phase of the program and there has not been time or scope to perform another iteration on the engine. The latest takeoff analysis is indicating that less thrust is required than was estimated in earlier studies, so the engine is throttled back more at takeoff and climbout. These shifts in requirements might imply a benefit to shrinking the engine down while maintaining climb thrust. At this stage, a trade study on engine size, FPR, use of heat addition and acoustic capability, factoring in results from the nozzle tests would be desirable.

3 AEROACOUSTIC NOZZLE

3.1 NOZZLE GEOMETRY

The GE nozzle concept contains two jet noise reduction technologies. To simulate the engine conditions during two key points of the takeoff (sideline and cutback), two interchangeable nozzles were designed and fabricated to be installed and tested on the NASA HFJER rig.

3.2 CFD

CFD and a stress and thermal analysis were conducted throughout the model design phases to ensure a robust scale model system design.

3.3 RANS N+2 NOZZLE PLUME ANALYSIS

RANS CFD was run on the scale model hardware design to look at the plume generated by the nozzle. The CFD domain is shown in Figure 10 along with the mesh of the 180 degree sector of the scale model. The dimension of the CFD domain is 30 nozzle diameters wide at the inlet, 50 nozzle diameters wide at the outlet, and 80 nozzle diameters in length. A non-uniform pure hexahedral mesh with approximately 12 million cells/elements was created using ICEM CFD mesher. The maximum cell squish is 0.44 and the maximum aspect ratio is about 800. The majority of the cells are concentrated near the nozzle exit region for accurate resolution of the shear layers.

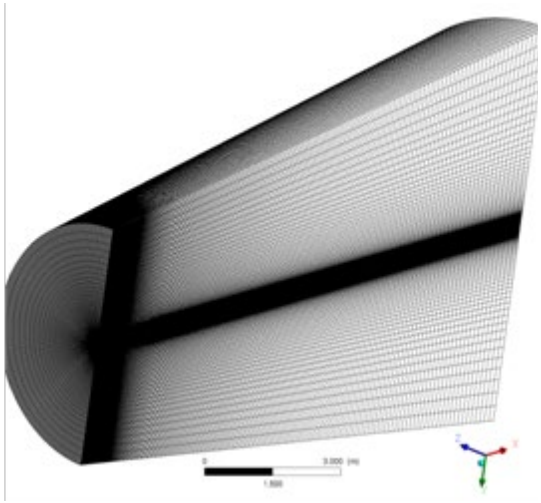

Figure 10 CFD domain and mesh of the half sector of the scale model with symmetric boundary conditions.

Steady Reynolds-averaged Navier-Stokes (RANS) simulations were performed using ANSYS CFX with the SST model for turbulence, total energy option for heat transfer, automatic option for turbulent wall functions, and ideal air was used for the fluid. In the simulations total pressure and temperature components are specified at the inlet boundaries. At the exit, atmospheric static pressure is specified.

In this study, one iteration of domain/mesh refinement was performed to examine the grid effect. The final ~12M cell hexahedral mesh, described above, was generated by improving the CFD domain and mesh based on the CFD results from an initial mesh. Figure 11 shows the contours of velocity magnitude at the symmetric plane from the two sets of meshes. The nozzle exit region has better resolution with the improved mesh.

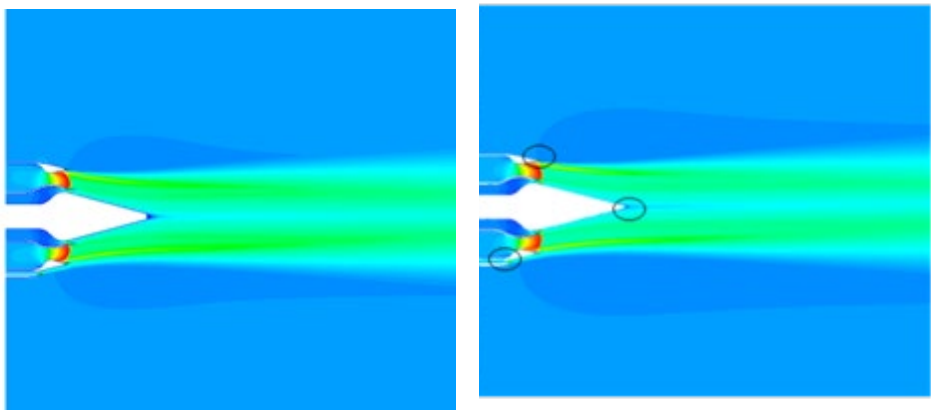

Figure 11 Contours of velocity magnitude at the symmetric plane. Left: original mesh; right: improved mesh.

3.3.1 SIDELINE RANS CFD RESULTS

Figure 12 shows contours of velocity, static pressure, and Mach number through a plane cutting through the centerline of the nozzle, focused near the nozzle exit. These results show that there is a region of separated flow at the exit of the primary exhaust.

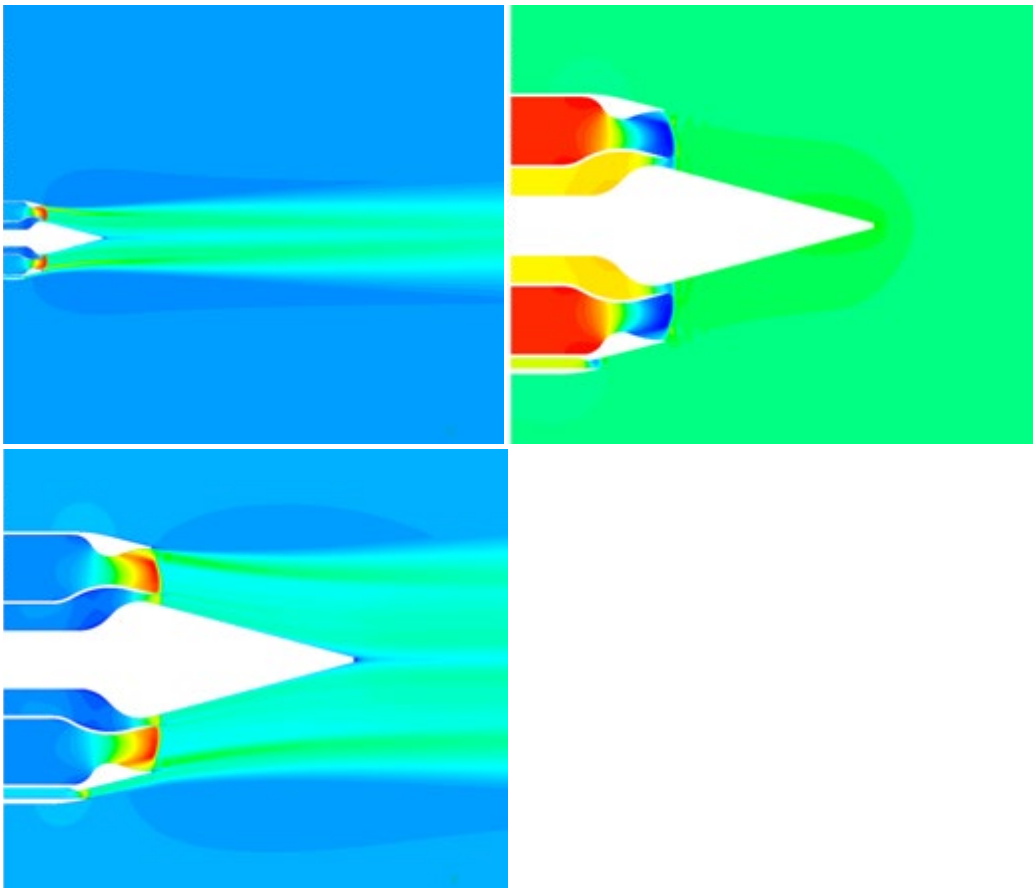

Figure 12 Contours of velocity magnitude, static pressure and Mach number at the symmetric plane.

Figure 13 shows contours of total temperature in a plane cut through the centerline of the nozzle showing the extent of the potential core of the exhaust system.

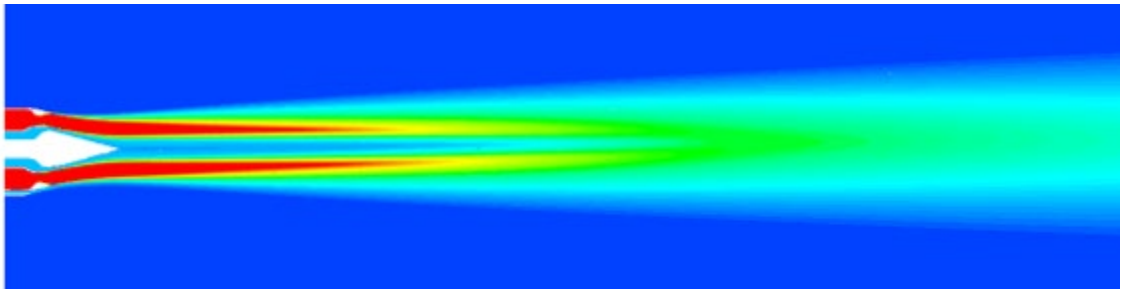

Figure 13 Contours of total temperature at the symmetric plane.

Figure 14 shows contours of turbulent kinetic energy (tke) in a plane cut through the centerline of the nozzle, showing the extent of the potential core of the exhaust system.

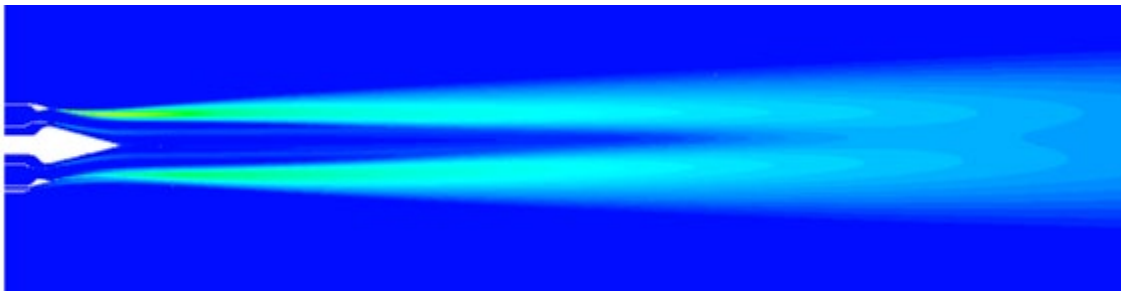

Figure 14 Contours of turbulent kinetic energy (m2/s2) at the symmetric plane.

Figure 15 shows contours of total temperature on cross-sectional cut planes at 5 axial locations down the jet plume. For the sideline configuration the equivalent diameter of the scale model is 0.14 m.

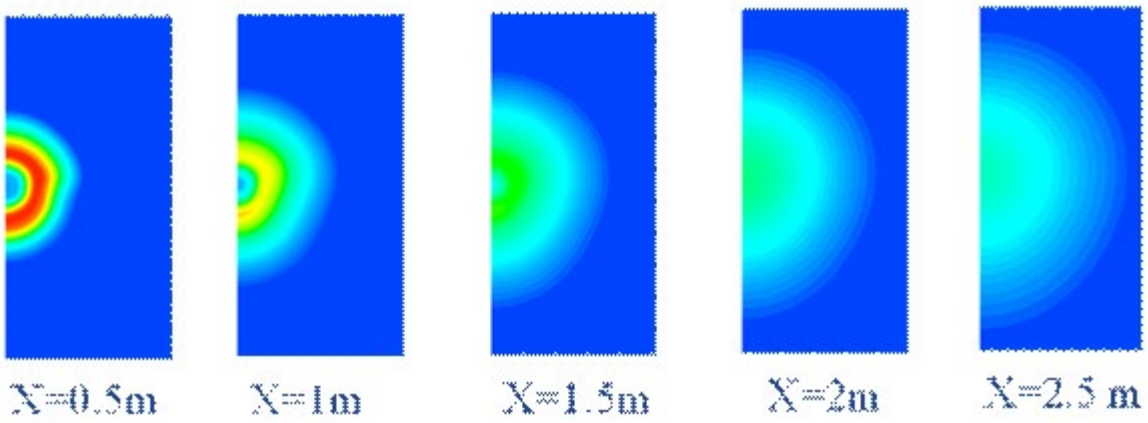

Figure 15 Contours of total temperature (R) at different axial locations.

Figure 16 shows contours of the tke on cross-sectional cut planes at 5 axial locations down the jet plume.

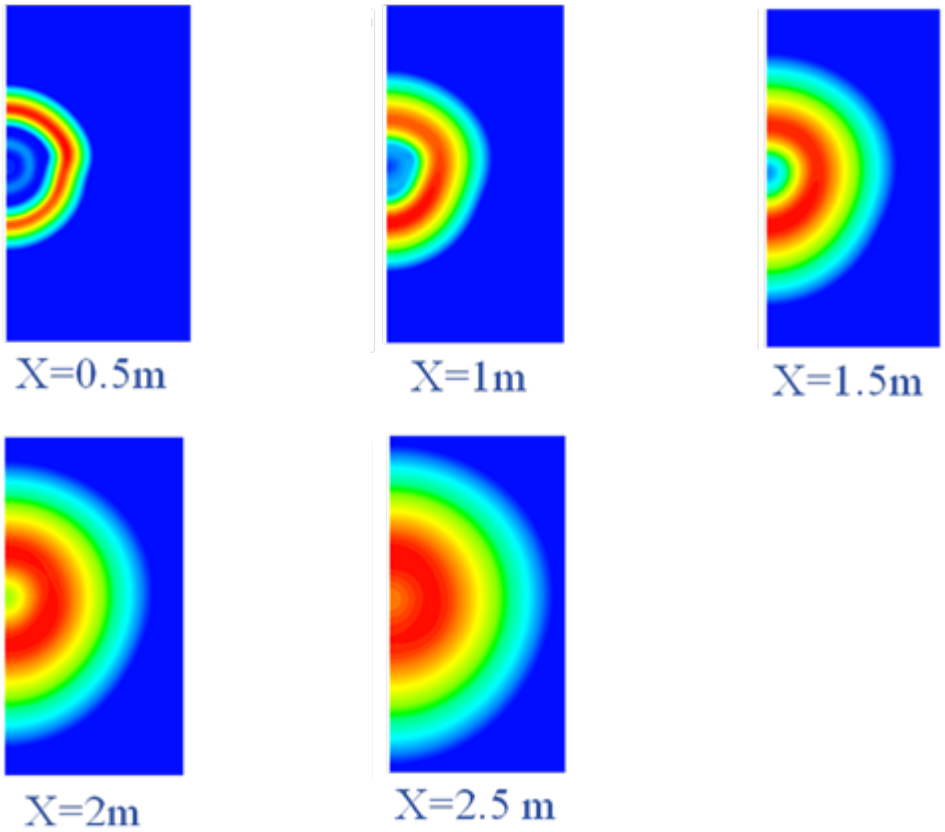

Figure 16 Contours of turbulent kinetic energy at different axial locations.

3.3.1 CUTBACK RANS CFD RESULTS

Figure 17 shows contours of velocity, static pressure, and Mach number through a plane cutting through the centerline of the nozzle, focused near the nozzle exit. These results show that there is a region of separated flow at the exit of the primary exhaust, although not as sizable as the sideline case.

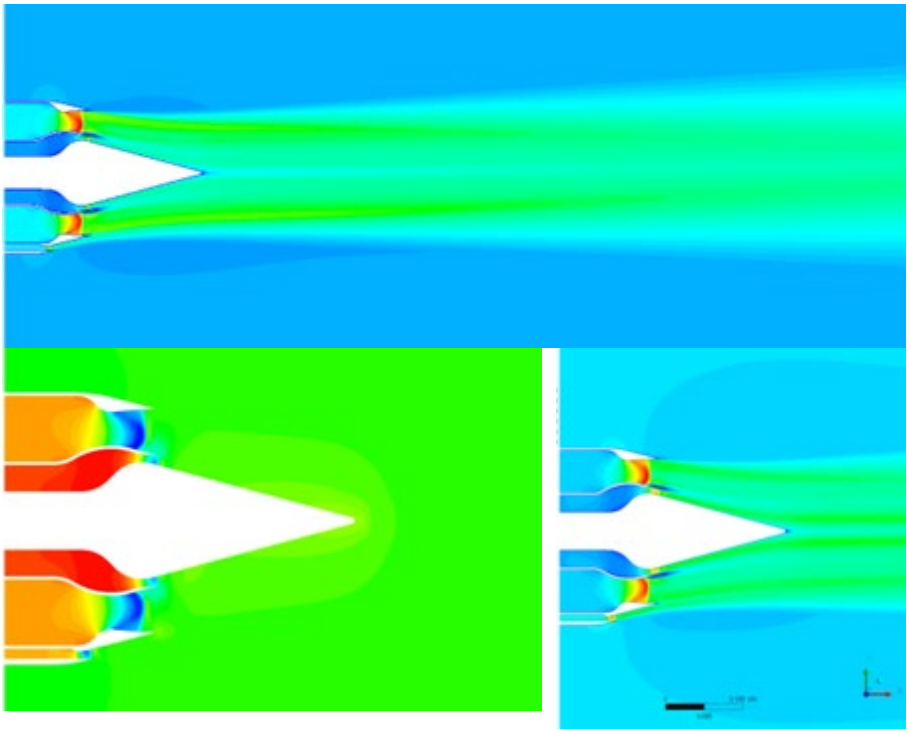

Figure 17 Contours of velocity magnitude, static pressure and Mach number at the symmetric plane.

Figure 18 shows contours of total temperature in a plane cut through the centerline of the nozzle showing the extent of the potential core of the exhaust system.

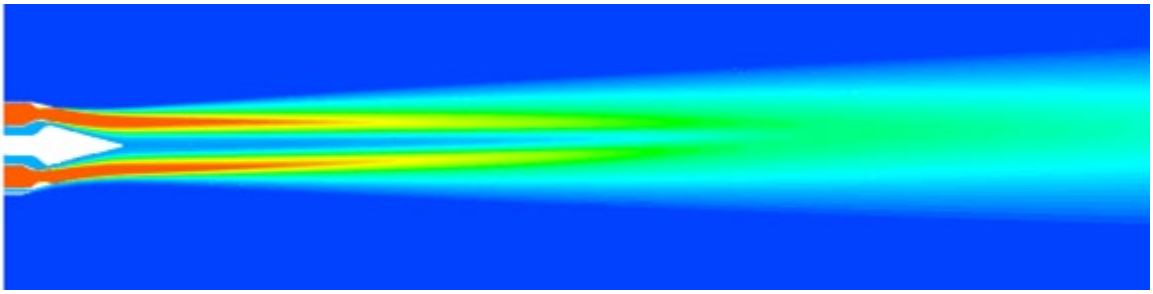

Figure 18 Contours of total temperature at the symmetric plane.

Figure 19 shows contours of turbulent kinetic energy (tke) in a plane cut through the centerline of the nozzle, showing the extent of the potential core of the exhaust system.

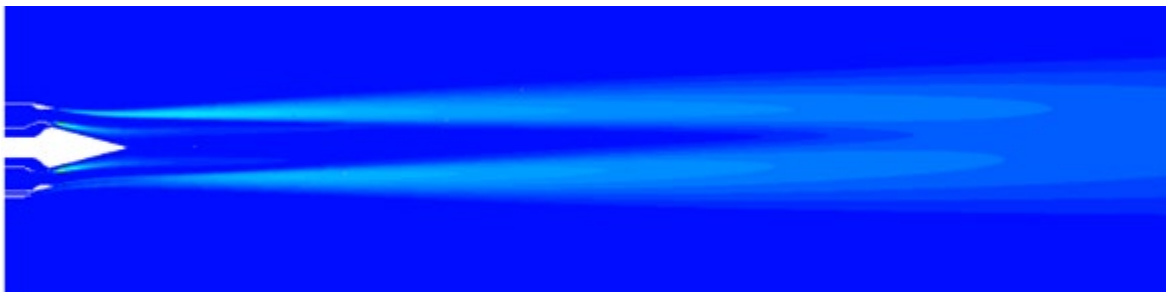

Figure 19 Contours of turbulent kinetic energy at the symmetric plane.

Figure 20 shows contours of total temperature on cross-sectional cut planes at 5 axial locations down the jet plume. For the cutback configuration the equivalent diameter of the scale model is 0.15m.

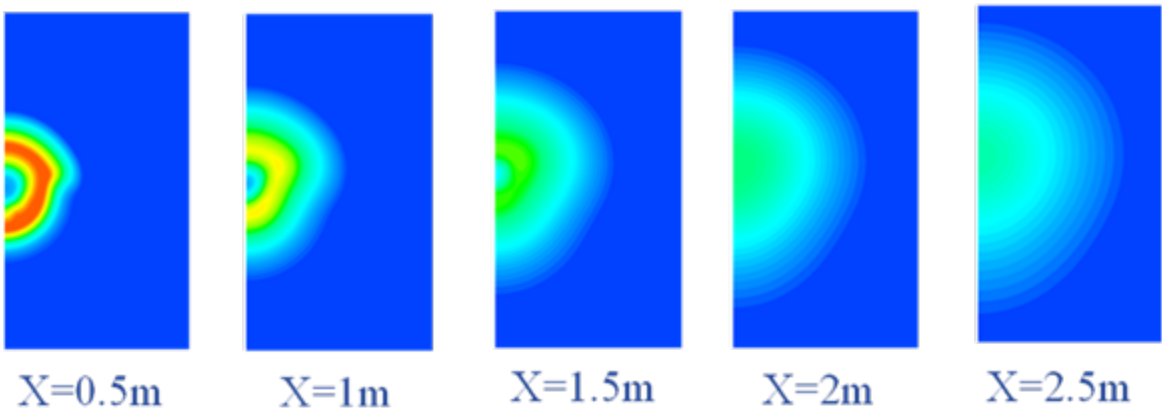

Figure 20 Contours of total temperature at different axial cuts.

Figure 21 shows contours of the tke on cross-sectional cut planes at 5 axial locations down the jet plume.

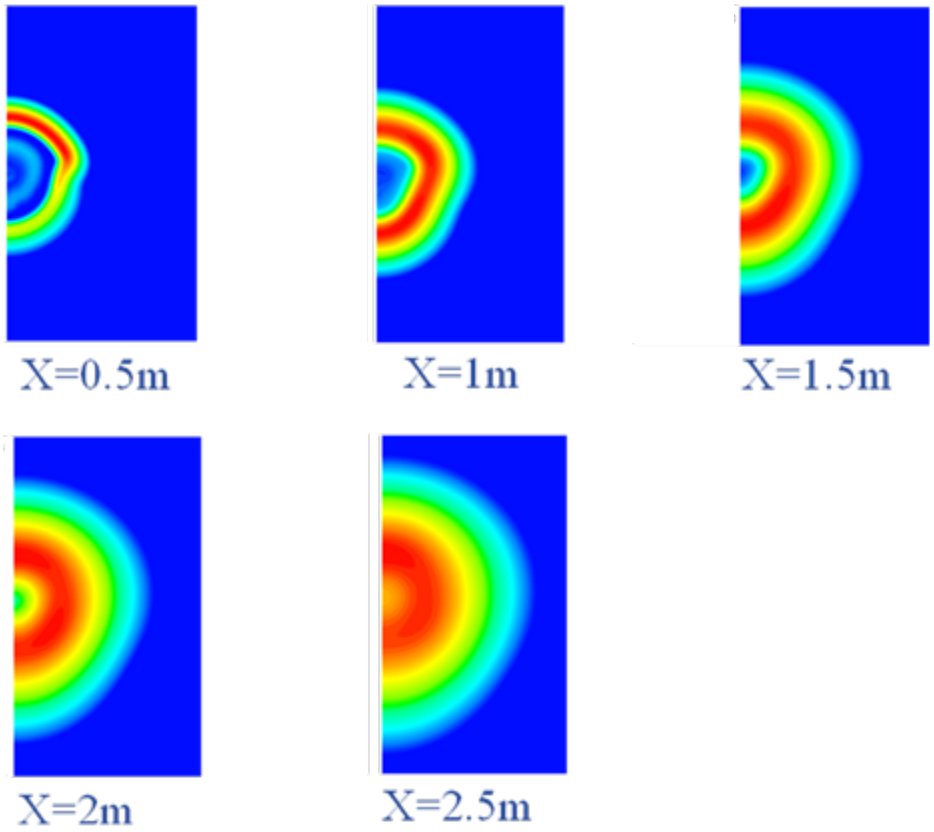

Figure 21 Contours of turbulent kinetic energy at different axial locations.

3.4 LES SIMULATIONS

LES continues to run for the GE nozzle and the corresponding reference nozzle at equivalent cutback cycle conditions. These are being run on the model scale geometry tested with flight simulation so they can be compared directly to each other as well as directly to the experimental data. At the time of this report the simulations are still running.

3.4.1 REFERENCE NOZZLE LES

Figure 22 illustrates the CFD domain and mesh of the scale model reference nozzle. The dimension of the CFD domain is 30 nozzle diameters wide at the inlet, 50 nozzle diameters wide at the outlet, and 65 nozzle diameters in length. A non-uniform pure hexahedral mesh with approximately 24 million cells/elements was created using the Gridgen mesher. The majority of the cells are concentrated near the nozzle exit region for accurate resolution of the shear layers.

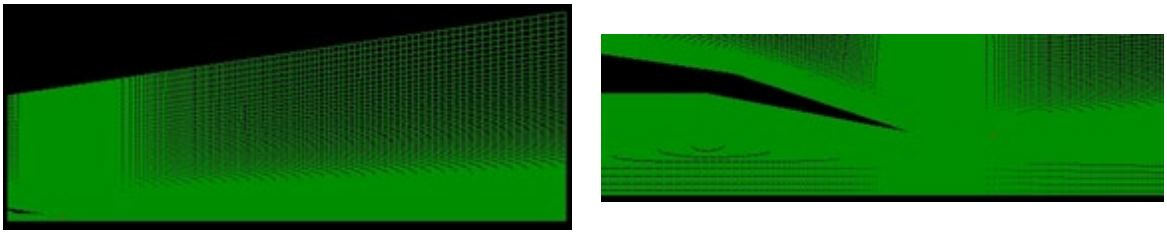

Figure 22 Center-plane mesh of the scale model reference nozzle with a diameter of 4 in.

The LES calculation was performed using FDL3DI. The code has been modified to account for the non-zero ambient stream. The calculation is running in parallel with 104 CPUs.

Figure 23 shows the contours of the non-dimensional axial velocity from the intermediate solution. The image on the left shows the progression of the external flow through the domain. Including external flow has increased the required computational time more than expected and has resulted in the solution not being complete at the time of this report.

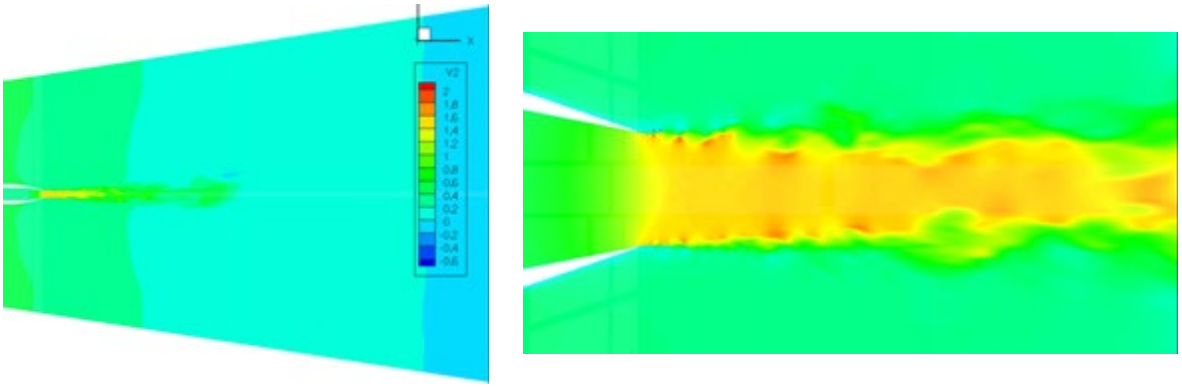

Figure 23 Contour of the non-dimensional axial velocity. (Intermediate solution from FDL3DI).

3.4.2 GE NOZZLE LES

Figure 24 illustrates the CFD domain and mesh of the scale model GE nozzle. The dimension of the CFD domain is 30 nozzle diameters wide at the inlet, 50 nozzle diameters wide at the outlet, and 65 nozzle diameters in length. A non-uniform pure hexahedral mesh with approximately 29 million cells/elements was created using the Gridgen mesher. The majority of the cells are concentrated near the nozzle exit region for accurate resolution of the shear layers.

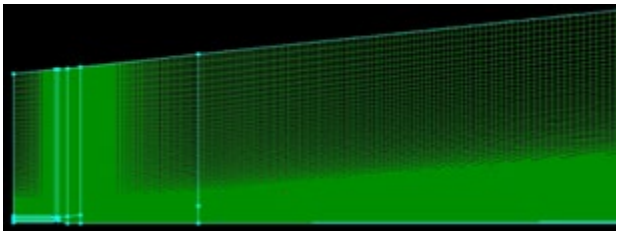

Figure 24 Center-plane mesh of the model scale GE nozzle.

The LES calculation was performed using FDL3DI. The code has been modified to account for the multiple inlet streams. The calculation is running in parallel with 128 CPUs.

3.5 TEST

Testing of the GE nozzle was conducted in the NATR/HFJER in the AAPL facility at NASA GRC in May and June of 2011. The test schedule was tight due to program requirements and an annual test facility shutdown at the end of the test window. Testing on the GE nozzle as well as a single stream reference conic nozzle was completed on schedule. The GE nozzle, as described in previous sections included two noise reduction technologies.

3.5.1 TEST SET-UP AND SCOPE

Figure 25 shows two photos of the nozzle installed on the HFJER.

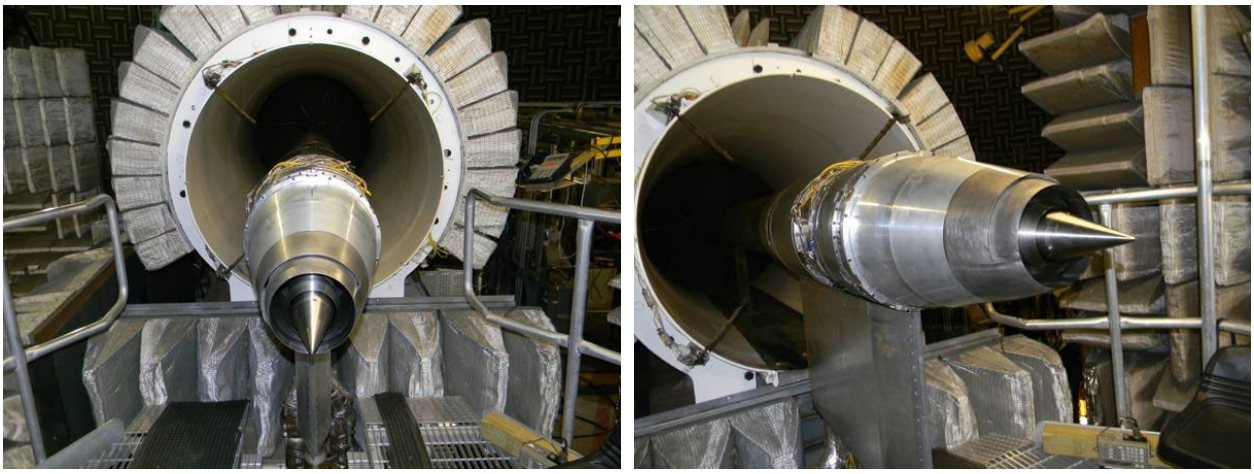

Figure 25 Photos of GE nozzle installed in HFJER.

Figure 26 shows a close-up photo of the GE nozzle looking up at the ceiling of the AAPL facility. The blue structure in the bottom of the photo is the ceiling mounted microphone array used in this test. NASA was responsible for all data acquisition, and transferred the microphone data and corresponding facility and model aerodynamic data to GE in a timely manner.

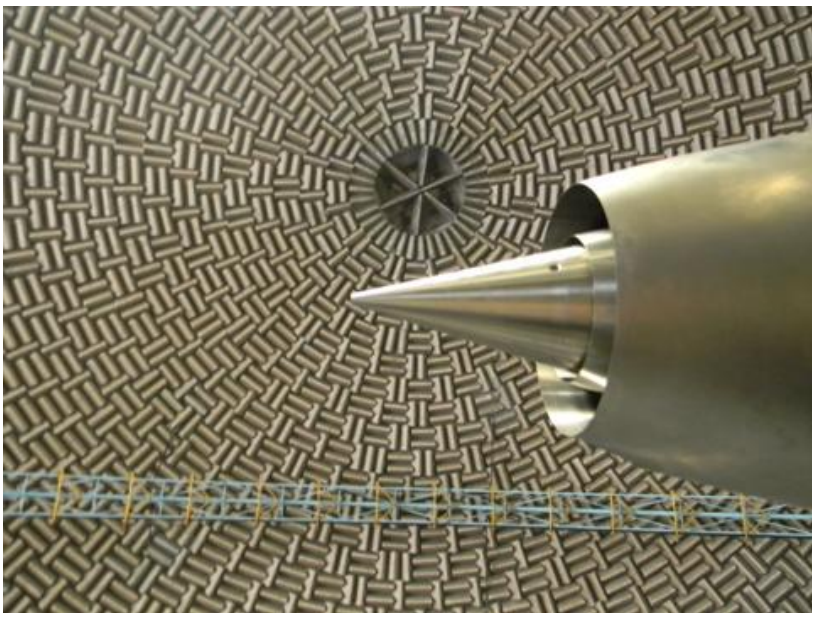

Figure 26 Close-Up photo of the GE nozzle, showing the AAPL ceiling and ceiling mounted microphone array.

3.5.2 TEST RESULTS

The test data presented in this section has been scaled to full scale. The scale factor is determined by scaling the thrust of the test condition closest to the engine condition required, based on a take-off profile provided by Lockheed Martin.

Both static and flight data are extrapolated to the corresponding altitude based on the provided flight path. The Effective Perceived Noise level (EPNL) is calculated using the aircraft speed again from the take-off profile. The flight data includes a shear layer correction in the processing and the static data uses a pseudo EPNL for comparison and reference.

Figure 27 shows the EPNL vs thrust for the cutback configuration for three different heat addition cycles for static conditions, along with the corresponding reference nozzle data. A couple of things to notice on these figures is that for the reference nozzle the noise levels are louder for higher levels of heat addition, although if more higher condition data was taken it appears the trend starts to reverse. Comparing each cycle of the GE nozzle to the reference nozzle there is a clear cross-over point where at lower power settings the reference nozzle is quieter that the GE nozzle and then at higher power settings the trend reverses. This is the expected trend as the IVP concept works better at higher power settings. However, looking at the no heat addition cycle the noise trend at lower thrust levels is approximately constant. This strongly indicates that there is an extra noise source, likely from the flow separation see previously in the CFD. This is a much larger impact than was expected. The performance of the no heat addition cycle at higher levels of thrust is very promising, with reductions from 2 – 4 EPNdB seen relative to the reference nozzle.

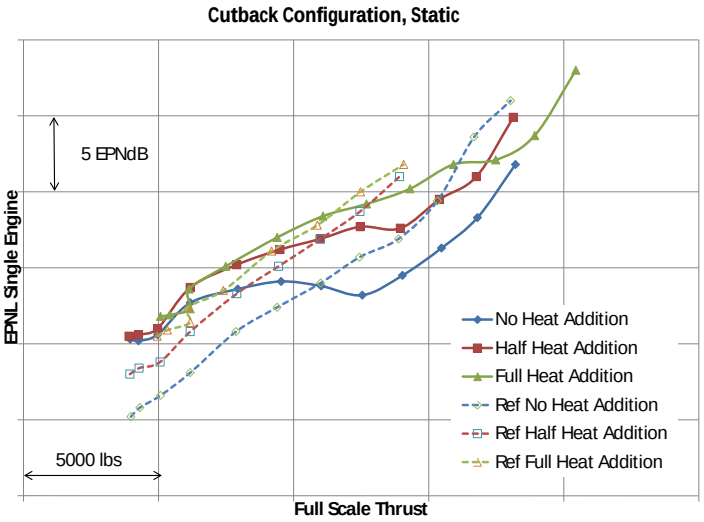

Figure 27 EPNL for Cutback Configuration, Static Conditions Processed to Flyover.

Figure 28 shows the same configurations with the corresponding flight simulation cases.

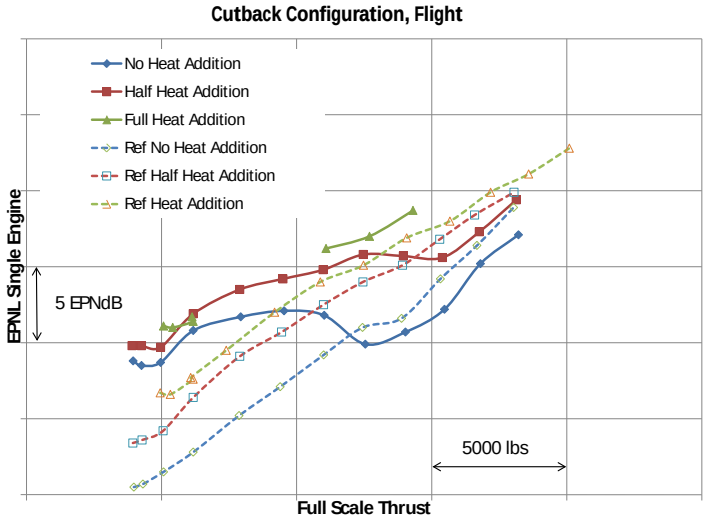

Figure 28 EPNL for Cutback Configuration, Flight Conditions Processed to Flyover.

Figure 29 shows the Perceived Noise Level (PNL) for the cutback configuration as a function of directivity angle for all of the no heat addition cycle conditions for the static data. The GE nozzle is shown on the left and the reference nozzle is on the right.

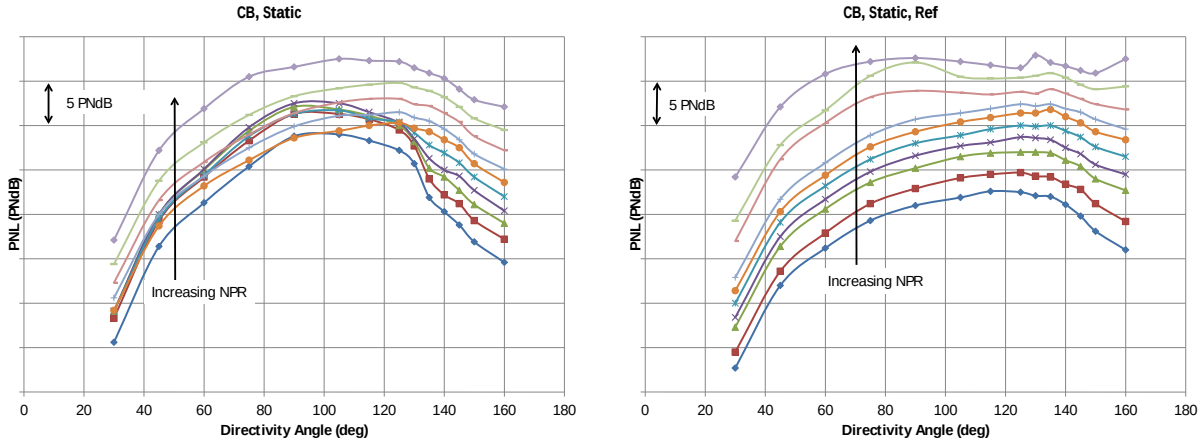

Figure 29 PNL for Cutback Configuration, Static Conditions, Processed to Flyover, No Heat Addition Cycle Conditions, Test Nozzle on Left, and Reference Nozzle on Right.

Figure 30 through Figure 33 show Sound Pressure Level (SPL) spectra for the same conditions at 60, 90, 125, and 150 deg, respectively. At angles up to 125 deg and frequencies above approximately 1000 Hz the excess noise is seen. This extra separation noise is in the Noy weighted region of the spectra and significantly impacts the EPNL values.

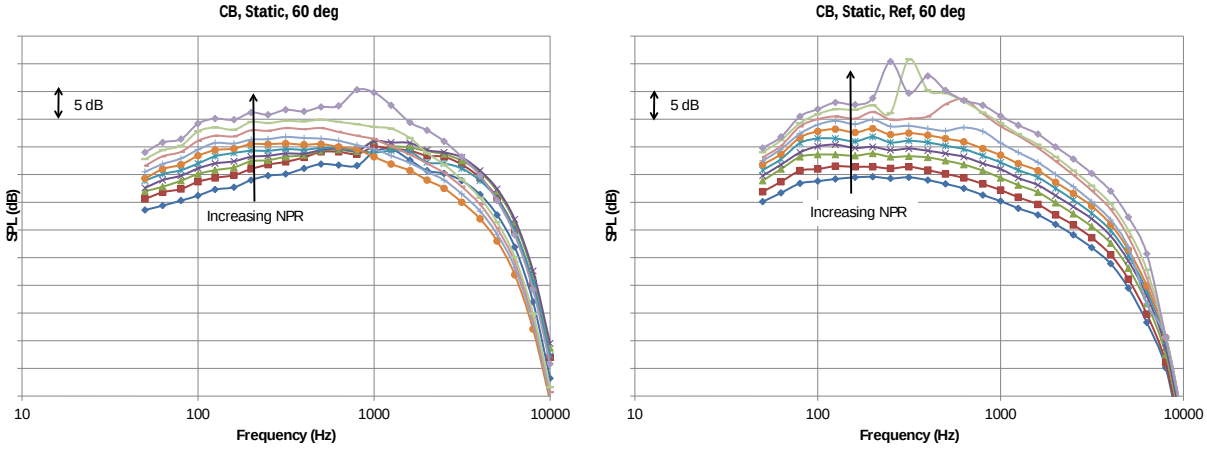

Figure 30 SPL at 60 deg for Cutback Configuration, Static Conditions, Processed to Flyover, No Heat Addition Cycle Conditions, Test Nozzle on Left, and Reference Nozzle on Right.

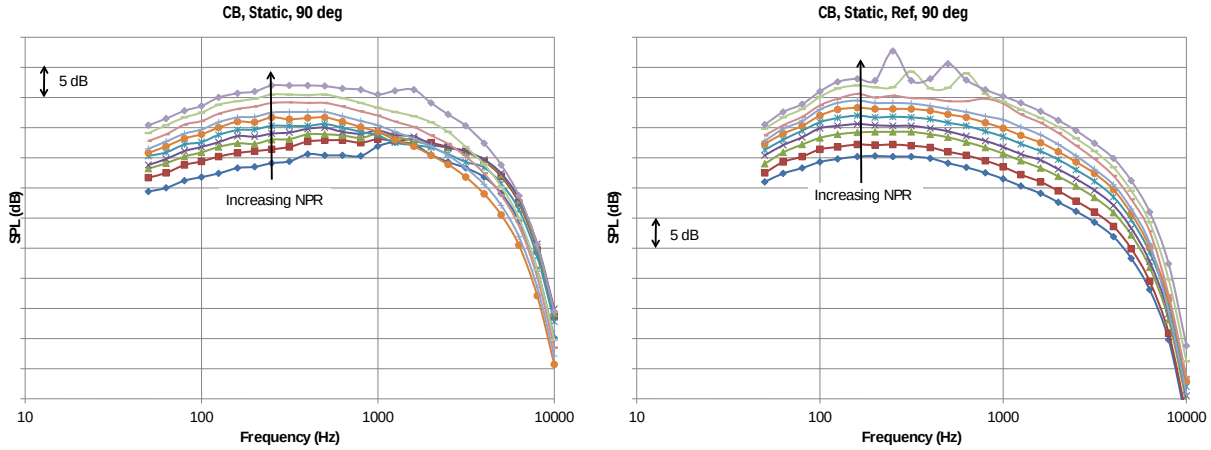

Figure 31 SPL at 90 deg for Cutback Configuration, Static Conditions, Processed to Flyover, No Heat Addition Cycle Conditions, Test Nozzle on Left, and Reference Nozzle on Right.

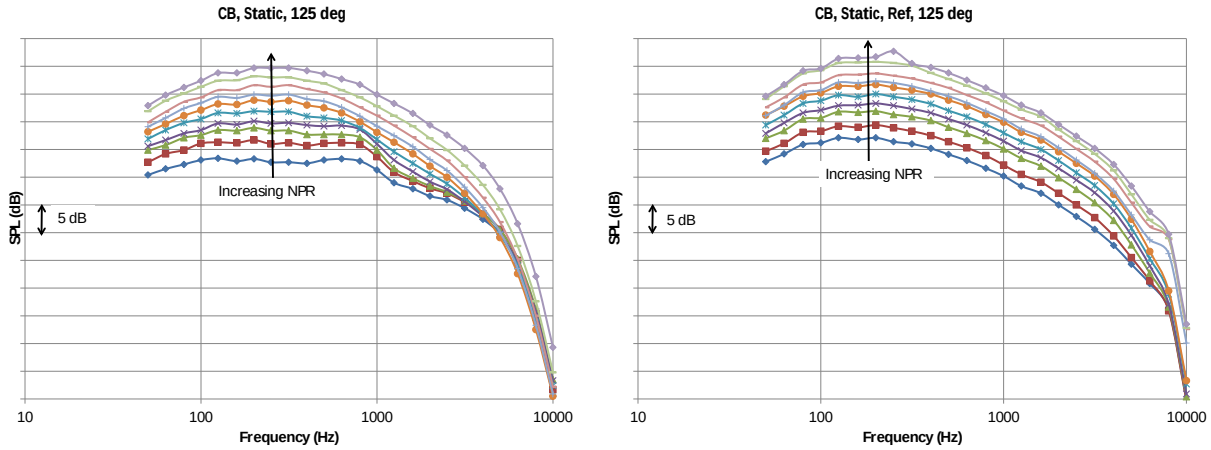

Figure 32 SPL at 125 deg for Cutback Configuration, Static Conditions, Processed to Flyover, No Heat Addition Cycle Conditions, Test Nozzle on Left, and Reference Nozzle on Right.

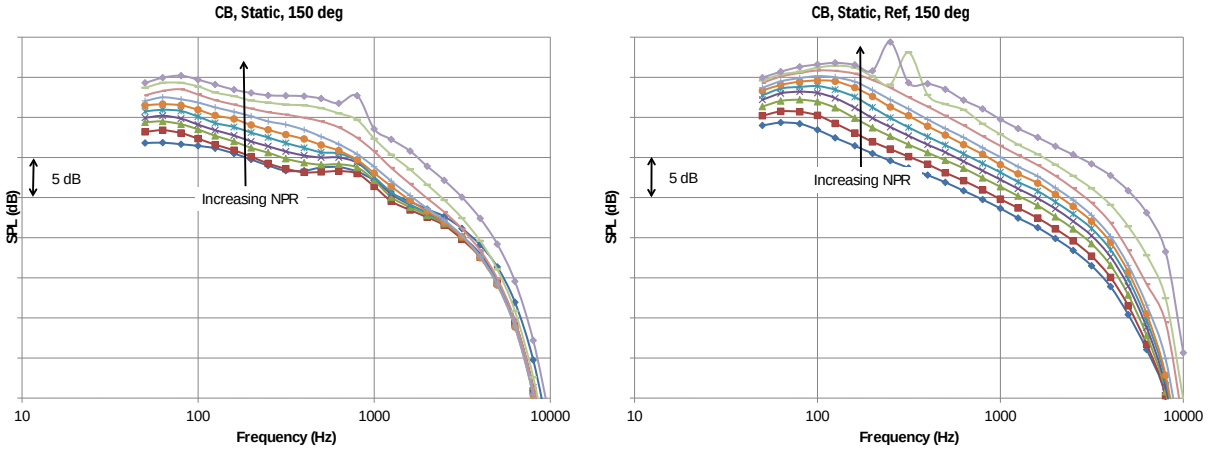

Figure 33 SPL at 150 deg for Cutback Configuration, Static Conditions, Processed to Flyover, No Heat Addition Cycle Conditions, Test Nozzle on Left, and Reference Nozzle on Right.

Figure 34 shows the PNL directivity for the corresponding flight cases. Figure 35 through Figure 39 show the SPL spectra at angles of 60, 80, 90, 120, and 150 deg, respectively. Again at frequencies greater than 1000 Hz excess noise is seen due to the flow separation.

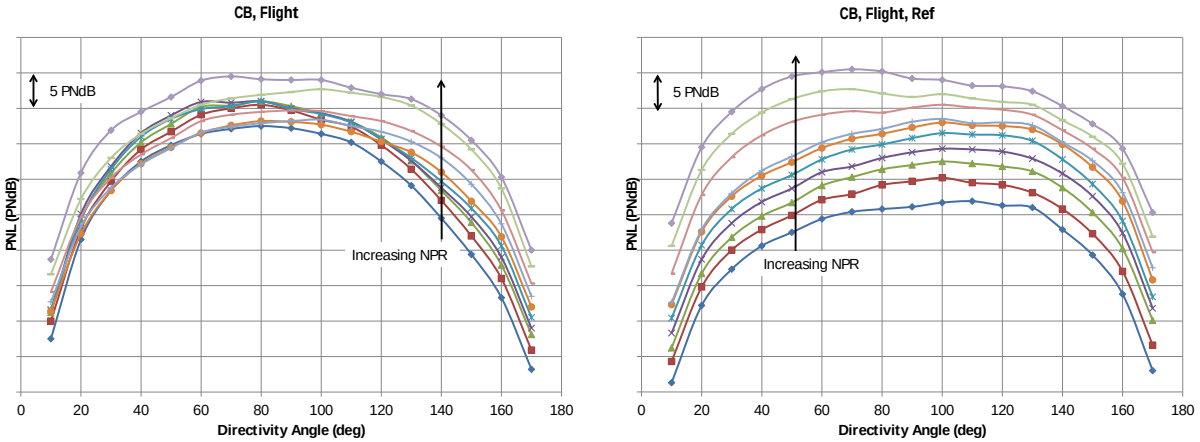

Figure 34 PNL for Cutback Configuration, Flight Conditions, Processed to Flyover, No Heat Addition Cycle Conditions, Test Nozzle on Left, and Reference Nozzle on Right.

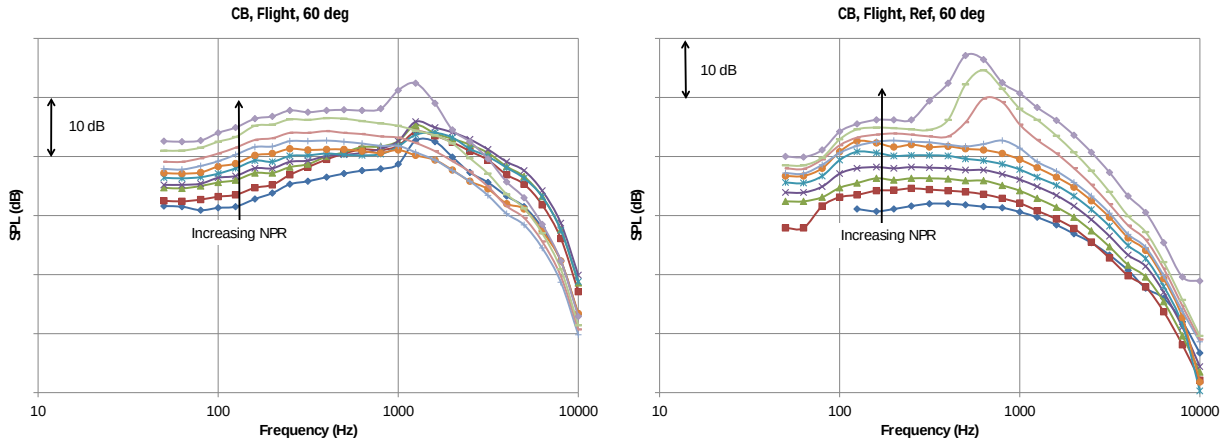

Figure 35 SPL at 60 deg for Cutback Configuration, Flight Conditions, Processed to Flyover, No Heat Addition Cycle Conditions, Test Nozzle on Left, and Reference Nozzle on Right.

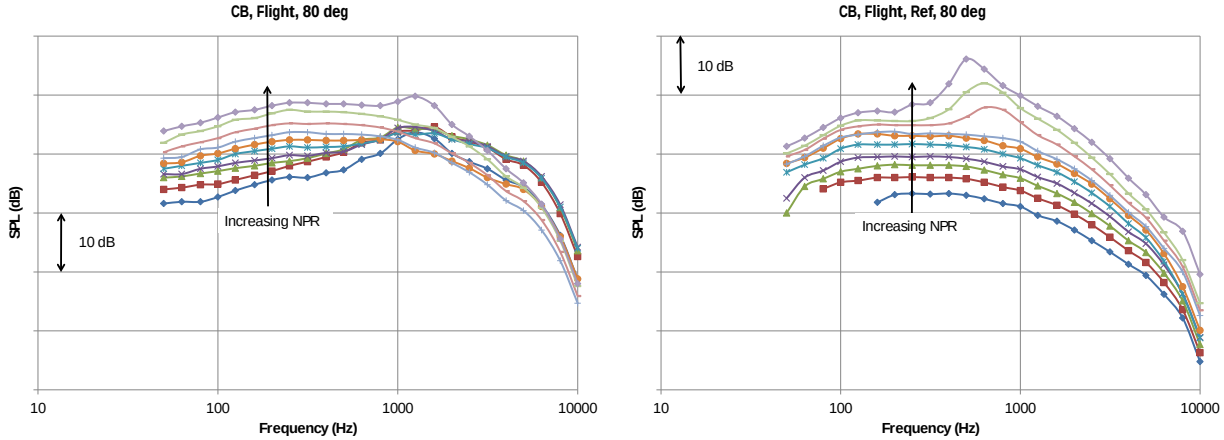

Figure 36 SPL at 80 deg for Cutback Configuration, Flight Conditions, Processed to Flyover, No Heat Addition Cycle Conditions, Test Nozzle on Left, and Reference Nozzle on Right.

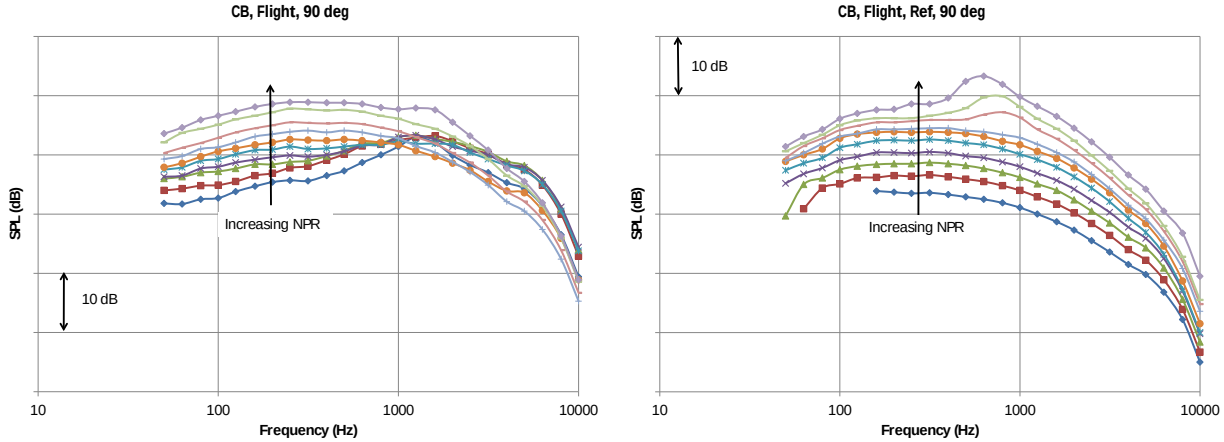

Figure 37 SPL at 90 deg for Cutback Configuration, Flight Conditions, Processed to Flyover, No Heat Addition Cycle Conditions, Test Nozzle on Left, and Reference Nozzle on Right.

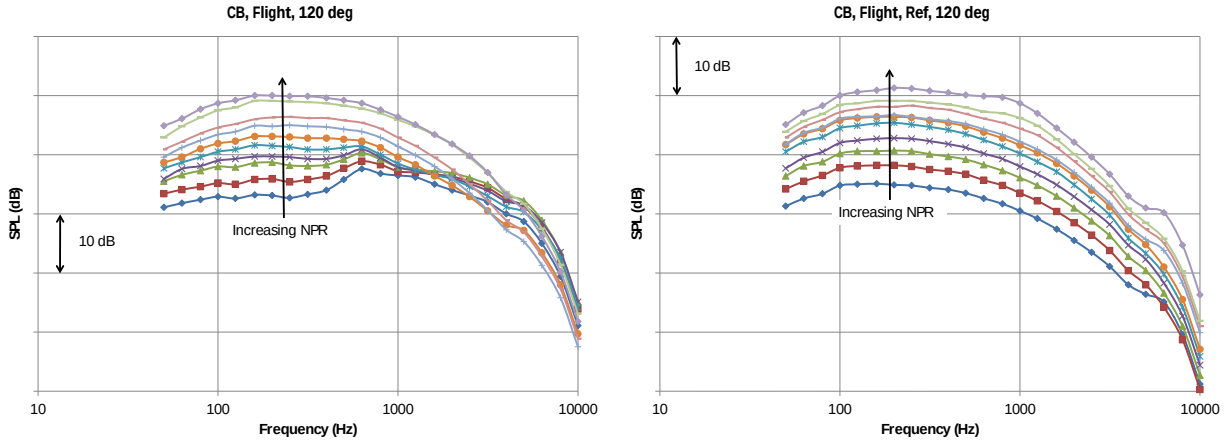

Figure 38 SPL at 120 deg for Cutback Configuration, Flight Conditions, Processed to Flyover, No Heat Addition Cycle Conditions, Test Nozzle on Left, and Reference Nozzle on Right.

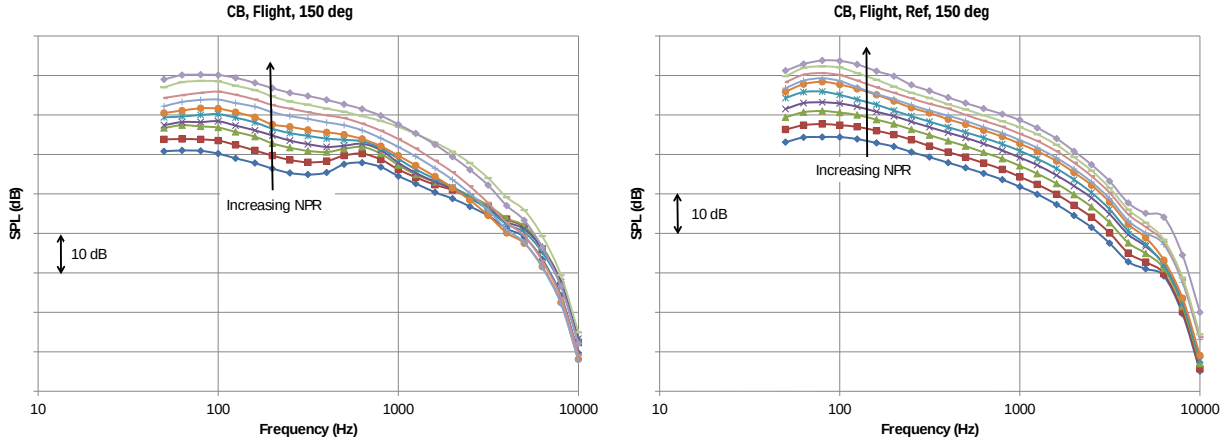

Figure 39 SPL at 150 deg for Cutback Configuration, Flight Conditions, Processed to Flyover, No Heat Addition Cycle Conditions, Test Nozzle on Left, and Reference Nozzle on Right.

Figure 40 shows the EPNL vs thrust for the sideline configuration at static conditions for all three heat addition cycles along with the corresponding reference nozzle data. The trends are similar to those seen in the cutback configuration, the no heat addition cycle is the quietest and the GE nozzle is generally louder than the reference nozzle up to higher conditions.

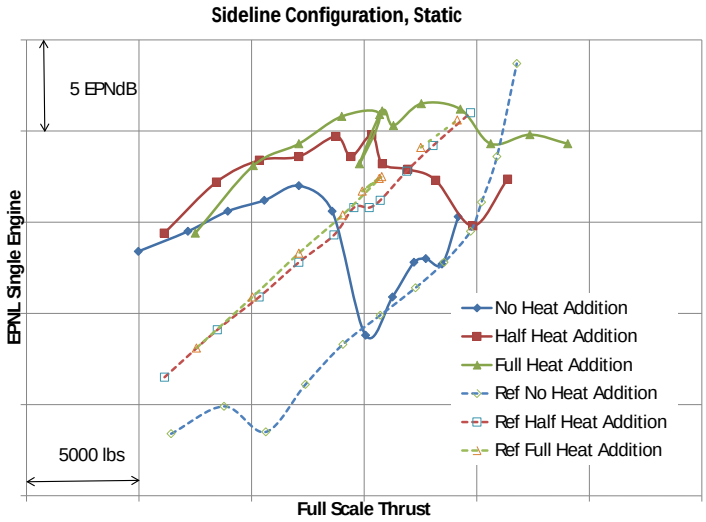

Figure 40 EPNL for Sideline Configuration, Static Conditions Processed to Sideline.

Figure 41 shows the same configurations with the corresponding flight simulation cases. Again, the no heat addition cycle shows a dramatic cross-over relative to the reference nozzle. As will be evident in the following data the excess noise was much worse for the sideline configuration compared to the cutback geometry. The sideline nozzle geometry has a larger area ratio (exit area to throat area) than the cutback configuration.

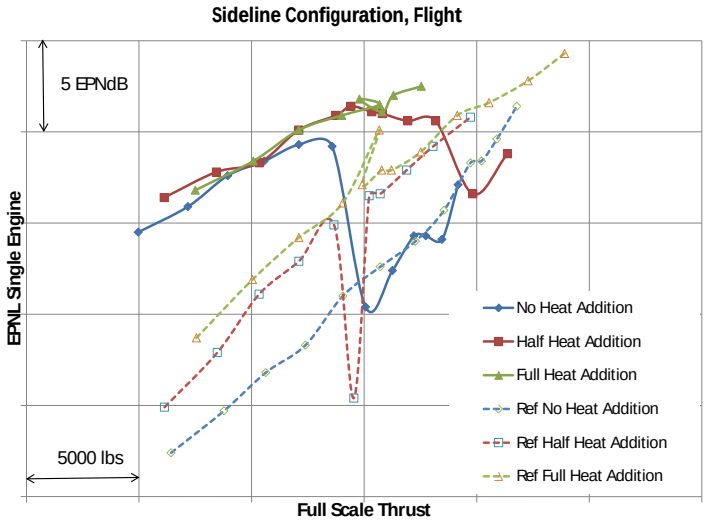

Figure 41 EPNL for Sideline Configuration, Flight Conditions Processed to Sideline.

Figure 42 shows the PNL directivity for the sideline configuration for all of the no heat addition cycle conditions for the static data. The GE nozzle is shown on the left and the reference nozzle is on the right.

There are some very interesting trends in the GE nozzle data, as the lowest set of data at a primary nozzle pressure ratio in the middle of the range tested. This agrees with the EPNL plots shown previously, which showed a dramatic change in noise level at that thrust level.

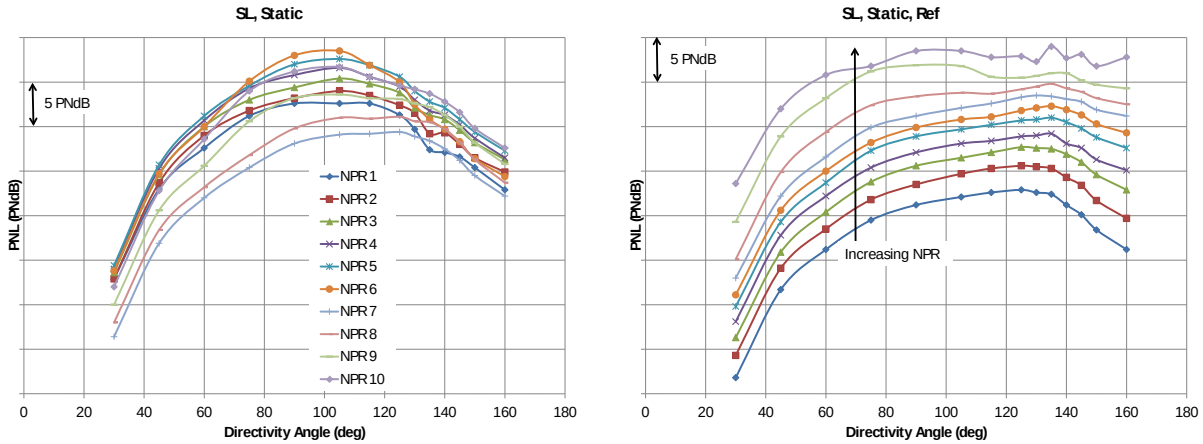

Figure 42 PNL for Sideline Configuration, Static Conditions, Processed to Sideline, No heat addition Cycle Conditions, Test Nozzle on Left, and Reference Nozzle on Right.

Figure 43 through Figure 46 show the SPL spectra for the same conditions at 60, 90, 125, and 150 deg, respectively. One thing that really sticks out is the two broad tones seen at the lower primary nozzle pressure ratios. The two tones are at approximately 600 and 800 Hz. Only the tone at 800 Hz was seen in the cutback configuration.

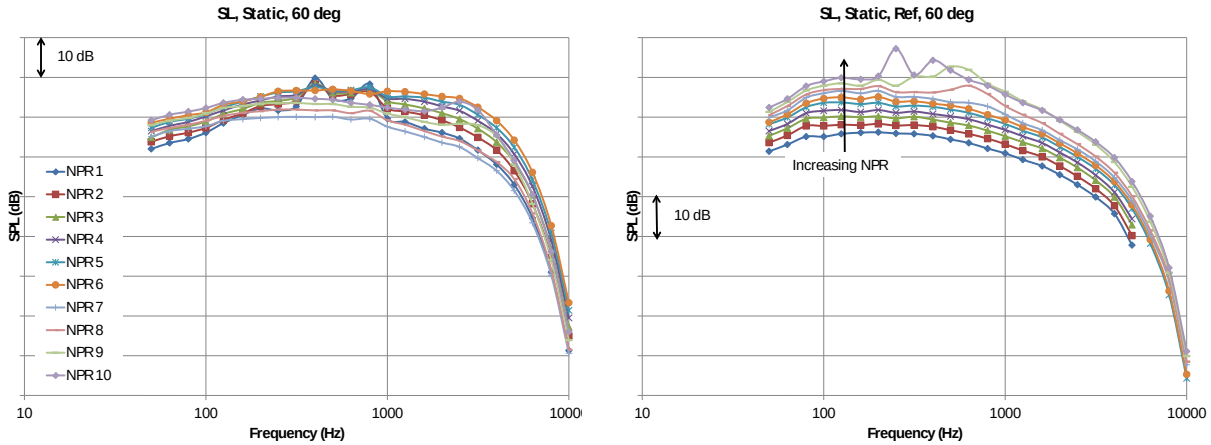

Figure 43 SPL at 60 deg for Sideline Configuration, Static Conditions, Processed to Sideline, No Heat Addition Cycle Conditions, Test Nozzle on Left, and Reference Nozzle on Right.

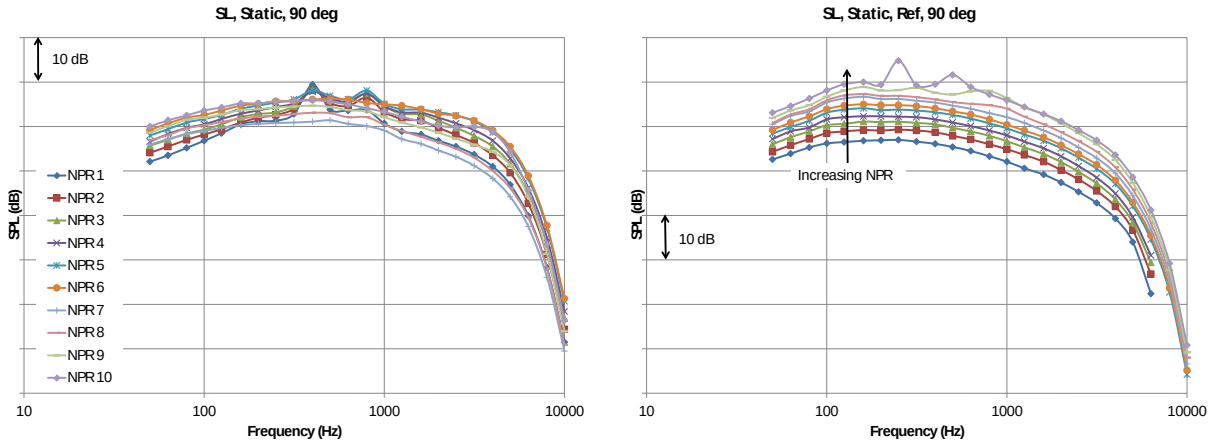

Figure 44 SPL at 90 deg for Sideline Configuration, Static Conditions, Processed to Sideline, No Heat Addition Cycle Conditions, Test Nozzle on Left, and Reference Nozzle on Right.

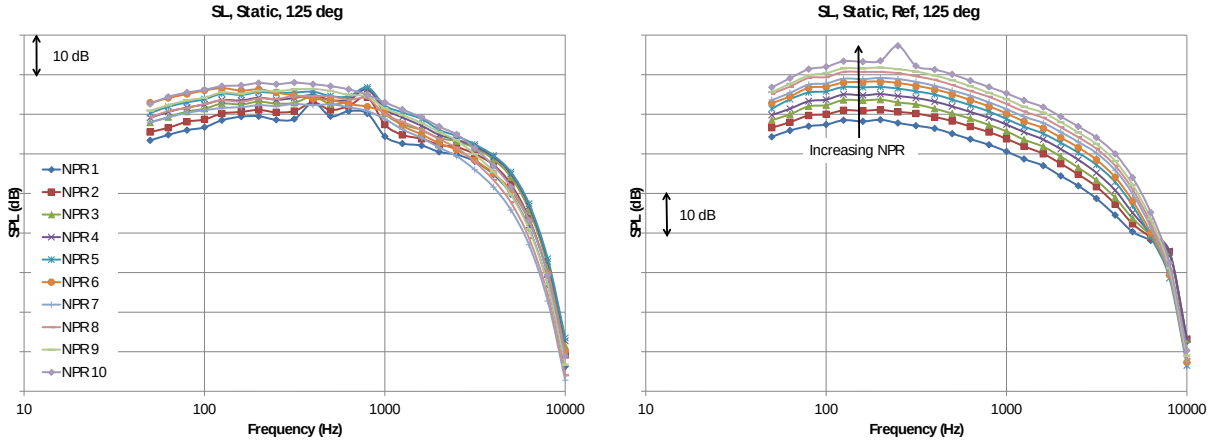

Figure 45 SPL at 125 deg for Sideline Configuration, Static Conditions, Processed to Sideline, No Heat Addition Cycle Conditions, Test Nozzle on Left, and Reference Nozzle on Right.

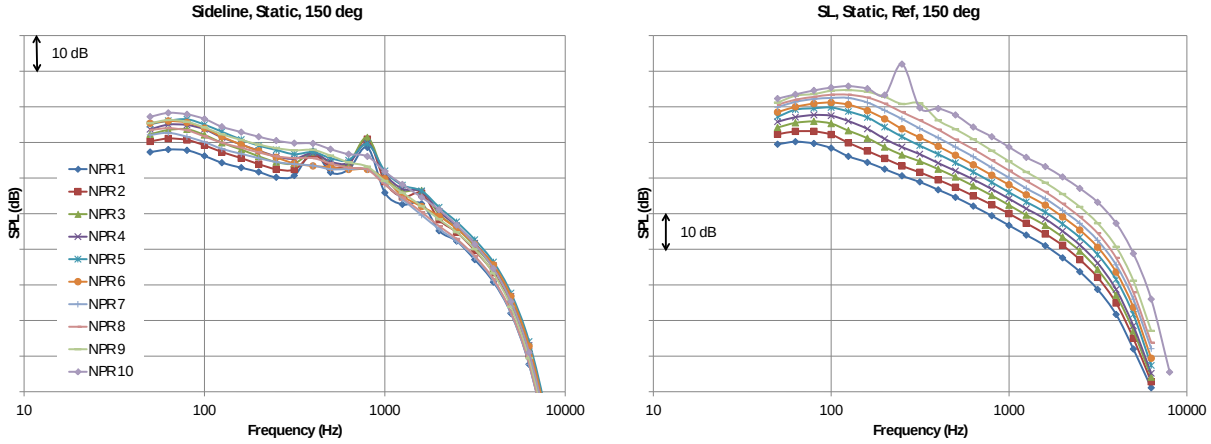

Figure 46 SPL at 150 deg for Sideline Configuration, Static Conditions, Processed to Sideline, No Heat Addition Cycle Conditions, Test Nozzle on Left, and Reference Nozzle on Right.

Figure 47 shows the PNL directivity for the corresponding flight cases. Figure 48 through Figure 52 shows the SPL spectra at angles of 60, 80, 90, 120, and 150 deg, respectively. The twin peaks from the shield are pretty much eliminated with flight, although the excess noise from the nozzle flow separation is seen up to primary nozzle pressure ratio in the middle of the range tested above 1000 Hz.

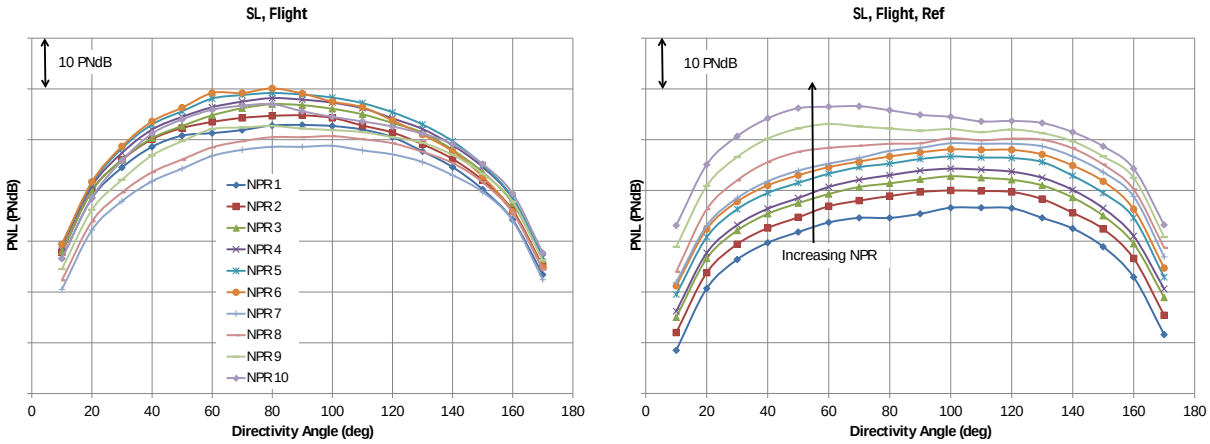

Figure 47 PNL for Sideline Configuration, Flight Conditions, Processed to Sideline, No Heat Addition Cycle Conditions, Test Nozzle on Left, and Reference Nozzle on Right.

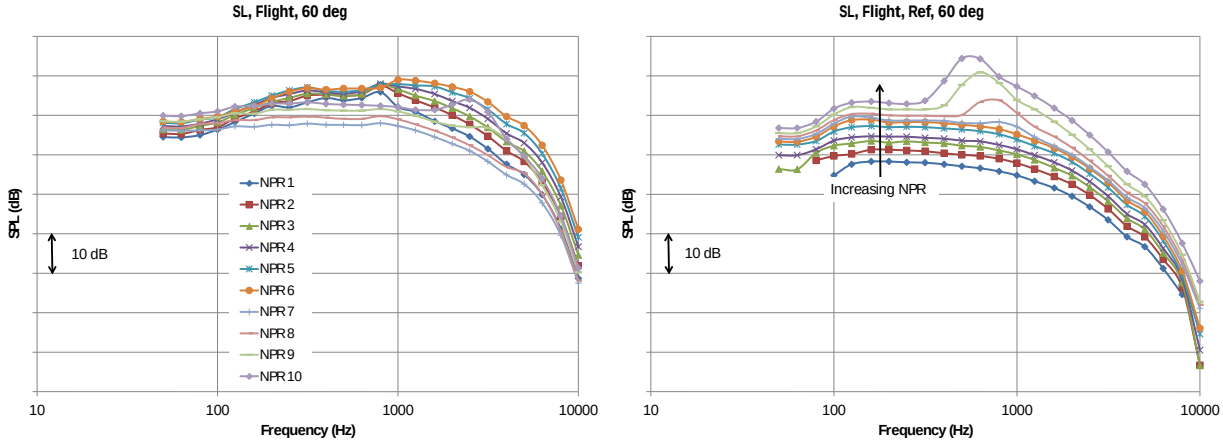

Figure 48 SPL at 60 deg for Sideline Configuration, Flight Conditions, Processed to Sideline, No Heat Addition Cycle Conditions, Test Nozzle on Left, and Reference Nozzle on Right.

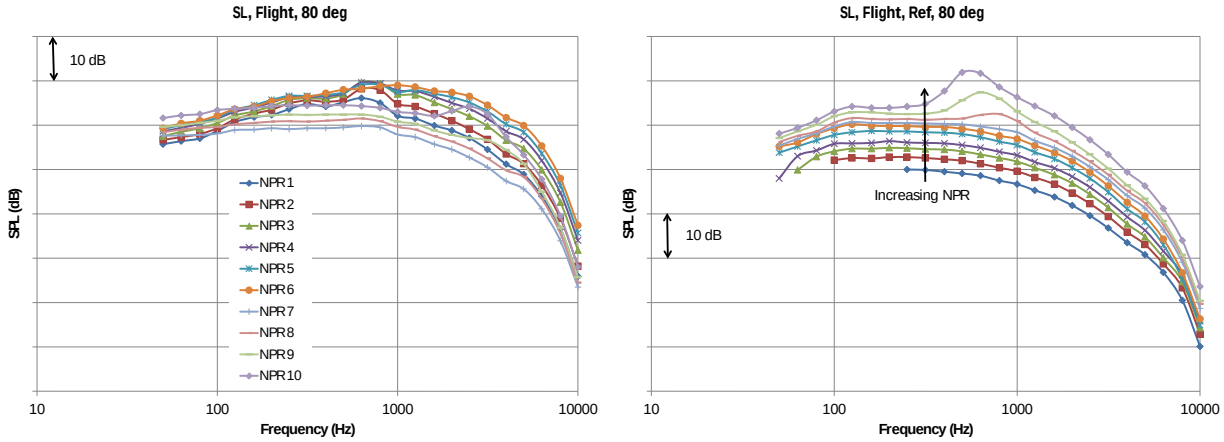

Figure 49 SPL at 80 deg for Sideline Configuration, Flight Conditions, Processed to Sideline, No Heat Addition Cycle Conditions, Test Nozzle on Left, and Reference Nozzle on Right.

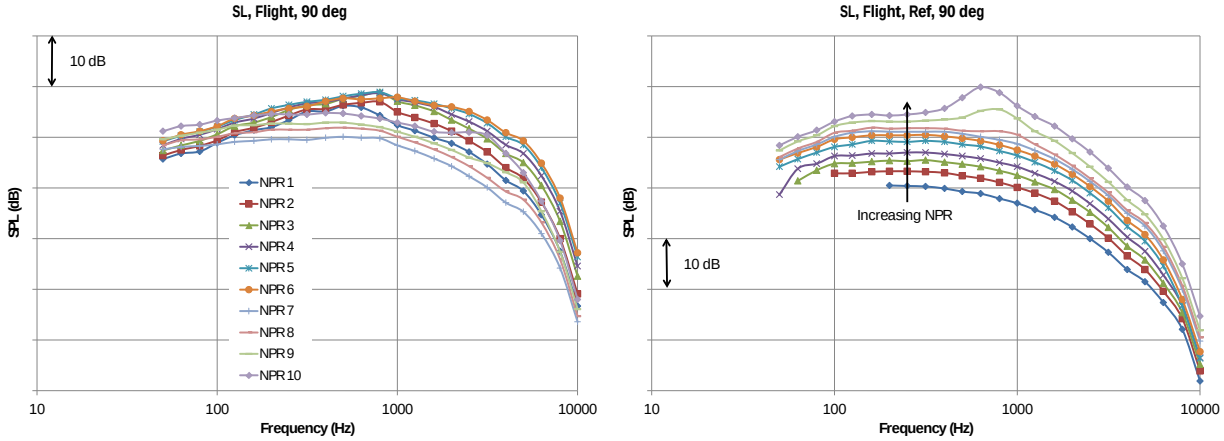

Figure 50 SPL at 90 deg for Sideline Configuration, Flight Conditions, Processed to Sideline, No Heat Addition Cycle Conditions, Test Nozzle on Left, and Reference Nozzle on Right.

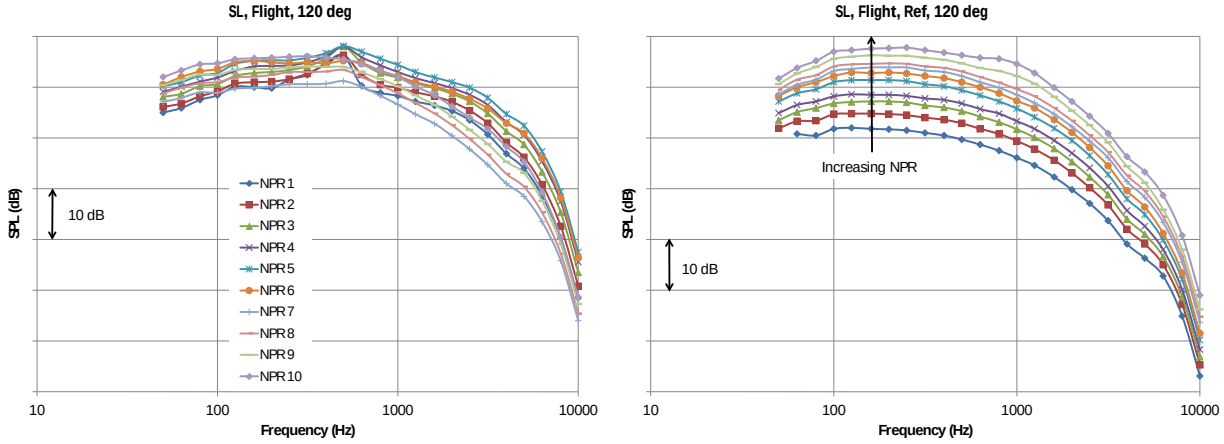

Figure 51 SPL at 120 deg for Sideline Configuration, Flight Conditions, Processed to Sideline, No Heat Addition Cycle Conditions, Test Nozzle on Left, and Reference Nozzle on Right.

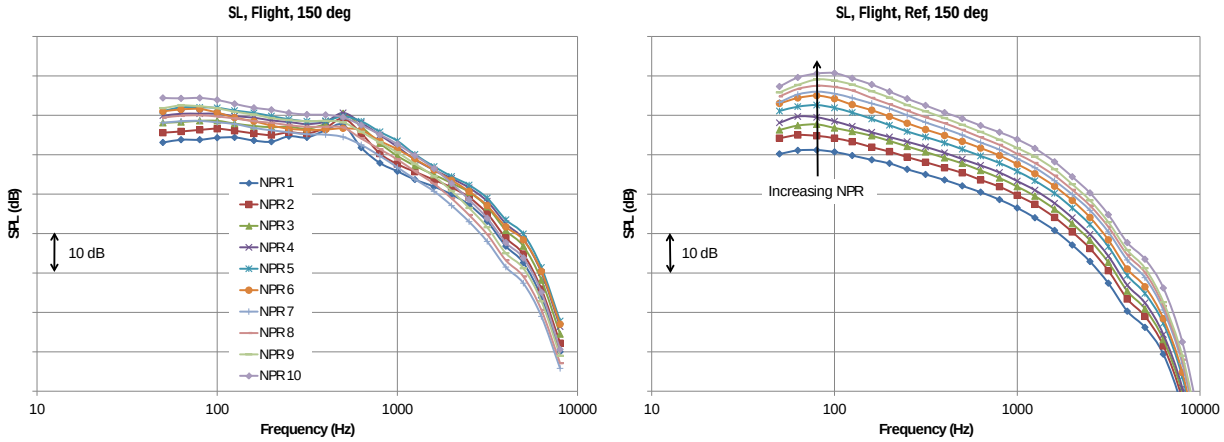

Figure 52 SPL at 150 deg for Sideline Configuration, Flight Conditions, Processed to Sideline, No Heat Addition Cycle Conditions, Test Nozzle on Left, and Reference Nozzle on Right.

3.5.3 TEST SUMMARY

Testing was completed with the majority of the planned test points acquired. Both static and flight simulated data was acquired for two geometric configurations corresponding to the cutback and sideline variable geometry configurations. Three cycles were run for the three levels of heat addition. A reference nozzle was also run at equivalent mass averaged exhaust velocity conditions to provide a reference to compare noise levels to. The reference is a single stream conic nozzle. The test data was processed to full scale by matching thrust at an engine condition corresponding to a take-off profile provided by Lockheed Martin.

The two jet noise reduction technologies continue to show promise and seem to work together to some extent. The cross-over point where the jet noise reduction technologies show noise reduction was a bit lower in terms of power setting (or exhaust) velocity than expected. This was due to a larger impact of flow separation at the primary nozzle exit. The geometry was designed for a heat addition cycle and thus had a very wide range of areas required for all of the operating conditions (including take-off, top of climb, approach, and cruise) This resulted in an area ratio of the primary nozzle contour that is required for the overall system to reach the different areas and provide excellent performance at cruise conditions. The CFD showed some separation at these noise conditions but the impact on noise was much more than expected. However, starting at approximately half way up the cycle line the reduction seen with the jet noise reduction technologies were close to as expected. Heat addition did not show any benefit at the take-off conditions of interest, although if the application had a need for a higher exhaust velocity there is evidence that this could provide a benefit for other applications.

3.5.4 SYSTEM NOISE ASSESSMENT

System noise assessments of the jet noise have been made at various points in the program. For the Lockheed Martin final quad-jet thrust requirements and flight path, from the previous NASA N+3 program, and GE assumed airframe noise levels, a cumulative margin of approximately 23 EPNdB to the Stage 3 requirements was estimated. The initial N+2 quad-jet updated for thrust requirements, aircraft weight, airframe noise estimates provided by Lockheed Martin, and an N+2 propulsion system resulted in an estimation of approximately 32 EPNdB cumulative margin to Stage 3. The cumulative margin to stage

3 increased significantly because the engines were throttled back further for take-off. For the latest N+2 tri-jet configuration, again the thrust requirements, aircraft weight and trajectory have been updated, and the estimated cumulative margin to Stage 3 is approximately 22 EPNdB. The margins for sideline and cutback remain fairly consistent to the original N+3 margins although the heat additions cycle is not showing a benefit for take-off anymore. This is because, similar to as mentioned in earlier sections the engine is being throttled back significantly for take-off now in an effort to hold the engine size constant, and the jet noise reduction technologies are not showing as much benefit as they did for the higher exhaust velocity settings.

Figure 53 shows the EPNL vs thrust plots from the testing at NASA for both cutback and sideline along with the predicted level of the jet noise reduction technologies from previous databases and the same procedure used throughout the N+3 program to estimate system level noise. At these conditions the engine is throttled back and the prediction shows no benefit for the heat addition cycle, and very modest benefit for the jet noise reduction technologies. This agrees with the test data, as the predicted level is very close to the reference nozzle measured noise level at the same thrust values. With the nozzle flow lines cleaned up to eliminate the flow separation that causes the excess noise the test data should match the predicted noise levels very well.

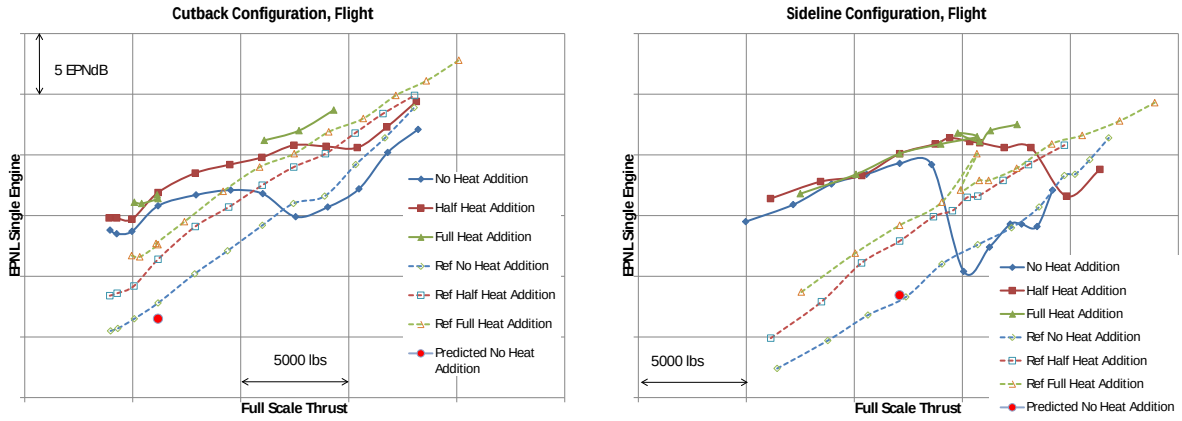

Figure 53 EPNL vs Thrust for cutback and sideline configurations including latest noise prediction.

4 INLET FLOW CONTROL ASSESSMENT

The Lockheed Martin supersonic inlet concept has features unique compared to commercial aircraft and introduces distortion which interacts with the fan to generate noise. Technologies are compiled that can help mitigate the distortion and otherwise reduce noise from the inlet/fan module.

4.1 VIABLE TECHNOLOGIES FOR ENGINE INLET NOISE CONTROL

A list of viable inlet noise control technologies that were found in published literature is summarized. Techniques were broadly classified as passive and active. Passive methods were further classified as geometry based or flow based. Active control strategies included in this list employed a feedback algorithm that used a set of sensors as an input. The algorithm outputs an appropriate control signal to the actuators to achieve noise reduction. Method, Advantage, Penalty along with one reference from each of these techniques is included below.

4.1.1 PASSIVE METHODS (GEOMETRIC MODIFICATIONS)

Absorbent Acoustic Liners

Method: Provide an impedance boundary condition to attenuate wave reflections

Advantage: Works well for high freq. noise as the distance of propagation over the acoustic lining is several wavelength

Penalty: Not effective at low freq. -> requires longer lengths of ducting

Ref: “Advanced turbofan duct liner concepts”, Bielak, Premo, Hersh, NASA CR 1999-209002

Rotor Spacing and Vane Count

Method: Spacing and Vane Count chosen so as to avoid propagation of the cut on modes

Penalty: Increase in engine size and weight, performance concerns

Ref: “Rotor Wake/ Stator interaction noise: prediction vs data”, Topol, Journal of Aircraft, 30, 1993, pp. 728-735

Swept and Leaned Stator

Method: combination of swept and leaned vane-> leading to viscous wake decay & more wakes intersecting the vane, causes additional noise cancellation

Advantage: Relatively Simple

Penalty: Increase in engine size and weight, higher aerodynamic loss

Ref: Envia, Aeroacoustics, 1, no. 1, 2002, pp. 43-64, Fan noise reduction: an overview

Flow Control Obstructions

Flow Control Obstructions (Triangular, Sinusoidal and Cylindrical) placed in a circumferential manner in front of rotor

Method: Noise from the obstruction is equal in magnitude and opposite in phase compared to the primary tone. Magnitude and phase are controlled by axial dist. between the rotor and obstruction and angular position of the control obstruction

Penalty: Loss in Engine Efficiency, Increased Weight

Ref: “Experimental Validation of tonal noise control from subsonic axial fans using flow control obstructions” Gerard, Berry, Masson, Gervais, Journal of Sound and Vibration, Vol. 321, 2009, pp. 8-25

Others (Geometry Based)

- Vortex Generators-> Mix out Wake (Needs Consideration to shape, size and location)
    - Micro Vortex Generator(Lin. J. C , Control of Turbulent Boundary- Layer Separation using Micro Vortex Generators, AIAA 1999-3404)
    - MEMS Controlled Vortex Generator (Tillman, Kimmel, Addington, Myatt, Flow Control Research and Applications at the AFRL's Air Vehicle Directorate, 2004-2622)
- Riblets (Walsh, M. J., Drag Characteristics of V-Groove and Transverse Curvature Riblets. AIAA Viscous Flow Drag Reduction. Vol. 72, 1980, (ed.Gary R. Hough), pp. 169-184.)

Passive Methods (Flow Based)

Steady Blowing

Location: Jets placed downstream of Rotor Blade Trailing Edge.

Method: Circumferential position of Jets varied to vary the phase of the secondary sound field relative to primary one (Rotor-Stator)

Advantage: Reduction in Blade Passage tones (max 9.5dB), but increase in broadband sound due to jets

Penalty: Loss in Engine efficiency

Ref: “Technology Approach to aero engine noise reduction”, Neise and Enghardt, Aerospace Sci and Tech. 2003

Unsteady Blowing

Location: Jets placed downstream of Rotor Blade Trailing Edge.

Method: Pulsating flow of air jets was synchronized with the Blade Passage Frequency (BPF)

Advantage: Low mass flow needed for control (Mjet/Mfan ~1%).Fan Pressure raised by 15%. Reduction in Blade Passage tones by about 20dB.

Penalty: Increase of energy in Higher harmonics due to air pulse-impeller blade interaction

Ref: “Technology Approach to aero engine noise reduction”, Neise and Enghardt, Aerospace Sci and Tech. 2003

Trailing edge blowing

Method: Flow supplied through the shaft along the labyrinth of internal passages that start from the blade root and terminate at a series of trailing edge ports in rotor. Wakes issuing from the rotor blades are made more uniform so as to cause less unsteady forces on the stator, reducing the tonal noise

Advantage: blowing rate of only 1.6-1/8% to achieve in far-field tone power at the first 3 harmonics (as high as 12.4 dB PWL)

Penalty: Need for additional plumbing in the vanes, Structural issues, Loss in engine efficiency

Ref: “Low Speed fan noise reduction with trailing edge blowing” Sutliff, Tweed, Fite, Envia, Intl Journal of Aeroacoustics, 1, 2002, pp. 275-305

Dielectric Plasma Discharge Actuators

Method: Generates a body force which imparts momentum without addition of mass. Introduces large scale vorticity that promote mixing, Could be employed to promote mixing and reduce wakes behind the vanes or at the inlet BL

Advantage: capable of minimizing radiated aerodynamic noise. can be operated in cont. and pulsed modes, no moving parts, consume little power. Low integration, maintenance and operating costs. Compact and effective

Penalty: Effectiveness only at low speeds
Ref: Reduction of Fan and Compressor Wake deficit using plasma actuation for tonal noise reduction , Lemire, Duc Vo, Journal of Turbomachinery, Vol. 133, 2011,
Active Noise Control of Bluff Body flows Using Dielectric Barrier discharge Plasma Actuators, Kozlov and Thomas, AIAA 2009-3245

Boundary layer suction on the duct circumference

Noise produced by the interaction of the B.L. (with large intake turbulence and spatial and temporal variations) with the blade tip

Method: Generate a thin uniform Boundary Layer that interacts with rotor blade tip

Advantage: 15dB reduction in few of the far field tones upon 5% removal of main flow

Penalty: could produce cut on residual distortion that could propagate downstream to increase far field sound

Ref: “Reduction of fan noise by annulus boundary layer removal” Moore, Journal of Sound and Vibration, 43, 1975, pp. 671-681

Herschel Quinke Tubes

Technique is based on Acoustic Noise Cancellation

Method: Employ an array of H-Q tubes at the inlet of a turbo fan. The exit of the HQ tube produces out-of phase sound at certain frequencies which cancel with the generated noise

Advantage: No Moving Parts

Disadvantage: Works only for a certain band of freq.

Ref: “Burdisso, R.A. and Smith, J.P., “Control of Inlet Noise from Turbofan Engines Using Herschel-Quinke Waveguides,” 6th AIAA/CEAS 2000-1994, (2000).

Serrated Blades

Method: Fan Blades are serrated for mixing wakes therefore attenuate Fan noise (at BPF and Spectrum of Freq. related to wake turbulence)

Advantage: No Moving Parts, Economical
Disadvantage: Acoustic benefits were not evaluated.

Ref: Gliebe, P., Serrated Fan Blade, US Patent: 6733240 B2, May 11 2004.

Tip Platform Extensions

Method: Employ pressure side tip extensions to minimize tip leakage flow in an axial flow fan with serrated trailing edge

Advantage: No Moving Parts

Penalty: Acoustic benefit yet to be quantified

Ref: Arturk, A., Camci, C., Axial Flow fan Tip Leakage Flow Control using tip platform extensions

Other Passive Methods (Flow Based)

Active Vortex Generator (McManus and Magill, Separation Control in Compressible and Incompressible Flows Using Pulsed Jets, AIAA 96-1948)

High Frequency Control, [Powered Resonance tube arrays] (Ganesh Raman (IIT), Valdis Kibens, William Bower)

Active Methods

Active Noise Cancellation (ANC)-1

Method: Loud Speakers as Actuators and Microphones as Sensors, Loud Speaker used to generate anti phase sound field. LMS Algorithm and Modal Control Concept used to reduce the tonal frequencies (Blade Passage Freq.)

Advantage: Effective in reducing the BPF by about 25dB. Modal Controller (Conceptually based)

Penalty: Complex

Ref: “Active Control of noise from Turbomachines-Control algorithms and experimental results”, Maier and Zillman, 30th International Cong, Dan Haag, 2001

Active Noise Cancellation-2

Method: Stator vanes equipped with two piezo actuators each on suction and pressure side Microphone mounted on the inlet duct acted as sensors. Feedback Control was employed to suppress tonal noise

Advantage: Up to 7dB reduction in BPF tones

Penalty: Complex

Ref: “Control of Fan Noise by Active Stators”, Zilman, Maier, Bouty, Antoine, Just, Borchers, Enghardt, Tapken, 2001.

Active Noise Cancellation-3

Method: blowing air jets into the blade tip. The actuating jets were mounted on fan casing. Microphone mounted on the inlet duct acted as sensors

Advantage: low weight, low mass injection

Penalty: Complex

Ref: “Technology Approach to aero engine noise reduction”, Neise and Enghardt, Aerospace Sci and Tech. 2003

Active flow and Noise suppression

Method: Radial rods (Actuators) equally spaced circumferentially on a ring in a fan duct. Flush Mounted Microphones on the fan duct upstream of rods. Distance with which rod protrudes into the duct was adaptively adjusted in response to microphone respectively using the steepest decent algorithm. Control effectiveness depend on the modal content and number and position of control rods

Advantage: Induce noise reduction as high as 25dB

Penalty: Aerodynamic loss, Weight, Low noise reduction at higher fan speed (which incl. more modes)

Ref: “Wake generator control of inlet flow to cancel flow distortion noise”, Kota and Wright, Journal of Sound and Vib., 195, (2006), 94-113

Active Noise Cancellation-4

Method: Active Airfoils on Stators (Active Noise cancellation of rotor-stator noise). Perforated metal cavities in the stators that formed resonators driven by compression drivers

Advantage: low weight, low mass injection

Penalty: Weight concerns and complex

Ref: Sawyer and Fleeter, Journal of Propulsion and Power, 18, 2002, pp. 100-106

Active Noise Cancellation-5

Method: Helmholtz resonators mounted on the circumference of the duct act as actuators for ANC

Advantage: Could produce local (inlet or exhaust noise cancellation) or global noise suppression. Simultaneous inlet and exhaust noise cancellation.

Penalty: Location sensitive, Weight, Complex
Ref: "Active resonators for control of Multiple spinning modes in an Axial flow fan Inlet", Walker, Hersh, Heidelberg, Sutliff, Spencer, 96-1740.

Other Active Methods

Advanced Strut-Wake Mixing (Passive/Active)

Spatially modulated time delay air jets -> reduced far field noise, superior to spatially uniform pulsed jets

(Guo, AIAA 2006-2847, Low Noise Actuator Design for Active flow Control)

Contributed from Lockheed-Martin

Variable Aux Lip Thickness
Variable Lip Thickness
Distortion Reduction (Bleed, Vanes, Microvanes)
Embedded Accessories
Zero Length Diffusor
Mixed Compression Inlet

Once this list was collected the concepts were arranged in categories as shown in Figure 54. They were ranked in the following categories; acoustic benefit, cost, and risk. The cost category included the impact on SFC and weight. The risk category included mechanical/structural, manufacturability, system integration, reliability, serviceability, and risk in ability to achieve performance, and risk in ability to achieve benefit. Each of the categories could be assigned a value of 0, +/-1, 3, and 5, as appropriate. The final benefit score is the acoustic benefit and the final risk score is the average of the cost and risk values. This technology ranking is one way to provide a semi-quantitative prioritization of technologies based on expert opinions. Figure 55 shows the results on Figure 54 plotted as risk vs benefit. On this plot the most attractive technologies to pursue are those on the upper left corner. In this case, those were essentially design practices commonly followed. The other technologies can be downselected based on the acceptable level of risk for the expected benefit.

			Cost		Risks (0/1/3/5)								
	Technology	Acoustic Benefit (1/3/5)	DSFC (0,+-/1/3/5)	Weight (0, +-1/3/5)	Mechanical / Structural	Manufacturability	System Integration	Reliability	Serviceability	Risk in ability to achieve performance	Risk in ability to achieve benefit	Benefit Score	Risk Score
Geometry Based	Absorbent Acoustic Liners	5	1	3	0	0	0	0	0	0	0	5.0	0.5
	Rotor Spacing and Vane Count	5	0	3	0	0	0	0	0	0	0	5.0	0.4
	Swept and Leaned Stator	5	0	1	0	0	0	0	0	0	0	5.0	0.1
	Flow Control Obstructions	3	1	1	0	1	1	1	0	1	3	3.0	1.1
	Herschel Quincke Tubes	3	1	3	1	1	1	1	1	1	1	3.0	1.3
	Serrated Struts	3	0	0	1	1	1	1	0	1	3	3.0	0.9
	Tip Platform Extensions	1	1	1	1	1	1	1	0	3	3	1.0	1.4
	Vortex Generators on Struts (Active/Passive)	3	1	1	0	1	1	1	0	1	3	3.0	1.1
Flow Based Control	Unsteady Blowing (Closed/Open loop)	3	1	1	1	3	3	3	1	1	3	3.0	1.9
	Trailing Edge Blowing (Closed/Open loop)	3	3	1	1	3	3	3	1	1	3	3.0	2.1
	Boundary layer Blowing/Suction (Closed/Open loop)	1	3	1	1	3	3	3	1	1	3	1.0	2.1
	High Frequency Control (Powered Res.Tubes)	1	1	1	1	3	3	3	1	1	5	1.0	2.1
	Spatially Modulated air jets (Open loop)	3	1	1	1	3	3	3	1	1	3	3.0	1.9
Active (Feed-back) Control	Dielectric Plasma Discharge (Closed/Open loop)	3	1	3	1	5	5	5	1	1	5	3.0	3.0
	Active Noise Cancellation (Includes different sensors (eg: microphone)-actuator (loudspeaker, piezo actuators) and feedback control methods). Locations of the sensor-actuators varied (e.g. blade tip, duct) depending on the mode to be suppressed	5	1	3	1	3	5	5	1	1	3	5.0	2.5
Advanced Concepts	Advanced Strut-Wake Mixing	3	0	0	1	3	1	1	0	1	3	3.0	1.1
Contributed by LM	*Variable Aux Lip Thickness*											1	3
	Variable Lip Thickness											2	5
	Distortion Reduction -Bleed											1	1
	Distortion Reduction -Vanes											1	3
	Distortion Reduction -MicroVanes											1	4
	Embedded Acessories											4	2
	Zero Length Diffusor											5	5
	Mixed Compression Inlet											4	4

Figure 54 Spreadsheet of Potential Flow/Noise Control Technologies for Inlet/Fan Noise Reduction.

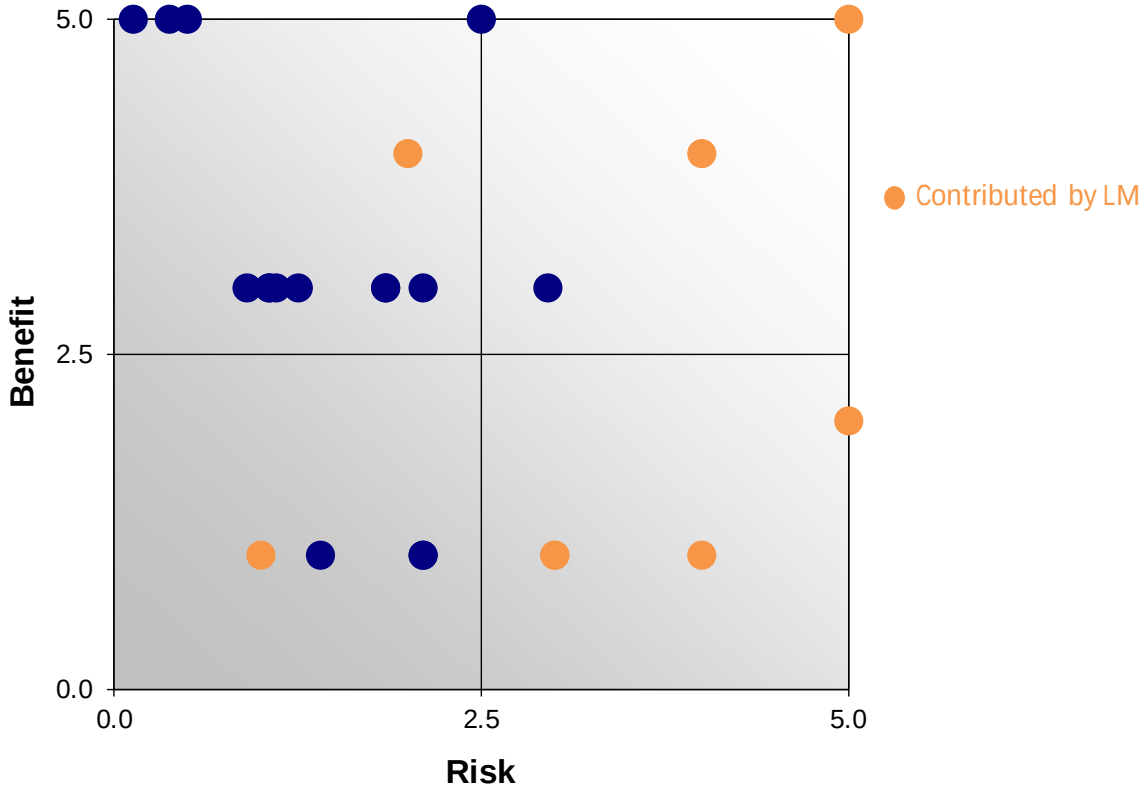

Figure 55 Plot of Risk vs Benefit for Inlet Flow/Noise Control Technologies.

5 INLET DISTORTION EVALUATION

This task included a high fidelity aeroacoustic assessment of the impact of the Lockheed Martin supersonic inlet in front of a fan module. The first step was the choice of fan module to use in the evaluation. There is not a detailed design available of a variable cycle engine for the exact engine configuration being developed in these NASA studies. There was a two stage fan tested in the past after the end of the HSR program, and there were a number of single stage fans tested at NASA in the 9x15 wind tunnel with acoustic data. In the end the SDT fan with low vane count was chosen, although this is a single stage fan the main noise source of concern with the supersonic inlet is the distortion from the struts interacting with the first stage of the fan. The other primary reason this module was chosen was that analysis has been done on this fan configuration and the approach has been validated with experimental data.

The first step in the process was to couple the supersonic inlet with the SDT fan module. The inlet provided by Lockheed Martin was scaled down by 40% to match the fan cowl diameter.

The inlet and SDT fan hub are merged together, iteratively to ensure the total amount of diffusion is maintained, and does not cause a build-up of low momentum fluid which could lead to separation at the fan hub.

Figure 56 shows some sample meshes around the fan blade leading edge near the hub and near the tip region. This is a fairly complicated meshing procedure, with hand tuning required to capture all of the effects of different regions of the flowfield.

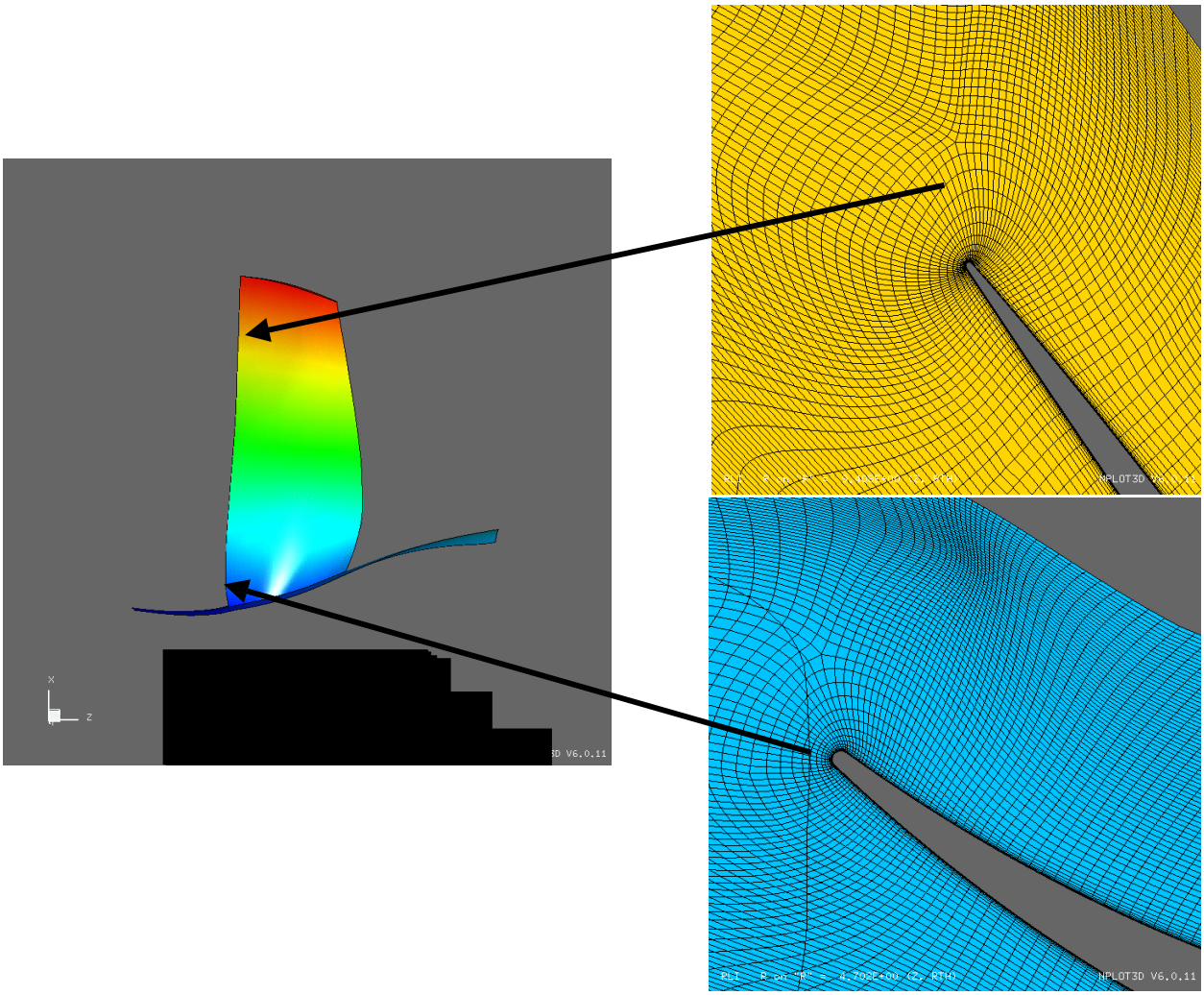

Figure 56 Sample grid mesh at hub and near case tip of fan blade.

A steady calculation is run first to establish the flow and boundary conditions, especially for the fan and OGV discharge pressures.

Figure 57 shows the Massflow at the inlet and exit of all components through the calculation iterations. This shows that the solution has converged.

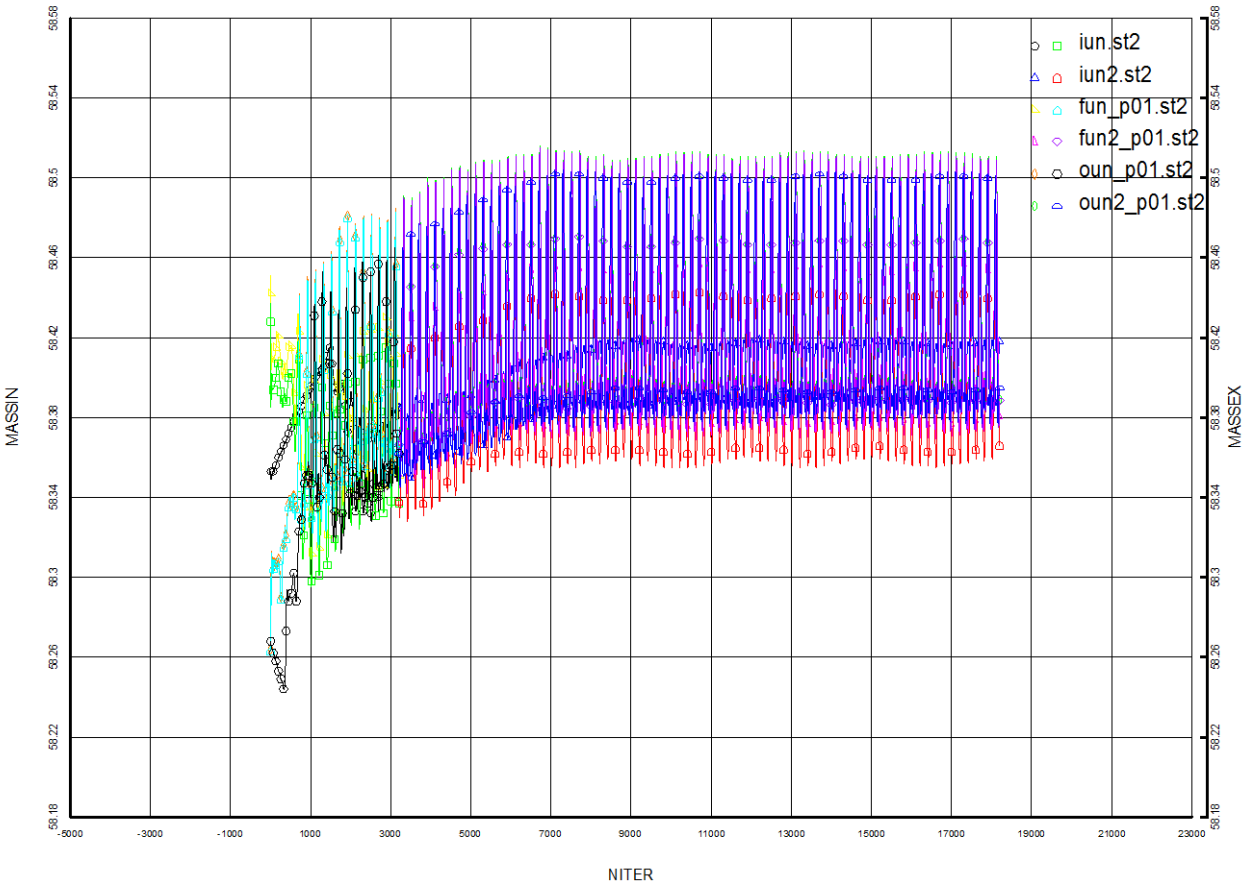

Figure 57 Massflows at the inlet and exit of all components.

Figure 58 shows the total pressure at the inlet and exit of all components over the analysis iterations. The difference between the lower lines and the upper lines signifies the pressure rise across the fan. The difference between the two lower lines corresponds to the inlet pressure loss, and the difference between the two upper lines corresponds to the pressure loss across the OGVs.

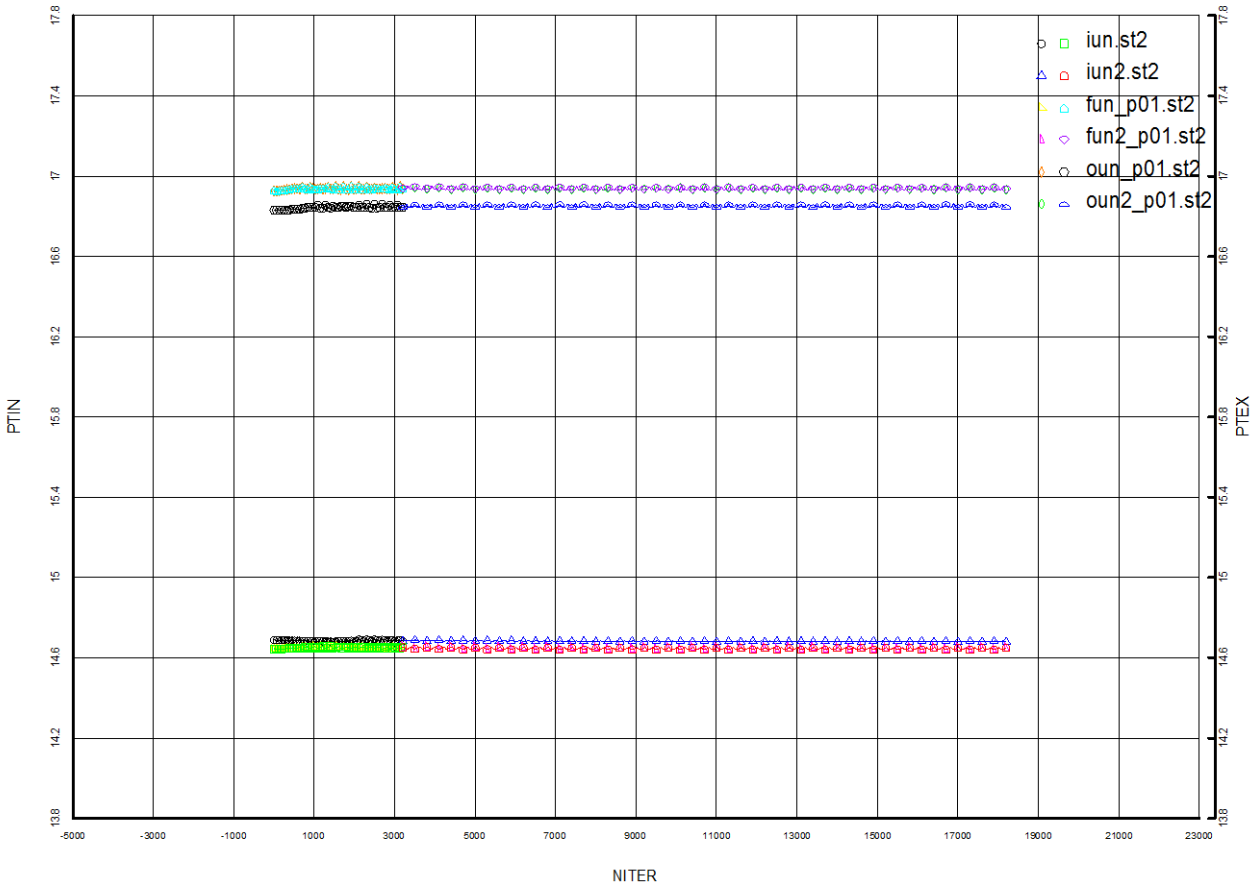

Figure 58 Total pressures at the inlet and exit for all components.

Figure 59 shows similar information for the static pressure. The difference between the two inner lines is the static pressure rise across the fan. The difference between the two lower lines is the static pressure rise through the inlet, and the difference in the two upper lines is the static pressure rise across the OGVs.

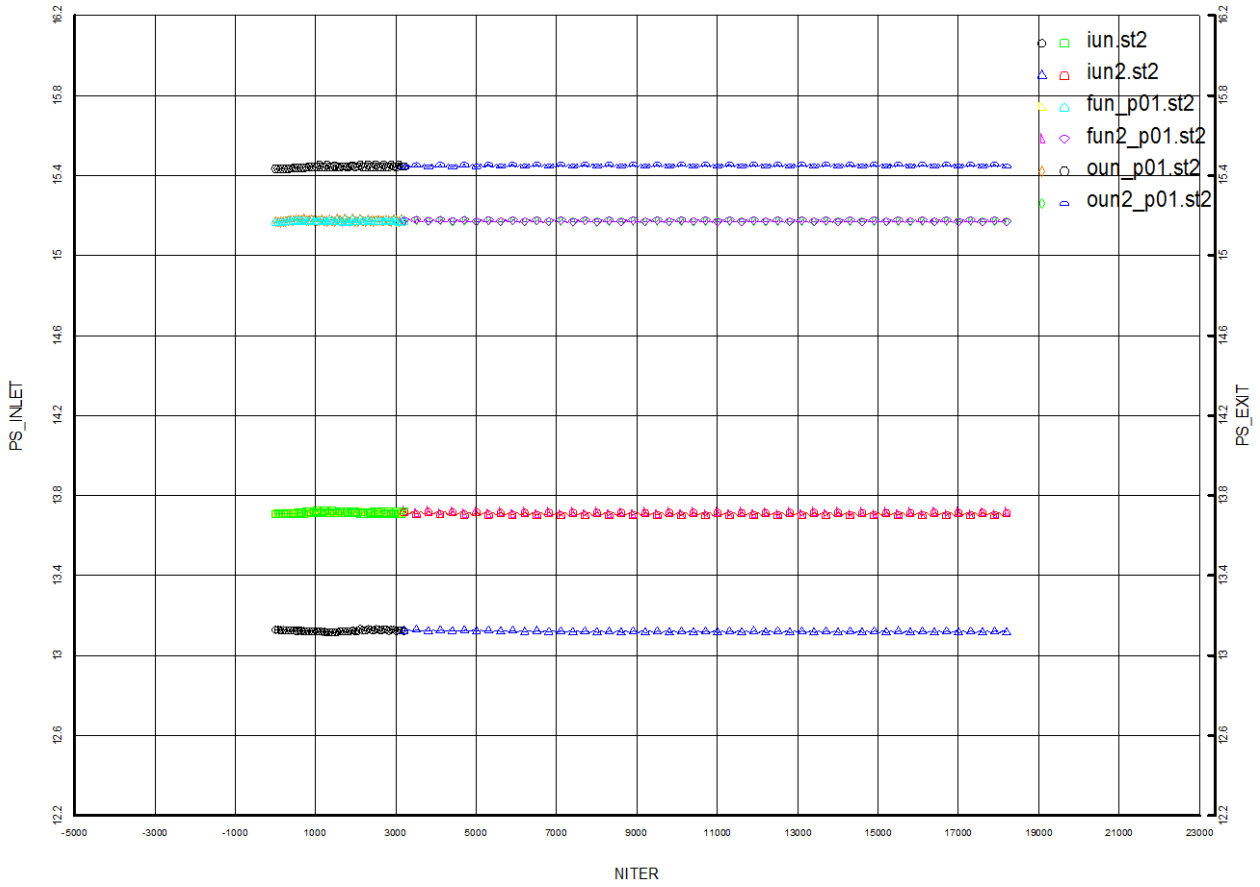

Figure 59 Static pressure at the inlet and exit over all components.

Figure 60 shows the progression of the inlet distortion ingested and segmented by the rotors, then merged with the fan rotor wakes. These more complex wakes then interact with the OGVs.

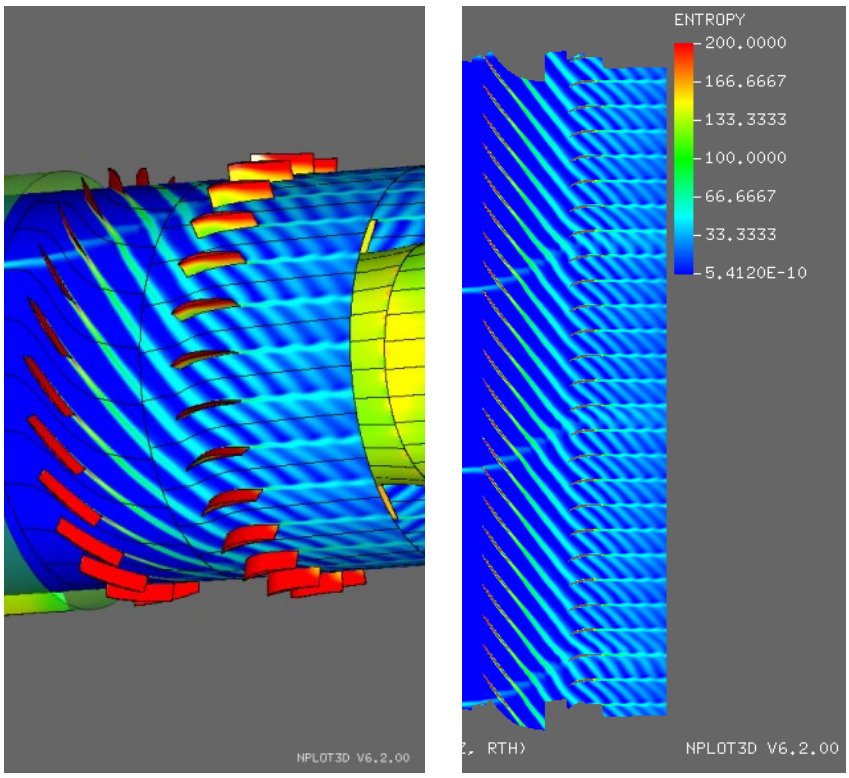

Figure 60 Progression of the inlet distortion through the fan and OGVs.

Figure 61 shows a cross-sectional view of the wakes (entropy) at different axial stations. The image at the left shows the view just downstream of the fan. The image on the right shows the more complicated entropy field after passing through the OGVs.

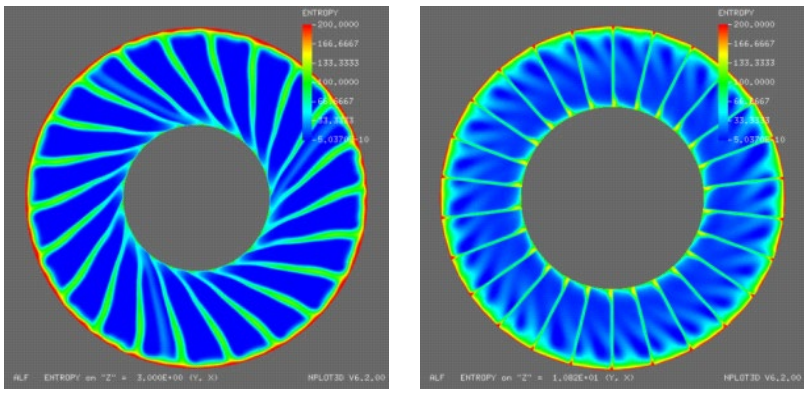

Figure 61 Wake (entropy) visualizations at different axial stations.

Figure 62 Shows static pressure plots through two different planes and unwrapped for easier visualization. The image on the left is at the fan rotor mid-span and the image on the right is through the fan rotor near the casing. The lattice patterns are generated by pressure wakes from the fan and reflections from the inlet features.

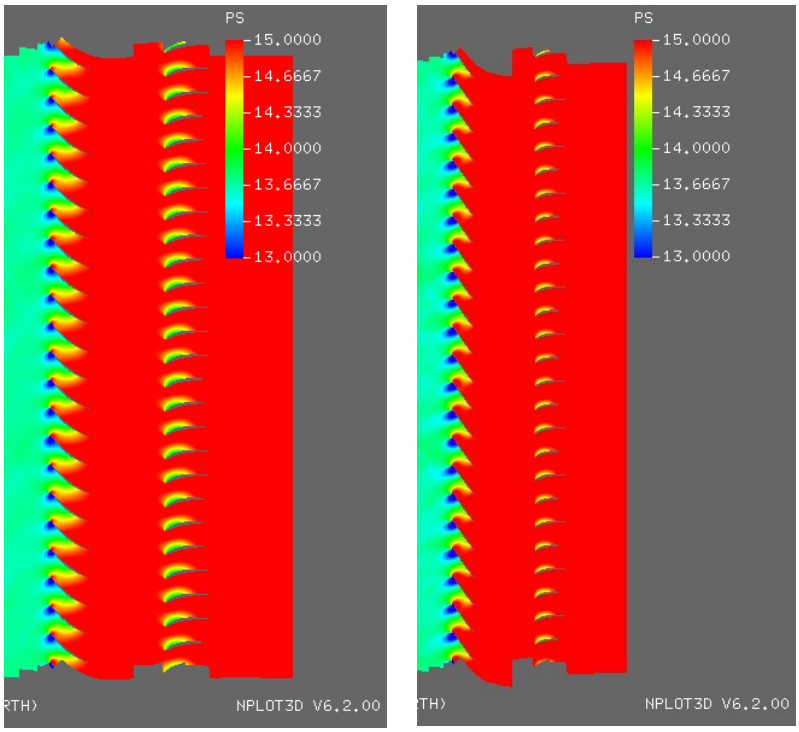

Figure 62 Static pressure plots through two planes.

5.1 ACOUSTICS ANALYSES

The time accurate data from the nonlinear unsteady RANS calculations contains the acoustic signature mixed with the hydrodynamic fluctuations. To separate out the radiating (acoustic) component, the following procedure is used.

1. A Fourier transform in time using one blade passage of time data is carried out over an axial plane through which the acoustic intensity flux (sound power transmitted) is desired. In the simulations only the blade passing frequencies are captured as all blades are assumed identical and the inflow is uniform.
2. For each blade passing frequency, an eigenvalue problem is then posed as described in Ref [1]. The solution of this eigenvalue problem yields axial acoustic wave numbers as the eigenvalues and the corresponding eigenvectors correspond to the acoustic modes in the duct (assuming that it is infinitely long with a constant cross-section). The duct modes correspond to the more familiar Bessel (or Hankel) functions for uniform flows and are characterized by a spin number and a radial number (m, n). These modes are then used, assuming orthonormality, to compute the acoustic power contained in each mode. Acoustic power in each mode is then summed up to calculate the total power at that blade passing frequency.

5.1

The above procedure has been used to calculate the acoustic power radiated due to two sources: (1) inlet distortion interaction with the fan, and (2) fan wake interaction with the OGV. Both source produce noise at the blade passing frequency and although some source characterization is possible by analyzing the circumferential mode orders, we chose to perform two sets of simulations – one with the OGVs present and another with the OGVs removed. In the second case, the tone noise would solely come from the inlet distortion interaction with the fan. Note that in these calculations the fan tip speed is subsonic and there is no blade passing noise due to the potential field radiating out (becoming "cut on").

The acoustic decomposition is carried out on an axial plane just upstream of the fan. Time accurate data is sampled at this plane. A total of 200 samples are collected that comprise one blade passage time. A Fourier Transform in time is applied to this data to obtain blade passing harmonic amplitudes; this is schematically shown in Figure 63. Each blade passing harmonic is then further decomposed into acoustic (radiating) and hydrodynamic (non-radiating) fields using the Eigenvalue decomposition method described in Ref [1], also sketched schematically in Figure 64.

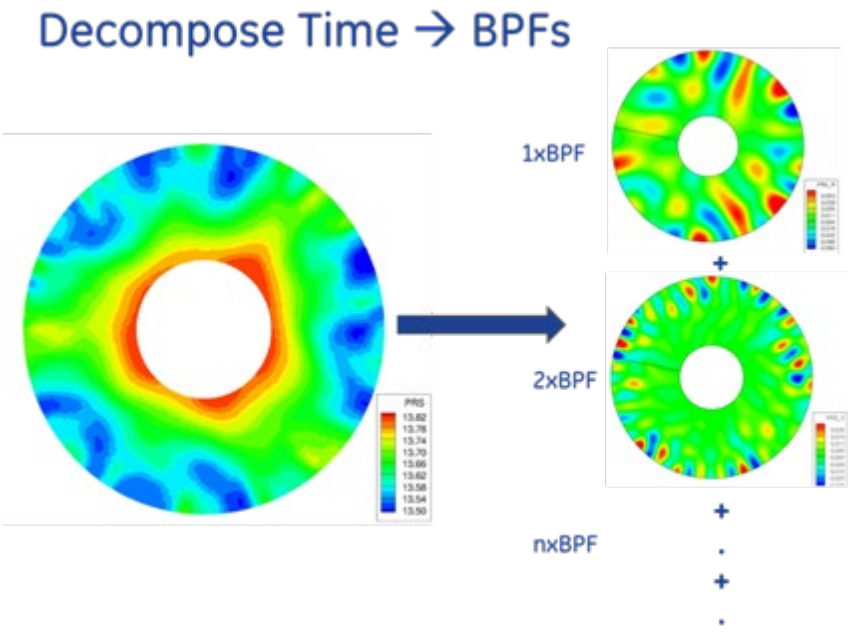

Figure 63 A schematic showing Fourier decomposition of the time-accurate data at an axial plan into blade passing harmonics.

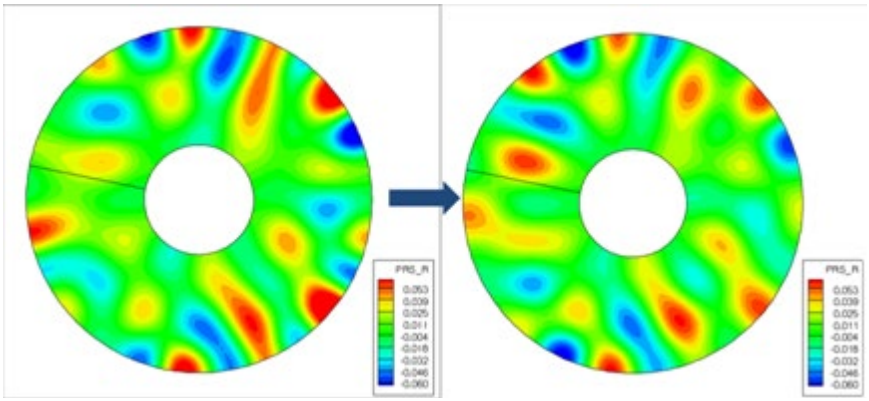

Figure 64 Schematic showing a harmonic perturbation field (full field on left) and radiating part only on right.

Figure 65 compares the acoustic power in the first four blade passing harmonics from two calculations: one that includes only the inlet distortion and the fan (this would only include the inlet distortion interaction with fan noise source) and second that includes OGVs in addition to the inlet distortion and the fan. There is a very slight difference in the sound power levels between the two calculations suggesting that the inlet distortion-fan interaction source dominates for the inlet radiated noise. This is quite interesting considering the fact that the inlet distortion does not appear as strong as the fan wakes. The noise generation mechanism however is the interaction of inlet distortion vortical energy with the downstream bladerow, which follows almost a fifth power law with the relative velocity. The relative flow speed seen by the fan is much higher than that seen by the OGV, which could explain why the inlet

distortion-fan interaction is so strong. In addition, the inlet distortion is non-uniformly spaced azimuthally, which essentially allows the interaction mechanism to scatter acoustic energy into very low order azimuthal modes, most of which are cut-on in the duct and hence there are more channels for transferring energy. While in the fan-OGV interaction case, there are just a handful of circumferential modes that are cut-on and hence only a small portion of the acoustic energy gets transmitted. This is demonstrated in Figure 66, which shows the amplitude of the cut-on acoustic modes that are generated at first blade passing frequency due to the inlet distortion interaction (on the left) versus for that generated via fan-OGV interaction mechanism (on the right).

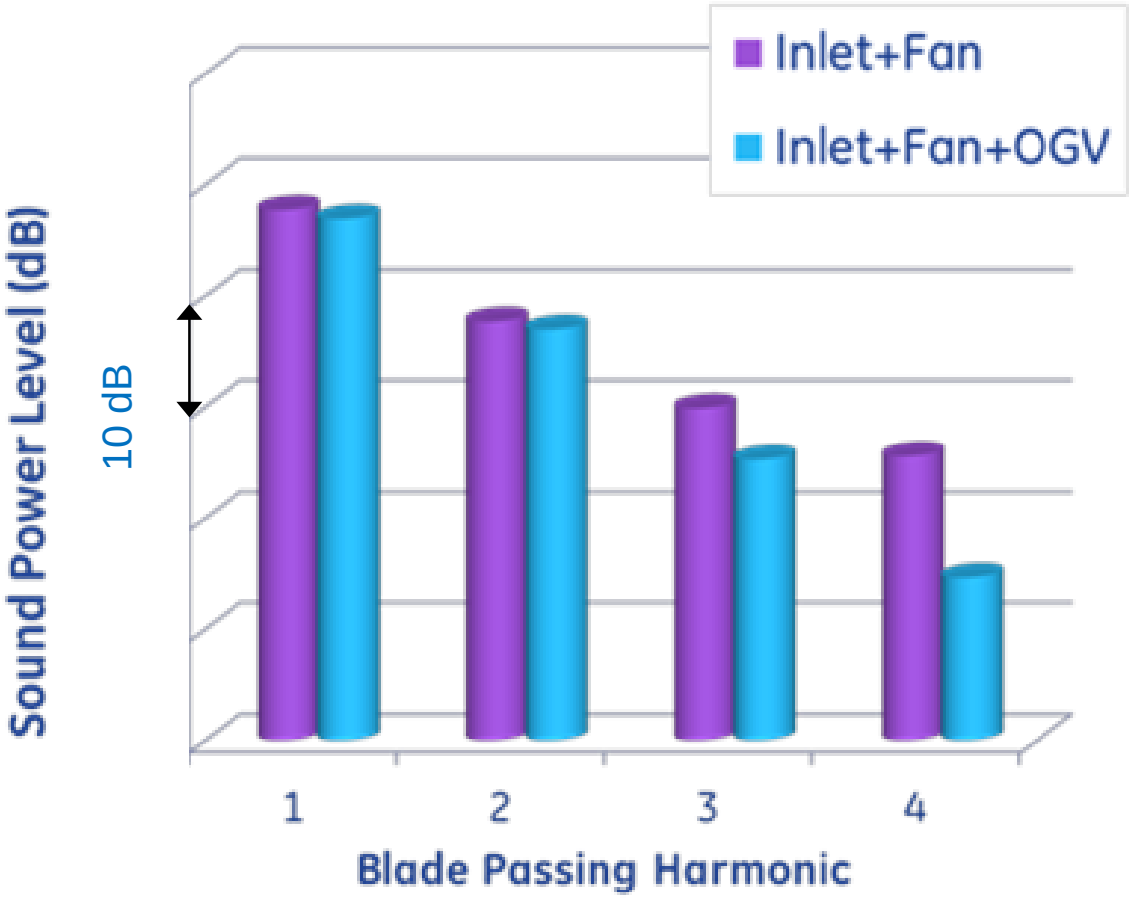

Figure 65 Sound power level at an axial plane just in front of the fan due to the inlet distortion-fan interaction and the combined inlet distortion-fan-OGV interaction.

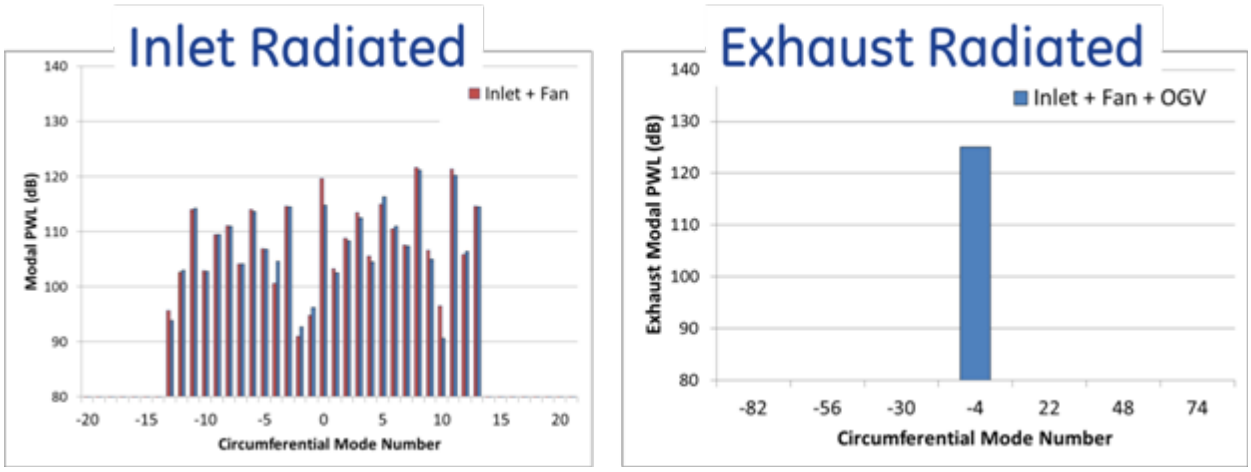

Figure 66 Circumferential mode power for inlet radiated acoustic power from inlet distortion-fan interaction (left) versus aft radiated from fan-OGV interaction (right).

It is a little disconcerting to see that the levels for the case where the OGVs are absent are higher (for higher harmonics) than for the case when the OGVs are present. One possible reason for this is the possibility that the operating condition in the presence of the OGV changes ever so slightly to change the inlet distortion, or the incidence of the fan blade. But the dominant mode and the overall power level are within 2 dB.

The conclusion for the acoustics analyses of the time-accurate simulation is as follows: inlet distortion-fan interaction appears to be the dominant noise generation mechanism for the configuration attempted here. High fan tip speed and large mode density are two potential reasons why this result is observed.

6 SUMMARY

This report covers the activity in Phase 1 of the N+2 NRA – System Level Experimental Validations for Supersonic Transport Aircraft. Three main activities were included in this portion, an updated conceptual design of a propulsion system to meet the N+2 goals with technologies appropriate within the associated timeframe, a demonstration of two jet noise reduction technologies in the exhaust, and an assessment of the noise impact of the supersonic inlet with the fan module and associated technologies that can improve the noise impact.

The proposed engine concept incorporated advanced technologies such as Cooled Cooling Air (CCA) with modulated turbine cooling flow, high pressure (HP) controlled area turbine nozzle (CATN), variable area bypass injector (VABI), low noise/high performance exhaust, and heat addition. The maximum T4 of the engine was set to meet the cruise NOx requirement. During the course of the N+2 Phase 1 the Lockheed Martin vehicle was changed from a 4 engine to a 3 engine application. Further iterations of the 3 engine application changed relative levels of the thrust characteristics and another iteration of the conceptual engine design needs to be performed. Specifically higher fan pressure ratio engines should be evaluated to better match the engine characteristics to the thrust requirements.

A scale model exhaust system was designed incorporating two jet noise reduction technologies. This scale model included struts to transfer the outer secondary flow into the center of the exhaust. RANS CFD was used to help design and evaluate the struts to ensure the flow could be transferred efficiently.

Large Eddy Simulation continues to run on one configuration of this GE nozzle as well as a reference nozzle, also tested to provide a baseline. The model was fabricated and tested at NASA GRC's NATR in AAPL. The test was completed on schedule and farfield acoustic data was acquired for static and flight conditions for three cycle lines simulating three heat addition settings. Two physical geometries were fabricated to simulate the cutback and sideline variable geometry settings. The results showed that flow separated from the primary nozzle exit due to too much overexpansion for the lower nozzle pressure ratio cycle conditions. The nozzle design was for a full heat addition cycle and the required area variation over all elements of the flight envelope results in a non-optimum area ratio of the nozzle at take-off conditions. This flow separation resulted in excess noise at the lower power settings of the cycles and the GE nozzle was louder than the reference nozzle. At higher power settings the expected noise reduction was seen. The cycles with heat addition operation did not show any benefit, although at higher power settings it is trending in that direction.

System level noise assessments for the latest tri-jet thrust requirements and flight profile estimate margin to meet the N+2 noise goals, however the test data, for the reasons discussed above, had excess noise at these levels. Since the engine is throttled back so much at these new tri-jet thrust requirements this type of nozzle is not predicted to be much quieter than the reference nozzle, a perfectly mixed exhaust. The engine fan pressure ratio and airflow size needs to be re-evaluated based on the latest thrust requirements and in all likelihood a higher fan pressure ratio/smaller engine could better meet the overall system requirements and result in engine settings where this nozzle concept will be more effective again.

A list of viable technologies were collected and ranked/prioritized to address the unique features of the Lockheed Martin supersonic inlet and its impact on noise. The supersonic inlet has unique features which introduce distortion, which translates to noise as it interacts with the fan. The technologies included flow control to improve the distortion as well as other concepts to improve the acoustics. The technologies were than rated based on acoustic benefit, risk and cost. This provided a ranked/prioritized list of technologies for future consideration.

An aeroacoustic assessment was performed on the Lockheed Martin inlet and the SDT fan with and without a low vane count set of OGVs. The fan configuration was chosen as it captures the primary interaction of the inlet distortion hitting the fan, and it has been used previously to validate the aeroacoustic tools. The results showed that the inlet distortion interacting with the fan is a larger noise source than the fan wakes interacting with the OGVs. This will become important as the exhaust jet noise reduction technologies are matured and levels are reduced.

7 NEXT STEPS

Due to the change from a four to three engine powered aircraft and other changes in the overall thrust requirements a short study needs to be performed on the propulsion system looking at different fan pressure ratios. This can rebalance the engine relative to the thrust requirements. An acoustic assessment will be part of this study to ensure that the final fan pressure ratio chosen will continue to meet the noise goals.

The aeroacoustic nozzle must be redesigned based on the experience and learnings from the completed testing. The nozzle will be designed for a cycle without the heat addition. This will reduce the overall area variations required by the variable geometry exhaust and reduce the area ratio at take-off conditions. RANS and LES will be used to ensure there is no separation at the take-off conditions. The remaining data (phased array and PIV) taken by NASA will be used to help redesign the exhaust system. This data will also be used to validate the LES that is currently still running.

The promising (highly ranked) technologies for fan/inlet noise should be analyzed using CFD to determine their effect on controlling the distortion. A more representative fan module should replace the SDT fan used in the current aeroacoustic assessments. The best performing flow control technologies should be used in the full aeroacoustic analysis to see what effect they will have on the inlet/fan noise generation.

8 ACKNOWLEDGEMENTS

This work was funded by the NASA N+2 Supersonic program administered by Peter Coen at the NASA Langley Research Center under prime contract (Lockheed Martin) NNC10CA02C. The authors recognize numerous individuals from both GE Global Research and GE Aviation, and Lockheed Martin for their technical guidance. NASA GRC conducted the scale model exhaust testing flawlessly and many thanks go out to all who contributed to that effort.

9 REFERENCES

[1] A. Sharma, S. K. Richards, T. H. Wood, and C. Shieh, "Numerical Prediction of Exhaust Fan-Tone Noise from High-Bypass Aircraft Engines," *AIAA Journal*, vol. 47, no. 12, 2009.

Appendix C.—Stanford Final Report

Development of Adjoint-Based Design Capabilities for Equivalent Area Distributions for the NASA/LMCO Supersonics N+2 Efforts

Juan J. Alonso, Francisco Palacios, Michael Colonno, Jason Hicken, Trent Lukaczyk
Stanford University, Stanford CA 94305, USA

This report describes the efforts of the Stanford University (SU) Team over the past 12 months in the development of new adjoint-based techniques for the design of supersonic aircraft that must match a particular equivalent area distribution at constant lift coefficients. This tool is meant to be part of a larger effort that will culminate in a design module that can be incorporated into larger multidisciplinary analysis and optimization capability that Lockheed/NASA are seeking. The report focuses on the description of the complete capability including the flow analysis, the formulation and implementation of an adjoint solver for the equivalent area distribution, and the shape design process of a trijet supersonic aircraft proposed by LMCO. This shape design effort is rather challenging and unconventional due to three factors: the complexity of the geometric details involved that require a full unstructured flow and adjoint solver methodology, the *apriori* grid adaptation process needed for capturing the shock and expansion waves in the near-field (without the need for additional mesh adaptation), and the selected objective function for the calculation of sensitivities and the ultimate application in aircraft design.

I. Introduction

As part of the NASA Supersonics Project N+2 effort and in collaboration with LMCO, SU had agreed to develop and adjoint-based capability for the inverse shape design of supersonic configurations that must match a target equivalent area distribution (chosen for its beneficial properties). The long-term intent is to incorporate such a capability into a generic multi-disciplinary analysis and optimization (MDAO) framework that, in addition to aerodynamic performance and sonic-boom considerations, incorporates other important aspects of the design in order to reach a balanced, realizable, low-boom aircraft.

The main objective of our effort during the Base Program (approximately 12 months for the SU portion of the work) was to derive, implement, and test a preliminary version of an adjoint solver that is able to produce sensitivities (gradients) of cost functions derived from the aircraft's equivalent area distribution with respect to arbitrary numbers of design variables that affect the shape of the aircraft. Owing to the properties of adjoint solvers, the entire vector of sensitivities (the gradient) can be obtained with a single flow solution followed by a single adjoint solution, thus leading to large computational efficiencies. The intent expressed in the proposal for the SU part of the effort was to further refine and validate this equivalent-area adjoint capability during the first year option, and to incorporate such a capability into a broader MDAO environment. The direction that we have also followed is to ensure that our implementations are sufficiently generic so that they can be used in other contexts (such as the FUN3D code or the OpenMDAO environment).

A schematic view of our approach to low-boom shape design is depicted in Fig. 1 below. This figure emphasizes that the low-boom shape design module consists of various components that must be integrated themselves, prior to full integration with a true MDAO environment. In particular, geometries need to be created and modified for design purposes, meshes must be deformed during the optimization procedure,

flow and adjoint solutions must be calculated (according to a new formulation described in this report) and gradients must be computed in order to supply them to the optimization procedure. This report focuses on:

- The description of our geometry treatment (using both a parametric CAD approach and a free-form deformation box approach),
- The mesh deformation algorithm (based on the work of Campbell) in order to resolve the near-field pressure distribution accurately,
- The formulation of the adjoint solver for low-boom design (based on cost functions related to the equivalent area distribution), and
- The results of various optimization runs that we have been pursuing and that leverage all other components

The report does not focus on the details of the unstructured flow solver that we are using, or the optimization algorithms that drive the results presented.

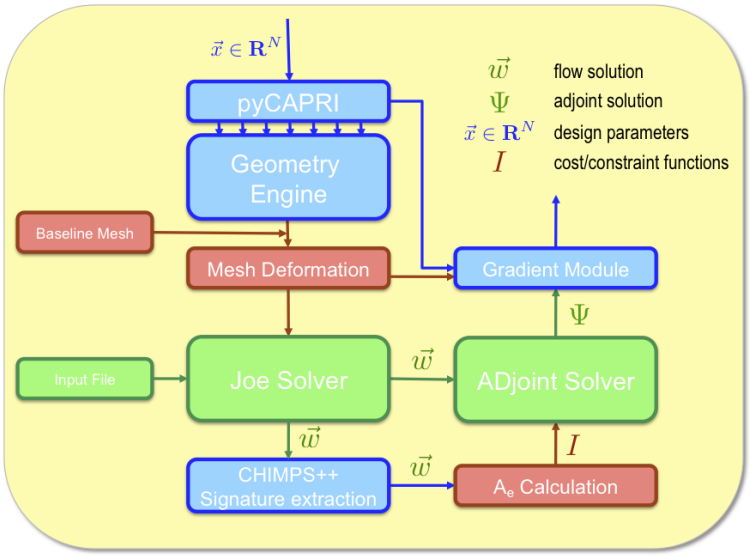

Figure 1. Overall Approach to Supersonic Low-Boom Shape Optimization

II. Parametric CAD Geometry Interface: pyCAPRI

Ideally, the designer would like optimization to be performed directly on variables which are convenient for design, here referred to as parametric variables. The sweep of a wing section or the width of the fuselage at a given station are examples of parametric variables. These are distinguished from other design variables in that a change in their value results in a change of the parametric geometry throughout the model and not just a local change to a given node or cell of a computational model. Hence, changing a parametric variable requires that that models geometry be regenerated (to use CAD terminology) or recomputed from the current parametric inputs via interaction with the relevant software. In order to compute the sensitivity of the performance metrics of interest (derived from the computed equivalent area distributions) using CFD analysis, the following general procedure must be reliably performed for a given vector of design variables, $\vec{x}$:

1. Geometry generated for $\vec{x}$:

2. Surface mesh created and analysis conducted for $G(\vec{x})$

3. Geometry perturbed about $G(\vec{x})$ for each x_i of interest:

4. Recreate or deform the surface mesh for δG_i

5. Compute the sensitivities in the coordinates of the surface mesh corresponding to δG_i, $\partial\vec{r}/\partial x_i$

With the sensitivies of the surface mesh to the geometry known, the sensitivies of the performance with respect to the parametric geometry can be found by combining these results in an appropriate fashion to the sensitivies of the performance with respect to the surface mesh. Assuming the sensitivity of a performance metric, J, is known with respect to the position of a surface node, r_j, the parametric sensitivity of node j with respect to design variable i can be found via a dot product (chain rule),

$$\frac{\partial J}{\partial x_i} = \frac{\partial \vec{r}_j}{\partial x_i}\frac{\partial J}{\partial \vec{r}_j} = \frac{\partial x_j}{\partial x_i}\left(\frac{\partial J}{\partial x_i}\right) + \frac{\partial y_j}{\partial x_i}\left(\frac{\partial J}{\partial y_j}\right) + \frac{\partial z_j}{\partial x_i}\left(\frac{\partial J}{\partial z_j}\right) \tag{1}$$

Note that x is used in this context both as a Cartesian spatial coordinate (x, y, z) and as the vector of design variables $(\vec{x})$. In other sections of this report, the analytical tools to compute the sensitivities of the performance metric to the position of a surface node are discussed; here we discuss the tools developed to compute $\partial\vec{r}/\partial x_i$ for an arbitrary parametric solid or surface model. CAPRI [ref: Bob Haimes] was chosen as the basis for development of a geometry interface. CAPRI is a CAD-neutral software interface with a wide range of functionality for querying, modifying, and regenerating CAD models. In order to make CAPRI platform independent and compatible with the current and future framework, a Python interface was required. In addition, multithreaded (locally parallel) execution of query commands involving the entire surface mesh was required to accelerate the performance of surface mesh regeneration. pyCAPRI is an implementation of CAPRI in Python which utilizes the NumPy high-performance Python array functionality. Internally, a combination of C++ and Fortran 90 code interfacing to the CAPRI API is wrapped in Python and exposed to the user as a single module. Parallelization is currently achieved through OpenMP [ref: http://openmp.org].

pyCAPRI has been tested both with simple geometries and a few of the surface meshes used in this study for full vehicle configurations. Fig. 2 shows three variations of an SST solid geometry, varying two parameters (one of several fuselage thicknesses and the sweep of the leading edge / fuselage intersection). pyCAPRI itself is a general tool for the analysis involving parametric CAD models which is being applied to this work to determine spatial perturbations described in the steps above. Specifically, the perturbation of the surface mesh is achieved through a mapping to local surface parametric coordinates (u, v) which are preserved through a regeneration of a model for a small change in $x = x + \delta x$. The algorithm is summarized below:

1. Create a surface mesh corresponding to $\vec{x}$

2. Map the spatial coordinates of the surface mesh to (u, v) surface coordinates in the local surface

3. Regenerate the geometry with the new vector of design variables, $x = x + \delta x$

4. Map the (unchanged) (u, v) coordinates to new spatial coordinates $\rightarrow$ analysis

III. A priori anisotropic grid adaptation for sonic-boom simulations

Sonic-boom propagation methods typically rely on the CFD solver to model the strongest nonlinearities in the flow. Consequently, the near-field pressure signature must be extracted a sufficiently large distance from the configuration: one or more body lengths below the aircraft is common. Capturing the pressure signature accurately at these distances is challenging, because strong shocks can be dissipated by the numerical scheme before they reach the extraction location.

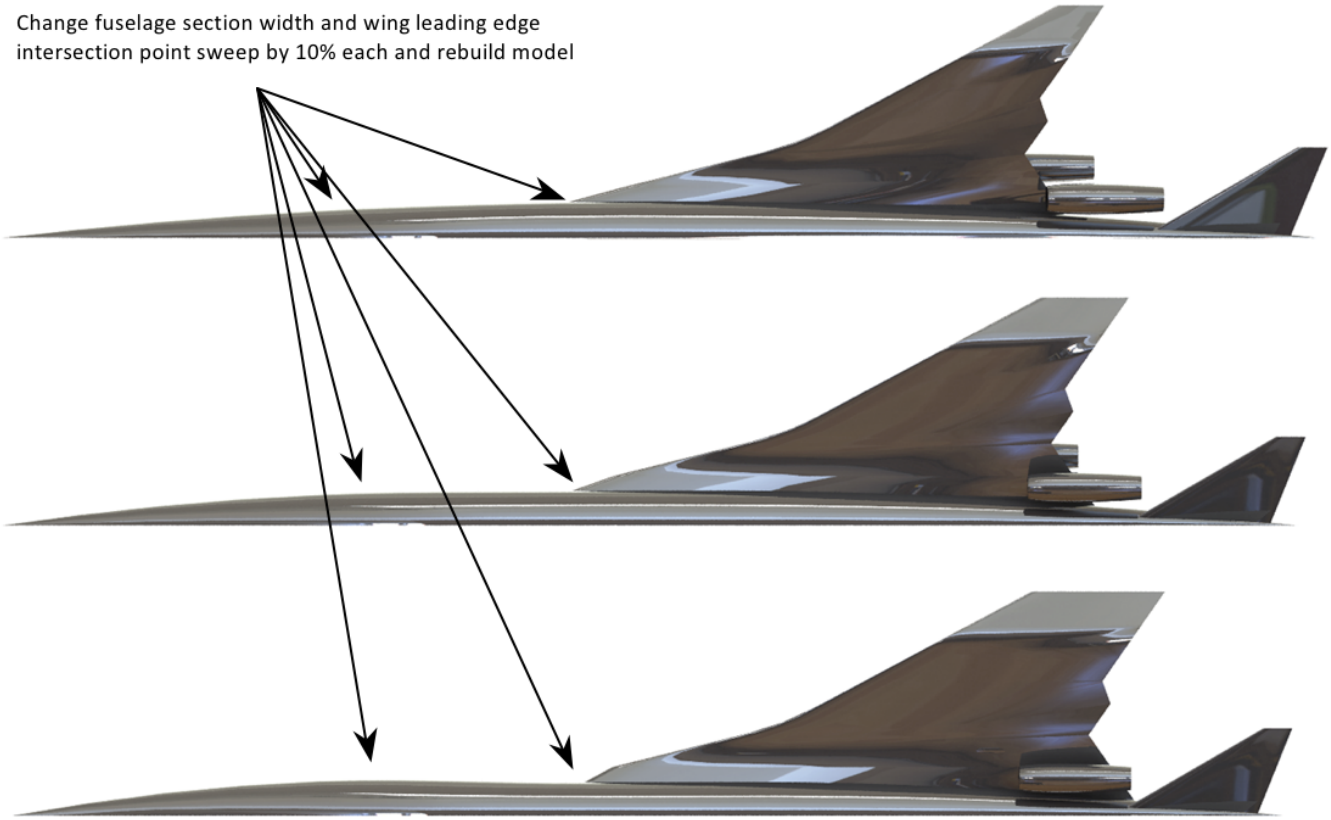

Figure 2. Parametrically varying surface geometry of SST concept vehicle via pyCAPRI API calls from Python. Note that much of the surface varies significantly though only two of approximately 150 parameters are varied.

Grid adaptation can be used to reduce numerical dissipation and thereby improve the pressure-signature accuracy. Using isotropic adaptation based on the solution gradient, Choi *et al.* found that the number of nodes required to accurately capture the near-field pressure is order 10^7 for a node-based unstructured solver. This motivates the use of anisotropic output-based adaptation; indeed, several studies have shown that the adjoint-weighted residual method coupled with metric-based anisotropic adaptation can reduce the number of solution degrees of freedom an order of magnitude relative to isotropic adaptation.[1,2]

While automated *a posteriori* grid adaptation is attractive for general flows, *a priori* adaptation can be more efficient if the locations of critical flow features are well known. A common example is refinement of the boundary layer in Reynolds-averaged Navier-Stokes simulations. Recently, Campbell *et al.*[3] proposed a simple, yet remarkably effective, *a priori* mesh adaptation strategy for sonic-boom prediction. Numerical experiments suggest that their approach produces accurate pressure signatures with order 10^6 degrees of freedom, which is comparable to *a posteriori* output-based adaptation methods. Therefore, for this work we follow reference[3] and use the *a priori* grid adaptation approach described in the following sections.

A. Radial stretching and conical shearing

The *a priori* grid adaptation method of Campbell *et al.*[3] consists of two transformations applied to a baseline grid: 1) a radial stretching to reduce the number of nodes required to reach the near-field analysis location, and 2) a conical shearing to align the cells with the free-stream Mach angle. These transformations are described in more detail below.

Applying the stretching and shearing transformation too close to the aircraft may create volume cells that intersect with the geometry. Consequently, a cylindrical region with its axis parallel to the x-axis is placed around the configuration, and nodes inside this region are not modified. The sectional shape of the cylinder is composed of two ellipses with a common spanwise (major) axis length of $(1+\epsilon)b$, where b is the span and $\epsilon = 0.1$ is a safety margin. The upper and lower ellipses have semi-minor axis lengths of $(1+\epsilon)z_{\max}$ and $(1+\epsilon)z_{\max}/2$, respectively, where $z_{\max}$ denotes the upper bound of z on the geometry.

Stretching in the radial direction precedes as follows. Consider an arbitrary point in cylindrical coordinates $\mathbf{x} = (x, r, \beta)$. Let $\mathbf{x}_{\text{cyl}} = (x, r_{\text{cyl}}, \beta)$ denote the point where the line through $\mathbf{x}$ and $(x, 0, \beta)$ pierces the cylinder defining the fixed-node region. Stretching is applied if $r > r_{\text{cyl}}$, in which case the stretched coordinates are given by $\mathbf{x}_{\text{str}} = (x, r_{\text{str}}, \beta)$ where

$$r_{\text{str}} = r_{\text{cyl}} + \lambda(r - r_{\text{cyl}}),$$

and λ is the stretching factor. We have used $\lambda = 3$ in the present work.

Once a node is stretched radially, it is sheared to align the grid with the Mach cone. As with stretching, this transformation is applied only to nodes outside the fixed-node cylinder described above. First, the stretched point $\mathbf{x}_{\text{str}}$ and its corresponding $\mathbf{x}_{\text{cyl}}$ are expressed in a coordinate system that has its x-axis parallel with the free-stream velocity and its origin at the nose of the configuration. In this new coordinate system, the Mach cone that $\mathbf{x}_{\text{cyl}}$ lies on is determined, and $\mathbf{x}_{\text{str}}$ is projected onto this Mach cone along the line parallel to the free-stream.

B. Repairing invalid cells after adaptation

The stretching and shearing transformation may create inverted cells, i.e. cells with negative volumes, particularly along the boundary of the fixed-node region. To repair these invalid cells, we use the simultaneous untangling and smoothing procedure proposed by Escobar *et al.*.[4] For completeness, we describe this procedure briefly below.

Let v denote a vertex in the grid and $N(v)$ the local submesh of tetrahedral elements connected to v. We define an objective function for the node v using a sum of modified quality measures for the elements in $N(v)$:

$$K_v = \sum_{m=1}^{N(v)} \eta_m^*,$$

where η_m^* is a modified version of the inverse mean ratio:

$$\eta_m^* = \frac{|S_m|^2}{3\left[h(\sigma_m,\delta)\right]^{(2/3)}}, \qquad h(\sigma_m,\delta) = \frac{1}{2}\left(\sigma_m + \sqrt{\sigma_m^2 + 4\delta^2}\right).$$

Here, S_m denotes the nodally-invariant Jacobian matrix of element m. The scalars $|S_m|$ and σ_m are the Frobenius norm and determinant of S_m, respectively.

If the parameter δ is set to zero then $h = \sigma_m$, and we recover the usual inverse mean ratio quality measure, i.e. $\eta^* \to \eta$ as $\delta \to 0$. However, η is singular for collapsed elements whereas η^* remains defined for all elements provided $\delta > 0$. Hence, the role of the function h is to globalize the objective function K_v, so that we may apply suitable continuous optimization algorithms to minimize K_v.

For each cell that is inverted, we loop through its nodes v and attempt to minimize K_v using a safe-guarded Newton's method. Nodes on the surface of the geometry are not permitted to move, and nodes on the symmetry plane have their y-coordinate held fixed.

We begin the untangling process with $\delta = 0.1$ and decrease δ after each sweep through the inverted cells; we have found that this iterative process helps keep the objective function Hessian well conditioned during the first few iterations. All inverted cells are typically removed after three or fewer iterations.

C. Baseline and transformed grids

The baseline grid for this work was created using the StarCCM meshing package, which is based on Delaunay tetrahedralization. A strength of this software is its ability to precisely define volume, surface, and edge refinement regions. Volume regions of cells may be sized with sources generated from primitive shapes or imported shapes from a CAD file. Surfaces may be sized by region by splitting imported surface patches. Edges may be sized by defining feature curves on which cell edges are forced to snap.

The meshing process is characterized by the following three steps. First, a surface mesh of the aircraft is imported. Typically the surface is in Parasolid file format, because it provides StarCCM with patch information useful for splitting the surface into refinement regions. Next, the the aircraft surface is integrated with the farfield geometry. In the case of external symmetric flow problems like the present study, the surface is intersected with a symmetry plane. The result of this operation is shown in Figure 3. Finally, the mesh is populated with information to control the size of cells in specified locations.

Several regions of the baseline mesh were targeted for refinement. In particular, a volume refinement source was added below the aircraft to capture the near-field pressure signature in the final transformed grid. In addition, the surface mesh was refined in regions of high curvature using feature curves. The refinement achieved around the leading and trailing edges is shown in figure 4.

The baseline grid used for this study is shown in Figure 5(a). For a Mach number of 1.8 and angle of attack of 3 degrees, the stretching and shearing operations transform the baseline grid into the grid shown in Figure 5(b). The anisotropic cells are clearly aligned with the Mach angle.

IV. Surface sensitivity using continuous adjoint methodology

The objective of this section is to quantify the influence of geometry modifications on the pressure distribution on the trijet surface or at an arbitrary location within the domain of interest (typically the near-field). Conventional adjoint implementations are aimed at reducing a cost function computed from the pressure distribution on the surface that is being modified. In the present case, apart from the traditional functionals defined on the airplane surface (drag, lift, etc.), we will use two objective functions which depends on the near-field pressure: pressure coefficient on the near-field, and equivalent area distribution.

The fluid domain Ω is bounded by a disconnected boundary $\delta\Omega$ which is divided into a "far field" component Γ_∞ and a wall boundary S. Ω has been further divided into two subdomains Ω_i and Ω_o separated by the near-field boundary Γ_{nf}. Note that Γ_{nf} will be remain fixed throughout the optimization process, nor the solid surface S.

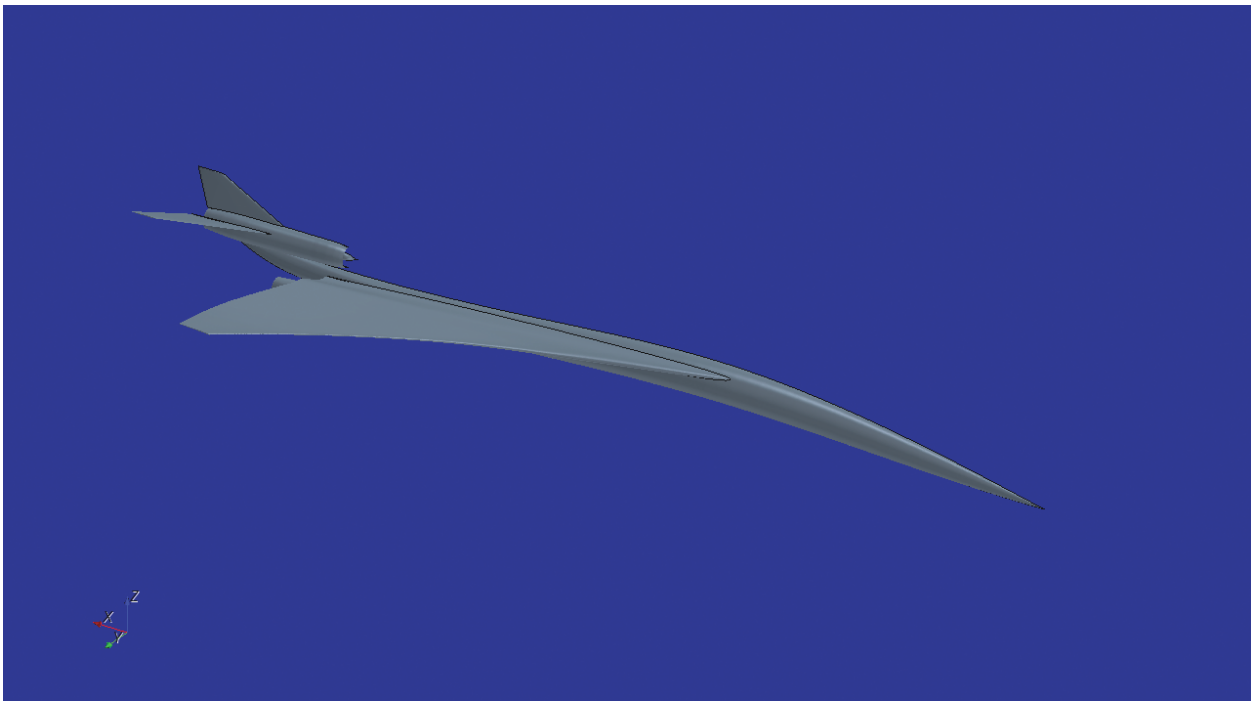

Figure 3. Half-body aircraft geometry.

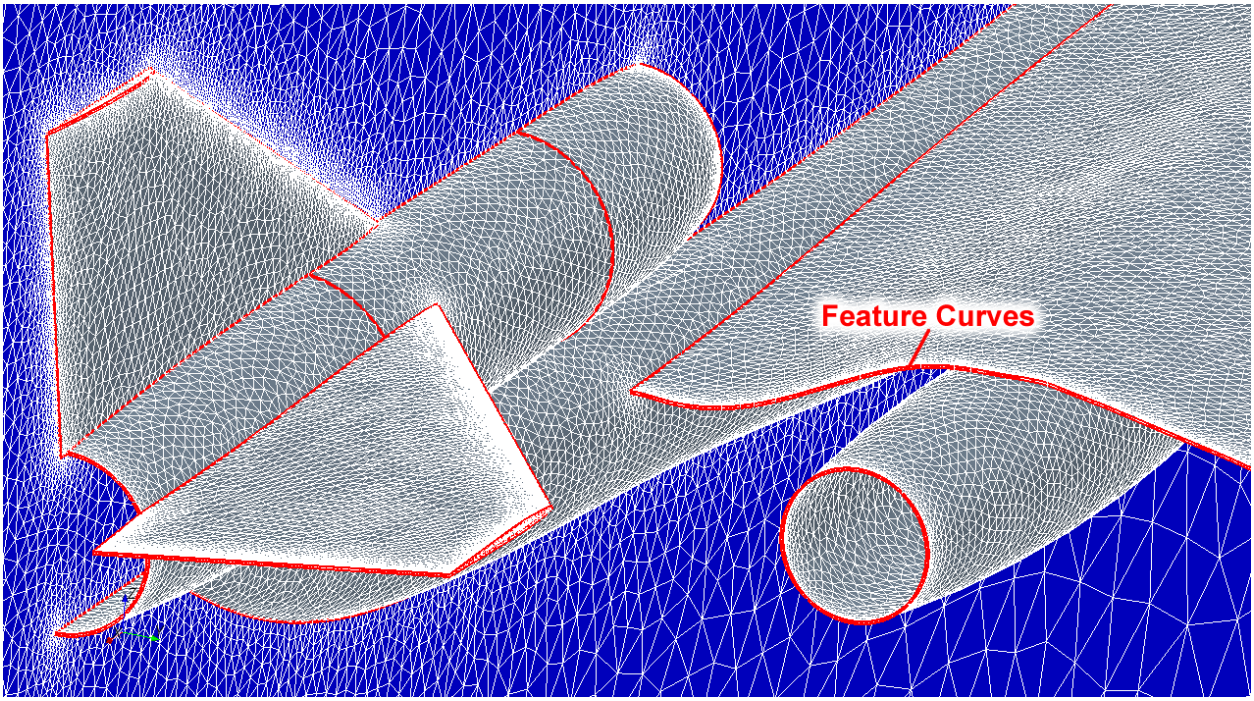

Figure 4. Detail showing surface and symmetry-plane mesh near empennage.

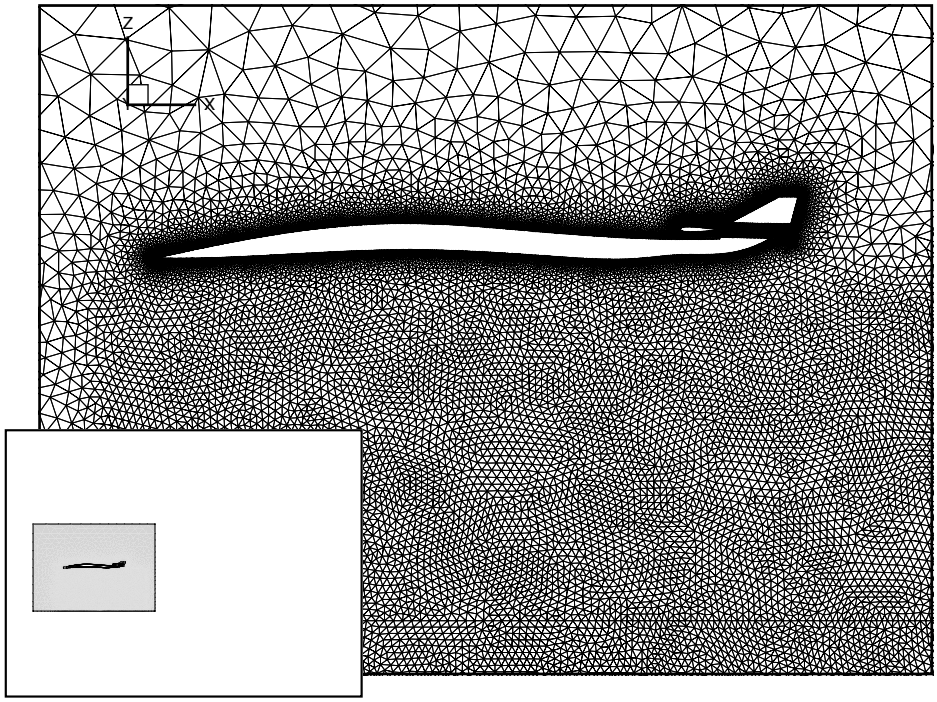

(a) initial grid

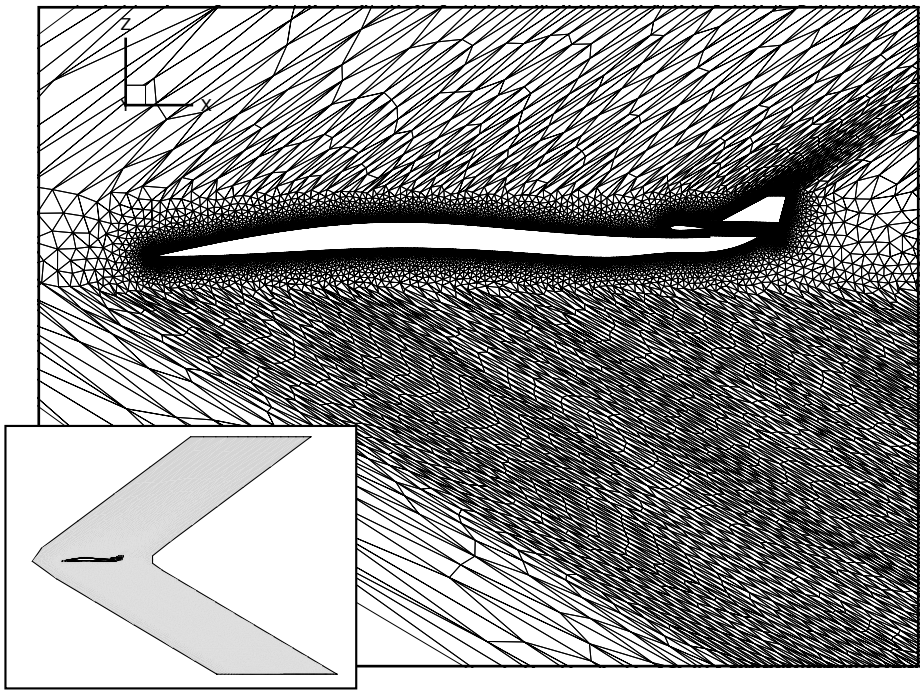

(b) transformed grid

Figure 5. Cells on the symmetry plane of the initial and transformed grids. The inset plots show the shape of the far-field boundary at the symmetry plane.

A typical optimization problem seeks the minimization of a certain cost function J with respect to changes in the shape of the boundary S. We will concentrate on functionals defined as integrals over the solid surface S, and integrals over the near-field boundary Γ_{nf},

$$J = \int_S \vec{d}\cdot(P\vec{n}_S)\,ds + \int_{\Gamma_{nf}} \frac{1}{2} f(x)(P-P_\infty)^2\,ds = \int_S j_S\,ds + \int_{\Gamma_{nf}} j_{nf}\,ds \tag{2}$$

where P is the value of the pressure, $\vec{n}_S$ is a normal vector to the solid surface S, $f(x)$ is a function that only depends on the spatial coordinates, P_∞ is the pressure at the infinity, and $\vec{d}$ is a constant vector that we will define later on. The goal is to compute the variation of the above functional under deformations of S.

Upon and infinitesimal deformation δS of the control surface S on the normal direction $\vec{n}_S$, the cost function varies due to the change in the solution induced by the deformation.

$$\begin{aligned}
\delta J &= \int_{\delta S} j_S\,ds + \int_S \delta j_S\,ds + \int_{\Gamma_{nf}} \delta j_{nf}\,ds \\
&= \int_S (\partial_n j_S - 2H_m j_S)\delta S\,ds + \int_S \vec{d}\cdot(\delta P\vec{n}_S + P\delta\vec{n}_S)\,ds + \int_{\Gamma_{nf}} \frac{\partial j_{nf}}{\partial P}\delta P\,ds \\
&= \int_S \vec{d}\cdot(\partial_n(P\vec{n}_S) - 2H_m(P\vec{n}_S))\delta S\,ds + \int_S \vec{d}\cdot\delta P\vec{n}_S\,ds - \int_S \vec{d}\cdot P\nabla_S(\delta S)\,ds + \int_{\Gamma_{nf}} f(x)(P-P_\infty)\delta P\,ds \\
&= \int_S \vec{d}\cdot\delta P\vec{n}_S\,ds + \int_{\Gamma_{nf}} f(x)(P-P_\infty)\delta P\,ds + \int_S \vec{d}\cdot(\partial_n(P\vec{n}_S) + \nabla_S P - 2H_m(P\vec{n}_S))\,\delta S\,ds \\
&= \int_S \vec{d}\cdot\delta P\vec{n}_S\,ds + \int_{\Gamma_{nf}} f(x)(P-P_\infty)\delta P\,ds + \int_S (\vec{d}\cdot\vec{\nabla}P)\delta S\,ds
\end{aligned} \tag{3}$$

where we have used $\delta\vec{n} = -\nabla_S(\delta S)$ that holds for small deformations,[?] and H_m is the mean curvature of S computed as $(\kappa_1+\kappa_2)/2$, and (κ_1,κ_2) are curvatures in two orthogonal directions on the surface. Here ∇_S represents the tangential gradient operator on S. Note that we have done an integration by parts and we have used the gradient operator on local coordinates on S.

Once we are able to evaluate the variation of the objective function, we note that the variation is subject to the steady Euler flow equations $\vec{\nabla}\cdot\vec{F} = 0$, where $\vec{F}$ are the convective fluxes. To tackle the variation of the flow variables δP in the objective function evaluation Eq. 3 we resort to the adjoint state $\Psi = (\psi_1, \vec{\varphi}, \psi_5)$, where $\vec{\varphi} = (\psi_2, \psi_3, \psi_4)$. Starting with the linearized Euler's flow equations, taking the product with Φ, and integrating over the domain one gets

$$0 = \int_\Omega \Psi(\vec{\nabla}\delta\vec{F})\,d\Omega = \int_\Omega \Psi\vec{\nabla}(\vec{A}\delta U)\,d\Omega = \int_{\Omega_i} \Psi\vec{\nabla}(\vec{A}\delta U)\,d\Omega + \int_{\Omega_o} \Psi\vec{\nabla}(\vec{A}\delta U)\,d\Omega \tag{4}$$

where $\vec{A}$ is the Jacobian of $\vec{F}$ in conservative variables, and the entire domain has been splitted between the subdomains Ω_i, and Ω_o. Integrating by parts

$$\begin{aligned}
0 &= -\int_{\Omega_i} (\vec{\nabla}\Psi)\vec{A}\delta U\,d\Omega_i + \int_S \Psi\left(\vec{n}_S\vec{A}\right)\delta U\,ds + \int_{\Gamma_{nf}} \Psi_i\left(\vec{n}_{nf}\vec{A}\right)\delta U\,ds \\
&- \int_{\Omega_o} (\vec{\nabla}\Psi)\vec{A}\delta U\,d\Omega_o - \int_{\Gamma_{nf}} \Psi_o\left(\vec{n}_{nf}\vec{A}\right)\delta U\,ds + \int_{\Gamma_\infty} \Psi_i\left(\vec{n}_\infty\vec{A}\right)\delta U\,ds
\end{aligned} \tag{5}$$

Note that the integral over the far-field can be forced to vanish with the appropriate choice of boundary conditions, and the integral over the solid boundary S gives

$$\int_S \Psi\left(\vec{n}_S\vec{A}\right)\delta U\,ds = \int_S (\vec{n}\cdot\delta\vec{v})(\rho\psi_1 + \rho\vec{v}\cdot\vec{\varphi} + \rho H\psi_5)\,ds + \int_S (\vec{n}\cdot\vec{\varphi})\,\delta P\,ds \tag{6}$$

where we have used the boundary condition $\vec{v}\cdot\vec{n}_S = 0$ to evaluate the jacobian $\vec{A}$. To eliminate the dependence on $\vec{n}\cdot\delta\vec{v}$ we will use the linearized boundary condition on the surface S to obtain

$$\begin{aligned}\int_S \Psi\left(\vec{n}_S\vec{A}\right)\delta U\,ds &= -\int_S ((\delta S\partial_n\vec{v})\cdot\vec{n}_s + \delta\vec{n}_s\cdot\vec{v})(\rho\psi_1+\rho\vec{v}\cdot\vec{\varphi}+\rho H\psi_5)\,ds + \int_S(\vec{n}\cdot\vec{\varphi})\,\delta P\,ds\\ &= -\int_S((\delta S\partial_n\vec{v})\cdot\vec{n}_s - \nabla_s(\delta S)\cdot\vec{v})\,\vartheta\,ds + \int_S(\vec{n}\cdot\vec{\varphi})\,\delta P\,ds\\ &= -\int_S((\partial_n\vec{v}\cdot\vec{n}_s)\,\vartheta + \nabla_s(\vec{v}\,\vartheta))\,\delta S\,ds + \int_S(\vec{n}\cdot\vec{\varphi})\,\delta P\,ds, \end{aligned} \tag{7}$$

to obtain this last expression we have used the linearized boundary conditions, the value of $\delta\vec{n}_S$ at the surface, and we have also done an integration by parts. On the other hand, the integrals supported on Γ_{nf} can be combined in the single integral

$$\int_{\Gamma_{nf}}\Delta\Psi\left(\vec{n}_{nf}\cdot\vec{A}\right)\delta U\,ds \tag{8}$$

where $\Delta\Psi = \Psi_i - \Psi_o$ is the difference between the values of Ψ above and below the near-field boundary. Finally the domain integrals vanish provided the adjoint equation

$$\vec{\nabla}\Psi\cdot\vec{A} = \vec{A}^T\cdot\vec{\nabla}\Psi = 0 \tag{9}$$

is satisfied. And the equation 4 can be written as

$$-\int_S((\partial_n\vec{v}\cdot\vec{n}_S)\,\vartheta + \nabla_S(\vec{v}\,\vartheta))\,\delta S\,ds + \int_S(\vec{n}_S\cdot\vec{\varphi})\delta P\,ds + \int_{\Gamma_{nf}}\Delta\Psi\left(\vec{n}_{nf}\vec{A}\right)\delta U\,ds = 0. \tag{10}$$

where $\vartheta = (\rho\psi_1+\rho\vec{v}\cdot\vec{\varphi}+\rho H\psi_5)$, the last step is to subtract equations 3 and 10 to obtain the complete variation of the functional as:

$$\begin{aligned}\delta J &= \int_S\vec{d}\cdot\delta P\vec{n}_S\,ds + \int_{\Gamma_{nf}} f(x)(P-P_\infty)\delta P\,ds + \int_S(\vec{d}\cdot\vec{\nabla}P)\delta S\,ds\\ &+ \int_S((\partial_n\vec{v}\cdot\vec{n}_s)\,\vartheta + \nabla_S(\vec{v}\,\vartheta))\,\delta S\,ds - \int_S(\vec{n}_S\cdot\vec{\varphi})\delta P\,ds - \int_{\Gamma_{nf}}\Delta\Psi\left(\vec{n}_{nf}\vec{A}\right)\delta U\,ds\\ &= \int_S(\vec{d}\cdot\vec{n}_S)\delta P\,ds - \int_S(\vec{n}_S\cdot\vec{\varphi})\delta P\,ds + \int_{\Gamma_{nf}} f(x)(P-P_\infty)\delta P\,ds - \int_{\Gamma_{nf}}\Delta\Psi\left(\vec{n}_{nf}\vec{A}\right)\delta U\,ds\\ &+ \int_S\left(\vec{d}\cdot\vec{\nabla}P + (\partial_n\vec{v}\cdot\vec{n}_S)\,\vartheta + \nabla_S(\vec{v}\,\vartheta)\right)\delta S\,ds \end{aligned} \tag{11}$$

where we have rearranged the different terms to have a more clear view of those which are involved in the evaluation of the objective function gradient.

A. Surface and near-field pressure based functionals

Eq. 11 is the key to evaluate the functional sensitivity with respect to deformations on solid surface S. In order to do that, we firstly define the vector $\vec{d}$ as

$$\vec{d} = \begin{cases} \left(\frac{1}{C_\infty}\right)(\cos\alpha\,\cos\beta, \sin\alpha\,\cos\beta, \sin\beta), & C_D & \text{Drag coefficient,}\\ \left(\frac{1}{C_\infty}\right)(-\sin\alpha, \cos\alpha, 0), & C_L & \text{Lift coefficient,}\\ \left(\frac{1}{C_\infty}\right)(-\sin\beta\,\cos\alpha, -\sin\beta\,\sin\alpha, \cos\beta), & C_{SF} & \text{Side force coefficient,}\end{cases} \tag{12}$$

where α is the angle of attack, β is the angle of sideslip, $C_\infty = 0.5v_\infty^2\rho_\infty A_z$, and v_∞ and ρ_∞ denote the infinity values of velocity and density. All the positive components of the normal surface vectors in the

z-direction are summed up in order to calculate the projection A_z, but a pre-specified reference area can also be used in a similar fashion.

The admisible adjoint boundary conditions, which eliminate the dependence on the fluid flow variation are:

$$\begin{cases} \vec{n}_S \cdot \vec{\varphi} = \vec{d} \cdot \vec{n}_S \\ \vec{\nabla}\Psi \left(\vec{n}_{nf} \cdot \vec{A} \right) = f(x)(P - P_\infty) \end{cases} \tag{13}$$

And the variation of the objective function is

$$\delta J = \int_S \left(\vec{d} \cdot \vec{\nabla} P + (\partial_n \vec{v} \cdot \vec{n}_s)\, \vartheta + \nabla_s (\vec{v}\, \vartheta) \right) \delta S \, ds \tag{14}$$

where $\frac{\partial J}{\partial S} = \left(\vec{d} \cdot \vec{\nabla} P + (\partial_n \vec{v} \cdot \vec{n}_s)\, \vartheta + \nabla_s (\vec{v}\, \vartheta) \right)$ is what we have called the surface sensitivity, which provides a measure of the variation of the objective function with respect to infinitesimal variations of the surface shape in the normal direction. This value is computed at each surface node of the numerical grid. In Fig. A and Fig. A the shape sensitivity for the drag and lift coefficients using the baseline configuration is shown.

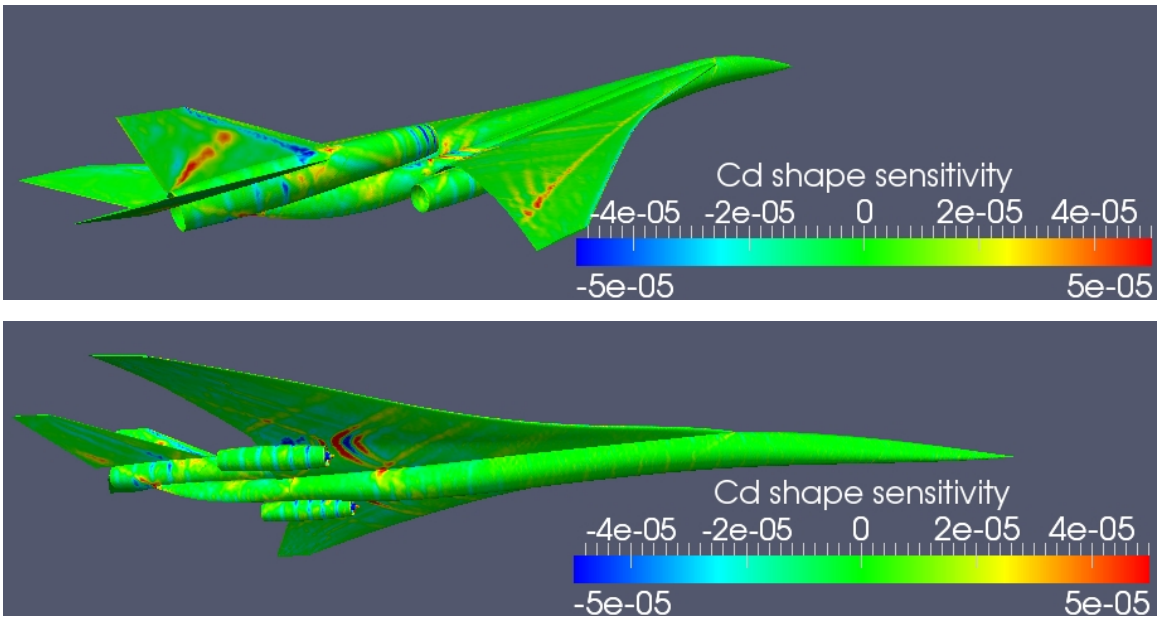

Figure 6. Shape sensitivity of the Drag coefficient (baseline configuration).

B. Equivalent Area-based functional

As we have seen, in optimal shape design problems, continuous adjoint formulations restrict the form of the objective functions that can be computed in the near-field. Essentially, the variation of the cost function with respect to the pressure must have the following form so that the appropriate boundary terms are cancelled in the formulation:

$$\delta J = \int_{-L}^{L} f(x)(P - P_\infty)\delta P \, dx, \; -L < x < L \tag{15}$$

where $f(x)$ is a function that can only depend on the spatial coordinates at the near-field plane. Note that, if $f(x) = 2/\rho_\infty A U_\infty^2$ the objective function is just the area integral of the pressure coefficient on the near-field,

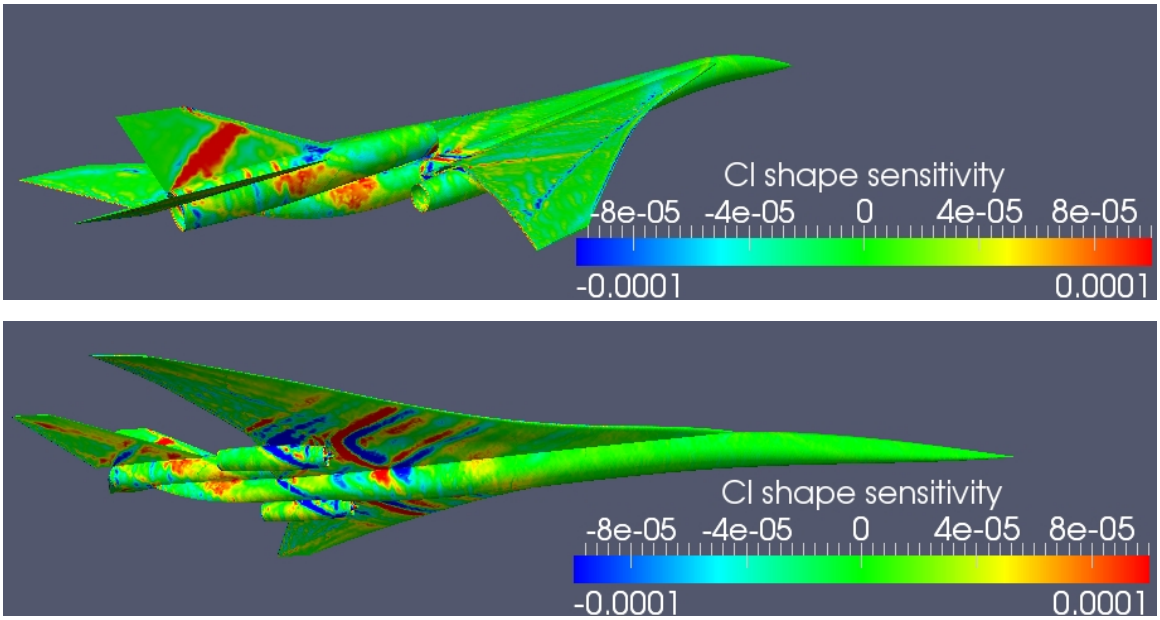

Figure 7. Shape sensitivity of the Lift coefficient (baseline configuration).

where the area within the limits of integration is given by A. Using classical supersonic aerodynamics, we know that the equivalent area distribution $A_e(x;\theta)$ at a particular azimuthal angle θ is given by

$$A_e(x;\theta) = \int_0^x C(P - P_\infty)(x-t)^{1/2}\, dt, \tag{16}$$

where $C = 4\frac{\sqrt{2\beta r}}{\gamma \rho_\infty M_\infty^2}$. In the following we assume that we are on an azimuthal plane $\theta = \theta_0$ and drop the dependence of the area distribution on the azimuthal angle θ. In order to pose an inverse design problem whereby we attempt to match a target equivalent area distribution and, at the same time, satisfy the requirement expressed by Eq. 15, the logical approach is to formulate the problem using a least-squares minimization formulation. For purposes of illustration, let's minimize the weighted sum of the square of the differences between the computed equivalent area and the target equivalent area at four different points (x_0, x_1, x_2, x_3) in the near field, with weights $(\omega_0, \omega_1, \omega_2, \omega_3)$, and target equivalent areas $(A_t(x_0), A_t(x_1), A_t(x_2), A_t(x_3))$. Obviously, the procedure can be easily extended to an arbitrary number of such points, thus making it completely general, even for cases where we might be interested in designing equivalent area distributions at multiple azimuthal planes, θ, as would be the case to avoid simply reducing the sonic boom under the flight track while the boom intensity increases off the flight track.[?]

For this problem formulation, the objective function can be written as:

$$J = \omega_1 \left[A_e(x_1) - A_t(x_1)\right]^2 + \omega_2 \left[A_e(x_2) - A_t(x_2)\right]^2 + \omega_3 \left[A_e(x_3) - A_t(x_3)\right]^2, \tag{17}$$

where we have assumed that $A_e(x_0) = A_t(x_0) = 0$. In order to check if the variation of this objective function satisfies the requirement in eq. 15, the variation of eq. 17 is given by:

$$\begin{aligned} \delta J &= 2\omega_1 \left[A_e(x_1) - A_t(x_1)\right] \delta A_e(x_1) + 2\omega_2 \left[A_e(x_2) - A_t(x_2)\right] \delta A_e(x_2) \\ &+ 2\omega_3 \left[A_e(x_3) - A_t(x_3)\right] \delta A_e(x_3). \end{aligned} \tag{18}$$

On the other hand, the variation of the equivalent area, $A_e(x)$, with respect to the pressure yields:

$$\delta A_e(x) = \int_0^x C(x-t)^{1/2} \delta P\, dt. \tag{19}$$

Using this last expression it is possible to separately evaluate the variation of the non-zero equivalent areas at the three chosen points as follows:

$$\begin{aligned}
\delta A_e(x_1) &= \int_{x_0}^{x_1} C(x_1 - x)^{1/2} \delta P \, dx, \\
\delta A_e(x_2) &= \int_{x_0}^{x_1} C(x_2 - x)^{1/2} \delta P \, dx + \int_{x_1}^{x_2} C(x_2 - x)^{1/2} \delta P \, dx, \\
\delta A_e(x_3) &= \int_{x_0}^{x_1} C(x_3 - x)^{1/2} \delta P \, dx + \int_{x_1}^{x_2} C(x_3 - x)^{1/2} \delta P \, dx \\
&+ \int_{x_2}^{x_3} C(x_3 - x)^{1/2} \delta P \, dx,
\end{aligned} \tag{20}$$

where, for the sake of simplicity, we have substituted the dummy variable of integration t by x. Using the variation of the equivalent area that we have computed in eq. **??**, it is possible to rewrite the variation of the objective function as:

$$\begin{aligned}
\delta J &= 2\omega_1 \left[A_e(x_1) - A_t(x_1) \right] \int_{x_0}^{x_1} C(x_1 - x)^{1/2} \delta P \, dx \\
&+ 2\omega_2 \left[A_e(x_2) - A_t(x_2) \right] \left(\int_{x_0}^{x_1} C(x_2 - x)^{1/2} \delta P \, dx + \int_{x_1}^{x_2} C(x_2 - x)^{1/2} \delta P \, dx \right) \\
&+ 2\omega_3 \left[A_e(x_3) - A_t(x_3) \right] \left(\int_{x_0}^{x_1} C(x_3 - x)^{1/2} \delta P \, dx + \int_{x_1}^{x_2} C(x_3 - x)^{1/2} \delta P \, dx \right. \\
&+ \left. \int_{x_2}^{x_3} C(x_3 - x)^{1/2} \delta P \, dx \right),
\end{aligned} \tag{21}$$

To simplify the notation, we will use:

$$\begin{cases}
\Delta A_e(x_1) = 2\omega_1 \left[A_e(x_1) - A_t(x_1) \right] C \\
\Delta A_e(x_2) = 2\omega_2 \left[A_e(x_2) - A_t(x_2) \right] C \\
\Delta A_e(x_3) = 2\omega_3 \left[A_e(x_3) - A_t(x_3) \right] C,
\end{cases}$$

Rearranging the integrals in eq. 21, it is possible to write the variation of the objective function as

$$\begin{aligned}
\delta J &= \int_{x_0}^{x_1} \left(\Delta A_e(x_1)(x_1 - x)^{1/2} + \Delta A_e(x_2)(x_2 - x)^{1/2} + \Delta A_e(x_3)(x_3 - x)^{1/2} \right) \delta P \, dx \\
&+ \int_{x_1}^{x_2} \left(\Delta A_e(x_2)(x_2 - x)^{1/2} + \Delta A_e(x_3)(x_3 - x)^{1/2} \right) \delta P \, dx \\
&+ \int_{x_2}^{x_3} \left(\Delta A_e(x_3)(x_3 - x)^{1/2} \right) \delta P \, dx.
\end{aligned} \tag{22}$$

In conclusion, the inverse equivalent area shape design problem can be reinterpreted as an optimization of a functional of the near-field pressure distribution with a particular weighting function:

$$J = \int_{-L}^{L} f(x)(P - P_\infty) \, dx, \; -L < x < L, \tag{23}$$

where

$$f(x) = \begin{cases}
0 & , \text{ if } -L < x < x_0, \\
\Delta A_e(x_1)(x_1 - x)^{1/2} + \Delta A_e(x_2)(x_2 - x)^{1/2} + \Delta A_e(x_3)(x_3 - x)^{1/2} & , \text{ if } x_0 < x < x_1 \\
\Delta A_e(x_2)(x_2 - x)^{1/2} + \Delta A_e(x_3)(x_3 - x)^{1/2} & , \text{ if } x_1 < x < x_2 \\
\Delta A_e(x_3)(x_3 - x)^{1/2} & , \text{ if } x_2 < x < x_3, \\
0 & , \text{ if } x_3 < x < L,
\end{cases}$$

and $\Delta A_e(x_i) = 2\omega_i \left[A_e(x_i) - A_t(x_i)\right] C$ as given in eq. 22, $C = 4\frac{\sqrt{2\beta r}}{\gamma \rho_\infty M_\infty^2}$, and where ω_1, ω_2, and ω_3 are arbitrary weights chosen by the designer. It is important to note that this formulation of the problem fits perfectly within a continuous adjoint framework. The application of this formula to an arbitrary number of points in the near-field is straightforward. Furthermore, this formula also gives us some clues about how to choose $f(x)$ in a three-dimensional environment.

1. Sample 2D Equivalent Area Distribution Redesign

Using the equivalent area distribution as a functional on an optimal shape design process requires the imposition of a jump in the adjoint variables on the near-field. In order to do that, the original grid is divided by a horizontal line (2D) or plane (3D), and the points on the line/plane are duplicated, both planes and coordinates are exactly the same except the connectivity of the elements. This process is done automatically with an in-home tool developed for this project. After the domain division, the jump condition is imposed using the fluxes that connect both domains.

To test the complete methodology we have proposed an equivalent area inverse design problem: starting with an airfoil NACA 4412, at Mach 2.0 and angle of attack 0.0deg, the objective is to obtain the equivalent area distribution of an airfoil NACA 0012. In Fig. 8 the flow solution (left), and the adjoint solution (right) for the NACA 4412 are plotted (density variable). To reduce the computational cost an apriori adapted grid is used (see Fig. 9, left).

In this problem the near-field is located at one chord length from the airfoil, and the objective is to recover the equivalent area of a NACA 0012 airfoil. As design variables we have used a total of 50 Hick-Henne bump functions distributed along the entire airfoil (upper and lower side), and a quasi-Newton method is used as optimizer, gradients are computed using the technique described in this work.

In Fig. 10 the original NACA4412 and the designed airfoil with the area distribution of a NACA0012 are plotted. Finally, in Fig. 9 (right) the optimization history is shown, after 10 iterations we have almost recovered the NACA 0012 equivalent area distribution. It is important to note that, although the equivalent area distribution is the same as in the NACA0012, the designed airfoil shape differs from the NACA0012. On the other hand, the design variables, and the fact that the optimizer has found a local minimum prevent the complete convergence of the functional to the exact value of the equivalent area.

2. Sample 3D Equivalent Area Distribution Redesign Using NASA/LMCO Trijet Configuration

As an initial example of the entire methodology for equivalent-area-based adjoint design, this section shows a sample calculation where the baseline trijet configuration supplied by LMCO is analyzed, the resulting equivalent area distribution is arbitrarily altered (including changes to the area of the base of the equivalent area distribution and, therefore, the lift of the configuration), and the configuration is redesigned using the FFD parameterization described earlier in order to match as closely as possible the target equivalent area distribution for the entire aircraft.

This test case is viewed as a validation of the entire design procedure and of the procedure we have followed to compute the adjoint sensitivities of functions of the equivalent area distribution. It is, however, not intended to be a realistic design test case: a more typical use of this design procedure may focus on fixing shortcomings of the equivalent area distribution in a localized portion of the signature. In addition, realistic design processes may (or may not) require that the overall lift be fixed. In this example we were interested in finding out if, even with lift changes that may require angle of attack variations, the target equivalent area distributions could be achieved.

Fig. 12 shows the results of the initial iteration of our sample design process. After an initial flow and adjoint solutions, these two solutions are combined to compute the surface shape sensitivity of the cost function. In other words, Fig. 12 shows both the upper surface (top) and the lower surface (bottom) sensitivities: by how much will change our cost function (based on the difference between the actual equivalent area and the target equivalent area) if each point on the surface of the aircraft were to move normal to the surface? The plots also show the C_p distribution on the upper and lower surface of the configuration.

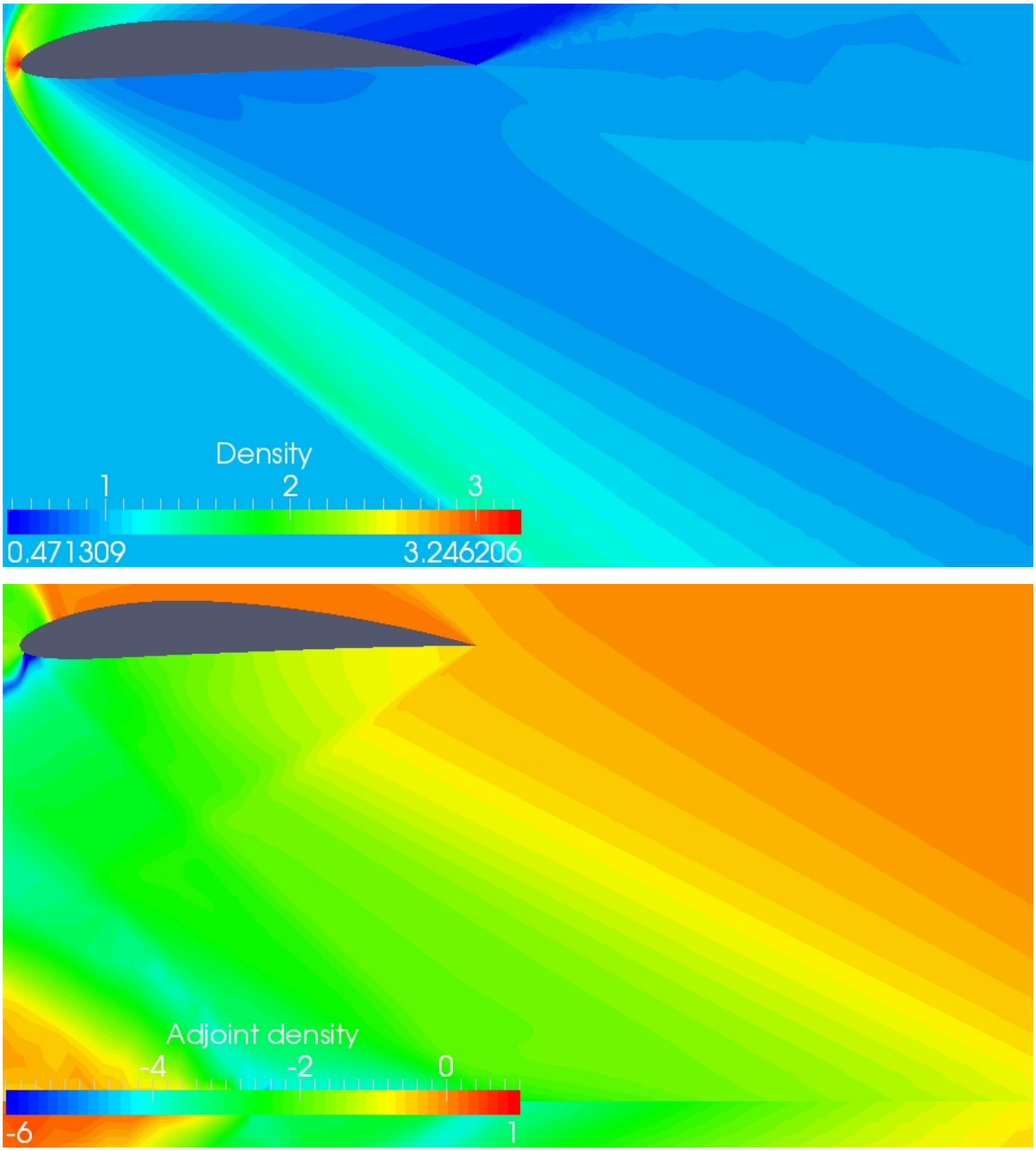

Figure 8. Flow (left), and adjoint (right) solution for the NACA 4412 and the equivalent area distribution functional.

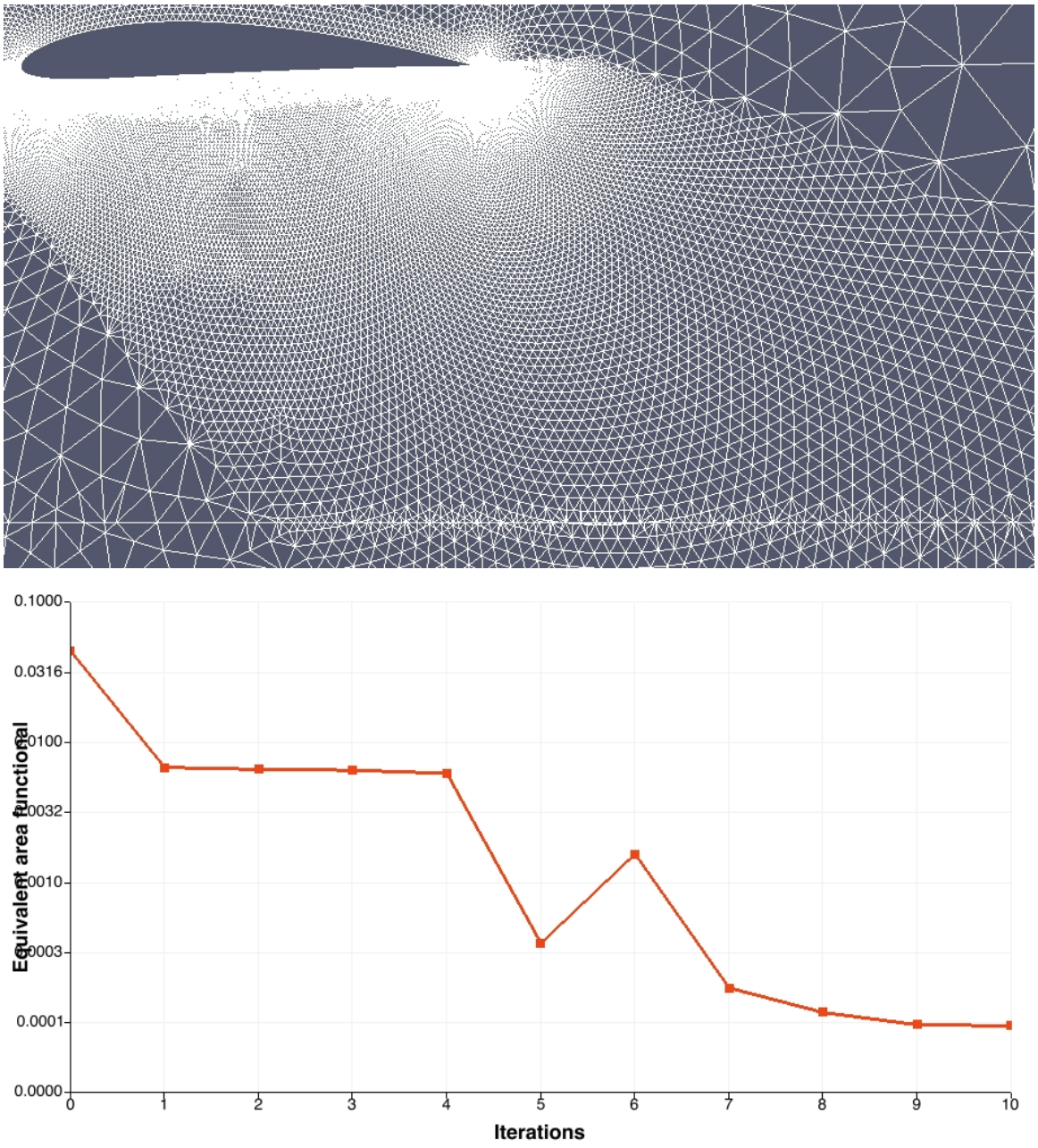

Figure 9. A priori adapted numerical grid (left), and optimization evolution using logaritmical scale (right).

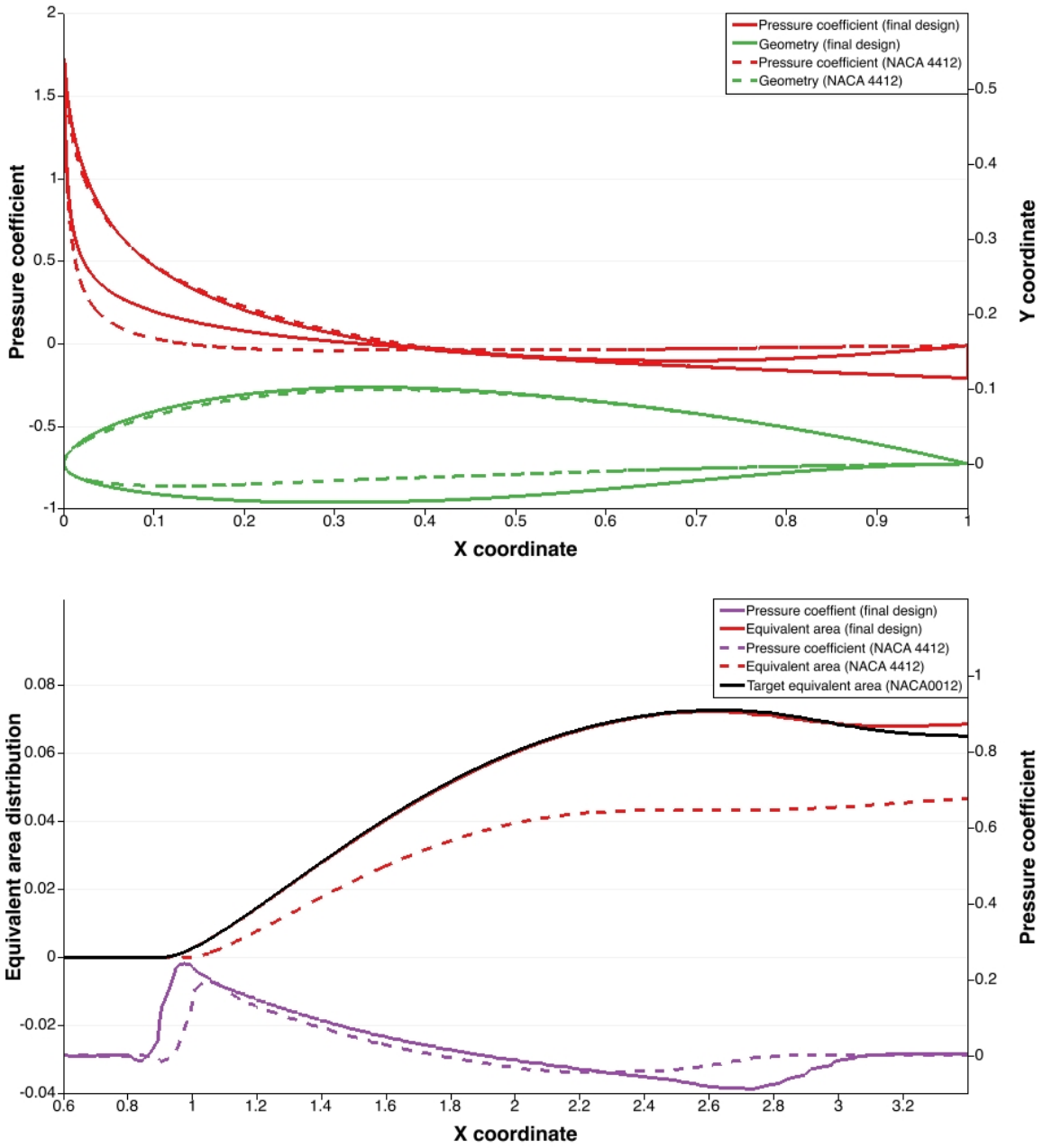

Figure 10. Optimization results, geometry and pressure distribution (left), equivalent area distribution, and near-field pressure (right).

Note that these results (even without an actual optimization) are quite revealing: they point to the areas of the configuration where the impact on the cost function of the equivalent area distribution is largest and, therefore, the areas where the parameterization of the surface shape should be active. Owing to the supersonic flow nature of this problem (regions of dependence/regions of influence) it is clear that the largest contributions in order to reduce the difference between the target area distribution and the existing one are on the lower surface of the configuration ahead of the nacelles/inlets. In fact these areas of high influence can be seen to reflect in complicated ways off of the various surfaces of the configuration, making it nearly impossible to be able to figure such patterns out using designer's intuition alone.

Fig. **??** shows a large view and some details of the adjoint variable distribution (for the density variable) in the symmetry plane, on the surface of the aircraft, and on a cutting plane perpendicular to the incoming free stream.

Fig. **??** shows the Mach number distribution in the symmetry plane and the location of the near field plane

V. Design variable definition, and mesh deformation

For these initial results, a Free-Form Deformation (FFD)[?] strategy has been adopted. In FFD an initial box encapsulating the object (wing, fuselage, etc.) that we want to redesign is parameterized as a Bézier solid. A set of control points are defined on the surface of the box, depending on the order of the chosen Bernstein polynomials. The solid box is parameterized by the following expression

$$X(u,v,w) = \sum_{i,j,k=0}^{l,m,n} P_{i,j,k} B_i^l(u) B_j^m(v) B_k^n(w), \tag{24}$$

where $u, v, w \in [0,1]$, and the B^i being the Bernstein polynomial of order i. The Cartesian coordinates of the points on the surface of the object are then transformed to the parametric coordinates of the Bézier box. Control points of the box become design variables, as they control the shape of the solid, and thus the shape of the surface grid inside. The box embedding the geometry is then deformed by modifying its control points, with all the points inside the box inheriting a smooth deformation. Once the deformation has been applied, the new Cartesian coordinates of the object of interest can be recovered by inverting the mapping.

Once the boundary displacements have been computed using the FFD strategy, a classical spring method is used in order to reallocate the rest of vertexes of the unstructured mesh. The method is based on the definition of a stiffness matrix, k_{ij}, that connects the two ends of a single bar (mesh edge). Equilibrium of forces is then imposed at each mesh node

$$\left(\sum_{j \in \mathcal{N}_i} k_{ij} \vec{e}_{ij} \vec{e}_{ij}^{\mathsf{T}} \right) \vec{u}_i = \sum_{j \in \mathcal{N}_i} k_{ij} \vec{e}_{ij} \vec{e}_{ij}^{\mathsf{T}} \vec{u}_j \tag{25}$$

where the displacement $\vec{u}_i$ is unknown and is computed as a function of the known current displacements $\vec{u}_j$, being $\mathcal{N}_i$ the set of neighboring points to node i and $\vec{e}_{ij}$ the unitary vector in the direction connecting both points. The system of equations is solved iteratively by a conjugate gradient algorithm with Jacobi preconditioning.

VI. Simulation and shape design framework

The simulations and optimal shape design cases presented in this work have been done using the SU^2 suite (Stanford University Unstructured). SU^2 is a computational tool for the optimal shape design of airplanes composed by a group of softwares (written in C++), and scripts (written in Python). Next, a brief description of the main software is presented:

- SU2 CFD (Computation Fluid Dynamics Code). This is the software for performing the fluid dynamics simulation, this code is able to solve the direct, continuous adjoint, and linearized problems for the

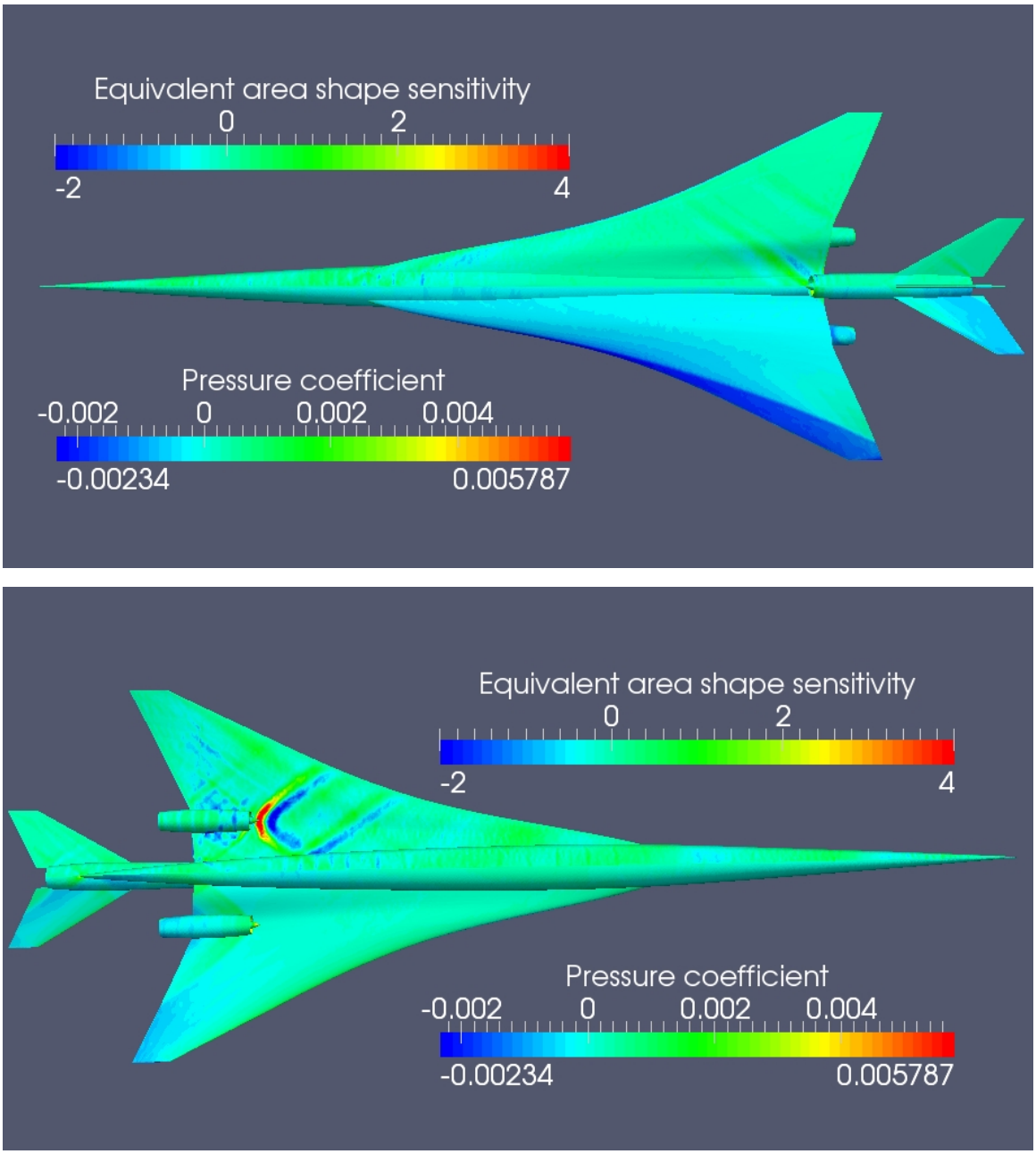

Figure 11. Upper and lower surface C_p and shape sensitivity distributions

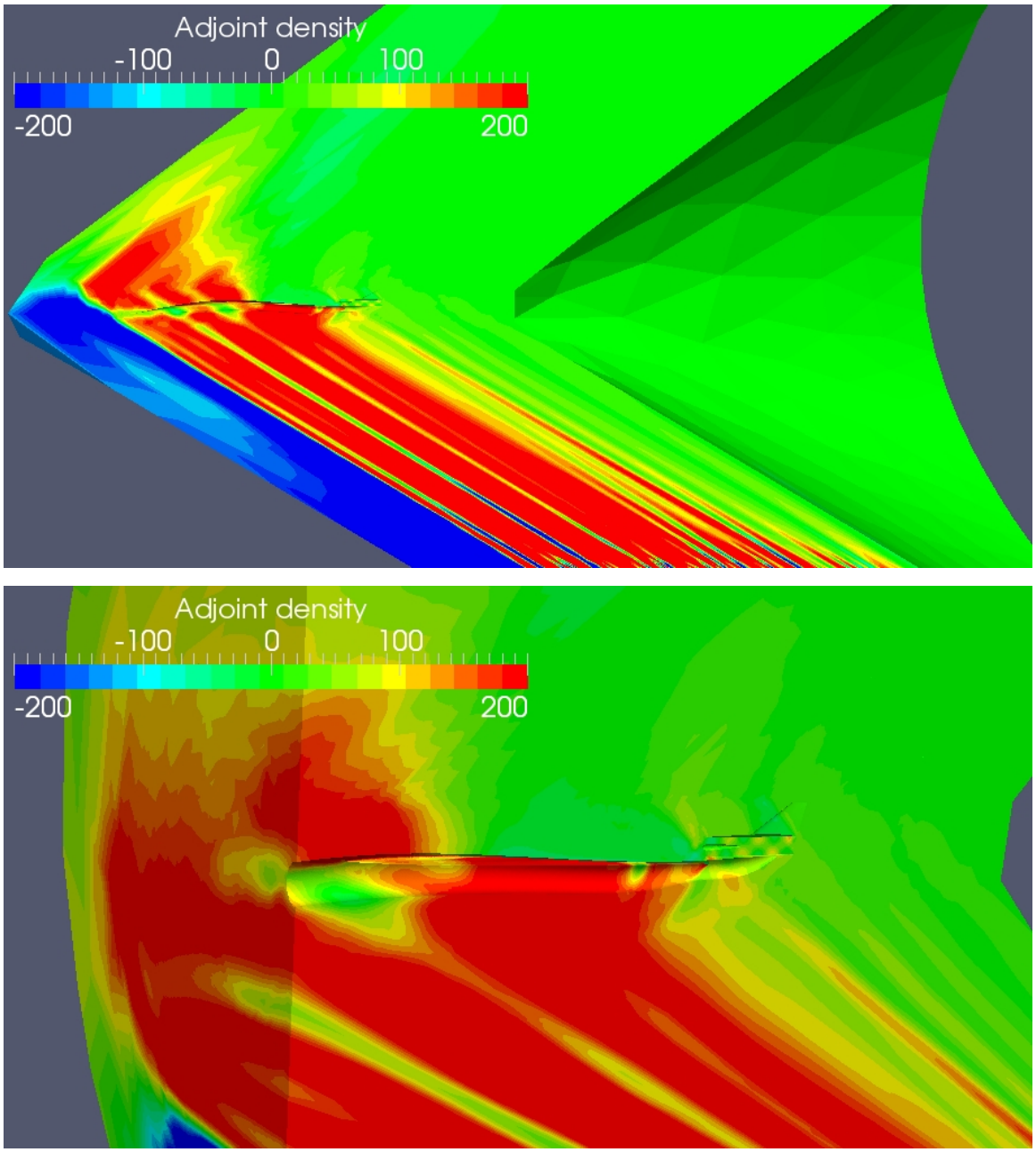

Figure 12. Adjoint of density variable: overall view and detail.

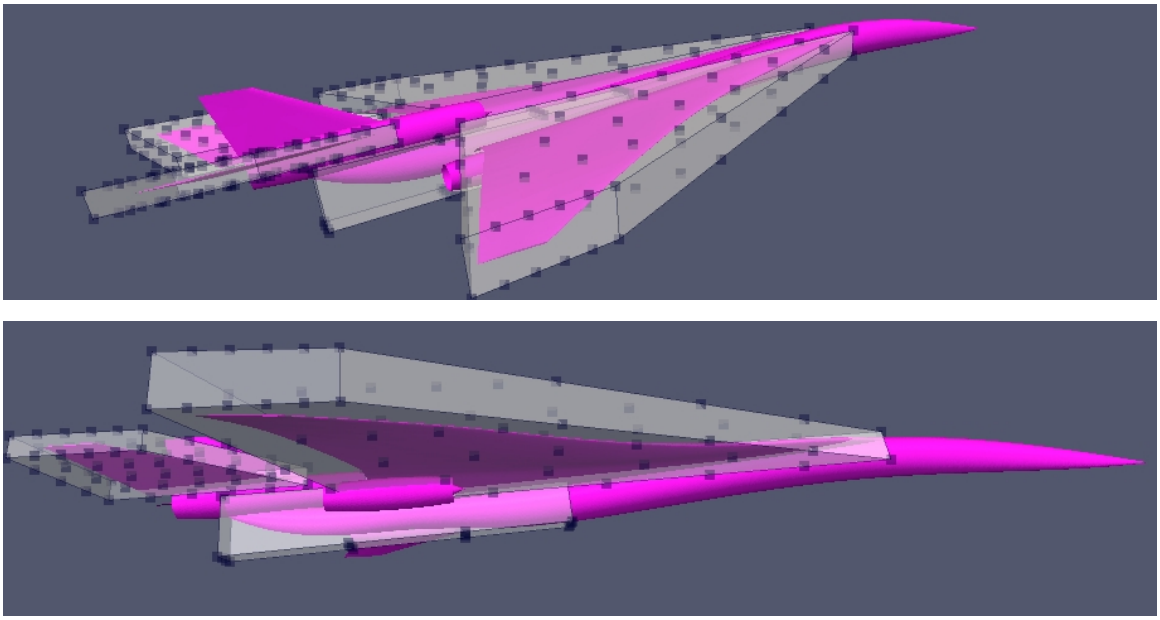

Figure 13. Free Form Deformation boxes used in the current optimization.

potential, Euler, Navier-Stokes and RANS equations. It uses a Finite Volume Method formulation, and an edge based structure, the code is fully parallel, explicit/implicit, and it uses an agglomeration multigrid to accelerate the convergence to the steady state.

- SU2 GPC (Gradient Projection Code). This is the software for computing the partial derivative of a objective function with respect to variations on the aerodynamic surface. The code SU2 GPC uses the surface sensitivity, the flow solution, and the definition of the geometrical variables to evaluate the derivative of a particular functional.
- SU2 MDC (Mesh Deformation Code). This is the software for performing the geometrical deformation of an aerodynamic surface, as well as the volumetric grid deformation. Once the kind of deformation is defined, the software SU2 MDC performs the grid deformation using a spring analogy. To perform the 3D surface deformations a Free Form Deformation method is used.
- SU2 MAC (Mesh Adaptation Code). This is the software for grid adaptation using different techniques based on the analysis of the fluid solution, adjoint solution and linearized problem.
- SU2 GDC (Geometrical Design Code). This is the software for computing the value of geometrical functional, and its gradient that depend exclusively on the geometry of the aircraft.

All this softwares interact one with the other using a serie of Python scripts that automate the entire optimization loop.

VII. Shape optimization of the complete trijet geometry

In this section we will show the shape optimization of the trijet supersonic aircraft using adjoint based techniques. The governing equations are the Euler's equations, and the baseline configuration is Mach 1.8, and angle of attack 3.0. An unstructured grid, with all the geometrical details (6 millions cells) will be used, with this methodology a complete trijet optimization with more than 100 design variables can be obtained in one day using 10 cores.

In the design process we have used a maximum number of 108 design variables, which produce a variation on the thickness and camber in three different locations of the aircraft: main wing, horizontal tail plane, and rear fuselage. The Free Form Deformation boxes for the main and secondary wing have $(5, 4, 1)$ degrees in (i, j, k) local direction, and the rear fuselage box has $(3, 3, 1)$ degrees in the local directions. On the other hand, a coordinate movement of the control points has been implemented to obtain a camber, thickness and a volume variation of the aircraft. In Fig. 14 it is possible to appreciate the different Free Form Deformation boxes used in this work.

In this work we have performed three different optimization test: unconstrained drag minimization, drag minimization with a constrained lift (value 0.14), and inverse design problem to obtain a target equivalent area distribution. It is important to highlight that the process is completely automated.

The optimization results presented in this work make use of the *SciPy* library (`http://www.scipy.org`), a well-established open-source software for mathematics, science, and engineering. The SciPy library provides many user-friendly and efficient numerical routines for the solution of non-linear constrained optimization problems, such as conjugate gradient, Quasi-Newton or sequential least-squares programming algorithms. At each design iteration, the SciPy routines only require as inputs the values and gradients of the objective functions, computed by means of our continuous adjoint approach, as well as the set of chosen constraints.

A. Drag minimization problem

Starting with the baseline geometry, and using two Free Form Deformation boxes (main wing, and horizontal tail plane), we have performed an unconstrained drag minimization problem to check the quality of the gradients obtained with the continuous adjoint methodology. In Fig. 15 it is possible to study the upper an lower side of the trijet after and before the shape optimization.

In Fig. 16 (left) we show the rear part of the aircraft with especial emphasis in the drag reduction on the nacelles and the modifications of the horizontal tail plane. Finally in Fig. 16 (right) we show the evolution of the optimization. In this case the drag coefficient has been reduced in a 50% with respect to the original configuration, note that we have used a quasi-Newton method of Broyden, Fletcher, Goldfarb, and Shanno (BFGS) as optimization method.

B. Drag minimization problem, with lift constraint

As in the previous case we have started with the baseline geometrical configuration (6 millions cells). The objetive is to reduce the drag coefficient maintaining the original lift coefficient (Cl = 0.14). In this case we will use a Sequential Least SQuares Programming optimization algorithm (SLSQP) with constraints as optimizer. The design variable definition is done with two Free Form Deformation boxes (main wing, and horizontal tail plane). In Fig. 17 we show the upper and lower part of the trijet (baseline and optimized configuration).

In Fig. 16 (left) we show the rear part of the aircraft with especial emphasis in the drag reduction on the nacelles and the modification of the horizontal tail plane. Finally in Fig. 16 (right) we show the evolution of the optimization, in this case the drag coefficient has been reduced a 20% with respect to the original configuration.

C. Equivalent Area inverse design problem

References

[1]Loseille, A., Dervieux, A., and Alauzet, F., "Fully anisotropic goal-oriented mesh adaptation for 3D steady Euler equations," *Journal of Computational Physics*, Vol. 229, No. 8, 2010, pp. 2866–2897.

[2]Park, M. A. and Darmofal, D. L., "Validation of an output-adaptive, tetrahedral cut-cell method for sonic boom prediction," *AIAA Journal*, Vol. 48, No. 9, Sept. 2010, pp. 1928–1945.

[3]Campbell, R. L., Carter, M. B., Deere, K. A., and Waithe, K. A., "Efficient unstructured grid adaptation methods for sonic boom prediction," *26th AIAA Applied Aerodynamics Conference*, No. AIAA–2008–7327, Honolulu, Hawaii, Aug. 2008.

[4]Escobar, J. M., Rodríguez, E., Montenegro, R., Montero, G., and González-Yuste, J. M., "Simultaneous untangling and smoothing of tetrahedral meshes," *Computer Methods in Applied Mechanics and Engineering*, Vol. 192, No. 25, 2003, pp. 2775–2787.

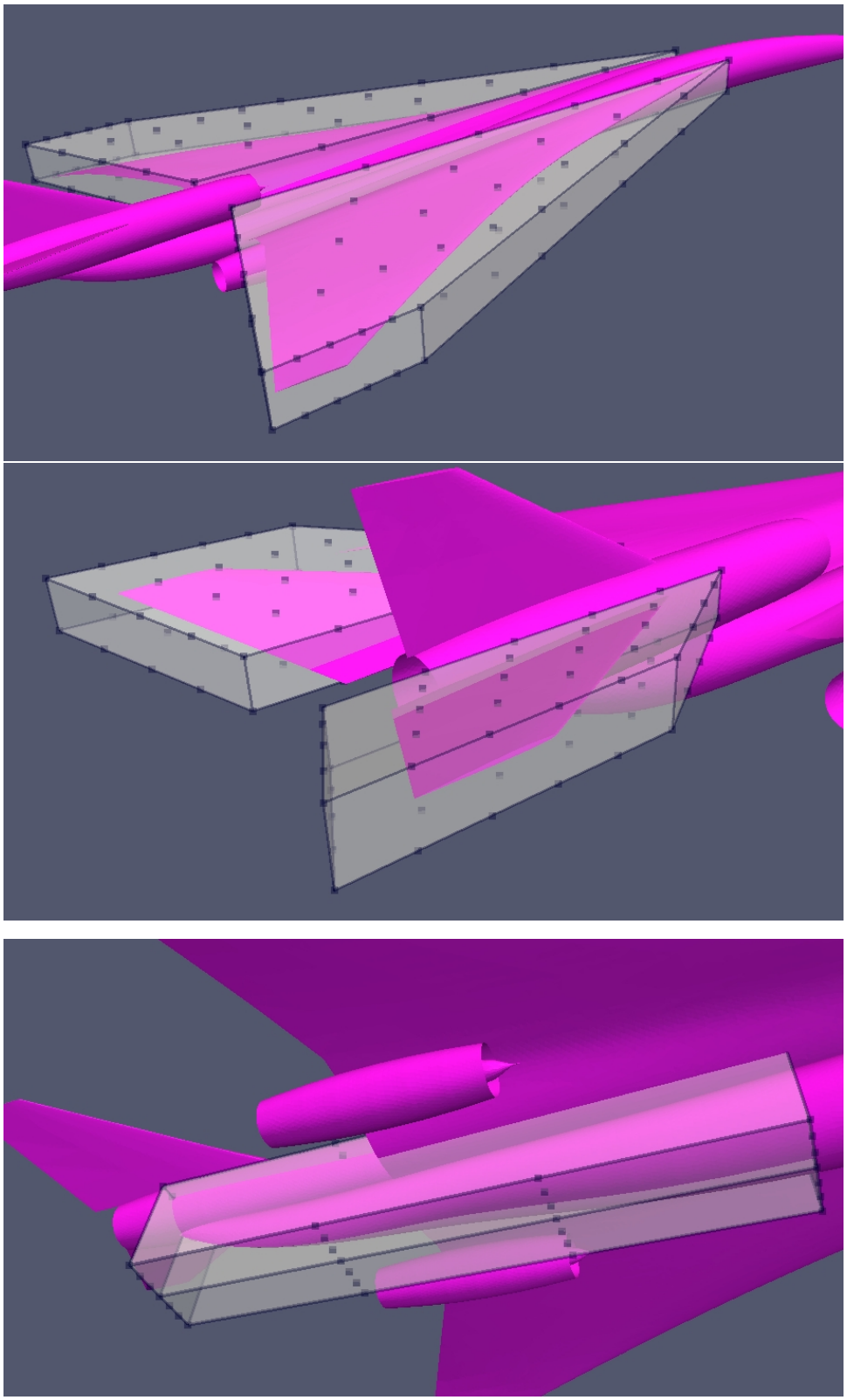

Figure 14. Free Form Deformation boxes used in the optimization process.

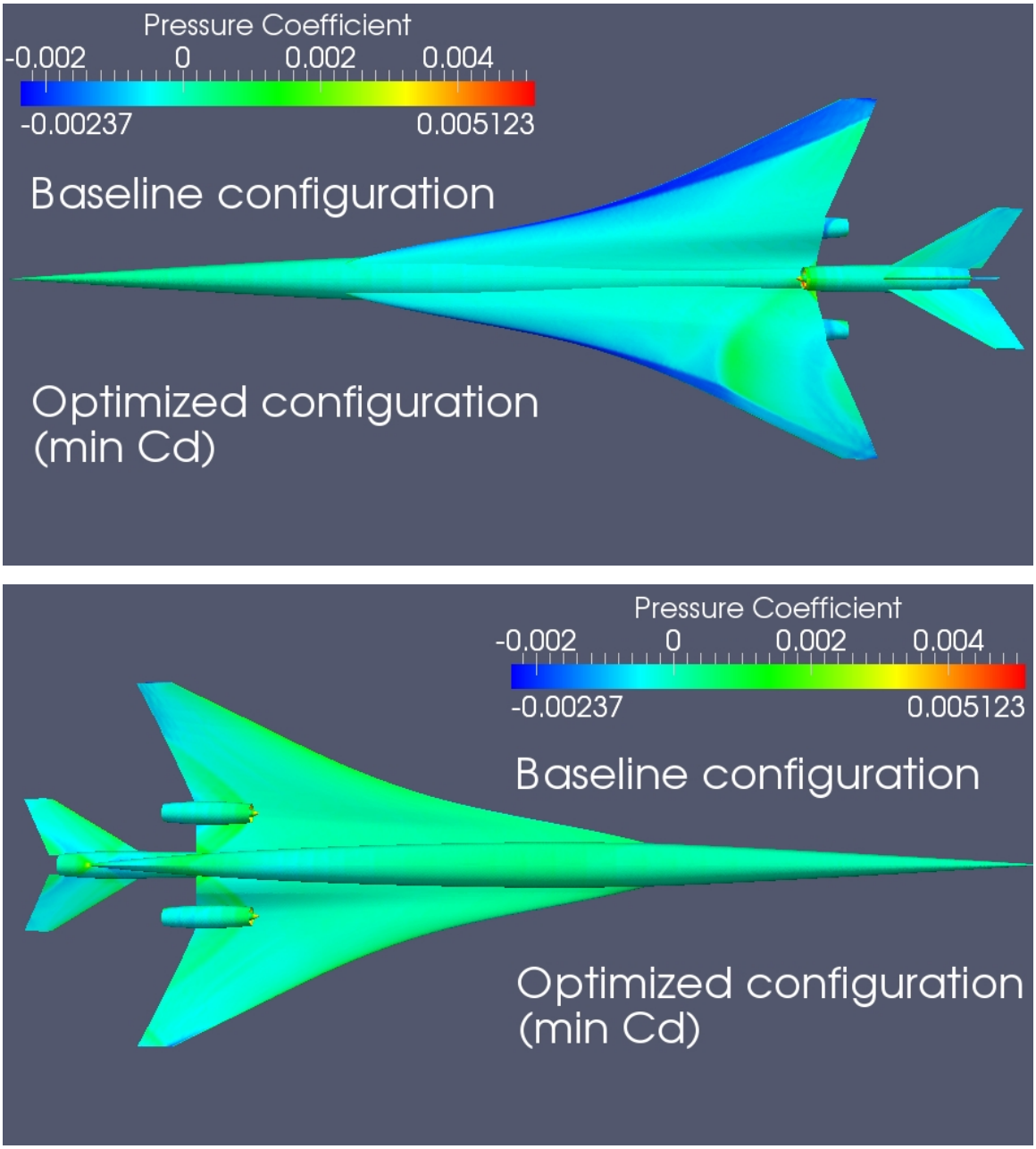

Figure 15. Shape design optimization (min Cd), upper and lower surfaces of the trijet.

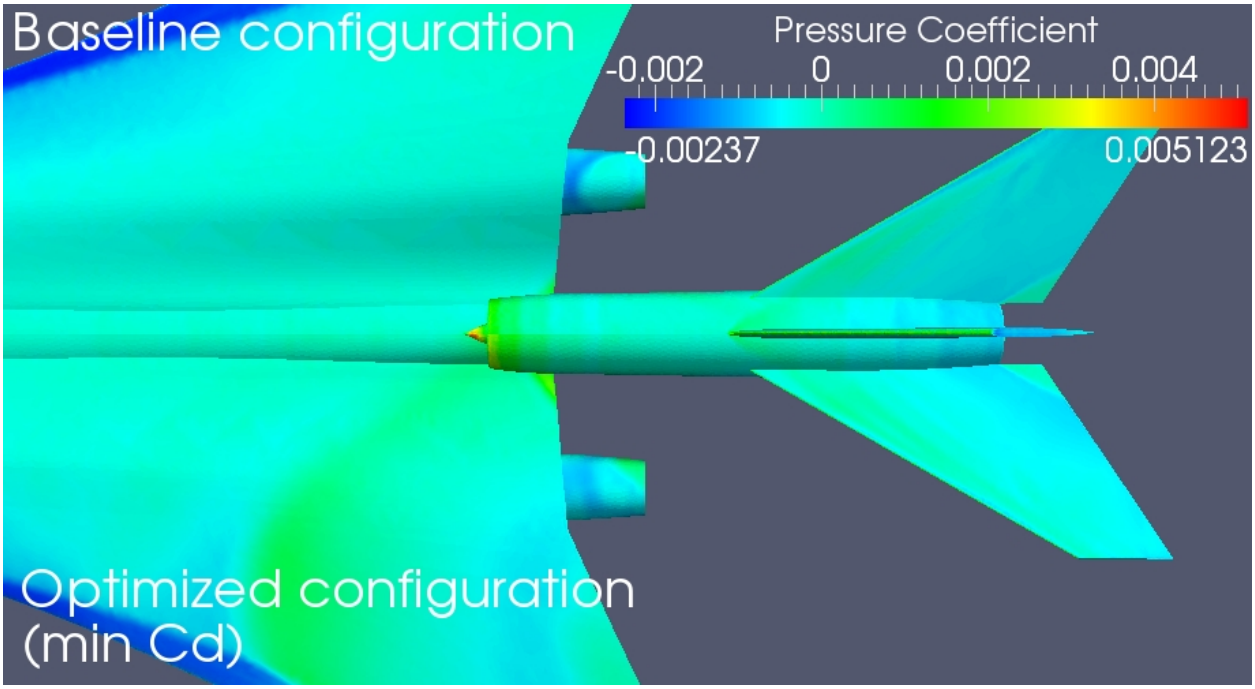

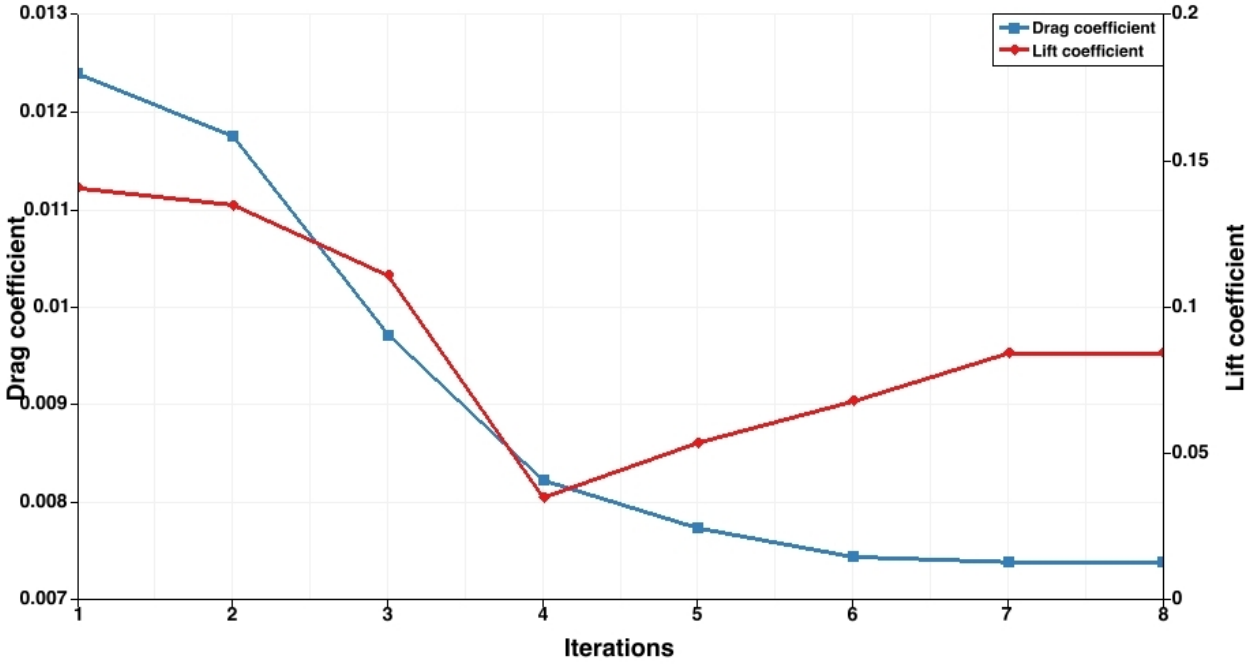

Figure 16. Detail of the shape design optimization (min Cd), and evolution of the optimization (right)

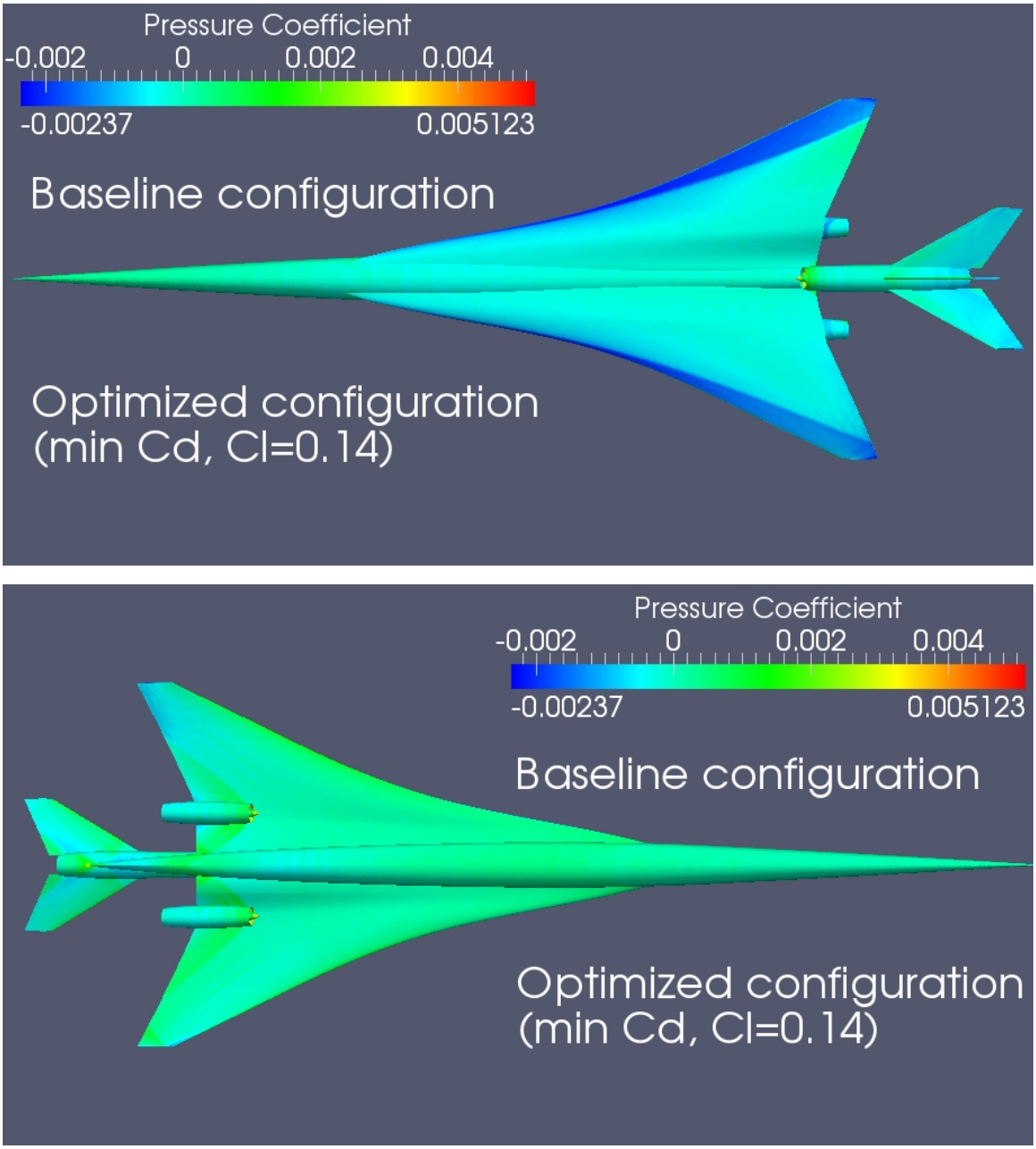

Figure 17. Shape design optimization (min Cd, Cl=0.14), upper and lower surfaces of the trijet.

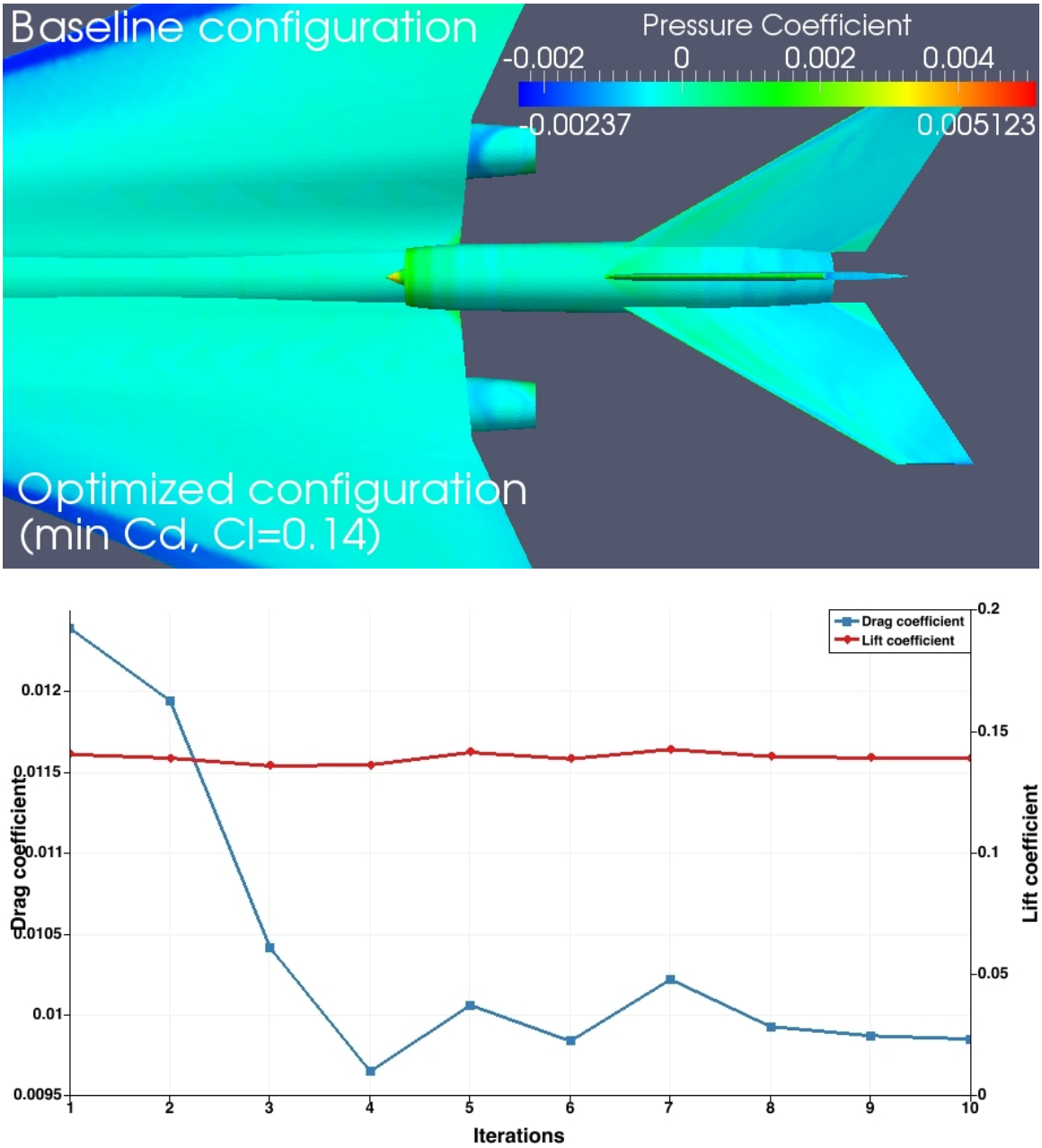

Figure 18. Detail of the shape design optimization (min Cd, Cl=0.14), and evolution of the optimization (right)

Appendix D.—Acronym List

Acronym	Definition
AIAA	American Institute of Aeronautics and Astronautics
AAPL	Aero-acoustic Propulsion Laboratory
ALR	Aft Lift Relaxation
ANSI	American National Standards Institute
AoA	Angle of Attack
ARMD	Aeronautics Research Mission Directorate
BFL	Balanced Field Length
BPR	Bypass Ratio
CAD	Computer Aided Design
CATIA	Computer-Aided Three-Dimensional Interactive Application
CFD	Computational Fluid Dynamics
CG	Center of Gravity
DOE	Design of Experiments
EINOx	Emission Index for NOx
EIS	Entry Into Service
EoC	End of Cruise
EPNL	Effective Perceived Noise Level
FAA	Federal Aviation Administration
FAR	Fuel/Air Ratio
GE	General Electric
GRC	Global Research Center
GT	Georgia Tech
GTOW	Gross TakeOff Weight
IML	Inner Mold Line
IRAD	Independent Research and Development
LA	Linear Actuator
L/D	Lift to Drag Ratio
LM	Lockheed Martin
MDAO	Multi-disciplinary Analysis and Optimization
MSA	Model Support Apparatus
MTOW	Max Takeoff Weight
NASA	National Aeronautics Space Administration
NATR	Nozzle Aeroacoustics Test Rig
NLF	Natural Laminar Flow
NRA	NASA Research Announcement
OD	Outer Diameter
OptSig	Optimum Signature
OEI	One Engine Inoperative
OEW	Operational Empty Weight

OML	Outer Mold Line
OPR	Overall pressure ratio
POD	Point of Departure
PAX	Passenger
PL	Perceived Loudness
PLdB	Perceived Loudness DeciBels
PLR	Programmed Lapse Rate
PR	Pressure Ratio
QR	Quarterly Review
QSST	Quiet Small Supersonic Transport
RCD	Rapid Conceptual Design
RH	Relative Humidity
RMS	Root Mean Square
ROC	Rate Of Climb
RRLW	Rolls-Royce Liberty Works
SF	Scale Factor
SFC	Specific Fuel Consumption
SLS	Sea Level Static
SOA	State Of the Art
SoC	Start of Cruise
SST	Supersonic Transport
TC	Technology Configuration
TE	Trailing Edge
ToC	Top of Climb
TOFL	Takeoff Field Length
TOGW	Takeoff Gross Weight
TRL	Technology Readiness Level
WBS	Work Breakdown Structure

Appendix E.—Revision Status

Revision	Date	Comments
N/A	09/16/2011	Initial submission of the non-proprietary Final Report per Contract NNC10CA02C
Rev 1	1/31/2012	Updated Final Report to include LM3 97-0231 Wind Tunnel Test results per Contract NNC10CA02C

References

1. NASA Langley Research Center. A.4 Supersonics Project (SUP3). NSPIRES - NASA Research Opportunities Online. [Online] 2009. http://nspires.nasaprs.com/external/viewrepositorydocument/cmdocumentid = 161745/ROA-2008_Amend%207_Append_A_4.pdf.
2. Lockheed Martin Corporation. N+3 Supersonic Systems Studies Final Report. s.l.: NASA/CR—2010-216796, August 2010.
3. Stanford Final Report covering N+2 Phase I Supersonic Validations program
4. RRLW Final Report covering N+2 Phase I Supersonic Validations program
5. GE GR Final Report covering N+2 Phase I Supersonic Validations program
6. Darden, Christine. Sonic Boom Minimization with Nose Bluntness Relaxation. s.l.: NASA, 1979. NASA TP-1349.
7. Morgenstern, J.; "Optimum Signature Shaping for Low Sonic Boom," AIAA-2012-3218, 30th Applied Aerodynamics Conference, June 2012.
8. Lyman, Victor. Calculated and Measured Pressure Fields for an Aircraft Designed for Sonic-boom Alleviation. s.l.: AIAA-2004-4846, 2004.
9. Morgenstern, John. Wind Tunnel Testing of a Sonic Boom Minimized Tail-Braced Wing Transport Configuration. s.l.: AIAA-2004-4536, 2004.
10. Morgenstern, J.; "Distortion Correction for Low Sonic Boom Measurement in Wind Tunnels," AIAA-2012-3216, 30th Applied Aerodynamics Conference, June 2012.
11. Morgenstern, J.; "How to Accurately Measure Low Sonic Boom in Supersonic Wind Tunnels," AIAA-2012-3215, 30th Applied Aerodynamics Conference, June 2012.
12. Morgenstern, J.; Buonanno M. and Norstrud, N.; "N+2 Low Boom Wind Tunnel Model Design and Validation," AIAA-2012-3217, 30th Applied Aerodynamics Conference, June 2012.
13. Lyman, Victor and Morgenstern, John, "Calculated and Measured Pressure Fields for an Aircraft Designed for Sonic-boom Alleviation." 22nd Applied Aerodynamics Conference, AIAA-2004-4846, 16-19 August 2004.
14. Morgenstern, John; "Wind Tunnel Testing of a Sonic Boom Minimized Tail-Braced Wing Transport Configuration." 10th AIAA-ISSMO Multidisciplinary Analysis and Optimization Conference, AIAA-2004-4536, Sept. 2004.

REPORT DOCUMENTATION PAGE	Form Approved OMB No. 0704-0188

1. REPORT DATE *(DD-MM-YYYY)*	2. REPORT TYPE	3. DATES COVERED *(From - To)*
01-02-2013	Final Contractor Report	

4. TITLE AND SUBTITLE
Advanced Concept Studies for Supersonic Commercial Transports Entering Service in the 2018 to 2020 Period
Phase I Final Report

5a. CONTRACT NUMBER
NNC10CA02C

5b. GRANT NUMBER

5c. PROGRAM ELEMENT NUMBER

6. AUTHOR(S)
Morgenstern, John; Norstrud, Nicole; Sokhey, Jack; Martens, Steve; Alonso, Juan, J.

5d. PROJECT NUMBER

5e. TASK NUMBER

5f. WORK UNIT NUMBER
WBS 475122.02.03.01.02

7. PERFORMING ORGANIZATION NAME(S) AND ADDRESS(ES)
Lockheed Martin Corporation
Palmdale, California 93599

8. PERFORMING ORGANIZATION REPORT NUMBER
E-18569

9. SPONSORING/MONITORING AGENCY NAME(S) AND ADDRESS(ES)
National Aeronautics and Space Administration
Washington, DC 20546-0001

10. SPONSORING/MONITOR'S ACRONYM(S)
NASA

11. SPONSORING/MONITORING REPORT NUMBER
NASA/CR-2013-217820

12. DISTRIBUTION/AVAILABILITY STATEMENT
Unclassified-Unlimited
Subject Categories: 05 and 07
Available electronically at http://www.sti.nasa.gov
This publication is available from the NASA Center for AeroSpace Information, 443-757-5802

13. SUPPLEMENTARY NOTES

14. ABSTRACT
Lockheed Martin Aeronautics Company (LM), working in conjunction with General Electric Global Research (GE GR), Rolls-Royce Liberty Works (RRLW), and Stanford University, herein presents results from the "N+2 Supersonic Validations" contract's initial 22 month phase, addressing the NASA solicitation "Advanced Concept Studies for Supersonic Commercial Transports Entering Service in the 2018 to 2020 Period." This report version adds documentation of an additional three month low boom test task. The key technical objective of this effort was to validate integrated airframe and propulsion technologies and design methodologies. These capabilities aspired to produce a viable supersonic vehicle design with environmental and performance characteristics. Supersonic testing of both airframe and propulsion technologies (including LM3: 97-023 low boom testing and April-June nozzle acoustic testing) verified LM's supersonic low-boom design methodologies and both GE and RRLW's nozzle technologies for future implementation. The N+2 program is aligned with NASA's Supersonic Project and is focused on providing system-level solutions capable of overcoming the environmental and performance/efficiency barriers to practical supersonic flight. NASA proposed "Initial Environmental Targets and Performance Goals for Future Supersonic Civil Aircraft". The LM N+2 studies are built upon LM's prior N+3 100 passenger design studies. The LM N+2 program addresses low boom design and methodology validations with wind tunnel testing, performance and efficiency goals with system level analysis, and low noise validations with two nozzle (GE and RRLW) acoustic tests.

15. SUBJECT TERMS
Aircraft configuration; Aircraft descriptions; Aircraft design; Aircraft development; Aircraft evaluation; Aircraft flight tests; Aircraft performance; Aircraft simulation; Aircraft structures; Aircraft testing

16. SECURITY CLASSIFICATION OF:			17. LIMITATION OF ABSTRACT	18. NUMBER OF PAGES	19a. NAME OF RESPONSIBLE PERSON
a. REPORT	b. ABSTRACT	c. THIS PAGE			STI Help Desk (email:help@sti.nasa.gov)
U	U	U	UU	308	19b. TELEPHONE NUMBER *(include area code)* 443-757-5802